②

AFWAL-TR-88-4229

DYNAMIC CONSTITUTIVE/FAILURE MODELS

A. M. Rajendran and
T. Nicholas, Eds.

University of Dayton
Research Institute
300 College Park Avenue
Dayton OH 45469

December 1988

Final Report for Period 10 May 1988 - 11 May 1988

DTIC
SELECTED
21 FEB 1989
E

MATERIALS LABORATORY
AIR FORCE WRIGHT AERONAUTICAL LABORATORIES
AIR FORCE SYSTEMS COMMAND
WRIGHT-PATTERSON AIR FORCE BASE, OHIO 45433-6533

89    2    21    096

# NOTICE

WHEN GOVERNMENT DRAWINGS, SPECIFICATIONS, OR OTHER DATA ARE USED FOR ANY PURPOSE OTHER THAN IN CONNECTION WITH A DEFINITELY GOVERNMENT-RELATED PROCUREMENT, THE UNITED STATES GOVERNMENT INCURS NO RESPONSIBILITY OR ANY OBLIGATION WHATSOEVER. THE FACT THAT THE GOVERNMENT MAY HAVE FORMULATED OR IN ANY WAY SUPPLIED THE SAID DRAWINGS, SPECIFICATIONS, OR OTHER DATA, IS NOT TO BE REGARDED BY IMPLICATION, OR OTHERWISE IN ANY MANNER CONSTRUED, AS LICENSING THE HOLDER, OR ANY OTHER PERSON OR CORPORATION; OR AS CONVEYING ANY RIGHTS OR PERMISSION TO MANUFACTURE, USE, OR SELL ANY PATENTED INVENTION THAT MAY IN ANY WAY BE RELATED THERETO.

THIS REPORT HAS BEEN REVIEWED BY THE OFFICE OF PUBLIC AFFAIRS (ASD/CPA) AND IS RELEASABLE TO THE NATIONAL TECHNICAL INFORMATION SERVICE (NTIS). AT NTIS, IT WILL BE AVAILABLE TO THE GENERAL PUBLIC, INCLUDING FOREIGN NATIONS.

THIS TECHNICAL REPORT HAS BEEN REVIEWED AND IS APPROVED FOR PUBLICATION.

THEODORE NICHOLAS
Project Engineer
Metals and Behavior Branch

ALLAN W. GUNDERSON
Technical Manager
Metals and Behavior Branch

FOR THE COMMANDER

JOHN P. HENDERSON, Chief
Metals and Behavior Branch

IF YOUR ADDRESS HAS CHANGED, IF YOU WISH TO BE REMOVED FROM OUR MAILING LIST, OR IF THE ADDRESSEE IS NO LONGER EMPLOYED BY YOUR ORGANIZATION PLEASE NOTIFY AFWAL/MLLN, WRIGHT-PATTERSON AFB, OH 45433- 6533 TO HELP US MAINTAIN A CURRENT MAILING LIST.

COPIES OF THIS REPORT SHOULD NOT BE RETURNED UNLESS RETURN IS REQUIRED BY SECURITY CONSIDERATIONS, CONTRACTUAL OBLIGATIONS, OR NOTICE ON A SPECIFIC DOCUMENT.

# REPORT DOCUMENTATION PAGE

Form Approved
OMB No. 0704-0188

| 1a. REPORT SECURITY CLASSIFICATION | 1b. RESTRICTIVE MARKINGS |
|---|---|
| Unclassified | |

| 2a. SECURITY CLASSIFICATION AUTHORITY | 3. DISTRIBUTION/AVAILABILITY OF REPORT |
|---|---|
| | Approved for public release; |
| 2b. DECLASSIFICATION/DOWNGRADING SCHEDULE | distribution unlimited |

| 4. PERFORMING ORGANIZATION REPORT NUMBER(S) | 5. MONITORING ORGANIZATION REPORT NUMBER(S) |
|---|---|
| UDR-TR-88-110 | AFWAL-TR-88-4229 |

| 6a. NAME OF PERFORMING ORGANIZATION | 6b. OFFICE SYMBOL (If applicable) | 7a. NAME OF MONITORING ORGANIZATION |
|---|---|---|
| University of Dayton Research Institute | | Air Force Wright Aeronautical Laboratories Materials Lab (AFWAL/MLLN) |

| 6c. ADDRESS (City, State, and ZIP Code) | 7b. ADDRESS (City, State, and ZIP Code) |
|---|---|
| 300 College Park Avenue Dayton, Ohio 45469 | Wright-Patterson Air Force Base Ohio 45433-6533 |

| 8a. NAME OF FUNDING/SPONSORING ORGANIZATION | 8b. OFFICE SYMBOL (If applicable) | 9. PROCUREMENT INSTRUMENT IDENTIFICATION NUMBER |
|---|---|---|
| Air Force Wright Aeronautical Laboratories, Materials Lab. | AFWAL/MLLN | F33615-86-C-5064 |

| 8c. ADDRESS (City, State, and ZIP Code) | 10. SOURCE OF FUNDING NUMBERS | | | |
|---|---|---|---|---|
| Wright-Patterson Air Force Base Ohio 45433-6533 | PROGRAM ELEMENT NO. | PROJECT NO. | TASK NO. | WORK UNIT ACCESSION NO. |
| | 62102F | 2418 | 04 | 50 |

11. TITLE (Include Security Classification)

Dynamic Constitutive/Failure Models

12. PERSONAL AUTHOR(S)
A. M. Rajendran and T. Nicholas, Eds.

| 13a. TYPE OF REPORT | 13b. TIME COVERED | 14. DATE OF REPORT (Year, Month, Day) | 15. PAGE COUNT |
|---|---|---|---|
| Final | FROM 5/10/88 TO 5/11/88 | December 1988 | 494 |

16. SUPPLEMENTARY NOTATION

| 17. COSATI CODES | | | 18. SUBJECT TERMS (Continue on reverse if necessary and identify by block number) |
|---|---|---|---|
| FIELD | GROUP | SUB-GROUP | Impact, High Strain Rate, Spall, Composite, Concrete, Metals, Failure, Plastic Flow, Brittle, Computer Codes |
| 20 | 11 | | |
| 20 | 14 | | |

19. ABSTRACT (Continue on reverse if necessary and identify by block number)

The objective of this report is to identify and explore solutions to critical issues in modeling material behavior under high loading rates for use in computer codes. The report will bring together a critical mass of active presentors involved in various aspects of modeling the response of nonreactive materials to high strain rate loading. Attention will be focused on issues that require interactions between experimentalists, material scientists, applied mechanicians and model builders, and developers of advanced computer codes.

| 20. DISTRIBUTION/AVAILABILITY OF ABSTRACT | 21. ABSTRACT SECURITY CLASSIFICATION |
|---|---|
| ☑ UNCLASSIFIED/UNLIMITED ☐ SAME AS RPT. ☐ DTIC USERS | Unclassified |

| 22a. NAME OF RESPONSIBLE INDIVIDUAL | 22b. TELEPHONE (Include Area Code) | 22c. OFFICE SYMBOL |
|---|---|---|
| Theodore Nicholas | (513) 255-1347 | AFWAL/MLLN |

DD Form 1473, JUN 86    Previous editions are obsolete

# FOREWORD

The work described in this report represents the results of a workshop conducted by the University of Dayton Research Institute under Contract No. F33615-86-C-5064. The contract was administered under the direction of Dr Theodore Nicholas (AFWAL/MLLN). This report contains the papers presented at the Workshop on **DYNAMIC CONSTITUTIVE/FAILURE MODELS** which was held at the *Bergamo Conference Center* of the University of Dayton, Dayton, OH, on 10 and 11 May, 1988. The proceedings were edited by Dr Nicholas of the Air Force Materials Laboratory and Dr A.M. Rajendran, the principal investigator on the contract for the University of Dayton.

The symposium was supported with funds provided by the Air Force Armament Laboratory, Eglin AFB, FL, the Army Research Office, Durham, NC and the Army Materials Technology Laboratory, Watertown, MA. The support of Dr Tony Chu of AMTL, Dr Yuki Horie of ARO, and Mr William Cook of AFATL in organizing the workshop is gratefully acknowledged. A special word of appreciation is extended to Ms JoAnn Jones for her tireless efforts in organizing and administering the many details of the workshop. Thanks are also extended to all of the speakers and participants without whom this workshop could not have been successful.

| Accession For | | |
|---|---|---|
| NTIS GRA&I | ☒ | |
| DTIC TAB | ☐ | |
| Unannounced | ☐ | |
| Justification | | |
| By | | |
| Distribution/ | | |
| Availability Codes | | |
| Dist | Avail and/or Special | |
| A-1 | | |

DTIC COPY INSPECTED 1

iii

# TABLE OF CONTENTS

# INTRODUCTION

Many important impact engineering applications rely on numerical simulations using finite element/difference computer codes for analysis. Several unique codes have been developed in recent years incorporating novel concepts such as slide line logics, erosion, rezoning, dezoning, etc. The modeling of material behavior in computer codes, while achieving improved sophistication in recent years, still lags behind our present knowledge of dynamic behavior and failure. Accurate descriptions of the dynamic inelastic behavior of materials for metals, ceramics, and composites in computer codes must include the effects of strain rate, loading history, high pressure, high temperature, large deformation, and internal damage.

An ideal model for a computer code must satisfy several requirements. First, it must accurately represent the physical processes. Second, the model must be mathematically tractable and easily incorporated into the styructure of existing codes. Third, it must be easy to calibrate the model, i.e., obtain the material model constants, in a simple manner from a limited set of experimental data. These require the input and coordination of material scientists, experimentalists, and applied mechanicians. Successful progress in this area will require careful attention to each of the areas and application of the latest advances in the state of the art in each area.

A workshop on **Dynamic Constitutive/Failure Models for Use in Computer Codes** was held at University of Dayton on May 10-11, 1988. The objective of the workshop was to identify and explore solutions to critical issues in modeling material behavior under high loading rates for use in computer codes. The workshop brought together a critical mass of active researchers involved in various aspects of modeling the response of non-reactive materials to high strain rate loading. The workshop focused on three main issues in material modeling for computer codes: determination of material parameters from impact experiments, computational effectiveness of constitutive and failure models, and developments in material modeling as related to the the physical processes involved in deformation and failure.

The workshop was organized into four sessions: Material Behavior, Dynamic Failure Modeling, Brittle Materials and Composites, and Numerical Simulations. The papers covering the work presented at the workshop are contained in this report. The author presenting the work is highlighted in bold in the Table of Contents.

# SECTION I

# MATERIAL BEHAVIOR

# RECENT RESULTS AND CONTINUED DEVELOPMENT OF THE MTS MODEL

Paul S. Follansbee
Los Alamos National Laboratory
Los Alamos, NM 87545

## ABSTRACT

A review is given of the development of the Mechanical Threshold Stress (MTS) Model as a description of deformation in metals, particularly at high strain rates. The model is based on the use of internal state variables to represent the current structure or state of the material. Equations are written for the variation of the yield stress with strain rate and temperature and for the evolution of the state variables with strain, strain rate and temperature. The deformation behavior of several metals has been analyzed using this approach, and the results of these investigations are summarized. Ongoing research to extend the model to include the effects of deformation twinning and multiple strengthening mechanisms is described

## INTRODUCTION

The variation of material strength with the applied strain rate is an important consideration in the design of hardware for impact loading. The magnitude of the flow stress at a given strain rate $\dot{\varepsilon}$, strain $\varepsilon$, and temperature T, as well as the strain-rate sensitivity m, where

2

$$m = \frac{\partial \log \sigma}{\partial \log \dot{\epsilon}} \tag{1}$$

influence the response to impact loading. The strength determines the resistance to plastic flow at any instant. The strain-rate sensitivity affects the resistance to instability, as does the temperature dependence of the flow stress and the work hardening rate. The requirement for accurate descriptions of the magnitude of the flow stress, the strain-rate sensitivity, and the temperature dependence of the flow stress, and the need for these "constitutive relations" over a wide range of strains, strain rates, and temperatures is a serious challenge to the materials scientist.

Many previous investigators have noted that the flow stress increases rapidly when the strain rate is raised above roughly 1000 s$^{-1}$. Generally this behavior is observed in a plot of flow stress at some constant strain level as a function of strain rate. In mild steel, however, this increased strain-rate sensitivity is found in a plot of the <u>yield stress</u> versus strain rate. The data in the high strain rate regime has often been shown to be described by an equation of the form

$$\sigma = \sigma_b(\epsilon) + \beta\dot{\epsilon} , \tag{2}$$

where the constant $\beta$ may or not be a function of strain. Measurements in copper, for instance, show that over the strain rate regime of $10^3$ to $10^4$ s$^{-1}$ and for a strain of $\epsilon=0.15$, the constant $\beta$ equals 0.00312 MPa·s and $\sigma_b$ equals 248 MPa [1]. Experiments at strain rates higher than $10^4$ s$^{-1}$ are difficult to perform; to estimate strength levels at higher strain rates a common approach has been to extrapolate Eq. (2) beyond the regime over which it has been fit. This practice, however, must be exercized with caution. In copper, for

3

example, the flow stress predicted at $\dot{\varepsilon} = 10^5$ s$^{-1}$ is 560 MPa which is roughly twice that measured at $\dot{\varepsilon} = 10^4$ s$^{-1}$, and at $\dot{\varepsilon} = 10^6$ s$^{-1}$ the estimated flow stress is 3368 MPa!

In addition to the rapid increase in the flow stress predicted by Eq. (2), the strain-rate sensitivity also is predicted to increase dramatically. In fact, the strain-rate sensitivity for a material obeying such a law is

$$m = \frac{\beta \dot{\varepsilon}}{\sigma_b + \beta \dot{\varepsilon}} \qquad (3)$$

which indicates that the strain-rate sensitivity approaches unity at very high strain rates, whereas for most materials it is on the order of 1/30 at quasi-static strain rates.

Thus, Eq. (2) predicts that the flow stress as well as the strain-rate sensitivity rise dramatically at strain rates in the impact regime. This calls attention to the generality of Eq. (2) as a description of material behavior at very high strain rates.

In support of Eq. (2), several investigators have argued that at these high strain rates deformation becomes controlled by dislocation drag forces which lead to the high strain rate sensitivity predicted by Eq. (1). Following previous investigators [2,3], Follansbee et al [4] and Regazzoni et al [5] showed that conditions for drag control were not satisfied by the copper test results and that Eq. (2) was an inappropriate description. Subsequently, Follansbee and Kocks [6] analyzed copper data through the use of an internal state variable model based on the previous work of Kocks [7] and Mecking and

4

Kocks [8]. The purpose of this paper is to review key features of the model, termed the Mechanical Threshold Stress (MTS) model, and to provide a status on its continued development and extension to other materials. In the next section the MTS model will be reviewed. The measurements required to establish the model parameters are then described, and a summary of the results on copper is presented. Measurements on a low carbon steel, which appear to be well described by Eq. (2) are reanalyzed, and it is shown that an alternate interpretation is possible. Ongoing work to extend the model to other crystal structures and more complicated engineering materials is reviewed in the final section.

THE MTS MODEL

Deformation is assumed to be controlled by the kinetics of the thermally activated interactions between dislocations and obstacles. Generally at any instant, or for any given microstructural condition,

$$\frac{\sigma}{\mu} = \frac{\sigma_a}{\mu} + \sum_{i=1}^{n} s_i(\dot{\varepsilon},T) \frac{\hat{\sigma}_i}{\mu} \tag{4}$$

where $\sigma$ is the applied stress, $\sigma_a$ is an athermal stress, $\mu$ is the temperature dependent shear modulus, $\hat{\sigma}$ is the mechanical threshold stress characterizing the stress that is required in the absence of any contribution from thermal activation energy to overcome obstacle "i", and s characterizes the ratio of the applied stress (minus any athermal stress) to the mechanical threshold stress at temperatures above absolute zero. In writing Eq. (4) it has tacitly been assumed that the contributions from individual obstacles are linearly additive. This is an approximation which is often made but which lacks

5

fundamental basis (except in a few specific cases). One of the goals of our current work is to investigate the regimes of applicability of this equation. As defined above, $\hat{\sigma}_i$ represents an internal state variable which characterizes the strength, as well as the density, of obstacle "i". The ratio of the applied stress (at a given temperature and strain rate) to the mechanical threshold stress is given by s, which, when deformation is thermally activated, can be written as

$$
s_i = \left\{ 1 - \left[ \frac{kT}{g_{0i}\mu b^3} \log \frac{\dot{\varepsilon}_{oi}}{\dot{\varepsilon}} \right]^{1/q_i} \right\}^{1/p_i} \quad , \tag{5}
$$

where $g_{oi}$ is the normalized total activation energy, k is the Boltzmann constant, b is the burgers vector, and $\dot{\varepsilon}_{oi}$, $q_i$, and $p_i$ are constants. When dislocation drag effects become important, Eq. (5) must be modified; the procedure to do this has been outlined previously [9].

During strain hardening, the density of defects (primarily dislocations) increases, which leads to an evolution of $\hat{\sigma}_D$ with strain. Hardening can be described with a differential evolution equation of the form

$$
\theta = \frac{d\hat{\sigma}_D}{d\varepsilon} = \theta_0 \left[ 1 - F \left( \frac{\hat{\sigma}_D}{\hat{\sigma}_{Ds}(\dot{\varepsilon}, T)} \right) \right] \quad , \tag{6}
$$

where $\theta_0$ is (usually) a constant on the order of $\mu/20$, F is a function (F=1 implies a Voce law), and $\hat{\sigma}_{Ds}$ is the saturation stress. Note that evolution is also a strain rate and temperature dependent process, with different kinetics than described by Eq. (5). Equation (6) implies a temperature and strain-rate dependent limit to the mechanical threshold stress characterizing dislocation/dislocation interactions. One equation used to describe $\hat{\sigma}_{Ds}(\dot{\varepsilon}, T)$

6

in FCC metals is

$$\log\left(\frac{\dot{\epsilon}}{\dot{\epsilon}_{Ds}}\right) = \frac{A}{kT} \log\left(\frac{\hat{\sigma}_{Ds}}{\hat{\sigma}_{Dso}}\right) \tag{7}$$

where $\dot{\epsilon}_{Ds}$, A, and $\hat{\sigma}_{Dso}$ are constants. In FCC metals, A and $\dot{\epsilon}_{Ds}$ scale with the stacking fault energy [10]. The constant A increases with an increase in $\gamma_{SFE}$, and, in fact, in very high $\gamma_{SFE}$ materials, such as aluminum and pure BCC metals, the strain-rate and temperature dependence of $\hat{\sigma}_{DS}$ becomes negligible.

In copper, measurements [6] have indicated that $\theta_o$ is a weak function of strain rate at low strain rates, but that at strain rates greater than ~10$^3$ s$^{-1}$ $\theta_o$ increases linearly with strain rate. The source of this effect is thought to be the initial high stresses (and, thus, the initial high dislocation generation rate) required to accommodate the high strain rates at yield in a relatively dislocation free material [9]. The generality of this behavior is not yet known.

The MTS model is essentially described by Eqs. (4) through (7), although a few of the details, such as the $\theta_o(\dot{\epsilon})$ dependence and the definition of the function F in Eq. (6), are described elsewhere [6]. Although there appear to be a sufficient number of adjustable constants in these equations to fit any test data, it is important to emphasize that most of these parameters have well-defined limits. Some of these limits have already been discussed. The constants p and q in Eq. (5) are restricted to $0 < p \leq 1$ and $1 \leq q \leq 2$ [11]; generally, we have found that p~2/3 and q~1 work well for dislocation/dislocation interactions whereas p~1 and q~2 work well for dislocation/solute atom and dislocation/interstitial atom interactions. The constant $\dot{\epsilon}_o$ in Eq.

7

(5) also is restricted to $10^7 \leq \dot{\varepsilon}_o \leq 10^{10}$ s$^{-1}$ and because this constant is inside a logarithmic term, it is not necessary to determine a precise value. The athermal stress $\sigma_a$ in Eq. (4) is used to incorporate any long-range obstacle, such as a grain boundary or large dispersoid, into the analysis. It is the yield stress in well annealed pure FCC metals, and in copper was estimated as 40 MPa [6]. In FCC alloys, or in BCC metals, $\sigma_a$ is more difficult to measure; thus, in non dispersion strengthened materials, we always choose a small number within the range of 40 to 100 MPa, depending on the grain size.

The normalized total activation energy $g_o$ is an important parameter, but it too is constrained within well defined limits. For dislocation/dislocation interactions, we have found $g_o \sim 1$, whereas for short-range interactions, such as dislocation/solute atom or dislocation/interstitial atom interactions $g_o \sim 0.1$. (In Eq. (5) $g_o$ is dimensionless because $\mu b^3$ has been factored out. Multiplying $g_o$ by $\mu b^3$ gives $g_o$ in the units of energy.) The point is that there are no free or floating constants in the MTS model; all of the parameters are constrained by the physical mechanisms that Eq. (4) through (7) attempt to describe.

FITTING THE MTS MODEL TO DATA

Because the model is based on the evolution of internal state variables, experimental methods are required to measure these variables as well as to evaluate Eq. (5) under conditions where these variables are constant. This implies that it is insufficient to simply use monotonic stress-strain curves measured over a wide range of temperature and strain rates. Ideally, one would use in situ temperature and strain rate change tests, but these tests are difficult under high strain rate conditions of particular interest to our

8

studies. We are therefore forced to use prestrain and reloading operations, separated by an unloading step. The prestrain temperature, strain, and strain rate are chosen to yield a systematic variation in the value of the state variable(s), which will then be probed through reload tests at various strain rates and temperatures. The reload tests are used to evaluate Eq. (4) and (5) and only the <u>yield stress</u> as a function of reload test temperature and strain rate is of interest. This implies that several identical samples are required for a single evaluation of Eqs. (4) and (5). Variations in prestrain conditions are used to generate the data required for fitting to Eqs. (6) and (7). If wide variations in prestrain strain, strain rate and temperature are of interest, then the test matrix can be large. The copper results described in Ref. [6], for instance, cover prestrain strain rates from $10^{-4}$ to $10^4$ s$^{-1}$, strains to 1, and only room temperature deformaticn, and the results in this paper represent ~600 separate compression tests. Thus a significant disadvantage of the modeling procedure adopted in the MTS model is the required data base. Fortunately as experience with more and more materials is gained, the required size of this data base is decreasing.

APPLICATION OF THE MODEL

In copper one interesting result found by fitting the MTS model to the extensive data set described above was that the strain-rate sensitivity of strain hardening (Eq. (7)) exceeded the strain-rate sensitivity at constant structure (found from Eqs. (4) and (5)). Furthermore, the strain hardening rate increased abruptly at high strain rates which leads to the "increased" strain-rate sensitivity observed in a plot of applied stress at constant strain versus strain rate plotted on a logarithmic scale (figure 1). This implies that constant strain is not a good basic of comparison for flow stress

measurements obtained over a wide range of strain rates in copper. When flow stress values at constant mechanical threshold stress are plotted on the axes of figure 1, there is no increase observed in the strain-rate sensitivity at high strain rates and the strain-rate sensitivity decreases. To further illustrate this strain-rate history effect, figure 2 shows stress-strain curves for two annealed copper specimens, one loaded (prestrained) to a strain of $\varepsilon=0.15$ at a strain rate of $\dot\varepsilon=10^4$ s$^{-1}$ and the other prestrained to $\varepsilon=0.15$ at $\dot\varepsilon=1.4\times10^{-4}$ s$^{-1}$. Each of these specimens was reloaded at 295K and $\dot\varepsilon=10^{-3}$ s$^{-1}$; the reload stress-strain curves are also shown in figure 2. Although valid questions have been raised about the accuracy of dynamic stress-strain measurements, the quasi-static reload stress-strain curves can be measured with precision. Note that the reload yield stress for the specimen prestrained at $\dot\varepsilon=10^4$ s$^{-1}$ exceeds that of the specimen prestrained at the lower strain rate by 33%. The conclusion is that the dynamically prestrained specimen has hardened more than the quasi-statically prestrained specimen. In figure 3, these results are combined with measurements at prestrain strain rates between $\dot\varepsilon=10^{-4}$ s$^{-1}$ and $\dot\varepsilon=10^4$ s$^{-1}$ and are plotted on semi-logarithmic coordinates. It is evident that the strain-rate dependent hardening becomes more important when the strain rate is raised above $10^3$ s$^{-1}$. Thus, the dramatically increased strain-rate sensitivity seen in the flow stress (at $\varepsilon=0.15$) measurements in figure 1 is a result of the enhanced hardening that has occurred, rather than of any change in deformation mechanism.

The MTS formalism is capable of distinguishing between the strain-rate sensitivity at constant structure and that of strain hardening. Furthermore, the increased strain-rate sensitivity has been identified as arising from the strain hardening term, and this effect is more naturally described using the MTS formalism than using Fq. (2). To illustrate this latter point, figure 4

shows isothermal stress-strain curves at strain rates from $10^{-4}$ s$^{-1}$ to $10^6$ s$^{-1}$. The predictions at strain rates of $10^5$ s$^{-1}$ and $10^6$ s$^{-1}$ represent extrapolations of the model, which has been fit to measurements at strain rates up to $10^4$ s$^{-1}$. Note that the shape of the curves is found to change dramatically; at the highest strain rate, the initial strain hardening is high and the saturation stress (described by Eq. (7)) is reached rapidly. Thus, the stress-strain curves approach elastic, perfectly-viscoplastic behavior *at* very high strain rates. Figure 5 shows predicted stress-strain curves for adiabatic conditions for an initial temperature of 295K. Temperature is explicitly treated in the MTS model. To compute adiabatic stress-strain curves, one has only to calculate the temperature rise through a heat balance of the form

$$\Delta T = \frac{\psi}{\rho c_p} \int \sigma(\varepsilon) \, d\varepsilon \quad , \tag{8}$$

where $\rho$ is the density, $c_p$ the heat capacity, and the factor $\psi$ expresses the fraction of plastic work converted to heat $(0.85 < \psi < 0.95)$. Note that at a strain of 2 the flow stress at a strain rate of $10^5$ s$^{-1}$ is predicted to be roughly equal to that at a strain rate of $10^6$ s$^{-1}$, although the temperature is higher at the higher strain rate (629 K versus 584 K at $10^5$ s$^{-1}$).

Temperature changes are an example of a history effect that the MTS model is capable of following, primarily because hardening (or softening) is modeled differentially. Strain rate changes offer a similar challenge to the modeling procedure. Table I lists the constant $\beta$ in Eq. (2) measured for copper over the strain-rate range of $10^3$ s$^{-1}$ to $10^4$ s$^{-1}$ for initially annealed material and for samples given a prestrain of 0.0513, 0.105, and 0.163 at a strain rate of $10^{-3}$ s$^{-1}$ followed by the dynamic loading. (We use Eq. (2) here only as a

11

convenient representation of roughly a hundred separate measurements.) Table
II lists the constant $\beta$ predicted using the MTS model described above. The
model **does not** predict exactly linear stress versus strain rate behavior, but
for comparison with the results in Table 1, a line (Eq. (2)) has been fit to
predictions of the model for monotonic dynamic loading, and for quasi-static
loading followed by dynamic loading, at strain rates from $10^3$ s$^{-1}$ to $10^4$ s$^{-1}$.
Since the model has not been fit to data from **prestrains** with strain rate

Table 1.   Summary of Measurements of Dynamic Flow Stress in Copper

| Dynamic Strain | $\beta$, $10^{-3}$ MPa·s, $(10^3$ s$^{-1} \leq \dot{\varepsilon} \leq 10^4$ s$^{-1})^*$ | | | |
| | Prestrain at $\dot{\varepsilon} = 0.001$ s$^{-1}$ | | | |
| | 0 | 0.513 | 0.105 | 0.163 |
| --- | --- | --- | --- | --- |
| 0.05 | 1.4 | 0.2 | 0.7 | 1.3 |
| 0.10 | 2.9 | 1.2 | 1.3 | 1.5 |
| 0.15 | 3.1 | 1.7 | 2.0 | 1.1 |
| 0.20 | 2.7 | 1.8 | 1.7 | 1.0 |

\* Standard deviation on estimate of $\beta \simeq 0.5 \times 10^{-3}$ MPa·s.

Table 2.   Summary of Predictions of Dynamic Flow Stress in Copper

| Dynamic Strain | $\beta$, $10^{-3}$ MPa·s, $(10^3$ s$^{-1} \leq \dot{\varepsilon} \leq 10^4$ s$^{-1})$ | | | |
| | Prestrain at $\dot{\varepsilon} = 0.001$ s$^{-1}$ | | | |
| | 0 | 0.513 | 0.105 | 0.163 |
| --- | --- | --- | --- | --- |
| 0.05 | 1.3 | 1.2 | 1.1 | 1.1 |
| 0.10 | 2.1 | 1.9 | 1.8 | 1.7 |
| 0.15 | 2.5 | 2.3 | 2.2 | 2.1 |
| 0.20 | 2.7 | 2.6 | 2.5 | 2.4 |

changes, this comparison actually represents a fairly demanding test of the modeling procedures. Yet, it is evident that the model captures many of the trends noted in the measurements.

THE CASE OF MILD STEEL

The results for copper, as well as for several other FCC metals, indicate that strain-rate history effects strongly influence the stress-strain behavior, which complicates comparisons of flow stress at constant strain. In mild steel, however, measurements of <u>yield stress</u> over a wide temperature and strain-rate range by Campbell and Ferguson [12] (figure 6) show a similar increased strain-rate sensitivity at high strain rates as found in measurements of the flow stress at constant strain in copper. As indicated earlier, measurements of the yield stress represent true constant structure measurements which are not complicated by history effects; thus, the observed behavior in mild steel has been interpreted as evidence of a transition in deformation mechanism in the high strain rate regime [13]. Plotting the measurements shown in figure 6 on coordinates suggested by Eq. (5), however, leads to a different interpretation of the data. Figure 7 shows this plot for $p=1/2$, $q=3/2$, $\tau_a=50$ MPa, and $\dot{\varepsilon}_o=10^7$ s$^{-1}$. Note that the measurements all fall roughly along the same curve, that the data at low temperatures and high strain rates are well represented by a straight line on these coordinates, and that the data at the lowest strain rates and highest temperatures show an approach to an athermal limit (or, perhaps, the contribution of dynamic strain aging). In the linear regime, the mechanical threshold stress is found to equal 536 MPa (in shear stress) and the normalized total activation energy is $g_o=0.087$. The conclusion is, therefore, that there is no transition within

13

the high strain rate regime and that the deformation within this regime is well-represented by standard thermal activation theory (and is not well-represented by Eq. (2)). This conclusion has a significant influence on the predicted strength levels at strain rates beyond the regime of the measurements.

STATUS OF THE CONTINUED DEVELOPMENT AND APPLICATION OF THE MTS MODEL

1. The Contribution of Deformation Twinning

The mild steel measurements illustrate one complication found in many materials. Equation (5) is valid only over a certain regime of temperature and strain rate. The tail at high temperatures shown in the data in figure 7 is not described by the same set of constants (or even by the same equation) that represent the linear regime. Measurements in AISI 1018 steel, shown in figure 8, indicate a similar tail at high temperatures as well as a flattening of the curve at the lowest temperatures and highest strain rates. This reduction in the temperature dependence and strain-rate dependence of the yield stress in iron [14] and iron base alloys at low temperatures has been observed previously and identified as indicating a significant contribution of deformation twinning [15]. Indeed, metallographic examination of the 1018 steel samples showed the presence of extensive twinning for samples deformed 10% at 77K and a strain rate of 5000 s⁻¹ (the data points with the lowest value on the abscissa) but only mild twinning when the deformation was carried out at a strain rate of $10^{-3}$ s⁻¹. Twinning is a deformation mechanism that is found in many materials, particularly low stacking fault energy FCC metals and in BCC metals where the high temperature and strain-rate sensitivity of the yield stress can lead to high stresses (exceeding the stress required to

14

nucleate and grow twins) at low temperatures or high strain rates. As illustrated by the 1018 steel data, deformation twinning can lead to deformation at stresses below those required for deformation solely by a slip mechanism. The stress level at which twinning predominates is also a sensitive function of grain size [16] and grain orientation.

As shown above, the contribution of twinning can affect the kinetics at constant structure. Furthermore, deformation twinning can alter the hardening behavior. The hardening expressed by Eq. (6) occurs by the generation of dislocations; if a significant amount of deformation is being accommodated by deformation twinning, then the hardening rate may decrease. Indeed, this has been observed in Fe-25 at.% Be single crystals [17] and in polycrystalline Cu-Sn alloys [18]. Conversely, if the twin interfaces act as obstacles to dislocation motion, then additional hardening may occur; this has been observed in Hadfield steels [19] and in several other metals [15]. Clearly, the effect of deformation twinning on the deformation kinetics and on the hardening behavior is complicated. But, it is equally clear that this is an important contribution which requires further study in order that it can be incorporated into the formalism of the MTS model.

## 2. Modeling Multiple Strengthening Mechanisms

Copper was chosen for our initial studies for two reasons. First, it demonstrates the strong strain-rate sensitivity at high strain rates which has intrigued investigators for many decades. Secondly, it is a model FCC metal, which is strengthened moderately by the presence of grain boundaries but mostly by the generation and storage of dislocations. Since dislocation motion in FCC metals is not influenced by a large Peierls barrier, the strain-rate

sensitivity in copper arises from the kinetics of dislocation/dislocation interactions. These interactions are well-described by Eqs. (4) and (5) over a wide range of conditions. The situation in BCC metals, however, is quite different. The Peierls barrier represents a large, short-range, barrier to dislocation motion, which gives a higher strain-rate and temperature dependence to the yield stress in these metals. As in FCC metals, strain hardening occurs by the generation and storage of dislocations, which implies that the strengthening in even a model BCC metal, such as iron, niobium, or molybdenum, is a combination of the intrinsic lattice resistance along with the resistance provided by stored dislocations. With continued strain hardening, the dislocation density increases and the strain-rate and temperature dependence of the yield stress, which combine effects of dislocation interactions with short-range obstacles (the Peierls barrier) and interactions with long-range obstacles (other dislocations), continually changes. The situation becomes further complicated by the addition of solute atoms, interstitial atoms, and dispersoids. It is common in engineering metals (stainless steels, for example) to have strengthening contributions from several mechanisms.

Modeling these combined strengthening mechanisms represents a significant challenge. Equation (4) is a first approximation, but the true behavior may be significantly more complicated than this. Ideally, an equation of the form of Eq. (4) is desired with a limited number of internal state variables (or even a single one) that evolve according to Eq. (6). The use of Eq. (4) with a single evolving internal state variable, characterizing the strength of dislocation/dislocation interactions, has been successfully applied to Ti-6Al-4V [20], which is a two-phase alloy strengthened by interstitial oxygen and substitutional aluminum and vanadium, and to Nitronic 40, which is an

16

austenitic stainless steel, strengthened by interstitial nitrogen along with several substitutional additions. In both of these systems deformation twinning becomes prevalent at low temperatures and high strain rates, which further emphasizes the points of the previous section.

To further study multiple strengthening mechanisms, a series of experiments has been designed in nickel, two nickel-carbon alloys, a nickel-aluminum alloy, and a ternary nickel-aluminum-carbon alloy. In these systems it is possible to independently investigate strengthening by dislocation/dislocation interactions, dislocation/interstitial atom (C) interactions, dislocation/solute atom interactions (Al), and dislocation/dispersoid ($Ni_3Al$) interactions, and to give several combinations of these mechanisms. The unique feature of this study is the attempt to separate the deformation kinetics at constant structure from the kinetics of structure evolution using the MTS formalism over a wide range of prestrain strains and strain rates. It is hoped that this study will lead to new insight concerning the difficult question of how to model the effects of simultaneous strengthening mechanisms.

### 3. Some Preliminary Results

In addition to the extensive series of measurements in copper, Nitronic 40 stainless steel, Ti-6Al-4V, AISI 1018 steel, and the nickel alloys described above, work is currently in progress on Armco iron, AISI 4340 steel (in the soft, two-phase, alpha iron plus pearlite condition), tungsten, uranium, and U-.75Ti. As expected the history effect, or strain-rate and temperature dependence of the strain hardening, which was so dominant in the copper results, is not observed in the other metals listed above. Furthermore, an interesting (although only preliminary) observation is that the very rapid

17

dislocation storage rate found at high strain rates in copper has not been observed in metals of crystal structure other than FCC. That is, in Ti-6Al-4V [20], tungsten, pure iron, uranium, and U-.75Ti, the mechanical threshold stress following dynamic prestrain is essentially equal to that following quasi-static prestrain to the same strain level. This implies an absence in these metals of the enhanced strain-rate sensitivity within the strain-rate regime of $10^3$ s$^{-1}$ to $10^4$ s$^{-1}$ that has been observed in copper and other FCC metals. It is of course quite possible that this effect has been delayed to higher strain rates, but this will require verification.

SUMMARY

Application of the MTS model to the analysis of deformation in several FCC metals has increased our understanding of the influence of strain rate, particularly high strain rate, on the strength and strain-rate sensitivity in these metals. The rising scrain-rate sensitivity at high strain rates that is observed in copper and other FCC metals appears to be a result of rapid dislocation generation and storage. Because the MTS model can differentiate between the strain-rate sensitivity at constant structure (mechanical threshold stress) and the strain-rate sensitivity of evolution, it is well suited to model this effect, although questions remain concerning why FCC metals behave this way at high strain rates.

Numerous constitutive equations have been proposed to describe the dynamic deformation of metals. Many of these expressions are designed to capture general behavior and to be easily evaluated within computer codes, while others claim a more "physical" basis and attempt to describe greater subtleties in the material behavior. In copper, the data in figures 2 and 3

18

provide a stringent test of a constitutive description because the strain-rate history effect requires a strain-independent formulation. There are many proposed dynamic constitutive equations that can predict the prestrain stress-strain curves in figure 2. However, there are few that can predict the reload behavior illustrated in this figure. An equation that does not predict this behavior does not accurately represent the strain-rate sensitivity and, therefore, should be extrapolated carefully beyond the regime in which it has been fit and should not be used in calculations (such as instability calculations) where the strain-rate sensitivity is an important property.

Analysis of the measurements in mild steel by Campbell and Ferguson [12] showed that the data is well described using Eqs. (4) and (5), and that there is no need in invoke a transition in deformation mechanism at the high strain rates. A similar conclusion has recently been reached by Nojima [21]. This is an important conclusion because, as has been emphasized throughout this paper, the estimates of flow stress at strain rates beyond those easily achieved in the laboratory depend on the form of the equation used to model the experimental results. In several recent analyses of dynamic fracture in steel, Eq. (2) has been used to represent the Campbell and Ferguson data [22,23]. If the strain rates in the vicinity of the growing crack exceed the maximum strain rate used by Campbell and Ferguson (see figure 6), then the flow stress and the strain-rate sensitivity have been overestimated in these analyses.

The application of the MTS model to engineering metals requires continued development of the model. The influence of deformation twinning on the strain-rate sensitivity at constant structure and on the rate of strain hardening must be analyzed and eventually incorporated into the formalism. Similarly, the effect of multiple strengthening mechanisms on both the strain-

19

rate sensitivity at constant structure as well as the rate of structure evolution requires further study. It is yet unclear how to incorporate into the model the effect of heterogeneous plastic flow (including adiabatic shear), which seems to dominate material behavior during, for instance, armor penetration. Finally, we emphasize that the model as formulated here is not ideally suited for large-strain deformation (such as modeled in figures 4 and 5) because it makes no account of the texture changes that accompany large strains and of the stress-state dependence of these texture changes. There is complementary work underway to develop the textural evolution analyses and models to predict these effects [24,25]. Eventually, we hope to combine these models with the deformation kinetics models described in this paper to yield a complete constitutive description of metal deformation over a wide range of strains, strain rates, and temperatures.

# REFERENCES

1. Follansbee, P.S., Regazzoni, G., and Kocks, U.F., "High-Strain-Rate Measurements of Dislocation Mobility," The Mechanics of Dislocations, American Society for Metals, Metals Park, OH, 237, 1985.

2. Klahn, D., Mukherjee, A.K., and Dorn, J.E., "Strain Rate Effects", 2nd Int. Conf. on The Strength of Metals and Alloys, American Society for Metals, Metals Park, OH, 951, 1970.

3. Frost, H.J. and Ashby, M.F., "Motion of a Dislocation Acted on by Viscous Drag Through an Array of Discrete Obstacles," J. Appl. Phys. 42, 5273, 1971.

4. Follansbee, P.S., Regazzoni, G., and Kocks, U.F., "The Transition to Drag-Controlled Deformation in Copper at High Strain Rates," Mechanical Properties at High Strain Rates, The Institute of Physics, Conf. Ser. No. 70, London, 71, 1984.

5. Regazzoni, G., Kocks, U.F., and Follansbee, P.S., "Dislocation Kinetics at High Strain Rates," Acta Metall. 35, 2865, 1987.

6. Follansbee, P.S., and Kocks, U.F., "A Constitutive Description of the Deformation of Copper Based on the Use of the Mechanical Threshold Stress as an Internal State Variable," Acta Metall. 36, 81, 1988.

7. Kocks, U.F., "Laws for Work-Hardening and Low-Temperature Creep", ASME J. Engr. Matl. Tech. 98, 76, 1976.

8. Mecking, H., and Kocks, U.F., "Kinetics of Flow and Strain-Hardening," Acta Metall. 29, 1865, 1981.

9. Follansbee, P.S., "The Rate Dependence of Structure Evolution in Copper and its Influence on the Stress-Strain Behavior at Very High Strain Rates," Impact Loading and Dynamic Behaviour of Materials, C.Y. Chiem, H.-D. Kunze, L.W. Meyer, Eds., DGM Informationsgesellschaft, Germany, Vol. 1, 315, 1988.

10. Mecking, H., Nicklas, B., Zarabova, N., and Kocks, U.F., "A Universal Temperature Scale for Plastic Flow," Acta Metall. 34, 527, 1986.

11. Kocks, U.F., Argon, A.S., and Ashby, M.F., "Thermodynamics and Kinetics of Slip," Prog. Mater. Sci. 19, Pergamon Press, NY, 1975.

12. Campbell, J.D., and Ferguson, W.G., "The Temperature and Strain Rate Dependence of the Shear Strength of Mild Steel," Phil. Mag. 21, 63, 1970.

13. Rosenfield, A.R., and Hahn, G.T., "Numerical Descriptions of the Ambient Low-Temperature, and High-Strain Rate Flow and Fracture Behavior of Plain Carbon Steel," Trans. of the ASM 59, 963, 1966.

14. Erickson, J.S., and Low, J.R., Jr., "The Yield-Stress Temperature Relation for Iron at Low Temperature," Acta Metall. 5, 405, 1957.

15. Reed-Hill, R.E., "Role of Deformation Twinning in Determining the Mechanical Properties of Metals," The Inhomogeneity of Plastic Deformation, American

Society for Metals, Metals Park, OH, 285, 1973.

16. Armstrong, R., Codd, I., Douthwaite, R.M., and Petch, N.J., "The Plastic Deformation of Polycrystalline Aggregates," Phil. Mag. 7, 45, 1962.

17. Bolling, G.F., and Richman, R.H., "Continual Mechanical Twinning, Part II: Standard Experiments," Acta Metall. 13, 723, 1965.

18. Vöhringer, O., "Deformation Twinning in Polycrystalline α-Copper Alloys," 2nd Int. Conf. on Strength of Metals and Alloys, American Society for Metals, 294, 1970.

19. Raghavan, K.S., Sastri, A.S., and Marcinkowski, M.J., "Nature of Work-Hardening Behavior in Hadfield's Manganese Steel," Trans. TMS-AIME 245, 1569, 1969.

20. Follansbee, P.S., and Gray, G.T. III, "An Analysis of the Low Temperature, Low and High Strain Rate Deformation of Ti-6Al-4V," Met. Trans., To appear.

21. Nojima, T., "Constitutive Equations of Some Kinds of Steels at High Rates of Strain," Impact Loading and Dynamic Behaviour of Materials, C.Y. Chiem, H.-D. Kunze, and L.W. Meyer, Eds., DGM Informationsgesellschaft, Germany, Vol. 1, 357, 1988.

22. Freund, L.B., and Hutchinson, J.W., "High Strain-Rate Crack Growth in Rate-Dependent Plastic Solids," J. Mech. Phys. Solids, 33, 169, 1985.

23. Hack, J.E., Chen, S.P., and Srolovitz, D.J., "A Kinetic Criterion for Quasi-Brittle Fracture," Acta Metall., To appear.

24. Kocks, U.F., Stout, M.G., and Rollett, A.D., "The Influence of Texture on Strain Hardening," To be published in Proc. 8th Int. Conf. on Strength of Metals and Alloys, Tampere, Finland, Pergamon Press, 1988.

25. Kocks, U.F., "Constitutive Behavior Based on Crystal Plasticity," Unified Constitutive Equations for Creep and Plasticity, A. K. Miller, ed., Elsevier Applied Science, New York, NY, 1987.
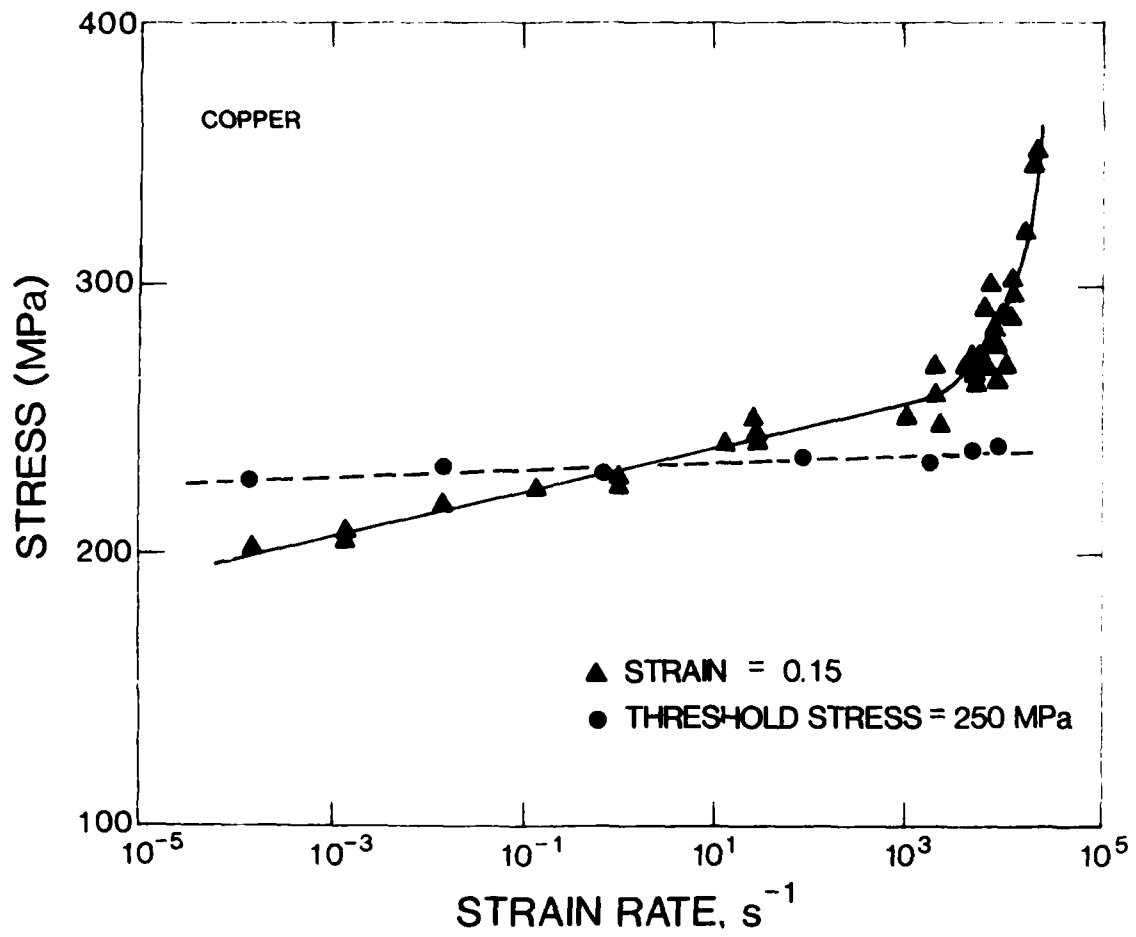
Figure 1. Flow stress in copper at $\varepsilon=0.15$ versus applied strain rate (triangles) compared with flow stress at $\hat{\sigma} = 250$ MPa (circles).
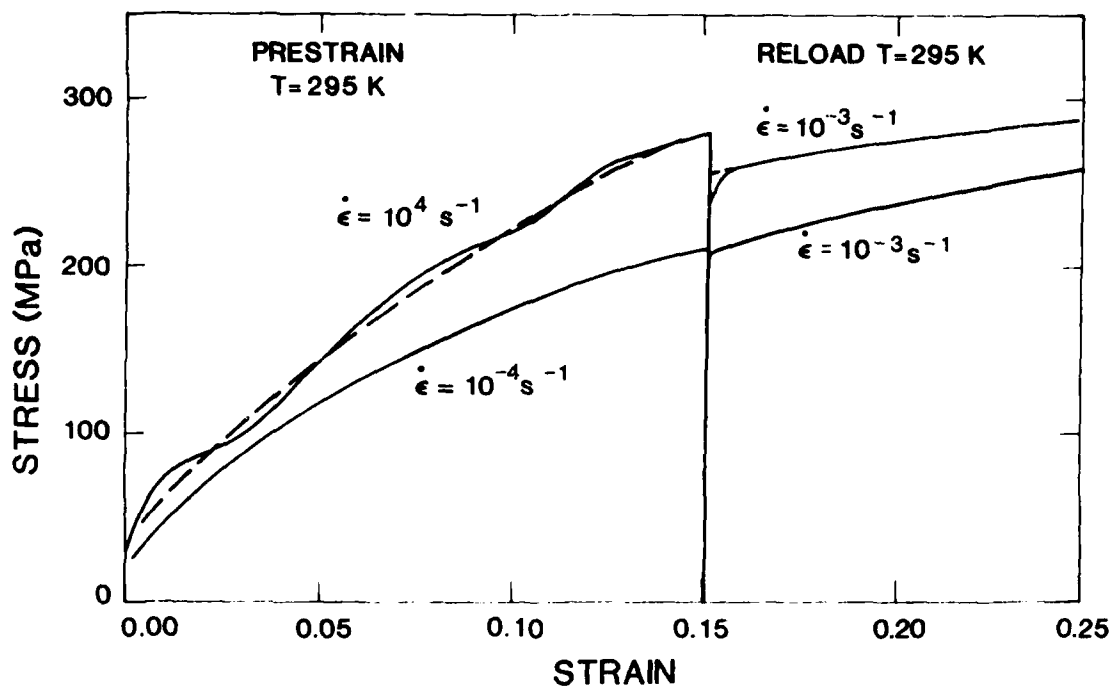
Figure 2.  Quasi-static and dynamic stress-strain curves in copper
and subsequent quasi-static stress-strain curves on these
two specimens.
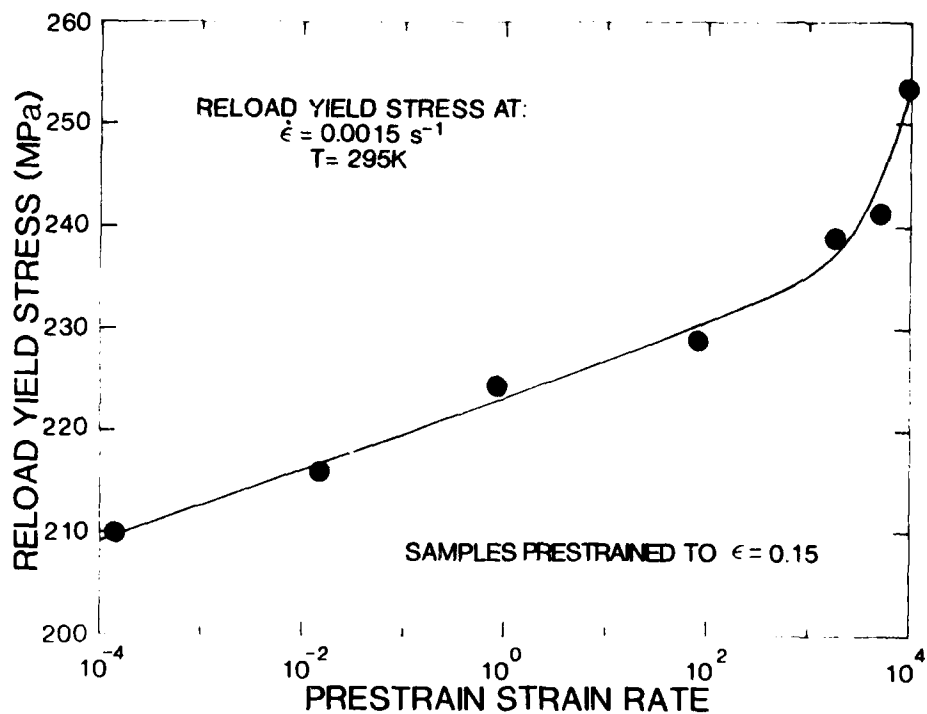


Figure 3.  Quasi-static, room temperature, reload yield stress
measurements on copper specimens prestrained 15% at the
indicated strain rates.

24
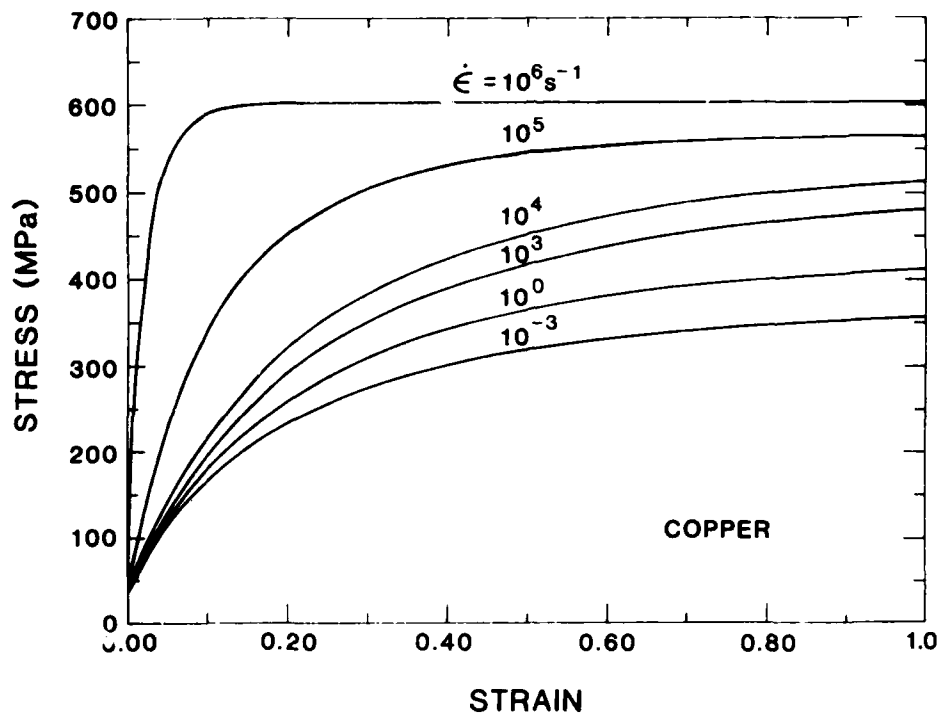
Figure 4.  Predicted isothermal stress-strain curves in copper.
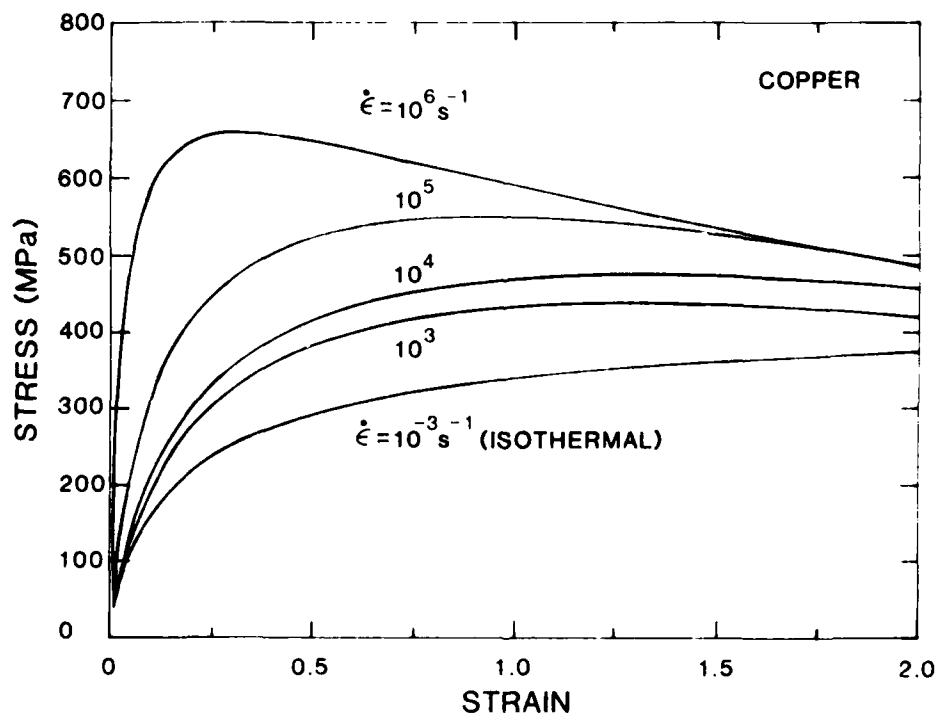


Figure 5.  Predicted adiabatic stress-strain curves in copper.

25
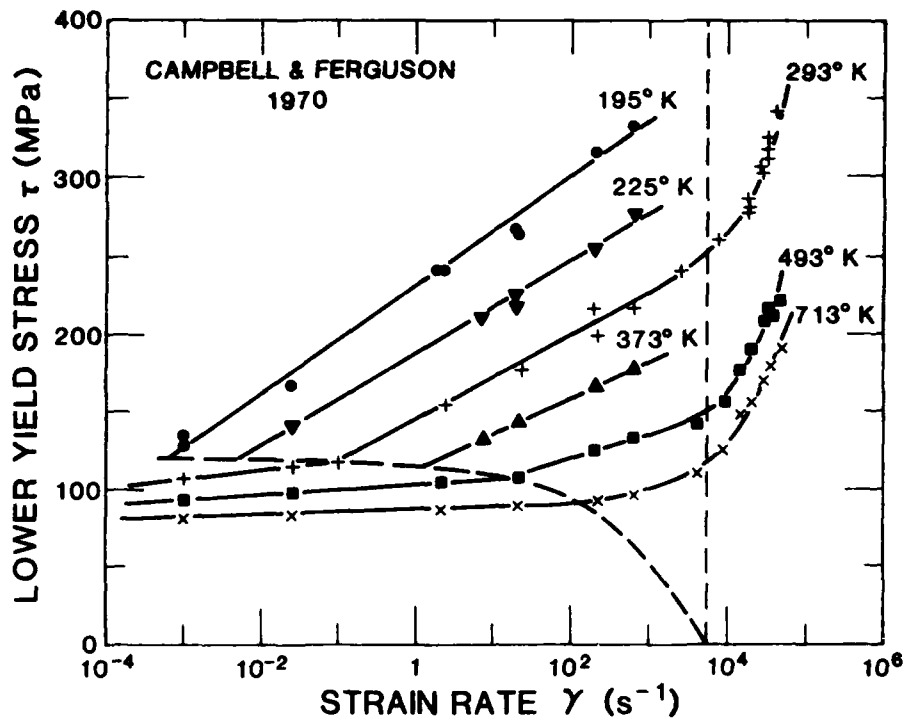
Figure 6. Yield stress (in shear) measurements of Campbell and Ferguson [12] in mild steel. The dashed lines were suggested by Rosenfield and Hahn [13] as lines separating different deformation regimes.
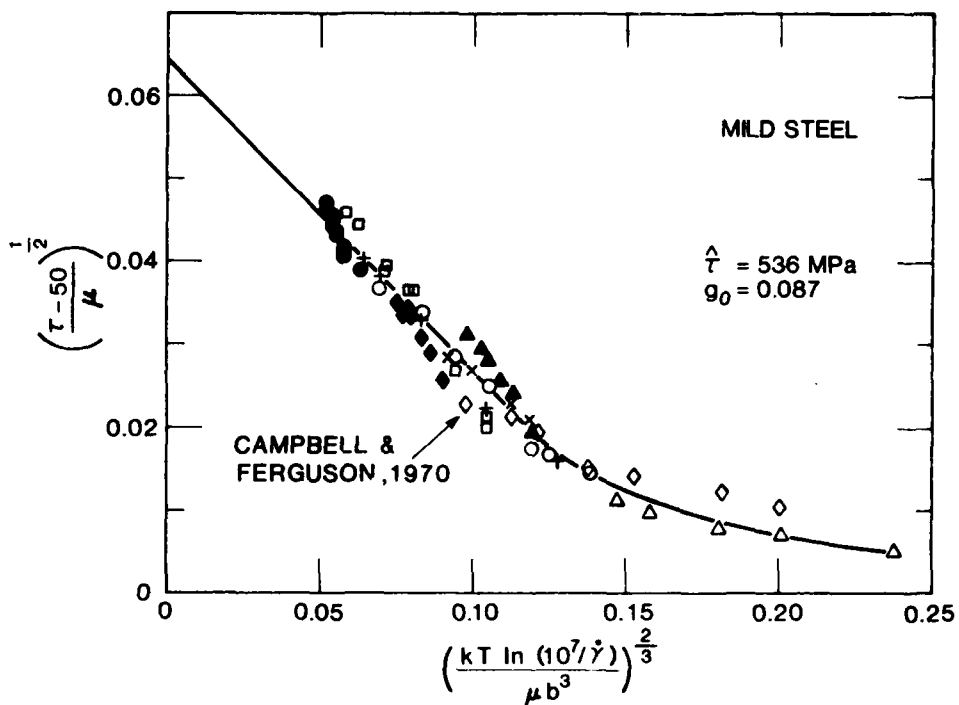


Figure 7. The data of Campbell and Ferguson [12] plotted on coordinates suggested by Eqs. (4) and (5). Note that most of the data fall along a straight line suggesting a single rate controlling, thermally activated, deformation mechanism.

26
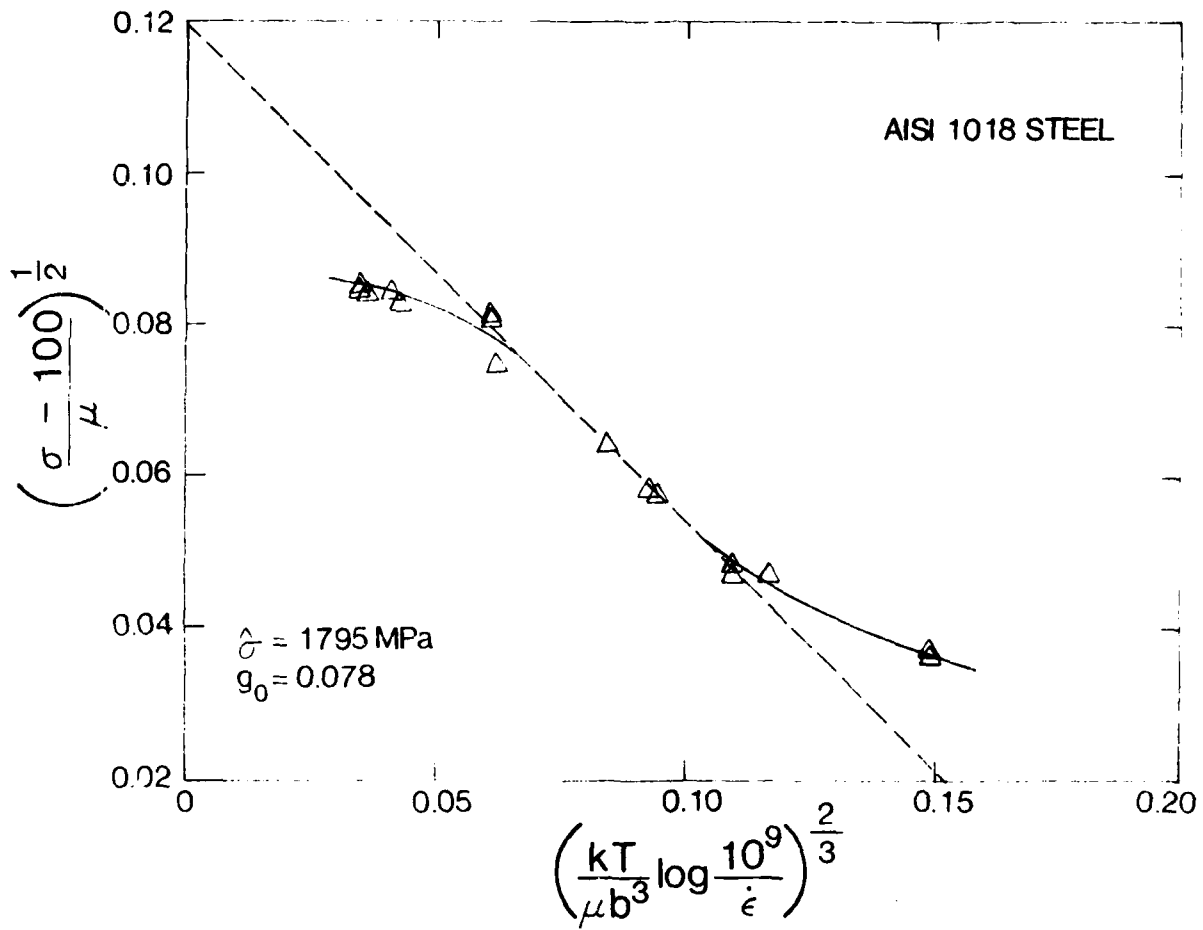
Figure 8.  Yield stress measurements in AISI 1018 steel plotted on coordinates suggested by Eqs. (4) and (5).

# CONSTITUTIVE MODELS FOR PLASTIC FLOW AT ULTRA HIGH STRAIN RATES

Rodney J. Clifton
Division of Engineering
Brown University
Providence, RI 02912

## ABSTRACT

Results of pressure-shear experiments on the dynamic plastic response of metals at shear strain rates of $10^5$- $10^6$ s$^{-1}$ are summarized. The flow stress for high purity metals is found to be sensitive to the rate of strain and relatively insensitive to the accumulated plastic strain. Conversely, for high strength alloys the flow stress is relatively insensitive to the rate of strain but sensitive to the accumulated plastic strain. For the case of high purity metals an elementary model is presented which associates the observed phenomena with the dynamics of dislocation motion in a three-dimensional dislocation cell structure.

## EXPERIMENTAL RESULTS

Direct measurements of the stress-strain behavior of metals at high strain rates can be made at strain rates of $10^3 - 10^4$ s$^{-1}$ using Kolsky bar expriments and at strain rates of $10^5 - 10^7$ s$^{-1}$ using pressure-shear plate impact experiments. Both types of experiments involve the plastic deformation of a specimen sandwiched between two elastic bodies. In the case of Kolsky bar experiments, the specimens are solid bars for compression tests and thin-walled tubes for torsion tests. In the pressure-shear experiments the specimens are thin plates. In all these configurations, the basic concept - due to Kolsky [1] - is to use the elastic waves in the bounding bodies to determine the nominal stress and strain rate in the specimen, once the stress state in the specimen becomes essentially homogeneous. Integration of the strain rate provides the strain required for plotting dynamic stress-strain curves.

28

For this presentation, the primary interest is in the regime of very high strain rates covered by the pressure-shear experiment. The experimental configuration is shown in Figure 1. A detailed description of the technique has been given by Klopp and Clifton [2]. Briefly, a thin specimen attached to an elastic flyer plate is subjected to pressure-shear loading by impacting a parallel elastic anvil plate that is inclined relative to the direction of approach. After several reverberations between the elastic plates, the state of stress in the specimen is essentially homogeneous. Then, the nominal longitudinal and shear strain rates in the specimen are

$$\dot{\epsilon} = \frac{u_0 - u_{fs}}{h} \tag{1}$$

$$\dot{\gamma} = \frac{v_0 - v_{fs}}{h} \tag{2}$$

where $u_0$, $v_0$ are the normal and transverse components of the flyer velocity and $u_{fs}$, $v_{fs}$ are the normal and transverse particle velocity of the free surface of the anvil; h is the specimen thickness. The normal and shear tractions at the specimen-anvil interface are

$$\sigma = \frac{1}{2} \rho c_1 \, u_{fs} \tag{3}$$

$$\tau = \frac{1}{2} \rho c_2 \, v_{fs} \tag{4}$$

where $\rho c_1$, and $\rho c_2$ are respectively the impedances for elastic longitudinal waves and elastic shear waves in the anvil. For Hampden tool steel plates which are commonly used these values are $\rho c_1 = 45.5$ GPa/mm/$\mu$s and $\rho c_2 = 24.8$ GPa/mm/$\mu$s.

From Eqs. (1) to (4) the quantities which must be measured to allow dynamic stress-strain curves to be obtained are the velocities $u_0$, $v_0$, $u_{fs}$, $v_{fs}$. The velocities $u_0$, $v_0$ are obtained from the angle of inclination of the plates and the velocity of impact, which is determined from the time at which the flyer contacts five

accurately spaced pins mounted at the muzzle of the barrel. The velocities $u_{fs}$ and $v_{fs}$ are obtained from a combined normal velocity interferometer (NVI) and transverse displacement interferometer (TDI)[3]. Diffracted beams required for the TDI are obtained from a 200 lines/mm diffraction grating that is copied onto the polished rear surface of the anvil by means of a photo-resist technique.

The very high strain rates of the pressure-shear experiments are obtained by using relatively thin specimens with thicknesses h that are in the range of 0.3 mm to 3 $\mu$m. The corresponding gage lengths for Kolsky bar experiments are of the order of 3 mm and larger. The smaller thicknesses in the pressure-shear experiments, and consequently the higher strain rates, are allowable because these are plane wave experiments which are free of lateral inertia effects and end-friction effects until unloading rarefactions arrive from lateral boundaries. For the lateral dimensions of these experiments (projectile diameter is 62.5 mm), plane wave conditions hold for approximately 1 $\mu$s. Thus, pressure-shear experiments allow one to determine dynamic stress-strain curves at strain rates of $10^5$ to $10^7$ s$^{-1}$ up to strains of 0.1 to 10, respectively. The flatness required to ensure plane wave conditions can be obtained by lapping, for thicknesses greater than approximately 35 $\mu$m. The highest strain rates (i.e. $10^7$ s$^{-1}$) are obtained for vapor deposited specimens with thicknesses of the order of 3 $\mu$m.

Experimental results have been obtained for three high purity metals (aluminum, copper, and iron) and three commercial alloys (6061-T6 aluminum, 4340 VAR steel, and 21-6-9 stainless steel) [4-6]. Here we consider the case of OFHC copper, which is representative of the behavior of the high purity metals and a 4340 VAR steel (600°C temper) which is indicative of the main features of the response obtained for the alloys.

Dynamic stress-strain curves for OFHC copper specimens that were cut from a cylindrical bar, annealed, and lapped to final thickness, are shown in Figure 2. (Details of the experiments are given in Table I.) The steeply rising part of each

curve should be disregarded because this segment is generated before a homogeneous state of stress has been established. After the steep rise the flow stress (and the strain rate - see Eqs. (2) and (4)) becomes essentially constant. Although two of the curves show a small positive slope and two show a small negative slope, the slopes are small relative to the strain hardening found at lower strain rates - for which the quasi-static and torsional Kolsky bar results shown are representative. As shown in Figure 2, the flow stress in the pressure-shear experiments is several times larger than the flow stress in torsional Kolsky bar experiments and quasi-static torsion experiments.

Dynamic stress-strain curves for vapor-deposited copper specimens are shown in Figure 3. The specimens deformed at strain rates of $4.4 \times 10^5$ $s^{-1}$ and $8.5 \times 10^6$ $s^{-1}$ were prepared by RF sputtering and the specimen deformed at the strain rate of 7.1 $\times 10^6$ $s^{-1}$ was prepared by vacuum evaporation of resistance heated OFHC samples. Again, after a steep rise the flow stress becomes essentially constant. The stress levels are much higher than those shown in Figure 2 for specimens cut from bar stock. The exceptionally high flow stress obtained at the strain rate of $4.4 \times 10^5$ $s^{-1}$ (Cf. Figure 2) is an indication that differences in microstructure between the bulk material and vapor-deposited material are playing an important role in the observed response. Further study of vapor-deposited specimens is required to clarify the roles of microstructure and high strain rates in causing the large flow stresses shown in Figure 3.

As an indication of the different behavior observed for metal alloys, dynamic stress-strain curves for 4340 VAR steel (600°C temper) are shown in Figure 4. In contrast to the behavior for the high purity metals, the flow stress does not increase strongly with an increase in strain rate from $10^3$ $s^{-1}$ to $10^5$ $s^{-1}$.

## Modeling High-Rate Plastic Flow for High Purity Metals

Two characteristic features of the plastic response of high purity metals at the high strain rates of pressure-shear experiments are the relatively strong rate sensitivity and the relatively weak strain hardening. The weak strain hardening is observed even at the modest strains of, say, 3% in the experiments at the lowest strain rate. These features differ markedly from those observed in high purity metals at low strain rates and in structural alloys at high strain rates. Thus, from these observations alone, it would appear that new or revised microstructural models are required to explain the observed phenomena. However, Follansbee and Kocks [7] have shown that some of the observed behavior can be explained by a model based on consideration of the same model of thermally activated motion past obstacles that has been developed for interpreting experimental results at strain rates up to $10^4$ $s^{-1}$. Their model attributes the increased flow stress with increasing strain rate to the development of microstructures which, for a given plastic strain, are more resistant to the motion of dislocations. This enhancement of hardness with increasing rates of deformation has been established by measuring initial yield stress or "threshold stress" at $0°K$ of specimens which have been deformed previously at various strain rates. At the highest strain rates shown in Figure 2, the model of Follansbee and Kocks [7] predicts the reported stress-strain curves reasonably well. However, at the lower strain rates their model tends to show more strain hardening than is observed.

To assist in the clarification of the micromechanical processes responsible for the plastic response at high strain rates, a pilot study of the dislocation structures induced by the pressure-shear loading has been conducted by Gray [8]. Transmission electron micrographs have been made of dislocation networks in the specimens tested at shear strain rates of $0.82 \times 10^5 s^{-1}$ and $2.73 \times 10^5 s^{-1}$. Two of these micrographs

are shown in Figure 5. The dislocation structure consists primarily of cell walls with nearly dislocation-free spaces between the walls. The cells appear to be roughly spherical in shape, with a mean diameter that decreases with increasing stress or strain rate. Multiple slip appears to have occurred throughout the grains as there is very little evidence of linear features that are indicative of slip on a dominant glide plane. No shear bands appear to have formed. A few twins were observed in the specimen deformed at the lower strain rate; however, their effect appears to be small since the volume fraction of twinned material is small and the dislocation configurations near the twins appear to be unaffected by the presence of the twins. Overall, the dislocation configurations suggest that plastic deformation of OFHC copper under pressure-shear loading at strain rates of $10^5 s^{-1}$ is a relatively homogeneous and stable process.

Dislocation structures generated in copper by unidirectional deformation have been discussed by Mughrabi [9]. For single slip, in Stage II, the resolved shear stress for plastic deformation is found to vary inversely with the spacing of multipole bundles as well as with the spacing of free segment lengths of primary dislocations which bow out from the bundles [10,11]. For multiple slip, which occurs in polycrystals and in single crystals with highly symmetric orientations, a three-dimensional cell structure is observed [12,13]. Göettler [11] reports that for high purity copper single crystals the mean cell diameter varies inversely with the resolved shear stress according to

$$\overline{D} = \frac{49}{\overline{\tau}_r} \tag{5}$$

where the resolved shear stress $\overline{\tau}_r$ is in MPa and the mean diameter $\overline{D}$ is in microns. This relationship agrees with experimental results over the range of stresses investigated: 12 MPa to 70 MPa [11]. For comparison with the reported pressure-shear experiments the resolved shear stress in Eqn (5) must be estimated

from the applied shear stress in simple shear, $\bar{\tau}$, which is measured in the experiments. Because the orientations of the grains relative to the loading direction is unknown, only crude approximations are possible.

One means of estimating the resolved shear stress $\bar{\tau}_r$ is to assume that the grains are randomly oriented and that the shearing rate for each slip system is related to the shearing stress by a relation of the form

$$\dot{\gamma}^k = \alpha \left[\frac{\tau_r^k}{\tau_0}\right]^n \tag{6}$$

where $\alpha$, $\tau_0$, and n are constants. Under these conditions Hutchinson [14] has shown that the macroscopic shear strain rate $\bar{\dot{\gamma}}^p$ in simple shear is related to the applied shear stress $\bar{\tau}$ by

$$\bar{\dot{\gamma}}^p = 2\alpha \left[\frac{\bar{\tau}}{\bar{\tau}_0}\right]^n \tag{7}$$

in which $\alpha$, n are the same constants as in (6) and $\bar{\tau}_0$ satisfies

$$\bar{\tau}_0 \leqslant g(n)\tau_0 \tag{8}$$

where g(n) is tabulated in [14]. If, as in the Taylor theory of plastic flow of polycrystals, one assumes that the plastic strain is the same in all grains, then for a simple shearing deformation the shearing rate is given by

$$\bar{\dot{\gamma}}^p = \dot{\gamma}_{12}^p = \alpha \sum_{k=1}^{12} \left[\frac{\tau_r^k}{\tau_0}\right]^n (m_1^k n_2^k + m_2^k n_1^k) \tag{9}$$

where $n_1^k$ $m^k$ are unit normal vectors in the directions normal to the slip plane and parallel to the slip direction for the $k^{\text{th}}$ slip system, respectively. To estimate a representative resolved shear stress it is further assumed that the stress state is essentially uniform so that

34

$$\tau_r^k \simeq \bar{\tau} \; (m_1^k \, n_2^k + m_2^k \, n_1^k) \tag{10}$$

where $\bar{\tau} = \sigma_{12}$ is the applied shear stress. Substitution of Eqn. (10) into (9) gives

$$\bar{\gamma}^p \simeq \alpha \left[\frac{\bar{\tau}}{\tau_0}\right]^n \sum_{k=1}^{12} |m_1^k \, n_2^k + m_2^k \, n_2^k|^{n+1} \tag{11}$$

where absolute values have been taken to ensure $\tau_r^k \, \gamma^k \geqslant 0$ for all k. The inequality (8) is actually quite a tight upper bound and can be used as an equality for approximation purposes.

Then, from (7), (8), (10) and (11) one obtains

$$\sum_{k=1}^{12} |\frac{\tau_r^k}{\bar{\tau}}|^{n+1} \simeq \frac{2}{[g(n)]^n} \, . \tag{12}$$

Equation (12) can be used to estimate a nominal value of $\tau_r^k$, say $\bar{\tau}_r$, by noting that for $n \geqslant 3$ (as reported for the high strain rate deformation of OFHC copper [5]), the few terms corresponding to the most favorably oriented slip systems (i.e. largest values of $\tau_r^k$) provide the primary contribution to the sum. If one assumes that there are M equivalent favorably oriented slip systems with a nominal resolved shear stress $\bar{\tau}_r$, then Eqn. (12) provides the estimate

$$\bar{\tau}_r \simeq \left\{\frac{2}{M[g(n)]^n}\right\}^{\frac{1}{n+1}} \bar{\tau}. \tag{13}$$

For face centered cubic crystals the number of favorably oriented slip systems is usually small, say $1 \leqslant M \leqslant 5$. For M = 2, 3, 4 and for n = 3, g(3) = 1.54, the corresponding values of the factor multiplying $\bar{\tau}$ are 0.72, 0.65, and 0.61, respectively.

35

In the subsequent discussion we take $\bar{\tau}_r = 0.65\ \bar{\tau}$ as our estimate of the resolved shear stress.

For the shear stresses $\bar{\tau}$ of 178 MPa and 213 MPa corresponding to the cell wall structures shown in Figures 5(a) and 5(b) the values of $\bar{D}$ obtained from (5) for $\bar{\tau}_r = 0.65\ \bar{\tau}$ are $\bar{D}$ = 423nm and $\bar{D}$ = 354nm, respectively. These values are viewed as comparable to the observed cell diameters of approximately 600nm and 450nm for Figs. (5a) and (5b), respectively. Comparison can also be made with the estimate for mean cell diameter given by Staker and Holt [13]:

$$D = \frac{10.5\mu b}{\bar{\tau}} \tag{14}$$

where $\mu$ is the shear modulus and b is the Burgers vector ($\mu$ = 45.2 GPa and b = 2.56 x $10^{-10}$m for copper). Holt [15] has dervied a relation of the form (14) by considering the modulation of the dislocation density of an array of parallel screw dislocations. The mean cell diameter is identified with the wavelength of the modulation and the stress is taken to be proportional to the square root of the dislocation density in obtaining the form (14). The cell diameters obtained from (14) for the shear stresses $\bar{\tau}$ = 178 MPa and $\bar{\tau}$ = 213 MPa are $\bar{D}$ = 682 nm and $\bar{D}$ = 570 nm, respectively. Thus, it appears quite likely that Eqns. (5) and (14) provide a reasonably accurate correlation of cell size and resolved shear stress even for the range of high stresses generated in the pressure-shear impact experiment.

In view of the apparent correlation of the flow stress with the mirostructure through Eqns. (5) and (14) it is of interest to examine the implications of these equations for the associated dislocation mechanisms of plastic flow. To this end it is interesting to note that for a dislocation segment pinned at two points, separated by a distance $a_c$, the critical resolved shear stress $\tau_{rc}$ required for a Frank-Read source to operate is

$$\tau_{rc} = \frac{\beta \mu b}{a_c} \tag{15}$$

where $\beta$ is a factor that is reported to be approximately 1.1 for edge segments and 1.5 for screw segments [9]. Substituting $\mu$ and b for copper into Eqn. (15) and taking $\beta \simeq 1.3$ one obtains

$$a_c \simeq \frac{15}{\tau_{rc}} \tag{16}$$

where $\tau_{rc}$ is in MPa and $a_c$ is in microns. If we identify the resolved flow stress of Eqn. (5) with the critical resolved shear stress of Eqn. (16) we obtain the following relationship between the critical pinning distance $a_c$ and the mean cell diameter $\bar{D}$.

$$a_c \simeq 0.3 \, \bar{D} \tag{17}$$

Equation (17) suggests that those dislocations whose strong pinning points are separated by distances greater than approximately $0.3\bar{D}$ are sufficiently free to bow out from the cell wall and sweep across the cell under the driving force of the applied stress. Pinning distances of the order indicated by Eqn. (16) appear to be reasonable. Thus, it appears that the relationship (5) between the flow stress and the mean cell diameter is associated with a dislocation mechanism in which the stress is required to be sufficiently large to overcome the line tension which develops as dislocations bow out to cross the clear space of the cell.

Consider next the relationship between the applied stress and the rate of deformation for the dislocation mechanism of dislocations bowing out from a cell wall and sweeping across the clear interior of the cell. The rate of deformation associated with the passage of a dislocation can be expressed as

$$\gamma = \frac{Ab}{V\Delta t} \tag{18}$$

where A is the area swept by the dislocation, per volume V, per time $\Delta t$. To estimate the time $\Delta t$, assume that the dislocation velocity $v_d$ and resolved shear stress $\tau_r$ are related by

$$\tau_r = \frac{Bv_d}{b[1 - v_d^2/c_2^2]^{1/2}} \tag{19a}$$

or,

$$v_d = \frac{\tau_r b}{B\left[1 + \left(\frac{\tau_r b}{Bc_2}\right)^2\right]^{1/2}} \tag{19b}$$

where B is the drag coefficient and $c_2$ is the elastic shear wave speed; for high purity copper, B and $c_2$ are approximately $1.7 \times 10^{-11}$MPa s$^{-1}$ [16] and 2.25 kms$^{-1}$, respectively. In Eqns. (19), B is the drag coefficient measured at low dislocation velocities; the relativisitic correction is introduced to limit the dislocation velocity by the elastic shear wave speed.

The interval $\Delta t$ required for a dislocation to cross the diameter of a cell is

$$\Delta t = \int_0^{\bar{D}} \frac{dx}{v_d(\tau_r(x))} \tag{20}$$

where $v_d(\tau_r)$ is the function defined by (19b). Once the spatial dependence of $\tau_r$ is known, the interval $\Delta t$ can be obtained by the integration of Eqn. (20). An idealized stress distribution $\tau_r(x)$ along the path of a central dislocation segment is shown in Figure 6. The stress $\tau_r(x)$ is viewed as the superposition

$$\tau_r(x) = \bar{\tau}_r + \tau_{CW}(x) + \tau_{ID}(x) + \tau_{LT}(x) + \tau_{LR}(x) \tag{21}$$

38

where the quantities on the right side are the resolved shear stresses due to, respectively, the applied stress $\bar{\tau}$, the multipole dislocations in the cell wall, the impinging dislocation from a neighboring cell, the line tension of the bowed dislocation, and the long range stress field. The term $\bar{\tau}_r$ can be viewed as constant over the diameter of a cell. The stress field $\tau_{CW}(x)$ due to multipoles is a short-range field that decays quickly on the scale of distances comparable to cell wall thicknesses. The stress field $\tau_{ID}(x)$ varies as approximately

$$\tau_{ID}(x) = \frac{\mu b}{2\pi(h + x)} \tag{22}$$

where h is the thickness of the cell wall. The stress due to the bowing of the dislocation can be represented by

$$\tau_{LT}(x) = \frac{\mu b}{4\pi R(x)} \log \frac{R(x)}{5b} \tag{23}$$

where R is the radius of curvature of the bowed dislocation. The long range stress field can be idealized as

$$\tau_{LR}(x) = \tau_A \cos\left(\frac{2\pi x}{\lambda}\right) \tag{24}$$

where the amplitude $\tau_A$ and the wavelength $\lambda$ are constants. The long range stress field is expected to correlate with the dislocation cell structure. The wave length $\lambda$ for two dimensional dislocation networks are reported to be 5-6 times the spacing of the multipole bundles which form the mesh of the network [9]. By analogy it is expected that the wavelength $\lambda$ for a three dimensional cell structure is several times the mean diameter of the cells. The amplitude $\tau_A$ is reported to be approximately the same as the flow stress, say $\tau_A = 0.9 \, \bar{\tau}_r$ [9]. Again these values are obtained for

39

two-dimensional dislocation networks which are reported for stage II hardening; however, the similarity between the two and three dimensional dislocation structures is sufficiently strong that overall characteristics of the long range stress fields are expected to be similar.

For the mechanism being investigated the dislocation to be bowed out from the cell wall is initially in an equilibrium position for the stress fields $\bar{\tau}_r$, $\tau_{CW}(x)$, $\tau_{LT}(x)$, and $\tau_{LR}(x)$. As the impinging dislocation approaches, the dislocation is bowed out under the stress field $\tau_{ID}(x)$. Because of the large amplitude of $\tau_{ID}(x)$ and the short range of influence of the stresses $\tau_{CW}(x)$, a central segment of the bowed dislocation moves beyond the range of $\tau_{CW}(x)$ during an interval of time that is small relative to the time required for the dislocation to sweep across the cell. This small contribution to the total time $\Delta t$ in Eqn. (20) will be neglected. For the remainder of its travel across the cell a central segment of the dislocation is driven forward by the stress fields $\bar{\tau}_r$, $\tau_{ID}(x)$, and $\tau_{LR}(x)$; it is held back by the stress field $\tau_{LT}(x)$. From Eqn. (22) the value of $\tau_{ID}$ at $(h + x) = \bar{D}/2$ is approximately 8 MPa for $\bar{D} = 450$nm. Similarly, from Eqn. (23), the value of $\tau_{LT}$ for $R = \bar{D}/2$ is approximately -20 MPa. The net value of these opposing stresses is small compared to the applied stress $\bar{\tau}_r$. Furthermore, the value of the long range stress field $\tau_{LR}$ is expected to be near its maximum positive value in cells which are being swept by moving dislocations. Thus, as a first approximation, the effect of $\tau_{ID}$ and $\tau_{LT}$ on the time $\Delta t$ will be regarded as negligible and $\Delta t$ will be estimated from Eqn. (20) by taking $\tau_r$ to be constant at an effective value $\tau_{eff} = \bar{\tau}_r + \tau_A \approx 1.9\,\bar{\tau}_r$. That is,

$$\Delta t \approx \frac{\bar{D}B\left[1 + \left(\tau_{eff}/\tau_c\right)^2\right]}{\tau_{eff}b} \qquad (25)$$

where $\tau_c = Bc_2/b$ is the critical resolved shear stress that would cause dislocations to move at the elastic shear wave speed $c_2$ in the absence of relativistic effects; for

copper, $\tau_c$ is equal to 149 MPa. The times $\Delta t$ obtained from Eqn. (25) for the respective shear rates are shown in Table II as $(\Delta t)_{24}$. The times, although short on the scale of the time resolution of macroscopic experiments, are long relative to the time scale on which the inertia of accelerating dislocation is important [17]. Thus, the neglect of the inertia of dislocations in the analysis appears to be acceptable. The time increments obtained from Eqn. (25) can be substituted into Eqn. (18) to obtain an estimate of the volume V in which only one dislocation cell is active simultaneously. The results can be stated more simply if the volume V is represented as the number, N, of close-packed cells of diameter $\bar{D}$ which comprise the volume V (i.e. $V = N\bar{D}^3/\sqrt{2}$). Then, for $A = \pi\bar{D}^2/4$, Eqn. (18) becomes

$$\dot{\gamma} = \frac{\pi\sqrt{2}\ b}{4N\bar{D}\Delta t} . \qquad (26)$$

For the assumed case of three, equivalent, favorably oriented slip systems the shearing rate $\dot{\gamma}$ in Eqn. (26) is $\dot{\gamma}^p/(3 \times .65)$ where $\dot{\gamma}^p$ is the measured shear strain rate. The values of N obtained from Eqn. (26) for shots 4 and 6 are given in Table II. These values indicate that, according to the model, only a small fraction of the cells would be active simultaneously.

For the model being considered, the value of N is expected to be approximately 12 --- the number of cells in contact with a given cell in a close-packed array of spherical cells. This expectation is based on the requirement that under nominally steady conditions each impinging dislocation would cause one, and only one, dislocation to sweep across an adjoining cell. If N were much less than 12 then one would expect that the dislocation density would increase strongly, cell sizes would decrease, and the flow stress would increase. If N were less than 1, then more than one dislocation would be sweeping across a cell simultaneously. Intersection of these dislocations would lead to entanglements and marked refinement of the cell structure.

On the other hand, if N were much greater than 12, some impinging dislocations would not be able to free a single dislocation as they arrived at the cell walls shared with adjoining cells. Under these conditions deformation would not be sustained at the nominal strain rate in some region of the grain.

If only a small fraction of the cells operate simultaneously, then one can expect that the one dislocation that is sweeping across one of the N cells of a group is subjected to internal stress fields which provide only slightly more resistance to its motion than the resistance provided for other dislocations which are not sweeping across cells concurrently. Thus, the sweeping dislocation should be viewed as being driven by a stress that is only slightly greater than the threshold stress at which it is prevented from sweeping across the cell. Under these conditions, our previous assumption that the net retarding effects of the terms $\tau_{LT}(x) + \tau_{CW}(x)$ are offset by the driving stress $\tau_{ID}(x)$ of the impinging dislocation should be revised. Instead, we assume that there is a distance $\alpha \bar{D}$ over which the dislocation motion is retarded such that the effective stress is reduced by an amount $\tau_0$. The additional transit time is

$$(\Delta t)_r \approx \frac{\alpha \bar{D} B \left[ 1 + \left( \frac{(\tau_{eff} - \tau_0)}{\tau_c} \right)^2 \right]^{1/2}}{(\tau_{eff} - \tau_0) b} . \tag{27}$$

The shearing rate can be obtained by substituting the sum of the time increments of Eqns. (25) and (27) into Eqn. (26). In making this substitution we note that in (25) the distance of travel under the driving stress $\tau_{eff}$ should be reduced to $(1 - \alpha)\bar{D}$ since travel over the distance $\alpha \bar{D}$ occurs under the reduced driving stress, $(\tau_{eff} - \tau_0)$, of Eqn. (27). The resulting expression for the shearing rate can be written as

$$\dot{\gamma} = \frac{\pi\sqrt{2}\; b^2\, \tau_{eff}}{4NB D^2 \left\{ \left[1 + (\tau_{eff}/\tau_c)^2\right]^{\frac{1}{2}} + \alpha f(\tau_{eff}) \right\}}$$ (28)

where

$$f(\tau_{eff}) = \frac{\left[1 + \left(\frac{\tau_{eff} - \tau_0}{\tau_c}\right)^2\right]^{\frac{1}{2}}}{(1 - \tau_0/\tau_{eff})} - \left[1 + (\tau_{eff}/\tau_c)^2\right]^{\frac{1}{2}}.$$

Equation (28) is the form of the predicted relationship between the shear stress and the shearing rate. For $\alpha = 0$, or $\tau_0 = 0$, the retarding effects of the stress fields $\tau_{cw}(x)$ and $\tau_{LT}(x)$ vanish and Eqn. (28) reduces to the form used for evaluating N in Table II. For parameter values $0 < \alpha < 1$ and $0 < (\tau_0/\tau_{eff}) < 1$ the term $\alpha f$ in (28) reduces the strain rate at a given value of $\tau_{eff}$ or, equivalently, reduces the value of N for which the strain rates obtained from (28) agree with measured values.

In order to convert Eqn. (28) into a constitutive equation between the flow stress $\bar{\tau}$ in simple shear and the shear strain rate $\dot{\bar{\gamma}}^p$ we use $D = K\mu b/\bar{\tau}$ (Cf. Eqn. (14)), where K is a constant, to eliminate D. The resolved shear stress $\bar{\tau}_r$ and shearing rate $\dot{\gamma}$ are replaced by $\kappa\bar{\tau}$ and $\dot{\bar{\gamma}}^p/(M\kappa)$, respectively, where $\kappa$ and M are constants (e.g. for the assumed case of three equivalent slip systems the constants are $M = 3$ and $\kappa = 0.65$). Substitution of these expressions into (28) gives the constitutive equation

$$\dot{\bar{\gamma}}^p = \frac{C\bar{\tau}^3}{B\mu^2 q((\kappa + \eta)\bar{\tau};\; \alpha,\; \xi)}$$ (29)

where C is a dimensionless constant,

$$C = \frac{\pi\sqrt{2}\; M\kappa(\kappa + \eta)}{4NK^2}$$ (30)

and $q((\kappa + \eta)\bar{\tau};\; \alpha,\; \xi))$ is the dimensionless quantity enclosed in { } in Eqn. (28).

The effective stress is replaced by $(\kappa + \eta)\bar{\tau}$ where $\eta\bar{\tau}$ represents the long-range stress-field $\tau_{LR}$. The factor $(1 - \tau_0/\tau_{eff})$ is replaced by $\zeta$.

Except for $\tau_{eff} \gg \tau_c$ or $\tau_{eff} \simeq \tau_0$, the quantity q in Eqn. (29) varies slowly with $\bar{\tau}$ and the shearing rate varies as $\bar{\tau}^3$. For $\tau_{eff} \gg \tau_c$ the quantity q becomes proportional to $\bar{\tau}$ and the shearing rate varies as $\bar{\tau}^2$. Such proportionality between $\dot{\gamma}^p$ and $\bar{\tau}^2$ at ultra-high shearing rates has also been predicted by Grady [18] based on an analysis of wave profiles for steady shock waves. As $\tau_{eff}$ reduces to $\tau_0$ the predicted plastic strain rate $\dot{\gamma}^p$ reduces to zero. Thus, $\tau_0$ represents a threshold stress, below which the model being considered is not applicable. At these lower stress levels, the waiting times before dislocations can overcome obstacles by means of thermal motion are significant and would have to be included in Eqn. (27).

Equation (29) is plotted in Fig. 7 for comparison with measurements of the pressure-shear experiments on specimens lapped from bulk material. Values used for the parameters are those discussed in the text (e.g. N = 12, M = 3, $\kappa$ = 0.65) as well as those which are representative of the resolved shear stress distribution $\tau_R(x)$ shown in Fig. 6 (i.e. $\alpha$ = 0.1, $\zeta$ = 0.1, $\eta$ = 0.5). The constant K is taken to be K = 8.5, which is the average of the values corresponding to Eqns. (5) and (14) obtained from Refs. [11] and [13], respectively. The curve passes through several data points, but appears to be steeper than the overall trend of the data. This discrepancy in the steepness of the curve can be reduced by extending the model to account for waiting times required to overcome obstacles at low stress levels. The resulting retardation of dislocation motion at low stress levels would preferentially reduce the strain rate at the lower stress levels and thereby reduce the slope of the curve in Fig. 7.

## CONCLUDING REMARKS

Overall, the agreement between the predictions of the model and the results of the experiments is viewed as supportive of the basic elements of the model. Although many approximations are made, the model describes a real dislocation mechanism in which all constants are obtained from measurements and observations made by others without consideration of ultra-high strain rate experiments. Of course, the model is deterministic and one can expect that if only a small fraction of the cells operate simultaneously, then the dislocation mechanism is a highly stochastic process involving the mutual interactions of many dislocations. Consequently, elementary models which do not take explicit account of the statistical characteristics of the dislocation configurations can be expected to be limited in their prediction capability. Fully successful modeling appears to require insightful modeling of the interaction of dislocations and the evolution of dislocation structures. On the other hand, the modeling of the resistance of the lattice to the motion of dislocations appears to be less critical to the development of a satisfactory description. Furthermore, if only one dislocation is sweeping across a cell at a time, then the modeling of the mutual interaction of high velocity dislocations should be relatively unimportant to the development of successful constitutive models for plastic flow at high strain rates.

# REFERENCES

1. Kolsky, H., "An Investigation of the Mechanical Properties of Materials at Very High Rates of Loading," Proc. Phys. Soc. London, Series B, 62, 676, 1949.

2. Klopp, R.W. and Clifton, R.J., "Pressure-Shear Plate Impact Testing," Metals Handbook: Mechanical Testing, Vol. 8, 9th Edition, 230, 1985.

3. Kim, K.S., Clifton, R.J., and Kumar, P., "A Combined Normal and Transverse Displacement Interferometer with an Application to Impact of Y-cut Quartz," J. Appl. Phys. 48, 4131, 1977.

4. Klopp, R.W., Clifton, R.J., and Shawki, T.G., "Pressure-Shear Impact and the Dynamic Viscoplastic Response of Metals," Mechs. of Mat'ls. 4, 375, 1985.

5. Huang, S., Clifton, R.J., "Dynamic Plastic Response of OFHC copper at High Shear Strain Rates," Proceedings of IUTAM Symposium on Macro- and Micro-Mechanics of High Velocity Deformation and Fracture, held in Tokyo, Japan.

6. Klopp, R.W., "Plasticity of Aluminum and Iron at High Shear Strain Rate and High Pressure," Ph.D. Thesis, Brown University, Providence, R.I., 1987.

7. Follansbee, P.S. and Kocks, U.F., "A Constitutive Description of the Deformation of Copper Based on the Use of Mechanical Threshold Stress as an Internal State Variable," Acta Met. 36, 81, 1988.

8. Gray, George T., III, Private Communication.

9. Mughrabi, H., "Description of the Dislocation Structure After Unidirectional Deformation at Low Temperatures," in Constitutive Equations in Plasticity, edited by A.S. Argon, MIT Press, 199, 1975.

10. Essman, U., "Elektronenmikroskopische Untersuchung der Versetzungsanordnung verformter Kupfereinkristalle," Phys. Stat. Sol. 17, 725, 1966.

11. Gottler, E., Doctorate Thesis, Technical University, Braunschweitz, West Germany, 1973.

12. Edington, J.W., Phil. Mag. 19, The Influence of Strain Rate on the Mechanical Properties and Dislocation Substructure in Deformed Copper Single Crystals," 1189, 1969.

13. Staker, M.R., and Holt, D.L., "The Dislocation Cell Size and Dislocation Density in Copper Deformed at Temperatures Between 25 and 700°C," Acta Met. 20, 569, 1972.

14. Hutchinson, J.W., "Bounds and Self-Consistent Estimates for Creep of Polycrystalline Materials," Proc. Roy. Soc. Lond. A 348, 101, 1976.

15. Holt, D.L., "Dislocation Cell Formation in Metals," J. Appl. Phys. 41, 3197, 1970.

16. Jassby, K.M., and Vreeland, T., Jr., "An Experimental Study of the Mobility of Edge Dislocations, Phil. Mag. 21, 1147, 1970.

17. Campbell, J.D. Simmons, J.A. and Dorn, J.E., "On the Dynamic Behavior of a Frank-Read Source," J. Appl. Mech. 28, 447, 1961.

18. Grady, D.E., "Strain-Rate Dependence of the Effective Viscosity Under Steady-Wave Shock Compression," Appl. Phys. Lett. 38, 825, 1981.

19. Senseny, P.E., Richman, M.H., and Duffy, J., "The Influence of Annealing Temperature on the Strain Rate Sensitivity of Copper in Torsion," J. Appl. Mech. 42, 245, 1975.

20. Hartley, K.A. and Duffy, J., Private Communication.

21. Tanimura, S. and Duffy, J., "Strain Rate Effects and Temperature History Effects for Three Different Tempers of 4340 VAR Steel," International Journal of Plasticity, 2, 21, 1986.

| Shot No. | Projectile Velocity $V_0$, mm/$\mu$s | Skew Angle $\theta$,° | Pressure $p \approx -\sigma_{11}$ MPa | Shear Stress MPa | Shear Rate x$10^5$ s$^{-1}$ | Shear Strain $\gamma$ | Specimen Thickness mm |
|---|---|---|---|---|---|---|---|
| 01 | 0.183 | 23.2 | 3840 | 209 | 1.93 | 0.065 | 0.2870 |
| 02 | 0.190 | 26.6 | 3870 | 236 | 2.84 | 0.065 | 0.2337 |
| 04 | 0.179 | 22.0 | 3770 | 213 | 2.73 | 0.065 | 0.1829 |
| 06 | 0.093 | 18.0 | 2010 | 178 | 0.82 | 0.065 | 0.1753 |
| 08 | 0.176 | 20.0 | 3770 | 486 | 71.0 | 2.0 | 0.0030 |
| 09 | 0.188 | 20.0 | 4010 | 523 | 85.0 | 2.0 | 0.0026 |
| 10 | 0.180 | 18.0 | 3880 | 482 | 4.40 | 0.280 | 0.0380 |
| 11 | 0.174 | 22.0 | 3676 | 250 | 4.33 | 0.280 | 0.1034 |
| 13 | 0.189 | 22.0 | 3987 | 274 | 11.3 | 0.280 | 0.0432 |

Table I. Summary of Results on OFHC Copper

| Shot No. | $\overline{D}$ nm | $\overline{\tau}$ MPa | $\overline{\tau}_r$ MPa | $(\Delta t)_{24}$ nsec | $\overline{\dot{\gamma}}^p$ $\mu$sec$^{-1}$ | N |
|---|---|---|---|---|---|---|
| 04 | 450 | 213 | 138 | 0.231 | 0.273 | 18.9 |
| 06 | 600 | 178 | 116 | 0.323 | 0.082 | 32.4 |

Table II. Computed Values of $\Delta t$ and N for Shots 4 and 6
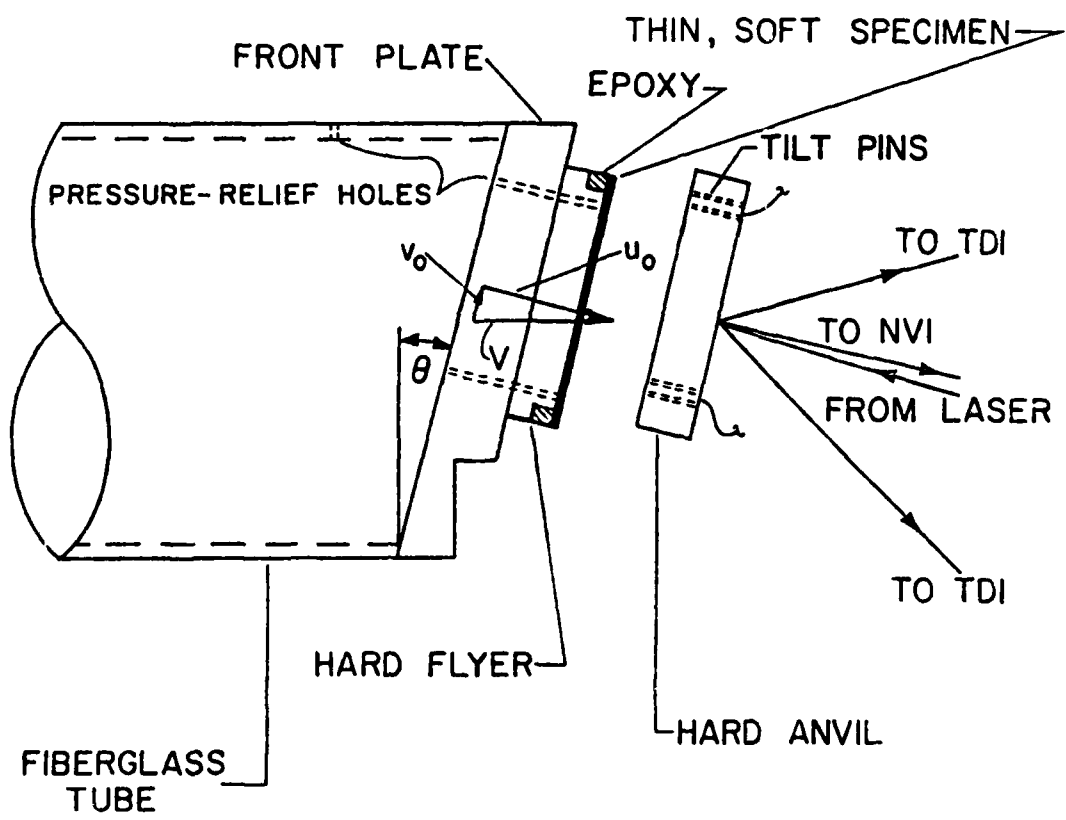
**Figure 1.** Schematic of Configuration for High Strain Rate Pressure-Shear Plate Impact Experiment.

49
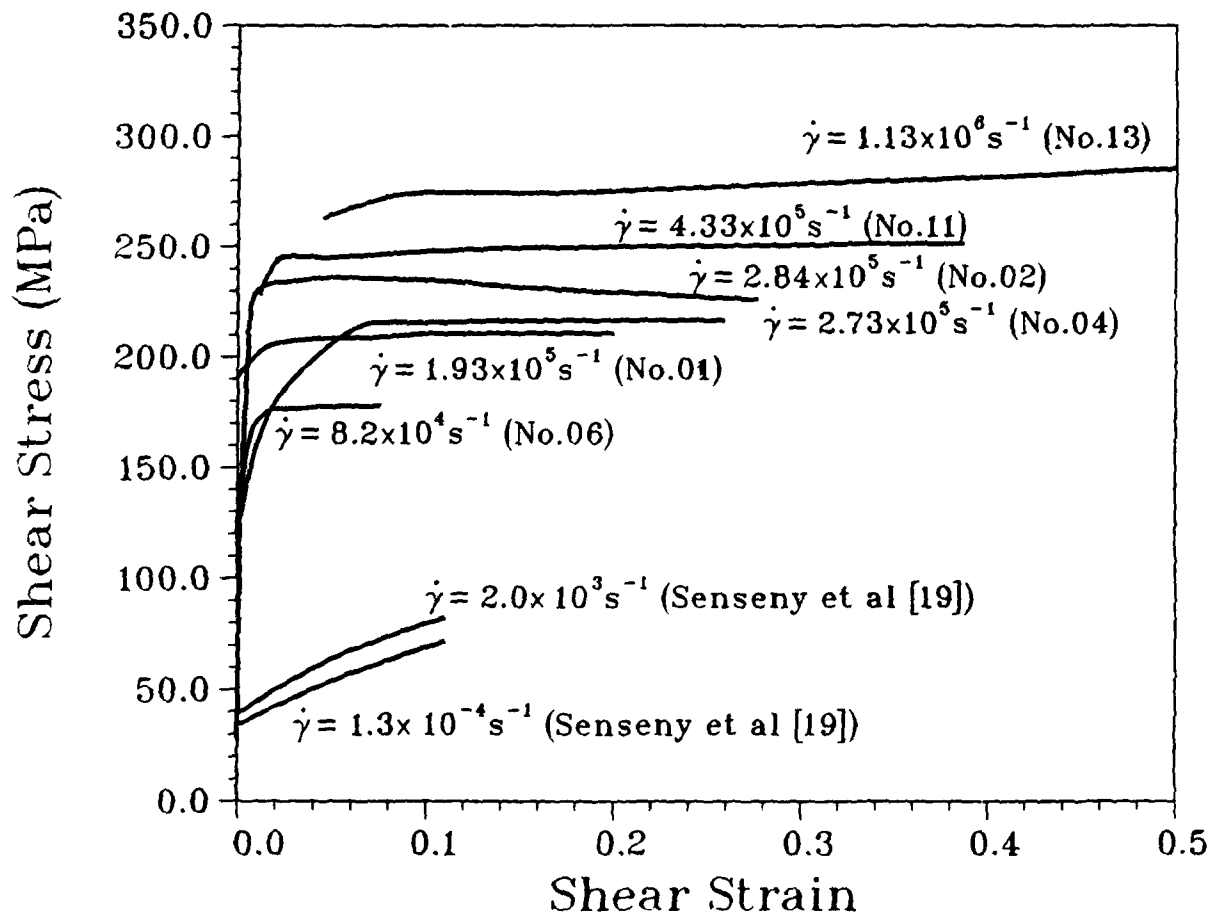
# Bulk OFHC Copper



Figure 2. Dynamic Stress-Strain Curves for OFHC Copper Specimens Lapped from Bulk Material.

50

# Deposited OFHC Copper
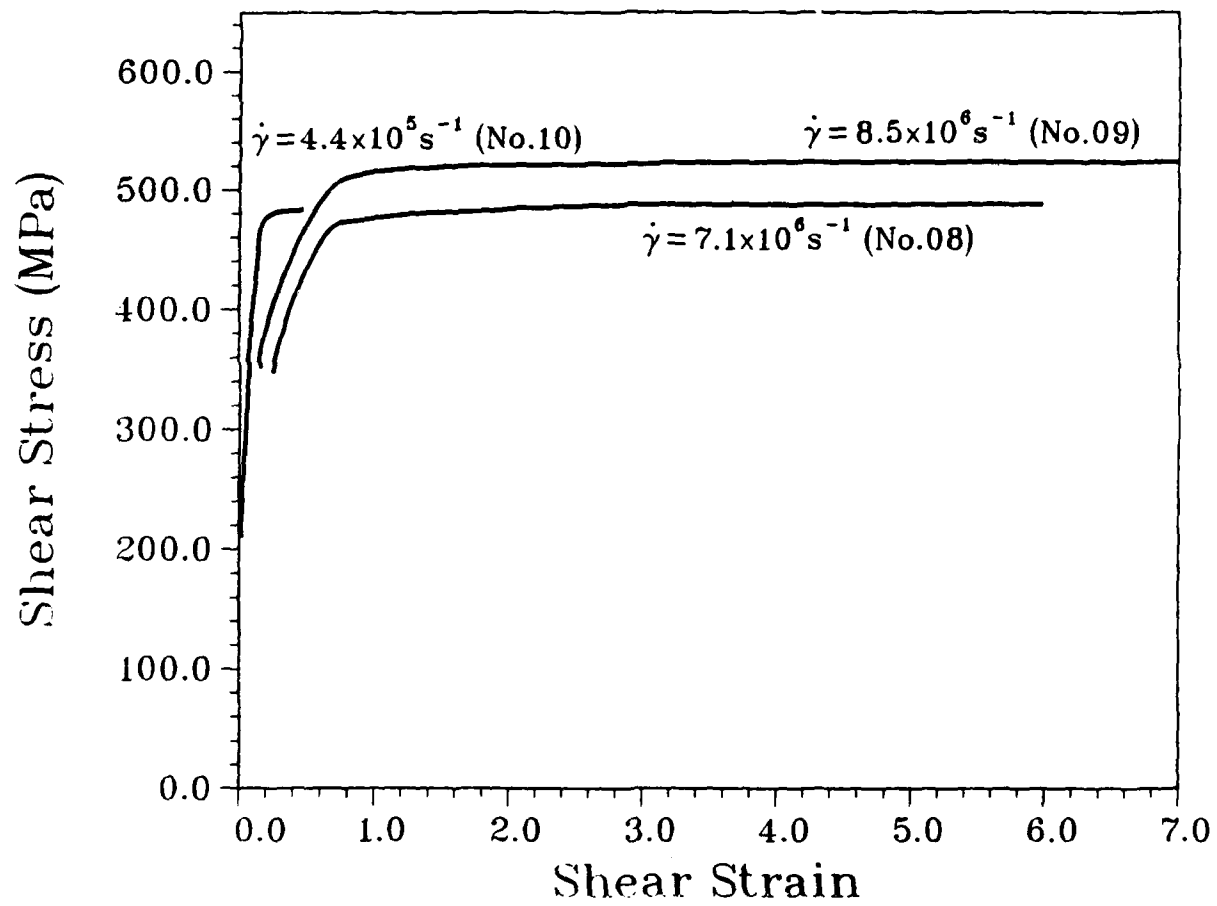


**Figure 3.** Dynamic Stress-Strain Curves for Vapor-Deposited Copper Specimens.
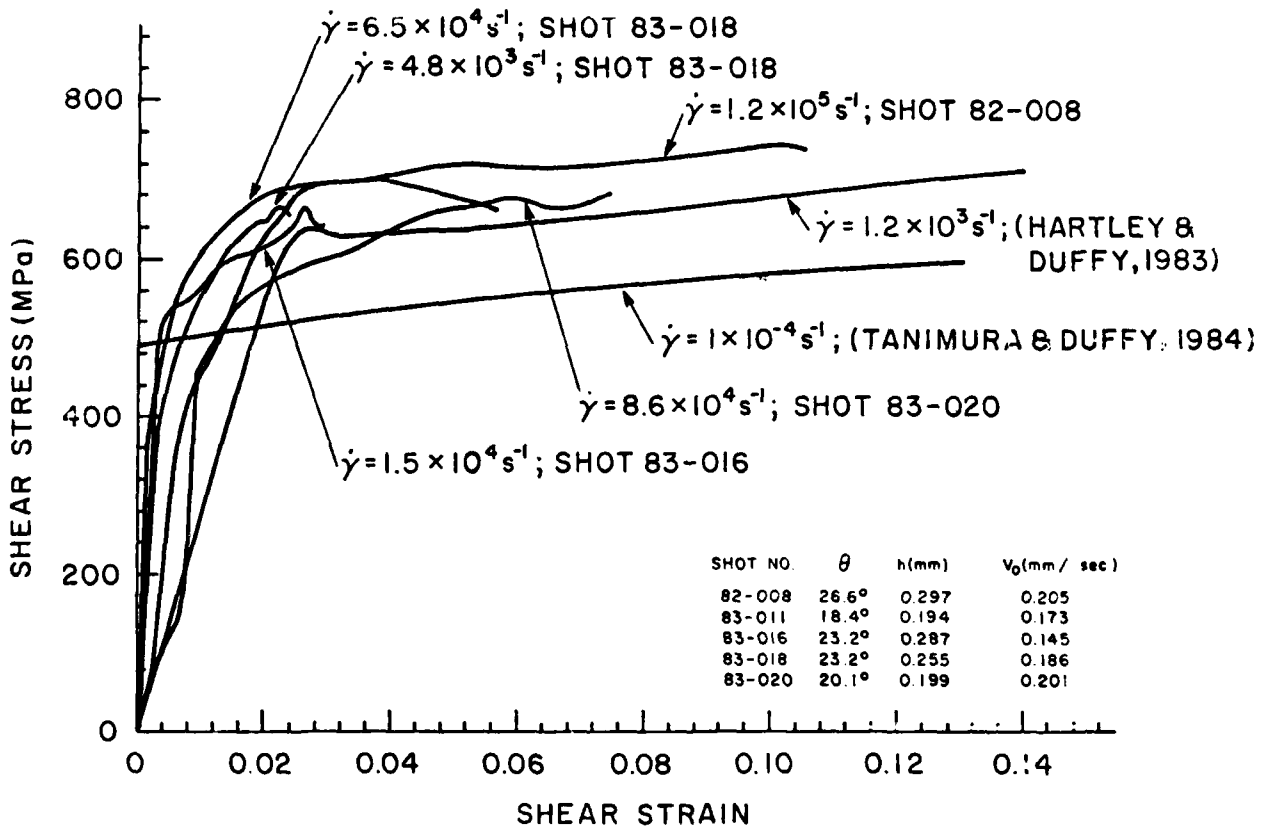
**Figure 4.** Dynamic Stress-Strain Curves for 4340 VAR Steel (600 °C Temper).

52
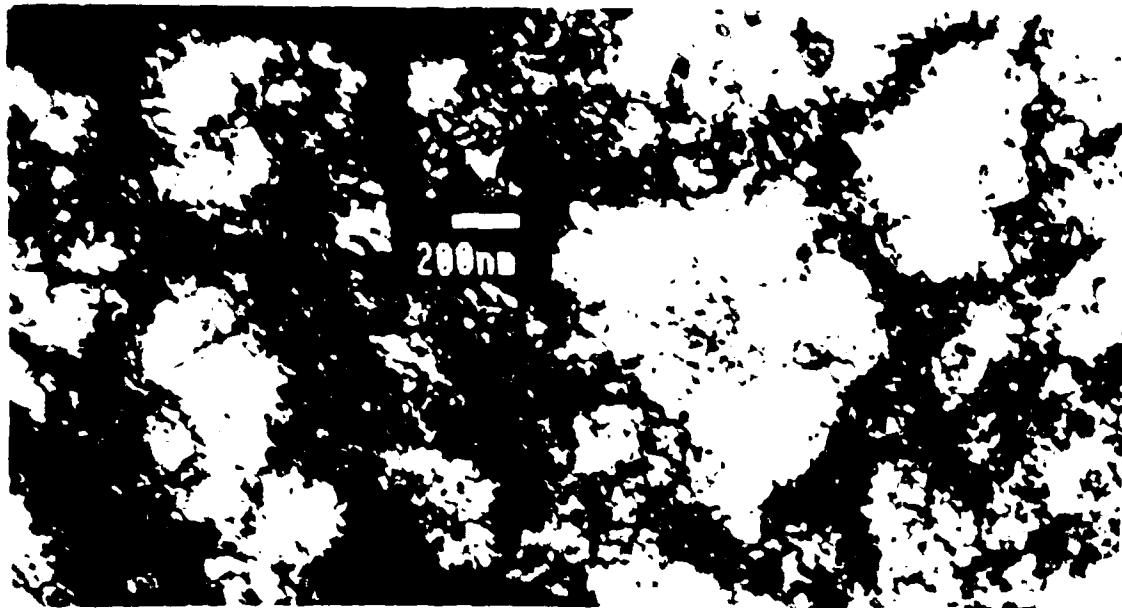
(a)     Shot No. 6



(b)     Shot No. 4

**Figure 5.**    TEM Micrographs of Dislocation Cell Structures Generated in
Pressure-Shear Plate Impact (From  Gray [8]).

53
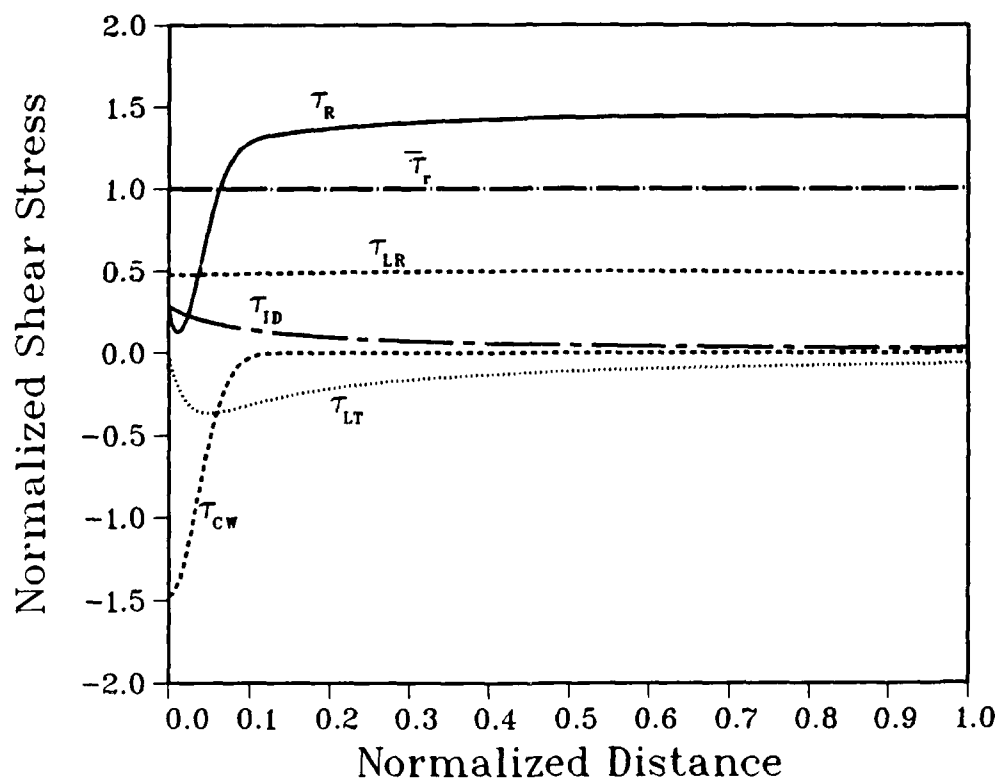
**Figure 6.** Resolved Shear Stress Distribution Experienced by the Center of a Curved Dislocation as it Sweeps Across the Diameter of a Dislocation Cell (Relative Amplitudes correspond to Dislocation Cells in Copper with $\bar{D}$ = 500 nm and h = 50 nm).

# OFHC Copper
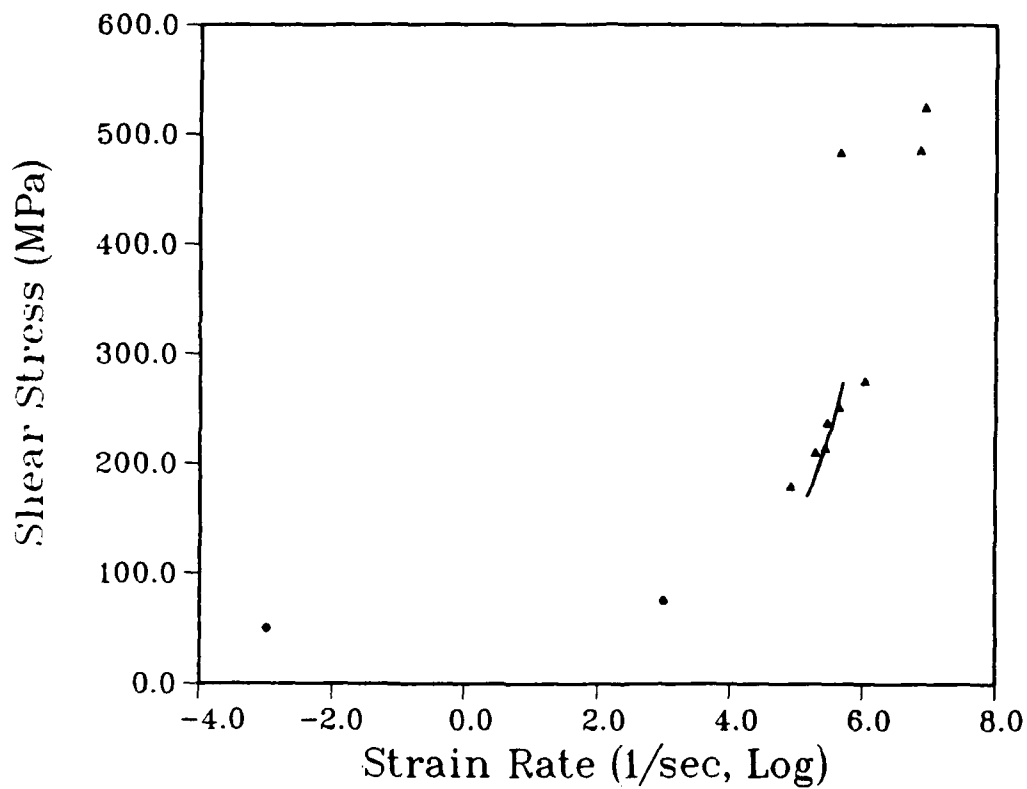


Figure 7.  Strain-Rate Sensitivity of OFHC Copper and Comparison with
Predictions of Equation (29).

55

# SOME RESULTS OF DOUBLE SHOCK EXPERIMENTS IN PMMA AND OFHC COPPER

Dattatraya P. Dandekar,  Paula J. Gaeta, and  Markos Hankin

U.S. Army Materials Technology Laboratory, Watertown, MA  02172

## Abstract

This paper deals with the results of a few experiments performed to  (i) compare the deformation behavior of PMMA subjected to successive shocks and releases against when it is subjected to a single shock and release under plane wave conditions, and (ii)  determine the influence of such successive stimuli on the spall threshold of annealed OFHC copper.  In addition, this paper describes a technique developed to conduct shock wave experiments where an impact velocity of less than 0.1 km/s is to be reliably attained.  The results of experiments on PMMA indicate that the observed repeated shock-release wave profiles, up to a stress of 1.17 GPa, can be satisfactorily simulated numerically, using a constitutive equation used to reproduce a single shock-release profile.  The experiments on OFHC copper show that the spall threshold appears to be larger when the copper is subjected to tension following two successive compressions as compared to when it is subjected to tension following a single compression, i.e. in a conventional spall experiment.

# INTRODUCTION

The present work is part of an on going effort to determine the deformation behavior of solids subjected to successive shocks and releases under uniaxial strain conditions. In principle, the need for this type of information is critical only for those material properties which are progressively altered and to some extent irreversible, i.e. those properties which are stress/strain history dependent. Some of the properties which fall in this category are the spall threshold of ductile metals and alloys, elastic stress limits in elastic-plastic materials or workhardening materials, and compression parameter of powder material, i.e. void collapse in powder material. This work gives the results of a few experiments performed on PMMA and OFHC copper to determine their response to two pairs of successive shock and release waves. These experiments may thus be considered to be the first step taken in attaining the goal of determining and understanding the response of a solid to a multiple pair of successive shock and release waves. Two earlier papers dealing with the response of PMMA and Z-cut single crystal sapphire to two pairs of successive shock and release waves below their respective Hugoniot Elastic Limits were reported by Dandekar, Gaeta and Horie [1] and Horie and Dandekar [2]. This work elucidates (i) the deformation behavior of PMMA subjected to a successive pair of shock and release waves where the shock stress exceeds the Hugoniot Elastic Limit, and (ii) the effect of successive shocks on the spall threshold of OFHC copper in the annealed condition.

## EXPERIMENTAL DETAIL

A general configuration for the double shock-release wave (two successive shock and release waves) experiments is shown in Fig. 1. In these experiments the projectile consisted of two flat disks separated by a predetermined gap and mounted parallel to each other on an aluminum carrier. These disks were normal to the axis of the carrier or sabot and are identified as flyers 1 and 2 in Fig. 1. The target assembly consisted of several flat disks with mutually parallel opposing faces, between which manganin gages were embedded to determine the stress wave profiles generated in the disk materials due to the impact of the projectile on the target at a measured impact velocity. In the case of spall experiments in OFHC copper, where the stress profiles were not recorded, the target was monolithic, i.e. it consisted of a single disk. Typical dimensions of the disks of PMMA and OFHC copper used in the experiments performed for the present work are given in Table 1. In these experiments the flyers and targets were of the same diameters. The diameters of the disks making up the flyers and targets for PMMA and OFHC copper were $50 \pm 1$ mm. These diameters were large enough to insure continuance of uniaxial strain conditions for the time durations of measurements in PMMA and for inducement of tensions in OFHC copper targets. Table 1 shows that these experiments were performed by symmetric impact, the disk material, either PMMA or OFHC copper, being the same for both the flyers and target in a given experiment. The disks used in the double shock release wave experiments were flat to 6-8 light bands and their opposing faces were mutually parallel to within 10 μm.

The controlling variables in this type of experiment are shock durations, determined by the thickness of the two flyers, stress free state duration between the successive shocks, determined by the gap thickness, shock magnitudes of the successive shocks, jointly determined by the impedance of the flyers and the impact velocity. The observables in these

58
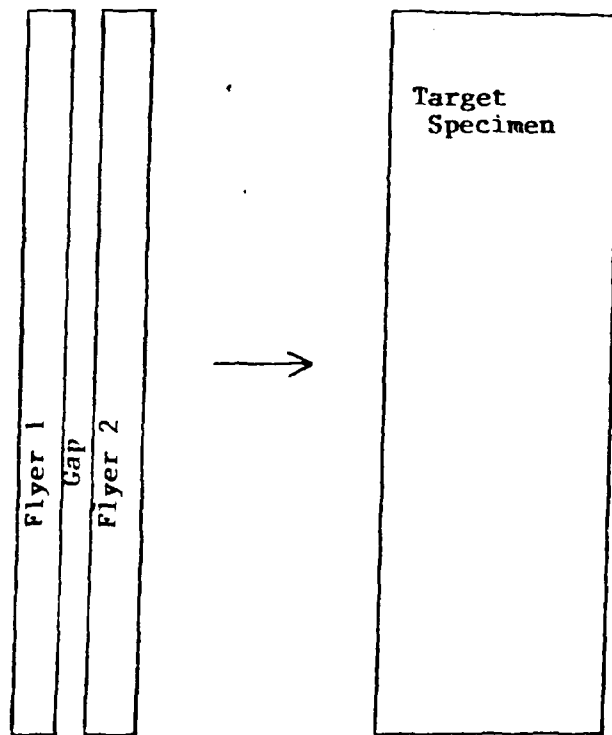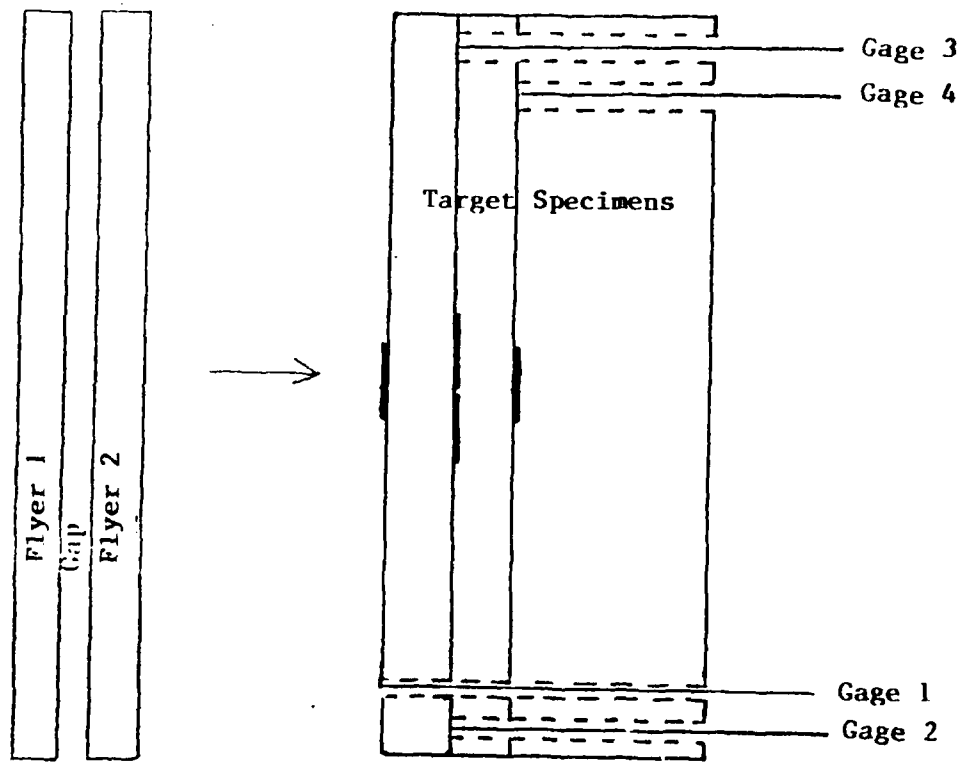
Figure 1. Configurations for Double Shock Experiments

# Table 1

## Tabulation of Parameters in OFHC Copper and PMMA Experiments

| Material | Experiment | Impact Velocity (km/s) | Flyer 1 Thickness (mm) | Gap (mm) | Flyer 2 Thickness (mm) | Target Thickness (mm) | Calculated Location of Tensile Planes from Impact Surface (mm) $P_1$ | $P_2$ | Location of Gages from Impact Surface (mm) Gages 2,3 | Gage 4 |
|---|---|---|---|---|---|---|---|---|---|---|
| OFHC Copper | 74201 | 0.0843 | 1.12 | 0.1 | 1.38 | 5.79 | 4.6 | 1 | | |
| OFHC Copper | 81103 | 0.0888 † | 1.42 | 0.06 | 1.47 | 5.81 | 4.4 | 1.6 | | |
| OFHC Copper | 80202 | 0.1176 | 1.45 | 0.15 | 1.54 | 5.89 | 4.5 | 3 | | |
| PMMA | 67002 | 0.4024 | 2.24 | NA | NA | 22.05 | | | 4.33 | 8.13 |
| PMMA | 70103 | 0.4001 | 3.33 | 0.59 | 3.16 | 22.55 | | | 4.34 | 8.63 |
| PMMA | 70204 | 0.4008 | 3.23 | 0.64 | 3.12 | 21.22 | | | 3.78 | 7.97 |
| PMMA | 71305 * | 0.6141 | 3.47 | 0.86 | 3.33 | 21.35 | | | 4.04 | 8.32 |
| PMMA | 72306 * | 0.6085 | 3.26 | 0.91 | 3.06 | 21.57 | | | 4.35 | 8.66 |

† Average velocity. In this experiment the scatter in the velocity readings was greater than normal.

* In these experiments a gage (gage 1) was located at the impact surface.

60

experiments were impact velocity, shock velocity in the target material and stress wave profiles at the various gage depths in the target material.

The impact velocity is measured with an uncertainty of ±0.5 %. The stress wave profiles are recorded by means of manganin foil gages, commercially available from Micromeasurements Inc.. The type of manganin foil gage used in this work is LM-SS-125CH-048. The precision of stress measurements is ± 2.5 %. The relative tilt of the projectile and target at impact was less than 0.5 mrad. As is evident from Table 1 the impact velocity required to conduct the experiments in OFHC copper was generally 0.12 km/s or less. Since it has been found to be difficult to accelerate a 1.5 kg projectile in the AMTL gas gun to 0.1 km/s or less, reliably and repeatably with gas pressure, a new approach had to be developed to conduct these experiments. The new approach consisted of developing a technique which uses atmospheric pressure to accelerate a projectile to a steady velocity of less than 0.1 km/s. In addition to this, a release mechanism for launching the projectile was developed. These two techniques are described below.

## Low Velocity Technique

According to the ideal gas theory the static pressure of a gas is given by:

$$P = (2/3) \, n \, (m V^2/2) \tag{1}$$

where n, m and V are gas density, molecular weight, and mean molecular velocity, respectively

In the case of a projectile moving down a gun tube into a vacuum with gas behind it, the pressure on the rear of the projectile is reduced since the gas molecules are hitting it at a reduced effective velocity: $V_e = (V - V_p)$ where $V_p$ is the projectile velocity. Thus we have:

$$P = \left( \frac{m \, n}{3} \right) V_e^2 \tag{2}$$

This relation will hold for the entire flight of the projectile provided the following assumptions remain valid: (1) The gas density, n remains constant - this implies that flow effects in the gun tube are negligible. (2) V remains constant - i.e. no temperature change.

If we also assume that there is no friction we can calculate the velocity of the projectile at the end of the barrel.

For the purposes of this calculation we can treat the atmosphere as a mixture of 80% $N_2$ and 20 % $O_2$. At 25 °C the molecular speeds of nitrogen and oxygen are 515 m/s and 482 m/s, respectively. Consolidating constants in equation (2) we have:

$$P = 0.8 \, C_1 \left( 515 - V_p \right)^2 + 0.2 \, C_2 \left( 482 - V_p \right)^2 \tag{3}$$

where $C_1$ and $C_2$ are nm/3 for $N_2$ and $O_2$, respectively.

At standard atmospheric pressure ( 0.101 MPa ) the values of $C_1$ and $C_2$ are 0.3808 and 0.4347 Pa $s^2/m^2$, respectively. These values are modified by a multiplicative ratio ( B/29.92 ) where B is the actual barometric pressure in inches of Hg. Since the

pressure acts on the rear face of a projectile of area (A) and mass (M), the acceleration of the projectile is given by:

$$a = \left( \frac{AB}{M} \right) \left[ 0.8\, C_1 \left( 515 - V_p \right)^2 + 0.2\, C_2 \left( 482 - V_p \right)^2 \right] \tag{4}$$

Equation (4) was integrated using a simple computer program which gives the velocity of the projectile when it reaches the end of the barrel. ( Note: temperature also has an effect on the equation by changing the mean molecular velocity but it varies the final projectile velocity by less than ± 0.5 % for temperature varying from 0 °C to 40 °C, so it was ignored).  Fig. 2 shows the results of the computer calculations for barometric pressures of 30" and 29" Hg.  Graphs of this type are used to determine the projectile mass needed to achieve the desired impact velocity.  Measured velocities have been within ± 3 % of the calculated values, often better.  So far, we have seen no trend in the errors so the assumptions used in calculating the projectile velocity appear to be valid to within experimental scatter.  Table 2 gives the values for a few of the experiments performed to date.

The projectile is held at the end of the gun barrel with a threaded mild steel rod which has a narrow neck machined in it ( Fig. 3 ).  To fire the projectile, we heat the necked down section of the rod with a propane torch until the neck yields.  This ensures that the projectile is released smoothly, with as little perturbation as possible.

63
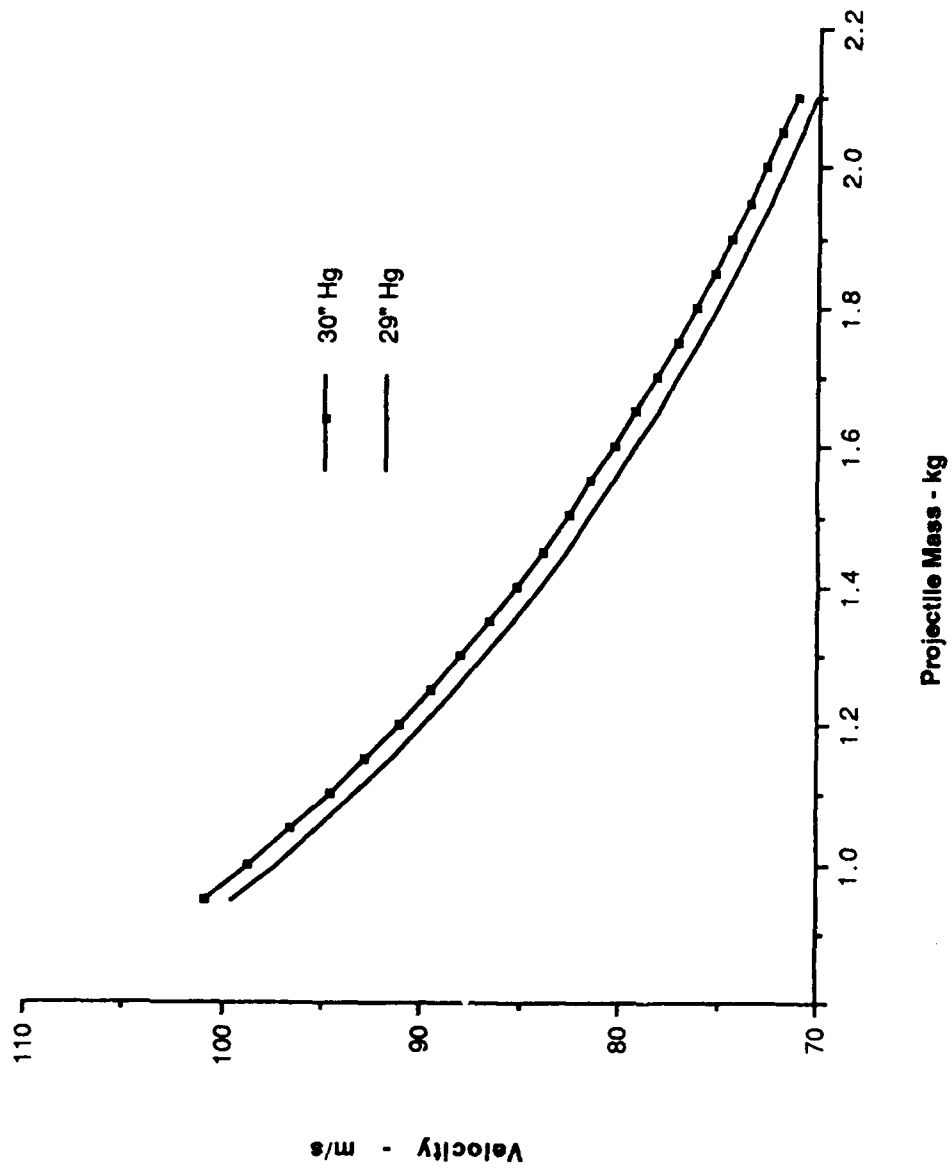
Fig. 2 - Calculated Velocity vs. Projectile Mass

## Table 2.

## Low Velocity Experiments:

### Observed & Caculated Velocity vs.Projectile Mass

| Projectile Mass ( kg ) | Observed Velocity ( m/s ) | Calculated Velocity ( m/s ) | Error (Observed/Calculated) |
|---|---|---|---|
| 1.020 | 96.9 | 97.8 | 0.991 |
| 1.263 | 90.4 | 89.1 | 1.015 |
| 1.400 | 87.4 | 85.2 | 1.026 |
| 1.405 | 87.4 | 85.1 | 1.027 |
| 1.434 | 84.3 | 83.5 | 1.010 |
| 1.445 | 82.7 | 84.0 | 0.985 |
| 2.013 | 74.9 | 73.0 | 1.026 |
| 2.146 | 72.5 | 70.1 | 1.034 |
| 2.162 | 71.2 | 70.2 | 1.015 |
| 2.170 | 71.9 | 70.2 | 1.025 |

Breech

Projectile

Gun Barrel

3/8-16 Threaded Steel Rod
w/ 1" section turned down
to .09" $\varnothing$

Al U-bracket

Al Plate

Vacuum Grease, 1/16" Rubber Sheet
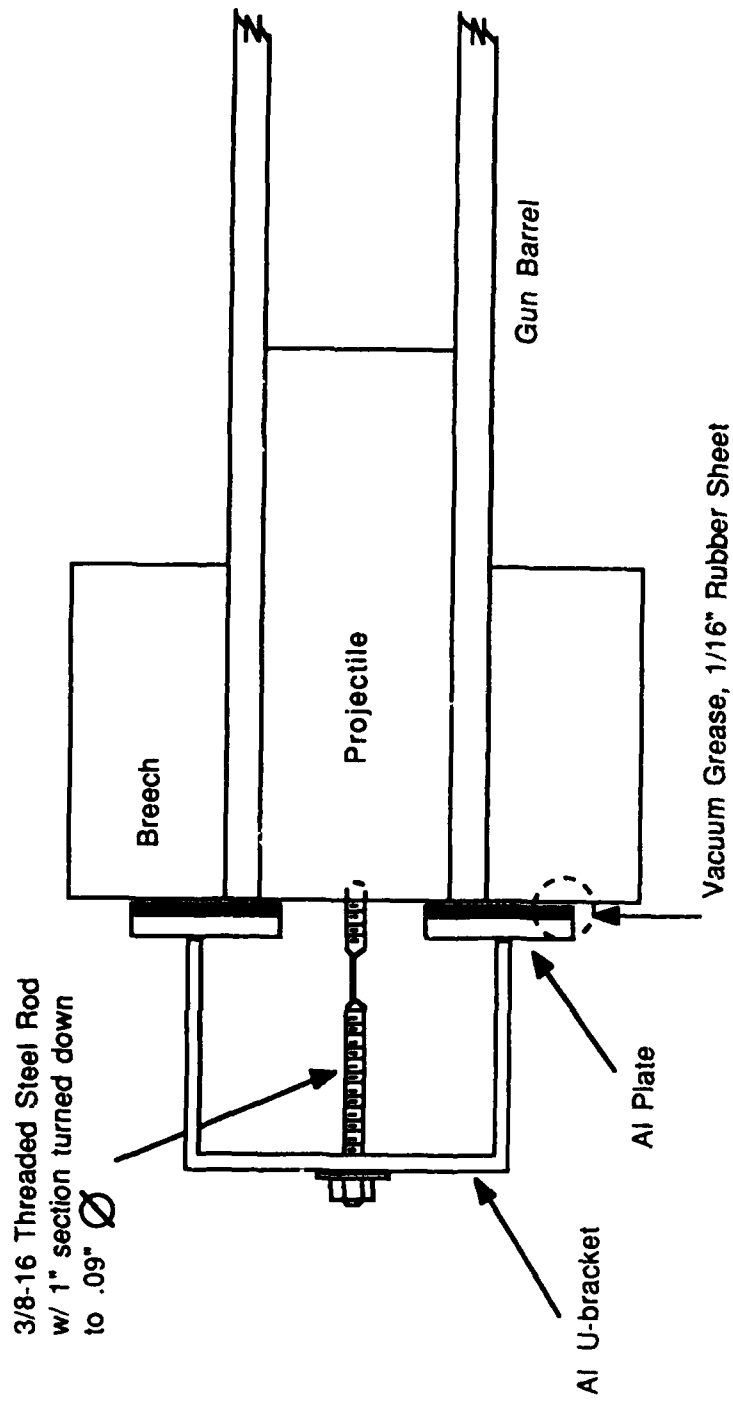
**Fig. 3 - Low Velocity Firing Fixture**

# RESULTS

## PMMA

Tables 1 and 3 give the information about the experimental configuration parameters and a summary of the results of the experiments performed on PMMA. These experiments were conducted to generate stresses in the neighborhood of 0.7 or 1.2 GPa.

As indicated in Table 1, at least one pair of manganin gages, Gages 2 and 3, were imbedded at the same depth in the PMMA to evaluate the repeatability of the manganin gage response under identical experimental conditions to two pairs of shock and release waves. Stress wave profiles recorded by gages 2 and 3 in experiments where the peak stresses were 0.75 and 1.17 GPa are shown in Fig. 4 (a) and (b). These figures show that the stress wave profiles recorded by the manganin gages located at the same depth in PMMA are similar with respect to one another within the accuracy and precision of measurements.

A visual summary of all stress wave profiles recorded by manganin foil gages in various experiments done on PMMA is shown in Figure 5 (a) and (b). Common features of these profiles are:

(i) Shock compression profiles are characterized by an initial shock followed by a more gradual rounding up to peak stress as has been observed by other workers [3 and 4]. This characterization of compression wave profiles is valid for both the first and for the second shock, following the release of the first shock. A superposition of these two shock profiles indicates that, within the resolution of the manganin foil gages, the rate sensitivity of PMMA, represented by the magnitude of the relaxation time, has not changed even when the magnitude of the compressive stress exceeds the HEL of PMMA.

(ii) The release wave profiles do not show any unusual features when the peak compressive stress is of the order of 0.75 GPa. This is true for the release wave profiles

67

Table 3

Summary of Double Shock Experiments in PMMA

| Experiment | 67002 | | 70103 | | 70204 | | 71305 | | 72306 | |
|---|---|---|---|---|---|---|---|---|---|---|
| | Shock & Release | | Shock & Release | | Shock & Release | | Shock & Release | | Shock & Release | |
| | first | second | first | second | first | second | first | second | first | second |
| VELOCITY (km/s) | | | | | | | | | | |
| impact | 0.4026 | NA | 0.4001 | NA | 0.4008 | | 0.6141 | | 0.6085 | |
| shock | | | | | | | | | | |
| measured | 3.162 | NA | 3.249 | NA | 3.123 | 3.196 | 3.337 | 3.338 | 3.197 | 3.223 |
| calculated | 3.303 | | 3.303 | | 3.303 | | 3.351 | | 3.350 | |
| particle | 0.2012 | | 0.20005 | | 0.2004 | | 0.30705 | | 0.30425 | |
| release | | | | | | | | | | |
| leading edge | 3.667 | NA | 3.824 | NA | 3.666 | 3.619 | 4.102 | NA | 4.116 | NA |
| calculated | 3.62 | | 3.62 | | 3.62 | . | 4.094 | | 4.088 | |
| trailing edge | 2.524 | NA | 2.597 | NA | 2.691 | 2.658 | 2.414 | NA | 2.466 | NA |
| STRESS (GPa) | | | | | | | | | | |
| measured | | | | | | | | | | |
| x=4m | 0.759 | NA | 0.743 | NA | 0.763 | 0.769 | 1.179 | 1.171 | 1.173 | 1.166 |
| x=8mm | 0.735 | NA | 0.717 | NA | 0.737 | 0.730 | 1.112 | NA | 1.130 | NA |
| calculated | 0.754 | | 0.770 | | 0.742 | 0.759 | 1.214 | | 1.157 | |
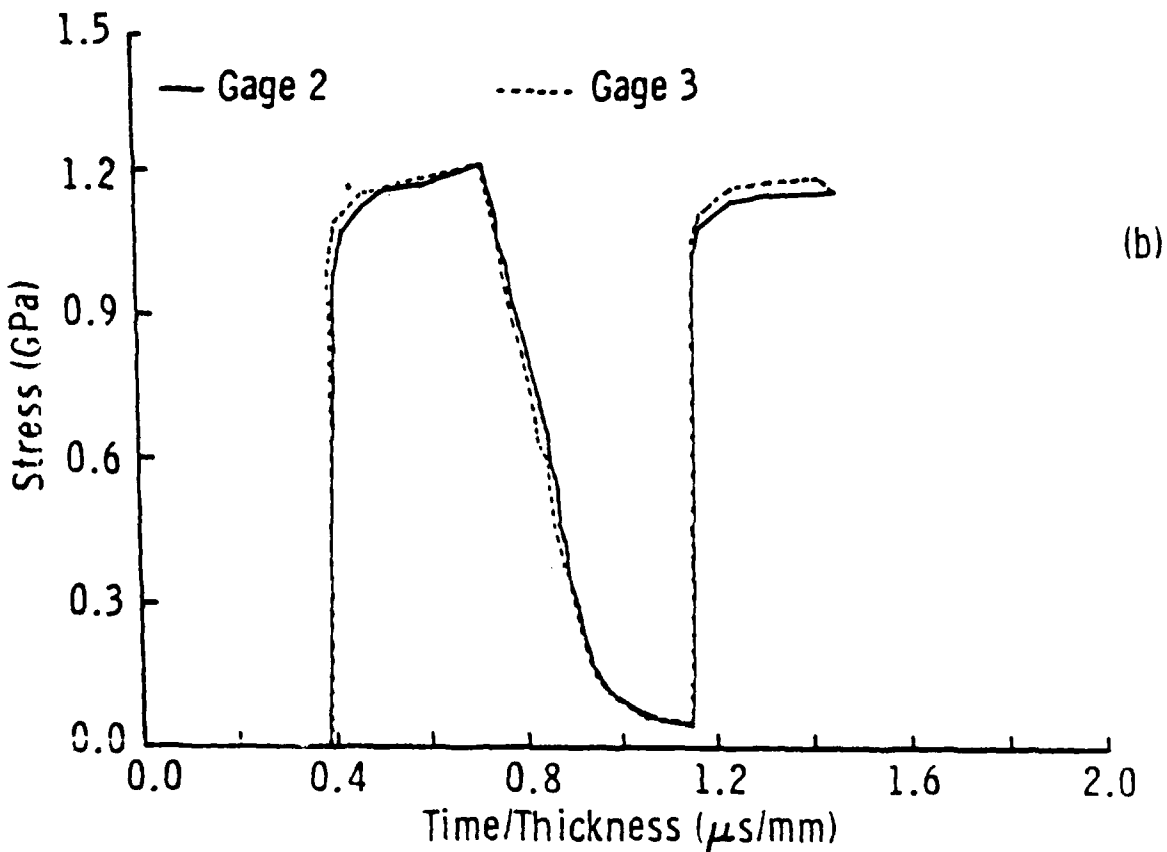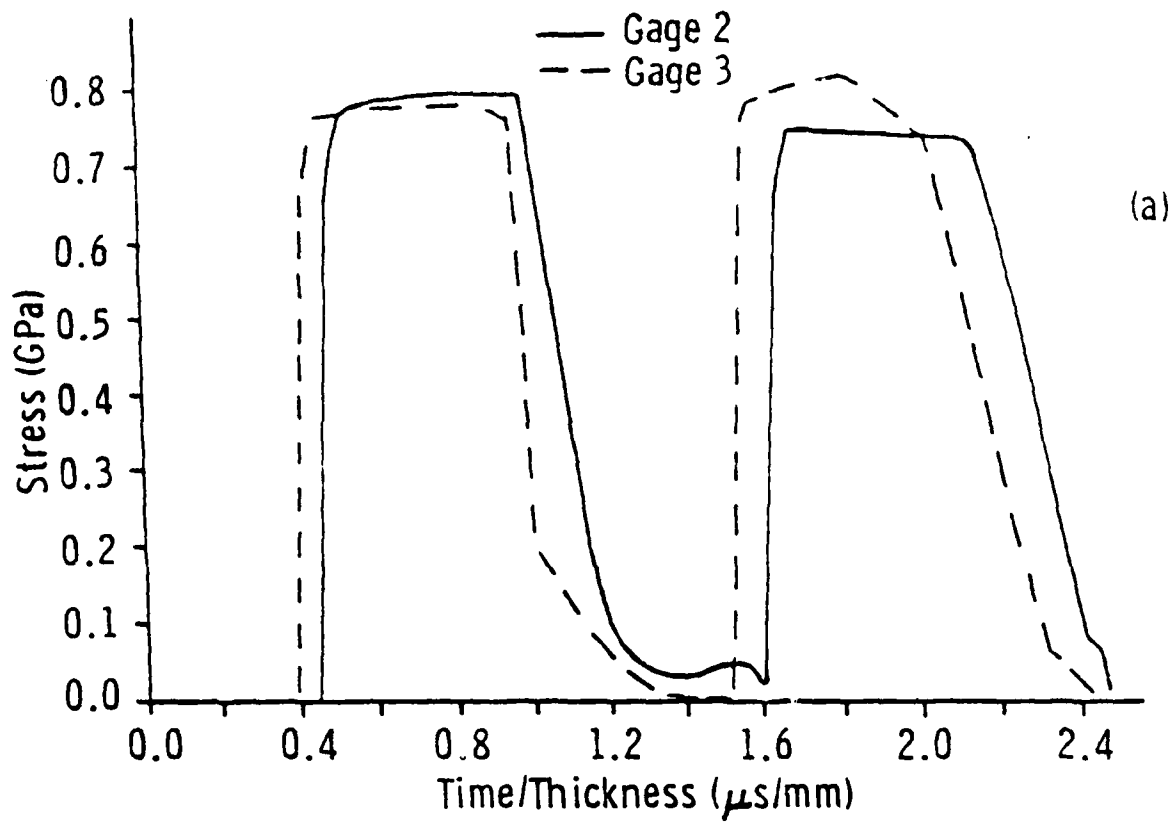
Figure 4. Stress Wave Profiles Measured by Two Gages at
the Same Location in PMMA at 0.7 GPa and 1.2 GPa.

69
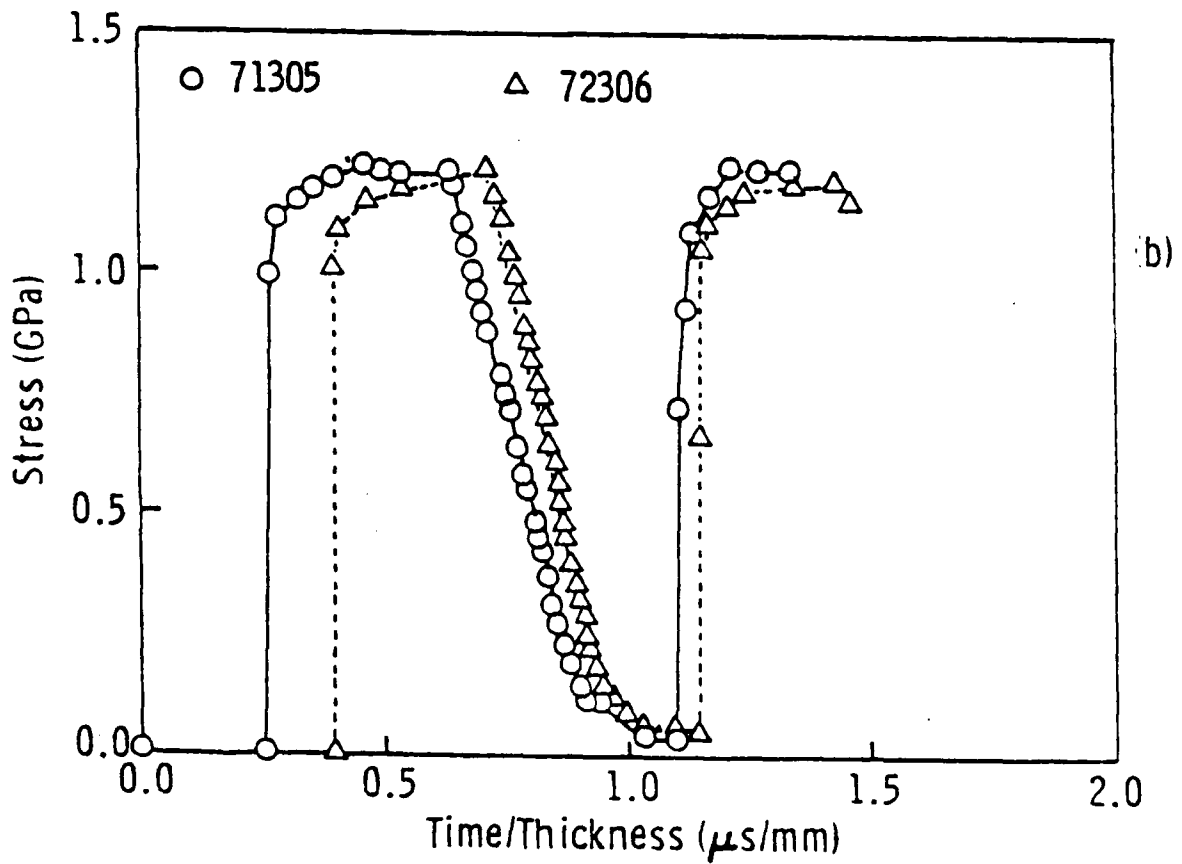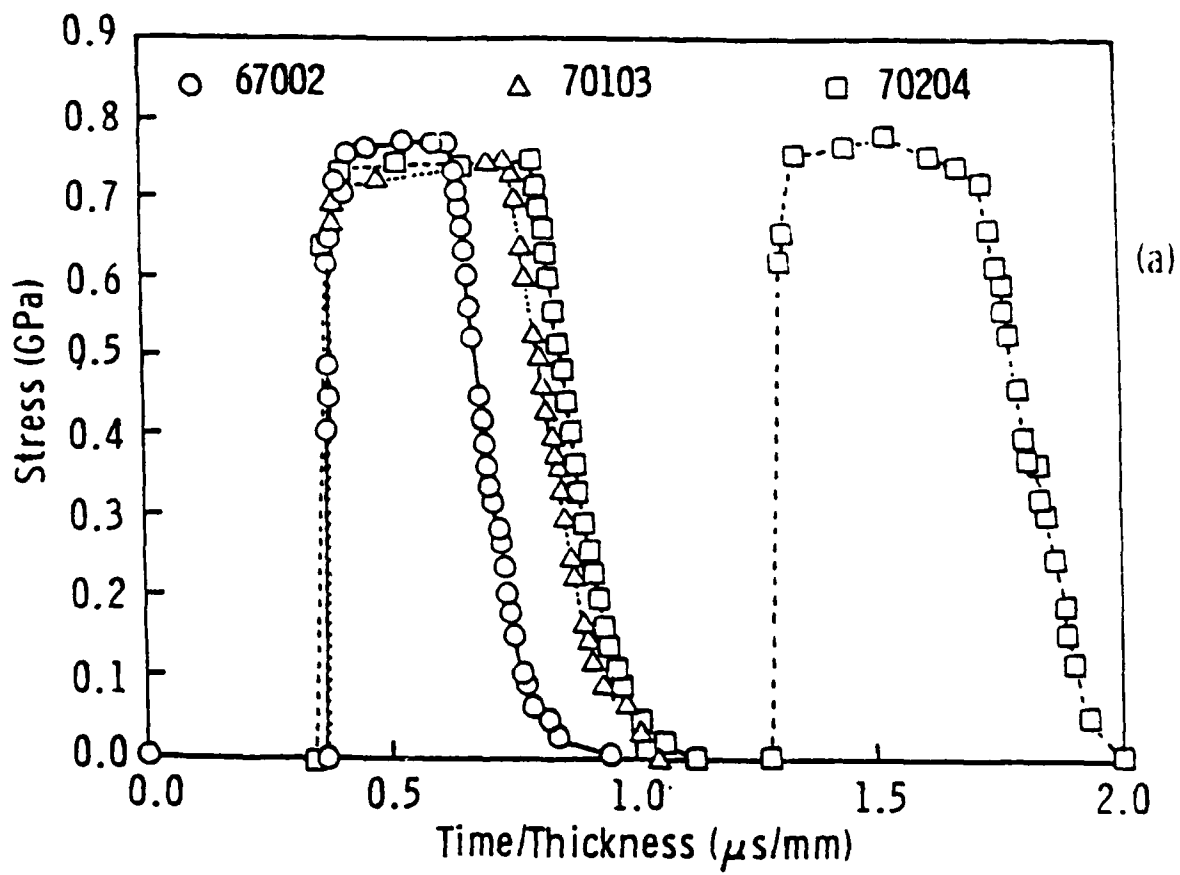
Figure 5. Stress Wave Profiles in PMMA at 0.7 GPa and 1.2 GPa.

following both the first and second shock waves. The release wave profiles show a well known dispersive character.

(iii) The release wave profile following the first shock wave amplitude of 1.17 GPa clearly shows a pattern similar to that of an elastic-plastic solid as also previously observed by Barker and Hollenbach [3]. Unfortunately, in the experiments 71305 and 72306 release wave profiles following the second shock were not recorded.

(iv) The magnitude of stress recorded by the manganin foil gages following the compressive shock state is very close to being stress free.

(v) None of the profiles show the existence of an HEL in PMMA which is consistent with the observations of other researchers.

Shock wave data gathered during the performance of the experiments on PMMA are analyzed by comparing the observed values of shock velocities, leading edge rarefaction wave velocities and stress with the values of the respective parameters on the basis of an elastic-plastic model for PMMA. An additional analysis is performed through numerical simulations of the observed wave profiles recorded in PMMA at 0.75 and 1.17 GPa.

The calculations of shock velocity, leading edge rarefaction velocities and peak stress are done by following the procedure outlined below.

Since the peak stress in PMMA is attained by the propagation of a single wave irrespective of the magnitude of stress, the jump condition

$$\sigma = \rho_0 U u \tag{5}$$

is applied to calculate stress ( $\sigma_t$ ) from the measured values of initial density ( $\rho_0$ ), shock velocity ( $U$ ) and peak particle velocity ( $u$ ). In the calculations of the shock wave and leading edge rarefaction wave velocities, use is made of measured variations in the values of elastic constants of PMMA under hydrostatic pressure to 1 GPa by Schock et al. [5].

The above mentioned data are used first to calculate mean pressure (P) corresponding to the stress given by (1) by using the relation

$$P = \frac{1 + v\,(P) \bullet \sigma_0}{3\,[\,1 - v\,(P)\,]} = K(P) \bullet \eta$$

(6)

Where $v\,(P)$ and $K(P)$ are the Poisson's ratio and the bulk modulus expressed as a function of pressure P, $\eta$ is the ratio of the change in volume ($\Delta V$) with respect to the initial volume ($V_i$) and $\sigma_0$ is the measured stress.

The variations of $v\,(P)$ and $K(P)$ are obtained from the data of Schock et al. [5]. The value of P allows us to calculate $V/V_i$ at P, i.e. the density of PMMA at P. This in conjunction with the mass and momentum conservation relations yield the following for shock velocity U:

$$U = \left( \frac{\rho\,(P) \bullet \sigma_0}{\rho_0\,[\,\rho\,(P) - \rho_0\,]} \right)^{\frac{1}{2}}$$

(7)

The leading edge velocity is simply the longitudinal sound speed at P which is obtained from the above mentioned high pressure data.

The results of these calculations are given in Table 3. The observed and calculated values of shock parameters are very close indeed. The observed values are also in good agreement with those measured by Barker and Hollenbach [3].

The numerical simulations of the experiments described above were done by using an elastic-plastic material model on a general purpose one dimensional wave propagation code called KOH. The equation of state used for PMMA was derived from the measurements of longitudinal and shear sound wave velocities in PMMA to 1 GPa by Schock et al.

72

[5]. The equation of state used for stresses below the Hugoniot Elastic Limit of PMMA (0.38 GPa) is:

$$P = 5.92\ r + 32.0\ r^2 + 80.0\ r^3 \qquad (8)$$

where r = the ratio of current density to initial density.

For stresses above 0.38 GPa the equation of state is:

$$P = 0.05 + 5.92\ r + 32.0\ r^2 + 80.0\ r^3 \qquad (9)$$

Since the HEL of PMMA is not observed because the plastic wave velocity exceeds the longitudinal wave velocity at 0.38 GPa, the equation of state is irreversibly adjusted such that at the transition pressure, 0.38 GPa, the Hugoniot has a smooth contact with the Raleigh line [2 & 6]. The results of numerical simulations of the wave profiles obtained in experiments performed on PMMA at impact velocities of 0.4088 and 0.614 km/s, corresponding to experiments 70204 and 71305, are shown in Fig. 6 and 7, respectively. The calculated (numerically simulated) and observed wave profiles shown in Fig. 6 and 7 are in very good agreement. In other words, the elastic-plastic model used in the present work generates wave profiles which match the observed double shock-release wave profiles in PMMA to 1.2 GPa.

## OFHC Copper

Shock experiments for OFHC copper were designed to determine whether or not the spall threshold of OFHC copper was history dependent. The basis for the postulate of history dependence of spall threshold of OFHC copper was the cumulative information pertaining to the observed low magnitude of the HEL compared to the spall threshold of ductile metals and alloys [7 & 8]. This relationship suggested that some plastic deforma-

73
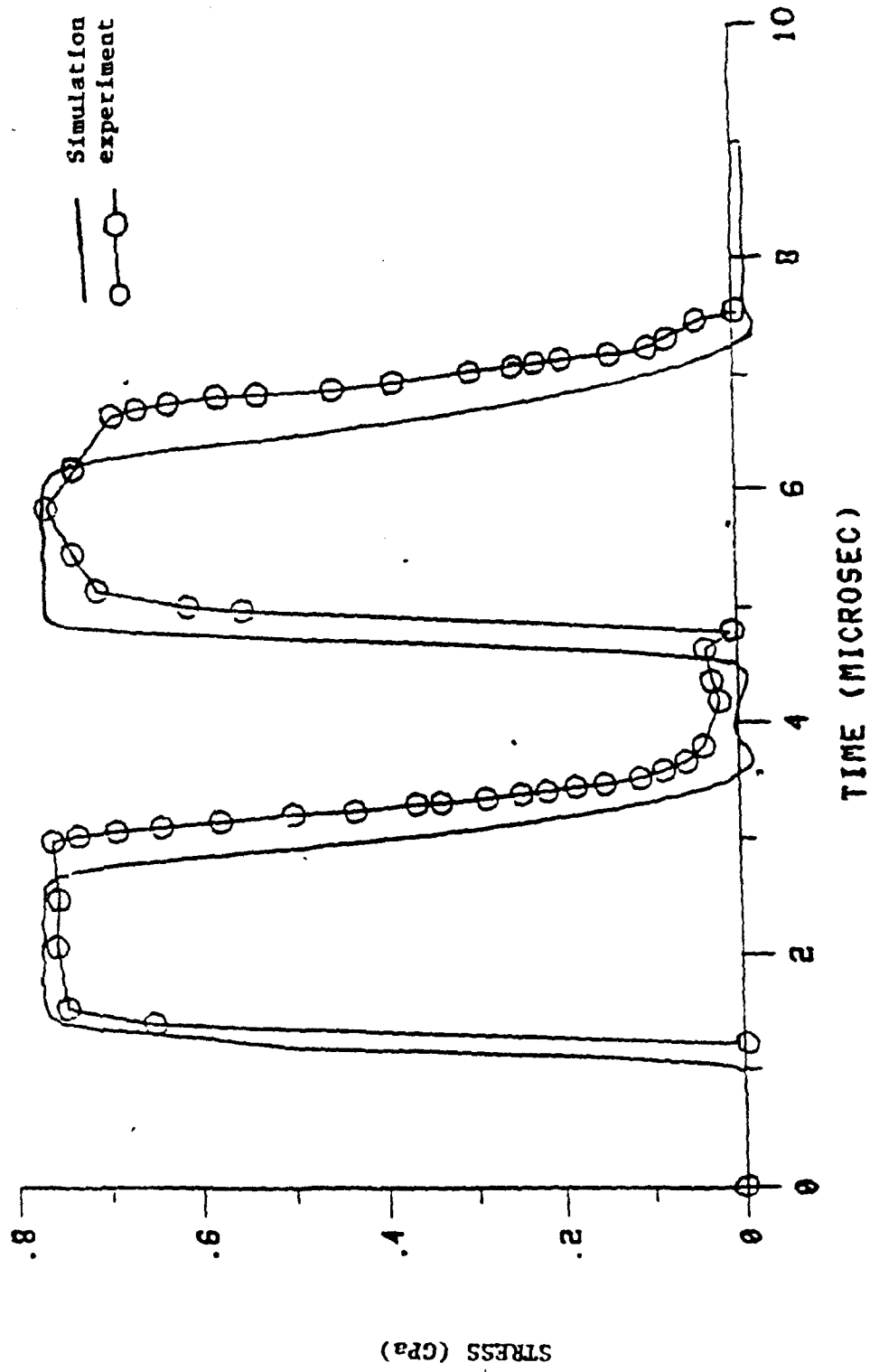
Figure 6. Numerical Simulation of Stress Wave Profile in PMMA at 0.7 GPa.

74
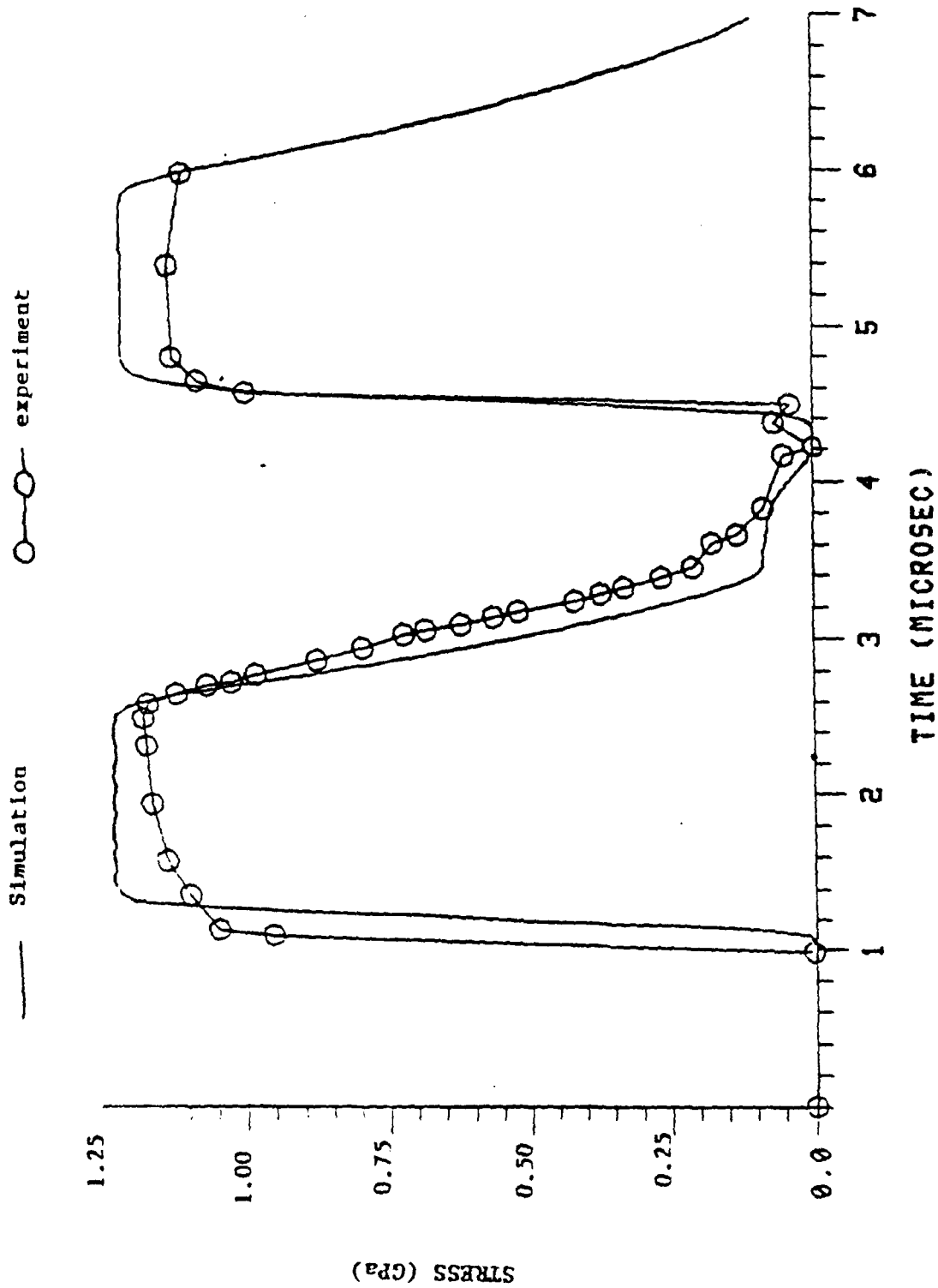
Figure 7. Numerical Simulation of Stress Wave Profile in PMMA at 1.2 GPa.

tion is necessary for the spallation of a ductile material. In other words, the spall threshold of a ductile material should be history ( stress/strain ) dependent. The present set of experiments was designed to determine the effect of single versus double precompression on the spall thresholds of OFHC copper.

The investigation of Stevens and Tuler [9] on hardened 1020 steel and fully hardened 6061-T6 aluminum showed that the effect of shock precompression to 12 GPa on the spall thresholds of these two materials was nonexistent. This simply implies that in these two materials the defect structures generated in the hardened condition were not significantly altered during the precompression and thus the spall threshold remained unchanged. In other words, history dependence of spall threshold is most readily discernable only in materials where there is scope for inducing changes in the microscopic defect structures of a ductile material when subjected to different histories.

The present investigation was, therefore, undertaken to determine the effect of two different shock precompressions on the spall threshold of OFHC copper. The copper used in the present investigation was of 99.99 % purity and was annealed at 400° C for an hour and then cooled.

A general configuration of the experiments performed on OFHC copper is shown in Fig. 1. In these experiments two thin flyer disks of copper separated by a predetermined gap were mounted on a projectile which impacted a thick OFHC copper disk target. These disks were 50 ± 1 mm in diameter. The thickness of the flyers varied between 1.12 and 1.54 mm, while the thickness of the targets was between 5.79 and 5.89 mm. The thickness of the gaps in these experiments varied from 0.06 to 0.15 mm.

The thickness of the two flyers, gap and target were chosen so that the two tension planes $P_1$ and $P_2$ developed in the target during shock wave experiments could be unambiguously identified (Fig. 8 & 9) in the recovered target. Space-time (Fig. 10) and stress-time diagrams (Fig. 8 & 9) show that a tension of a given magnitude develops at the plane $P_1$ after a single shock has propagated in that region of the target. Similarly, a tension of

**Figure 8** Photomicrograph of Recovered Copper Target, Experimental Configuration and Stress-Time Profiles at Locations P₁ and P₂
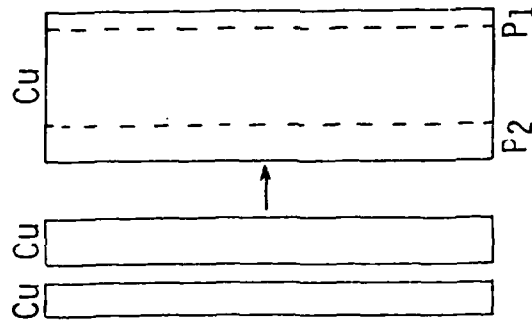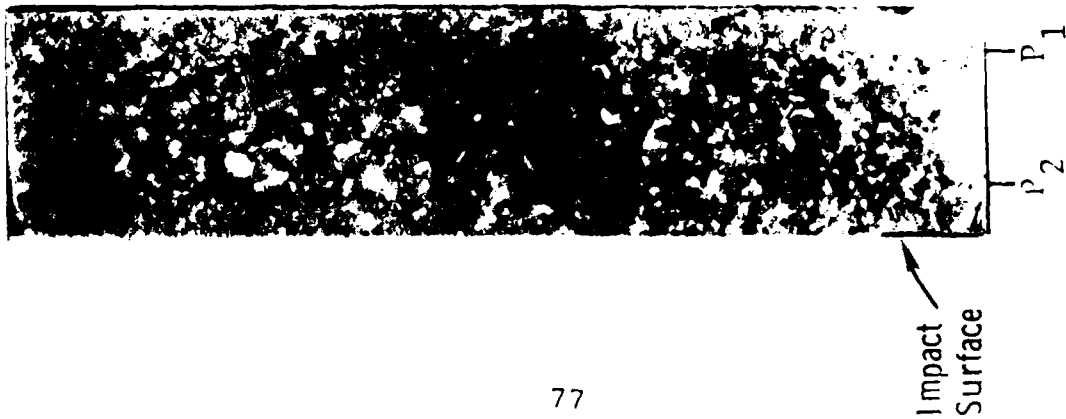
V = 0.0843 km/s

P₁ and P₂ are expected locations of tensile planes.

77
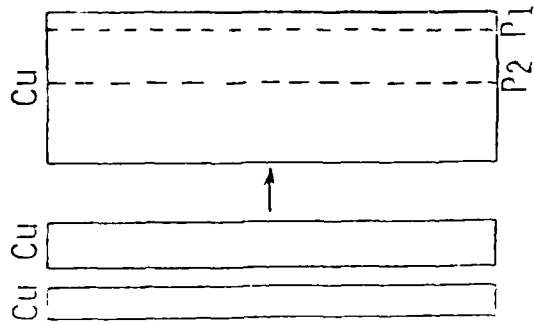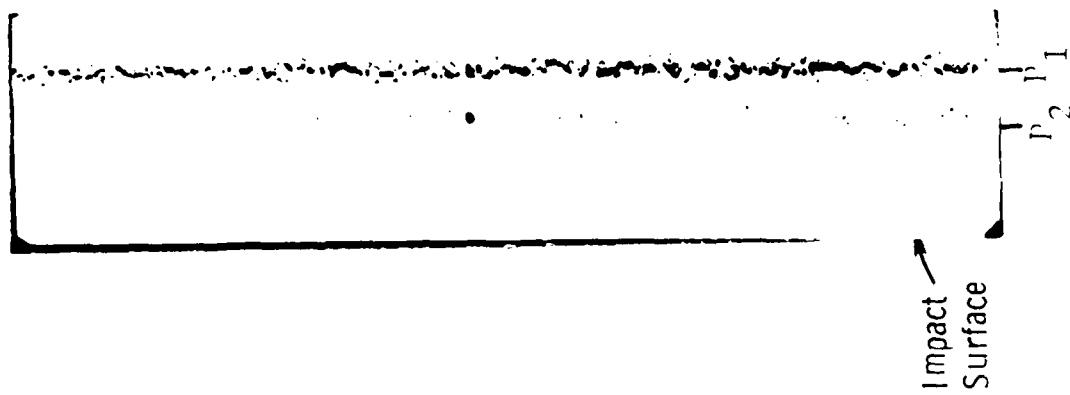
$V = 0.118 \ km/s$

$P_1$ and $P_2$ are expected locations of tensile planes.
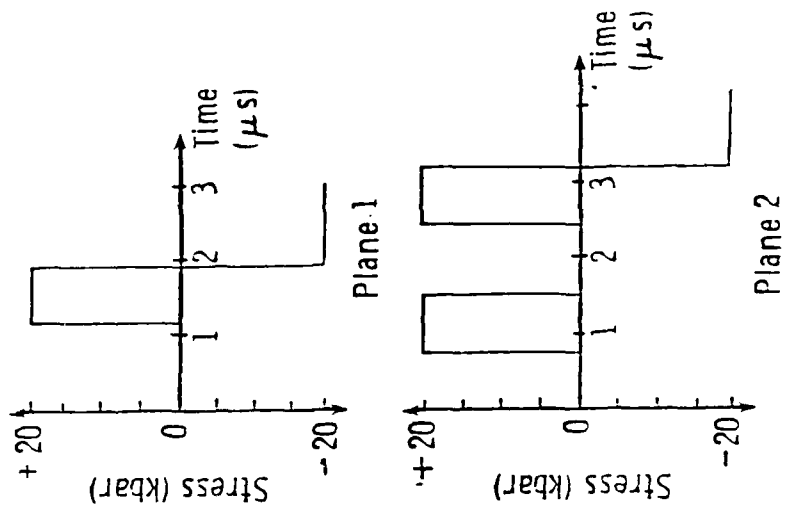
**Figure 9** Photomicrograph of Recovered Copper Target, Experimental Configuration and Stress-Time Profiles at Locations $P_1$ and $P_2$

78
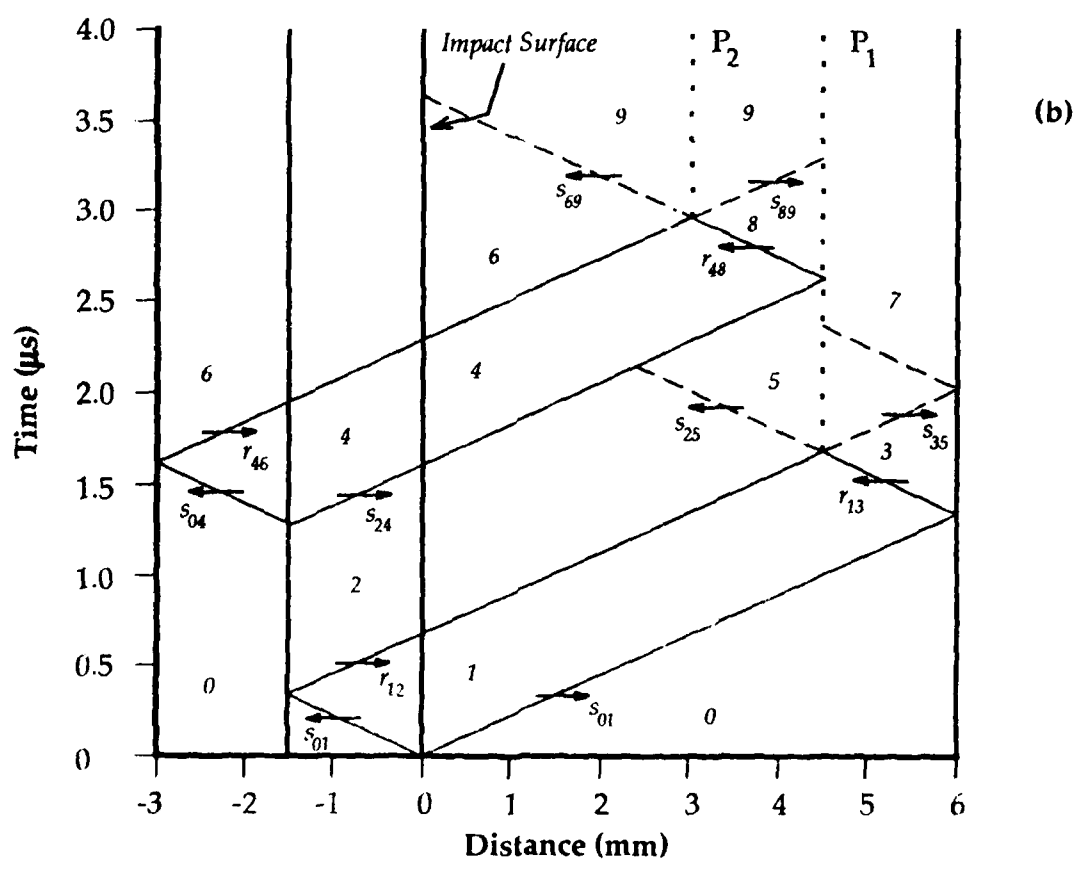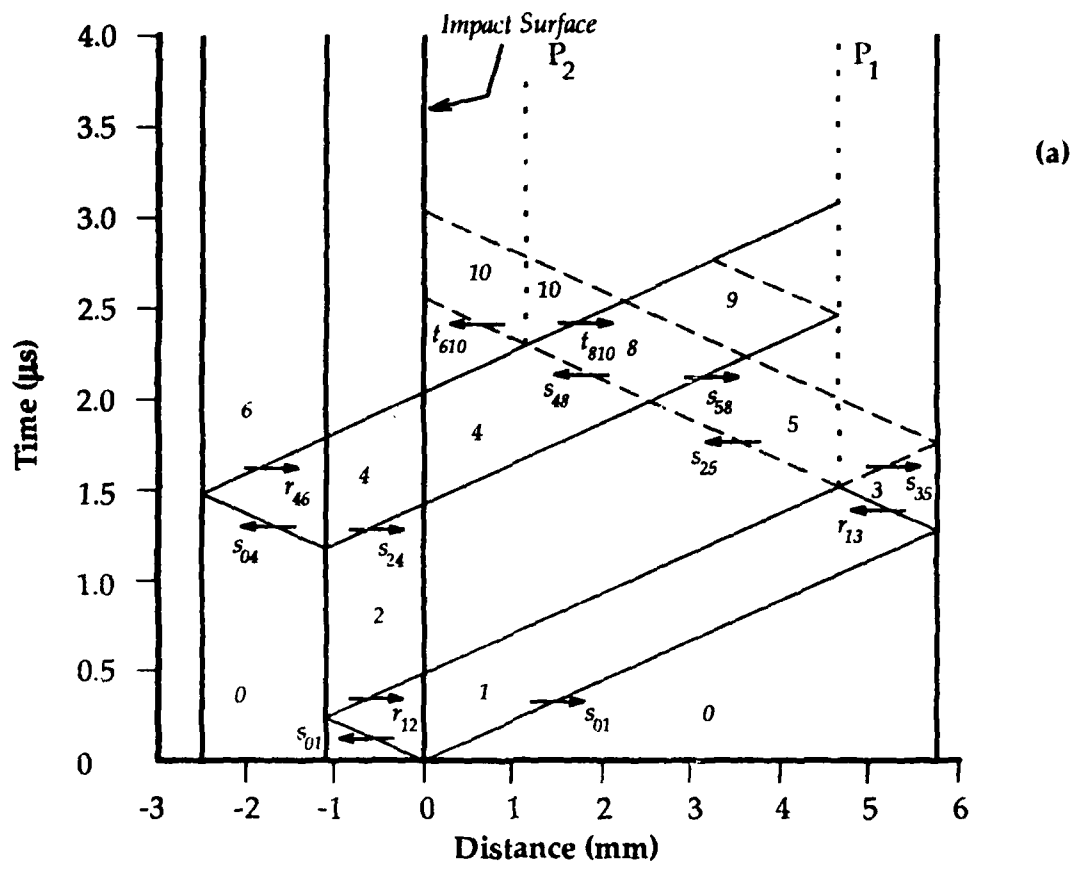
**Figure 10**    Distance-Time diagram for double shock in copper at impact velocities of a) 0.0843 km/s and b) 0.1176 km/s. Note: in a) spall occurs only at plane P1 while in b) spall occurs at both planes P1 and P2.

the same magnitude is developed at the plane $P_2$ after two successive shocks have traversed that region of the target. In other words, two different regions of the same copper target experience two different precompression histories before being subjected to tensions as a result of the interaction of two different sets of rarefaction waves. Pressures and pulse durations were calculated from impact velocity, flyer thickness, and gap thickness following standard procedures. Since it was not known whether the history of repeated precompression would reduce or increase the spall threshold of annealed OFHC copper, a tensile stress was chosen which was believed to be below the spall threshold of the material. The selection of this tensile stress was based on the information provided by Seaman et al. [10] on the spall threshold of dead soft OFHC copper. Their investigation showed that the minimum impact velocity required to cause spall in OFHC copper by symmetric impact was 0.0883 km/s. The pulse duration in this experiment varied between 0.4 and 0.8 µs. This specific experiment was done with a tapered flyer whose thickness varied from 0.79 to 1.58 mm. Therefore, the impact velocity chosen for our first two experiments was such that the tensile stress generated in the OFHC copper target would be less than that generated in the Seaman et al. [10] experiment with an impact velocity of 0.0883 km/s. The impact velocity chosen was 0.084 km/s. In 74201 the pulse duration of the first and second shock waves were 0.78 and 0.57 µs, respectively. The time difference between the inducement of the first and second shock wave pulses was 1.19 µs. The induced tensile stresses at the two planes $P_1$ and $P_2$ in the OFHC copper target were of the same magnitude, i.e. approximately 1.48 GPa. The target was recovered by a soft recovery technique, in a rag filled catcher tank. It was then sectioned, polished, etched and photomicrographed to examine for evidence of spallation in planes $P_1$ and $P_2$. Fig. 8 shows the photomicrographs of the OFHC copper target with planes $P_1$ and $P_2$ indicated on it. This figure shows the presence of a string of voids in plane $P_1$ and the absence of voids in plane $P_2$. In other words, contrary to expectations, OFHC copper spalled following one shock at a tensile stress of 1.48 GPa, yet the same target failed to spall under the same magnitude of

80

tensile stress following two shock compression pulses in and around plane $P_2$.
Photomicrographs of this target, even at 100X magnification, failed to show the presence
of voids in and around $P_2$. This figure also shows that the tilt, although not measured
during the experiment, was very small.

The second of the three experiments in OFHC copper (81103) was conducted at an
impact velocity approximately equal to that of the first experiment. The flyer thicknesses,
however, were nearly equal to each other so that the pulse duration of the two shocks
would be about the same (0.69 and 0.72 $\mu s$). Both the tilt and the scatter in the velocity
readings were relatively large but the results again showed the presence of voids at plane
$P_1$ and the absence of voids at plane $P_2$. This reinforces the conclusion drawn from the
first experiment that the spall threshold of OFHC copper appears to be affected by the
stress history.

Fig. 11 shows photomicrographs of shocked (from 74201) and unshocked OFHC
copper specimens. The material used in the present experiments corresponds to small
grained annealed OFHC copper investigated by Christy et al. [11]. However, in their ex-
periments the OFHC copper was subjected to stress exceeding 3.0 GPa. Nevertheless, one
of the failures shown in small grained OFHC copper bear similarity to those observed in
the present work. In both investigations a number of spherical voids were found to be nu-
cleated inside the grains in addition to those at the grain boundaries and grain boundary
triple points. An example of this observed in the present work is shown in Fig. 11.

Presently, only two mechanisms [12 & 13] for void growth have been proposed
but neither of them has been experimentally verified. The growth of microvoids is thought
to occur by generation and movement of dislocations. This requires the observation of
dislocation configurations in the neighborhood of voids. Christy et al. [11] used high
voltage transmission electron microscopy (1500 kV) to obtain microstructural information
on the voids produced by impact on OFHC copper to elucidate the formation mechanism of
the observed voids. Their work illustrated the presence of an elongated void which was

81

Figure 11 Photomicrograph of Unshocked and Recovered Shocked Copper Specimens (4μ/cm)

surrounded by heavily populated dislocations thought to be produced by shear strains required for the growth of a microvoid. This observation remains to be incorporated in a void growth model. Christy et al. [11] did present the volume fraction of voids formed upon spalling computed as a function of impact pressure for various metallurgical conditions. We plan to compare the volume fraction of voids formed in their small grained OFHC copper with those formed in our OFHC copper subjected to much smaller stresses.

In summary, stress history appears to affect the spall threshold of OFHC copper. The mechanism underlying this effect needs to be proposed and tested not only in annealed OFHC copper but in other ductile metals and alloys. Some of the important variables which need to be controlled in future experiments are (i) metallurgical parameters (grain size, impurity content, predeformation, including shock hardening), (ii) similar crystallographic metals and alloys and (iii) experimental parameters like pulse width and tensile stresses.

## SUMMARY

(i) Repeated shock release profiles in PMMA when shocked to 1.17 GPa can be satisfactorily simulated numerically by using a single constitutive equation used to simulate a single shock-release wave profile.

(ii) The effect of shock history (double shock induced precompression) in annealed OFHC copper is to raise the spall threshold value compared to that obtained from conventional spall experiments. In other words, the spall threshold of annealed OFHC copper is not an invariant

# REFERENCES

1. Dandekar, D. P., Gaeta, P. J., a..d Horie, Y., "Double-Shock and Release Experiments in PMMA and Z-Cut Sapphire", in Proceedings of the APS Conference on Shock Waves in Condensed Matter 1987, S. C. Schmidt and N. C. Holms, ed. El Services Science Publisher, New York, 1988.

2. Horie, Y., and Dandekar, D. P., "Computer Simulation of Double Shock-Release Experiments in PMMA". To appear in the proceedings of DYMAT, September 19-23, 1988.

3. Barker, L. M., and Hollenbach, R. E., "Shock Wave Studies of PMMA, Fused Silica, and Sapphire", J. Appl. Phys., 41, (1970), p. 4208.

4. Schuler, K. W., "Propagation of Steady Shock Waves in Polymethylmethacrylate", J. Mech. Phys. Solids, 18, (1970), p. 277.

5. Schock, R. N., Bonner, B. P., and Louis, H., UCRL Report-51508, Lawrence Livermore National Laboratory, California (1974).

6. Zhang, B. P., and Muller, F., "The Dynamic Behavior of Polymethylmethacrylate in the Low Pressure Range", High Temp. - High Press., 16, (1984) p. 475.

7. Davison, L. and Graham, R. A., "Shock Compression of Solids", Phys. Rep., 55, (1979), p. 255.

8. Jones, O. E. and Graham, R. A., "Shear Strength Effects on Phase Transition Pressures Determined from Shock-Compression Experiments" in Accurate Characterization of High Pressure Environment, National Bureau of Standards, Special Publication Number 326, (1971), p. 229.

9. Stevens, A. L., and Tuler, F. R., " Effect of Shock Precompression on the Dynamic Fracture Strength of 1020 Steel and 6061-T6 Aluminum", J. Appl. Phys., 42, (1971) p. 5665.

10. Seaman, L., Barbee, Jr., T. W., and Curran, D. R., "Dynamic Fracture Criteria of Homogeneous Materials", Report No. AFWL-TR-71-156, Kirtland AFB, New Mexico, Dec. 1971.

11. Christy, S., Pak, H., and Meyers, M. A., "Effect of Metallurgical Parameters on Dynamic Fracture by Spalling of Copper" in Metallurgical Applications of Shock Wave and High-Strain-Rate Phenomena, (1986) p.835.

12. Meyers, M. A., and Aimone, C. T., "Dynamic Fracture (Spalling) of Metals", Prog. Mat. Sci., 28, (1983), p. 1.

13. Stevens, A. L., Davison, L. and Warren, W. E., "Spall Fracture in Aluminum Monocrystals: A Dislocation-Dynamics Approach", J. Appl. Phys., 43, (1972), p. 4922.

# SECTION II

# DYNAMIC FAILURE MODELING

# RESEARCH ISSUES RELATED TO DYNAMIC FAILURE MODELS

Spencer T. Wu

Air Force Office of Scientific Research

## INTRODUCTION

Traditionally a good material model implies that the model can be used to describe the constitutive relations of a material (usually in a phenomenological way with the "continuum mechanics" approach) and be able to be implemented effectively in a computer code. To consider dynamic failures of materials and structures subjected to high energy release, a model should be able to represent the material behavior at both the macroscopic and microscopic levels such that the local and global failures of the material systems can be predicted.

This paper addresses research efforts in the development of rational models for predicting the dynamic failure of solid materials. In Section 2, subject areas involved are described. In Section 3, concerns on the development of better dynamic models are discussed. Based on these discussions, research issues to be focused are listed in Section 4. Concluding remarks are provided in Section 5.

## 2. Subject Areas Involved

Failure modes of materials are dominated by the loading characteristics and the structures of materials. For materials subjected to high strain-rate type loadings, dynamic effects such as stress wave propagations cannot be ignored. Hence the emphases in the investigation of dynamic failures may be quite different from those as in the static conditions. Current research efforts involved in the development of dynamic failure models are in the subject area of : deformation and fractures, transient effects, experimental and computations techniques.

Fracture mechanics and investigation of failure mechanisms have progressed well in the last twenty years. Material failures and structural instabilities can all be better described with the knowledge of microstructural behavior. E.g., interface and bond related issues. Nevertheless, dynamic fractures are not addressed only until recently when crack behavior such as curvings and branchings are correlated with the microstructural response. In most of the dynamic analysis, phenomena related to microcrack/microvoid initiations, growth and coalescence, are not explicitly included in the model.

Transient dynamic effects may cause the failure modes appeared differently because of the high frequency loading actions and residual properties in the materials. Shock induced phenomena were observed due to physical changes such as generation of

dislocations as well as chemical changes such as phase changes. Research studies in the last several years have provided clear descriptions of many phenomena related to transient effects. Further study is needed in many interdisciplinary areas to understand the dynamic failures of materials.

Development of experimental techniques is critical in providing information for determining the response mechanisms of the materials. Modern developments including acoustic emission techniques, scanning and imaging techniques have greatly improved understanding of deformation induced phenomena, e.g., transmission electron microscope examinations of adiabatic shear bands in metallic alloys. However, reliable experiemntal data for developing rational material models, especially for brittle materials, remain scattered.

Computation effectiveness is a major issue in the development of a good analytical model. I.e., the computation time has to be optimized in conjunction with the other issues including numerical stability and accuracy. Many special "elements" and criteria have been developed for dealing with some of the mathematical difficulties, e.g., singularities; rezoning in the numerical simulation. With the advancement in knowledge in the area of mechanics and materials, it is important that the physical processes be included in the computational model.

## 3. Concerns on the Development of Dynamic Failure Models

Research efforts progressed recently have improved understanding of failure mechanisms of materials. Concerns on further understanding of the material behavior, advancing measurement techniques and computational developments are described below.

Material Behavior: Efforts in the investigation of the formation and processing of "microcrackings' and their relations to macroscopic behavior are important in the development of failure models. Microstructural responses such as void collapse in brittle materials may not only dominate the fracture mechanisms of the materials but contribute to the transition from brittle to ductile deformations. Continued study of the microstructural behavior is needed to understand the response of a material system. Normally a comprehensive model is always developed first with the static conditions. For the problem under consideration, it seems that the development of micro-macro relations in dynamic sense may have the advantage of comparing the wave equations at different levels. To investigate in-depth the material response, it is necessary that the energy released mechanisms at microscopic levels be identified for all forms of energy, heat or shock waves. For newly developed materails such as fiber reinforced composites, the bond and shear effects at the interface may behave differently as the traditional materials. Hence, the dynamic mechanistic principles involved may also be different for such materials and structures.

Measurement Techniques:   Insitu measurements are in general quite complicated in the determination of responses of complex material systems. It is more difficult to study the dynamic response of materials because (ususally) the response histories of the materials cannot be entirely interpreted based on the measured data.   This is especially true under inelastic and nonlinear conditions. A jointed effort between experimental and analytical studies has to be developed. E.g., Non-destructive measurements against nonlinear mathematics.

Computational Development:   Computational efforts need to follow the approaches of the methods of analysis.   To investigate the failure of inhomogeneous material systems, modern statistical mechanics approaches such as percolation theory and fractal concepts may be useful. The formulation of the problem will be different from the conditions developed in the past. I.e., an integrated effort of the computation has to be established in the analysis.   There are certainly conditions where better mathematical formulations are needed, e.g., the "FEM" formulation for mixed mode conditions at the interface of the fiber and the matrix in a fiber composite system. All of these require more research studies in the area of computational mechanics.

## 4. Research Issues to be Focussed

Based on the developments and the needs as described, research issues to be further addressed are listed below.

### a. Rapid Energy Release Mechanisms

Identify clearly the deformation and damage mechanisms to be used as bases for developing sound theories to explain the material and structural failures under very rapid energy releasing conditions (including nonequilibrium states).

### b. Microstructural and Macro-behavior Relations

Establish quantitative relations between the microstructural parameters and material properties, and correlate the material response with the structural response for complex composite systems.

### c. Measurement Techniques

Develop further the measurement techniques, jointly with the modern development in other related disciplines such as non-linear mathematics, to determine the nonlinear material and structural response.

### d. Computational Development

Develop integrated computational efforts to optimize the numerical simulation of the physical and chemical processes.

## 5. Concluding Remarks

In this paper, a few notes on the development of dynamic failure models are addressed based on the state-of-the-art developments. As this paper is addressed primarily toward the research community, the mission oriented issues are not included in the discussions. The author would like to thank his colleagues at AFOSR for useful discussions related to this subject area.

# DAMAGE INITIATION MODELS IN IMPACT INDUCED DUCTILE FAILURE

Ian M. Fyfe
Department of Aeronautics and Astronautics
University of Washington, Seattle, WA 98195

## INTRODUCTION

That dynamic effects can play an important role in the ductile failure process has been recognized for quite some time; but the complexity of the process is such that it is extremely difficult to identify whether the various mechanisms of failure are influenced by changes induced by inertia, adiabatic heating, or material strain rate sensitivity, and to what degree. However, if one considers only the initiation of damage by the nucleation of small voids or cracks the problem becomes, more tractable, and it is also possible that, even if both inertia and strain rate did play roles, the experimental and theoretical considerations of dynamically induced loading could be combined with the quasi-static case to determine the material parameters required to predict failure. Although this paper deals mainly with the macro-level of damage initiation as characterized by localization and the loss of structural integrity, the importance of the micromechanics aspects, both in providing the basis of a model and defining damage, is also considered.

One of the earliest studies on failure initiation was that carried out by Considère [1], who developed a criterion for diffuse necking in tensile specimens. More recently the influence of strain rate sensitivity on tensile testing was examined in some detail by Hart [2], and a general survey of the deformation processes leading to failure was presented by Backofen [3]. However, the realization that void nucleation and growth was the underlying mechanism was further responsible for renewed interest in this area, with the result that a greater understanding of

the whole process has resulted. The growth of voids under plastic deformation was analyzed by Rice and Tracy [4], who noted the amplification of the growth rate due to stress triaxiality, an observation also made experimentally by Hancock and Mackenzie [5]. The determination of the conditions which lead to nucleation has been extensively studied, but unfortunately, these difficult measurements have led to conflicting observations as to when nucleation occurs. Several papers [6], [7] and [8] have combined both the theoretical and experimental aspects to shed some light on the subject by showing that void nucleation is also a function of the mean stress, and that the nucleation strain decreases with an increase in mean tensile stress.

A complicating factor in trying to define nucleation is introduced by the observation that as nucleation occurs at second phase particles or other inclusions, the process also depends on particle size; so that both particle-matrix decohesion, and particle cracking are contributing factors, [9]. Thus nucleation can occur almost immediately after yield, and can continue althrough the deformation process. However, at some point during deformation a proliferation point is reached where the nucleation increases dramatically, [6]. It is thus generally agreed that damage, and void nucleation in particular, is a statistical concept. Pan, Sage and Needleman recognised this statistical feature of nucleation in the failure analysis described in [10]. In addition a detailed study of ductile failure in Swedish iron by Thomson and Hancock [11] suggests that a bimodal distribution may be a more realistic model.

In this paper, experimentally determined failure strains, obtained under both quasi-static and impact loading conditions, are plotted as a function of the mean stress. These results are then examined in terms of a number of models that have been developed to predict this particular type of damage. By this means it is hoped to better define the varies levels of material damage so that a closer link can be made between the microscopic definition of damage, and the continuum concepts of instability and localization. It is also hoped to show the compatabilty

93

between different experimental techniques, and so define areas which require additional study.

## NUCLEATION AND LOCALIZATION THEORIES

The complexity of ductile failure is such that models are of necessity limited to a narrow range of deformations and constitutive equations, an example being the stability criterion of Considère which is suitable only as a means to predict instability in a simple tensile test. This limitation also occurs in the micromechanics area where models usually only apply to a particular mechanism, when indeed a number of mechanisms may be acting simultaneously. The classic example being the nucleation of voids by both the decohesion of second phase particles from the matrix, and the cracking of the particles. To examine all possible micromechanics models is clearly beyond the scope of this paper, and so the choice is restricted to a particular model that appears to be both compatible with the type of experiments associated with impact loading, and the continuum variables of these experiments.

### Nucleation

A model which meets the above requirements was developed by Goods and Brown [7], and is based on the concept that a critical value of normal stress $\sigma_c$ must be exceeded at the particle-matrix interface in order that void nucleation may occur. If the stress at the particle interface is assumed to be composed of a local stress $\sigma_{loc}$ and a superimposed hydrostatic stress $\sigma_m$, this model can then be expressed in the form

$$\sigma_{loc} + \sigma_m \geq \sigma_c \tag{1}$$

The value of $\sigma_{loc}$ reflects the contributions of the microstructure, such as particle volume fraction and the dislocation density which has accumulated at the particle. In the absence of any recovery or annealing the dislocation density $\rho_{loc}$, increases linearly with strain, and, assuming that $\sigma_{loc}$ is proportional to the square root of the density, then the nucleation strain,

$\epsilon_N$ can be obtained from the relation:

$$\sqrt{\epsilon_N} = \frac{1}{H}(\sigma_c - \sigma_m) \tag{2}$$

where H is a material constant.

The above model, although obviously a very much idealized one, does give the expected trend as to the effects of hydrostatic pressure on the nucleation strain. However, as nucleation is essentially a continuing process with material deformation, the particular strain represented by the above equation is susceptible to a number of interpretations. From a continuum point of view to interpret this strain as the one controlling the satistical distribution seems reasonable, but from a microscopic viewpoint it could well be defined as the proliferation strain, or the strain required to nucleate a single void.

## Localization

It is generally recognised that localization is triggered by both geometric and thermal conditions. In the case of dynamic experiments, geometric triggered localization is difficult to measure, and when it does occur, as in the case of diffuse tensile necking, it greatly adds to the problems associated with data analysis.

As geometric necking does not occur in torsional experiments, the formation of shear bands in this configuration are usually considered to be due to thermal instabilities. A model described by Dodd and Bai [12], and Staker [13] can be applied, which has the form

$$\gamma_c = -Cn/AB(\partial \tau / \partial T)|_{\gamma, \dot{\gamma}} \tag{3}$$

where n is the strain hardening exponent in a power-law model, $\tau$ is the flow stress in shear, T is the temperature, and C ($\rho c_v$) is the volume specific heat. The parameters and A and B are the fractions of plastic work converted to heat, and the fraction of heat conducted away from the deforming zone respectively. It is generally assumed that A ($\simeq 0.9$) and that B =1 for

adiabatic deformation and B< 1 for nonadiabatic deformations. Other criteria where different material behavior is assumed are described by Dormeval [14].

Where geometric localization does occur, as in the radial expansion of thin rings, the theories developed by Hill [15], Stören and Rice [16], and Needleman and Rice [17] might be applied. The pertinent relations as given by Hill are

$$\epsilon^* = \frac{n}{1 + \rho} \tag{4}$$

and

$$\tan\Psi = \sqrt{-\rho} \qquad \rho = \epsilon_1/\epsilon_2 \tag{5}$$

where $\epsilon^*$ is the strain at localization, $\Psi$ is the angle between the principal strain axis and the normal to the localized neck, $\epsilon_1$ and $\epsilon_2$ are the strains in the major and minor axes respectively. For the thin ring expansion, where $\rho = -1/2$, the strain at localization is equal to 2n. If the theory given in [16] had been used the results would be very slightly higher than those obtained from Eq. (4). In the case of axisymetric straining, the model described in [17] has the form

$$\epsilon^* = \sqrt{(1 + 3n)(1 - n)/3} \qquad n \leq 1/3 \tag{6}$$

The above equation applies in the diffuse neck, and is the bifurcation that just precedes failure.

A geometric localization model for torsional deformations was developed by Dodd and Atkins [18], but as this model contains both the shear band length and an undefined parameter, it is difficult to use. It should be recognised that the above quasi-static theories are very much dependent on the constitutive models chosen, and in this paper only materials which can be described fairly accurately by a power-law are considered; further it is assumed that the value of n applies to the flow stress appropriate to the strain-rates of interest.

96

## EXPERIMENTAL CONFIGURATIONS

Introducing dynamic data into the considerations of the above models does not materially alter the number of mean stress levels that can be reached, but it does allow a wider variety of experiments to be considered. In this paper we concentrate on three experimental configurations, these being the high mean stress case associated with the plate impact test, the intermediate condition of simple tension, and the zero mean stress case which results from the torsion configuration. In addition only two materials were considered, 6061-T6 aluminum and VAR 4340 Rc=33 steel, whose material properties are given in Table 1.

Values for the critical mean stress of Eq. (2) under quasi-static conditions have been obtained by Argon and Im [6] for three materials using a combined experimental analysis technique on notched tensile specimens. For the three materials tested, spherodized 1045 steel, Cu-0.6 pct Cr, and maraging steel they determined that the ratio of critical stress to the

TABLE 1

| | Y | E | n | $\partial \tau / \partial T^\dagger$ | $C^\dagger$ | $\gamma_i{}^*$ | $\sqrt{\epsilon}$ |
|---|---|---|---|---|---|---|---|
| | *MPa* | *GPa* | | *(kPa/°C)* | *(kPa/°C)* | | |
| 4340 | 831 | 213.0 | 0.065 | -830 | 3600 | 0.313 | 0.425 |
| 6061-T6 | 295 | 71.3 | 0.050 | -491 | 2533 | 0.285 | 0.406 |

† Refs. 12 and 13     * (A=0.9, B=1)

respective Young's moduli to be 0.0085, 0.008 and 0.009, respectively. The narrow range of these values allows a reasonable estimate of $\sigma_c$ to be made. On the dynamic side, one of the classic failure experiments is spallation created by plate impact, and for this paper the results presented in [19] will be used. One of the characteristics of this type of experiment is that the stress level required to cause failure increases slightly as the pulse duration shortens. In this paper the stress values for the shorter duration pulses are not used, assuming that the increase is due to inertial constraints.

In the tension configuration, failure is examined in radially expanded thin rings, and the techniques used are as described in [20] and [21]. To obtain the required expansion of a thin ring specimen, an exploding wire system was used to generate a symmetric and axial uniform pressure pulse which propagated radially through the medium surrounding the wire to uniformly impinge on the inner surface of the specimen. One of the configurations, used and not reported in [20], is shown in figure 1, where the wire to be exploded is on the axis of a fluid-filled cylindrical cavity. The specimen is positioned on the outer wall of this cylindrical region and, when loaded by the pressure pulse from the exploding wire, the specimen is free to expand radially. In the configuration shown, the expansion of the ring is controlled by using steel dies with different inner diameters chosen to halt the expansion of the ring at displacement values where the failure process occurs; in particular, the point where necking, if it occurs, is first observed. The rapid deceleration of the ring could well alter the microstructure of the material, but it does not affect the ability to determine the strains at which these events occur. Additional tension data were also obtained from reference [22].

The torsional data were obtained from a number of experiments, both quasi- static and dynamic, varying somewhat in detail and sophistication depending on both the objectives, and when the experiments were carried out. The aluminum data were those reported by Culver [23], while in the case of the 4340 steel, the work of Tanimura and Duffy [24], and Olsen, Azrin and Tsangarakis [25] was used. To allow this data to be compared with the others, the shear strain was converted to equivalent strain by dividing by the square root of three.

## RESULTS AND DISCUSSION

Data from the above cited experiments are presented, where, to conform to the requirements of Eq. (2), the damage level is the square root of the effective plastic strain at various points in the failure process. As is to be expected with the various definitions of failure in use, the damage level can vary over a wide range, and the results are presented in such a fashion that similar damage levels are connected.

### Plastic Instability

As is to be expected the ductile failure processes are usually preceded by plastic instabilities, for which the theories outlined earlier should apply. In the case of 4340 steel the test configurations were such that diffuse necking was not to be expected, but in both the torsion and ring experiments, localized bands or instabilities were observed. The bands which occur in the thin ring configuration subjected to impact loading ($\dot{\epsilon} \approx 1 \times 10^3$/sec.) can be seen in figure 2, and the hoop strain at which these bands form, $\epsilon_\theta = 0.15$, is in very close agreement with the 2n value as predicted by Eq. (4). In quasi- static expansion of these rings, the data was somewhat scattered, but the average value was only slightly lower.

For the torsion case the experimental instability strains given in [25] are shown in figure 3. These results are interesting in that instability was reported for both the dynamic and quasi-static configurations. When the dynamic instability strains are compared with the theoretical results (see Table 1) the thermal instability model of Eq. (3) provided good agreement. An indirect conformation of the above results is given by [26], who reported that in 4340 Rc=39 torsionally created adiabatic shear bands became evident when the shear strains reached approximately 0.14. This value is also shown in figure 3. The presence of instabilities under quasi- static conditions is usually attributed to an increase in the number of voids just prior to fracture, [18]. However, as reported in [25], little evidence of void nucleation could be found.

This is in accord with the thin ring experiments, where localization is purely geometric, and as can be seen in figure 4a, very few voids are present in the localized region.

The above instability strains reported for impact loading, are also in agreement with the values reported in [13], where the failure occurred in explosively loaded cylinders, with a mean stress that was probably quite different from that experienced by either the expanding rings or the torsional specimens.

In the case of 6061-T6 aluminum alloys there is no clear demarkation between failure and instability. In the thin ring experiments, localized necking of the type shown in figure 2 was not to be expected, mainly because the rings were too narrow, and so the standard diffused necking preceded failure. Culver [23] found that torsional shear band instabilities were present under both quasi-static and dynamic loading conditions, which was also the case for 4340, [25]. The theory given in Eq. (3) was again in good agreement with the dynamic experiments, but in both cases the instability strains for the quasi-static tests were lower than the dynamic. As the quasi-static tests are nonadiabatic (B< 1)the theory of Eq. (3) requires that the instability strains should be larger than the dynamic, and as suggested in [18] another mechanism may be the cause. In addition the aluminum experiments had quasi-static instabilities which were synonymous with failure, that this may be the influence of is voids is suggested by the necked region in figure 4b. These instability results are summarized in figures 5 and 6.

Failure

In figures 5 and 6 the failure strains of the cited experiments are plotted as a function of the mean tensile stress. In general the failure strain was the residual strain after impact, measured at the point of fracture. However, for the quasi-static results of references [20], [23] and [24] the strain where there was an abrupt drop in load was used. As mentioned above this was synonymous with instability in aluminum, but in steel both Culver [23] and Olsen et al

[25] observed localization well before failure.

Examining the experimental results for both materials in terms of Eq. (2), it would appear that H is indeed a material constant. The consistent change in the critical stress between the quasi-static and the dynamic is of more immediate concern. Although this shift indicates an increased ductility at high strain rates for both materials, the magnitude and direction of this change in ductility is probably due to a number of features associated with impact loading, in particular, the strain-rate sensitivity of the material, inertia and thermal effects, and the variation in defining damage levels. In this case neither material is inherently highly strain rate sensitive, as contrasted with 1020 steel. In both the plate impact and expanding ring configuration the deformation is constrained by inertia, in the plate impact this leads to the uniaxial strain condition, and hence the higher mean stress. However, in the thin ring configuration, or in simple tension, inertia forces act as constraints on the formation of the neck, but have almost no effect on the mean stress. Thus it is to be expected that when comparing the dynamic and static cases, the strains outside the necked region will be larger under dynamic conditions, but the strains in the necked region could be similar for both. A closer examination of the results indicate that the above is indeed the case. It thus appears that the main cause of the difference between the dynamic and static data lies in how failure or damage is defined.

If visible damage is used to define failure, then it is quite clear that not only void nucleation, but void growth must be considered. As can be seen in figure 4, where the necked region in thin rings under dynamic loading is compared, the 6061-T6 has very significant void growth prior to failure, which does not seem to be the case in 4340 steel. This factor is reflected in the fact that the ratio of dynamic to static failure strains is less in the steel than in the aluminum. When the effective plastic strain is determined from area reduction values, [22], it was

101

found that the damage level for static failure in the 4340 was within the range of values shown in figure 5, but for 6061-T6 the equivalent values were much higher than even the dynamic levels of figure 6. If the failure model of Eq. (6) is applied it also was in good agreement when applied to the 4340 steel, but predicted a very much higher value of failure strain for the 6061-T6. However, it was also shown in [17] that porosity based models greatly reduces this value. Again demonstrating the need to incorporate void growth concepts in general damage theories.

From a macroscopic viewpoint if Eq. (2) indicates the beginning of void proliferation, then to reach the higher damage levels of figures 5 and 6 an additional term must be added. This term can be interpreted as either the continued nucleation of voids beyond the proliferation point, or as a void growth component of the damage strain. The following expression would satisfy either of these the contributions to the damage level.

$$\sqrt{\epsilon_D} = \frac{g\sigma_c}{H} + \frac{1}{H}(\sigma_c - \sigma_m) \tag{7}$$

where g is a growth parameter which increases monotonically with damage. If the additional term in the above equation represents continued nucleation, then it also implies that the extra nucleation is from sites which require a higher critical stress to nucleate. This could represent a bimodal distribution of nucleation sites. If the void growth interpretation is used, and if damage strain is considered to be the sum of the nucleation and growth strains, then it can be readily shown that the growth strain required decreases with increasing mean tensile stress. This result is in accord with the calculations of Rice and Tracey [4] who found that as the mean tensile stress increased, the far field strain required to cause acceptable void growth decreased. It is also in accord with the fact, that at zero mean stress, larger strains are required to reach the level of damage where failure occurs. This latter requirement is also in accord with the nucleation interpretation in that, if void growth is small more voids must be nucleated, as for

102

example in void sheets. As mentioned earlier the stability strains as reported by Giovanola [26] agreed with those of [25]. In the case of the failure strains, when corrections were made to allow for the difference in hardness, the results were found to correspond to values that would be predicted by Eq. (7).

## CONCLUSIONS

Although the experimental evidence is limited, using a consistent measure of damage indicates that the simple concepts on which Eq. (7) is based can provide a model which is compatible with macroscopic measures of damage, in that H and $\sigma_c$ are essentially constant. The required assumption that a well defined nucleation strain $\epsilon_N$ exists is consistent with the void proliferation concepts of reference [8]. The results consistently indicate that plastic instability occurs at strains lower than $\epsilon_N$, and suggests that plastic instabilities of both the local or diffuse kind do not require the formation of significant void levels for their existence.

Although from a continuum viewpoint, Eq. (2) cannot be applied in any general way to predict the onset of plastic instability, it could be used to predict the onset of failure, if ductile failure is defined as the point in the deformation where voids proliferate.

As void nucleation also depends on the size distribution of the nucleating particles, the nucleation strain of Eq. (2) could well be used to model some particular aspect of this distribution, rather than proliferation as suggested above. Unfortunately, materials research into the statistical nature of nucleation is as yet not fully developed, so, for the present, it is to be expected that nucleation levels will be interpreted in different ways. It would thus appear that, despite the simplicity of the model, Eq. (7) could serve as a useful tool in impact analysis.

# REFERENCES

1. Considère, "L'Emploi du Fer et de L'Acier dans Constructions," Ann. Ponts Chaussee, 9, 574, 1885.

2. Hart, E.W., "Theory of the Tensile Test," Acta Met., 15, 251, 1967.

3. Backhofen, W.A., "Deformation Processing," Met. Trans., 4, 2679, 1973.

4. Rice, J.R. and Tracey, D.M., "On the Ductile Enlargement of Voids in Triaxial Stress Fields," J. Mech. and Phy. Solids, 17, 201 1969.

5. Hancock, J.W. and Mackenzie, A.C., "On the Mechanisms of Ductile Failure in High Strength Steels Subjected to Multi-Axial Stress-States," J. Mech. Phys. Solids, 24, 147, 1976.

6. Argon, S. and Im, J., "Separation of Second Phase Particles in Spheroidized 1045 Steel, Cu-0.6Pct Cr Alloy, and Maraging Steel in Plastic Straining," Met. Trans. 6A, 839, 1975.

7. Goods, S.H. and Brown, L.M., "The Nucleation of Cavities by Plastic Deformation," Acta Met., 27, 1 1979.

8. LeRoy, G., Embury, J.D., Edwards, G. and Ashby, M.F., "A Model of Ductile Fracture Based on the Nucleation and Growth of Voids," Acta Met. 29, 1509, 1981.

9. Thompson, A.W., "Modeling of Local Strains in Ductile Fracture" Int. J. of Fracture, 26, 99, 1984.

10. Pan, J., Saje, M. and Needleman, A., "Localization of Deformation in Rate Sensitive Porous Plastic Solids," Int. J. of Fracture, 21, 261, 1983.

11. Thomson, R.D. and Hancock, J.W., "Ductile Failure by Nucleation, Growth and Coalesence." Int. J. of Fracture, 26, 99, 1984.

12. Dodd, B. and Bai, Y., "Ductile Fracture and Ductility," Academic Press, London, 1987.

13. Staker, M.R., "The Relation Between Adiabatic Shear Instability Strain and Material Properties," Acta Metall. 29, 683, 1981.

14. Dormeval, R., "The Adiabatic Shear Phenomenon," Materials at High Strain Rates, Elsevier, London-NewYork, 1987.

15. Hill, R., "On Discontinuous Plastic States, with Special Reference to Localized Necking in Thin Sheets," J. Mech. Phys. Solids, 1, 19, 1952.

16. Storen, S. and Rice, J.R., "Localized Necking in Thin Sheets," J. Mech. Phys. Solids, 23, 421, 1975.

17. Needleman, A. and Rice, J.R., "Limits to Ductility Set by Plastic Flow Localization," Mechanics of Sheet Metal Forming, Plenum Press, New York-London, 1978.

18. Dodd, B. and Aitken, A.G., "Flow Localization in Shear Deformation of Void-Containing and Void-Free Solids." Acta Metall.,31, 9, 1983.

19. Davison, L. and Graham, R.A., "Shock Compression of Solids," Physics Reports, 55, 255, 1979.

20. Rajendran, A.M. and Fyfe, I.M., "Inertia Effects on the Ductile Failure of Thin Rings," J. Appl. Mech. 49, 31, 1982.

21. Fyfe, I.M. and Rajendran, A.M., "Dynamic Pre-strain and Inertia Effects on the Fracture of Metals," J. Mech. and Phy. Solids 28, 17, 1980.

22. Structural Alloys Handbook Vol. 1-2, Battelle Columbus Ohio, 1986.

23. Culver, R.S., "Thermal Instability Strain in Dynamic Plastic deformations," Metallurgical Effects at High Strain Rates Plenum Press, New York, 1973.

24. Tanimura, S. and Duffy, J., "Strain Rate Effects and Temperature History Effects for Three Different Tempers of 4340 VAR Steel," Brown University Report DAAG29-81-K-0121/4, 1984.

25. Olson, G.B., Azrin, M. and Tsangarakis, N.T., "Plastic Shear Instability in 4340 Steel," AMMRC Report MS 84-2, Watertown, MA., August 1984.

26. Giovanola, J.H., SRI., private communication 1987.
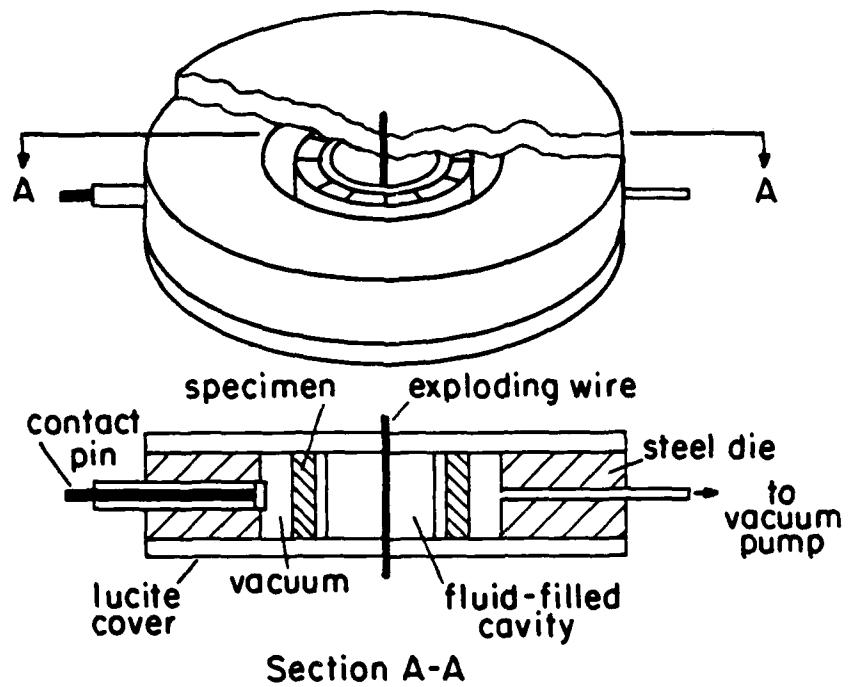
Figure 1.   Experimental Configuration for Thin Ring Expansion Tests
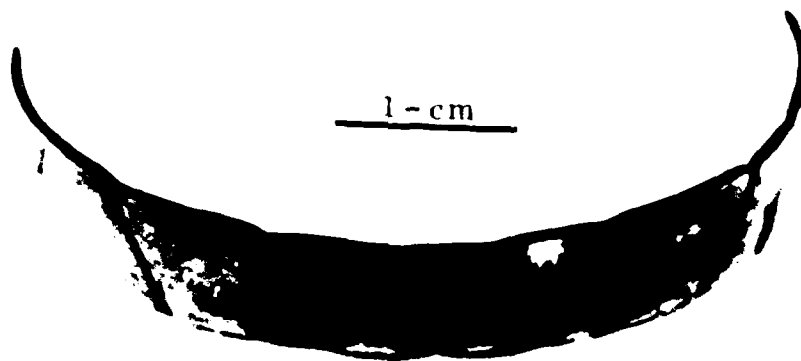


Figure 2.   Fragment from a Dynamically Expanded Thin Ring (4340 Steel)
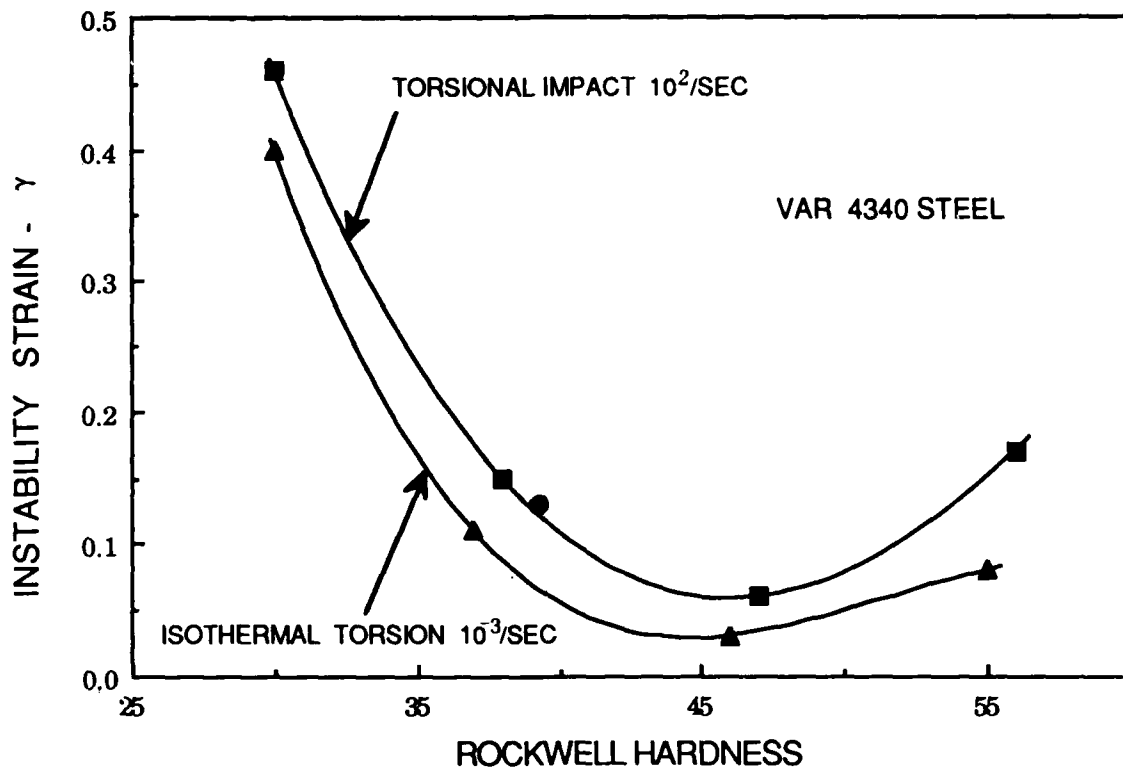
Figure 3.    Comparison of Instability Strains Measued In Adiabatic (■),  and
             Isothermal (▲) Torsion Tests of 4340 VAR Steel, after Olson et  al [25]
             Torsional Dynamic Instability (●) , after Giovanola [26]
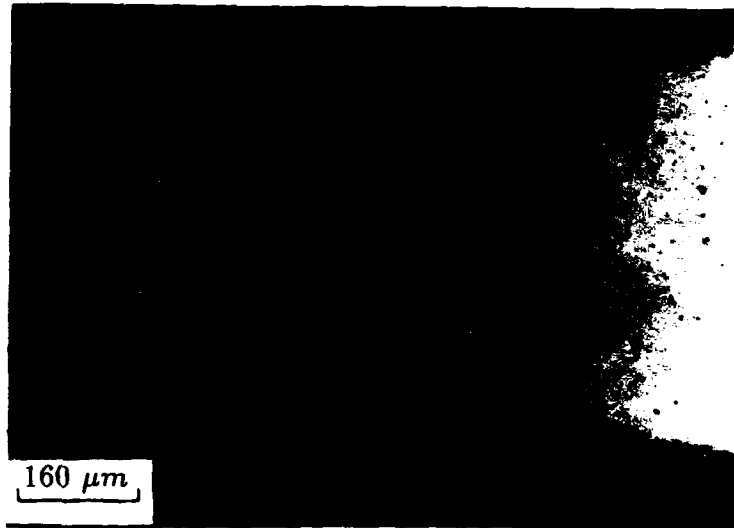
(a)
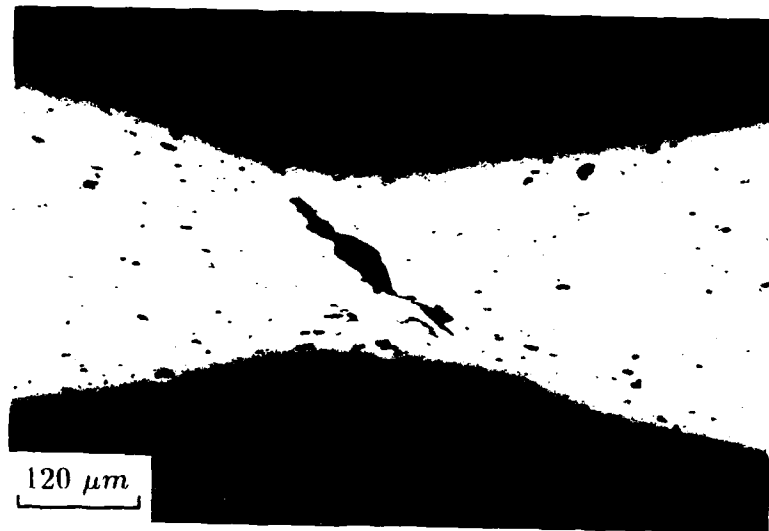


(b)

Figure 4.   Ductile Failure Damage in Thin Ring Specimens (polished not etched) under Dynamic Loading (a) 4340 VAR Steel, (b) 6061-T4 Aluminum
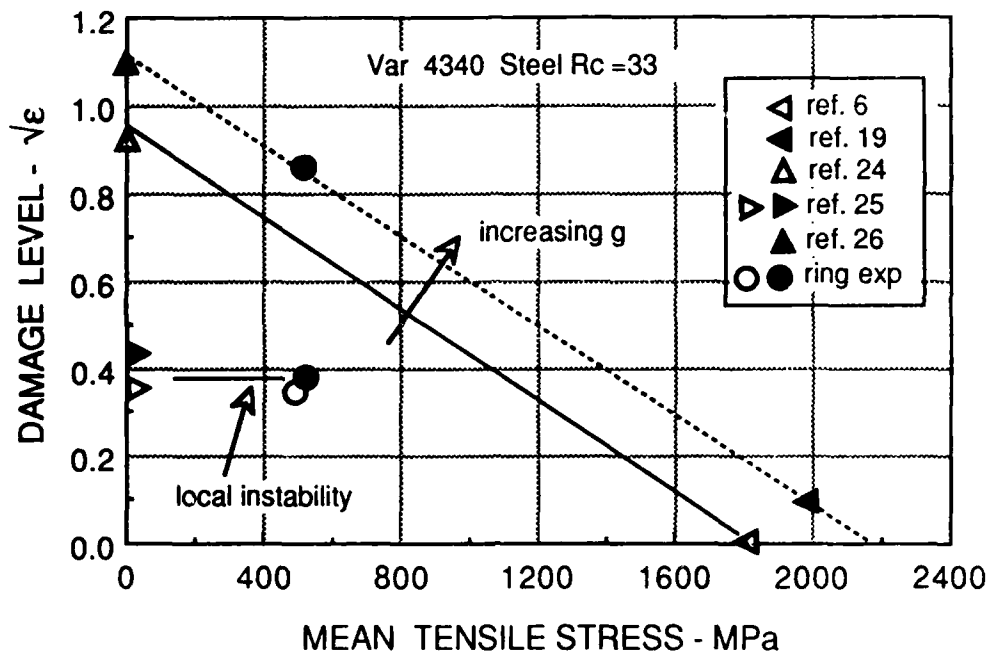
Figure 5. Damage Level as a Fui.ction of Mean Tensile Stress for 4340
Steel under Dynamic (-------) and Static (———)Loading
Conditions
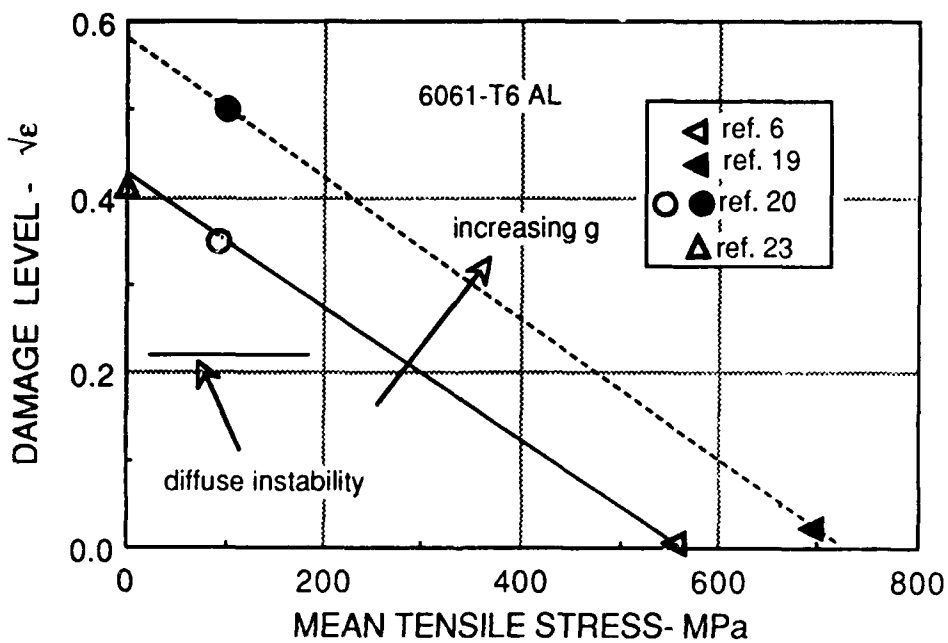


Figure 6. Damage Level as a Function of Mean Tensile Stress for 6061-T6
Aluminum under Dynamic (-------) and Static (———)Loading
Conditions.

# A VOID GROWTH BASED FAILURE MODEL TO DESCRIBE SPALLATION

## A.M. RAJENDRAN

Structural Integrity Division
University of Dayton Research Institute
Dayton, OH 45469

## ABSTRACT

A new dynamic failure model to describe void nucleation, growth, and coalescence in ductile metals is reported. The model is based on a pressure dependent yield criterion for compressible plastic flow. This three-dimensional, plasticity-based continuum damage model is incorporated into a finite difference, wave propagation code. A procedure to determine the failure model parameters is proposed. In this procedure, the model parameters are calibrated based on the ability to match the experimental free surface velocity history with code simulations. Model parameters for OFHC copper have been determined successfully using this procedure.

## I.    INTRODUCTION

Dynamic failure processes in metals have been studied extensively for the last few decades. There are numerous journal articles, technical reports, and conference proceedings on this subject. Investigators with widely varying backgrounds, such as applied mechanicists, metallurgists, and shock physicists have been contributing to the understanding of dynamic failure. The fundamental failure mechanism associated with dynamic fracture in ductile metals is one which considers the failure process as being initiated by the nucleation of voids around inclusions and their subsequent growth and coalescence as suggested by McClintock [1]. During the last two decades, different approaches have been taken by several investigators to apply this mechanism as a means of predicting ductile failure. Among them, Rice and Tracey [2] considered the growth kinetics of a single void in the matrix and

developed a model which showed the dependence of void growth rate on the triaxiality of the stress state. Hancock and MacKenzie [3] provided the experimental evidence to support this dependency on the stress state and used this model to predict failure initiation in notched tensile specimens under quasi-static loading conditions. Their study is obviously under low mean stress levels.

There are other experimental configurations in which this fundamental failure mechanism is frequently observed and reported. One such experiment involves impacting a flyer plate of one material against a target of the same or other material at a higher velocity. Fracture is induced in the target by tension arising from the interaction of reflected shock waves from the stress-free planes parallel to the plane of impact. The interesting feature is the growth and coalescence of voids under high mean stress levels leading to failure in the target plate; this type of failure is often referred to as spallation. A simple criterion in which stress, strain, pressure, or energy is assumed to reach a critical value is usually employed to model spallation in computer codes. This type of time independent failure model may work well when the spall is well above the threshold conditions. Tuler and Butcher [4] introduced a time dependent failure criterion. They assumed that failure occurs only after a critical value of damage is reached. However, there is no interaction between damage and stresses and therefore strength degradation due to damage cannot be modeled. This model has three parameters which have to be determined from spall experiments. Several other investigators [5-8] proposed models to predict the spall threshold. They considered the nucleation and growth rates of voids through rigorous mathematical modeling of the failure process. Meyers and Aimone [9] and Assay and Kerley [10] have reviewed the fundamental aspects of spallation and the modeling efforts by the various research workers.

The various approaches can be grouped into three categories: (1) micro-statistical approach, (2) physically motivated empirical approach, and (3) continuum mechanics based approach. The first

approach was mainly pursued by Curran and co-workers [11]. Based on the extensive micro-statistical analyses of the void sizes and orientations, they developed models to describe the void nucleation and growth processes. In the second ad hoc approach, the objective was to develop models, not based on any extensive analyses of microstructures or the kinetics of the failure processes, but mainly based on the ability to predict certain measured quantities such as the free surface velocity of the target plate. Under this approach most of the works had been strictly developed and limited to rectilinear motions. In most cases, the generalization of such theories to any other geometry is not possible. The third approach considered a general solution to the problem of spallation. Davison, Stevens, and Kipp [7] presented a theory of spall damage based on a unified and thermodynamically consistent treatment of elastic-viscoplastic deformation. A continuum mechanics approach was employed with a three-dimensional theory. Their theory contained numerous model parameters which are not easily obtainable.

The present paper describes a failure model which is based on microvoid nucleation and growth. The effect of damage (void volume fraction) on strength (flow stresses) is incorporated through associated flow rule based plasticity equations. An improved yield function is proposed to describe the effect of pressure and void volume fraction on the Von-Mises (effective) yield stress. The strain rate effect on the failure process is modeled through a viscoplastic matrix description. Model parameters are determined from a few split Hopkinson bar tensile tests data and a free surface velocity history of a target plate in a plate impact test. Using the proposed model, spallation in OFHC copper is successfully modeled.

II.   CONSTITUTIVE/FAILURE MODEL

We identify four phases in the constitutive modeling of damaged materials that were initially intact. The first phase of the modeling is the description of the intact material behavior. Prior to the development of damage, the aggregate is the fully

112

dense matrix material which is usually modeled by incompressible plastic flow theories. The second phase is the description of the damaged material. We require a model to describe the behavior of the aggregate material which contains microvoids/microcracks. In the third phase, depending on the nucleation mechanism, a mathematical description of the process will be required. This phase will also require a model to describe the growth of damage. The last phase of modeling is the coalescence of damage leading to total failure. In the present approach, separate modeling of the coalescence process is not needed. The void growth law is such that the growth rate is rapidly increased as the damage approaches its critical value.

## A. Matrix Material

The fully dense, void-free matrix material can be modeled through the state variable based viscoplastic constitutive equations of Bodner and Partom (B-P model) [12]. The B-P model in terms of equivalent plastic strain rate $\dot{D}_m^p$ and effective stress, $Y_m$ is given by,

$$\dot{D}_m^p = \frac{2}{\sqrt{3}} D_o \exp\left\{-\left[\frac{n+1}{2n}\right]\left[\frac{Z}{Y_m}\right]^{2n}\right\} \tag{1}$$

Z is a state variable. $D_o$ is the limiting value of the plastic strain rate. The value of $D_o$ is usually set to $10^8$/sec for metals. n is a parameter that is mainly related to strain rate sensitivity. The state variable Z describes the overall resistance of the material to plastic flow and it depends on the loading history. The evolution equation for Z is

$$\dot{Z} = m(Z_1 - Z)\,\dot{W}_p \tag{2}$$

where $\dot{W}_p$ is the plastic work rate. $Z_1$ is the maximum value that Z can attain and m is a parameter that embodies the strain hardening

113

behavior of the material. For highly strain hardening materials like copper, m is described by,

$$m = m_o + m_1 \, e^{-\alpha W_p} \qquad (3)$$

where $m_1$ and $\alpha$ are additional model parameters. For less strain hardening materials, $m_1$ and $\alpha$ are assumed to be zero. Rajendran et al [13] described the B-P model parameter evaluation scheme for three different metals. In their scheme, all the parameters were determined, from a few (at least three) tensile split Hopkinson bar stress-strain curves at different strain rates and the steady state value of the Hugoniot Elastic Limit (HEL), $\sigma_{HEL}$.

Until voids nucleate, the aggregate behavior can be described by the B-P model. The plastic flow in the void-free aggregate is incompressible, i.e., the sum of the principal or orthogonal plastic strains is equal to zero. However, the nucleation of voids will introduce dilatation and the plastic yield behavior will depend not only on the second invariant $J_2$, but also on the mean stress or pressure. The constitutive model for the aggregate must include these effects. For this purpose, we selected a yield-criterion-based plastic flow rule in which the pressure dependence enters explicitly into the calculations.

B. Modeling of Aggregate with Voids

We considered a yield-criterion-based approach in the constitutive model formulation. For randomly distributed voids or microcracks contained in the aggregate, the yield behavior will be influenced by not only the second invariant of the deviatoric stress ($J_2$) but also by the pressure or mean stress ($I_1$). The following form of the yield function has been considered:

$$A(\rho) \, J_2 + B(\rho) \, I_1^2 = \delta(\rho) \, Y_m^2 \qquad (4)$$

where A, B, and $\delta$ are functions of relative density, $\rho$. $Y_m$ is the effective stress in the material. (Note: the subscript 'm' means

114

matrix material and not a tensorial index.) Based on a critical total deformation energy, Doraivelu et al. [14] derived the following expressions for A and B:

$$A(\rho) = 2 + \rho^2 \tag{5}$$

and

$$B(\rho) = \frac{1 - \rho^2}{3} \tag{6}$$

The expression for $\delta(\rho)$ under dynamic loading regimes was given by Rajendran et al. [15]

$$\delta(\rho) = e^{-\beta\left[\frac{1-\rho}{\rho}\right]} \tag{7}$$

In general, this function is material dependent while the functions A and B are independent of the matrix material behavior. Thus, the yield condition for the aggregate can be written as:

$$\Phi = (2+\rho^2)\, J_2 + \frac{1-\rho^2}{3}\, I_1^2 - \delta(\rho)\, Y_m^2 = 0 \tag{8}$$

The viscoplastic strain rates in the aggregate can be calculated using the flow rule derived as:

$$\dot{\epsilon}_{ij}^p = \lambda\, \frac{\partial\Phi}{\partial\sigma_{ij}} \tag{9}$$

The proportionality factor $\lambda$ can be obtained using the flow rule in conjunction with the following relationship:

$$(1-f)\, Y_m\, \dot{D}_m^p = \sigma_{ij}\, \dot{\epsilon}_{ij}^p \tag{10}$$

where f is the void volume fraction and related to relative density $\rho$ through $f = 1-\rho$. Note that m is a subscript and not a tensorial index. The above expression was derived from the definition that the total plastic work in the aggregate is entirely due to the

plastic work done by the matrix. By combining Equations (9) and (10), $\lambda$ can be expressed by,

$$\lambda = \frac{(1-f) \ Y_m \ \dot{D}_m^p}{\frac{\partial \Phi}{\partial \sigma_{ij}} \ \sigma_{ij}} \tag{11}$$

The plastic strain rates in the aggregate can be written as:

$$\dot{\epsilon}_{ij}^p = \frac{(1-f) \ Y_m \ \dot{D}_m^p}{\frac{\partial \Phi}{\partial \sigma_{rl}} \ \sigma_{rl}} \ \frac{\partial \Phi}{\partial \sigma_{ij}} \ . \tag{12}$$

In the constitutive model formulation, the total strain rate is decomposed into elastic and plastic strain rates. The elastic strain rates, $\dot{\epsilon}_{ij}^e$ are related to the stress through Hooke's law as:

$$\dot{\epsilon}_{ij}^e = D_{ik} \ \dot{\sigma}_{kj} \tag{13}$$

where $D_{ik}$ is the inverse of elastic modulus matrix, $E_{ik}$.

Using the consistency condition which holds during the plastic flow, we can obtain an expression for $\dot{Y}_m$ as:

$$\dot{Y}_m = \frac{-\left( \frac{\partial \Phi}{\partial \sigma_{ij}} \ \dot{\sigma}_{ij} + \frac{\partial \Phi}{\partial f} \ \dot{f} \right)}{\frac{\partial \Phi}{\partial Y_m}} \tag{14}$$

An expression for $\dot{\sigma}_{ij}$ can be obtained from Equation (13) by replacing the elastic strain rate as the difference between total and plastic strain rates,

$$\dot{\sigma}_{ij} = E_{i\ell} \ (\dot{\epsilon}_{\ell j} - \dot{\epsilon}_{\ell j}^p) \ . \tag{15}$$

We now need an evolution equation to calculate f at any given instance of the loading history. The void volume fraction rate, $\dot{f}$,

116

contains two parts; one due to the growth of existing voids, and the other due to the nucleation of new voids.

## C.   Void Nucleation and Growth

The most widely used void nucleation model was the one that was initially used by Chu and Needleman [16] in their analysis of localized necking in biaxially stretched sheets.  The model was based on a mechanism in which voids are nucleated due to debonding of inclusions from the matrix.  The debonding can occur due to either a stress or a strain criterion or both.  The corresponding model is given by,

$$\dot{f}_n = F_\sigma \ (\dot{Y}_m + \dot{P}) + F_\epsilon \ \dot{D}_m^p \qquad (16)$$

where

$$F_\sigma = \frac{f_1}{s_1 \sqrt{2\pi}} \ e^{-\frac{1}{2} \left[\frac{Y_m + P - \sigma_N}{s_1}\right]^2} \qquad (17)$$

and

$$F_\epsilon = \frac{f_2}{s_2 \sqrt{2\pi}} \ e^{-\frac{1}{2} \left[\frac{D_m^p - e_N}{s_2}\right]^2} \qquad (18)$$

If the nucleation is due to only the matrix debonding from inclusions, then the total void volume nucleated must be consistent with the volume fraction of second phase particles.  Therefore, the values determined for the parameters $f_1$ and $f_2$ must meet this requirement.  $\sigma_N$ and $e_N$ are the mean equivalent stress and strain, respectively, around which the nucleation stress and strain are distributed in a Gaussian manner.  $s_1$ and $s_2$ are the standard deviations of the distributions.  These two parameters will control

117

the ranges of stress or strain over which most of the voids can be nucleated.

The growth law can be directly related to the dilatation due to growth of voids in the aggregate. By definition, the growth rate is given by,

$$\dot{f}_g = (1-f) \; \dot{\epsilon}^p_{ii} \tag{19}$$

where repeated index means summation and $\dot{\epsilon}^p_{ii}$ are plastic strain rates in the three principal directions and $f = 1-\rho$. By taking derivatives of the yield function with respect to the stress components and by summing up the plastic strain rates (12), the equation for void growth rate (19) can be written as

$$\dot{f}_g = \frac{3 \; \rho^2 \; \dot{D}^p_m \; (1 - \rho^2)}{\delta(\rho)} \; \{\frac{P}{Y_m}\} \tag{20}$$

The evolution equation for the void volume fraction is then given by the sum of $\dot{f}_g$ and $\dot{f}_n$ as:

$$\dot{f} = (1-f) \; \dot{\epsilon}^p_{ii} + F_\sigma(\dot{Y}_m + \dot{P}) + F_\epsilon \; \dot{D}^p_m \tag{21}$$

where $F_\sigma$ and $F_\epsilon$ are given by Equations (17) and (18). Six model parameters have to be determined to describe the void nucleation process, when the process is due to both stress and strain criteria.

When the stress state is triaxial with $(P/Y_m) \gg 1$, the nucleation process is stress-controlled; whereas under uniaxial stress states, such as in a thin ring cylinder or under plane stress condition, the mechanism is dominated by strain. It is fairly well established that under high strain rate and high pressure loading conditions, the void nucleation mechanism is dominated by the pressure (mean stress). To model the spall type failure, void nucleation due to $F_\epsilon$ in Equation (16) is negligible and in turn, we can set $F_\epsilon = 0$ in the calculations. Effectively, the void

118

volume fraction model will include only three parameters which can be determined from the plate impact tests data.

The rate Equations (1), (2), (12), (14), (15), and (21) must be solved numerically to describe the stress-strain response of a void contained aggregate material.  In particular, these equations were carefully rearranged to create a well-behaved set of first order ordinary differential equations.  These equations are solvable by a first order Diagonally Implicit Runge-Kutta (DIRK) scheme [17].  A first order DIRK scheme is designed to be stable, second order accurate, and efficient for stiff differential equations. The corresponding numerical algorithm was appended to the STEALTH finite difference code [18].  For this purpose several special purpose subroutines were developed.  Numerical exercises were conducted using these new subroutines.  The exercises were based on a plate impact test simulation.  (Note: a description of plate impact test is given in a later section.)  Results showed that the subincremental time steps of the DIRK scheme had to be unrealistically small to sustain a stable solution when $\delta(\rho)$ approached zero. Even for reasonably small time steps, a definite finite difference grid sensitivity was noticed due to the widening gap between the STEALTH time step and the DIRK scheme time step as $\delta(\rho)$ approached zero.  Further investigation revealed that this grid sensitivity was due to the exponential form of the $\delta(\rho)$ function (see Equation 8).  We investigated this aspect of the modeling as discussed in the following section.

D.  A New Form for $\delta(\rho)$

The conditions on the coefficient of the matrix effective stress in the yield function is $\delta(\rho) = 1$ at $\rho = 1$ and $\delta(\rho) = 0$ at $\rho = \rho_{cr}$.  We proceed initially with the form

$$\delta(\rho) = \frac{g(\rho) - g(\rho_{cr})}{g(1) - g(\rho_{cr})} \tag{22}$$

119

which satisfies the conditions on the $\delta$ function. However, a new function for $g(\rho)$ is proposed here as

$$g(\rho) = \left[\kappa - \frac{N}{|N|}(1 - \rho)\right]^N \tag{23}$$

The experimental observation of the spall signal indicated that the first derivative of $\delta(\rho)$ at $\rho = 1$, or

$$\beta = \delta'(1) = \frac{|N| / \kappa}{\left[1 - g(\rho_{cr}) / g(1)\right]} \tag{24}$$

should be much greater than unity. If $\beta$, $N$, and $\rho_{cr}$ are treated as model constants, the value for $\kappa$ can be solved from Equation (24) by an iterative scheme. Note that Equation (23) requires $\kappa > N(1 - \rho)/|N|$, for any real $N$. A negative real value of $N$ obviously allows $\kappa$ to be close to zero so that $\beta$ can become a large value without requiring large values of $|N|$ nor requiring $\rho_{cr} = 1$ in Equation (24). A negative value of $N$ also makes Equation (23) a hyperbolic power function which we find to be numerically more efficient than the exponential form. This fact has been substantiated through the numerical simulations of a plate impact test configuration.

III. PLATE IMPACT SIMULATIONS

In this section, the plate impact experimental technique is briefly described. Detailed discussions on planar plate impact can be found in References 19 and 20. Determination of the failure model parameters is aided through the simulation of plate impact tests. Simulations are carried out using the STEALTH one-dimensional finite difference code. The effect of each model parameter on the spall behavior is evaluated from the simulation results. A methodology to determine the parameters is outlined. The model also has been successfully used to describe spallation in OFHC copper.

## A.  Description of Plate Impact Test

The most commonly used test technique to determine high strain rate material properties is the plate impact experiment. This technique is schematically shown in Figure 1.  A flat flyer plate is impacted against a flat target plate.  The resulting free surface velocity history of the target is measured using a VISAR (velocity interferometer).  Using an embedded piezoresistive gage between the target and a plastic backing block as shown in Figure 1, the stress history can also be determined.

A typical free surface velocity history profile is given in Figure 2.  The first wave (point E) that propagates into the target plate is an elastic wave.  Depending on the impact velocity, a plastic wave (point P) follows the elastic wave.  The unloading wave that originates at the rear surface of the flyer arrives at point R.  Interaction of unloading waves from the free surfaces of the flyer and target plates lead to high triaxial tensile stresses in the target.  Usually, nucleation, growth, and coalescence of microvoids occur under such high stresses.  This failure process is often termed as spallation.

When the material inside the target fails, a compression wave originates from the spalled plane toward the target free surface. This compression wave arrival is at point S.  The velocity plot beyond point S is often referred to as the spall signal.   The velocity $\Delta V_s$ is related to the stress level at which nucleation of microvoids occur inside the target.  The nucleation stress level, $\sigma_N$, can be determined from a shock relationship,

$$\sigma_N = \frac{1}{2} \rho \ C \ \Delta V_s \qquad (25)$$

where $\rho$ is the mass density and C is the wave speed.

## B.  Physical Features

Impact of a 2-mm thick copper flyer against a 9-mm thick OFHC copper target is modeled using the STEALTH code.  The constitutive

and failure models described in Section 2 were used to characterize the high strain rate behavior of copper. Our first objective is to demonstrate the experimentally observed important physical features of the free surface velocity profile. In Figure 3, results from two different simulations are shown. In the first simulation, the model parameters were chosen so that the target spalls. A typical spall signal, as is usually observed in an experiment, can be seen in Figure 3. In the second simulation the spall is suppressed by choosing a zero value for the nucleation parameter, $f_1$. The complete unloading of the velocity history as indicated by the dotted line clearly demonstrates the absence of spall in the target.

In Figure 4, the velocity histories obtained from simulations at different impact velocities are shown. The most important physical features in the velocity profiles are the velocity level, $\Delta V_s$, and the time duration or period, $\tau_s$, of the wave transit between the spall plane and the free surface. The $\Delta V_s$ corresponds to a stress level around which rapid microvoid or microcrack nucleation occurs. If the impact velocity is greater than $\Delta V_s$, as in the cases of plots A, B, C, and D in Figure 4, then spallation will occur, as indicated by the spall signal. However, at an impact velocity of 50 m/s, it can be clearly seen that spall nucleation has not occurred. The tensile stresses in the target at this impact velocity are lower than the mean nucleation threshold stress $\sigma_N$ ($\approx16$ kbars). In the nucleation model, nucleation is assumed to occur at $\sigma_N \pm 3s$, where s is the standard deviation. Figure 5 shows that at velocity V = 100 m/s, the tensile peak stress was around 13 kbars, compared to a peak stress of 18 kbars in compression. This is due to void softening of material which reduced the stress levels.

The void volume fraction distribution levels in the target at three different times are shown in Figure 6. The distribution clearly shows that the maximum void volume fraction is at the spall plane which is around 2-mm (flyer plate thickness) from the free surface (x = 9-mm). Presence of voids at and around the spall

plane has been supported by metallographical studies conducted on different materials [11].

In Figure 7, the loading path at the spall plane of the target is shown. The void volume levels are shown by dotted lines. Initially the strength is independent of pressure as can be seen between points A-B. Damage nucleation has not yet initiated and therefore f remains zero. At B, the nucleation occurs. As the pressure increases, the void volume also increases between the loading points B-C. Strength rapidly decreases between points C-D. At one percent void (around D), the void contained aggregate can no longer sustain tensile pressure, so the pressure rapidly decreases as the void volume reaches 10 percent. Failure (coalescence of voids) occurs between points E-F. Both pressure and strength approach zero as the material completely fails.

## C.  Stability of the Solution

The integration of the ordinary differential equations for the constitutive model by a Diagonally Implicit Runge-Kutta (DIRK) scheme is known to be stable and at least second order accurate. But if the time intervals of the DIRK scheme are much smaller than the time step determined by the Courant criterion in the STEALTH wave propagation code, then the stability and accuracy of the solution becomes uncertain. Depending on the DIRK time step size, the STEALTH stable time step for a particular zone (or element), as determined from the Courant condition, may be reduced by an integer factor ranging from 2 to 10. This factor is initialized to one, indicating no reduction in the stable time step. Then the factor is either increased by one if the last DIRK time step is less than one tenth of the STEALTH time step, or decreased by one if the last DIRK time step is greater than two tenths of the STEALTH time step. This method allows a gradual, but not necessarily permanent, reduction in the STEALTH stable time step down to one tenth of the stable time step computed from the Courant condition. Since there is no mathematical criterion of stability for the entire solution, a few numerical exercises were devised to check for solution

stability and accuracy. These exercises involved several plate impact simulations. One effective numerical test was to determine if the total momentum and the total kinetic energy remained constant during a plate impact simulation. The solution was accepted only if this condition was met. The second exercise was to determine if the entire solution remained essentially the same if the grid size was varied. The results are shown in Figure 8 for two impact velocities, 200 m/s and 500 m/s for the three different grid sizes. It is possible to absolutely ensure stability and accuracy by forcing the STEALTH time interval to be the same as the DIRK scheme time interval, but this is costly in terms of programming effort and excessive computer time. In any case, numerical exercises to vary the numerical integration and stability parameters should be conducted to optimize the stability, accuracy, and computer time of the solution. The results so far indicate that the solution is stable and reasonably accurate.

### D. Sensitivity Study

It is important to evaluate the effects of various model parameters ($\sigma_N$, f, s, $\beta$, N, $f_{cr}$) on the numerically simulated failure process. For this purpose, we conducted a sensitivity study. The sensitivity of the dynamic failure model parameters on the solution (in the free surface velocity versus time plot) can be checked by varying the values systematically. The variation in the values of the three void nucleation parameters, ($\sigma_N$, $f_1$ and s) were examined first, and then the three void growth parameters ($\beta$, N, and $f_{cr}$) were examined.

An increase in the value of $\sigma_N$ causes the spall signal as shown in Figure 9 to occur later while the solutions during the rebound tend to merge together. Likewise, a decrease in the value of $f_1$ causes the spall signal as shown in Figure 10 to occur later while the solutions during the rebound tend to merge together. It appears the void nucleation parameters $\sigma_N$ and $f_1$ have a strong influence on the initial spall signal, but become a negligible influence on the void growth which affects the rebound.

124

The standard deviation s can be defined as a fraction of $\sigma_N$. The sensitivity study (see Figure 11) used three different fractions, 0.125, 0.25, and 0.5. Recall from Equations (16) and (17) that the model for void nucleation due to stress follows a Gaussian distribution with mean $\sigma_N$, which allows nucleation to occur for a stress range of $\sigma_N \pm 3s$. Since void nucleation in metals can only occur during tension, a practical upper limit for the fraction is one third. This prevents a negative lower bound for the nucleation stress range. Varying the stress standard deviation, s, has only minor effect on the spall signal or the rebound as shown in Figure 11.

The rebound peak of the spall signal increases for increasing values of the void growth parameters $\beta$ and $|N|$ as shown in Figures 12 and 13. The initial slope of the spall signal is less influenced by N than $\beta$. Further sensitivity studies showed that the void growth parameter $\beta$ seems to affect the slope significantly as shown in Figure 12. Taking advantage of the negligible influence of N on the slope, the parameter $\beta$ can be estimated by matching the spall signal slopes between the simulation and experiment. Varying $f_{cr}$ from 0.6 to 1.0 had a very minimal impact on the spall signal and the rebound. Therefore, we can arbitrarily choose a value of one for $f_{cr}$ which is consistent with the definition of f at failure.

In summary, the sensitivity study indicates that the failure model parameters can be systematically determined by matching the simulation results with the spall signal. $\sigma_N$ can be obtained from the relationship (25). The value for $\Delta V_s$ is available from the velocity history. The value for s can be arbitrarily chosen to be one-fourth of $\sigma_N$. A theoretical value of one can be assigned for $f_{cr}$. The only remaining parameters that need to be determined from the spall signal are, $f_1$, $\beta$, and N. $f_1$ can be determined by matching the spall arrival time. $\beta$ is chosen based on matching the slope of the spall signal and finally N is selected based on matching the rebound peak of the spall signal. We successfully employed

this scheme and determined the model parameters for OFHC copper. The following section describes this effort.

### E. Model Parameters for OFHC Copper

The constitutive and failure models discussed in Section 2 were used to describe OFHC copper at high strain rate loading. Rajendran and Bless [21] determined the B-P model parameters from split Hopkinson bar experimental data and the steady state value of $\sigma_{HEL}$. The corresponding parameters are given below.

| $D_o$ 1/sec | $m_o$ kbar$^{-1}$ | $m_1$ kbar$^{-1}$ | $\alpha$ kbar$^{-1}$ | n | $Z_o$ kbar | $Z_1$ kbar |
|---|---|---|---|---|---|---|
| $10^8$ | 1.1 | 15.0 | 150 | 0.4 | 8.0 | 65.5 |

The plate impact experiment on annealed OFHC copper reported by Rajendran et al. [15] was employed in the failure model parameter evaluation. A 2-mm copper flyer was impacted against a 9-mm copper target at an impact velocity of 185 m/s. The free surface velocity history of the target was determined by VISAR measurements. This velocity history was used in the model parameter calibrations.

Based on the sensitivity study discussed in the preceding section, the failure model parameters are estimated. Out of the six parameters $\sigma_N$, s, $f_{cr}$, $f_1$, $\beta$, and N determination of the first three are fairly straightforward. The value for $\sigma_N$ can be determined from formula (25) and the corresponding value was 16 kbar. In order to minimize the number of model parameters, by taking advantage of the fact that s and $f_{cr}$ are less sensitive to the failure processes, we arbitrarily assigned s = 0.25 $\sigma_N$ and $f_{cr}$ = 1. We showed earlier that the spall signal did not show significant differences for s = 2, 4, and 8. Similarly for $f_{cr} \geq 0.5$, the results showed similar trends and therefore a theoretical value of 1 was chosen for $f_{cr}$.

The remaining parameters $\beta$, N, and $f_1$ were determined by adjusting them until the simulated free surface velocity matched

well with the experimental data. Following the guidelines dis-
cussed in the preceding section, $f_1$ was adjusted to approximately
match the spall signal arrival time. B was modified until the
average slope between points A-B in Figure 14 matched with the
experimental data. Finally, the value of N was chosen so that the
peak velocity at C matched with the data. The corresponding
failure model parameters for OFHC copper are given below.

| $\sigma_N$ (kbar) | s (kbar) | $f_1$ | $\beta$ | N | $f_{cr}$ |
|---|---|---|---|---|---|
| 16 | 4 | 0.01 | 65 | -2.4 | 1 |

It can be seen from Figure 14 that the simulated free surface
velocity history using the newly developed dynamic failure model in
STEALTH finite difference code compared extremely well with the
experimental data. The model parameters were systematically
developed using standard high strain rate experimental techniques.
The developed model evaluation scheme can be extended to other
materials which fail under dynamic loading conditions due to void
nucleation, growth, and coalescence.

IV. CONCLUSIONS

Void nucleation and growth based constitutive and failure
models to describe spallation type failure processes in ductile
materials under dynamic loading conditions were presented. The
model is three dimensional and based on micromechanical parameters.
Strain rate dependency on the strength (flow stress) and the pres-
sure effect on the plastic flow were also included in the model
formulation. New subroutines incorporating a sophisticated numeri-
cal procedure were successfully developed to describe the failure
model in the STEALTH finite difference code. Numerical stability
of the stiff differential equations that describe the model was
demonstrated through plate impact simulations.

The matrix material description through the Bodner-Partom model introduces the necessary strain rate dependency into the model. The Bodner-Partom model parameters were determined from the split Hopkinson bar stress-strain data at three different strain rates and the steady state value of the Hugoniot Elastic Limit from the plate impact experiments. Rajendran et al. described the procedure to determine B-P model parameters elsewhere in Reference 13.

The pressure dependent yield function served as a plastic potential through which the damage growth and degradation of material strength were effectively modeled. The void nucleation and growth models contained six parameters. The plate impact test simulation results demonstrated that only three parameters, $f_1$, $\beta$, and N, have to be determined by adjusting them to reproduce the experimentally observed free surface velocity history of the target. It was also shown that the determination of the other three parameters ($\sigma_N$, s, $f_{cr}$) was straightforward and did not require any calibration.

This model can be implemented into any one-, two-, and three-dimensional finite difference/element wave propagation/dynamic codes. We successfully implemented it into the STEALTH finite difference code and determined the model parameters for OFHC copper. Generality of the proposed three-dimensional failure model in configurations other than plate impact tests is yet to be evaluated. The validity of the model parameters must be evaluated by conducting additional plate impact tests with different thicknesses of both the flyer plate and target.

## V.    ACKNOWLEDGEMENTS

# REFERENCES

1. F.A. McClintock, J. of Appl. Mech., 35, 363, (1968).

2. J.R. Rice and D.M. Tracey, J. Mech. Phys. Solids, 17, 201, (1969).

3. H.W. Hancock and A.C. MacKenzie, J. Mech. Phys. Solids 1, 213, 107, (1976).

4. F. R. Tuler and B.M. Butcher, Int. J. Fracture Mechs., 4, 431-437, (1968).

5. S. Cochran and D. Banner, J. of Appl. Physics, 48, 7, (1977).

6. A.M. Rajendran, Doctoral Dissertation, Dept. of Aero. and Astro., University of Washington, Seattle, (1980).

7. L. Davison, A.L. Stevens, and M.E. Kipp, J. Mech. Phys. Solids, 25, 11-28, (1977).

8. J.N. Johnson, J. Appl. Phys., 52, 4, 2812-2825, (1981).

9. M.S. Meyers and C.T. Aimone, Progress in Materials Science, 28, 1-96 (1983).

10. J.R. Assay and G.I. Kerley, Int. J. Impact Eng., 5, 69, (1987).

11. D.R. Curran, D.A. Shockey, and L. Seaman, J. Appl. Phys., 44, 4025, (1973).

12. S.R. Bodner and Y. Partom, J. of Appl. Mech., 42, 385-389, (1975).

13. A.M. Rajendran, S.J. Bless, and D.S. Dawicke, J. Eng. Mat. and Tech., 108, 75, (1986).

14. S.M. Doraivelu, H.L. Gegel, J.S. Gunasekara, J.C. Malas, J.T. Morgan, and J.F. Thomas, Int. J. Mech. Sci., 26, 9/10, 527-535, (1984).

15. A.M. Rajendran, D.J. Grove, and S.J. Bless, in Shock Waves in Condensed Matter, edited by S.C. Schmidt and N.C. Holmes (Elsevier Science Publishers B.V., 1987), 359.

16. C.C. Chu and A. Needleman, J. Engs. Mat. Tech., 102, 249-256, (1980).

17. Ala H. Al-Rabeh, Int. J. Computer Math., 21, 65, (1987).

18. R. Hoffman, Electric Power Research Institute Report No. NP-2080, (1981).

19.    C.H. Karnes, in Mechanical Behavior of Materials Under Dynamic Loads, edited by U.S. Lindholm, (Springer-Verlag, NY), (1968).

20.    J.R. Assay and J. Lipkin, J. Appl. Phys., 49, 4242, (1978).

21.    A.M. Rajendran and S.J. Bless, Air Force Wright Aeronautical Laboratory Report No. AFWAL-TR-85-4009, (1985).
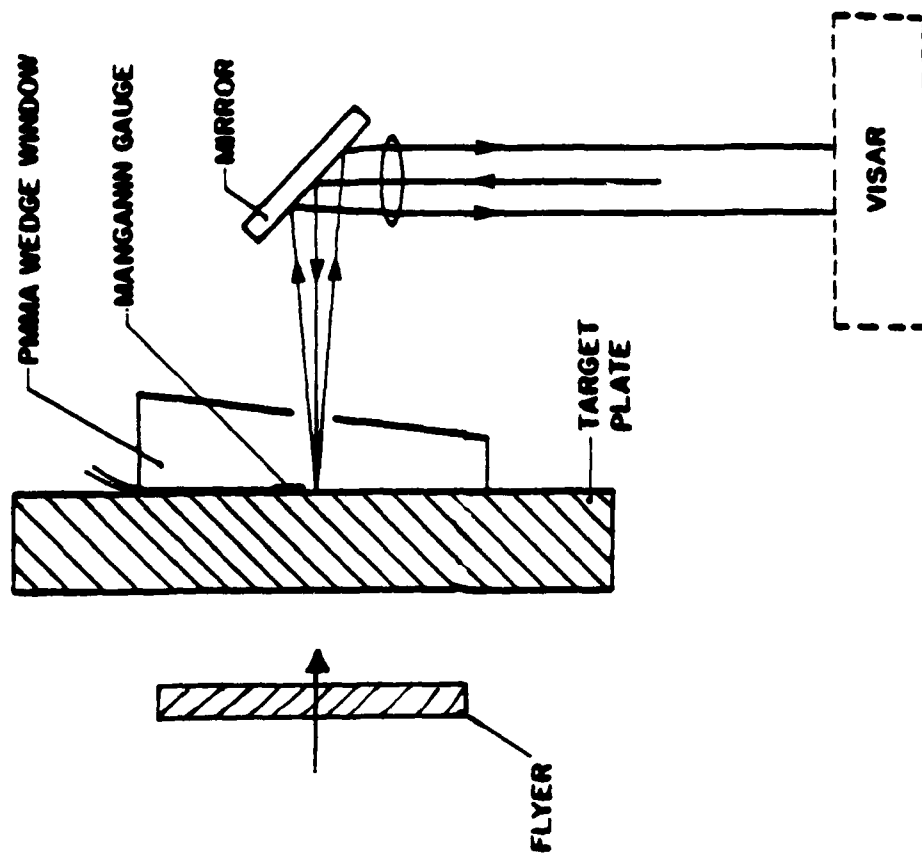
Figure 1. A Schematic of Plate Impact Test Along with the Diagnostics Setup.
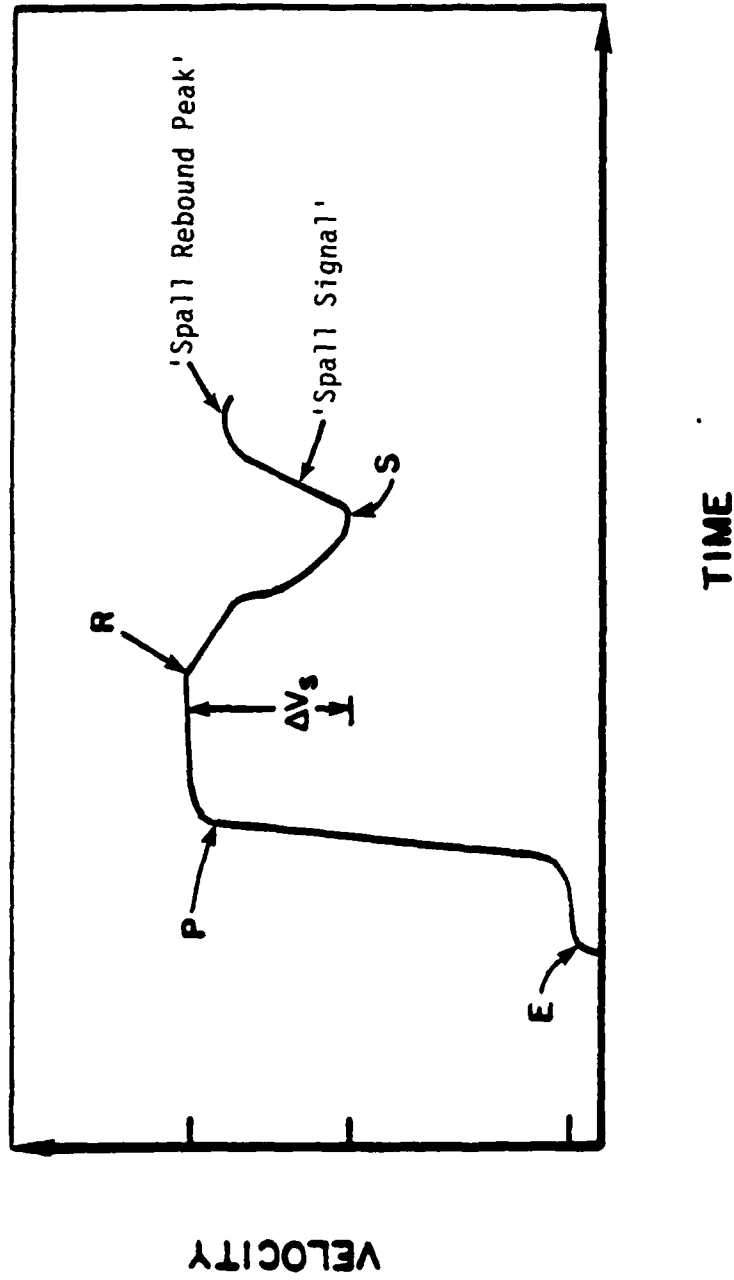
Figure 2.    Typical Free Surface Velocity of the Target Measured Using VISAR.

132
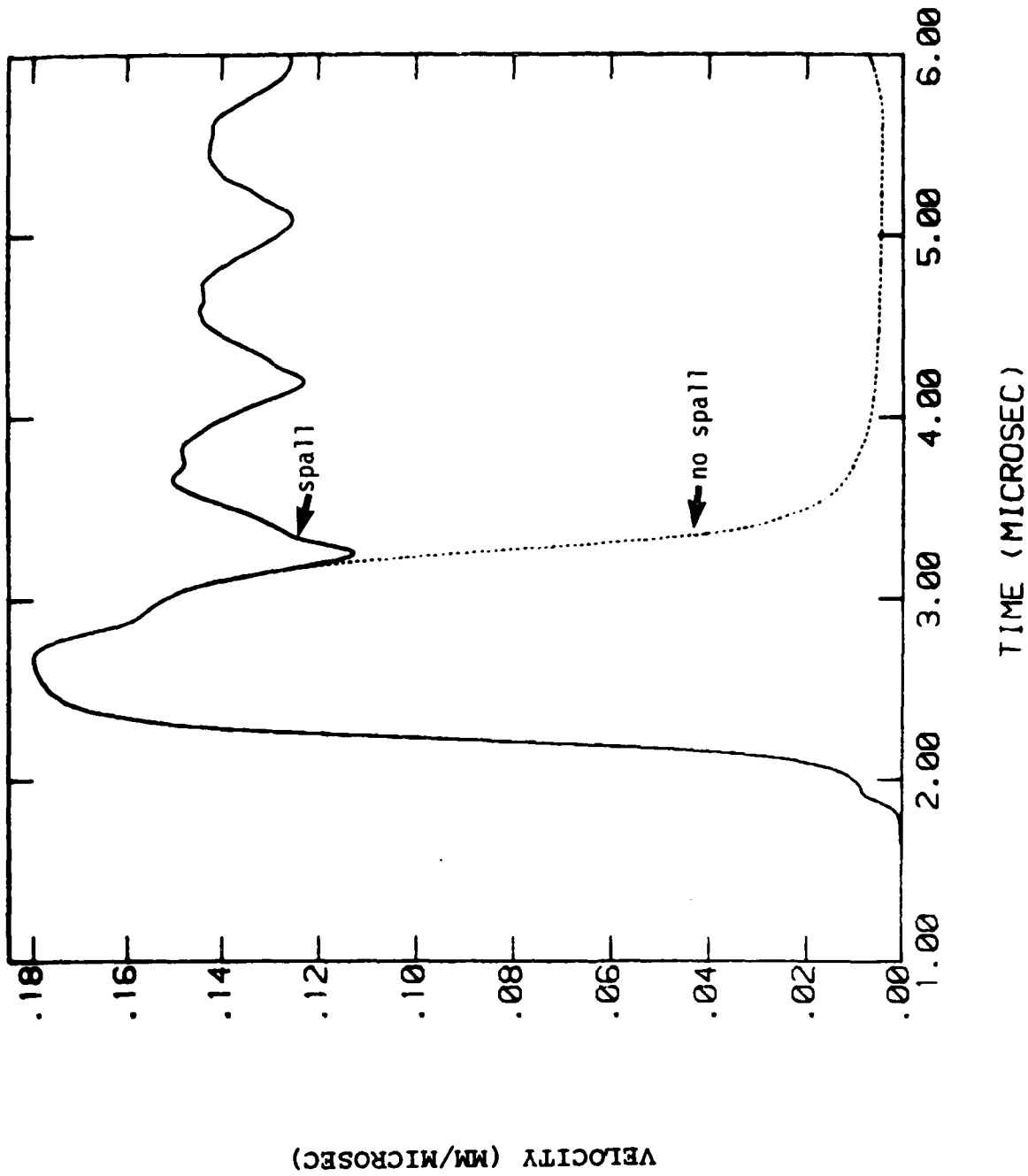
Figure 3.   Simulated Velocity History for a Target without and with Spall Failure.

133
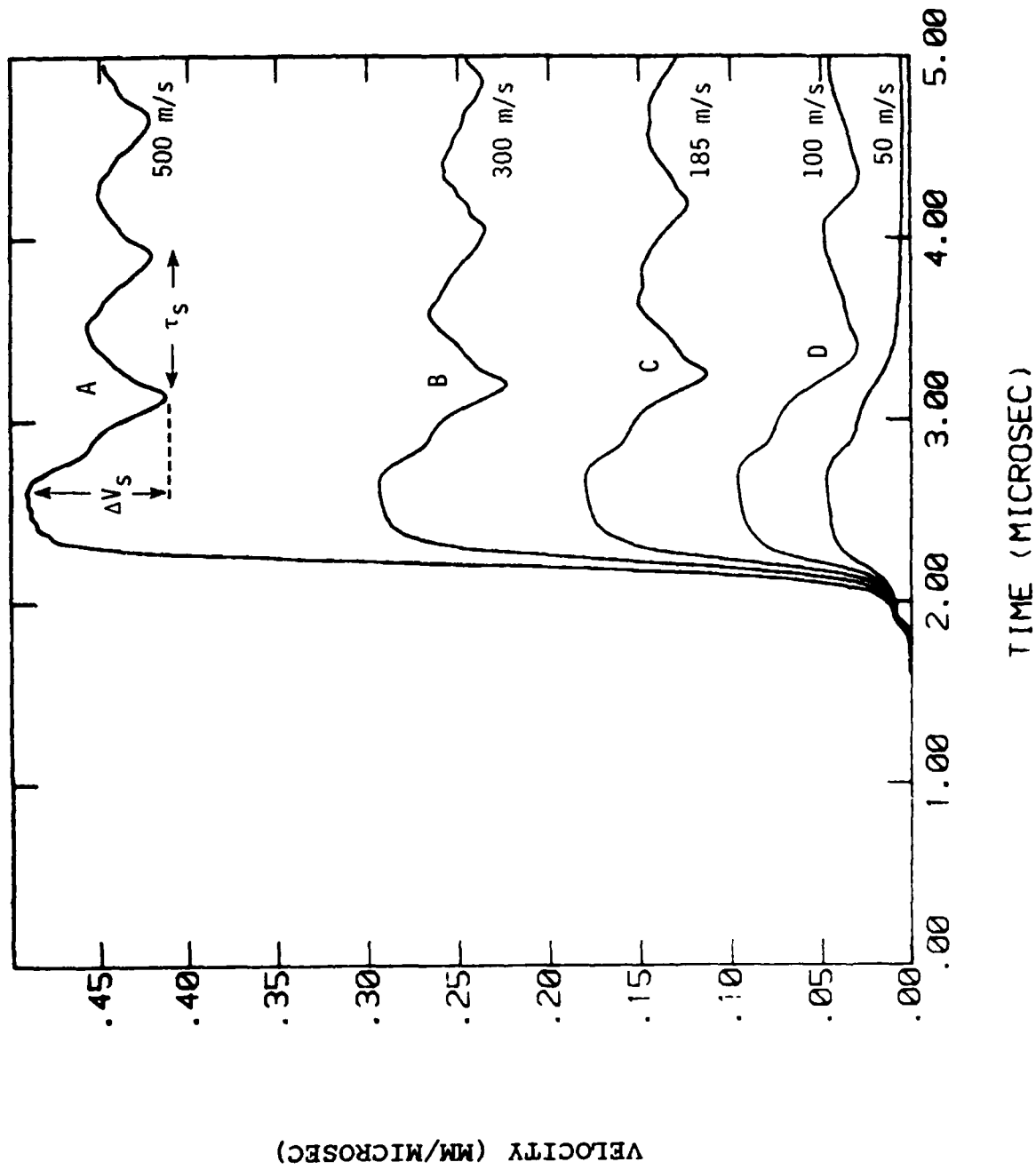
Figure 4. Simulated Free Surface Velocity Histories at Different Velocities. (Note: as velocity decreases, at V=50 m/s, no spall occurred.)

134
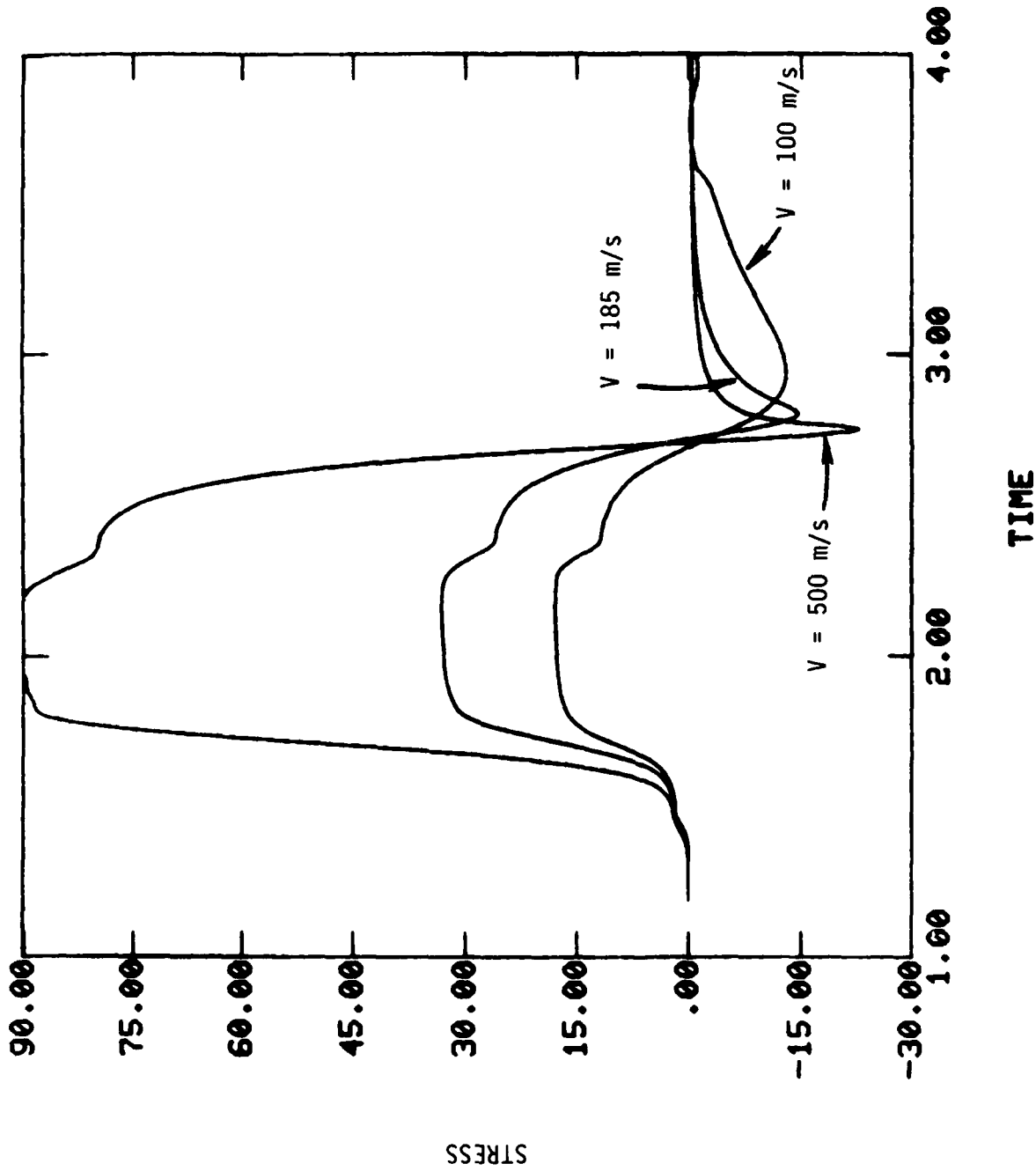
Figure 5. Simulated Stress History at the Spall Plane. Stress Relaxation under Tension is Shown for Three Impact Velocities - 100, 185, and 500 m/s. (Note: stress is -Ve in tension and +Ve in compression.)

135
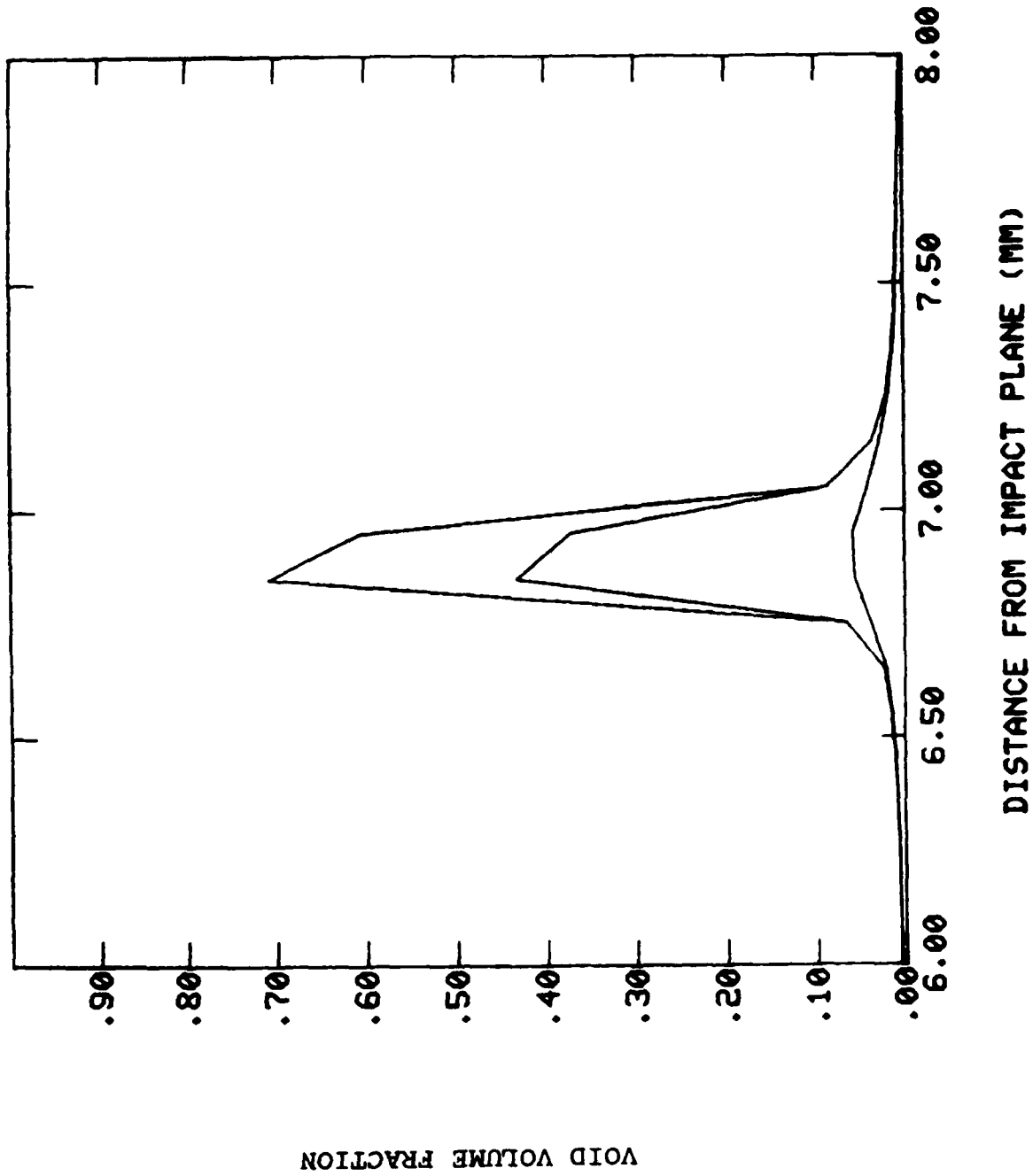
Figure 6. Model Simulated Void Distribution in the Impacted Target Plate for t = 3, 4, and 6 Microseconds.

136
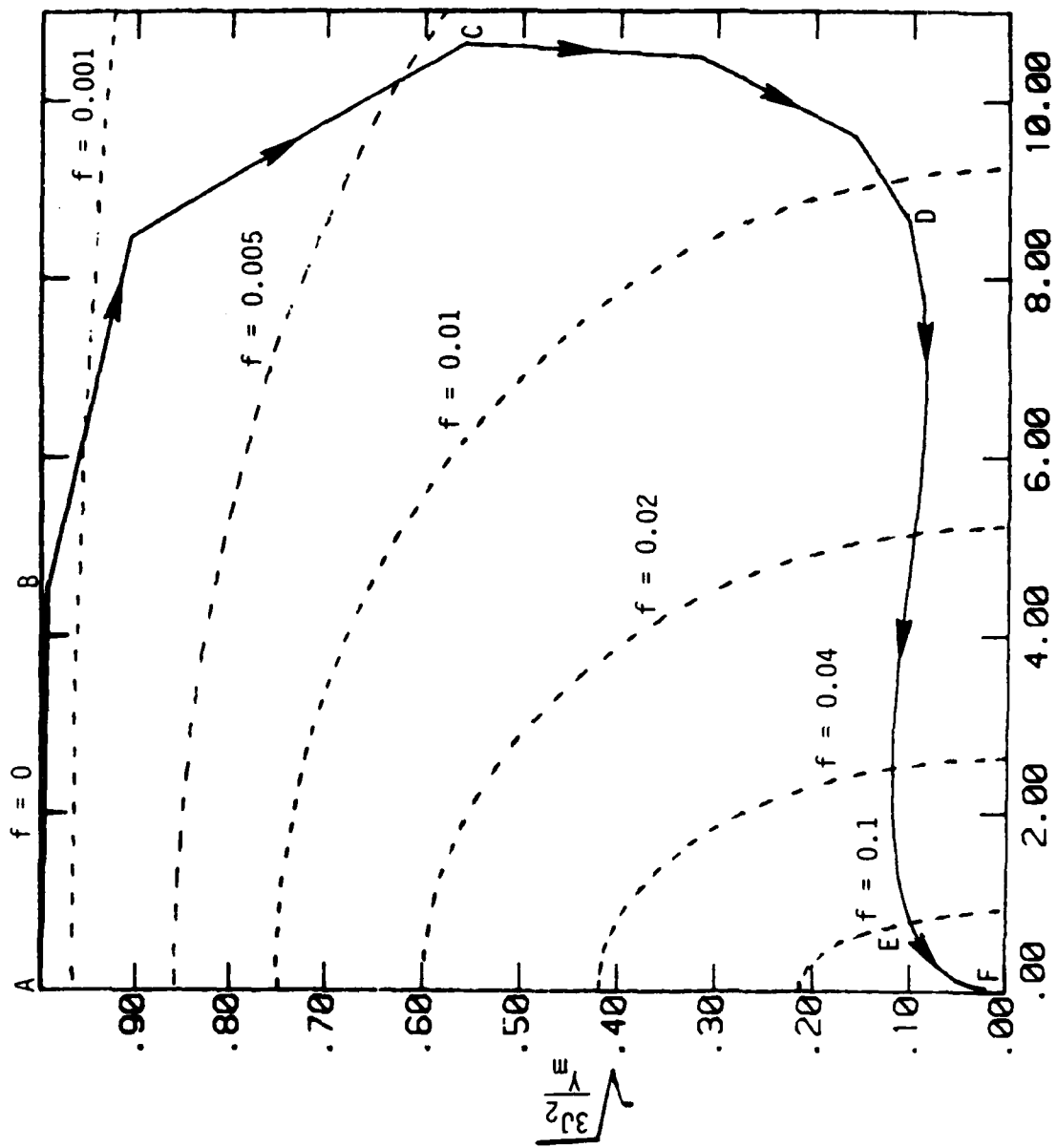
Figure 7. The Loading Path $\left(\sqrt{3J_2}/Y_m \text{ vs. } 3P/Y_m\right)$ at the Spall Plane in a Simulation.

137

TIME (MICROSEC)

VELOCITY (MM/MICROSEC)
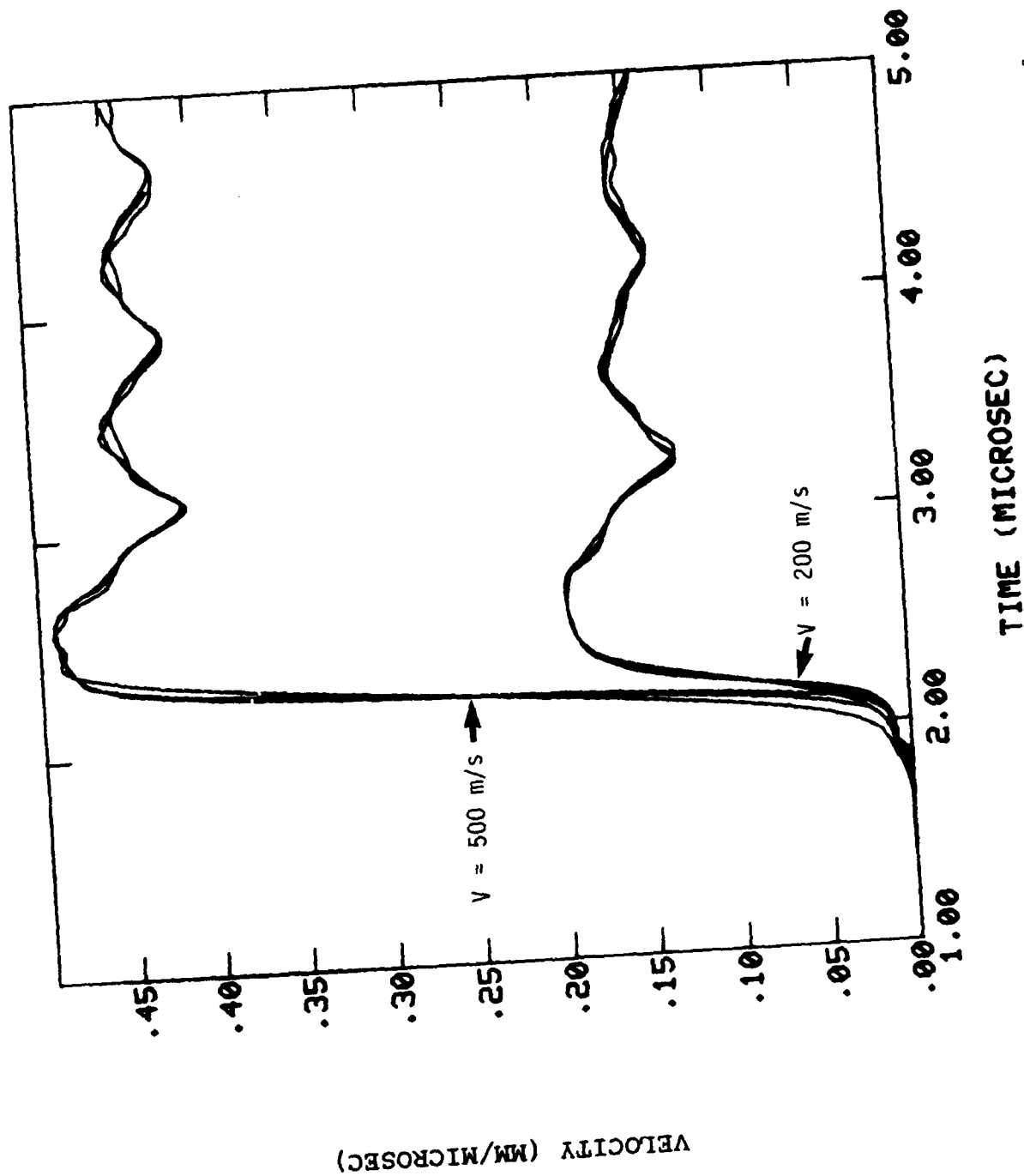
Figure 8. Demonstration of Grid (or mesh) Independency of the Solution for Three Different Grids at Two Velocities.

138

TIME (MICROSEC) SIGMAN

| | $\sigma_N$ = 1.2 GPa |
| --- | --- |
| $\circ$ | |
| — | = 1.6 GPa |
| $\triangle$ | = 2.0 GPa |
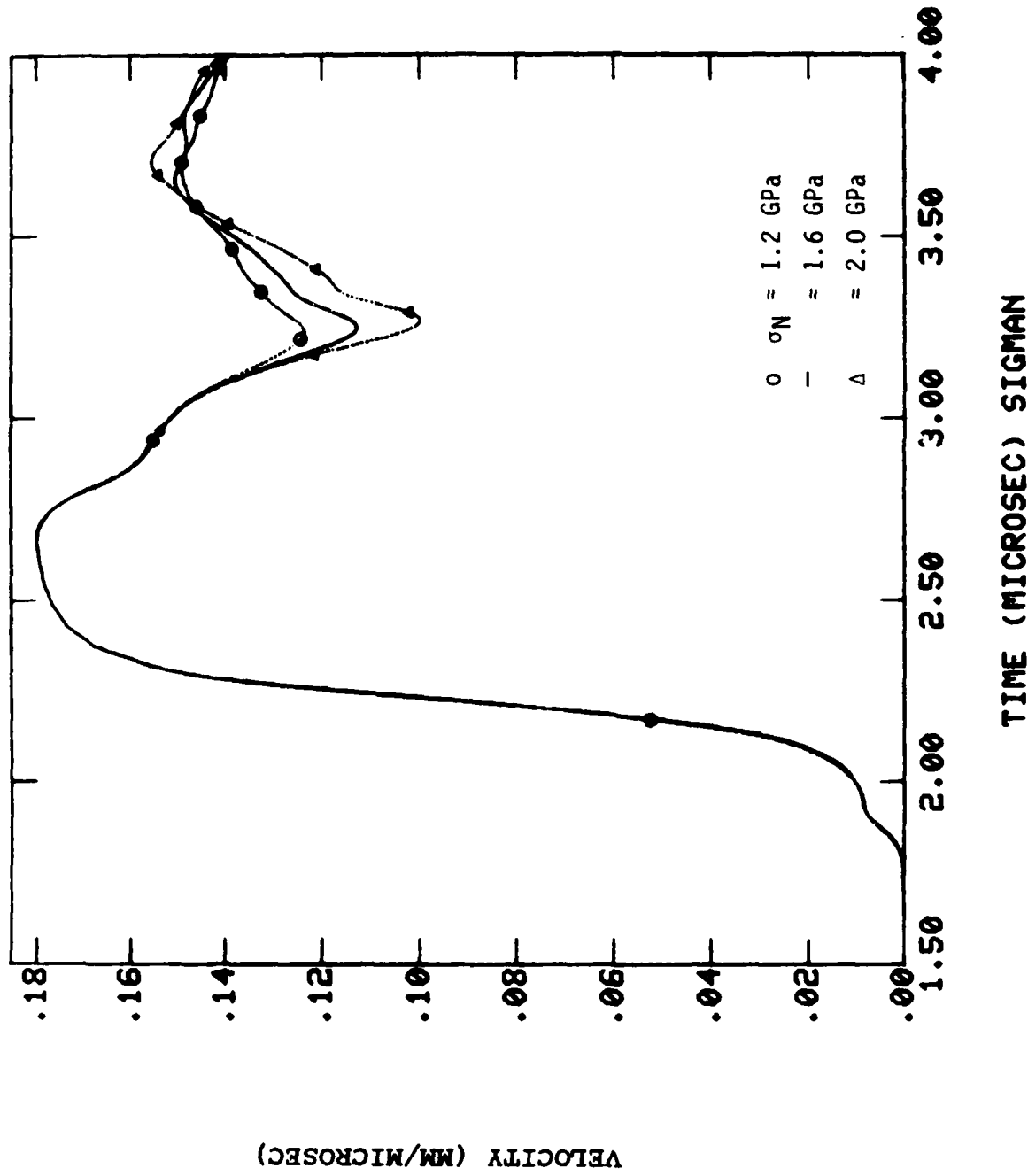
Figure 9.   Effect of Nucleation Parameter $\sigma_N$ in Equation (18) on the Spall Signal of the Free Surface Velocity History.
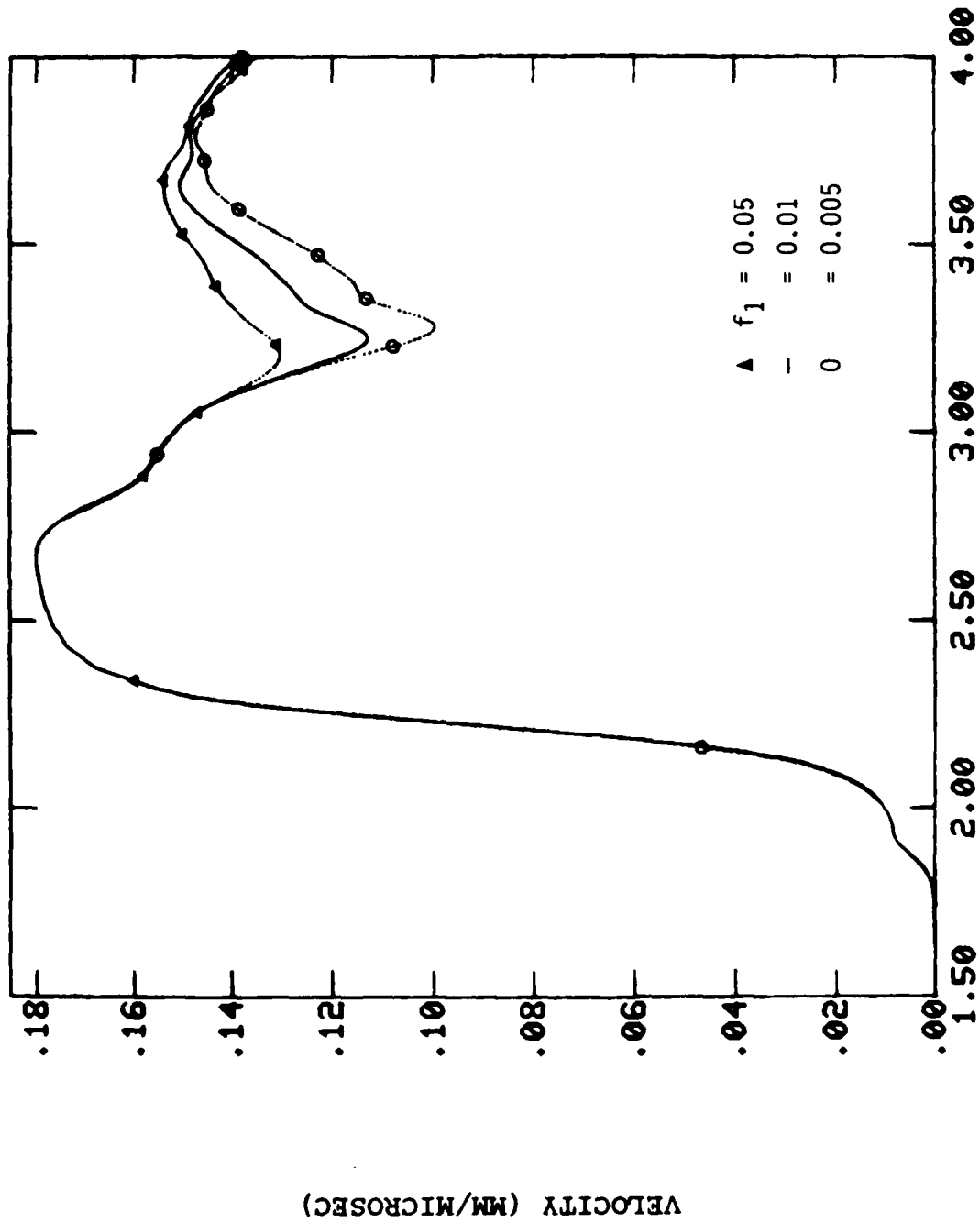
VELOCITY (MM/MICROSEC)

Figure 10. Effect of the Nucleation Parameter $f_1$ in Equation (18) on the Spall Signal of the Free Surface Velocity History.

140
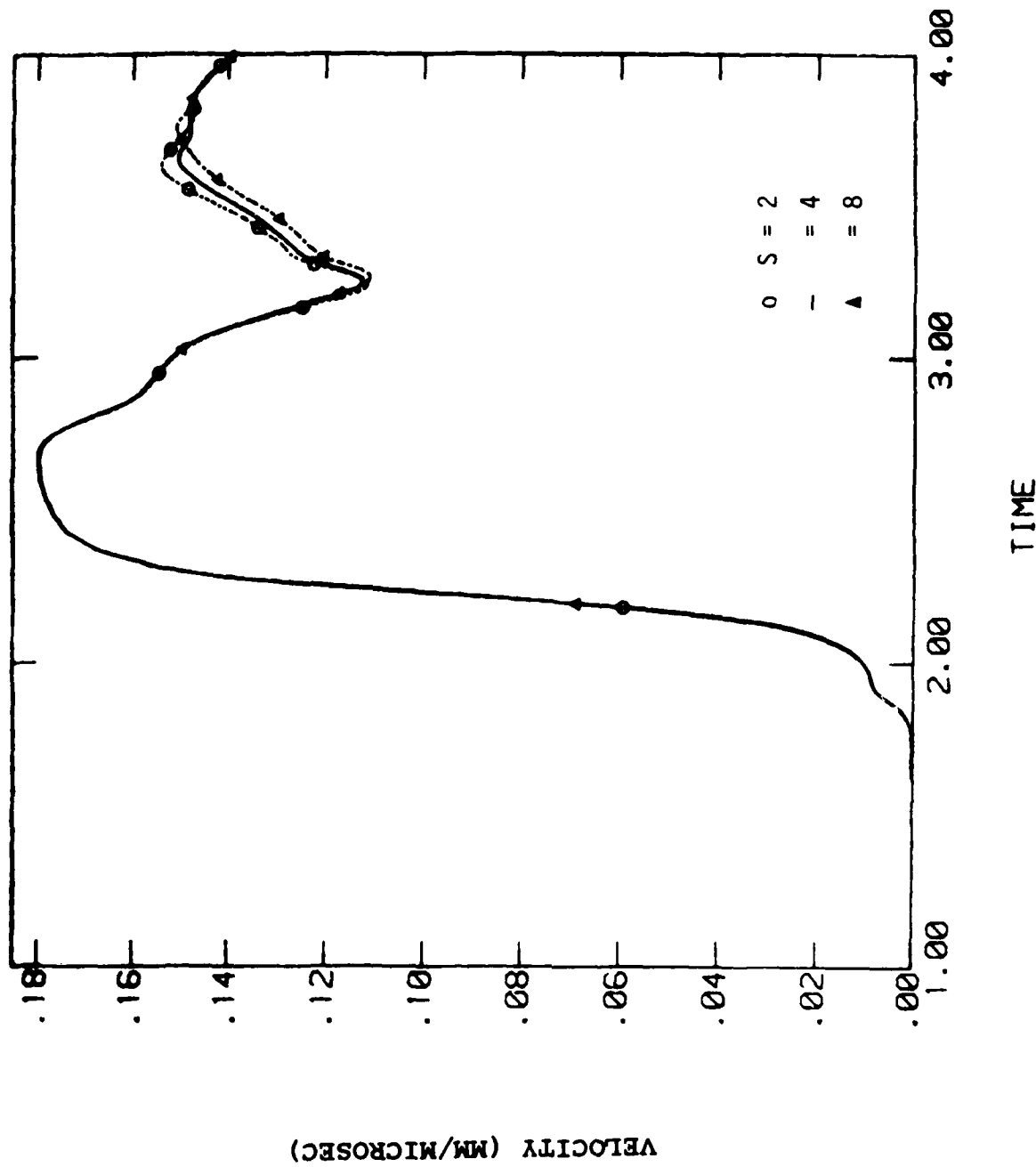
Figure 11.  Effect of Nucleation Parameter S in Equation (18) on the Free Surface Velocity History.

141
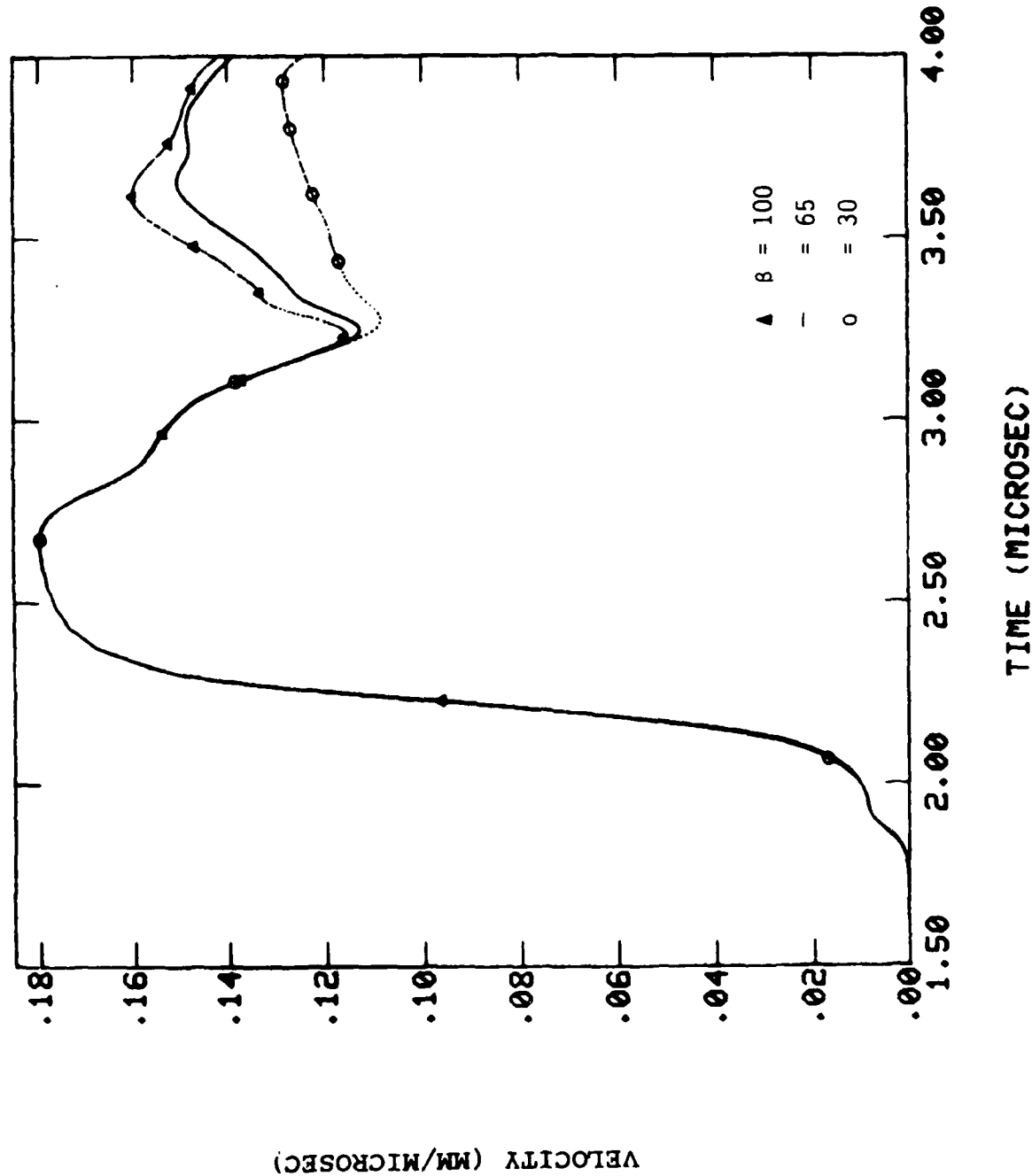
Figure 12.  Effect of Void Growth Parameter $\beta$ in the $\delta(\rho)$ Function on the Spall Signal of Free Surface Velocity History.

142
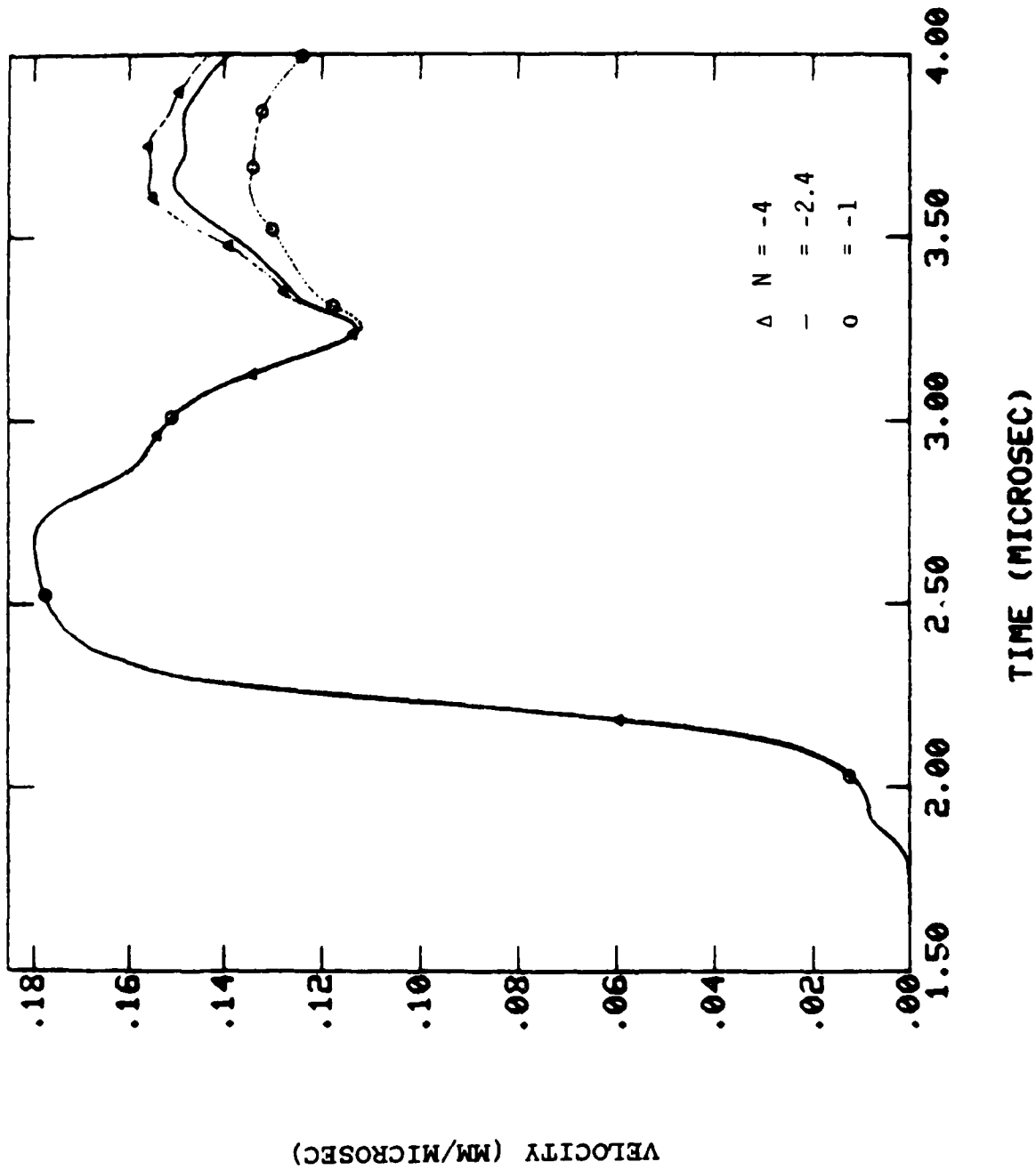
Figure 13.   Effect of N in the $\delta(\rho)$ Function on the Spall Signal of Free Surface Velocity History.
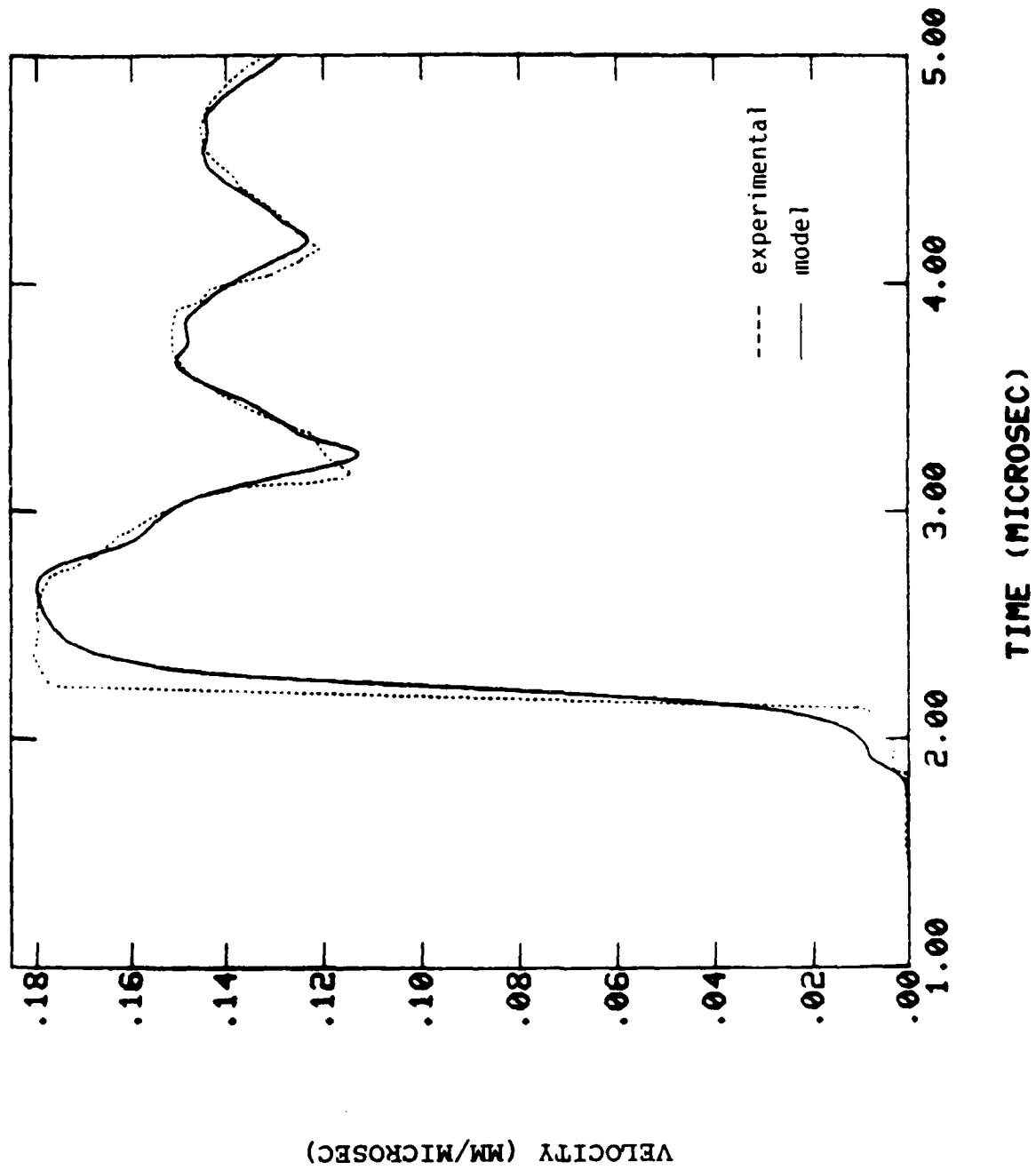
Figure 14.  Comparison Between Model Simulation and the Experimental Data
of the Free Surface Velocity History.

144

# MICROMECHANICS OF FAILURE AT HIGH STRAIN RATES:

## THEORY, EXPERIMENTS, AND COMPUTATIONS

S. Nemat-Nasser

Professor of Applied Mechanics and Engineering Sciences

University of California, San Diego, La Jolla, California 92093, U.S.A.

## Abstract

This paper examines the micromechanics of material failure by shear banding, void collapse and void growth, microcracking, and related phenomena at high strain rates. The following topics are discussed: (1) physical modeling and analytical formulation of void growth or void collapse in single crystals, where the effects of local anisotropic plastic deformation by slip, the rate of loading, and material ductility, on the change in the void geometry and subsequent failure mechanisms are reviewed; (2) a review of some recent experiments on void collapse in single and polycrystalline ductile materials, which seem to corroborate the theoretical predictions and demonstrate how a very ductile material can undergo brittle tensile fracturing normal to the applied compression, in the absence of any applied tensile loading; and (3) a phenomenological constitutive model for rate-dependent plasticity, including effects of the vertex structure and the temperature on the plastic flow.

## 1. Introduction

It is well known that large plastic deformation of ductile crystalline solids often leads to strain localization and shear banding which may persist and cause rupture. While this phenomenon has received considerable attention for quasi-static loading regimes, the corresponding dynamic case has been given far less attention numerically, analytically, and experimentally. Quantitative experimental observation of the flow and failure of solids at high and ultrahigh strain rates requires sophisticated and very expensive facilities and very skilled technical support. Because of this, few laboratories have been able to develop the required facilities in order to address the related fundamental scientific questions. Hence, many basic experimental issues associated with flow and failure modes of solids at high strain rates still remain unexplored.

In response to this paucity a new center, the Center of Excellence for Advanced Materials (CEAM), has recently been established at the University of California, San Diego, with the explicit objective of developing experimental, theoretical, and computational facilities and expertise, to study the basic problem of material performance at high strain rates. Figure 1 shows schematically the manner by which major efforts of this Center support each other with the aim of tailoring the microstructure of materials for optimal dynamic performance.

As is seen from Fig. 1, one of the major aims of CEAM is the modeling of inelastic deformation and the failure modes of advanced materials. This includes the numerical modeling of ductile rupture at high strain rates

146

which involves shear banding, adiabatic shearing, and related phenomena. Both micromechanically based and phenomenological constitutive models are considered.

This paper examines shear banding, void collapse, microcracking, and related phenomena at high strain rates, based on physical modeling experiments and phenomenological constitutive relations. These relations are developed within a framework which is sufficiently general to include a number of significant features. For example, the effects of thermal softening, the vertex structure of yielding, and the apparent increase in the flow stress with increasing strain rate, can be accommodated. Some of these issues are examined and illustrated in the following. In particular, the following topics are discussed: (1) physical modeling and analytical formulation of void growth or void collapse in single crystals, where the effects of local anisotropic plastic deformation by slip, the rate of loading, and material ductility, on the change in the void geometry and subsequent failure mechanisms are reviewed; (2) a review of some recent experiments on void collapse in single and polycrystalline ductile materials, which seem to corroborate the theoretical predictions and demonstrate how a very ductile material can undergo brittle tensile fracturing normal to the applied compression, in the absence of any applied tensile loading; and (3) a phenomenological constitutive model for rate-dependent plasticity, including effects of the vertex structure and the temperature on the plastic flow.

## 2. Physically Based Analytical Modeling of Void Growth and Void Collapse in Single Crystals

Plastic flow and failure mechanisms of ductile crystalline solids generally involve initiation and growth (under tension) or collapse (under compression) of microvoids. The process is highly rate-dependent, and whether or not the final failure regime is in a ductile or brittle mode for the same ductile crystalline solid, generally depends on the void configuration, on the state of stressing, and on the rate at which plastic flow takes place. Furthermore, even when the solid is a polycrystal with an overall isotropic response, its plastic deformation at the local crystal level is dominated by the local crystal anisotropy, and hence the growth or collapse of voids within a crystal is an anisotropic process, even under overall all-around uniform tensile or compressive forces. Such local plastic deformation occurs on specific geometric planes and is controlled by the rate of flow when slip is the predominant mode of plastic deformation.

Analytical studies of void growth and void collapse generally have been phenomenological and based on isotropic constitutive models; see, e.g., Nemat-Nasser et al. [1] for discussion and references. In an effort to include: i) the influence of local plastic anisotropic flow by plastic slip, and ii) the influence of the rate of plastic deformation on the mechanisms of void growth or collapse, a two-dimensional problem involving a double-slip system has been considered by Nemat-Nasser and Hori [2] and, for various far-field stress states imposed at moderate as well as at high and ultrahigh rates, void growth and void collapse have been studied

148

analytically; in a more recent work, Hori and Nemat-Nasser [3] have extended their results to fully three-dimensional cases.

In this section we briefly review the analytical formulation, present some numerical examples, and summarize the basic conclusions which seem to have important implications for ductile versus brittle response and failure modes of very ductile materials at high strain rates.

## 2.1 Formulation

High strain rate problems present enormous analytical difficulties because: i) the involved plastic deformation is highly rate-dependent; ii) plastic flow is anisotropic, occurring on geometric slip-planes; and iii) the inertia effects render the field equations extremely difficult to solve. The inertia terms may be neglected in formulating the constitutive models which may then be used in the general dynamic field equations that include the inertia terms. However, the effect of anisotropic plastic flow and the rate dependency of this flow must be included in the micromechanical modeling of constitutive relations involving void growth and void collapse in crystalline solids.

As an illustration, consider a face-centered cubic (fcc) single crystal containing a void, subjected to far-field stresses $\sigma_{ij}^{\infty}$. Denote by d and w, respectively, the deformation rate and spin tensors, and let superscripts e and p stand for the elastic and plastic parts of the corresponding rates. The stress rate corotational with the elastic spin is related to the elastic deformation rate by Hooke's law,

$$\overset{\circ}{\sigma}_{ij} + d^e_{kk}\,\sigma_{ij} - L_{ijkl}d^e_{kl} \quad, \tag{2.1}$$

where $L_{ijkl}$ is the elasticity tensor. The plastic part of the deformation is produced by slip on specific slip systems which, for an fcc model, will involve twelve active systems,

$$d^p_{ij} - p^\alpha_{ij}\,\dot{\gamma}^\alpha \qquad w^p_{ij} - \omega^\alpha_{ij}\,\dot{\gamma}^\alpha \qquad (\alpha\ \text{summed}),\ \alpha - 1,\ 2,\ \ldots,\ 12,$$

$$p^\alpha_{ij} = \frac{1}{2}\,(s^\alpha_i n^\alpha_j + s^\alpha_j n^\alpha_i), \qquad \omega^\alpha_{ij} = \frac{1}{2}\,(s^\alpha_i n^\alpha_j - s^\alpha_j n^\alpha_i), \qquad (\text{no sum on } \alpha) \quad . \tag{2.2}$$

Here $\dot{\gamma}^\alpha$ is the slip rate and $s^\alpha_i$ and $n^\alpha_i$ are the tangential and normal unit vectors of the $\alpha$-th slip system. Plastic flow by slip is assumed to follow the power-law, $\dot{\gamma} - \eta(\tau/\tau_r)^n$, where $\eta$, $\tau_r$, and n are regarded as material parameters, and $\tau$ is the resolved shear stress. The exponent n is very large, say, about 100 to 150, when the strain rate is relatively small, say, of the order of $10^3$ or less, and it is about unity for large strain rates. The quantity $\tau_r$ is the flow stress associated with a given slip system and, in general, depends on the accumulated slip on all other slip systems (cross-hardening), as well as the accumulated self-slip (self-hardening). It also depends on the temperature and hence the plastic work.

The slip-rate $\dot{\gamma}$, defined by the power law, has some serious limitations, especially at very high slip rates, where the exponent n is set equal to 1. An obvious limitation is that this does not place an upper value on the rate of slip. An alternative and still very simple model is to use an exponential relation of the form $\dot{\gamma} - \dot{\gamma}_M \exp\,(-a\tau_r/\tau)$, where $\dot{\gamma}_M$ is the upper value of the slip rate, and a is a numerical factor. Other, more physically based models have been proposed, but will not be discussed here.

150

## 2.2 Method of Calculation

In the sequel we confine attention to two-dimensional problems with two active slip systems; see Fig. 2. This is the problem associated with the actual experimental results which are discussed in Section 3. For a discussion and results of the general case, see Hori and Nemat-Nasser [3]. For details of the actual calculations, see Nemat-Nasser and Hori [2].

The far-field stress is assumed to be prescribed by giving the far-field stress rate $\dot{\sigma}$ as a function of time. The deformation of an initially circular void with radius $a_r$ is computed incrementally, using the following procedure:

1) At a specified time $t = t_0$, an elliptical cavity (see Fig. 2) with boundary $\Gamma(t_0)$ (i.e., $a_1$, $a_2$ and $\chi$ are prescribed) in an infinite elastoplastic solid is considered. The stress field $\sigma(t_0)$ is known. The solid is then subjected to a far-field incremental loading defined by stress rate $\dot{\sigma}^\infty$.

2) The instantaneous response is assumed to be purely elastic for a step loading $\Delta\sigma^\infty = \dot{\sigma}^\infty \Delta t$, and the instantaneous stress rate $\dot{\sigma}(t_0)$ and the incremental stress field $\Delta\sigma = \dot{\sigma}(t_0)\Delta t$ are calculated. The new stress field $\sigma(t_0+\Delta t)$ is then obtained as the sum of $\sigma(t_0)$ and $\Delta\sigma(t_0)$,

$$\sigma_{ij}(t_0+\Delta t) = \sigma_{ij}(t_0) + \Delta\sigma_{ij} + O(\Delta t^2). \tag{2.3}$$

3) From the current stress field $\sigma(t_0)$, the resolved shear stress on each slip system is calculated, and the current plastic deformation rate and spin tensors are obtained. The corresponding displacement gradient is then obtained from the sum of the elastic and plastic parts.

151

4) Ignoring the elastic contribution to the void shape change, and taking a sufficiently small time increment, the incremental small displacements of the points along the void boundary $\Gamma(t_0)$ are computed; this deformation by rate-dependent plastic flow is assumed to take place during the time increment $\Delta t$.

5) The new void geometry, in general, will not be elliptical. To continue the computation, an *equivalent* elliptical void with boundary $\Gamma(t_0 + \Delta t)$ is calculated, using the following criteria:

   a) The maximum distance from the center to the perimeter of the deformed void is taken to be the major semi-axis $a_1$ of the equivalent ellipse.

   b) The orientation of $a_1$ established in a) is taken to be the orientation of the major semi-axis, $\chi$.

   c) The aspect ratio of the equivalent ellipse is defined by $\rho = A/\pi a_1^2$, with A being the area of the deformed void.

This procedure can be continued until the aspect ratio of the equivalent ellipse becomes so small that the ellipse can be regarded to be a crack (void collapse), or until the aspect ratio attains a limiting value with the void area increasing in an unstable manner (self-similar expansion).

## 2.3 Tensile Cracking Normal to Applied Compression

Tensile cracks are generally formed in brittle materials in a direction normal to the applied *tensile* loads. Indeed, under mixed opening and sliding modes, cracks often curve and take on a direction normal to the

152

maximum applied tension, or *parallel* to the maximum applied compression; see Horii and Nemat-Nasser [4]. Hence, it defies intuition that *tensile cracks can form in a very ductile material normal to the applied compression*. The theoretical model of Nemat-Nasser and Hori [2] suggests that this indeed can happen during unloading when a pre-existing void is fully or partially collapsed into a crack by uni-axial compressive loads. Furthermore, whether or not a collapsed void will extend as a tensile crack and the extent to which it will grow, depend on the initial void size, the rate of compressive loading, and the material toughness.

The analysis is based on the simple assumptions that unloading occurs elastically and that the crack may grow if the Mode I stress intensity factor exceeds a given critical value. The Mode I stress intensity factor at the tip of a crack of length 2a (which is obtained by the extension of a crack of length $2a_1$ formed by a collapsed void), due to the superposition of accumulated stresses during loading and released stresses during unloading, is given by

$$K_I = \int_{a_1}^{a} \sigma_n^{(\ell)}(\varsigma) \ 2\sqrt{a} \ \frac{d\varsigma}{\{\pi(a^2-\varsigma^2)\}^{\frac{1}{2}}} + \sigma_n^{\infty(u)} \sqrt{\pi a}, \qquad (2.4)$$

where the subscript n denotes the stress component normal to the crack face, and where it is assumed that the crack faces remain traction-free, and that the far-field stresses existing prior to unloading are removed by the amount $\sigma_n^{\infty(u)}$. In Eq. (2.4) superscript $\ell$ on $\sigma$ stands for the magnitude of the stress during loading, and superscript u stands for the unloading stress. In the actual calculation the extended crack length defined by a, is chosen such that the value of $K_I$, calculated from (2.4), equals the

153

prescribed critical value of the stress intensity factor.

The calculation shows and experiment verifies that higher compressive loads are required at higher loading rates, in order to collapse a void. Hence, larger stress intensity factors are attained in complete unloading, when void collapse occurs at higher loading rates. Thus the response of the same material containing the same microvoids will not be the same when the loading rate is changed: the material becomes stronger but more brittle at higher (compressive) loading rates.

For a given material with known fracture toughness, from Eq. (2.4) one can estimate the minimum size of the void which, upon collapse into a crack, does not extend during unloading. This minimum void size decreases with increasing loading rates.

## 2.4 Results and Discussion

The process of void growth and void collapse and the subsequent failure mechanisms depend on the orientation of the slip systems, the state of stress, the rate of loading, and the initial void size. The following general results are obtained.

1) Even under all-around uniform compression, an initially spherical (circular in two dimensions) void quickly becomes nonspherical and may collapse into a crack. Depending on the rate of loading, the ductility of the material (which is also affected by the rate of loading), and the initial void size, the crack which is formed by the void collapse may extend in its own plane during the course of unloading,

154

leading to failure by a brittle type tensile fracture, even though the material has not been subjected to any overall tensile loads. This occurs at high strain rates for sufficiently large voids. The minimum void size required for such a failure decreases with increasing compressive loading rate.

2) Void collapse in compression and void growth in tension are basically different processes and one cannot be regarded as the reverse of the other. Thus, phenomenological models currently used to estimate ductile fracture, which do not distinguish between void growth and void collapse, are of limited usefulness.

3) An initially circular (in two dimensions) void may collapse into a crack, even under uni-axial tension, if the orientations of the slip systems are suitable. Similarly, overall shear stresses can collapse a void into a crack. However, under tensile loads, voids usually expand into ellipsoidal cavities which may then grow self-similarly in an unstable manner, leading to ductile failure.

4) Figures 3a and b give typical results for void collapse in uni-axial compression, using a double-slip plane deformation assumption. In Fig. 4 we show a typical result for a spherical void which is deforming into a complicated shape under all-around compression. Figure 5 shows void growth under all-round uniform tension, and Fig. 6 shows how a void can collapse even in uni-axial *tension*. These are presented here for illustration, and the interested reader is referred to Nemat-Nasser and Hori [2] and Hori and Nemat-Nasser [3] for more details and examples.

155

## 3. Experiments

The results of the void collapse calculations reported in Sec. 2 are in good accord with data reported by Butcher *et al.* [5] on porous aluminum, where it was observed that voids collapsed in aluminum under 70 kg/mm$^2$ uniform compression, with reference stress of 40-50 kg/mm$^2$. This is essentially what the computation of Nemat-Nasser and Hori [2] has revealed for stress rates as high as $10^4 \tau_r s^{-1}$, where $\tau_r$ is the reference stress.

In an effort to fully understand the failure mechanisms associated with dynamic void collapse in ductile metals and to verify the theoretical predictions, a systematic experimental program has been initiated by the author and coworkers at CEAM. Initial experiments are uni-axial and are done both quasi-statically (strain rate $\approx$ 0.001/s) in a servo-controlled hydraulic testing machine, and dynamically (strain rate $\approx$ 1000 to $10^4$/s) in a split Hopkinson bar apparatus. Test specimens are copper and mild steel coupons approximately 17.8mm by 8.9mm, with 0.9mm thickness. Both polycrystal and single-crystal copper as well as (polycrystal) 1018 steel coupons are tested. Polycrystal coupons are conventionally machined, and a circular hole of approximately 350 to 600$\mu$m is drilled through the thickness at the center. Single-crystal coupons are obtained from a large (25mm dia. by 150mm long) copper crystal. Orientation is determined from back reflection Laue photographs of the X-ray diffraction pattern. Coupons are then Electrical Discharge Machined (EDM) from the large crystal, and an EDM of about 120$\mu$m diameter circular hole is put through the thickness at the center. Coupons are supported against buckling by sandwiching them between semicircular cylindrical pieces of OFHC copper or steel. 17.8mm

156

dia. by 8.9mm high. The sandwiched assembly is held together in a steel annulus whose height is selected to limit the total compressive deformation to a predetermined amount of plastic strain. The assembly is held in the steel annulus with Styrofoam pillows. Supporting copper pieces (and specimens) are annealed at 650°C for one hour after machining. Records of hole shape are made with a scanning electron microscope before and after testing.

Figure 7 shows the collapsed void in single-crystal copper axially strained by about 21.4% at 1,100/s strain rate. The upper figure shows the shear bands. The crystal is cut in such a manner that two slip systems in the plane of the specimen are activated. Hence, the thickness remains essentially constant. Since one of the slip systems dominates, the deformed void rotates, and the final configuration is not quite normal to the axis of compression. The two lower figures in Fig. 7 are the electronmicroscopic record of the polished and etched specimen. As is seen, the collapsed void has extended as a crack in dynamic crack growth fashion, resulting in multi-branching which suggests a rather high crack-growth velocity. Experiments of this kind clearly have shown that the cracks extend in many different directions and not only in the direction of the cleavage plane of the crystal.

Figure 8 shows the void collapse (initial void size of about 600μm) in compression and subsequent crack growth in 1018 mild steel, at various indicated strain rates. Extensive crack branching is observed which is an indication of very high velocity crack growth. The tensile cracks initially run straight ahead for a distance and then branch out. The

resistance of the material to plastic flow during compressive loading and the extent of subsequent tensile cracking decrease with decreasing strain rate; compare the three experiments shown in Fig. 8.

It is therefore seen that *brittle-type tensile cracking is produced in very ductile single and polycrystals under purely compressive loads, in a direction normal to the applied compression.* The large local plastic flow during void collapse produces residual strains which, during unloading, create cracks. Since, in the absence of voids, the failure mode of the same material is by ductile rupture, it can be concluded that the compression-induced large plastic flows produce certain embrittlement and hence, change the mode of failure of the material. To completely understand the microstructural changes that result in such a response, detailed studies of the dislocation structure in the region close to the collapsed void are required. For detailed discussion and additional experimental results the reader is referred to Nemat-Nasser and Chang [6].

## 4. Computational Modeling

As commented on before, unstable flow by localized deformations is an integral part of large-deformation metal plasticity. Hence, effective numerical models must be capable of capturing localization by shear banding as a part of the solution. This, however, is an exceedingly difficult problem which has eluded the computational solid mechanics community. While there is extensive literature on the numerical study of various phenomena relating to the problems of necking and shear banding, they have involved specialized computer programs with special elements which must be

158

arranged *a priori* in a manner which anticipates the location and orientation of the shear bands. Furthermore, essentially all such calculations concerned quasi-static deformation.

In view of this, a coordinated effort involving collaboration with researchers at Sandia National Laboratory, at Lawrence Livermore National Laboratory, and ANATECH, has been initiated at CEAM in an effort to develop within the context of large-scale explicit computer codes, PRONTO and DYNA, constitutive models and associated algorithms which are capable of predicting localized deformations at high strain rates, say from $10^2$/s to $10^7$/s. In this section some preliminary results are reviewed and illustrative examples given. A more complete discussion is found in Nemat-Nasser *et al.* [7].

## 4.1 A Phenomenological Model

A simple rate-dependent phenomenological model can be based on the assumption that the plastic deformation rate tensor $\underset{\sim}{d}^p$ is decomposed into two components, one co-axial with the deviatoric part of the Kirchhoff stress, the other normal to this stress, when viewed as vectors in the deviatoric stress space. The first component contributes to the rate of plastic work and may be associated with the gradient of a smooth plastic potential. The second component has zero contribution to the rate of plastic work, but serves to model the structure of the vertex on the yield surface, which is an integral part of slip-induced plasticity.

More specifically, we write for the deformation rate tensor $\underset{\sim}{d}$, with components $d_{ij}$,

$$\underset{\sim}{d} = \underset{\sim}{d}^e + \underset{\sim}{d}^p ,  \tag{4.1}$$

where the elastic part $\underset{\sim}{d}^e$ is given by

$$\underset{\sim}{d}^e = \underset{\sim}{M} : \underset{\sim}{\dot{\tau}} ,  \tag{4.2}$$

with $\underset{\sim}{M}$ being the elastic compliance tensor, and $\underset{\sim}{\dot{\tau}}$ an *objective* rate of change of the Kirchhoff stress. For the plastic part of the deformation rate tensor we write,

$$\underset{\sim}{d}^p = \dot{\gamma}\underset{\sim}{\mu} + A\tau\underset{\sim}{\dot{\mu}} ,  \tag{4.3}$$

where

$$\underset{\sim}{\mu} = \underset{\sim}{\tau}'/(\sqrt{2}\,\tau) , \qquad \tau = (\tfrac{1}{2}\underset{\sim}{\tau}' : \underset{\sim}{\tau}')^{\frac{1}{2}} .  \tag{4.4}$$

Hence,

$$\underset{\sim}{\mu} : \underset{\sim}{\mu} = 1 , \quad \underset{\sim}{\mu} : \underset{\sim}{\dot{\mu}} = 0 .  \tag{4.5}$$

In (4.3), A is the noncoaxiality parameter (Nemat-Nasser [8]) which, in rate-independent plasticity, plays an essential part in giving the model its predictive capability in large plastic deformations that involve instability by localization; see Rice [9], Stören and Rice [10], Nemat-Nasser [8], Nemat-Nasser and Iwakuma [11], and Asaro [12].

For rate-dependent plasticity we assume that $\dot{\gamma}$ is defined in terms of the effective stress $\tau$, in the same manner as the slip rate in single

crystals is defined in terms of the corresponding resolved shear stress. For example, we may choose

$$\dot{\gamma} = \dot{\gamma}_r \ (\tau/\tau_r)^n \ , \tag{4.6}$$

where the exponent n is a very large number for low strain rates, say, up to $10^3/s$, and is approximately 1 for higher strain rates, and $\tau_r$ is the reference effective stress associated with simple shearing at reference strain rate $\dot{\gamma}_r$. In general, $\tau_r = \tau_r \ (\gamma, \ T)$, where $\gamma$ is the accumulated effective shear strain, and T is the temperature. Other forms such as

$$\dot{\gamma} = \dot{\gamma}_M \ \exp \ (-a\tau_r/\tau) \ , \tag{4.7}$$

where $\dot{\gamma}_M$ is the limiting value of the strain rate and a is a parameter, or a suitable version of (4.7), may be used. The presence of a large exponent n in (4.6) for low strain rates, followed by a linear relation for high strain rates, or, what is the same, the presence of the exponential function in (4.7), necessitates specialized effective algorithms, in order to ensure adequate accuracy of the numerical results.

## 4.2 Numerical Examples and Discussion

For illustration, assume isotropic elasticity and, with $\mu$ as the shear modulus, from (4.2) obtain

$$\underset{\sim}{\dot{\tau}}' = 2\mu \ \underset{\sim}{d}^{e'} = 2\mu(\underset{\sim}{d}' - \underset{\sim}{d}^p) \ . \tag{4.8}$$

Take the inner product of both sides with $\underset{\sim}{\mu}$, and using (4.3) and (4.5),

obtain

$$\dot{\bar{\tau}} + \dot{\gamma} = d ,$$ 
(4.9)

where

$$\bar{\tau} = \tau/(\sqrt{2}\,\mu) , \quad d = \underline{\mu} : \underline{d}' .$$ 
(4.10)

Moreover, since

$$\dot{\underline{\mu}} = \frac{\sqrt{2}\,\mu}{\tau} \, [\underline{1} - \underline{\mu} \otimes \underline{\mu}] : \underline{d}^{e'} ,$$ 
(4.11)

we have

$$\underline{d}^p = \dot{\gamma}\mu + \beta[\underline{1} - \mu \otimes \mu] : \underline{d}' ,$$ 
(4.12)

where

$$\beta = \sqrt{2}\,\mu A / (1 + \sqrt{2}\,\mu A) .$$ 
(4.13)

We set $A = 0$ when $\tau < \tau_r \, (\dot{\gamma}/\dot{\gamma}_r)^{1/n}$, with an analogous expression when (4.7) is used, so that for small $\tau$ and when the response is basically elastic, the second term in the right-hand side of (4.3) is zero.

Equation (4.6) is used for numerical results reported in this section. For $\tau < \tau_r$ and n large, this equation yields small values for the strain rate. When $\tau \geq \tau_r$, the strain rate becomes large, and, for large values of n, the model simulates rate-independent plasticity. For very large strain rates, $n = 1$ and the plastic flow is controlled by viscous drag associated with the phonon drag on dislocation motion.

162

Equation (4.9) is to be integrated at each time step in such a manner that the relation between $\dot{\gamma}$ and $\tau/\tau_r$, given by either (4.6) or (4.7), is satisfied. In an explicit code, at each time step the right-hand side of (4.9) is obtained in terms of the current nodal forces, by integrating the equations of motion. Then the integration of (4.9) in conjunction with (4.6) or (4.7), yields $\Delta\tau$ and $\Delta\gamma$ and hence, from (4.3) the increment in the plastic deformation rate, and from (4.8) the increment in the stress. The differential equation (4.9) varies its character over the range of values of $\dot{\gamma}$. Hence one may need to use different algorithms for different strain rate regimes.

We have obtained some tentative results on the basis of constitutive assumption (4.6), with $n = 100$ for $\dot{\gamma} \leq \dot{\gamma}_0$ and $n = 1$ for greater strain rates, where $\dot{\gamma}_0/\sqrt{3} = 10^4/s$. The computations are done using PRONTO 2D [13]. In this code the objective stress rate is obtained by first rotating the Kirchhoff stress from the current Eulerian triad to the associated Lagrangian triad, taking the material derivative of the resulting stress tensor and rotating back when necessary.

For a numerical example, Figs. 9a, b, c, and d show localization in uni-axial extension at $10^2$, $10^3$, and $10^4/s$ strain rates with $A = 0$ (i.e. no noncoaxiality). To ensure that localization occurs at the center of the bar, a slightly different hardening parameter is assigned to the central element. This is actually unnecessary since localization occurs (if it does) automatically at some point in the bar which however, cannot be predetermined. The calculations are made using the following expression for the flow stress:

$$\tau_r = \sigma_0 \left( 1 + \gamma/\gamma_0 \right)^N \exp \left( - \lambda \left( T - T_0 \right) \right) , \qquad (4.13)$$

where $\sigma_0$, $\gamma_0$, $T_0$, and $N$ are fixed parameters; for the examples reported here, we have assumed $\sqrt{3}\,\sigma_0 = 1.25$ GPa, $\dot{\gamma}_r/\sqrt{3} = 10^{-3}$/s, $\gamma_0/\sqrt{3} = 6.25 \times 10^{-3}$, $N = 0.08$, $T_0 = 294°$K, and $\lambda = 1.6 \times 10^{-3}/°$K. Also, the Young modulus $E = 2 \times 10^2$GPa, Poisson's ratio $\upsilon = 0.3$, and mass density $\rho = 7,833$ kg/m$^3$ are used. The change in temperature is calculated from $\dot{T} = a \tau \dot{\gamma}$, where 95% of plastic work is assumed being converted into heat.

The influence of the strain rate on localization is illustrated in Figs. 9b, c, and d. It is seen that at low strain rates, sharp shear bands occur, but at high enough strain rates no shear banding is predicted. This is basically due to the change in the exponent n from n = 100 for small strain rates to n = 1 for large ones. The effect of noncoaxiality is illustrated in Fig. 9e with $\beta = 0.975$. As is seen, sharper shear band are produced.

As a second example, we consider the void collapse problem, and again with A = 0 and other parameters as before, obtain results shown in Figs. 10b and 10c. As is seen, the resistance to void collapse is increased with increasing strain rate.

These and other related examples show that:

1) In the standard PRONTO environment, unstable deformation by shear localization can be captured without recourse to any special elements and without any special arrangement of the elements, by just using a reasonable suitably fine mesh structure and quadrilateral elements with

164

one-point integration;

2) The localized deformation is mesh size independent, as long as a reasonable number of meshes is used;

3) The shear band is sharper at lower strain rates;

4) At higher strain rates the bands are broad and tend to disappear at very high strain rates, a phenomenon which may, in part, be associated with the fact that exponent n in (4.6) is set equal to 1 at high strain rates.

## Acknowledgement

# References

1. S. Nemat-Nasser, T. Iwakuma, and M. Accorsi. Cavity Growth and Grain Boundary Sliding in Polycrystalline Solids. *Mech. of Mats.* 5, 317-329 (1986).

2. S. Nemat-Nasser and M. Hori. Void Collapse and Void Growth in Crystalline Solids. *J. Appl. Phys.* 62, No. 7, 2746-2757 (1987).

3. M. Hori and S. Nemat-Nasser. Mechanics of Void Growth and Void Collapse in Crystals. *Mech. of Mats.* 7, 1-13 (1988).

4. H. Horii and S. Nemat-Nasser. Brittle Failure in Compression: Splitting, Faulting, and Brittle-Ductile Transition. *Trans. of Roy. Soc. London* 319, No. 1549, 337-374 (1986).

5. B. M. Butcher, M. M. Carroll, and A. C. Holt. Shock-Wave Compaction of Porous Aluminum. *J. Appl. Phys.* 45, No. 9, 3864-3875 (1974).

6. S. Nemat-Nasser and S.-N. Chang. "Compression-Induced Void Collapse and Tensile Cracking in Ductile Single and Polycrystals; in preparation.

7. S. Nemat-Nasser, D.-T. Chung, and L. M. Taylor. Strain Localization at Ultrahigh Strain Rates; in preparation.

8. S. Nemat-Nasser. On Finite Plastic Flow of Crystalline Solids and Geo-Materials. *J. Appl. Mech.* 50, No. 4b, 1114-1126 (1983).

9. J. R. Rice. The Localization of Plastic Deformation. *Theor. & Appl. Mech.*, W. T. Koiter (ed.), North Holland Publishing Co., 207-220 (1976).

10. S. Stören and J. R. Rice. Localized Necking in Thin Sheets. *J. Mech. Phys. Solids* 23, 421-441 (1975).

11. S. Nemat-Nasser and T. Iwakuma. An Analytical Estimate of Shear Band Initiation in a Necked Bar. *Int. J. Solids Struct.* 18, No. 1, 69-83 (1982).

12. R. J. Asaro. Material Modelling and Failure Modes in Metal Plasticity. *Mech. of Mats.* 4, 343-373 (1985).

13. L. M. Taylor and D. P. Flanagan, PRONTO 2D, *A Two-Dimensional Transient Solid Dynamics Program*, SAND86-0594, Sandia National Laboratories, Albuquerque, NM (1987).
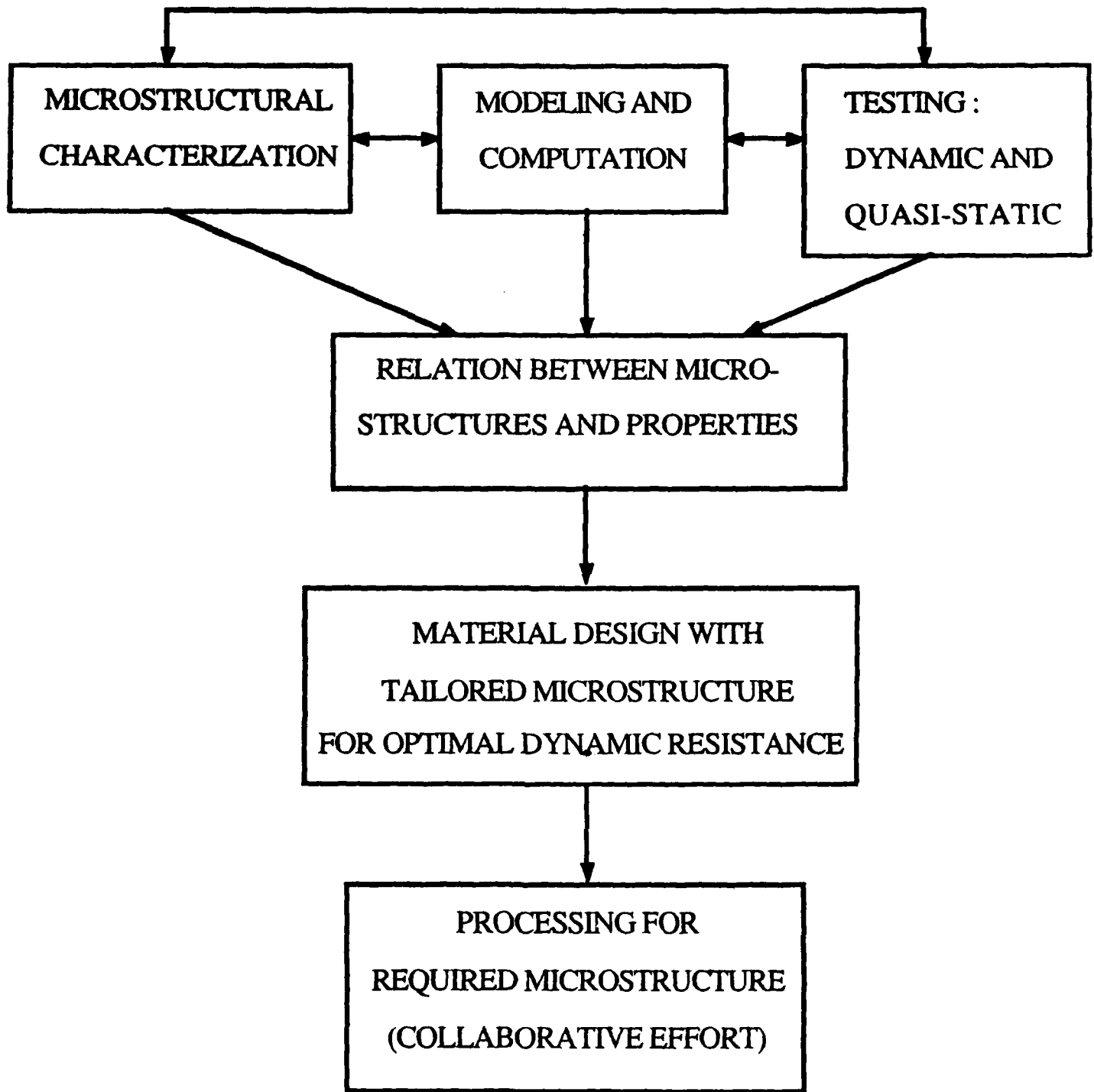
Figure 1. Major research components of the Center of Excellence for Advanced Materials (CEAM), University of California, San Diego. The Center's main objective is to design advanced materials with tailored microstructures for optimum performance in severe environments.

168
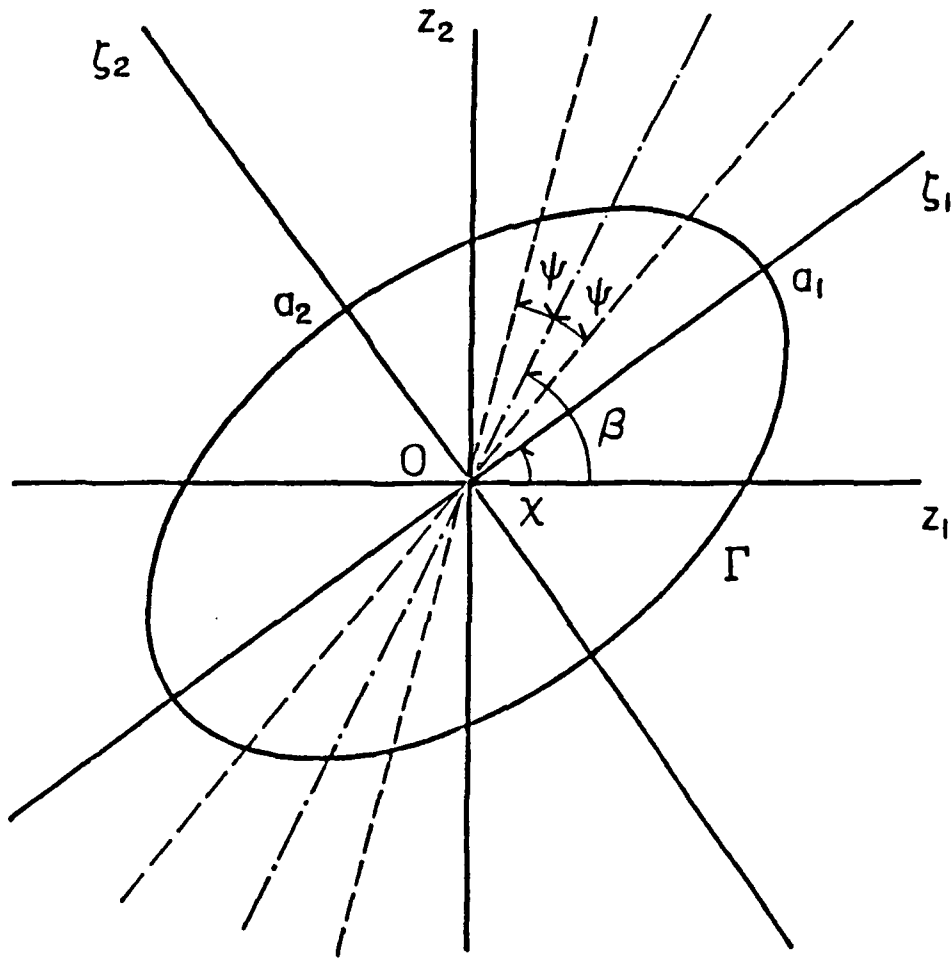
Figure 2.   Elliptical cavity in the $z_1, z_2$- and $\zeta_1, \zeta_2$-coordinate systems.

169
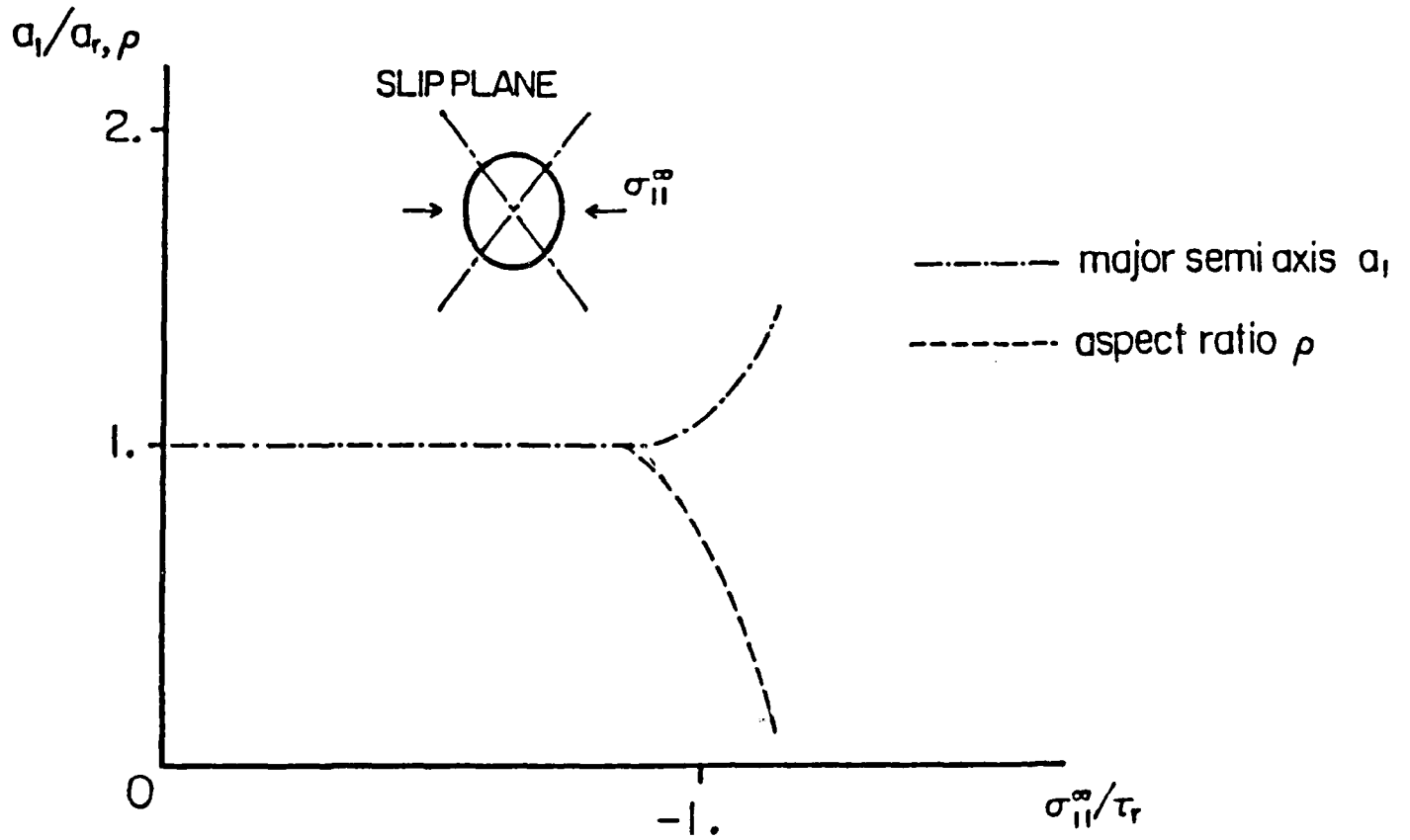
Figure 3.(a)   Change of aspect ratio $\rho$ and major semi-axis $a_1$   under uniaxial compression $\dot\sigma^\infty_{11}/\tau_r = -10^2/s$; $\beta = 0.5\pi$, and $\psi = 0.2\pi$. $a_r$ is the radius of the initial hole, and $\tau_r$ is the reference (yield) stress.
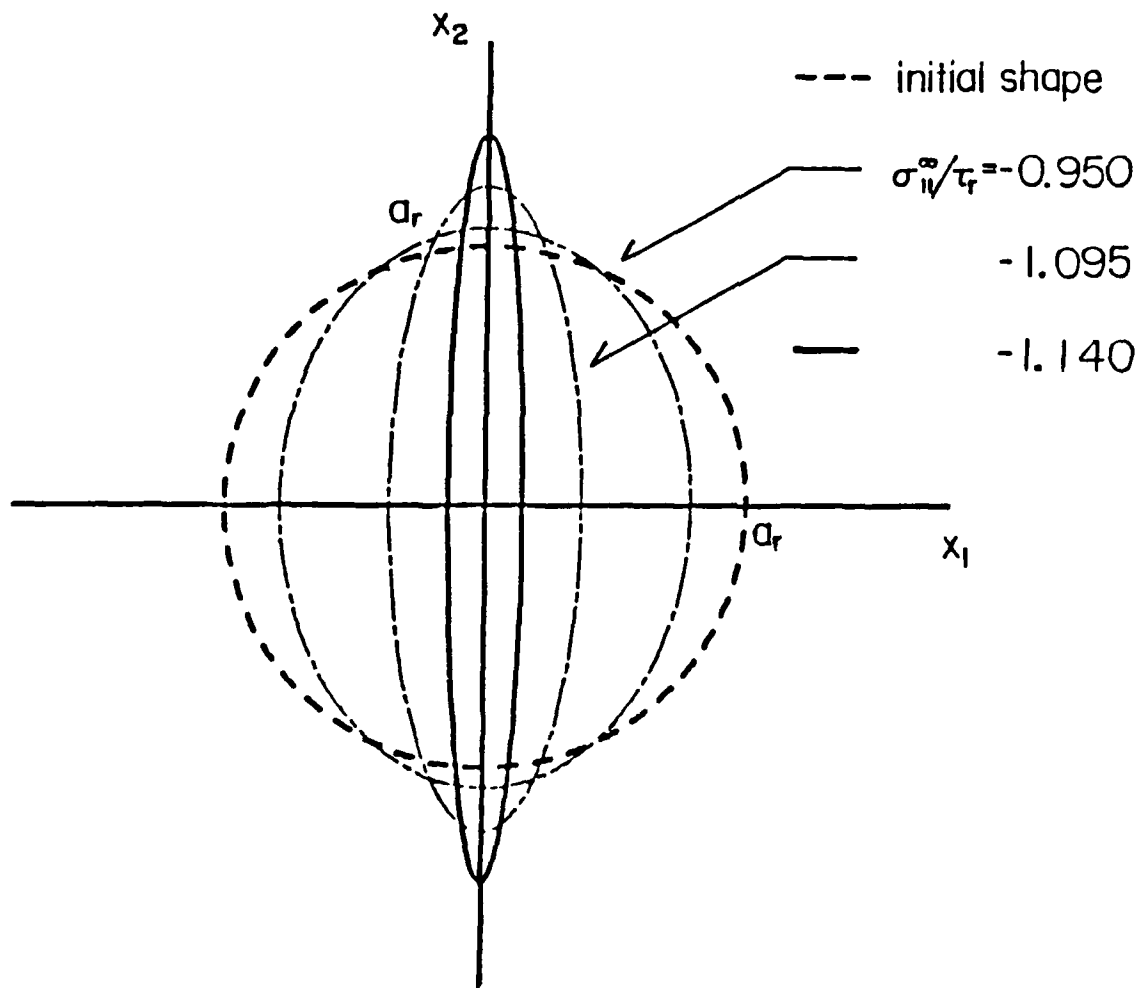
Figure 3.(b)  Deformed shape of initially circular void; the equivalent ellipse at $\sigma_{11}^{\infty}/\tau_r$ = -0.950, -1.095 and -1.140.
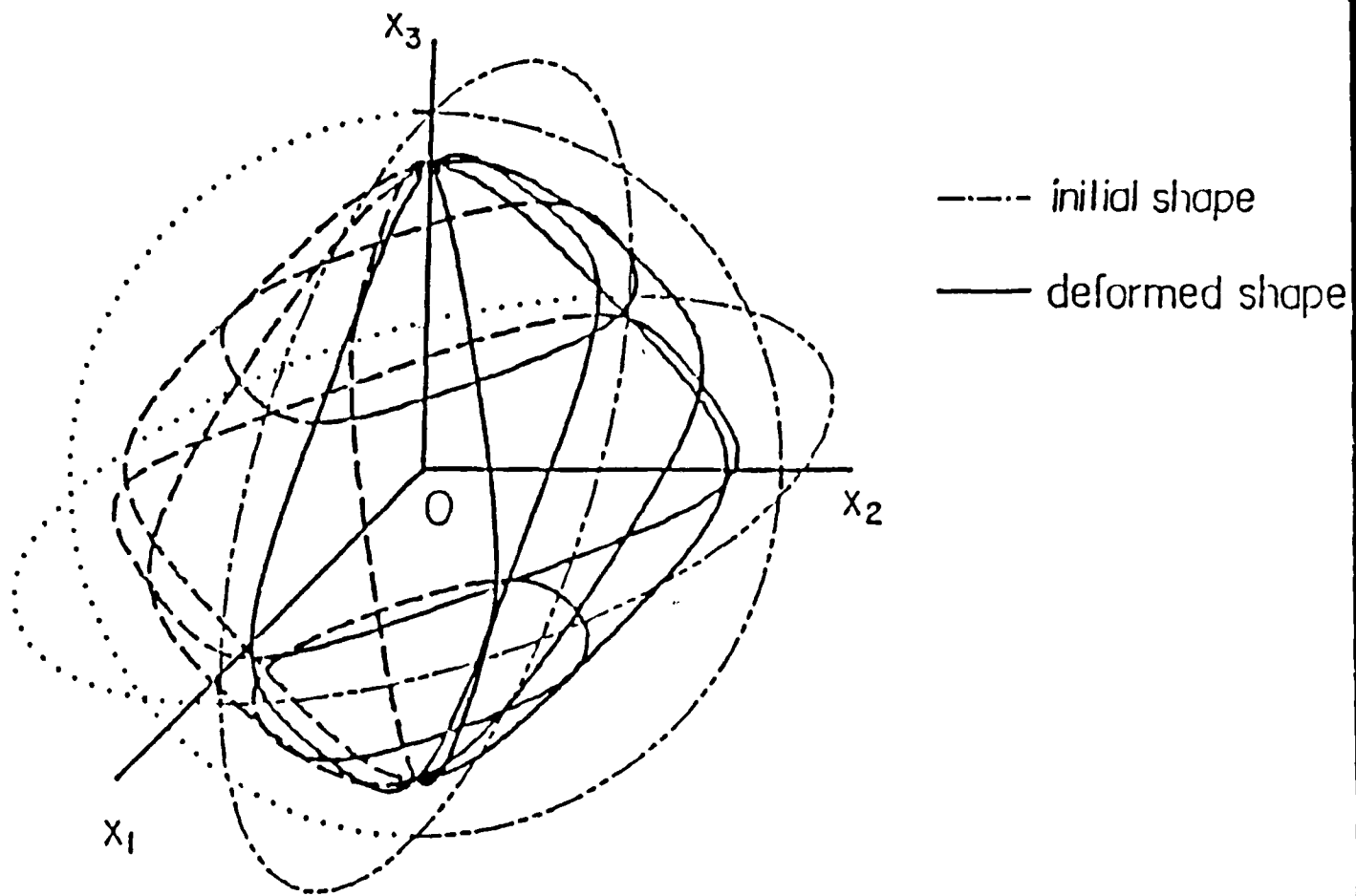
Figure 4. Deformed shape of initially spherical void after time increment $\Delta t = 0.5$ sec, under all-around uniform compression $\dot{\sigma}^{\infty}_{11}/\tau_r = \dot{\sigma}^{\infty}_{22}/\tau_r = \dot{\sigma}^{\infty}_{33}/\tau_r = -1/s$ for crystal with 12 slip systems; $\eta = 1$, $n = 1$, $\psi = 0.2\pi$.
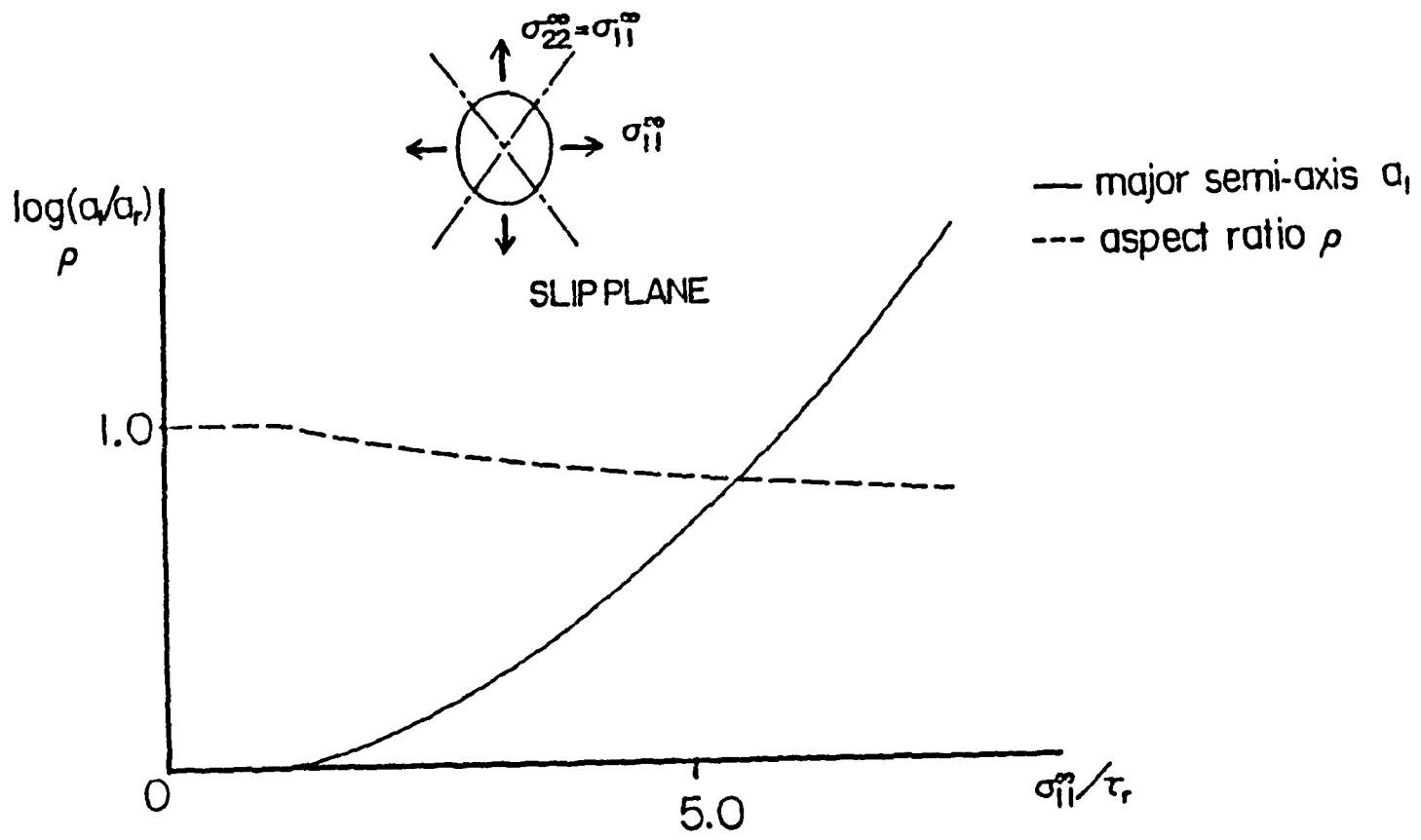
Figure 5. Change of aspect ratio $\rho$ and major semi-axis $a_1$ under all-around tensile loading $\dot\sigma_{11}^\infty/\tau_r = \dot\sigma_{22}^\infty/\tau_r = 10^5/s$; $\beta = 0.5\pi$, and $\psi = 0.2\pi$.
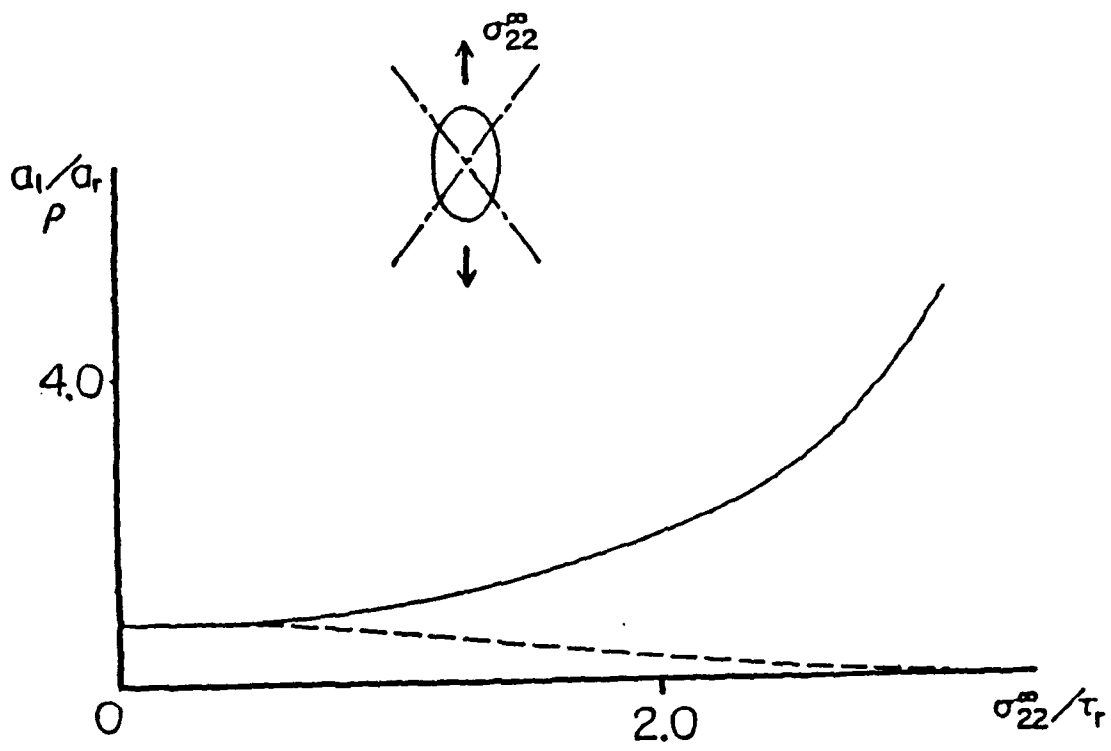
Figure 6. Change of aspect ratio $\rho$ and major semi-axis $a_1$ under uni-axial tension $\dot{\sigma}_{22}^\infty / \tau_r = 10^5/s$; $\beta = 0.5\pi$, and $\psi = 0.2\pi$.

void dia. 130 µm   (011) plane
21.4%   1100/sec

120 µm
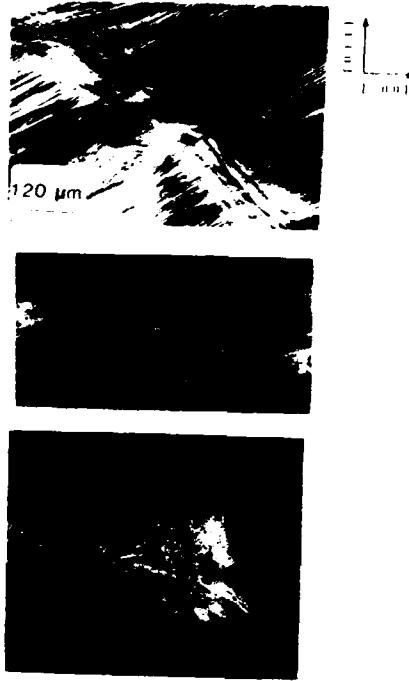
Figure 7.  Void collapse and subsequent tensile cracking  under  uni-axial compression  in  single  crystal  copper:  shear  bands  (upper  figure); collapsed void (middle figure); and tensile cracks (lower  figure)  at  the tip of collapsed void.
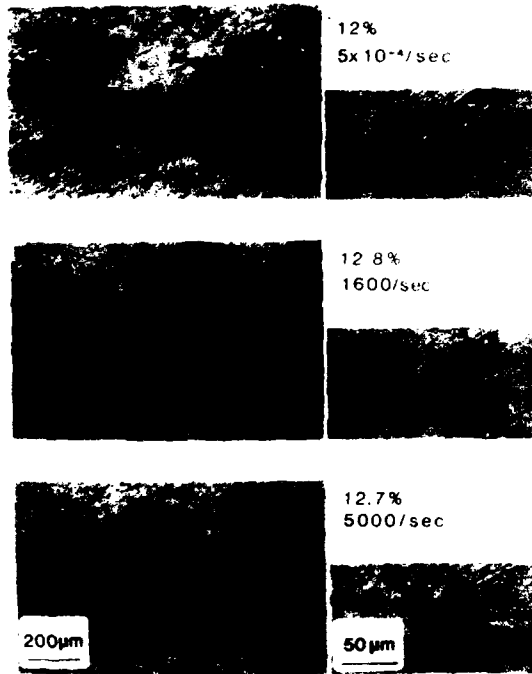
Figure 8. Void collapse and subsequent tensile cracking under uni-axial compression in 1018 steel: for a total of about 12% axial shortening, the void collapses completely (upper figure) at quasi-static loading, but not at higher strain rates (middle and lower figures). The corresponding tensile cracks, formed at the ends of collapsed voids, are shown in the right-hand figures.
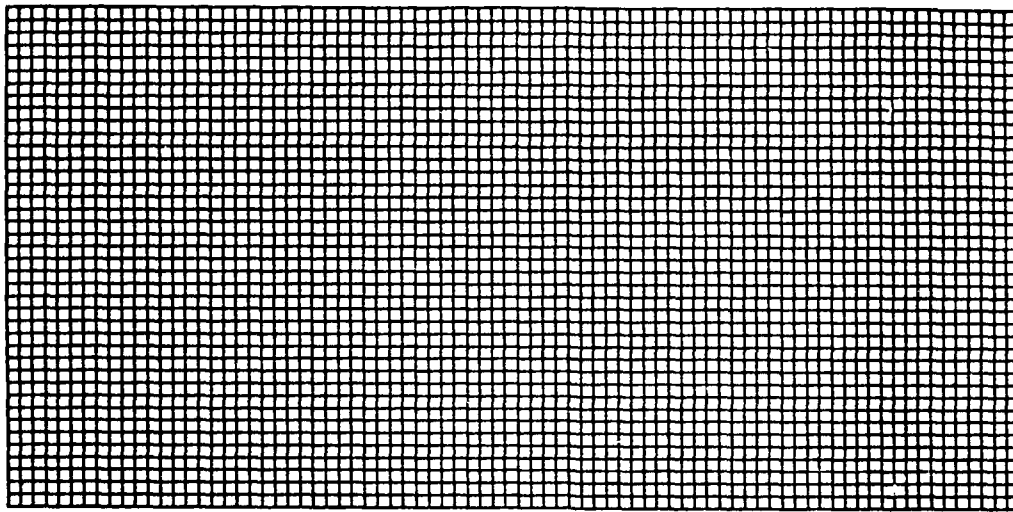
Figure 9. Uni-axial extension and shear banding at total extension of 13% of initial length:

(a) undeformed shape
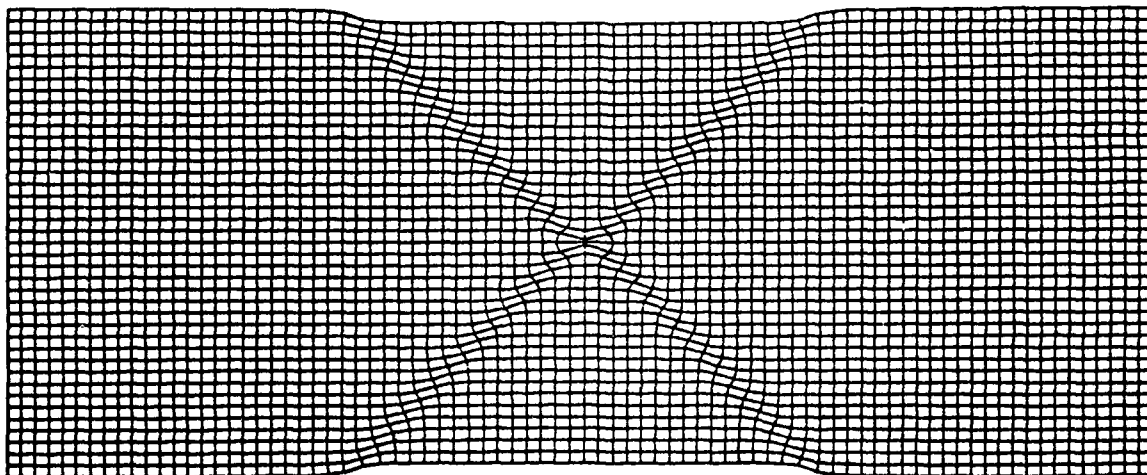


9.(b) at $10^2$/s strain rate
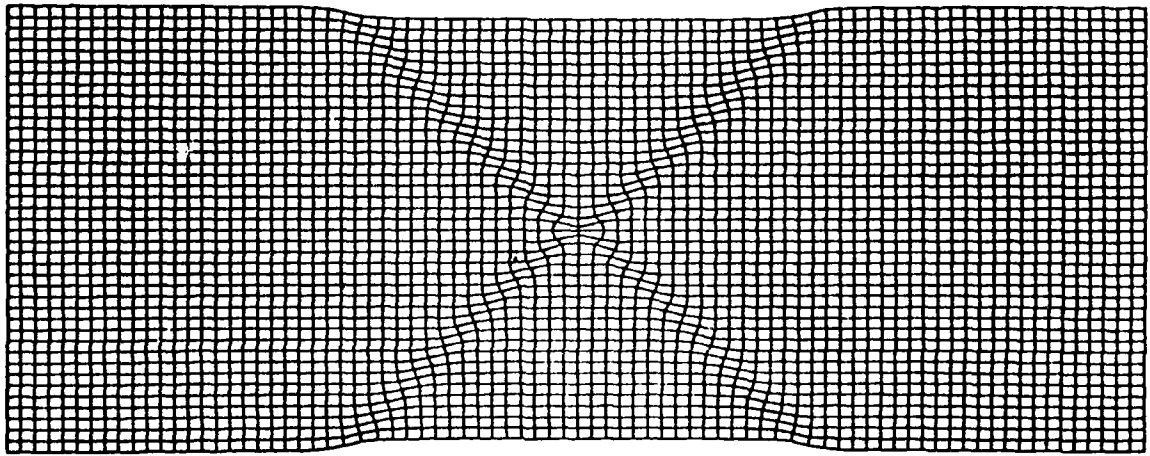
9.(c) at $10^3$/s strain rate
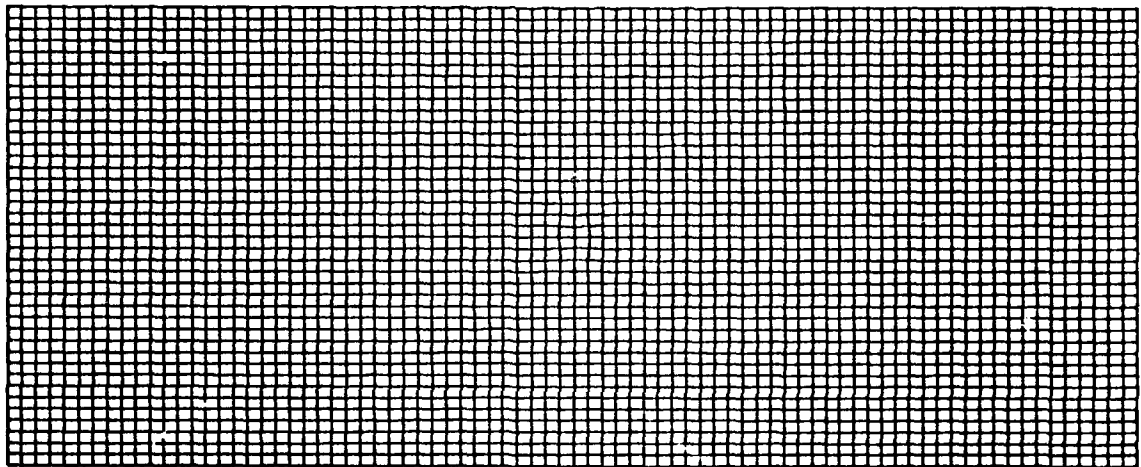


9.(d) at $10^4$/s strain rate
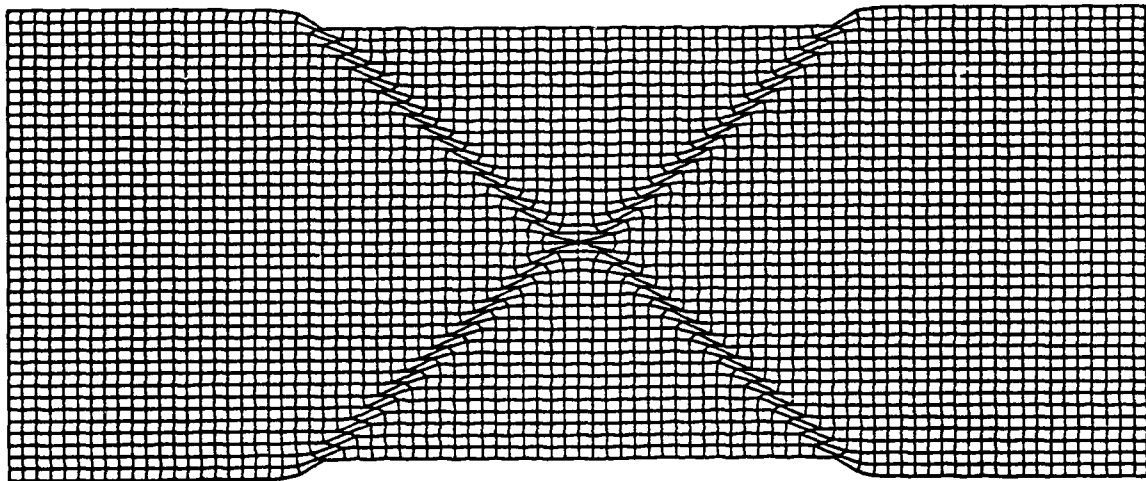
9.(e) at $10^2$/s strain rate with noncoaxiality
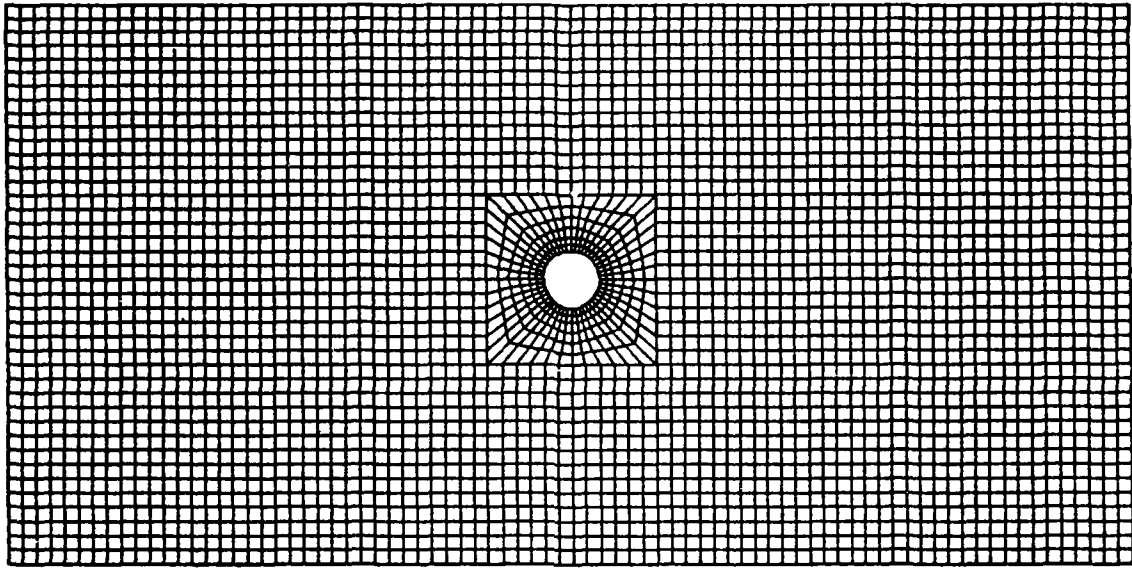
Figure 10.   Void collapse under uni-axial compression with total shortening
of 5%:

        (a) undeformed shape
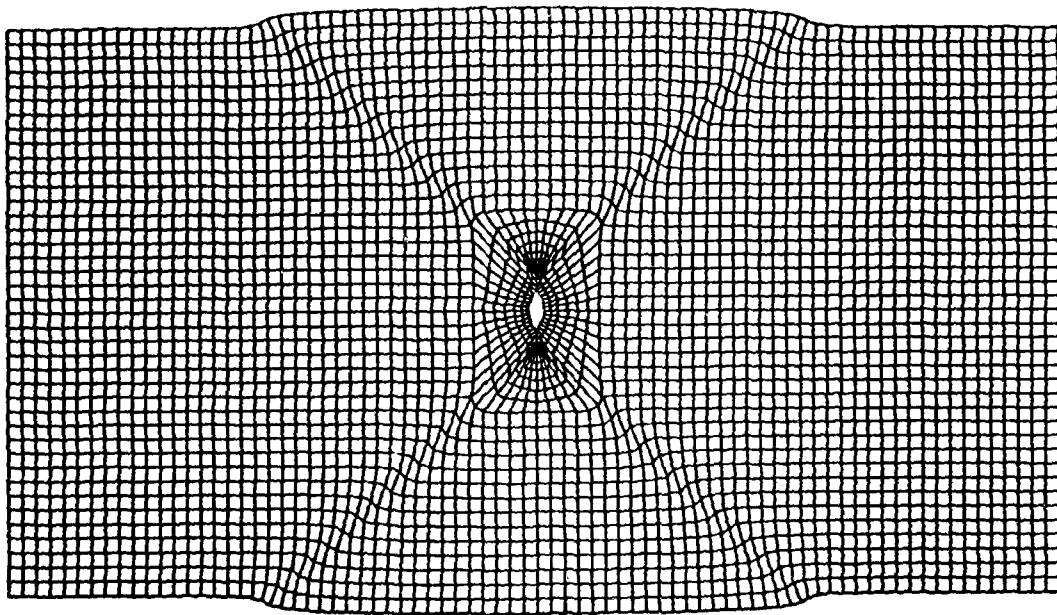
10.(b) at $10^2$/s strain rate
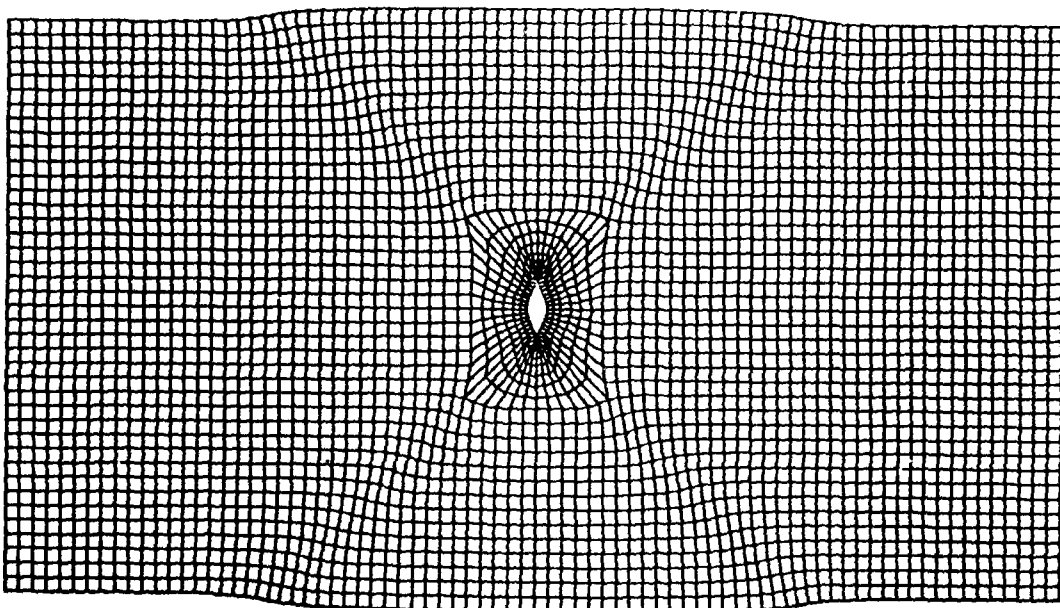


10.(c) at $10^3$/s strain rate

181

# SECTION III

# BRITTLE MATERIALS AND COMPOSITES

# IMPACT BEHAVIOR OF CERAMICS

By:

S. J. Bless
University of Dayton
Research Institute
Dayton, OH   45469

## INTRODUCTION

The behavior of ceramics under impact loading has become a topic of great importance in at least two current technological developments:   development of improved ceramic armor and development of ceramic engine components for aircraft.   It has become clear that the performance of ceramics under impact does not bear an obvious relationship to properties of ceramics as conventionally defined and determined.

The purpose of this paper is to describe the properties of ceramics that seem to be most closely related to impact behavior. We will then describe test techniques used to characterize the dynamic behavior of ceramics.   It will turn out that results are often contradictory, and a unified conceptual framework is yet to emerge.   Lastly, we will review the data available for alumina, which is probably the best studied ceramic, and for which critical ambiguities in behavior modes still exist.

# CHARACTERISTICS OF IMPACT LOADING

We concern ourselves here with impacts that are likely to result in penetration of the ceramic. In other words, we are dealing mainly with ceramic armor applications.

Ceramic armors should probably be grouped into two classes: light and heavy. Light ceramic armor employs tiles whose thickness is comparable with the diameter of the impactor, and whose width is typically 10 times the thickness. Such tiles are generally bonded to substrates of similar thickness to the tile. Impact occurs directly on the face of the ceramic. The main failure mode in such tiles is tensile failure on the back surface opposite the impact site. There are several published accounts of penetration mechanisms in such tiles [1,2].

Heavy ceramic armor is the application that is of most intense current interest. Heavy ceramic armor employs tiles that are typically several times thicker than the impactor diameter. Tiles are also usually relatively well confined by surrounding structure, including on the impact face. We do not know of any open publications on the mechanics of heavy ceramic armor. There are also very few restricted access publications that treat penetration and failure mechanisms; we point out [3] as a good source of information.

The first stage of impact onto a ceramic (or any other target) involves a shock phase. Shock stresses are very high, as shown in Figure 1. The deformation associated with shock loading is one-dimensional strain, which implies perfect lateral confinement. Tensile stresses develop in the ceramic after initial shock passage, due to the diverging flow (hoop stresses) behind the shock wave, and due to reflection of compressive waves as tensile waves at tile boundaries. In the case of heavy armor, it appears that the combination of compressive and tensile stresses ahead of the projectile induces a great deal of damage in the as yet unpenetrated ceramic.

The stress at the projectile interface after the shock decays is given approximately by:

$$\sigma = \frac{1}{2} \rho_p (u - v)^2 + Y_p \qquad (1)$$

where $\rho_p$ is the penetrator density, u is the impact velocity, v is the penetration velocity, and $Y_p$ is the flow stress of the projectile [4,5]. Using the approximation that v = 0 (i.e., the penetrator is defeated), Figure 2 graphs the stress from Equation 1. It can be seen that this stress is also very high, even relative to the strength of most ceramics.

The combination of the high impact stress and the degradation of the ceramic in front of the penetrator may result in ceramic failure ahead of the projectile. In this instance, much of the penetration takes place through ceramic that has been altered by previous compressive and/or tensile failure.

## PROPERTIES OF CERAMICS THAT AFFECT DYNAMIC BEHAVIOR

Before commencing this discussion, we want to warn of the danger of reification. We describe properties and failure modes according to an incomplete and still evolving set of concepts. At this time, it is best to approach all experimental data with as open a mind as possible, and avoid forcing new observations to fit into what may turn out to be an inadequate model for behavior. Nevertheless, we do hope that the discussion that follows will serve as a guide to the design of critical experiments, both to explore fundamental behavior modes and to provide engineering data for design. We also hope this discussion will aid modelers in identification of critical processes.

Impact response is, in general, governed by bulk properties. Failure occurs so rapidly that different regions of the ceramic cannot communicate with each other. Hence, where flaw size is important, it is the average, not the maximum flaw that determines behavior.

Other bulk properties also play critical roles. The elastic moduli, and in particular the bulk modulus, K, determines the ability of the ceramic to spread the load away from the impact site and avoid local failure. The equation of state (EOS) (e.g., the pressure-volume relationship at high pressure) determines the peak stress associated with impact, which in turn governs the intensity of shock waves in the impactor and in the ceramic. The initial intensity of the shock loading often is critical in determining the early breakup of the ceramic and the projectile.

The importance of bulk properties runs counter to the intuition of many ceramics engineers. The bulk response, for example, is probably one reason why, in general, results of impact testing exhibit much less scatter than is typical of mechanical tests at low deformation rates.

Probably the most important property of ceramics for resistance to penetration is compressive strength. Impact stresses

are initially very high, as shown in Figures 1 and 2. During most stages of the impact process, the ceramic is not free to expand laterally. Hence, the confined compressive strength is of primary importance. The confined compressive strength is synonymous with the Hugoniot Elastic Limit (HEL), which is the shock strength.

According to [6], the strength of brittle materials should be a function of the sum of the largest and smallest principal stresses,

$$\bar{P} = (\sigma_1 + \sigma_3)/2 \tag{2}$$

Hence, we have the general behavior sketched in Figure 3. Note that according to [7], many ceramics become ductile as $\bar{P}$ becomes very large.

Tensile strength is also a very important impact parameter. Many impact-induced failures are due to tensile stresses. The bulk tensile strength is also known as the spall strength. It is measured in shock experiments, and is the tensile strength under one-dimensional strain deformation. In impact events, material usually experiences tensile stresses only after very intense compressive loading. Thus, the dependence of tensile strength on compressive prestress is very important for brittle materials. In fact, this dependence is very sensitive for many brittle materials [8,9].

The propagation rate of tensile failure is also undoubtedly very important for determining impact response. This process may account for the loss of confinement in large tiles, as expansion of outer boundaries is communicated to the impact region. Tensile fracture in prestressed brittle materials can take place very rapidly because energy stored in the elastic field is transformed to kinetic energy of failed material. Most of the theoretical work on this subject has been carried out by Soviet authors; see for example [10,11].

It is clear that the properties after compressive failure, compressive, shear, and tensile, also strongly affect the penetration of ceramic tiles by projectiles. It has been observed that the strength of ceramics after compressive failure varies greatly among different ceramics. Figure 4, for example, shows shock Hugoniot curves for different types of materials. The Hugoniot is the shock loading path. The lower curve (labelled HYDR) is the hydrostat (e.g., compression curve for all principal stresses equal). The offset between these two curves is equal to two-thirds of the shear stress. (See, for example, [12] or [13] for a general discussion of shock loading states.) Some ceramics are observed to lose all shear strength at the HEL [14]; this behavior is termed "elastic-isotropic". Other ceramics [15] and glass [16] retain full shear strength above the HEL. Still other glasses and ceramics display gradual softening at high pressure [17,18].

After compressive failure, the ceramic material may be granulated. Granulated materials usually are described by a Coulomb relationship, in which the maximum shear stress,

$$S = (\sigma_1 - \sigma_3)/2 \tag{3}$$

is a linear function of $\bar{P}$;

$$S = \alpha + \beta \bar{P} \tag{4}$$

This behavior is also sketched in Figure 3 together with the original failure surface. It would be surprising, and contrary to shock observations [14] if the strength of granulated material can exceed the initial strength of material, so evidently when the failed material is fully compressed it either retains its initial ability to support shear stress or else the strength collapses as in the elastic-isotropic model. Referring to Figure 3 we can pose two of the most difficult questions in need of experimental investigation: What does the shape of the failure surface look like between point Y (failure under uniaxial

stress) and point H (failure under shock loading)? When the failure surface is reached between Y and H (at A for example), where is state B, to which the material releases? (See [6] for further discussion of this latter question.)

The behavior of ceramics during unloading is also largely unresolved. Figure 5 illustrates a load/unload cycle under one-dimensional strain. Metals load to failure, after which they have approximately constant shear strength. Ignoring the Bauchinger effect, they have the same strength on unloading. When metals are unloaded to zero driving stress, $\sigma_1 = 0$, the post shock microstructure closely resembles the starting material, and there is a trapped shear stress. Ceramics that retain shear strength behave similarly to metals until unloading commences. After the loading cycle is completed, ceramics are probably totally pulverized. The manner in which ceramics lose shear strength as pressure is relaxed probably has a critical relationship to penetration resistance.

Another property of ceramics that may affect impact response is dilatancy. Dilatancy refers to the tendency for a failed material to increase in volume due to cracks. It is manifested as an increase in mean stress if failure takes place at constant volume, or an (possibly violent) expansion takes place under stress boundary conditions. Historically, there appears to be two concepts for dilatancy. The first is a precursor to failure. This effect was first observed in rocks [19,20]. The second type of dilatant behavior arises when failed granulated material is forced to undergo additional shear strain. Grains slide over one another, rotate, and hence need to occupy more volume. Either type of dilatancy seems to imply strength enhancement under dynamic loading because dynamic loading usually implies a constant volume boundary condition; hence the mean stress increases from dilatancy, and an increase in mean stress usually implies an increase in strength.

The speed of release waves in failed material may also play a large role in armor mechanics. There seems to have been little

work in this area, except measurement of release wave speeds under shock loading conditions. We note here the theory for unloading wave speeds driven by dilatancy advanced in [21]. In addition, there is the self-sustaining brittle fracture model described in [10].

# EXPERIMENTAL TECHNIQUES

In order to evaluate the usefulness of experiments, we must be clear about the objectives of experiments. In the present context in which development of impact resistant systems are developed, the primary purpose of experiments is probably to validate and calibrate numerical analyses. Numerical analysis encompasses both constitutive models and computational algorithms. However, the best experiments are those which can be interpreted without supporting numerical analysis; for example, direct measurements of strength parameters as functions of stress state or load history. Calibration of codes by direct comparison to penetration experiments is hazardous. Any given experiment may not provoke all important modes of material response. In addition, some experiments may be relatively insensitive to critical material parameters; for example, high velocity penetration of metals is not very sensitive to strength parameters.

Plate impact experiments are the most accepted techniques to determine the dynamic properties of brittle materials. Figure 6 illustrates the basic impact configuration. A flat flyer plate strikes a flat target plate, inducing plane waves in both the flyer and target. If the impact region of the target is driven into the plastic region, then an elastic wave propagates into the target whose strength represents the elastic limit of the target material. This is, by definition, the HEL. As discussed above, the HEL is a primary impact property of ceramics.

Analysis of the wave profile also gives data for equation of state parameters and spall strength (see, for example [22]). The shape of the wave profile also allows one to estimate the extent of elastic-isotropic or elastic-plastic behavior above the HEL.

Measurement of spall stress as a function of driving stress is especially diagnostic for ceramics. Unlike metals, for which spall stress is relatively unaffected by prior compressive

failure, the spall strength of many brittle materials is strongly decreased if compressive failure occurs first. The nature of the decrease provides important clues as to the character of the compressive failure--microfracture versus microplasticity.

Actual traces observed in plate impact tests on ceramic targets are hardly ever as simple as the generic waveform sketched in Figure 6. There is usually a "ramp" from the first elastic arrival to the plastic wave top, as in Figure 7. The ramp indicates a departure from simple elastic-plastic behavior on loading. The usual interpretation of ramping invokes hardening (strengthening) after the first elastic arrival. Causes of strengthening of ceramics may be strain rate or pressure.

Release is also frequently not symmetric in ceramics, as shown in Figure 8. The relative steepening of the release waves in glass, for example, seems to be associated with a densification that is similar to a phase change [17].

Precursor decay also affects interpretation of HEL values in ceramics. In alumina, for example, it appears that specimens must be at least 10 mm thick to ensure that equilibrium values of HEL stress are achieved [23].

Most puzzling is the unsteady nature of shocks in some brittle materials. In particular, many glasses do not maintain a steady stress behind the plastic wave arrival [16]. Whether stress decay is due to anomalously fast release waves or relaxation of deviator stresses behind the shock arrival is not yet understood.

The basic plate impact test has been augmented in recent years by a number of specialized modifications that are very helpful for study of ceramics. First among these is the use of transverse stress gauges to directly measure the deviatoric stress behind shock waves [24,25]. Use of transverse gauges is considerably more accurate than the older technique of inferring transverse stress by comparing Hugoniot curves to hydrostats. Hydrostats for new ceramics are not always known. Ambiguity

191

concerning the hydrostat shape for failed material is not a concern.

Progress has also been made on recovery techniques for ceramics. Using techniques described in [26,27] ceramics have been recovered from about 100 m/s impact. Analysis of fractured material has been very valuable in determining failure modes which may aid development of more impact resistant materials. Using the self-trap technique [26], it is even possible to recover spalled material.

Double flyer plates also provide a new technique to probe the behavior of shock fractured material without uncertainties concerning additional damage during recovery [28]. It has been used to study alumina [28] and sapphire [29].

Pressure shear experiments may also be an important tool for future studies of ceramics. This technique was developed for study of large deformation in metals [30]. In the usual version of this experiment, an oblique impact plate strikes a target so as to induce particle velocities both normal to and parallel to the impact surface. The result is, a normal pressure wave followed by a shear wave. The combined loading may provide a means to achieve stress boundary conditions not otherwise achievable in dynamic experiments. Another version of the pressure shear tests employs a conventional flyer impactor; however, the rear surface of the target is oblique so that both compression and shear waves are produced when the impact-induced compression wave reflects from the rear surface. To date, only this latter configuration seems to have been used for brittle rocks [31], and there seems to be no pressure shear data for ceramics.

The conventional stress state for testing is one-dimensional stress. Dynamic tests are normally conducted with a Hopkinson bar. So far, only [32] have published dynamic failure stress data for ceramics with a split Hopkinson bar. While the data appears to be consistent, questions remain concerning stress equilibrium in the sample, since the strains involved are far

192

less than the limits for which the Hopkinson bar is normally considered valid.

The bar impact technique is another means of measuring the failure stress under one-dimensional stress. A flyer plate is made to impact the end of a long bar. Failure occurs at the impact surface, and an elastic wave propagates along the bar. The amplitude of the wave is the largest elastic stress support- able by the bar material. The test was successfully used to measure dynamic yield stress for metals [25]. It has also been applied to ceramics to measure failure stress [33]. It appears to be a valid technique to measure failure stress under one- dimensional stress. Moreover, as discussed in [21], the duration of the stress pulse and the radial expansion velocity are very sensitive to the post failure properties of the bar material. Thus this test may also be very useful for characterizing the behavior of failed ceramics. Work toward this end is currently underway at the University of Dayton.

We conclude this section on experimental techniques with an assessment. Compressive failure of ceramics can and should be characterized both by the bar impact test and the plate impact test. In addition, the plate impact test is needed to measure spall strength. Measurements at intermediate stress states must await development of a pressure-shear type experiment; this should be a high priority. Measurement of post-failure properties can be accomplished by double plate impact tests and bar impact tests. However, more analysis is required for the bar impact test in order to develop a sound interpretation algorithm.

# DYNAMIC RESPONSE OF POLYCRYSTALLINE ALUMINA

Alumina has been one of the most extensively studied ceramics under impact loading. However, there is still not a consistent picture of the nature of dynamic yielding in this material. Concentrating on polycrystalline alumina, we will first present those features of the dynamic response that are uncontroversial. Those properties that are still being debated will then be described.

## SHEAR STRENGTH ABOVE THE HEL

The shear strength of alumina is maintained at shock stresses above the HEL. This conclusion is based on several different types of measurements:

(a) The Hugoniot has a constant offset above the hydrostat [34,35].

(b) The initial release is elastic [36,37].

(c) Direct measurements of the lateral stress, using transverse gauges, show a constant shear stress above the HEL [15].

The issues that are still not clear concern the following questions:

(a) Is alumina rate dependent?

(b) Is dynamic yielding in alumina due to plasticity or microfracture?

(c) Is the spall strength maintained when shocked above the HEL?

## RATE AND PRESSURE EFFECTS

It has been noted by [26] and [32] that the strength of alumina calculated from shock data using the formula:

$$Y_d = \sigma_1 - \sigma_2 = \frac{1-2\nu}{1-\nu} \qquad \sigma_1 = \frac{1-2\nu}{1-\nu} * HEL \qquad (5)$$

is much larger than the static yield strength. For example, $Y_d$
43 kb for AD-85 (85 percent alumina), whereas the static strength
is 19 kbar. This has been interpreted by [32] as evidence for
rate dependence.

Other evidence for rate dependence at ultra high rates
comes from HEL decay studies. The HEL of very pure alumina
(Lucalox) increases by a factor two as $\sigma_1$ increases from 136 to
490 kbar [36]. Precursor decay is also observed in sintered
aluminas [25,38]. In 85 percent alumina, specimen thickness of
about 30 mm was required to measure "equilibrium" HEL values
[38], whereas in more pure aluminas (>94 percent), 10 mm thick-
ness was sufficient. In these studies, actual strain rates
associated with HEL values were not measured. Ramping of the
plastic wave in 85 percent alumina was also interpreted in [38]
as evidence for rate dependent behavior. Rate dependence in 94
percent alumina was studied over rates of $5 \times 10^4$ to $6 \times 10^5 s^{-1}$
using various plate impact techniques, and no rate dependency was
seen [39]. Bar impact data at strain rates of about $10^3 s^{-1}$ show
that the strengths of 94 percent and 99 percent alumina at this
rate do not differ appreciably from static values [33]. Much of
these data are summarized in Figure 9.

It is safe to conclude from these observations that some
aluminas are rate dependent, but only at very high rates, prob-
ably exceeding $10^5 s^{-1}$. Rate effects are not sufficient to
account for the discrepancy between $Y_d$ (Equation 5) and Y
measured from static or bar impact tests.

It seems likely that in part the high HEL values of
ceramics is due to the greater confining stress associated with
shock loading. Figure 10 presents data for the strength of
alumina as a function of confining pressure. The large influence
of pressure on strength of ceramics means that measurement of HEL
values is more important for these materials than for metals.

195

## FAILURE MECHANISM

On the basis of known deformation mechanisms in single crystal alumina [36] concluded that plastic flow via dislocation motion in polycrystalline alumina could not occur in a plate impact experiment and dynamic yielding in alumina is due to microfracturing. This conclusion is supported by work done by [37], who showed that alumina (AD-85) is degraded by the elastic precursor. In addition, experiments on heat treated samples show a correlation between fracture toughness and HEL values [41]. Recovery experiments on 85 percent alumina find microcracks in material shocked to near the HEL [42,43]. Microcracking at the HEL is also consistent with observations of loss of spall strength observed in some aluminas shocked to near or above the HEL [9,36].

On the other hand, some shock recovery experiments with pure aluminas have found grain plasticity dominates under shock loading, even above the HEL [44]. The interpretation of the HEL as a plastic yield threshold in these ceramics is also supported by observations that the spall strength does not change above the HEL in these same ceramics [45]. It has also been found that the HEL of a 94 percent alumina is increased by preshock [39], which is easiest to explain in terms of plastic failure mechanisms.

It is difficult to reconcile these contradictory observations for microfracture and microplasticity. Unfortunately, each team of investigators has used slightly different experimental techniques and ceramics from different sources. Since both interpretations are supported by several types of evidence-- recovery, spall strength variations, reshock properties--the best hypothesis is that the failure process is highly dependent on the original microstructure of the material. For example, it has been suggested that a very fine grain structure may favor ductile behavior.

SUMMARY

This summary reflects the our interpretation of the experimental evidence.

(a) The shear strength of alumina is maintained at high stresses surpassing the compressive strength.

(b) The increase in strength observed in plate impact experiments is probably due mainly to high confining pressure, not high strain rate.

(c) The occurrence of precursor decay does indicate some strain rate effect at ultra high rates.

(d) There is no agreement on whether dynamic yielding is due to plasticity or microfracture. It is likely tht the failure process varies with the microstructure and composition of the alumina.

(e) There is also lack of agreement on whether spall strength is retained in material shocked above the HEL.

# REFERENCES

1. Wilkins, M.L., Landingham, R.L., and Honodel, C.A., Fifth Progress Report of Light Armor Program, UCRL-50980, Lawrence Radiation Laboratory, Livermore, CA, January 1971.

2. Mayseless, M., Goldsmith, W., Virotek, S.P., and Finnegan, S.A., "Impact on Ceramic Targets," J. App. Mech., Vol. 54, p. 373, June 1987.

3. "Penetration Studies of Ceramic Armor Materials (U)," UCID-21183, September 1987.

4. Tate, A., "Further Results in the Theory of Long Rod Penetration," J. Mech. Phys. Solids, Vol. 17, p. 141, 1969.

5. Tate, A., "A Theory for the Deceleration of Long Rods After Impact," J. Mech. Phys. Solids, Vol. 15, pp. 387-399, 1967.

6. Glenn, L.A. and Janach, W., "Contrasting Fracture Models for Granite Under Dynamic Loading," J. Eng. Mat'ls. Tech., Vol. 100, pp. 287-293, 1978.

7. Heard, H.C. and Cline, C.F., "Mechanical Behavior of Polycrystalline BeO, $Al_2O_3$, and AlN at High Pressure," J. Matls. Sci., Vol. 15, pp. 1889-1897, 1980.

8. Rosenberg, Z., Yaziv, D., and Bless, S., "Spall Strength of Shock Loaded Glass," J. Appl. Phys., Vol. 58, p. 3249, 1985.

9. Bless, S., Yaziv, D., and Rosenberg, Z., "Spall Zones in Polycrsytalline Ceramics," Proc. Fourth APS Conf. on Shock Waves in Condensed Matter, Spokane, WA, 22-25 July 1985.

10. Cherepanov, G.P., Mechanics of Brittle Fracture, McGraw-Hill, 1979.

11. Nikolaevskii, V.N., "Limit Velocity of Fracture Front and Dynamic Strength of Brittle Solids," Int. J. Eng. Sci., pp. 41-56, 1981.

12. McQueen, R.G., Marsh, S.P., Taylor, J.W., Fritz, J.N., and Carter, W.J., "The Equation of State of Solids from Shock Wave Studies," High Velocity Impact Phenomena, ed. R. Kinslow, 1970.

13. Asay, J.R. and Lipkin, J., "A Self-Consistent Technique for Estimating the Dynamic Yield Strength of Shock Loaded Material," J. Appl. Phys., Vol. 49, pp. 4242-4247, 1978.

14. Graham, R.A. and Brooks, W.P., Phys. Chem. Solids, Vol. 32, p. 2311, 1971.

15. Rosenberg, Z., Yaziv, D., Yeshurun, Y., and Bless, S., "Shear Strength of Shock-Loaded Alumina as Determined with Longitudinal and Transverse Manganin Gauges," J. Appl. Phys., Vol. 62, p. 1120, 1987.

16. Bless, S.J., Rosenberg, Z., and Brar, N.S., "Strength of Soda Lime Glass Under Shock Compression," Shock Waves in Condensed Matter 1987, North Holland, pp. 309-312, 1988.

17. Cagnoux, J., "Deformation et Ruine d'un Verre Pyrex Soumis a Un Choc Intense," Thesis, Univ. Poitiers, 1985.

18. Mashimo, T., "Measurements of the Combined Compression Shear Shock Waves of Over 20 GPa in Sapphire," Shock Waves in Condensed Matter 1987, North Holland, pp. 285-287, 1988.

19. Brace, W.F., Paulding, B.W., and Scholz, C., "Dilatancy in the Fracture of Crystalline Rocks," J. Geophys. Res., Vol. 71, pp. 3939-3953, 1966.

20. Schock, R.N., "Stress Strain Behavior of Granodiorite and Two Graywackes on Compression to 20 Kilobars," J. Geophys. Res., Vol. 78, pp. 5922-5991, 1973.

21. Janach, W., "The Role of Bulking in Brittle Failure of Rocks Under Rapid Compression," Int. J. Mech. Min. Sci. & Geomech. Abstr., Vol. 13, pp. 177-186, 1976.

22. Bless, S.J., "Plate Impact Experiments," UDR-TR-88-05, The Metal Society Annual Meeting, Phoenix, AZ, January 1988.

23. Rosenberg, Z., Brar, N.S., and Bless, S.J., "Elastic Precursor Decay in Ceramics as Determined with Manganin Stress Gauges," J. Physique C3, pp. 707-712, September 1988.

24. Rosenberg, Z. and Partom, Y., "On the Lateral Stress Measurement in Shock Loaded Targets with Transverse Piezoresistance Gauges," Proc. 4th APS Conf. Shock Waves in Condensed Matter, Spokane, WA, July 1985.

25. Rosenberg, Z. and Bless, S.J., "Determination of Dynamic Yield Strengths with Embedded Manganin Gauges in Plate-Impact and Long-Rod Experiments," Exp. Mech., Vol. 26, pp. 184-186, September 1984.

26. Yaziv, D., "Shock Fracture and Recompaction of Ceramics," PhD. Thesis, Univ. of Dayton, June 1985.

27. Kumar, P. and Clifton, R.J., "A Star Shaped Flyer for Plate-Impact Recovery Experiments," J. Appl. Phys., Vol. 48, pp. 4850-4852, 1977.

28.  Yaziv, D., Bless, S.J., and Rosenberg, Z., "Shock Fracture and Recompaction of Ceramics," Proc. Fourth APS Conf. on Shock Waves in Condensed Matter, Spokane, WA, 22-25 July 1985.

29.  Dandekar, D.P., private communication, 1988.

30.  Abou-Sayed, A.S. and Clifton, R.J., "Pressure-Shear Waves in 6061T6 Aluminum," J. Appl. Phys., March 1976.

31.  Young, C. and Dubugnon, O., "A Reflected Shear-Wave Technique for Determining Dynamic Rock Strength," Ins. J. Rock. Mech., Min. Sci., 1977.

32.  Lankford, J., "Mechanisms Responsible for Strain-Rate Dependent Compressive Strength in Ceramic Materials," J. Am. Cer. Soc., C33, 64, 1981.

33.  Brar, N.S., Bless, S.J., and Rosenberg, Z., "Brittle Failure of Ceramic Rods Under Dynamic Compression," J. Physique C3, pp. 707-712, September 1988.

34.  Ahrens, T.J., Gust, W.H., and Royce, E.B., "Material Strength Effect in the Shock Compression of Alumina," J. Appl. Phys., Vol. 39, p. 4610 (1968).

35.  Maskimo, T., Hanaoka, Y., and Nagayoma, K., "Elastoplastic Properties Under Shock Compression of $Al_2O_3$ Single Crystal and Polycrystal," J. Appl. Phys., Vol. 63, pp. 327-336, 1988.

36.  Munson, D.E. and Lawrence, R.J., "Dynamic Deformation of Polycrystalline Alumina," J. Appl. Phys., Vol. 50, pp. 6272-6282, 1979.

37.  Rosenberg, Z., Yeshurun, Y., and Brandon, D.G., "Dynamic Response and Microstructure of Commercial Alumina," J. Physique, 46, C5-331, 1985.

38.  Yaziv, D., Yeshurun, Y., Partom, Y., and Rosenberg, Z., "Shock Structure and Precursor Decay in Commercial Alumina," Shock Waves in Condensed Matter - 1987, S.C. Schmidt, N.C. Holmes, editors, Elsevier Science Publishers B.V., 1988.

39.  Cagnoux, J. and Longy, F., "Is the Dynamic Strength of Alumina Rate-Dependent?", Shock Waves in Condensed Matter 1987, Elsevier, pp. 293-296, 1988.

40.  Lopatin, C. and Bless, S., "Dynamic Unloading Behavior of Soda Lime Glass," to be published J. Appl. Phys., 1988.

41.   Yeshurun, Y., Rosenberg, Z., Brandon, D.G., and Travitzky, N.A., "Effect of Heat Treatment on the Dynamic Response of Commercial 85 wt. % Alumina," _Materials Sci. & Engng._, Vol. 71, 1985.

42.   Yeshurun, Y., Brandon, D.G., Venkert, A., and Rosenberg, Z., "The Dynamic Properties of Two-Phase Alumina/Glass Ceramics," _J. Physique_ C3, pp. 11-18, September 1988.

43.   Louro, L.H.L., Linfors, A., and Meyers, M.A., "Stress-Wave-Induced Damage in Alumina," _J. Physique_ C3, pp. 333-338, September 1988.

44.   Cagnoux, J. and Longy, F., "Spallation and Shock-Wave Behavior of Some Ceramics," _J. Physique_ C3, pp. 3-10, September 1988.

45.   Longy, F. and Cagnoux, J., "Macro and Micro-Mechanical Aspects of Shock-Loading of Aluminas," _Impact Loading and Dynamic Behavior of Materials_, ed. C.Y. Chiem, H-D Kunze, and L.W. Meyer, pp. 1001-1008, 1988.

46.   Coon Porcelin data sheet.

47.   Rosenberg, Z., "Dynamic Uniaxial Stress Experiments on Alumina with In-Material Manganin Gauges," _J. Appl. Phys._ Vol. 57, pp. 5087-5088, 1985.

48.   Tracy, C.A., "A Compression Test for High Strength Ceramics," _J. Testing and Eval._, Vol. 15, pp. 14-19, January 1987.

49.   Arrowood, R. and Lankford, J., "Dynamic Characterization of an Alumina Ceramic," Report SWRI-6724, 30 November 1982.
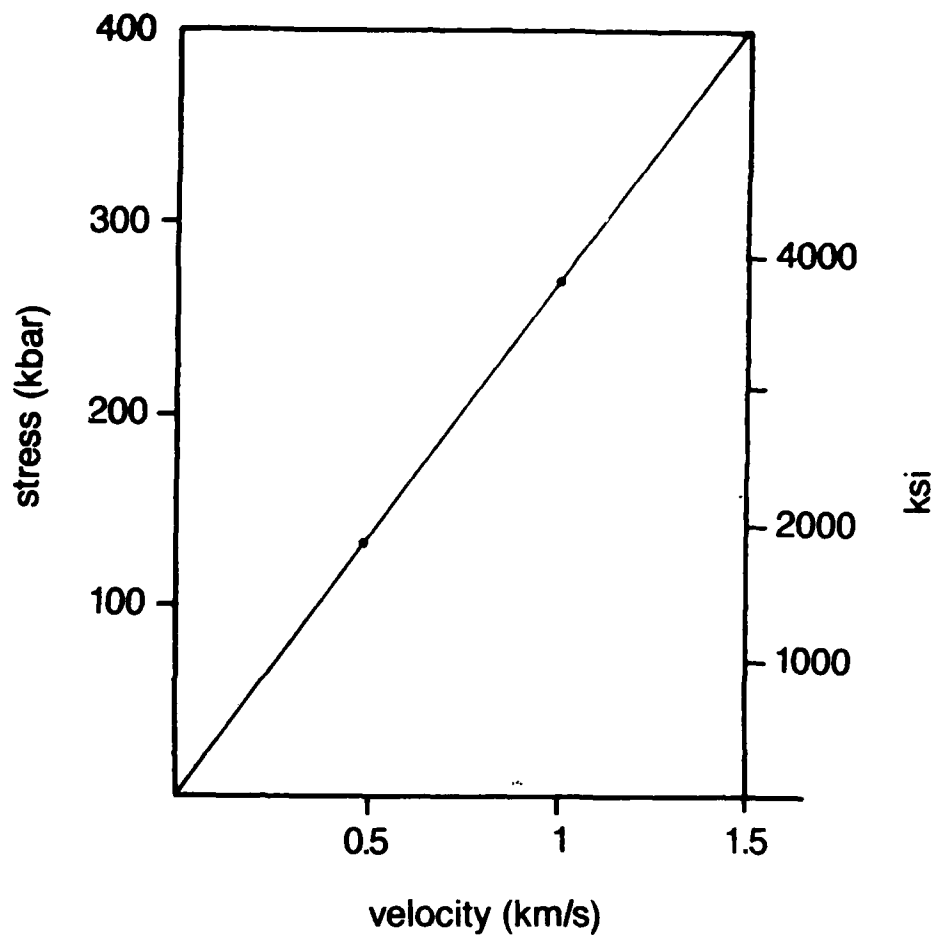
Figure 1.    Shock Stress as a Function of Impact Velocity for
Tungsten Projectiles Striking Alumina.
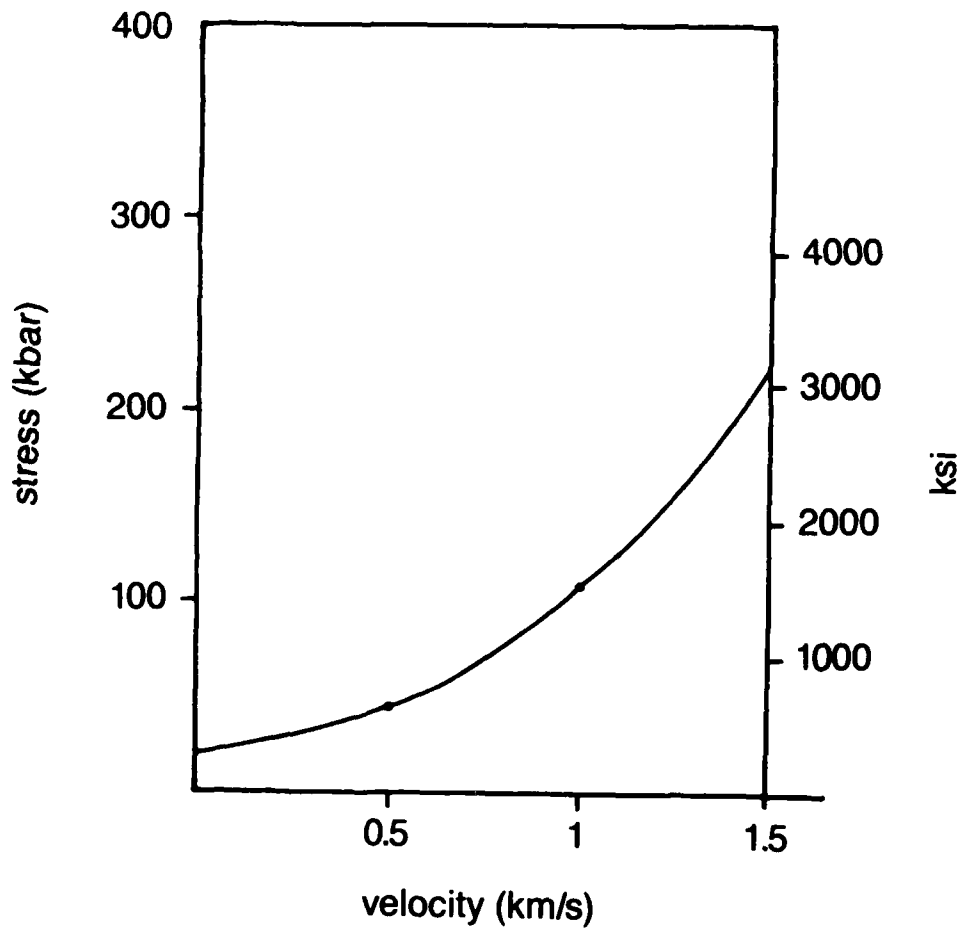
Figure 2.   Impact Stress as a Function of Velocity for Tungsten
Projectile of 20 kbar Dynamic Strength.
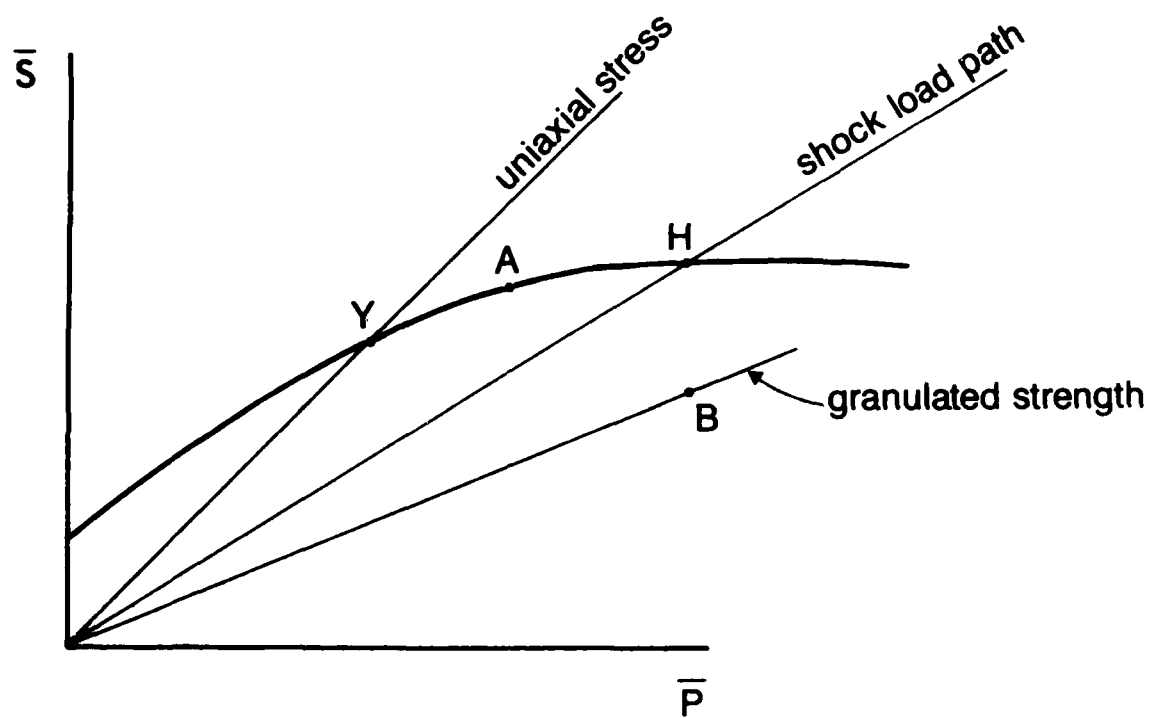
Figure 3. General Variation of Shear Strength, S, as a Function of $\overline{P}$. Here $\overline{S} = 1/2 \ (\sigma_1 - \sigma_2)$.
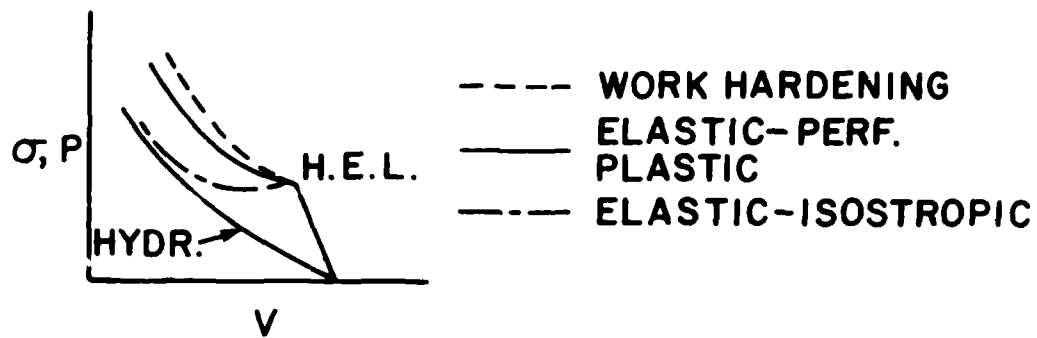
Figure 4.  Shock Loading Paths; Stress as a Function of
Volumetric Compression.
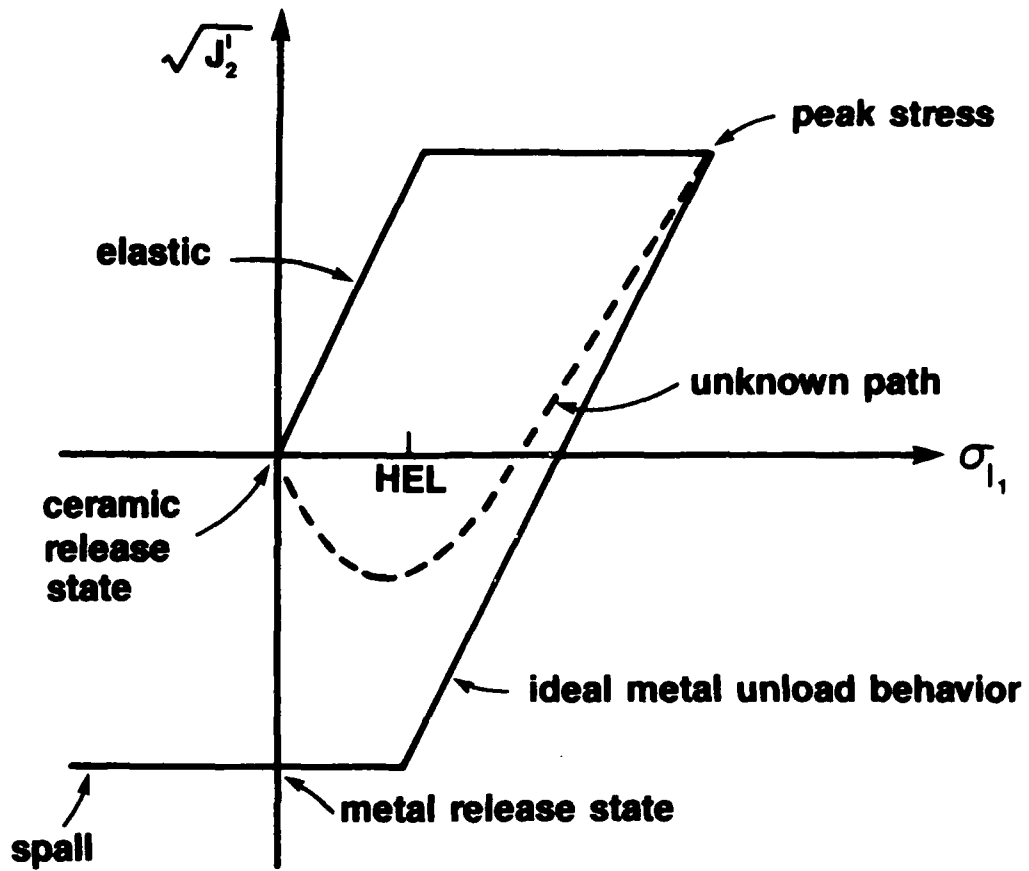
Figure 5.  One-dimensional Strain Load/Unload Path Deviatoric Stress as a Function of Principal Stress.

FLYER PLATE — MEASUREMENT STATIONS

$\sigma_x$

$\sigma_y$

SPECIMEN

"PLASTIC" WAVE

STRUCTURED RELEASE ⟹ INFORMATION ABOUT SHEAR STRENGTH

VELOCITY OR STRESS

SPALL SIGNAL ⟹ $\sigma_{u.t.s}$ AT $10^5$ s$^{-1}$

ELASTIC WAVE ⟹ $\sigma_y$ (COMPRESS.) AT $10^6$ s$^{-1}$

TIME

OUTPUT - AT MEASUREMENT STATIONS
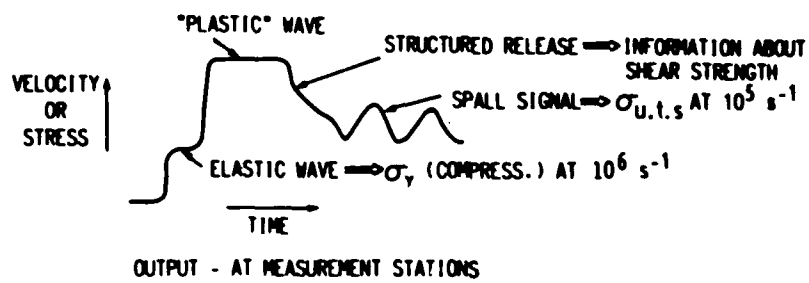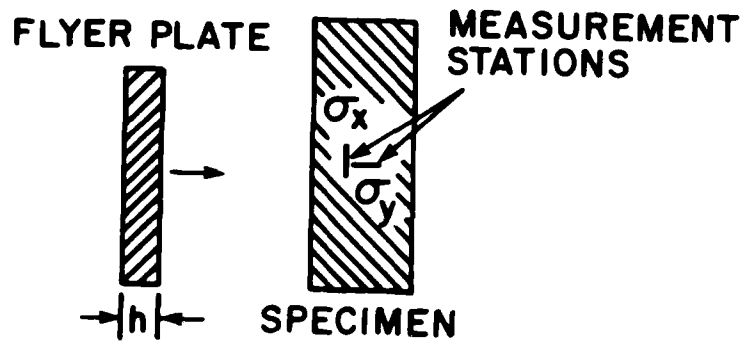
Figure 6.   Plate Impact Experiment.
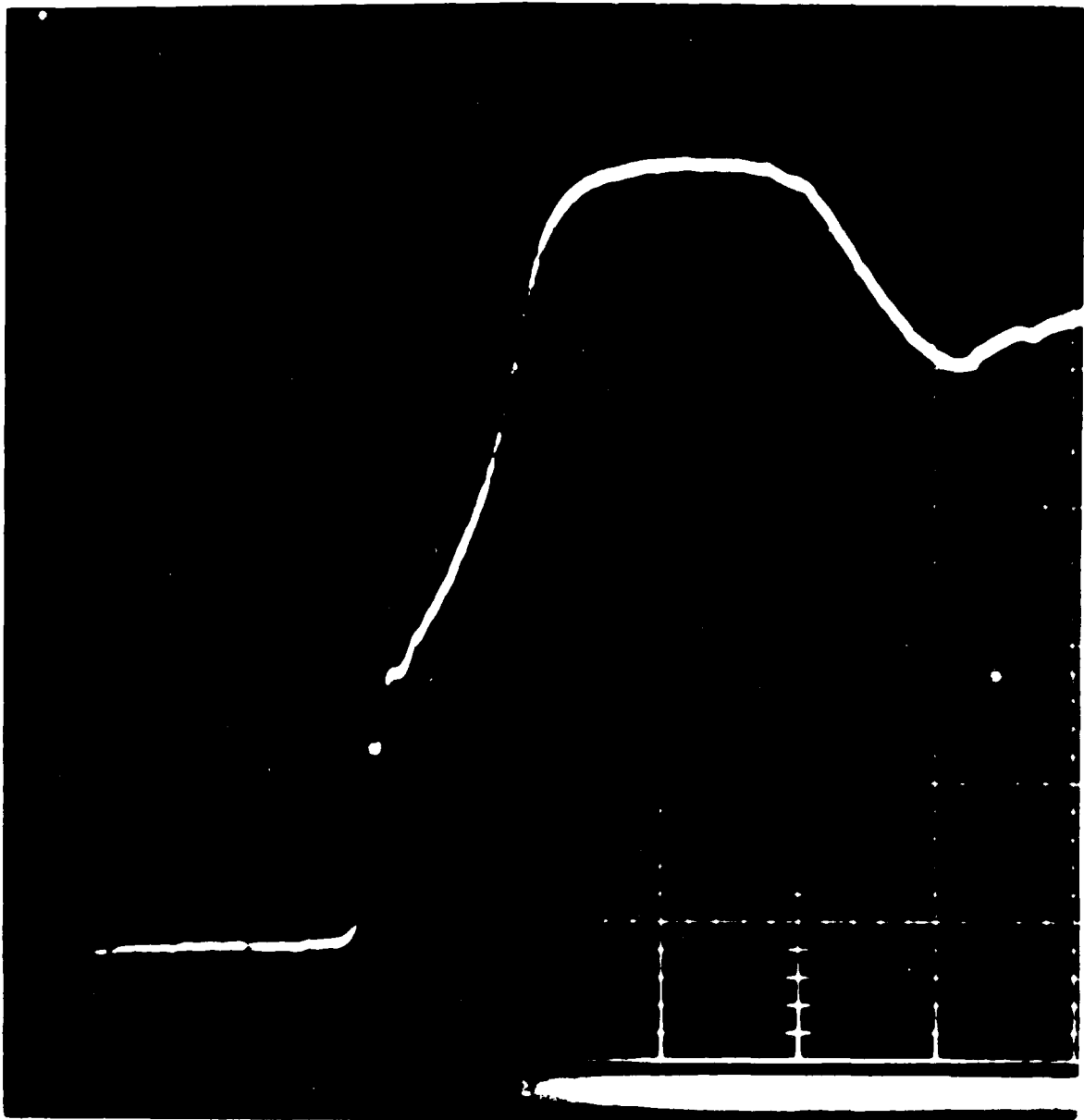
Figure 7.  Stress Time Signal as Commonly Observed in Ceramic
Targets.
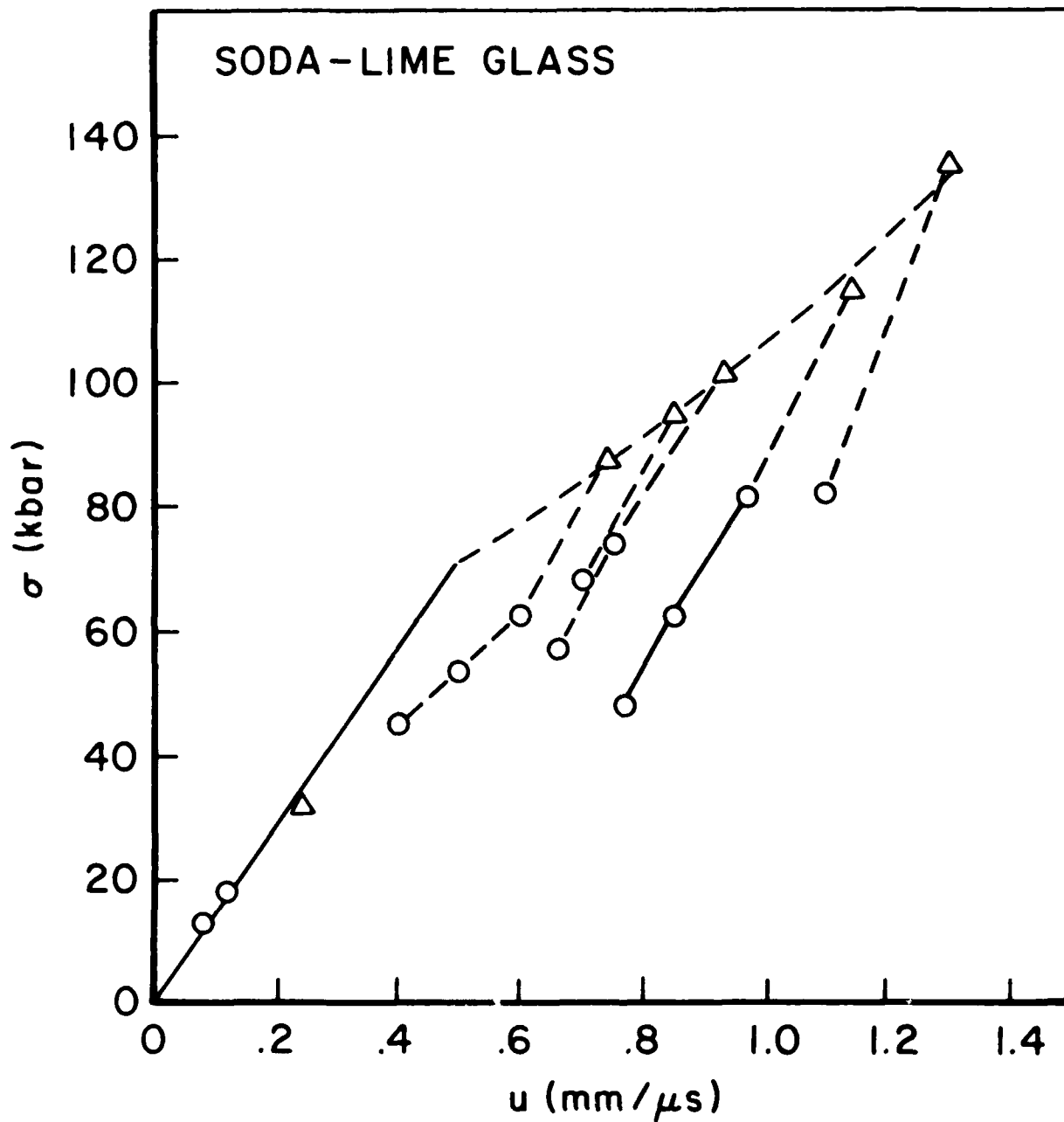
Figure 8.   Dynamic Unloading Paths in Soda Lime Glass (from [40]).
Triangles (Δ) are peak stress points and circles (o)
are points on release paths.
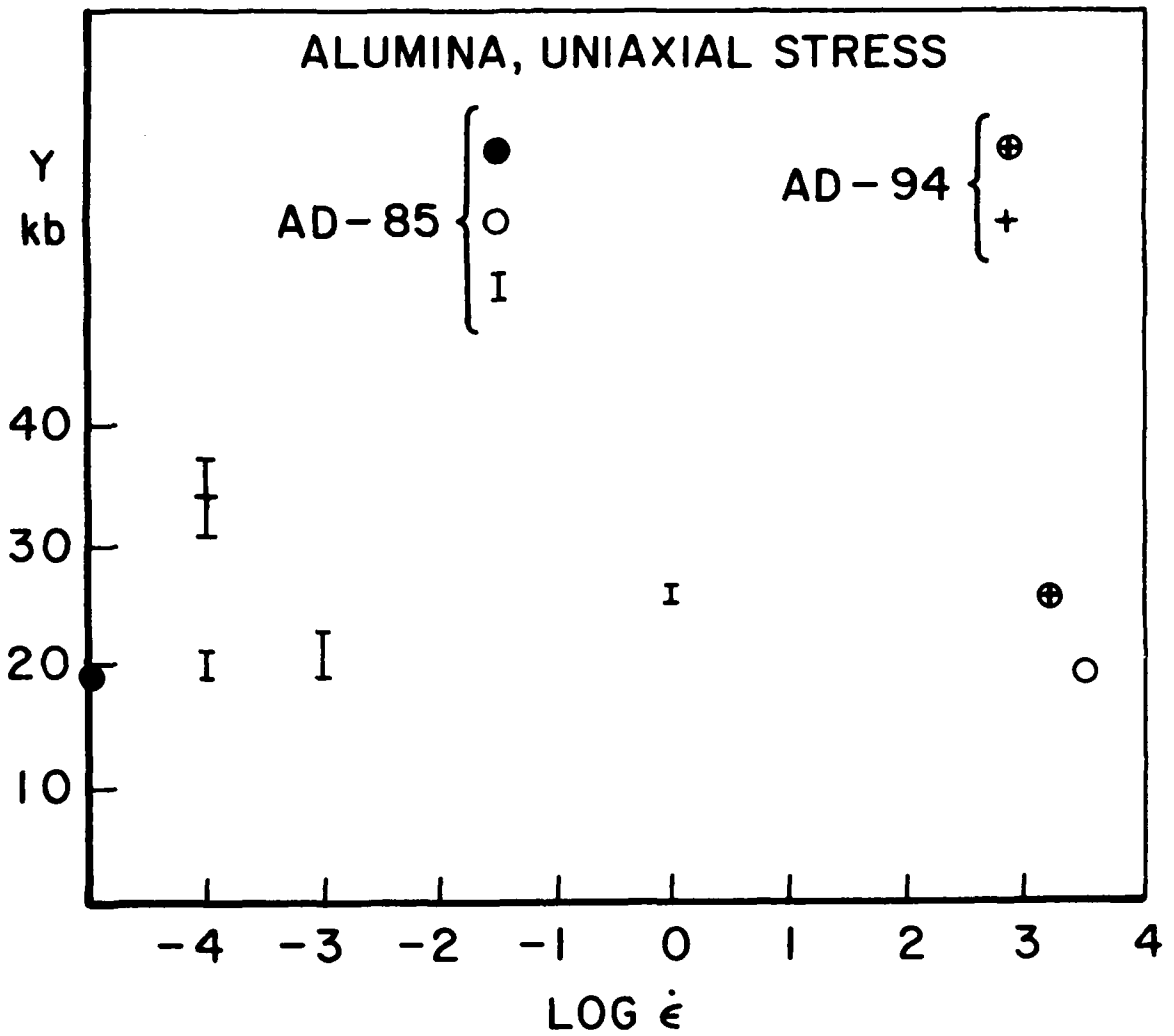
Figure 9. Yield Strength Under Uniaxial Stress Conditions as a Function of Strain Rate.

AD-85 is 85% alumina. Data sources are [46,47,32], respectively.

AD-99 is 94% alumina. Data sources are [33,48], respectively.
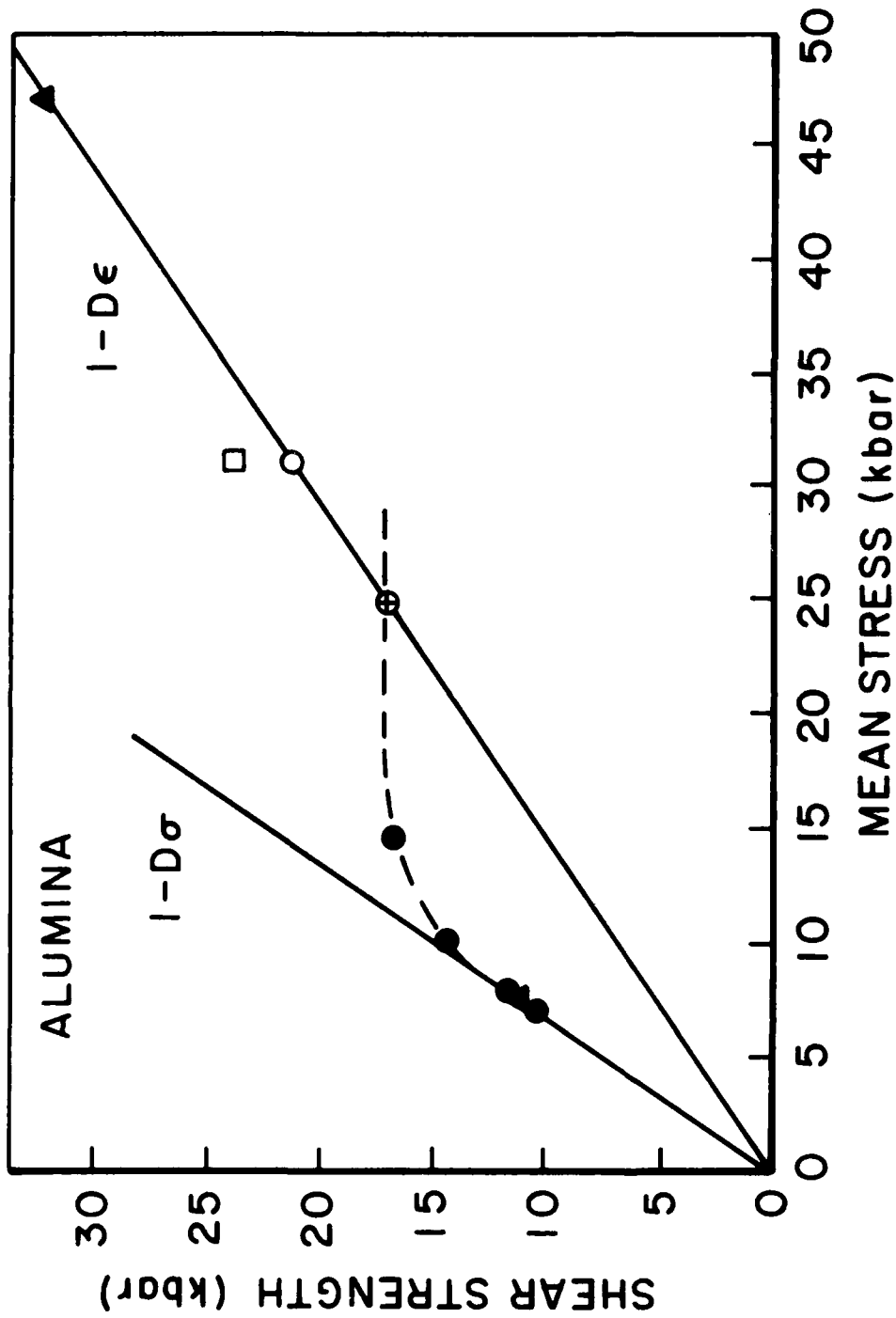
Figure 10.   Shear Strength of Alumina as a Function of Pressure.
Circles and sqaures are AD85: triaxial data from [49],
equilibrium HEL from [38], thin sample HEL from [37],
and direct shear measurement (square points) from
[37].  Triangles are for Lucalox (100% alumina) [36].

# A STRAIN RATE DEPENDENT BRITTLE FRACTURE MODEL
# BASED ON CONTINUUM DAMAGE MECHANICS*

E. P. Chen

Applied Mechanics Division III
Sandia National Laboratories
Albuquerque, New Mexico 87185

## ABSTRACT

Dynamic fracturing in brittle materials is studied in the present investigation using a strain rate dependent continuum damage model. A basic assumption of this model is the existence of a randomly distributed crack network in the material. Under applied tension, these cracks will grow and interact to relieve the stress. This is reflected globally by reducing the stiffness of the material. In compression, the material responds in an elastic/perfectly plastic manner. Explicit strain rate dependence has been included in the model. A brief description of the model will be given. Applications of the model to treat engineering scale problems will be discussed. *

## INTRODUCTION

An important aspect of many engineering applications of brittle materials involves the understanding of the fracture and fragmentation behavior of these materials under rapidly applied loads. Typically, many brittle solids have an existing flaw structure. Under applied loads, these flaws will grow and interact to relieve portions of the material volume of their load carrying capability. The process progresses until the total volume becomes incapable of carrying load and failure occurs. Thus, the dynamic fracture process in brittle materials may be modeled as a continuous accrual of damage where the damage is defined to be the

---

212

volume fraction of material that has been tension relieved by multiple crack growth and interaction. Such a model has been developed by the author and his coworkers [1-3]. In this model, the material behaves in an elastic/perfectly plastic manner under compressive loading conditions. Explicit strain rate dependence has been included in the model. A brief review of the model will be presented. The model has been implemented into the transient dynamic finite element codes PRONTO 2D [4] and DYNA2D [5]. To demonstrate the utility of the model, numerical simulations of the oil shale blasting and concrete penetration problems are presented.

## A BRIEF ANALYTICAL MODEL DESCRIPTION

The basic assumption of the damage model is that the material is permeated by an array of randomly distributed cracks which grow and interact with one another under tensile loading. The model does not try to treat each individual crack, but rather treats the growth and interaction of cracks as an internal state variable which represents the accumulation of damage in the material. This damage, D, is assumed to degrade the material stiffness following the equations derived by Budiansky and O'Connell [6] for a random array of penny-shaped cracks in an isotropic elastic medium:

$$\bar{K} = K\,(1 - D) \tag{1}$$

where K and $\bar{K}$ denote, respectively, the bulk modulus for undamaged and damaged material. The damage is related to the damaged Poisson's ratio, $\bar{\nu}$, and crack density parameter, $C_d$, through

$$D = \frac{16\,(1 - \bar{\nu}^2)}{9\,(1 - 2\nu)}\,C_d \tag{2}$$

The crack density parameter is related to the undamaged Poisson's ratio, $\nu$, and $\bar{\nu}$ by the following expression:

$$C_d = \frac{45}{16} \frac{(\nu - \bar{\nu})(2 - \bar{\nu})}{(1 - \bar{\nu}^2)[10\nu - \bar{\nu}(1 + 3\nu)]} \tag{3}$$

Thus, if the crack density parameter is known, the damaged Poisson's ratio can be calculated from Equation (3) and consequently, the damage parameter is found from Equation (2). The crack density parameter provides information about cracking in a given volume in that it is assumed to be proportional to the product of N, the number of cracks per unit volume, and $a^3$, the cube of the average crack dimension in the volume element under consideration, i.e.,

$$C_d \sim N a^3 \tag{4}$$

Following the work of Grady and Kipp [7], N is expressed as a Weibull statistical distribution function activated by the current bulk strain measure P/3K, where P is the pressure or mean stress $P = (\sigma_{xx} + \sigma_{yy} + \sigma_{zz})/3$, according to

$$N = k\left(\frac{P}{3K}\right)^m \tag{5}$$

In Equation (5), k and m are material constants to be determined from strain-rate dependent fracture stress data. Since the size of the fragments is determined by the intersecting crack network within the material volume, the crack dimension is thought to be proportional to the fragment size. Thus, the average crack dimension, a, is estimated from the nominal fragment diameter expression for dynamic fragmentation in a brittle material [8] as

$$2a \sim \left(\frac{\sqrt{20}\,K_{Ic}}{\rho\,C_s\,\dot{\varepsilon}_{max}}\right)^{2/3} \tag{6}$$

214

where $\rho$ is the mass density, $C_s$ is the uniaxial wave speed ($\sqrt{E/\rho}$), with E being the Young's modulus, and $K_{Ic}$ the fracture toughness of the material. Also, $\dot{\varepsilon}_{max}$ is the maximum volumetric strain rate experienced by the material throughout the fracture process. Note that Equation (6) provides the average crack size that has been activated by the applied load in the volume element under consideration. Thus, when the strain rate is low, only large cracks have been activated and the material can only separate into a few large pieces. On the other hand, under high strain rates, smaller cracks would also have been activated and the specimen can break into many small fragments. The proportionality constants from Equation (4) and Equation (5) can be absorbed into the constant k. Hence, the additional material parameters for this constitutive model, aside from the commonly defined ones, are k and m as given in Equation (5). When bulk tension occurs in the material, it is possible to calculate, at each time step, the damage parameter D from the above expressions. The stiffness is then degraded by the factor (1 - D). In this fashion, the post-damage responses of the material are represented. Note that the damage parameter D is an internal state variable which is evolutionary and irreversible in nature. In compression, the material is assumed to behave in an elastic/perfectly plastic manner.

The constants k and m in the analytical model are specific to the strain rate dependent fracture responses of the material under consideration. The procedure to determine the constants k and m from strain rate data has been given in [1] and will not be repeated here.

## OIL SHALE BLASTING

The damage model as implemented in DYNA2D was used to obtain results for the single cratering tests conducted in 1983-1984 at Anvil Points Mine near Rifle, Colorado, by Sandia National Laboratories [9,10]. A schematic of the experimental configuration is given in Figure 1 to show the pertinent parameters. These involve the depth of burial b, the length of the explosive column c, the diameter of the explosive 2d, the property of the

explosive, and the property of the oil shale. The explosive column was detonated from the bottom. The two single borehole cratering tests were essentially the same except that one test included stemming above the explosive column (SB-1), and in the other test, the explosive column was open to the surface (SB-2). The value of b = c = 2.5 m, and 2d = 0.162 m were fixed for these tests. The explosive used in the tests was IREGEL 1175U, whose pertinent properties are given in [10]. A core was taken from rock near the test site. The results of Fischer Assay analysis of this core are shown in Figure 2. The stratigraphy indicates the layered structure of the oil shale media. The mechanical properties for these grades of oil shale are required input to the damage model for numerical simulation purposes. These are listed in Table 1. The strain rate dependent fracture stress data,

**Table 1. Mechanical Properties of Oil Shale by Grade**

| Grade (gpt) | Density (kg/m$^3$) | Young's Modulus (GPa) | Poisson's Ratio | Shear Strength (MPa) | m | k (m$^{-3}$) | $K_{Ic}$ (N/m$^{3/2}$) |
|---|---|---|---|---|---|---|---|
| 8.7 | 2523 | 30.2 | 0.259 | 102 | 7 | $4.34 \times 10^{27}$ | 512000 |
| 10.1 | 2493 | 28.8 | 0.260 | 103 | 7 | $2.96 \times 10^{27}$ | 520000 |
| 11.4 | 2465 | 27.5 | 0.261 | 103 | 7 | $2.04 \times 10^{27}$ | 527000 |
| 13.5 | 2420 | 25.4 | 0.264 | 104 | 7 | $1.08 \times 10^{27}$ | 538000 |
| 15.8 | 2370 | 23.1 | 0.266 | 106 | 7 | $5.01 \times 10^{26}$ | 551000 |
| 17.3 | 2338 | 21.6 | 0.267 | 107 | 7 | $2.92 \times 10^{26}$ | 559000 |
| 21.2 | 2261 | 17.8 | 0.271 | 106 | 7 | $6.44 \times 10^{25}$ | 580000 |
| 24.0 | 2216 | 15.5 | 0.274 | 102 | 7 | $2.09 \times 10^{25}$ | 595000 |
| 25.5 | 2192 | 14.2 | 0.276 | 100 | 7 | $1.06 \times 10^{25}$ | 605000 |
| 29.0 | 2136 | 11.2 | 0.279 | 95 | 7 | $1.61 \times 10^{24}$ | 638000 |
| 38.6 | 2008 | 7.0 | 0.289 | 78 | 7 | $3.70 \times 10^{22}$ | 726000 |
| 51.1 | 1870 | 4.3 | 0.301 | 70 | 7 | $7.26 \times 10^{20}$ | 896000 |

however, have only been determined for 20 gpt (gallons per ton) grade oil shale (Figure 3) [9]. In this set of calculations, the constants k and m in the damage model are obtained based on the data in Figure 3. Note that the determination of k is dependent upon the

fracture toughness. Therefore, m = 7 for all grades of oil shale, but the value of k is different. The IREGEL 1175U explosive is modeled in the DYNA2D code as a material type which uses the JWL equation of state [5]. The relevant parameters can be found in [9] and are not repeated here.

The finite element mesh used in the calculations is shown in Figure 4. Two idealizations for the oil shale have been made. In the first case, the oil shale was approximated as an isotropic material having the properties of the 21 gpt oil shale. This represents the average of the oil shale grades in Figure 2. The second case treats the oil shale as a layered structure according to the stratigraphy in Figure 2. Measured and calculated shock wave parameters at a point 3.0 meters from the explosive column and 2.5 meters below the surface are compared in Figures 5 and 6. In Figure 5, the measured arrival time and those calculated from the isotropic and layered models are shown; and close agreement was found among all three values. Further, the peak radial stress calculated in the two simulations was within 10 percent of the measured one. The radial particle velocity measurement and calculations at this same point are shown in Figure 6. The peak velocity calculated by the isotropic model is the highest, while the layered model yielded the lowest value. These comparisons demonstrate the accuracy with which the numerical model calculates the transmission of the explosive induced shock waves.

The region of significant rock damage in the oil shale is usually measured by excavating the rock loosened by the blast. Comparisons between experimental and numerical results are shown in Figures 7 and 8. The layered model produced a smaller damaged rock zone than the isotropic one due to energy dissipation by the layer interfaces. However, in both cases, the calculated regions of damage were much larger than excavated craters.

To further investigate the fragmentation experienced in the tests, cores were taken from the rock beyond the crater. The cores showed extensive fragmentation, indicating

that fragmentation extended beyond the excavated region. A gradational scale was used to describe the extent of fracturing experienced by each part of the core. Five categories were chosen for this description:

1. Intact - for rock that appeared to have suffered no damage;

2. Fractured - for rock that contained isolated fractures;

3. Well Fractured - for rock that had an extensive network of intersecting fractures;

4. Rubble - for rock that had been fractured enough that it was a collection of fragments;

5. Pulverized - for rock that had been ground into small fragments (less than 0.5 cm in diameter).

Each section of core was assigned one of these categories. The categories of fragmentation used to describe the cores can also be compared to the numerical calculations of damage. The five degrees of fragmentation used in the core analysis were compared to different intervals of the damage coefficient. The result, shown in Figure 9, is a similarity between the numerical calculation and experimental measurement that suggests rock fragmentation can be calculated with reasonable accuracy using this damage model.


## CONCRETE PENETRATION

In this case, an attempt to simulate numerically the concrete penetration experiments conducted by Hightower and Forrestal [11] is made. In these experiments, steel penetrators with 6.0 CRH nose shapes, 6.1 - 6.3 in. diameters, 59 - 64 in. lengths, and 330 - 350 lb. weights were accelerated to impact velocities between 1000 - 2000 fps with a 12 in. diameter, smooth-bore, recoilless gun (Davis gun) into concrete slabs. Only normal penetration has been included in this test series. The geometry of the two-layered targets is shown in Figure 10. The construction of the concrete slabs is quoted from [11]: "All

targets were poured at the same time, and tests were conducted at 4, 24, and 48 months after construction. The concrete slabs were 16 ft. square and were 2 and 3 ft. thick. The 2-ft.-thick slabs were designed as two-way slabs (equal reinforcement in the lateral directions and no shear reinforcement), and the 3-ft.-thick slabs were designed as one-way slabs (principal reinforcement in one lateral direction, temperature reinforcement in the other direction, and shear reinforcement)."

Numerical simulations of the normal penetration processes in geological targets using the PRONTO 2D code have been considered previously by Chen [12]. In these calculations, both the penetrator and the target are treated as deformable bodies. The metal penetrators are usually modeled as elastic/plastic materials with strain hardening behavior. The targets are modeled by the soil and crushable foam model in PRONTO 2D [5]. A pilot hole is assumed along the expected penetrator path. For illustration purposes, the case of penetration into 4-month-old concrete target corresponding to the tests in [11] is considered. Only the first layer of the target has been included since it is enough to make the point. The finite element mesh is shown in Figure 11 where axisymmetry has been invoked. Material properties for the steel penetrator are not important since it will essentially not deform under the range of impact velocities considered here. For this reason, the material properties of the steel penetrator are not listed. Some concrete properties have been measured in [11] from core samples and these are shown in Figure 12. Other mechanical properties were taken from open literature and are listed in Table 2. For an impact velocity of 1340 fps, Figure 13 shows a deformed mesh plot at 3.0 ms. Calculated maximum deceleration 3900 g and exit velocity 1150 fps compare well with measured values of 4300 g and 1075 fps, respectively.

**Table 2. Typical Concrete Properties**

| | |
|---|---|
| Mass Density | 2.4 Mg/m³ |
| Young's Modulus | 20.7 GPa |
| Poisson's Ratio | 0.18 |
| Fracture Toughness | 2.75 MPa-$\sqrt{m}$ |

By comparing the observed failure surfaces in the target in Figure 14 with the calculated ones in Figure 13, numerical calculations certainly did not simulate the failure surfaces well. The reason for this discrepancy as well as the pilot hole assumption stems from the use of plasticity type of constitutive models. The use of plasticity type models allows only the dissipation of energy by continuous deformation and precludes fracturing as an additional mechanism for energy dissipation purposes. Thus, for these models, the physically observed material separation processes must be manually included by, for example, the pilot hole assumption, to arrive at the desired results. Otherwise, these fracture characteristics will be absent as evidenced from the fracture surfaces in Figure 13, as compared with those in Figure 14. Moreover, under oblique impact conditions, when the trajectory of the penetrator is not known a priori, the utility of the plasticity type models is even more restricted. In this regard, a fracture-based material model should be more appropriate. Since the previously described damage model has been implemented into PRONTO 2D, the same problem of normal impact of a steel penetrator at 1340 fps into a 2-ft.-thick concrete target slab has been calculated using the damage model. The same finite element mesh in Figure 11 is used. In order to use this model, the constants k and m in the damage model must be determined. This requires the strain rate dependent tensile strength data for concrete in the range of strain rates of 1 to 1000 /s. In lieu of these test data, they can be estimated from the fracture toughness value by an equation given in [13]:

$$\sigma_c = \left( \frac{9 \, E \, K_{Ic}^2}{16 \, Y^2 \, C} \right)^{1/3} \dot{\varepsilon}^{1/3} \qquad (7)$$

relating the tensile strength and strain rate. In Equation (7), E is the Young's modulus, Y is a crack geometric shape factor, and C is the shear wave speed. Assuming that the sub-scale cracks are penny-shaped, Y can be taken to be 1.12. Other constants can be obtained from Table 2. Figure 15 shows the result from this estimation procedure. The constants k and m can be determined from strain rate dependent fracture stress via a procedure given in [1]. The values of k and m corresponding to the results in Figure 15 are found to be $5.753230 \times 10^{21}/m^3$ and 6.0, respectively. Figure 16 shows the deformed mesh plot based on the damage model at 3.0 ms. The computation also used the element death feature in the PRONTO 2D [5] code. Hence, an element is deleted from the calculation when the damage level reaches 0.5. The preliminary result in Figure 16 compares well with the observed fracture surfaces in Figure 14. Although some problems, such as the calculated deceleration history does not agree well with the measured record, remain, the results in Figure 16 are encouraging. Work is in progress to refine the analysis based on the damage model. Further results will be communicated when they become available.

## SUMMARY

A continuum damage model has been applied to study the dynamic response of brittle materials with subscale crack populations. The model treats the dynamic fracture process as a continuous accrual of damage where the damage is defined to be the volume fraction of material that has been tension relieved by multiple crack growth and interaction. Numerical simulation of the oil shale blasting problem validates the utility of the damage model. A work-in-progress report on the simulation of the concrete penetration problem show interesting features. Further results will be communicated in a future report.

## REFERENCES

[1]  Taylor, L. M., Chen, E. P., and Kuszmaul, J. S., "Microcrack Induced Damage Accumulation in Brittle Rock Under Dynamic Loading," Journal of Computer Methods in Applied Mechanics and Engineering, 55, 301, 1986.

[2]  Chen, E. P., "Continuum Damage Mechanics Studies on the Dynamic Fracture of Concrete," Cement-Based Composites: Strain Rate Effects on Fracture, Materials Research Society Symposia Proceedings, Volume 64, S. Mindess and S. P. Shah, Editors, Materials Research Society, Pittsburgh, PA, 1986.

[3]  Chen, E. P. and Taylor, L. M., "Fracture of Brittle Rock Under Dynamic Loading Conditions," Fracture Mechanics of Ceramics, Volume 7, R. C. Bradt, A. G. Evans, D. P. H. Hasselman, and F. F. Lange, Editors, Plenum Press, New York, 1986.

[4]  Budiansky, B. and O'Connell, R. J., "Elastic Moduli of a Cracked Solid," International Journal of Solids and Structures, 12, 81, 1976.

[5]  Taylor, L. M., and D. P. Flanagan, "PRONTO 2D - A Two-Dimensional Transient Solid Dynamics Program," Report SAND86-0594, Sandia National Laboratories, Albuquerque, NM, March 1987.

[6]  Hallquist, J. O., "User's Manual for DYNA2D - An Explicit Two-Dimensional Hydrodynamic Finite Element Code With Interactive Rezoning," Report UCRL-52997, Lawrence Livermore National Laboratory, Livermore, CA, 1981.

[7]  Grady, D. E. and Kipp, M. E., "Continuum Modeling of Explosive Fracture in Oil Shale," International Journal of Rock Mechanics and Mining Sciences, 17, 147, 1980.

[8]  Grady, D. E., "The Mechanics of Fracture Under High-Rate Stress Loading," Preprints of the William Prager Symposium on Mechanics of Geomaterials: Rocks, Concrete and Soils, Edited by Z. P. Bazant, Northwestern University, Evanston, IL, 1983.

[9]  Kuszmaul, J. S., "Numerical Modeling of Oil Shale Fragmentation Experiments," Proceedings of the Society of Explosive Engineers, Mini Symposium on Blasting Research, San Diego, CA, 1985.

[10]  Parrish, R. L. and Kuszmaul, J. S., "Development of a Predictive Capability for Oil Shale Rubblization: Results of Recent Cratering Experiments," Seventeenth Oil Shale Symposium Proceedings, Golden, CO, 1984.

[11]  Hightower, M. M. and Forrestal, M. J., "Perforation of Thick Reinforced-Concrete Slabs," Report SAND84-1588, Sandia National Laboratories, Albuquerque, NM, February 1985.

[12]  Chen, E. P., "Finite Element Simulation of Penetration Into Geological Targets," Theoretical and Applied Fracture Mechanics, 8, 125, 1987.

[13]  Kipp, M. E., Grady, D. E., and Chen, E. P., "Strain-Rate Dependent Fracture Initiation," International Journal of Fracture, 16, 471, 1980.
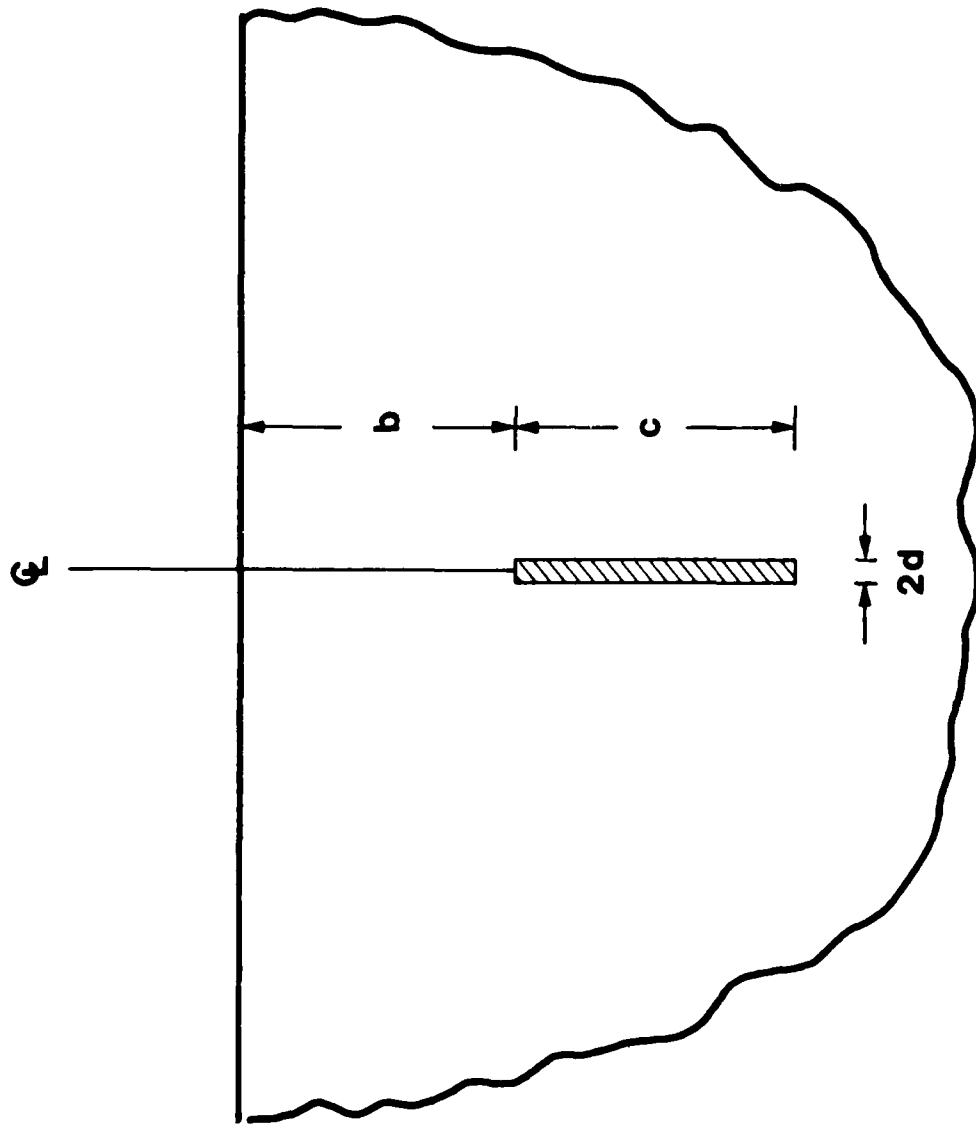
Figure 1. Oil Shale Single Crater Test Geometry
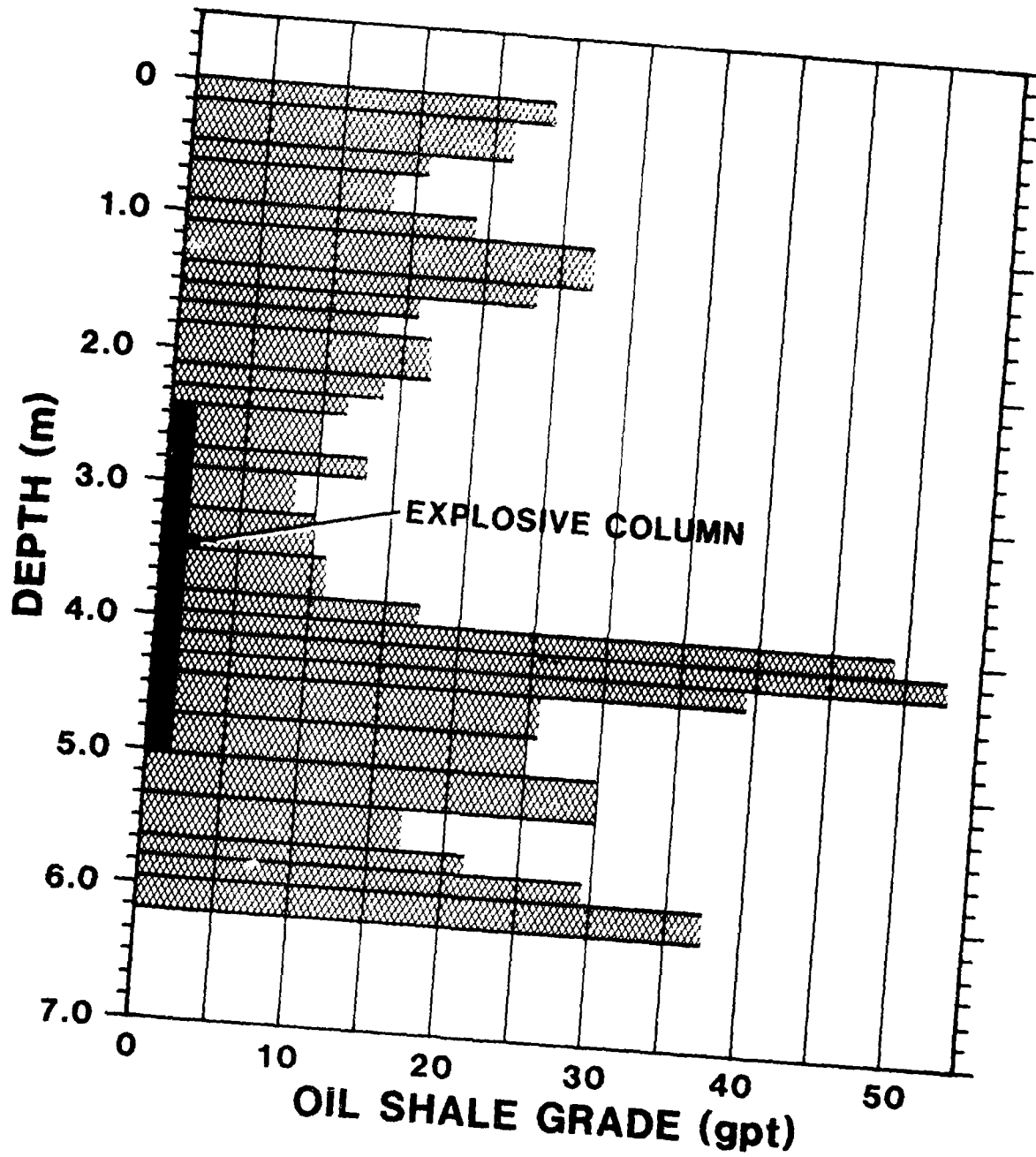
Figure 2.  Results of Fischer Assay Analysis of Core from Test Area
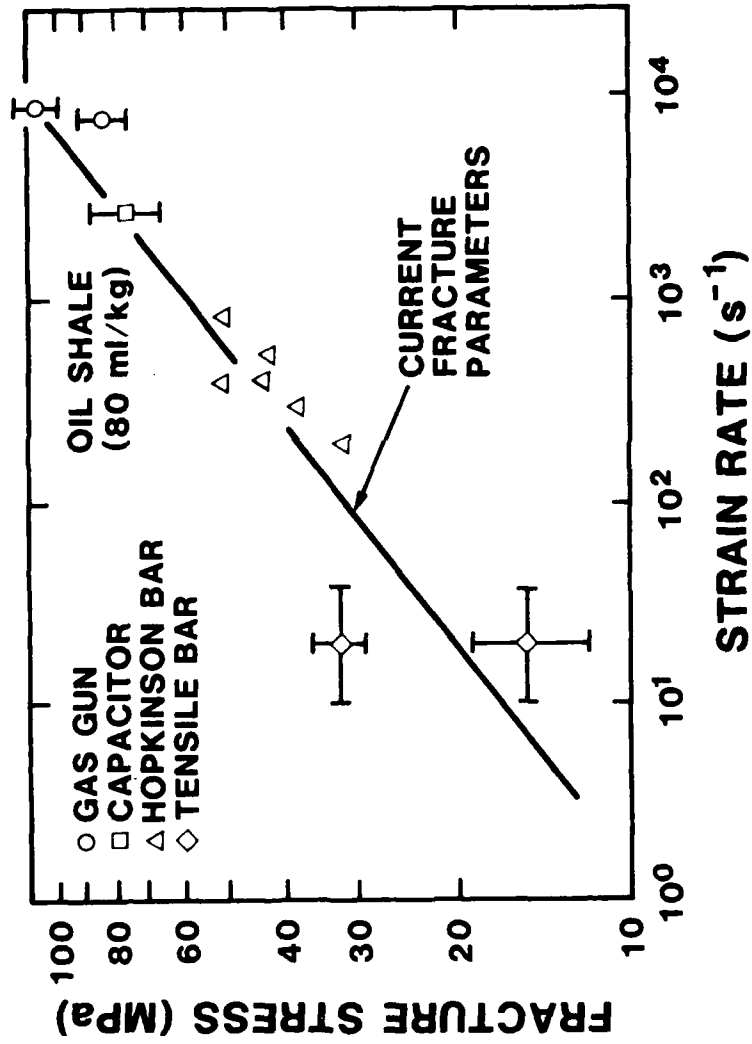
Figure 3. Strain Rate Dependent Fracture Stress Data for Oil Shale

225

SHALE GRADE
(gpt)

| 24.0 | 21.2 |
|---|---|
| 15.0 | 13.5 |
| 21.2 | 29.0 |
| 24.0 | 15.6 |
| 13.5 | 17.3 |
| 13.5 | 11.4 |
| 10.1 | 13.5 |
| 8.7 | 10.1 |
| 11.4 | 17.3 |
| 51.1 | 38.6 |
| 25.5 | |
| 29.0 | 21.2 |
| 17.7 | 38.6 |
| 29.0 | |
| 24.0 | |
| 38.6 | |
| 21.2 | |
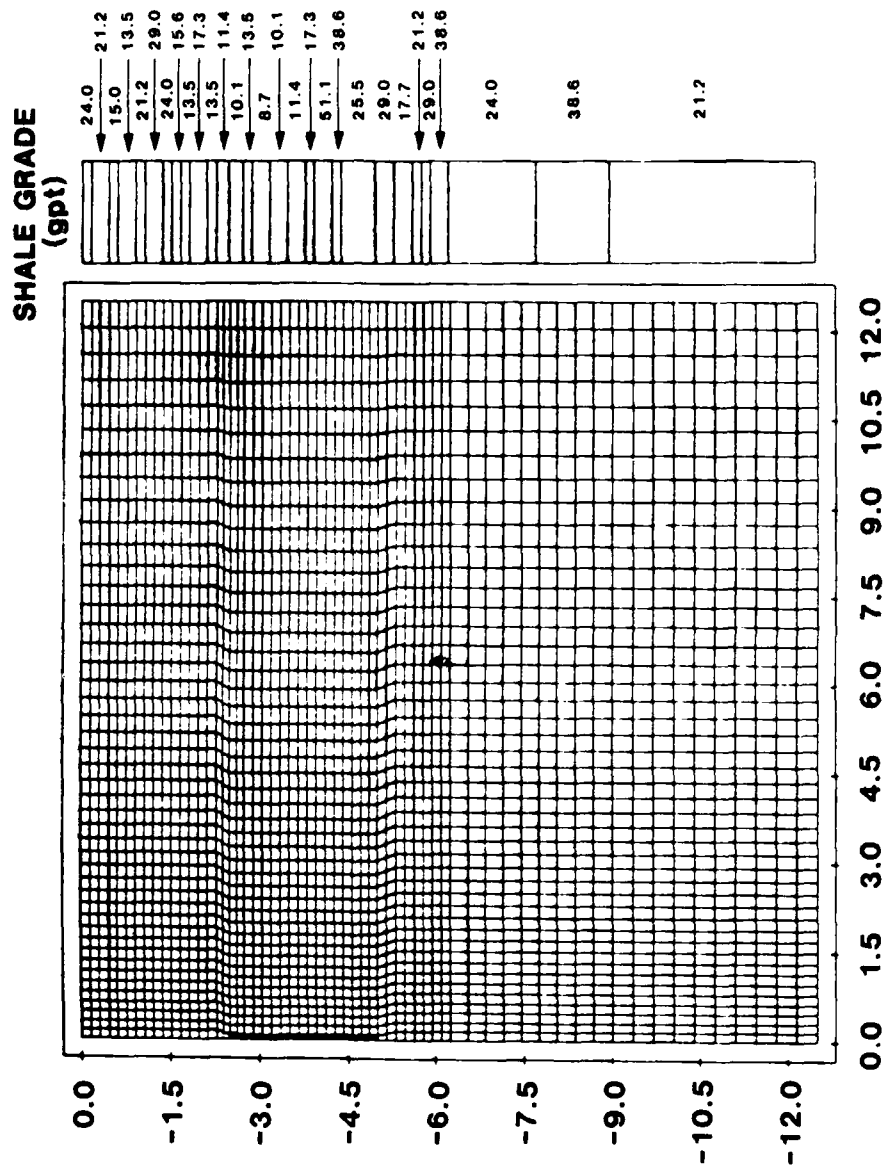
Figure 4.    Finite Element Mesh for Oil Shale Blasting Simulation

226
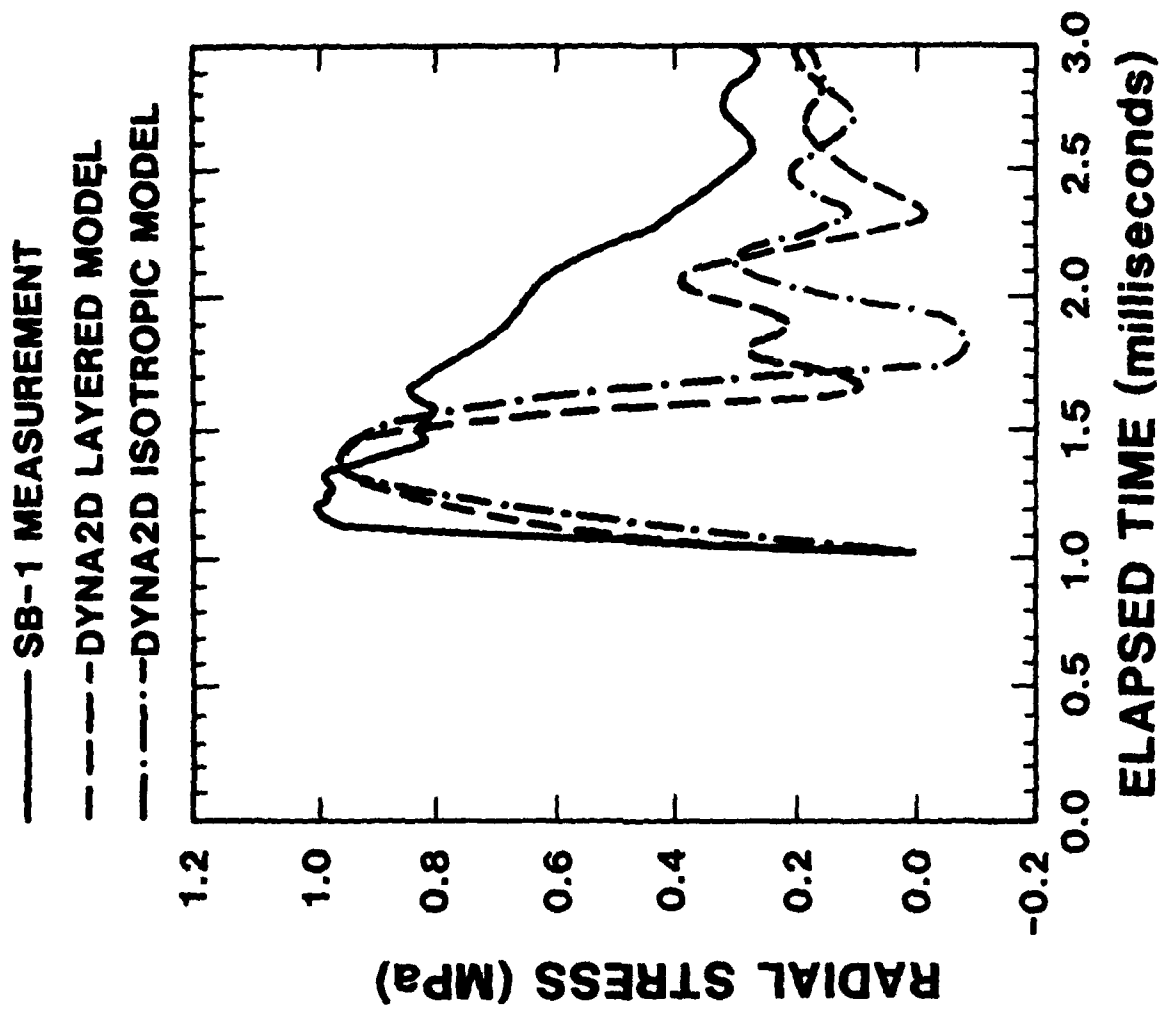
Figure 5.    Radial Stress Versus Time

SB-1 MEASUREMENT
DYNA2D LAYERED MODEL
DYNA2D ISOTROPIC MODEL

RADIAL VELOCITY (meters/second)

ELAPSED TIME (milliseconds)
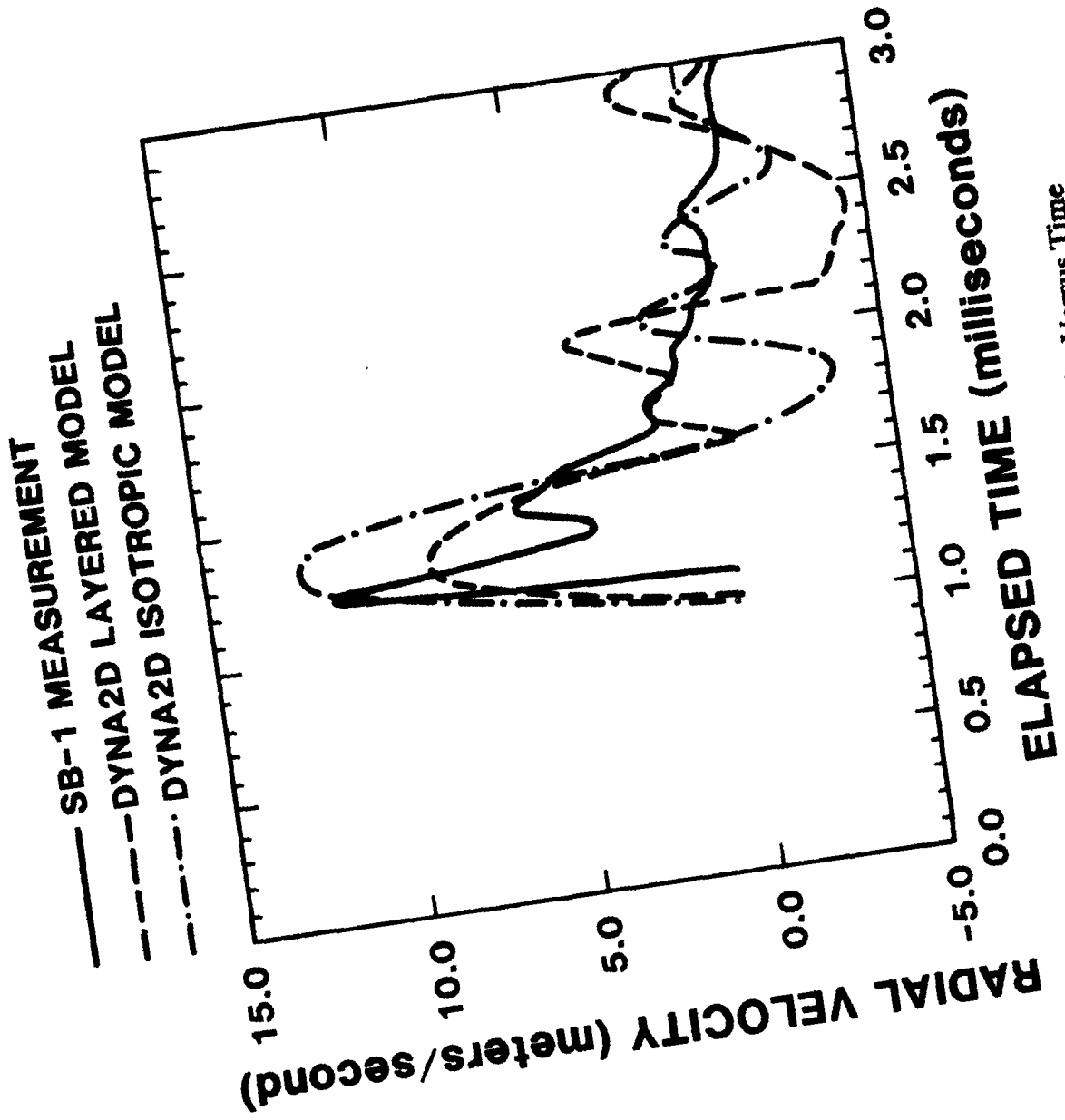
Figure 6.   Radial Velocity Versus Time

228
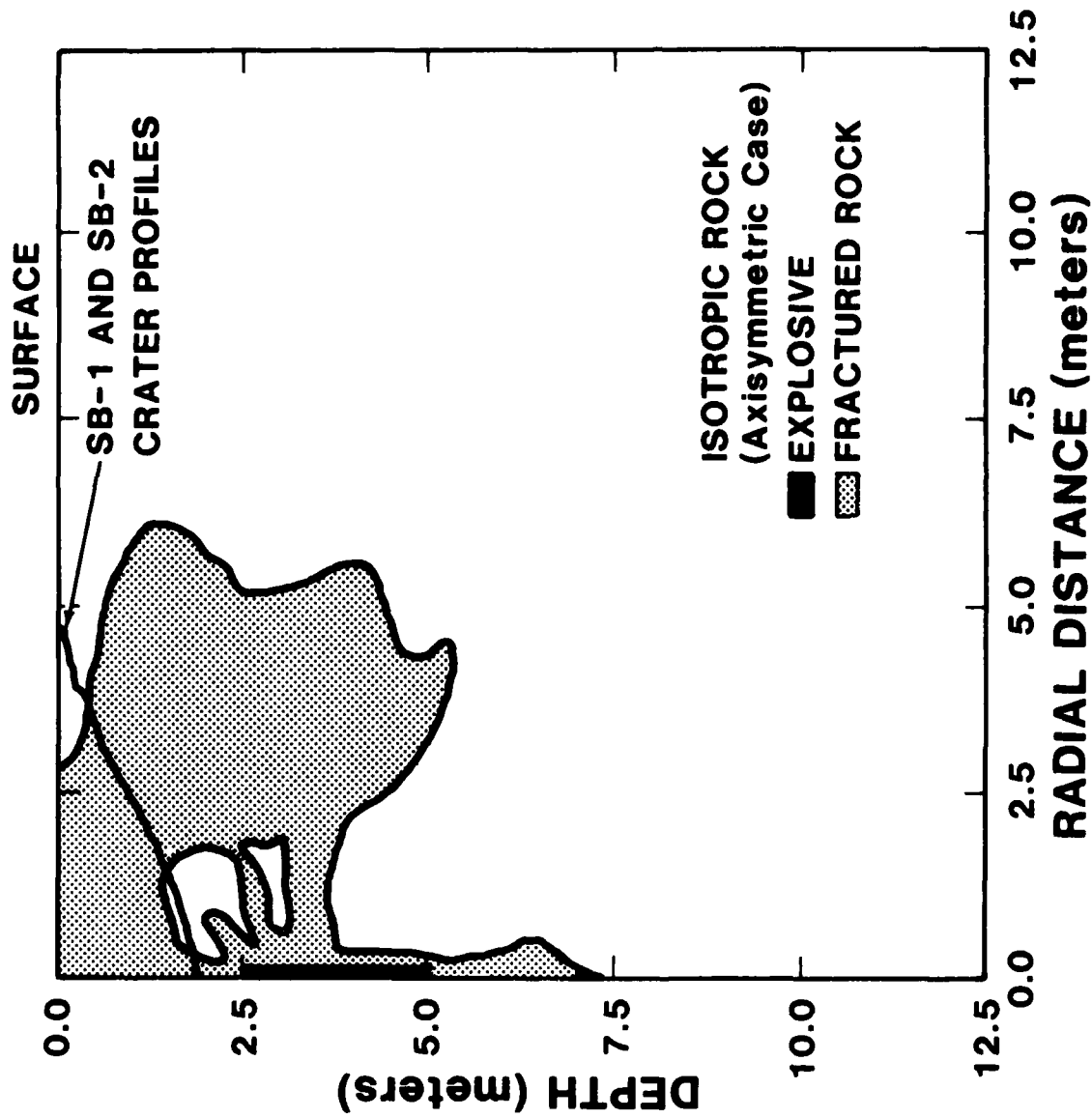
Figure 7.   Volume of Rock with Damage Exceeding 0.2 for the Isotropic Analysis Case

229
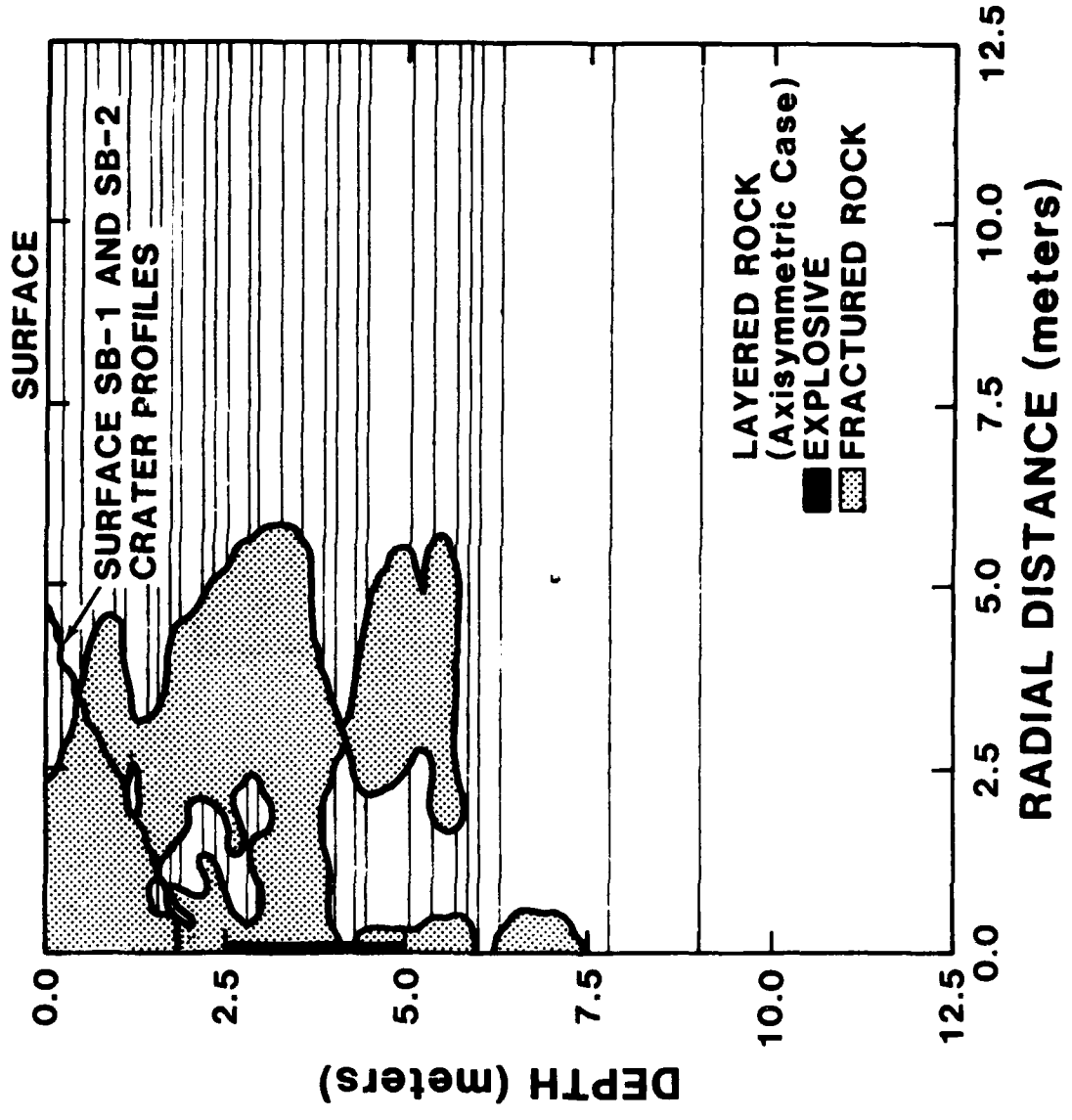
Figure 8. Volume of Rock with Damage Exceeding 0.2 for the Layered Analysis Case
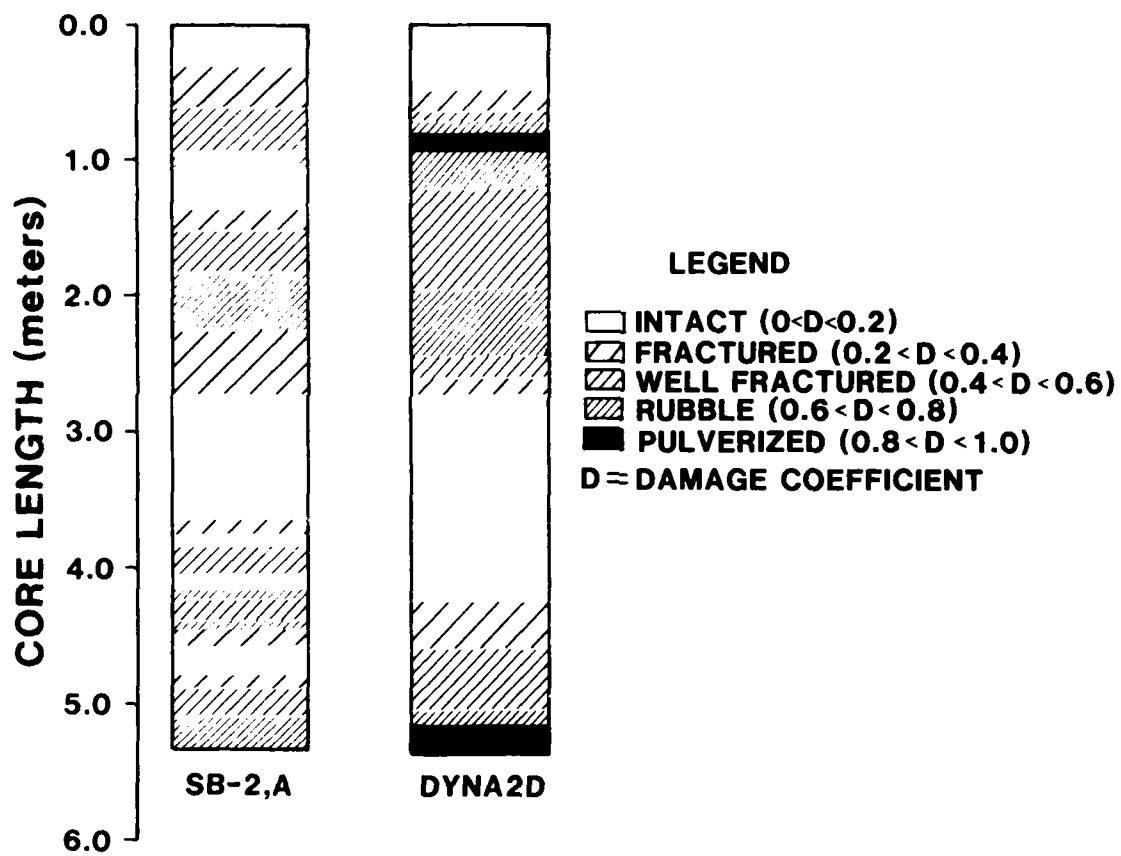
Figure 9.    Comparison of Core Sample with Model Predictions
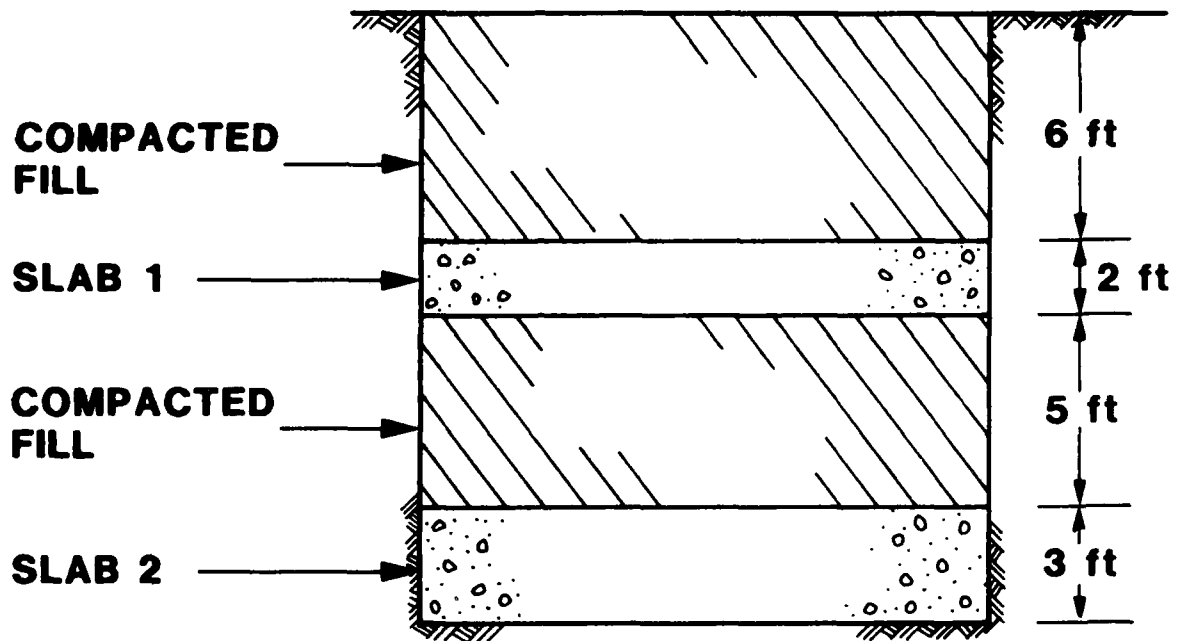
SLAB 1 - 5000 psi CONCRETE WITH 1 PERCENT REINFORCEMENT IN
THE LATERAL DIRECTIONS, #8s AT 7 in. EACH WAY, TOP
AND BOTTOM; GRADE 60.

SLAB 2 - 5000 psi CONCRETE WITH 2 PERCENT REINFORCEMENT IN
ONE LATERAL DIRECTION, #10s AT 7 in. TWO LAYERS
TOP AND BOTTOM; 1/2 PERCENT SHRINKAGE
REINFORCEMENT IN THE OTHER LATERAL DIRECTION, #8s
AT 12 in. TOP AND BOTTOM; AND #5s AT 6 in. EVERY
14 in. SHEAR REINFORCEMENT; GRADE 60.

Figure 10.   Geometry of the Two-Slab, Buried Target
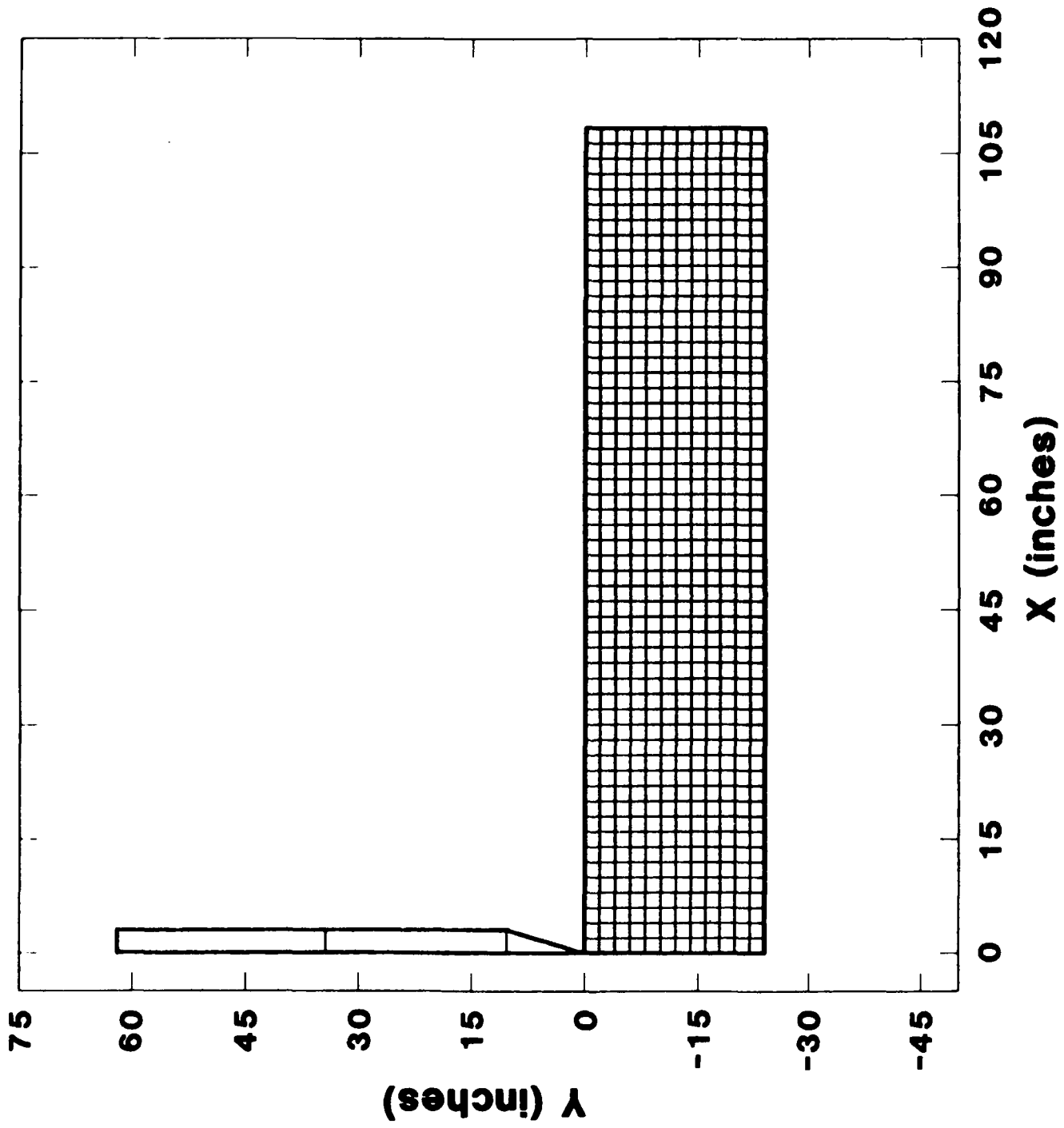
Figure 11. Finite Element Mesh for the Concrete Penetration Problem

233
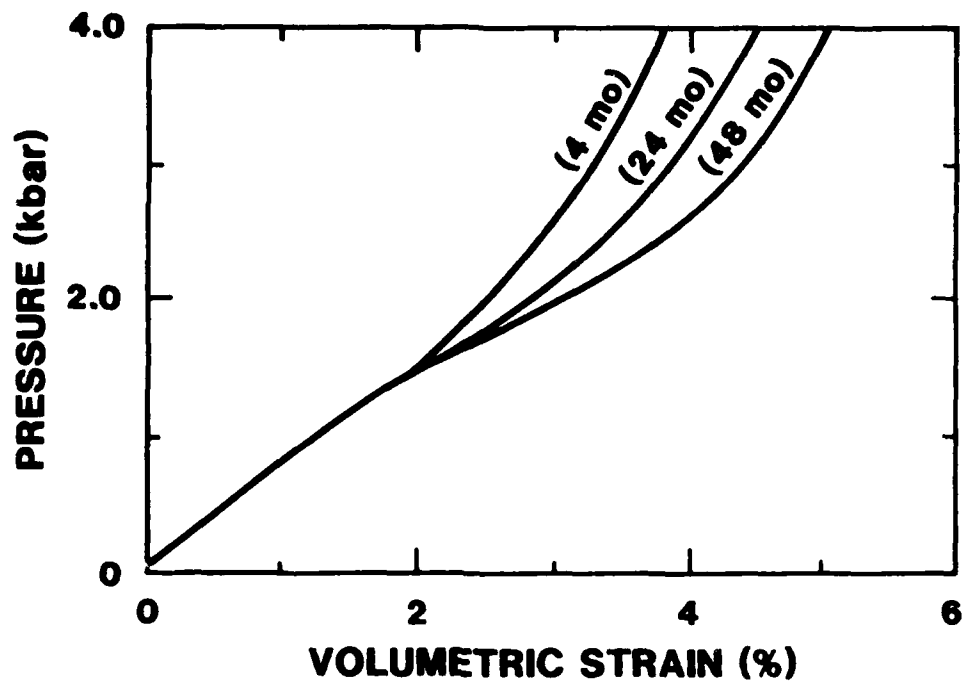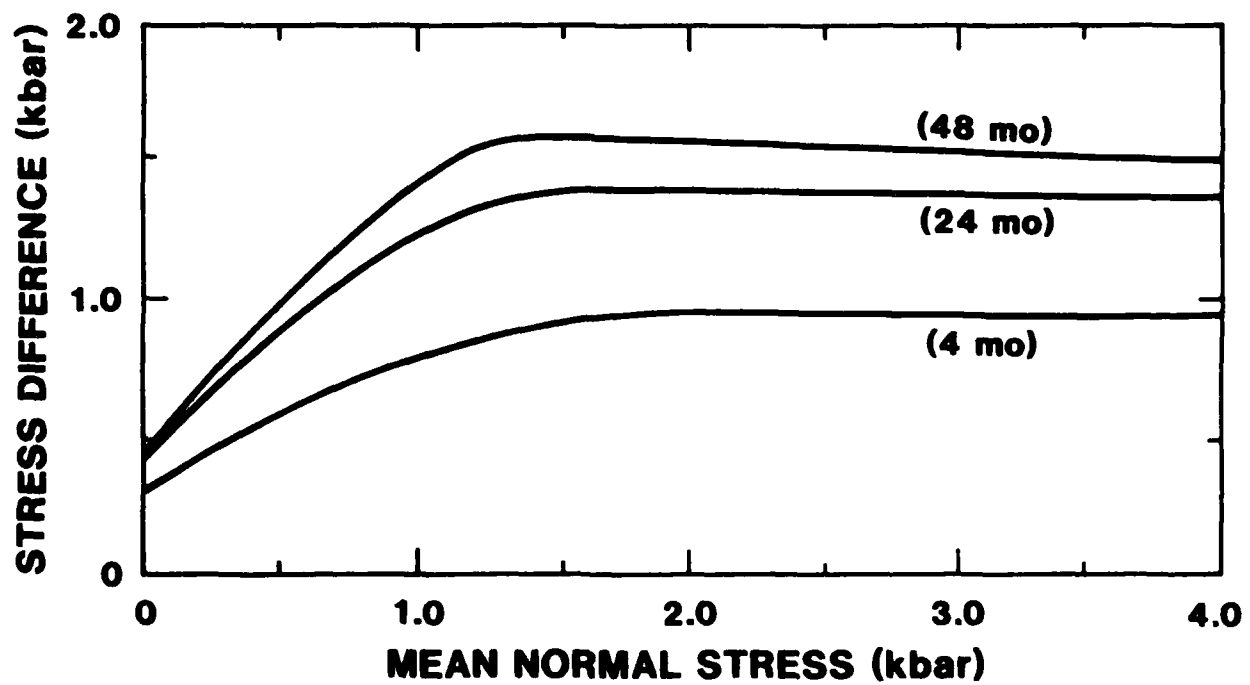
Figure 12.   Triaxial Material Test Data:  (a) Hydrostat; (b) Shear Failure
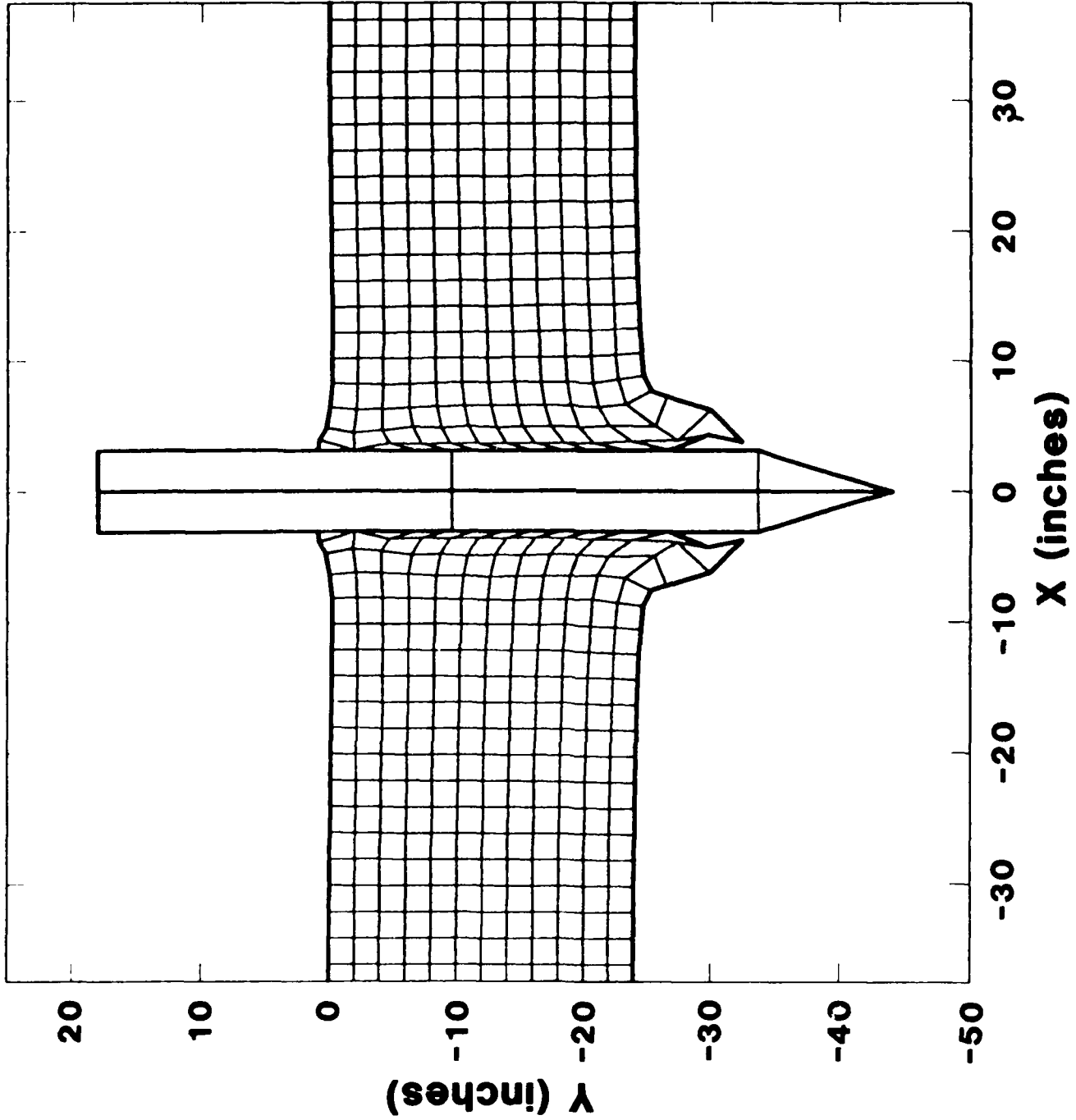
Figure 13. Deformed Mesh Plot of the Concrete Target at 3.0 ms
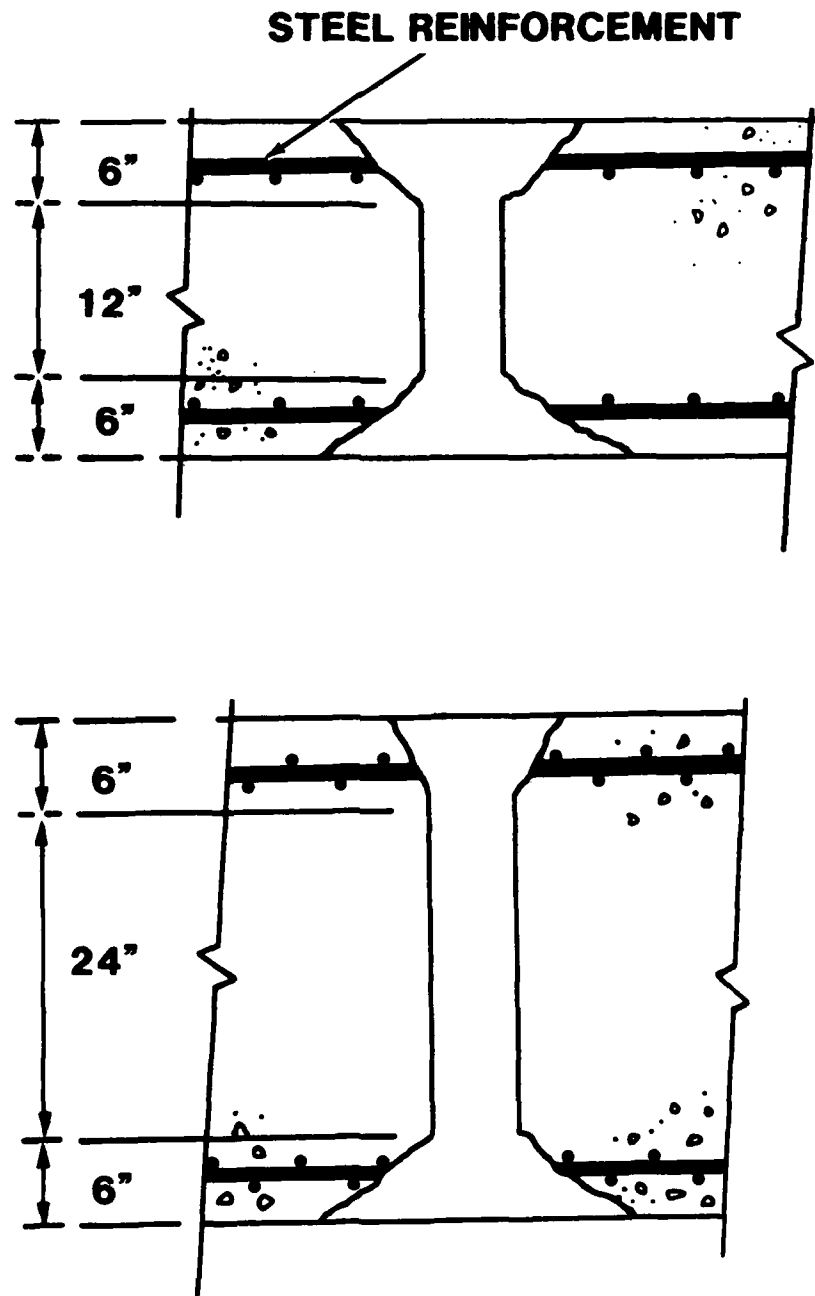
Figure 14. Illustration of Post-Test Concrete Slabs
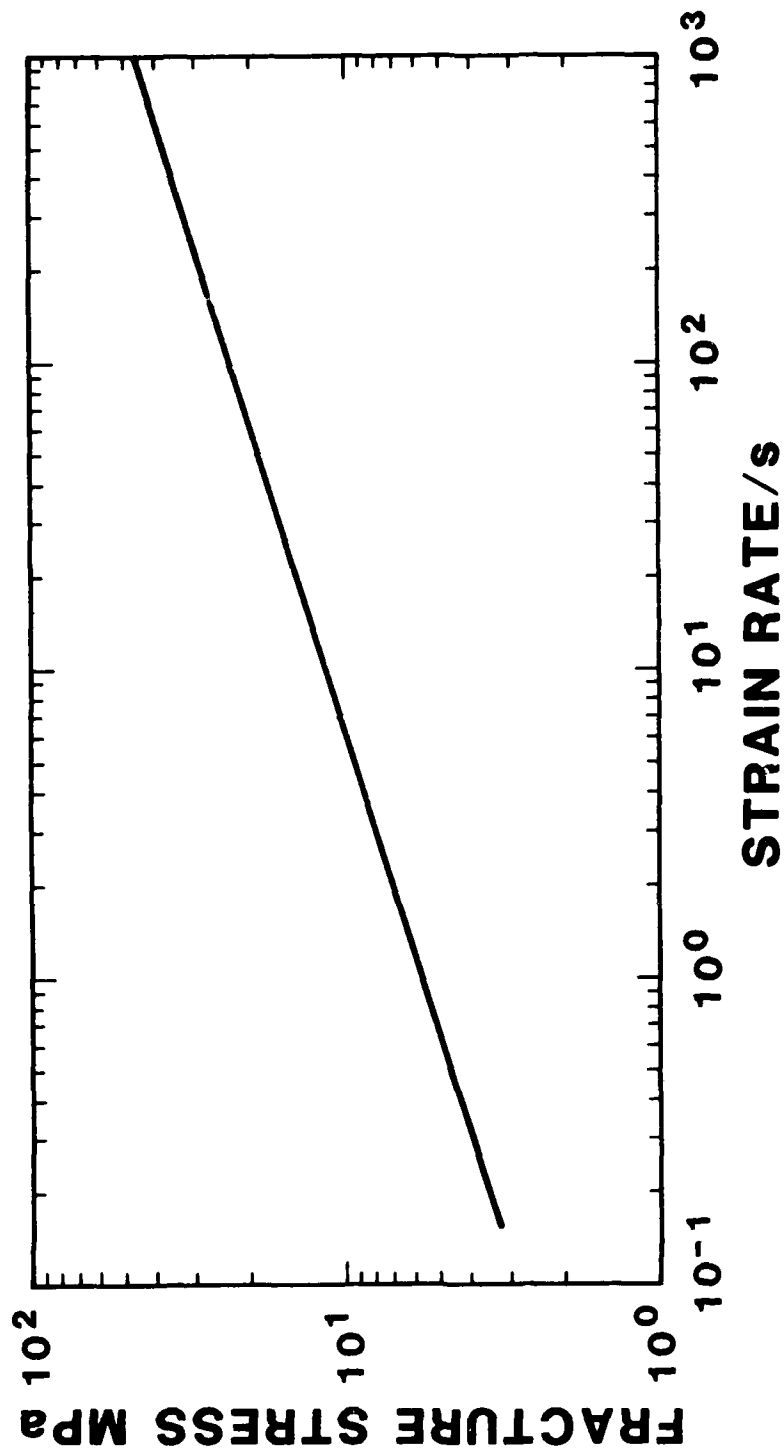
Figure 15.    Estimated Strain Rate Dependent Fracture Stress for Concrete
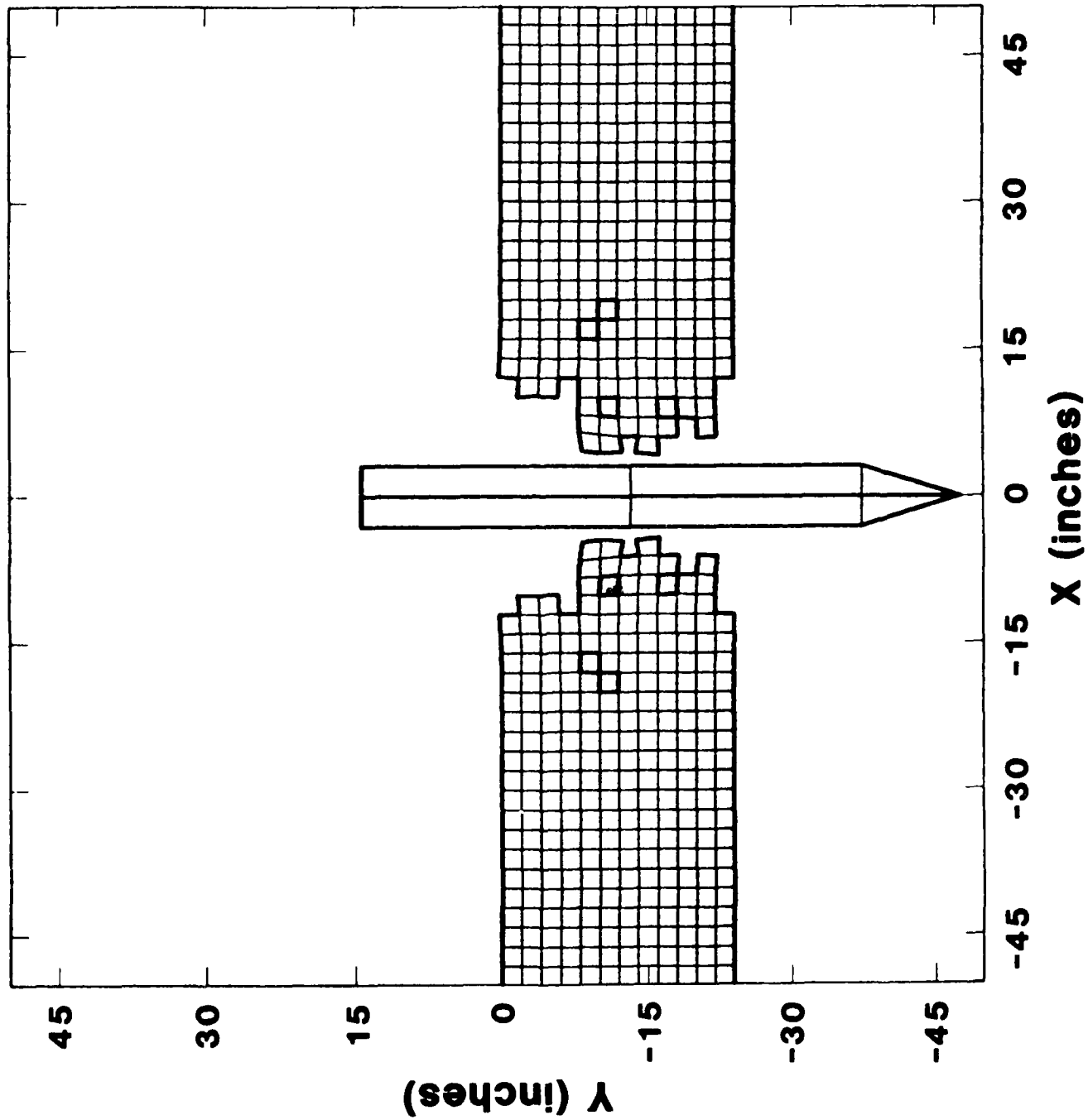
Figure 16. Deformed Mesh Plot of Concrete Target at 3.0 ms Using the Damage Model

238

# A Finite Element Material
# Model for
# Microfracture-Damaged Brittle Rock[1]

## L. S. Costin

Geotechnical Design Division

and

## C. M. Stone

Applied Mechanics Division 1

Sandia National Laboratories
Albuquerque, New Mexico 87185

## ABSTRACT

A continuum damage model based on the mechanics of microcrack growth has been implemented in the finite element code SANCHO. The model incorporates the effects of the nucleation, growth and coalescence of microcracks on the deformation of brittle materials, such as rock, under compressive loading. The material subroutine keeps track of both the magnitude and direction of microcrack growth in each element so that the induced anisotropy due to crack growth in preferred directions and the stress history dependence of microcrack growth are properly taken into account. In addition, the model allows for interaction among neighboring microcracks, which leads to coalescence and subsequent material failure or softening. A damage vector, which is calculated from the crack distribution in each element, is used as an internal variable to compute the effective elastic moduli at each stage of the deformation. The results of several sample calculations using the model are presented and methods for determining the required material parameters are discussed.

# 1 Introduction

The deformation of brittle materials, such as rocks and concrete under relatively low confinement, is accommodated primarily by the nucleation and growth of micro cracks. This deformation mechanism results in several phenomena characteristic of the response of brittle materials to stresses large enough to cause permanent damage. In particular, pressure dependent dilatancy, stress induced anisotropy, hysteresis with discrete memory, the progressive change in the apparent elastic moduli under increasing stress and the gradual softening of the material in the failure regime which eventually results in a localization of deformation along large fractures or shear zones are among the important phenomena that have proven difficult to include in any well developed constitutive theory for inelastic materials, such as classical plasticity.

In recent years there has been a large reported effort directed at developing new theories of non-linear material behavior that account for, in a continuum sense, some of the microstructural mechanisms associated with both brittle and ductile deformation. Continuum damage models, based on the original work of Kachanov [1], fall into this class of material model. Two major difficulties need to be addressed when attempting to formulate a damage model for implementation into a numerical code. First, the microstructural variables that must be recorded and used in the computation of the deformations may require an unduly large amount of storage capacity and manipulation of data. This problem will eventually be overcome by the use of larger and faster computers. The second problem is somewhat more critical to the success of damage models. Many damage models intended to simulate deformation in brittle materials are based on microcrack nucleation and growth, which is essentially a stress driven mechanism. As a result, they contain features that tend to lead to numerical instabilities. For example, corners on the damage (yield) surface, non-normality and strain-softening are common features of these models that are difficult to treat numerically. In addition, numerical codes are often insensitive to, and sometimes suppress, the development of localized deformation, an important failure mode in brittle materials. These problems are particularly acute for brittle materials which are modeled as time-independent, because they are not of a class for which uniqueness and stability of solutions can be proven [2].

In this report, we document the details of the implementation of a specific damage model based on the work of Costin and Holcomb [3-7] into SANCHO, a two-dimensional, large deformation finite element code [8]. Although the model was implemented into a specific finite element code, there is nothing in the model itself or in the methods employed in the numerical implementation of it that would prevent its installation into any other two-dimensional finite element code.

The model incorporates the effects of the nucleation, growth and coalescence of microcracks under compressive loading. In addition, the model allows for interaction among neighboring microcracks which leads to coalescence and subsequent material failure or softening. In order to deal with some of the numerical problems inherent in damaging and softening materials, such as those noted above, some modifications to the code and its solution techniques were required. These will be discussed in some detail. In the next section, the theory and equations on which the model is based are presented. Then, in Section 3, the numerical implementation of the model is discussed and the algorithms for solution of the model equations are presented. Section 4 demonstrates how to derive the model parameters from certain kinds of experimental data and how to estimate the value of some of the parameters in the absence of a complete set of data. Finally, the results of the analyses of some sample problems are presented in Section 5. Because of the complex nature of the model, no analytical solutions exists, even for simple boundary value problems. Therefore, the results obtained from the sample calculations are compared to experimental results. A user's guide for employing the material model in SANCHO is given in **Ref** [29].

# 2    Theory

## 2.1    Basic Definitions

Before proceeding to a discussion of the model equations, a few definitions need to be presented so that the terminology used is clear. First, the measures of stress and strain used in the model need to be defined. Since SANCHO is a finite deformation code, a finite strain measure is required. The microfracture damage model was originally developed under the assumption that the strains were infinitesimal [3]. However, the equations remain valid for the case of finite strains and large rotations, provided a rotationally invariant finite strain measure is used along with its appropriate work-conjugate stress [6]. To do this, the equations are written in terms of the Lagrangian (Green-St.Venant) strain, $E_{\alpha\beta}$, and the second Piola-Kirchhoff stress, $T^{\alpha\beta}$. Thus, the model can be used to describe material response at large strains, provided, of course, that the intact portion of the material being modeled remains linear and elastic. The nonlinear and possibly large strains are assumed to result from the growth and opening of tensile microcracks which are distributed throughout the intact material.

The motion of a body can be described by the equation

$$x^i = \mathbf{x}^i(X^\alpha, t) \tag{1}$$

where the particles of the body are identified by the material coordinates $X^\alpha$ and the points in space that a particle traverses during the motion are identified by the spatial coordinates, $x^i$ (tensors and vectors are denoted by bold-faced Roman letters). The function, $\mathbf{x}^i$, then, describes the motion of the particles, $X^\alpha$, as a function of time, $t$. Only material coordinates that coincide with the spatial coordinates in the reference configuration, $(t = 0)$, are considered, thus, $\mathbf{x}^i(X^\alpha,0) \equiv X^\alpha$.

The basic measures of deformation computed by SANCHO [8] during the solution process are the deformation gradient, $F_\alpha^k$, and the stretching rate, $d_{ij}$. The deformation gradient is defined as

$$F_\alpha^k \equiv \frac{\partial \mathbf{x}^k}{\partial X^\alpha} \tag{2}$$

and the stretching is given by

$$d_{ij} = \frac{1}{2}(v_{i,j} + v_{j,i}) \tag{3}$$

where the velocity is defined as

$$v^i(X^\alpha,t) \equiv \frac{\partial \mathbf{x}^i(X^\alpha,t)}{\partial t}. \tag{4}$$

The strain can be defined in terms of the deformation gradient

$$E_{\alpha\beta} = \frac{1}{2}(F_\alpha^k F_\beta^m g_{km} - G_{\alpha\beta}) \tag{5}$$

where the quantities $g_{km}$ and $G_{\alpha\beta}$ are the metric tensors in the spatial coordinates and the coordinates of the reference configuration, respectively. Similarly, the strain rate can be computed in terms of the deformation gradient and the stretching

$$\dot{E}_{\alpha\beta} = F_\alpha^k d_{km} F_\beta^m. \tag{6}$$

In SANCHO, the equations of motion are solved in terms of the Cauchy stress, $t^{km}$. Therefore, the second Piola-Kirchhoff stress computed in the constitutive subroutine must be converted to Cauchy stress using the following transformation

$$t^{km} = J F_\alpha^k T^{\alpha\beta} F_\beta^m \tag{7}$$

where $J = |\mathbf{F}|^{-1}$. In addition, the stress and strain tensors are usually separated into hydrostatic and deviatoric components. The deviatoric stress is defined as

$$T'^{\alpha\beta} = T^{\alpha\beta} - \frac{1}{3}T_\epsilon^\epsilon G^{\alpha\beta} \tag{8}$$

where $\frac{1}{3}T_\epsilon^\epsilon$ is the hydrostatic stress. Similar definitions apply to the deviatoric and hydrostatic components of the strain and strain rate tensors.

242

## 2.2 Model Equations

### 2.2.1 Stress Intensity Factor

A plane crack can be described adequately by specifying its size and orientation. In the model, it is assumed that all microcracks are preexisting penny-shaped features which can be described by the radius of the cracked surface, $a$, and a unit vector normal to the crack surface, $n$, as shown in Figure 1. A crack vector can then be defined as

$$\mathbf{a} = a\mathbf{n}. \tag{9}$$

In a polycrystalline medium like rock, compressive loads can generate local tensile stresses in the neighborhood of a microcrack. These local stresses generally arise from material property mismatches between grains or from contact stresses between grains with irregular grain boundaries [9,10]. The tensile stress due to deviatoric loading acting on any given crack is assumed to be proportional to the component of the deviatoric stress which is normal to the crack surface (Figure 1). Thus, the local tensile stress, $T_{\mathcal{L}}$, acting on $\mathbf{a}$ is given by

$$T_{\mathcal{L}} = \mathcal{F}(\mathbf{a}, \mathbf{n}, d, d_1) \, \mathbf{n}^T \cdot \mathbf{T}' \cdot \mathbf{n} \tag{10}$$

where $\mathbf{T}'$ is the applied deviatoric stress and $\mathcal{F}$ is a function of proportionality between the local tensile stress and the applied deviatoric stress and is, in general, a function of the crack size and orientation as well as two microstructural lengths. The distance $d$ is the nominal size of the local tensile region and $d_1$ is the initial average distance between neighboring cracks, thus, $d_1 \geq d$. Because the local tensile field is limited to perhaps a few grain diameters, crack growth causes the driving stress to be relieved as the crack propagates through the region. This effect is approximated by making $T_{\mathcal{L}}$ a function of $(d/a)$. A specific functional form of $\mathcal{F}$ will be derived later.

There is also a compressive stress acting on the crack due to the hydrostatic component of the applied stress (compressive stresses are taken to be negative). Thus, the total driving stress acting on any given crack can be expressed as the sum of the hydrostatic, $tr\mathbf{T}/3$, and the local tensile (deviatoric) components, $T_{\mathcal{L}}$, of the applied stress (Figure 1).

To formulate a crack growth criterion, a fracture mechanics approach is taken where the stress intensity at the crack tip, $K_I$, is used as a parameter that describes the state of stress at the crack tip. When $K_I$ reaches a critical value, $K_{Ic}$, the crack extends until $K_I \leq K_{Ic}$. For modeling purposes, the microcracks are assumed to be penny-shaped.

Considering a single crack, with orientation n, the elastic stress intensity factor may be approximated by

$$K_I = \frac{2}{\pi}\sqrt{\pi \mathbf{a} \cdot \mathbf{n}}\left[\frac{tr\mathbf{T}}{3} + \mathcal{F}(\mathbf{a},\mathbf{n},d,d_1)\,\mathbf{n}^T \cdot \mathbf{T'} \cdot \mathbf{n}\right]. \qquad (11)$$

Note that the two terms in equation (11) represent, respectively, the contributions of the hydrostatic and deviatoric components of the applied stress. The dot product, $\mathbf{a} \cdot \mathbf{n}$, is used in equation (11) to emphasize the notion that the stress intensity factor is calculated for a microcrack of size $a$ and orientation $n$.

## 2.2.2 Microcrack Interaction

As microcracks nucleate and grow during the deformation history, the separation distance between adjacent cracks becomes small enough that some interaction between the stress fields at the crack tips is inevitable. To include this interaction effect, we need to consider how the crack-tip stress intensity factor is affected by the stress fields of neighboring cracks. To do this, we first consider a collinear array of planar cracks (Figure 2). One solution to this problem, obtained by using a Laurent series expansion, is given by Isida [11]. A more recent solution, employing a "pseudo-traction" method, is given by Horii and Nemat-Nasser [12] and is shown in Figure 2. Since the solution was obtained by a numerical method, an approximate analytic form was derived. This is also shown in Figure 2. The basic result of this analysis is that, as cracks become more closely spaced, the stress intensity factor is amplified, resulting in crack growth at lower applied stresses. This effect is also present in arrays of non-collinear cracks but to a somewhat lesser degree [11]. Since collinear interaction is the most severe case, it represents a bound on the interaction effect of arrays of cracks (Figure 3). Unfortunately, no similar solution exists for the interaction of penny-shaped cracks. However, it can be assumed that the form of the solution for penny cracks will be approximately the same as that for planar cracks if we replace the planar crack length (Figure 2) with the penny crack radius. The additional factors arising from the differences in crack geometry between the two situations can be lumped into the scaling constant, $f$, which is defined below.

Combining the analytic approximation to the collinear crack solution given in Figure 2 with a term, $(d/a)$, which accounts for the effect of crack growth on the local driving stress, the proportionality function in equation (11) can be written as

$$\mathcal{F} \cdot f\left[\left(\frac{d}{\mathbf{a}\cdot\mathbf{n}}\right)\frac{1}{\left[1 - \left(\frac{\mathbf{a}\,\mathbf{n}}{d_1}\right)^2\right]^{\frac{1}{2}}}\right] \qquad (12)$$

where $f$ is a scaling constant that can be determined from experimental data. The term. $(d/a)$ is included to approximate the effect of crack growth on the local driving stress. Because the local tensile field is limited to a few grain diameters, crack growth causes the local stress to be relieved approximately in proportion to the ratio of $d/a$.

Figure 3 shows the effect of both local stress and crack interaction on the stress intensity factor (through the function $\mathcal{F}$) for the case of uniaxial compression with $d = d_1$. For small $a/d_1$, crack growth is stable because crack growth results in a decrease in driving force. As cracks grow closer together, the interaction effect becomes stronger and eventually unstable crack growth occurs just beyond the minimum point in Figure 3.

### 2.2.3 Damage Surfaces

In order to obtain a continuum description of microcrack damage, it is assumed that an ensemble of cracks contained in some region of the body behaves in a manner similar to an individual crack (accounting only for near-neighbor interactions). That is, the equation describing the response of an ensemble of cracks is assumed to be identical in form to that describing the response of a single crack (equation (11)) except that now a represents a measure of the mean size and density of cracks with normal n. The other parameters may also be thought of as average values associated with the continuum response.

When the applied loads reach a sufficient magnitude, the stress intensity factor associated with the most favorably oriented cracks reaches the critical value and these cracks begin to grow. This is the point where damage begins to accumulate. Letting $K_I = K_{Ic}$ in equation (11) and rearranging the terms results in the following expression

$$Y = \mathbf{n}^T \cdot \mathbf{T}' \cdot \mathbf{n} - \frac{tr\mathbf{T}}{3\mathcal{F}} \cdot \left[ \frac{\pi K_{Ic}}{2\mathcal{F}\sqrt{\pi \mathbf{a} \cdot \mathbf{n}}} \right] = 0. \tag{13}$$

For each direction. n. at a point in the material, $Y = 0$ (equation (13)) represents a surface in stress space. If the stress state is below this surface, the cracks with normals. n. are not growing. If the stress state is on the damage surface, then further loading will cause the cracks to grow. Thus, a will increase in such a way as to maintain $Y = 0$, provided, of course, that crack growth is in the stable region (Figure 3). The damage surface represented by $Y = 0$. then, behaves in a manner similar to a yield surface in the theory of plasticity. As damage accumulates, the damage surface moves outward. Thus, any unloading will put the stress state below the current damage surface and no further cracking can occur until the material is reloaded to a stress state on the current damage surface.

a constant state of incipient cracking. The surfaces of constant damage determined from the experiment were, within experimental error, straight lines as predicted by the model. In addition, when two successive surfaces were determined for the same sample, the second surface apparently had a steeper slope than the initial one, again in agreement with the model. Thus, Holcomb's experiments at least qualitatively confirm the existence of surfaces in stress space of constant damage. Recently, the existence of damage surfaces resulting from more complex loading histories which include the rotation of the stresses relative to the material have been confirmed by Holcomb and Costin [16].

## 2.2.4 Damage Parameter

The state of cracking at each point in a brittle rock can be specified by a crack function, $a(\theta, \phi)$, where $a$ is a function of the spherical angles $(\theta, \phi)$. Thus, for any spatial direction $(\theta, \phi)$, $a(\theta, \phi)$ represents the extent of crack growth that has taken place on cracks lying normal to that direction. The function $a$ can be computed uniquely from equation (13) at each stage of the deformation, provided that the crack growth is in the stable region (Figure 3). However, this function is not very useful as an internal state variable in a constitutive equation because it is not invariant with respect to the chosen coordinate system. It is desirable to define the crack damage such that it is invariant and represents some average measure of the state of cracking. Therefore we let the damage be the vector defined by

$$D_i = \frac{1}{a_o} \int_\Omega \mathbf{e}_i \cdot (\mathbf{a} - \mathbf{a}_o) H[K_I(\mathbf{n})]_i d\Omega \tag{14}$$

where $\mathbf{e}_i$ is a unit vector in the $i^{th}$ coordinate direction and $\Omega$ implies integration over the upper unit hemisphere. For convenience, $D$ is defined such that in the initial state, $D - 0$. The function $\mathbf{a}_o = a_o \mathbf{n}$ is the initial distribution of crack lengths. Any initial distribution of cracks can be defined as a reference virgin state. The function $H[K_I(\mathbf{n})]$ is defined by

$$H[K_I(\mathbf{n})] = \begin{Bmatrix} 1 \\ 0 \end{Bmatrix} \quad if \quad \begin{Bmatrix} K_I > 0 \\ K_I \leq 0 \end{Bmatrix}. \tag{15}$$

Thus, $D$ is defined so that only those cracks that are currently under deviatoric tension and participating in the damage process are accounted for. This is important when stress histories that include rotation of the principal directions relative to the material are being considered [5,16].

246

It is easiest to illustrate the utility of the damage surface concept by using the example of axisymmetric loading such as occurs in uniaxial or triaxial tests on rock. In this case, $T_{11} = T_{22} = -p$ and $T_{33} = -\sigma$ with $\sigma \geq p$. Figure 4 shows the results of a series of triaxial compression tests on Westerly granite reported by Brace et al. [10]. The data shown in the figure are the stress states at which yield occurred during tests performed at several different constant confining pressures, $p$. Yield was defined as the point where the volume strain first departed from the linear elastic curve (onset of dilatancy). Since the increase in volume strain is closely related to the growth of microcracks, Brace's yield point roughly corresponds to the point where crack growth begins in the most favorable direction. The data in Figure 4 are given in terms of the principal tensile (positive) deviatoric stress $T'_{11}$ versus the mean stress $-T_{kk}/3$. The reason for this is that for the chosen axes, the damage surface, equation (13), predicted by the model would be a straight line with a slope of $1/\mathcal{F}$, and an intercept of $\left[\frac{\pi K_L}{2\mathcal{F}\sqrt{\pi a}\,n}\right]$. As shown in Figure 4, the data are well represented by a straight line. The slope and intercept of a least-squares-fit line through such triaxial data can be used to determine material parameters such as $f$ and $d$. This will be discussed in more detail in Section 4.

More recent advances in rock mechanics testing has made it possible to determine more accurately the threshold of damage and to map damage surfaces in stress space without relying on the initiation of dilatancy, which is a rather crude measure of damage initiation. Newer techniques employ acoustic emission technology (AE) to detect crack growth by the sonic emissions radiated from growing cracks. Holcomb [13] has performed a series of experiments in which acoustic emissions were used to detect the initiation of microcrack growth and map the damage surfaces for triaxial stress paths. In these experiments, a sample of Westerly granite was first loaded hydrostatically to 5 MPa. Then the sample was loaded axially at constant lateral stress to an arbitrary stress somewhat less than the failure stress. This established a damage state in the sample as evidenced by the large number of acoustic emissions recorded during the initial loading. On unloading, no further acoustic emissions were recorded and none were recorded on reloading until the previous peak stress was reached, at which time the emission rate increased significantly. Thus, apparently no further damage occurred during unloading or reloading until the previous maximum stress was reached. This memory of the previous maximum stress is often referred to as the Kaiser effect [14] and has been demonstrated previously on other rocks [15]. The novel portion of Holcomb's experiment was that he then increased the confining pressure and reloaded until the rate of acoustic emissions began suddenly to increase rapidly, indicating that crack growth was again beginning to occur. By successively increasing the confining pressure and then loading axially (see Figure 5) until the acoustic emission marker was again reached, Holcomb was able to trace out a surface in stress space that corresponds to

247

model calculations of triaxial compression at different confining pressures using material parameters for Westerly granite (see Section 4). The portions of the curves beyond the peak stress in Figure 6 were computed by allowing the material to deform in a stable manner. Once the peak stress is achieved, crack growth would be unstable if more load were applied. Thus, in order to maintain stability, the stress is reduced by the amount required to arrest the crack growth. For the next load increment, the stress increases according to the programed stress path, resulting in re-initiation of the cracks, causing more unloading to occur in order to arrest them. In some sense, this is a stable unloading curve; however, the damage continues to increase because the cracks grow during every iteration. This type of unloading path has been duplicated in laboratory experiments by Wawersik and Fairhurst [18]. They found that in very brittle rocks such as basalt, unloading had to occur much faster than would be the case in an infinitely stiff loading. That is, energy had to be extracted from the specimen in order to keep the deformation stable in the post-peak regime. The model calculations shown in Figure 4 seem to indicate a similar response. Of course, some rocks, such as Indiana limestone [18], show increasing strain on the post-failure portion of the curve. Thus, in a stiff loading machine, such a material would remain stable past the peak stress, whereas, basalt would not. This type of response could be achieved by the model either by increasing the effect of damage on the elasticity of the material (increasing $C_1$ and $C_2$ in equation (18)) or by assuming that the majority of interactions are between non-collinear cracks (Figure 3).

Since the ratio $a/d_1$ determines the point of instability, the parameter, $d_1$, can be determined directly from the uniaxial compression strength of the material. Determination of model parameters is discussed in more detail in Section 4.

# 3   Numerical Implementation

The microcrack-damage model was implemented in the form of a material model subroutine in the finite element code SANCHO [8]. SANCHO is a special purpose code designed to compute the quasi-static, large deformation, inelastic response of planar or axisymmetric solids. A constant bulk strain, bilinear displacement isoparametric element is used for the spatial discretization. A self-adaptive dynamic relaxation scheme based on explicit central difference pseudo-time integration and artificial damping is used to generate the series of equilibrium solutions.

At each solution step in the calculation, the program estimates the strain state for the next solution step based on the previous converged solution and current boundary conditions. The deformation gradient is the primary information provided to the mate-

## 2.2.5 Constitutive Equation

The final part of the model is the constitutive equation that relates the strains to the imposed stresses and the state of damage. Because we are concerned only with situations in which the matrix material remains linearly elastic, we assume that the strains can be derived from an energy function in a manner similar to that described by Krajcinovic and Fonseka [17]. For example, the Gibbs energy potential, $\mathcal{G}$, can be assumed to be a quadratic function of the stresses and have a quadratic dependence on the damage as well. The strains are then given by

$$\mathbf{E} = \frac{\partial \mathcal{G}}{\partial \mathbf{T}} \tag{16}$$

which, for small strains, results in

$$\epsilon_{ij} = S_{ijkl}\sigma_{kl}. \tag{17}$$

The compliance matrix is given by

$$S_{ijkl} = \frac{1 + \nu}{E}\delta_{ik}\delta_{jl} - \frac{\nu}{E}\delta_{ij}\delta_{kl} + C_1(\delta_{ij})(D_iD_l\delta_{jk} + D_jD_k\delta_{il}) - C_2(\delta_{ij})(D_iD_j\delta_{kl}) \tag{18}$$

where $E$ and $\nu$ are the elastic constants of the virgin material and $C_1$ and $C_2$ are additional constants that account for the effect of crack damage on the deformation. The constant, $C_1$, determines the reduction in stiffness perpendicular to the damage vector (parallel to the major direction of crack growth), whereas, $C_2$ determines the additional volume strain (Poisson expansion) that results from crack opening. Note that because only mode I crack opening is assumed, the cracks do not affect the shear compliance. Thus, $C_1(\delta_{ij}) = C_2(\delta_{ij}) = 0$ for $i \neq j$. For purposes of implementation of the model into a large deformation code, we assume that the equations remain valid for large deformations, thus, we write equation (17) as

$$E_{\alpha\beta} = S_{\alpha\beta\gamma\delta}T^{\gamma\delta}. \tag{19}$$

## 2.2.6 Failure Criterion

In the model, failure of the material is assumed to occur when stable crack growth is no longer possible. This occurs when crack interaction becomes the dominant driving force for crack growth and the crack-tip stress intensity factor increases with increasing crack length, under constant stress (Figure 3). Thus, when any microcrack in any direction at a material point exceeds the critical value (critical $a/d_1$ ratio), the only way to maintain stability of the material is to unload. Figure 6 shows the results of

rial subroutine. The material subroutine then calculates the corresponding stress and damage states. Finally, dynamic relaxation is invoked to obtain a static equilibrium solution. Each iteration of this procedure leads to a new trial strain state and trial stress state that converge to a global static equilibrium solution after a few iterations. Convergence of the iterative procedure is assumed to occur when an internal measure of the global force imbalance is less than a user prescribed value.

## 3.1  Material Subroutine

The material subroutine first calculates the strain from the supplied deformation gradient (equation (5)). Then, the stresses resulting from those strains and the current state of damage are calculated using the inverse of equation (19). Equation (19) was inverted analytically by Gaussian elimination before being written into the subroutine so that no time consuming matrix manipulation is necessary. After the stresses are computed, the damage equation (equation (11)) is used to determine whether the stress state is above or below the damage surface (i.e. whether microcracks will grow, $K_I >$ $K_{Ic}$, or not, $K_I \leq K_{Ic}$). Since this equation is a function of the orientation of the crack, the crack function, a, is discretized into thirteen spatial directions (every $15°$ in-plane and one in the out-of-plane or hoop direction) covering the hemisphere over which the damage (equation (14)) will be integrated (see Figure 7). Thus, equation (11) is used thirteen times for each iteration within the subroutine to compute the damage surface associated with each possible crack orientation. If the stress state is outside the damage surface in one or more directions, the crack length in that direction is incremented by a given amount, $\Delta a$. The damage is then computed from equation (14). But altering the damage changes the stresses computed from the given strain state so, an iterative process within the material subroutine must be used to find the unique stress-damage solution. A schematic diagram of this process is shown in Figure 8. It should be noted here that iteration and convergence of the stress-damage solution is independent of the overall program solution and the global convergence criterion. The amount of crack growth allowed on each subiteration of the solution process, $\Delta a$, is determined by the user and should be chosen so that the solution can be obtained rapidly without any substantial over-shoot. As shown in Figure 8, for each increment of crack growth, the damage surface moves outward, whereas, the stress state relaxes back toward the damage surface. Thus, convergence of the solution is guaranteed as long as the crack growth remains in the stable region.

A unique solution of the stress-damage equations is also guaranteed if the damage state is such that an increment of crack length in a given direction is stable. That is, the material is on the rising portion of the stress-strain curve and the stress intensity

factor decreases with increasing crack length. If crack growth becomes unstable ($K_I$ increases with increasing crack length), the crack is allowed to grow to a limiting value and the element is identified as being in failure. Once an element has failed, its load carrying capacity (stiffness) is reduced progressively to zero. This is done over several solution steps rather than all at once in order to promote more rapid convergence of the code at each new equilibrium solution.

The damage is calculated by integrating equation(14) which has been simplified to account for the two-dimensional geometry. The in-plane components of the damage can be determined by integration through an angle of $\phi = 0$ to $\pi$, where $\phi$ is measured clockwise from the vertical z-axis. Since the crack function is discretized into twelve in-plane directions, each spanning an arc of 15°, the integration of equation (14) is over $d\Omega = d\phi = \pi/12$. In the subroutine, the out-of-plane component of the crack function is stored in the variable $a(1)$, whereas, the in-plane components are stored in $a(2)$ through $a(13)$. Thus, the R and Z components of the damage vector are given by

$$D(R, Z) \quad \sum_{i=2}^{13} \frac{(a(i) \quad a_o(i))}{a_o(i)} H(i)(\sin(\phi(i)), \cos(\phi(i)))d\phi \tag{20}$$

where $H(i)$ is the discrete function, given by equation (15), evaluated for each of the crack directions. $a(i)$, which are oriented at angles $\phi(i)$. The hoop or out-of-plane component of the damage is evaluated by giving the one crack direction that contributes to it a weighting equal to one in-plane crack direction, ie. $\pi/12$. Thus, $D(\theta)$ is given by

$$D(\theta) \quad \frac{(a(1) \quad a_o(1))}{a_o(1)} H(1)d\phi. \tag{21}$$

## 3.2 Solution Control

When the damage is low or moderate, the resulting increments in damage do not drastically affect the stresses; but, solving the stress-damage equations can be time consuming. In addition, when the stress state is near the point where failure of an element is beginning, small changes in the trial strain states may cause the element to fail during one iteration and then, because the stress was transferred to other neighboring elements, the element may jump back into the stable regime during the next trial iteration. This drastic shifting of the damage state from stable to unstable and back to stable as the solution process iterates can cause problems in obtaining a converged equilibrium solution. Thus, some additional control options were added to SANCHO to enhance the rate of convergence. First, the solution sequence was altered so that, at each load step, a converged solution is first obtained by keeping the damage fixed

251

at the value it had at the previous step. Because the damage is fixed, this amounts to obtaining an elastic solution with constant (but degraded) moduli, which can be done quite rapidly. Once the elastic solution is found, a flag is set activating the complete stress-damage solution and the program iterates until a new global solution, with the updated damage state, is found. When the damage is low or moderate, the increment of damage added during the current step does not alter the elastic moduli very much. Thus, since the solution with the full damage model is starting from a converged elastic solution with only slightly different moduli, convergence to the new damage solution is very rapid. This two step solution process reduces the computational time significantly over the time required to obtain the solution with the full stress-damage routine invoked from the beginning.

When elements are in, or near, the failure regime, where unstable crack growth can occur, a second solution strategy can be employed that both enhances the stability of the solution process and decreases the computation time. This is achieved at the expense of some accuracy in the equilibrium solution. This technique uses the two step process described above except that once the elastic solution is found, only one additional iteration is allowed with the stress-damage routine invoked. This amounts to computing an equilibrium stress state, then using that state to compute the new state of damage, but no further iterating is done. Thus, the solution is one of static equilibrium where the damage is compatible with the stress state but not with the strain state, i.e. equation (13) may be satisfied but not equation (19). However, the error does not appear to be very great, as will be demonstrated later. This method has the great advantage that equilibrium solutions are always sought under conditions of constant damage, which greatly eases problems associated with reliability of the global solution algorithm, especially in regions where elements are failing.

## 3.3 Post-Failure Decay

During the calculation of the crack vector, a, each crack direction at every Gauss point is checked. If a solution to equation (13) cannot be found, then the applied stresses and the crack size are such that the crack is unstable ($K_I$ increases with increasing $a$). When this occurs, the crack length in that direction is set to a fixed maximum length which is equal to $d_1$, the distance between neighboring cracks. Thus, it is assumed that unstable crack growth occurs, causing the crack to link up with its nearest neighbors. At this point, the material is presumed to have failed and its load carrying capacity is systematically reduced. This is done through a user specified "decay" parameter. When the material at an integration point has been identified as having failed, the stresses are computed using the current damage (including cracks that have been set

252

to the maximum length because of instabilities). Then, these stresses are multiplied by the decay parameter, which is a positive number less than one. This has the effect of isotropically reducing the stiffness of the material at that point. After each step, the decay parameter is updated by multiplying it by itself. For example, if the decay at a failing point is 0.9 at step $n$, it will be 0.81 at step $n+1$ and 0.73 at step $n+2$ and so on. Thus, when crack growth at a point is severe enough to cause local failure, the material is softened over the succeeding steps. Currently, only isotropic softening is implemented in the model; however, other more realistic schemes are being investigated.

## 3.4 Random Initial Crack Lengths

Under most circumstances, it is usually assumed that the initial microcrack length, $a_o$, is the same for all directions at all points in the material. In practice, however, this initial length will probably vary randomly from point to point and direction to direction. There is nothing in the model which precludes the use of a random variation to describe the initial microcracked state. An attempt has been made to allow the user to generate a randomly varying initial crack length for the material.

Defining an initial random microcracked state is done by assigning each element integration point an initial crack length for each of the thirteen crack directions. The random variation is generated in a pre-processing program that writes a file which is read by the analysis program. A different crack length (randomly varied) is written for each of the thirteen damage integration directions at each element integration point. The analysis program stores these initial crack lengths which, of course, results in increased program storage.

The pre-processing program generates the distribution of crack lengths in the following way. First, a random number generator is used to generate thirteen sets of numbers between 0 and 1 that are uniformly distributed. One set of numbers is generated for each crack direction. The number of random values in each set is equal to four times the number of elements associated with the damage model, since SANCHO uses four Gauss points per element. This initial randomizing process is done to ensure that cracks of a given length and orientation will be scattered randomly through the mesh. Thus, the thirteen crack lengths at each Gauss point will be different. Next, a mathematical distribution, which represents the physical crack length data, is used to generate the function that maps the random number associated with each crack direction, $i$, and Gauss point, $j$, into a set of crack lengths, $A_i^j$. The mapping function used for this process is derived from the inverse cumulative distribution function ($\text{CDF}^{-1}$) for the selected mathematical distribution. An average crack length for each integration direction is then computed by summing the individual crack lengths and dividing

by the total number of points. This computed length is then scaled by a normalizing length provided by the analyst and a scale factor is computed. Each individual crack length is then multiplied by this scale factor to get the final crack length. The analyst supplied crack length is necessary to scale the distributed crack lengths so that the initial crack lengths, averaged over the structure, will represent some reasonable value for the material.

Several standard mathematical distributions can be used as the second distribution used to generate the sets of microcrack lengths for each crack direction. These include the normal, lognormal, Weibull and the $S_B$ distributions. Each distribution type is best suited to a certain class of random variables. Since the exact distribution of the microcrack lengths is unknown, a mathematical description that provides a general modeling capability was employed. The $S_B$ distribution provides the capability to skew and to control the flatness or peakedness of the distribution [19]. Four parameters are required to characterize this distribution. These four parameters are: (1) $\epsilon$, the lower bound of the data, (2) $\lambda$, the range of the data, and (3-4) $\gamma$, $\delta$, the shape parameters that peak and skew the distribution. These parameters must generally be determined by analyzing the specific data.

For the pre-processing program used here, the inverse CDF for the $S_B$ distribution, which is used as part of the mapping function, was determined in an approximate manner using the results of Salas and Benzeden [20]. The values, $U_i^j$, obtained by operating on the sets of random numbers with the normal inverse CDF are then used to generate the set of crack lengths using the following relation

$$ A_i^j = \lambda \left[ \frac{G_i^j}{1 + G_i^j} \right] + \epsilon $$

where

$$ G_i^j = \exp[(U_i^j - \gamma)/\delta]. $$

An example using this distribution to generate an initial crack state is given in Section 5.3. A copy of the pre-processing program used to generate the set of initial crack lengths at each Gauss point is given in Ref [29]. For the analysis described in Section 5.3, it was assumed that the minimum crack length for Westerly granite was 0.5 mm and the maximum value was 1.4 mm. The minimum crack length was determined from acoustic emissions studies. The maximum crack length was assumed to be halfway between the minimum and the critical crack length ($d_1$). The remaining shape parameters were chosen, somewhat arbitrarily, to give the distribution a slightly skewed shape since the exact initial crack distribution was unknown. The average crack length was scaled to 0.7 mm which was the crack length used in calculations where it

254

was assumed that initial crack lengths were all the same. This was done so that the results from the calculations using the initially random distribution could be compared to the results of analyses using a constant initial crack length of 0.7 mm.

## 3.5 Thermal Strains

SANCHO adjusts the stretching tensor to compensate for thermal strains which are interpolated from material input data [8]. However, equation (19) which is used to compute the stress, contains the strain itself and not just the strain rate. In order to compute correctly the bulk response when the temperature is changing, the thermal strains are computed in a separate subroutine which is called by the material subroutine if a thermal problem is specified. The thermal strain is computed by reading the temperature from the temperature history file which is supplied from an external source [8]. Then the strain is interpolated from the temperature-strain data which is supplied as part of the material data string on cards 8 and 9. The thermal strain is then subtracted from the the diagonal components of the mechanical strain. A listing of this subroutine is given in **Ref** [29].

# 4   Determining Model Parameters

In this section, we will demonstrate a procedure for determining a set of model parameters from triaxial compression and microstructural data. For illustrative purposes, we will use published data on Westerly granite to develop the parameters shown in Table 1. Senseny [21] has used a procedure similar to the one described below to estimate model parameters for Algerie granite.

In using triaxial test data to determine model parameters, we tacitly assume the initiation of damage, as detected either through AE or volume strain measurement techniques, is due to the propagation of the most favorably oriented crack. If the specimens are compressed such that the greatest principal compressive stress, $-\sigma$, is in the 3-axis direction with the confining pressure, $-p$, applied in the 1 and 2 directions. then the positive principal components of deviatoric stress will be $T'_{11} = T'_{22} = 1/3(\sigma - p)$. Therefore, the most favorably oriented cracks will be those that have normals perpendicular the 3-axis. Thus, we can simplify equation (13) to

$$T'_{11} + \frac{T_{kk}}{3\mathcal{F}} = \left[\frac{\pi K_{Ic}}{2\mathcal{F}\sqrt{\pi a_o}}\right]. \tag{22}$$

By plotting the points of damage initiation for a series of triaxial tests on axes of $T'_{11}$ versus $-T_{kk}/3$, an initial damage surface for the most favorably oriented cracks is produced, as shown in Figure 4. Note that we use the abscissa of $-T_{kk}/3 = (\sigma + 2p)/3$ because compressive stresses are considered to be negative and, thus, $T_{kk}/3 < 0$.

By performing a linear least-squares fit through the initial damage points, a straight line is produced that corresponds to equation 22. From the inverse of the slope $(1/S_o = 2.18)$ and the intercept $(I_o = 18.9 \text{ MPa})$ of the line through the data, we can get

$$\mathcal{F}(a_o) = f\left[\left(\frac{d}{a_o}\right)\frac{1}{\left[1 - \left(\frac{a_o}{d_1}\right)^2\right]^{\frac{1}{2}}}\right] = \frac{1}{S_o} \tag{23}$$

and

$$\left[\frac{\pi K_{Ic}}{2\mathcal{F}\sqrt{\pi a_o}}\right] = I_o. \tag{24}$$

Using equations (23) and (24), either the initial crack length or the fracture toughness for microcracks can be calculated, provided one or the other is known. In general, it is easier to estimate the initial crack length from either average grain size measurements or from actual crack measurement data than to determine the fracture toughness for crack sizes of interest. This is because for small cracks, the fracture toughness depends somewhat on the crack size. Schmidt and Lutz [22] have performed a series of fracture toughness tests on Westerly granite. They found that for crack lengths in the range of 10 to 100 mm, the fracture toughness increased from 2.0 to 2.6 MPa$\sqrt{m}$. For crack lengths below 10 mm the fracture toughness decreased much faster with decreasing crack length. Extrapolating their data to crack lengths on the order of 1.0 mm, the fracture toughness is approximately 1.0 MPa$\sqrt{m}$.

From the data reported by Tapponnier and Brace [23], we can estimate the average grain size of Westerly granite to be approximately 1.0 mm. Typically, the microcracks present in the virgin material are of the order of one half to one grain diameter in length. Thus, we estimated the value of $a_o$ to be 0.7 mm. Inserting $a_o = 0.7$ into equation (24) along with the value of $\mathcal{F}$ from equation (23) and the appropriate values of the slope and intercept of the initial damage surface (Figure 4), the value of $K_{Ic}$ is computed to be 1.23 MPa$\sqrt{m}$. This is a value comparable to that derived from the data of Schmidt and Lutz [22].

The three remaining microstructural parameters remain to be determined. From the model we know that

$$d_1 > d > a_o. \tag{25}$$

The length, $d$, is the span of the region of tension caused by some local inhomogeneity. It is assumed that these regions are due to mechanisms such as grains of different elastic properties being compressed together. Most of the idealized tension producing mechanisms are on the order of the grain size, thus, $d$ can at most be two to three grain diameters. Experience has shown that a value of $d$, chosen so that the ratio $d/a_o$ is approximately equal to three, gives good results. Thus, a value of $d = 2.0$ mm was derived for Westerly granite.

The parameter $d_1$ represents some initial spacing of microcracks and, thus, is related to the initiation of failure by unstable crack growth. Ideally, one could determine a failure curve similar to the initial damage curve (Figure 4) and determine its slope $(S_f)$ and intercept $(I_f)$ where

$$S_f > S_o$$

and

$$I_f > I_o.$$

Then using

$$\left[ \frac{\pi K_{Ic}}{2 \mathcal{F} \sqrt{\pi a_f}} \right] \quad I_f \tag{26}$$

a value of $a_f$ could be determined and substituted into

$$\mathcal{F}(a_f) = f \left[ \left( \frac{d}{a_f} \right) \frac{1}{\left[ 1 - \left( \frac{a_f}{d_i} \right)^2 \right]^{\frac{1}{2}}} \right] - \frac{1}{S_f}. \tag{27}$$

The pair of equations (23) and (27) could then be used to solve for the remaining two model parameters $d_1$ and $f$. Unfortunately, a failure curve, in the sense used in the model, would be very difficult to determine. This is because, in an actual experiment, when failure begins by microcracks coalescing, the state of stress is very inhomogeneous. Thus, regions of high stress may fail, whereas, regions of lower stress may be far from failure. The average stress measured at the peak in the stress-strain curve is not representative of the failure stress in the model sense. If an AE location system were used during the tests, the stress state where localization of damage causes initiation of failure may be detectable. However, experiments reported to date are inconclusive on this point.

In lieu of a better method, the following fitting procedure can be used. First, we assume $d_1 = d$, then calculate $f$ from equation (23). Then, an axisymmetric finite element model of a uniaxial compression test is formulated, such as the one discussed in Section 6. An analysis is run with the tentative model parameters to determine the

value of stress at the peak of the stress-strain curve. This value is compared to uniaxial compressive strength data. If the predicted strength is too low, $d_1$ is increased and a new $f$ is determined; then, the procedure is repeated. If the predicted value is too high, more changes are required since $d_1 \geq d$. Usually, by adjusting $d$ and $d_1$ slightly, a good fit can be obtained. For Westerly granite, a value of $d_1 = d = 2.0$ mm proved quite good. This resulted in a value of 0.715 for $f$.

The two constitutive parameters, $C_1$ and $C_2$, are also best determined by comparing axial and volume strains predicted from a uniaxial compression analysis with experimental data. From equation(18), it can be seen that

$$C_1 \sim \frac{1 + \nu}{E} \tag{28}$$

and

$$C_2 \sim \frac{\nu}{E}. \tag{29}$$

Using the above values to start with, the results of an analysis can be compared to experimental data and the values adjusted to give the desired fit.


# 5    Example Problems

Because of the complex nature of the microcrack damage model, analytic solutions to even simple boundary value problems are not available. Thus, direct comparisons of solutions with analytic results for the purpose of model verification are not possible. However, in this section, results of some calculations using simple geometries and loading conditions are presented and compared with experimental results, where possible, both to assist in verification of the implementation of the model and to demonstrate its validity in regard to modeling brittle materials. In addition, the effect of different solution control schemes, discussed in Section 3.2, on the solution of a particular problem are shown.


## 5.1    Single Element in Compression

### 5.1.1    Model Behavior Compared to Experiment

In order to demonstrate the basic nature of the model, a simple calculation was performed using only a single axisymmetric element subjected to uniaxial compression (Figure 9a). The material parameters used in these calculations and all others presented

here were derived from a series of triaxial tests on Westerly granite [10], as discussed in Section 4, and are given in Table 1.

Figures 9b and 9c show the results of the single element analysis compared with the experimental results of Brace, et al. [10] that were used to determine the model parameters. The fit to the data is reasonably good, demonstrating the model accurately replicates the data on which the parameters are based. As will be demonstrated later, the stress states in uniaxial and triaxial tests are not usually homogeneous unless great care is taken to alleviate end constraints applied by the end platens. This causes some problems in using this type of test data to determine model parameters because the usual process of determining parameters assumes the data are derived from tests in which the stress is homogeneous.

The accumulation of damage during axisymmetric uniaxial loading is displayed in Figure 9(d). The three components shown in the figure are the components of the damage vector in the (R), (Z) and ($\theta$) coordinate directions, respectively (equations (20) and (21)). The damage begins to accumulate at approximately 35% of the peak stress, consistent with acoustic emission measurements [13] [15]. In addition, more damage is accumulated in the (R) and ($\theta$) coordinate directions than in the (Z) direction because cracks grow primarily parallel to the loading axis (Z-axis).

## 5.1.2  Comparison of Solution Techniques

Figure 10 shows the behavior of a single element, in plane strain, subjected to uniaxial compression. Three solutions are shown. The three curves were generated using (1) the two-stage stress-damage convergence scheme, described in Section 3.2, where the the second stage stress-damage solution is allowed to reach complete global convergence (designated "Elastic-Full Damage" in the figure); (2) the modified two-stage convergence scheme where the damage is updated after an elastic solution is found but no further iterating is allowed (designated "Elastic-Damage Update" in the figure); (3) a solution using the update method but with time (or, equivalently, strain) increments of half the size used in the other two calculations. A comparison of the three curves shows that the accuracy of the update method is quite reasonable, differing from the full damage solution only in the post-failure regime. Considering that the update method runs approximately five times faster than the full damage method and, for more complex problems, tends to be more reliable in the post-failure regime, it seems reasonable that this method should be used, at least for preliminary calculations. The effect of changing the solution step size is also shown in Figure 10. Because of the isotropic decay method used, the rate of decay is tied directly to the number of steps

used in computing the response in the post-failure regime. The decay parameter, of course, can be adjusted to give the same post-failure response for any number of steps.

## 5.2 Uniaxial and Triaxial Compression Test Simulations

Uniaxial and triaxial compression tests of rock and concrete are often used to obtain material property data for engineering analysis. Calculations using this test geometry are useful because both the load-deformation histories and the failure modes are easily confirmed by experiment.

Simulations of uniaxial and triaxial compression tests on Westerly granite at several confining pressures were run using the material parameters given in Table 1, with a uniform initial crack length, $a_o$. For comparison, calculations were run in both the plane strain and axisymmetric configurations.

The model geometry and finite element mesh used is shown in Figure 11. Since the initial crack length was isotropic, a plane of symmetry was assumed through the middle of the sample so only half of the model was actually used in the computations. The rock was divided into 100 elements for most computations. Computations with 400 elements and with 25 elements (in plane strain) were also performed to assess the effect, if any, of element size on the results.

For uniaxial test simulations, the top of the steel endcap was displaced downward at a steady rate until so many elements in the rock material failed that converged equilibrium solutions were no longer possible. In the triaxial tests, a hydrostatic stress (in-plane stress for plane strain calculations) was first imposed by applying a uniform pressure at the lateral boundaries in combination with enough axial displacement to achieve an isotropic in-plane stress state. Then, the axial displacement of the endcap was increased until the rock failed. During this loading, the lateral pressure was kept constant. In all cases, it was prescribed that no slip could occur between the endcap and the sample.

Engineering stress-strain curves were derived from each simulation by computing forces and displacements in a manner similar to what would be done in a laboratory experiment. That is, axial stress was derived by computing the total reaction force at the lower boundary and dividing by the original cross sectional area. Axial strain was derived by computing the net displacement of the ends of the rock and dividing by the original length. Lateral strain was derived by computing the net displacement between two points across the central portion of the specimen and dividing by the original thickness. The volume strain was then computed as the sum of the axial and

lateral strains.

## 5.2.1 Plane Strain Calculations

The first set of results is for the plane strain configuration. Figure 12 shows the stress-strain data derived from the simulated tests at three different confining pressures: $P_c = 0$, 10, and 50 MPa. The effect of pressure on the ultimate strength and the dilatant behavior of the material are in good agreement with laboratory experiments on Westerly granite [10]; although the magnitudes of calculated failure stresses are somewhat lower than those reported in the experiments because the experiments were conducted on axisymmetric specimens. However, as shown in Figure 13, the stress-strain response of material as derived from the simulated compression test differs somewhat from the response of the material under uniform uniaxial compression as derived from a single element plane strain calculation. This is because the stresses in the rock in the multiple element simulated compression test are not uniform.

Figure 14 shows the stress distribution, in terms of the von Mises equivalent stress $(\sigma = \sqrt{\frac{3}{2} T'_{ij} T'_{ij}})$, in the rock at a point near the peak stress for each of the three test conditions. The distributions are quite similar for all three cases with strong gradients near the ends of the rock and less severe gradients near the center. Across the center of the specimen there is about a 15% variation in stress. Vertically, from the platen to the center of the specimen there is a 20 to 30% variation in stress, depending on the confining pressure. Although even a simple linear elastic analysis shows that the stresses are not uniform in the sample because of the constraint of the endcaps, the present analysis also shows that once microcrack growth begins, these inhomogeneities in the stress field tend to be amplified because regions under greater deviatoric stress become more highly damaged and, therefore, less stiff compared to undamaged regions such as those near the endcaps. Thus, the stress is redistributed further and the gradients become more severe.

## 5.2.2 Effect of Element Size

Plane strain simulations were also run using 25 elements and 400 elements to model the rock material. A comparison of the results from uniaxial compression calculations using three different meshes is shown in Figure 15. There are some small differences in the response curves up to the point of maximum stress. However, the major differences occurred in the neighborhood of the maximum stress and on into the post failure regime. The predicted maximum stress varied from approximately 180 MPa (using 400 elements) to 200 MPa (using 25 elements).

### 5.2.3 Damage Distribution

The distribution of damage (magnitude of the damage vector, equations (20) and (21)) in the rock at the same stress states as those shown in Figure 14 is given in Figure 16 (plane strain calculation). Note that for the unconfined test, the maximum damage occurs in a region on the surface of the sample, just below the endcap but not at the corner where maximum deviatoric stresses occur. Also, there are large triangular regions at the ends of the sample that have sustained little or no damage. As the confining pressure is increased, these end regions become smaller and regions of high damage begin to appear in the center of the sample. This indicates that the mode of deformation changes considerably as confining pressure is applied. However, even at 50 MPa confining pressure, the damage in the central region of the sample is considerably greater than near the ends. Because high damage means that the microcrack density is large and, thus, the volume strain in this region is large, it could be expected that some nonuniformity in surface deformation should begin to appear well before the peak in the stress strain curve. Such observations have been made experimentally by Spetzler, et al. [24] and Kurita, et al. [25] using a sensitive holographic method to measure surface deformation of rock samples under triaxial test conditions.

### 5.2.4 Failure Modes

The damage contours shown in Figure 16 also indicate possible failure modes. In the unconfined test, the maximum damage is confined to near surface regions, giving rise to the possibility that macrofractures will form in these regions resulting in slabbing off of material near the surface. As confining pressure is applied, this mode changes to one of more confined damage in the central portion of the sample, possibly leading to fractures forming in the central region of the sample and propagating outward to the surface along directions of high damage, resulting in faulting across the specimen.

The progression of failure for the unconfined, plane strain case is shown in Figure 17. The darkened regions shown in each frame are regions where the elements have failed and are softening. The first frame shows the state of the sample just before the peak in the stress-strain curve. Failure of some elements begins before the peak in the stress-strain curve is reached. The failure zones spread rapidly as the deformation continues beyond the peak stress. The last frame shows the state of the sample at the end of the stress-strain curve. Computational reliability (convergence of solutions) could not be maintained beyond this point.

The mode of failure predicted in the unconfined case is quite typical of brittle materials in compression. If large fractures form in regions of heavy damage and failure

262

(Figure 17), it is easy to see that slabs of material will form and fall away. Experiments by Wawersik [9] and Wawersik and Brace [26] clearly show this kind of behavior in uniaxial compression in a very stiff load frame. Figure 18 shows a series of photographs of sectioned post-test samples taken from Wawersik [9]. The samples shown in the figure were loaded to states of failure similar to those shown in the simulation in Figure 17. By sectioning samples after testing, Wawersik [9] determined that large fractures form at the surface below the endcap (not at the corner) and propagate nearly parallel to the lateral surface, leaving an hourglass-shaped central region of intact material. In addition, it was evident from microscopic examination of samples that the central region was heavily damaged, whereas, the regions near the ends appeared to have significantly fewer microcracks.

The progression of failure in a test simulation with 50 MPa confining pressure is shown in Figure 19. The mode of failure is quite different from that shown in Figure 17 for the case of uniaxial compression. If the confining pressure is large enough, the mode of damage and failure shifts to one in which the damage is confined to the central interior of the sample, resulting in the formation of one or more large fractures that propagate outward at an angle toward the surface near the corner of the sample. This mode of failure has been carefully documented experimentally by Hallbauer et al. [27]. Figure 19 shows a similar result, in that the failure begins in the central region. With further deformation, zones of failure begin to appear at the surface below the ends. However, it is the central failure zone that spreads and finally consumes the central region of the sample.


### 5.2.5 Comparison with Axisymmetric Results

The results of simulated compression tests on Westerly granite in the axisymmetric mode are compared with the previously discussed plane-strain results in Figure 20 for uniaxial compression and triaxial compression at 50 MPa confining pressure. Failure of the sample occurs at a slightly higher stress in the axisymmetric case because of the added hoop constraint. However, in the axisymmetric case, it is the damage in the hoop direction which dominates the failure mode. Figure 21 shows the predicted progression of failure under axisymmetric uniaxial compression. The damage in the failed zones is almost entirely in the hoop direction, which would lead to the formation of axial fractures causing the sample to split into long pie-shaped segments.

Because of the constraint imposed by end conditions, it appears that conditions of both plane-strain and axisymmetry may exist simultaneously in a compression test sample, leading to multiple sets of fractures. An example of this type of brittle failure in compression is shown in Figure 22. The figure shows a uniaxial compression sample

of aluminum-filled epoxy tested by Olsson and Jones [28]. The sample clearly shows two sets of fractures. Hourglass fractures appear through the sample, leaving a cone-shaped piece of intact material at each end of the sample. In addition, several axial fractures are shown. Thus, it appears that the ends of the sample reflect conditions consistent with plane strain deformation and failure, whereas, the failure mode evident in the central portion of the sample reflects axisymmetric deformation.

## 5.3 Uniaxial Compression with Random Initial Crack Lengths

All of the above calculations were performed starting with an initially isotropic distribution of microcracks. For comparison, a uniaxial compression, plane-strain calculation was performed using randomly generated initial crack lengths for each direction at each Gauss point. Crack lengths were allowed to vary from 0.5 to 1.4 mm in such a way that the average initial crack length over the entire model was 0.7 mm, the same as in the isotropic case. The random variation in initial crack lengths was generated using the pre-processing program described in Section 3.4. With the random initial crack lengths, the material at each integration point is different, so no symmetry in the model could be assumed. Figure 23 shows the state of damage near the maximum stress and the failed zones in the sample late in the post-failure regime. Due to the lack of symmetry, damage appears to be localizing into a band angled across the sample. However, because the shear stiffness in the model is not affected greatly by the damage, a shear zone does not form. Instead, failure bands similar to those in the isotropic case eventually form, leading to hourglass fracturing.

# 6   Concluding Remarks

The material model discussed in this report allows for a good representation of the behavior of brittle damaging materials such as rock, concrete and ceramics. The model is best suited for application to problems where a detailed knowledge of the stress and deformation states as well as the location and extent of regions of potential failure are required. To date, the model has been used extensively in the analysis of laboratory experiments to determine the extent and uniformity of deformation under simple and complex load paths. In addition, the model has been used in conjunction with experimental techniques such as acoustic emission location to study and identify the conditions under which localization of damage and deformation occur. This is an important step in understanding the formation of faults and joints in geologic media and the sudden failure of some kinds of concrete structures. Future applications may

264

include the analysis of ceramic components, especially the effects of thermal stresses and fatigue on service life.

Because this type of model is rather new and the version discussed in this report is the first attempt to implement such a model, several changes and improvements to the model and its implementation are planned for the near future. There are two major changes which will be made to address more completely the problem of calculating the stresses in the post-failure regime. First, the sequencing of failure will be addressed by incorporating a feature that allows the material at only one integration point at a time to go into failure. Once the most critical (most highly stressed) of the points that have reached the failure condition is identified, it will be identified as having failed and a new equilibrium solution will be sought in order to determine the new stress distribution resulting from a failure at one integration point. The remaining elements will then again be checked to see whether any are still at the failure condition; if so, the most critical will be allowed to fail. The process continues until no more integration points are at the failure condition. Thus, at each solution step, the stresses resulting from re-distribution of loads due to failing regions in the structure will be properly accounted for.

The second change to be made improves the calculation of stresses at a point that is in failure. In the current version, the stresses are isotropically reduced to simulate the reduction in load carrying capacity of a fractured element. This is somewhat unrealistic in that the material can support stress parallel to the fracture and can also support some shear stress. To correct this shortcoming, the stresses will be calculated by rotating them to the reference frame of the critical fracture. The orientation of the unstable fracture is known from the crack function, $a(n)$. The effect of the fracture is to reduce to zero the normal and shear components of stress on the crack plane. Once this is done, the stress tensor is rotated back to the global coordinate system and returned to the program. Thus, the stresses at a failing point will be reduced anisotropically in a way consistent with the growth of the macrocrack.

Finally, it is hoped to extend the improved version of the model to a fully three-dimensional version. The main problem in doing this is the large amount of storage required to represent the crack function accurately. For two dimensions, thirteen storage locations are required for each integration point just to store the crack orientation and magnitude information. In three dimensions, this would increase to 144 storage locations per integration point. Additional research is required to determine the minimum number of directions needed to accurately integrate the crack function before a three-dimensional version of the model can be effectively implemented.

# REFERENCES

[1] Kachanov, L. M., "On the Creep Fracture Time," *Izv. AN SSR, Otd. Tekhn. Nauk*, 8, 26, 1958.

[2] Rudnicki, J. W. and Rice, J. R., "Conditions for the Localization of Deformation in Pressure-Sensitive Dilatant Materials," *J. Mech. Phys. Solids*, 23, 371, 1975.

[3] Costin, L. S., "A Microcrack Model for the Deformation and Failure of Brittle Rock," *J. Geophys. Research*, 88, NO. B11, 9485, 1983.

[4] Costin, L. S. and Holcomb, D. J., "A Continuum Model of Inelastically Deformed Rock Based on the Mechanics of Microcracks," *Proc. Internat. Conference on Constitutive Laws for Engin. Mat.*, C. S. Desai and R. H. Gallagher, eds., Univ. of Arizona, Tucson, Arizona, 1983.

[5] Costin, L. S., "A Microcrack Damage Model for Brittle Rock," *Report, SAND83-1590*, Sandia National Laboratories, 1983.

[6] Costin, L. S., "Damage Mechanics in the Post-Failure Regime," *Mech. Materials*, 4. 149, 1985.

[7] Costin, L. S. and Stone, C. M., "Implementation of a Finite Element Damage Model for Rock," *Proc. Second Internat. Conference on Constitutive Laws for Engin. Mat.*, Desai. C. S., Krempl. E., Kiousis, P. D., and Kundu, T.. eds.. Univ. of Arizona, Tucson, Arizona. 1987.

[8] Stone, C. M., Krieg, R. D. and Beisinger, Z. E., "SANCHO: A Finite Element Computer Program for the Quasistatic, Large Deformation, Inelastic Response of Two-Dimensional Solids," *Report SAND84-2618*, Sandia National Laboratories. 1985.

[9] Wawersik, W. R., "Detailed Analysis of Rock Failure in Compression Tests," *Ph.D. Thesis*, Univ. of Minnesota. Minneapolis. MN, 1968.

[10] Brace, W. F., Paulding. B. W., and Scholz, C., "Dilatancy in the Fracture of Crystalline Rocks," *J. Geophys. Res.*. 71. 3939. 1966.

[11] Isida, M., "Method of Laurent Series Expansion for Internal Crack Problems." in *Mechanics of Fracture, Vol. 1*, G. C. Sih. Ed., Noordhoff. Leyden, 1973.

266

[12] Horii, H. and Nemat-Nasser, S., "Estimate of Stress Intensity Factors for Interacting Cracks," Earthquake Research and Engineering Laboratory Technical Report No. 83-7-55, Dept. of Civil Engineering, Northwestern Univ., Evanston, IL, July, 1983.

[13] Holcomb, D. J., "Using Acoustic Emissions to Determine In-situ Stress: Problems and Promise," *Geomechanics*, AMD vol 57, ASME, 11, 1983.

[14] Kaiser, J., "An Investigation Into the Occurrence of Noises in Tensile Tests or a Study of Acoustic Phenomena in Tensile Tests," *Ph.D. Thesis*, Tech. Hochsh. Munchen, Munich, Germany, 1950; English Trans.: Lawrence Radiation Laboratory Rept. UCRL-Trans-1082(L), June, 1964.

[15] Kurita, K. and Fujii, N., "Stress Memory of Crystalline Rock in Acoustic Emission," *Geophys. Res. Lett.*, 6, 9, 1979.

[16] Holcomb, D. J. and Costin, L. S., "Detecting Damage Surfaces In Brittle Materials Using Acoustic Emissions," *J. App. Mech.*, 53, 536, 1986.

[17] Krajcinovic, D. and Fonseka, G., "The Continuous Damage Theory of Brittle Materials," *J. App. Mech.*, 48, 809, 1981.

[18] Wawersik, W. R. and Fairhurst, C., "A Study of Brittle Rock Fracture in Laboratory Compression Experiments," *Int. J. Rock Mech. Min. Sci.*, 7, 561, 1970.

[19] Pearson, R. G., "Potential of the $S_B$ and $S_{BB}$ Distributions for Describing Mechanical Properties of Lumber," *Wood and Fiber*, 12, 4, 244, 1980.

[20] Salas, J. D. and Benzeden, E., "Probability Distribution Functions," *Proc. Computer Workshop in Statistical Hydrology*, Hydrology and Water Resources Program, Dept. Civil Eng., Colorado State Univ., Fort Collins, CO, 1978.

[21] Senseny, P. E., "A Microcrack Model for the Deformation and Strength of Algerie Granite," *Proc. 27$^{th}$ US Symp. on Rock Mech.*, University of Alabama, Tuscaloosa, Alabama, 1986.

[22] Schmidt, R. A. and Lutz, T. J., "$K_{Ic}$ and $J_{Ic}$ of Westerly Granite - Effects of Thickness and In-Plane Dimensions," *ASTM STP 687*, ASTM, 166, 1979.

[23] Tapponnier, P. and Brace, W. F., "Development of Stress-Induced microcracks in Westerly Granite," *Int. J. Rock Mech. Min. Sci. Geomech. Abstr.*, 13, 103, 1976.

[24] Spetzler, H., Soga, N., Mizutani, H., and Martin III, R. J., "Strain Fields Associated With Fracture Under High Pressure, Viewed With Holographic Interferometry," *High Pressure Research: Applications in Geophysics*, Academic Press, Inc., 1977.

[25] Kurita, K., Swanson, P. L., Getting, I. C., and Spetzler, H., "Surface Deformation of Westerly Granite During Creep," *Geophysical Research Letters*, 10, 1, 75, 1983.

[26] Wawersik, W. R. and Brace, W. F., "Post-Failure of a Granite and Diabase," *Rock Mech.*, 3, 5, 1971.

[27] Hallbauer, D. K., Wagner, H. and Cook, N. G. W., "Some Observations Concerning the Microscopic and Mechanical Behaviour of Quartzite Specimens in Stiff, Triaxial Compression Tests," *Int. J. Rock Mech. Min. Sci. & Geomech. Abstr.*, 10, 713, 1973.

[28] Olsson, W. A. and Jones, A. K., "Mechanical Properties of an Aluminum-Filled Epoxy," *Report SAND85-2133*, Sandia National Laboratories, 1985.

[29] Costin, L. S. and Stone, C. M., "A Finite Element Material Model for Microfracture-Damaged Brittle Rock," Report SAND87-1227, Sandia National Laboratories, 1987.

## Table 1: Model Parameters

| Parameter | Westerly Granite |
|---|---|
| E (GPa) | 60 |
| $\nu$ | 0.25 |
| $C_1$ (1/MPa) | $8.3 \times 10^{-4}$ |
| $C_2$ (1/MPa) | $2.0 \times 10^{-4}$ |
| $a_o$ (m) | 0.0007 |
| $d$ (m) | 0.002 |
| $d_1$ (m) | 0.002 |
| $K_{Ic}$ $(MPa\sqrt{m})$ | 1.23 |
| f | 0.715 |
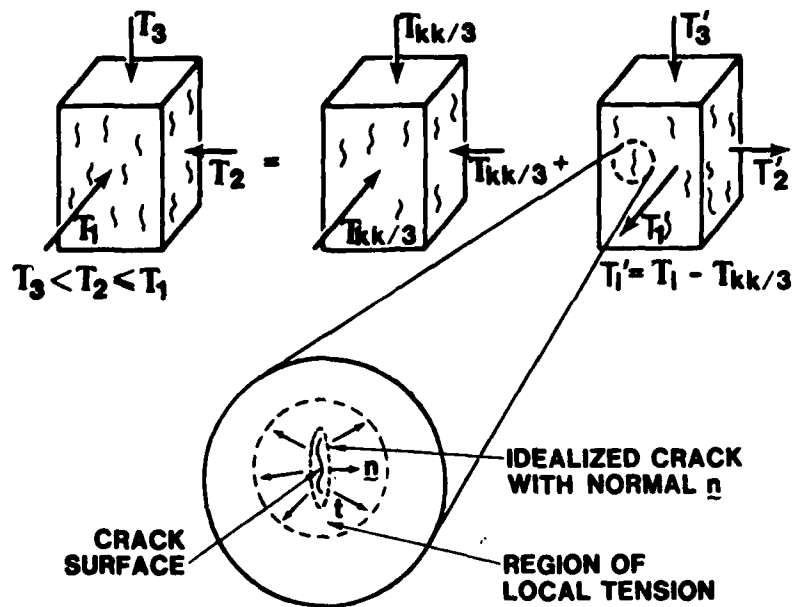
**Figure 1**

Idealization of a microcrack in rock. The local region of tension is proportional to the positive component of the deviatoric stress normal to the crack surface.

**INTERACTION OF COLLINEAR CRACKS**

APPROXIMATION FUNCTION

$$\frac{1}{\left|1-\left(\frac{a}{d_I}\right)^2\right|^{1/2}}$$

PSEUDO - TRACTION SOLUTION

$\frac{K_I}{\sigma\sqrt{\pi a}}$

$a/d_I$
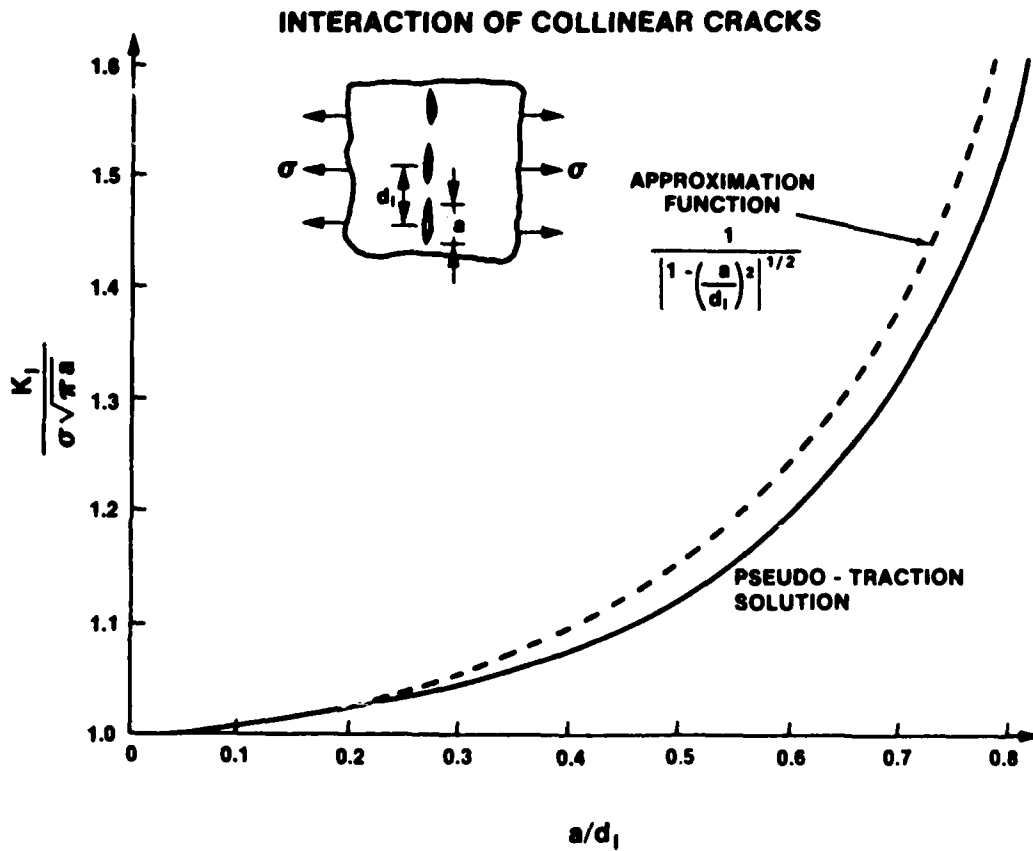
**Figure 2**

The effect of interaction between an array of collinear cracks on the stress intensity factor. Pseudo-traction solution is that of Horii and Nemat-Nasser [12].

271

**UNIAXIAL COMPRESSION**
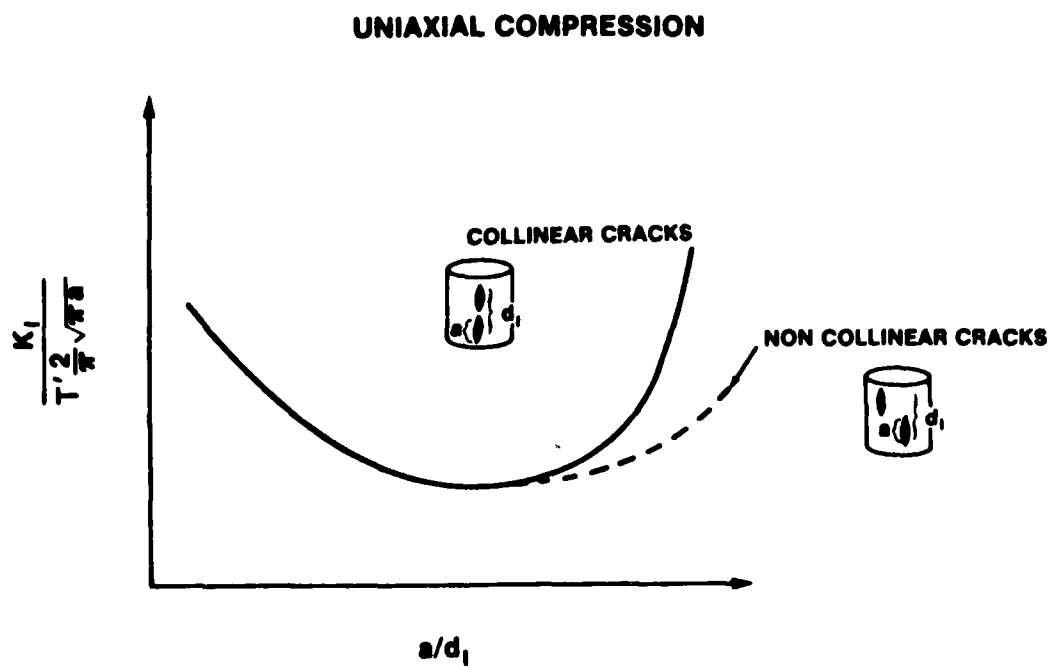
**Figure 3**

The effect of interaction between an array of collinear cracks on the stress intensity factor of a penny crack in a local tensile region.
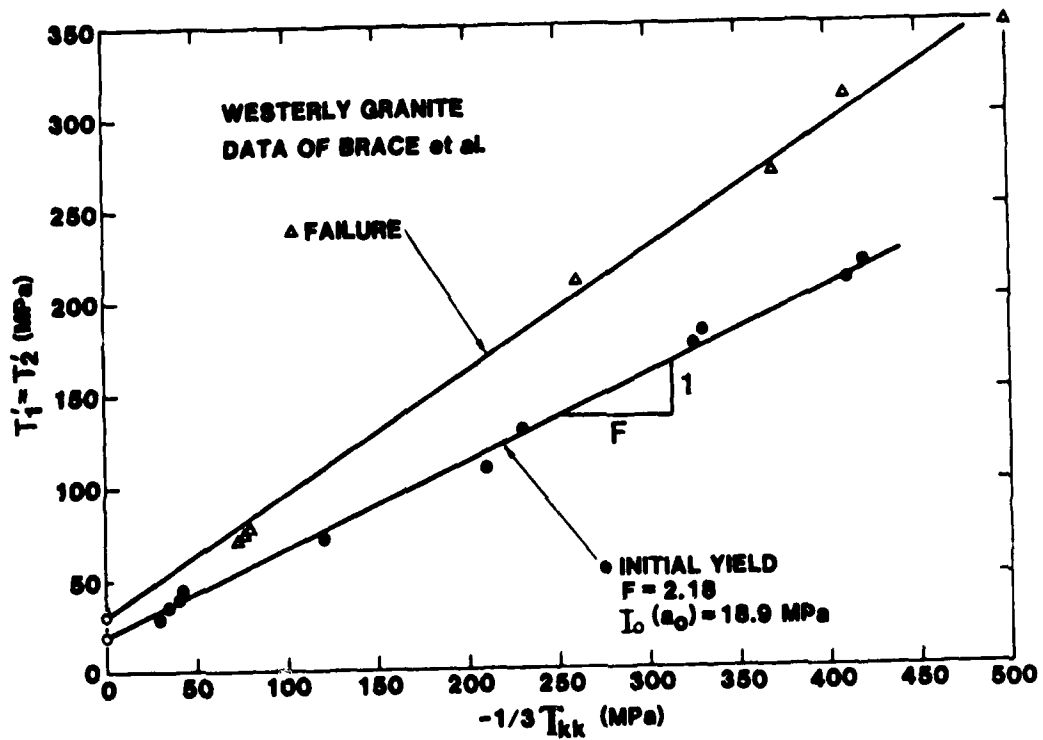
**Figure 4**

Initial damage (yield) surface and failure surface for Westerly granite. The solid lines are the model approximations to the data of Brace et al. [10].

273
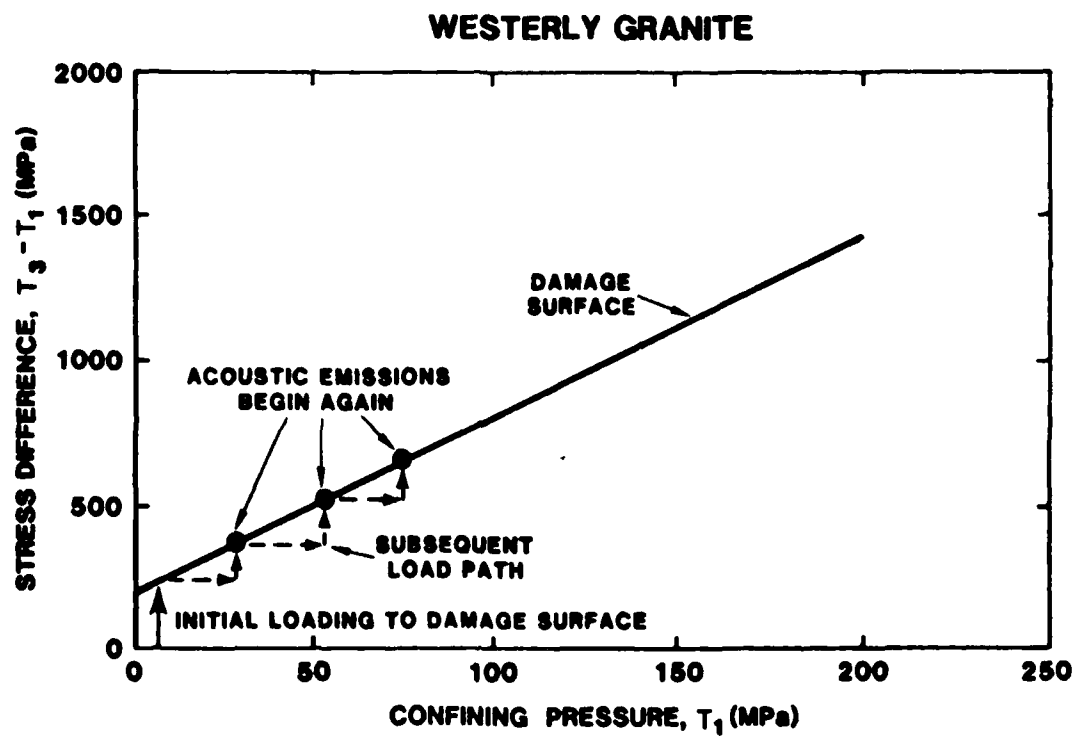
**WESTERLY GRANITE**

Figure 5

Load path followed by Holcomb [13] during triaxial
tests on Westerly granite to determine points on a
single damage surface by using the Kaiser effect.

274
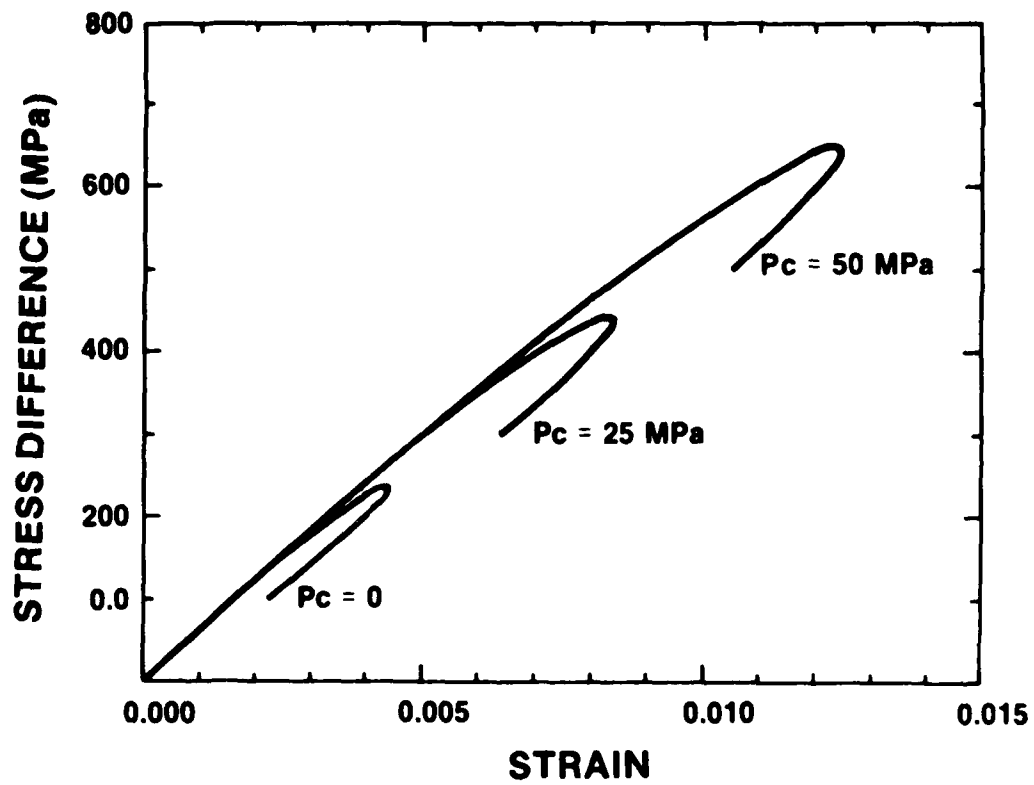
**Figure 6**

Model simulations of triaxial tests on Westerly gran-
ite at different confining pressures $(T_{11} = P_c)$. Stress
difference is $T_{33} - P_c$.
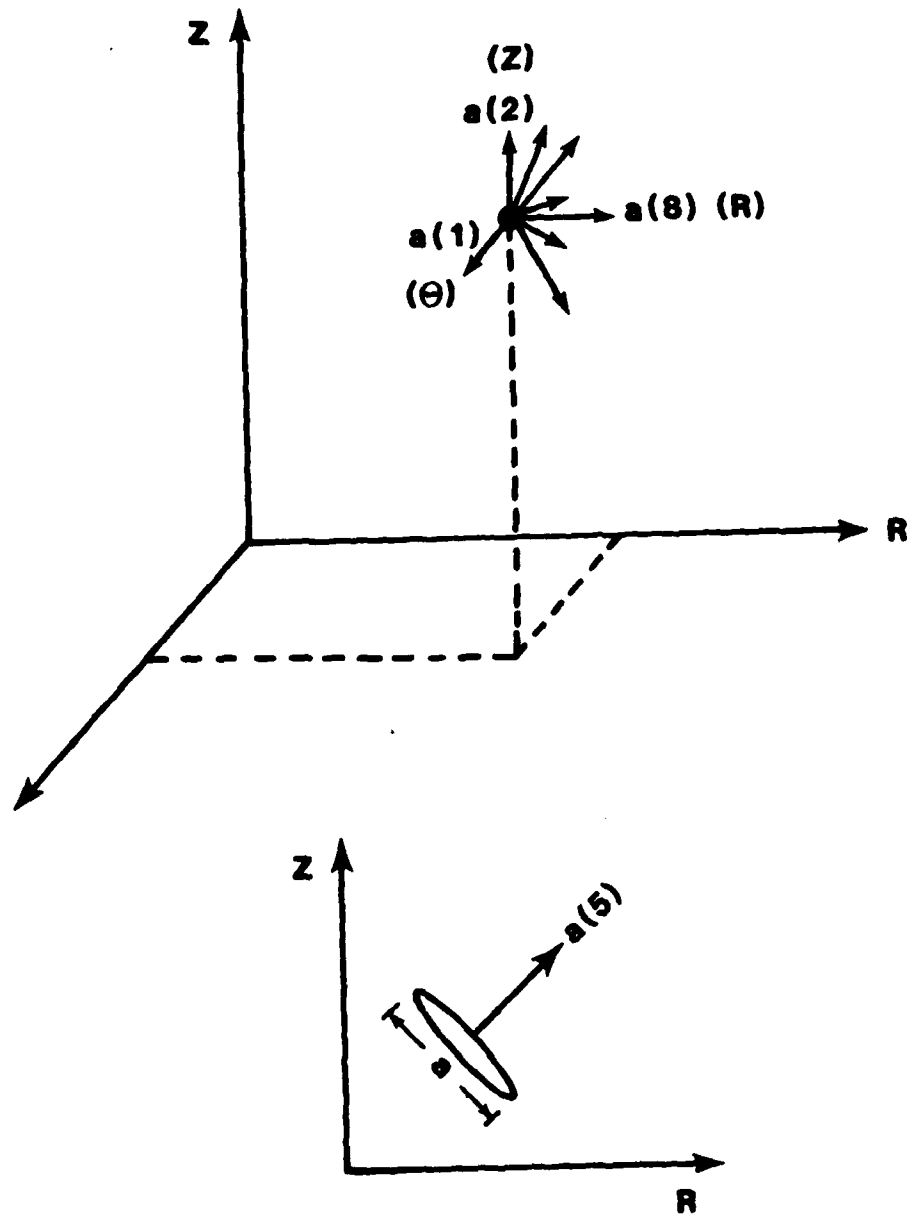
**Figure 7**

Schematic showing the assumed microcrack array at each
Gauss point ($\mathbf{a} = [a(1), a(2), \ldots, a(13)]$).

276
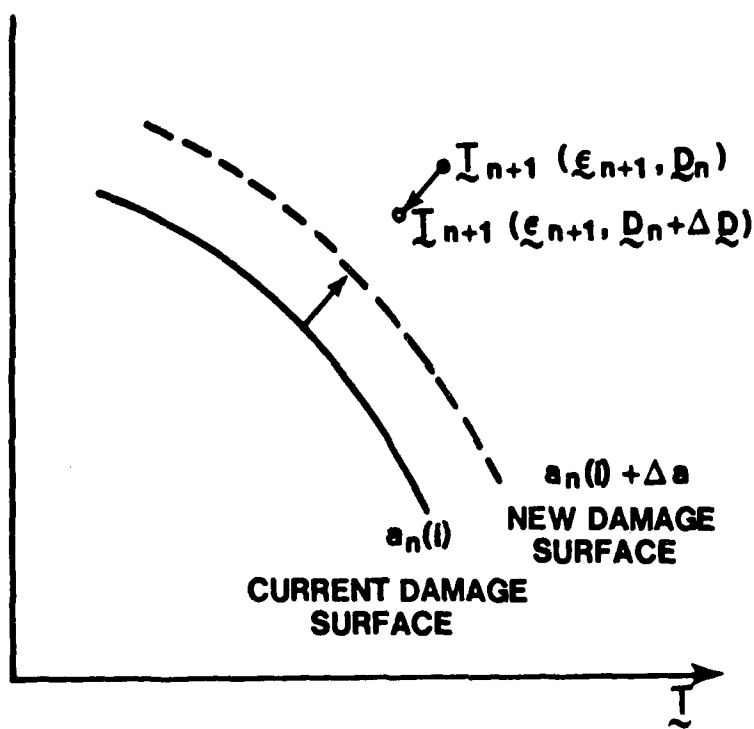
**Figure 8**

Schematic of convergence process for the solution of the stress-damage equations. Crack array component, $a_n(i)$, at solution step $n$ is incremented by $\Delta a$ until the computed stress, $T$, relaxes to the damage surface.
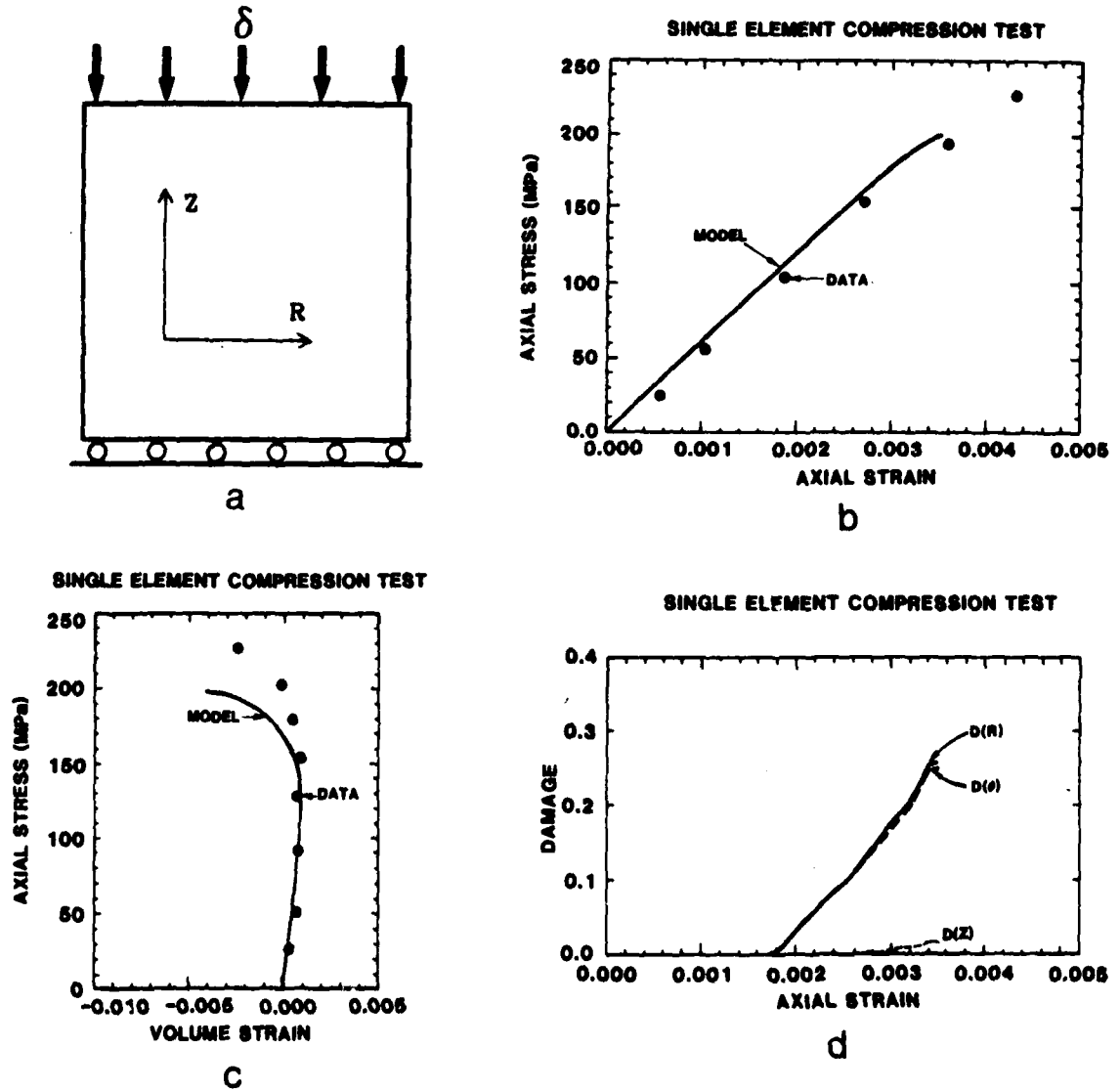
**Figure 9**

Results of a single axisymmetric element in compression compared to the uniaxial compression data of Brace, et al. [10]. (a) Single element model. (b) Axial stress-strain curve. (c) Axial stress-volume strain curve. (d) Three components of the damage vector as a function of the axial strain.

278
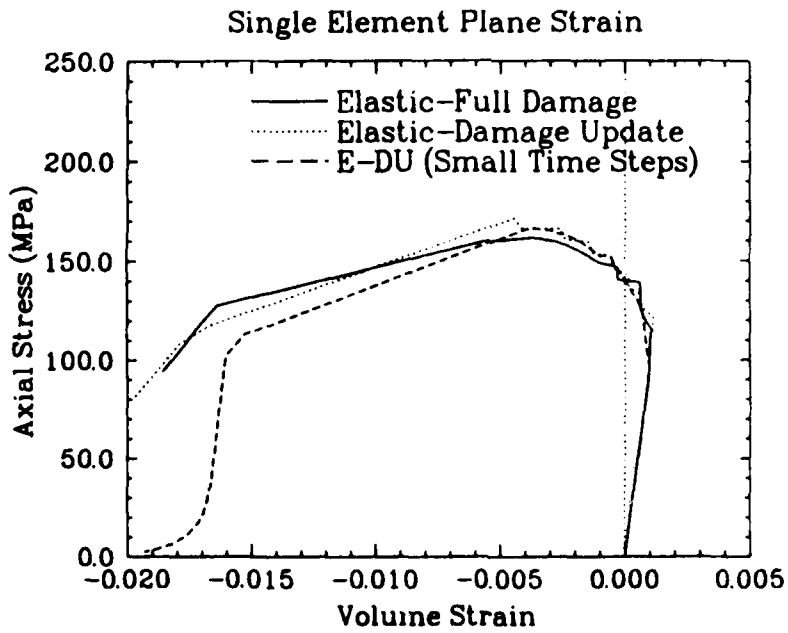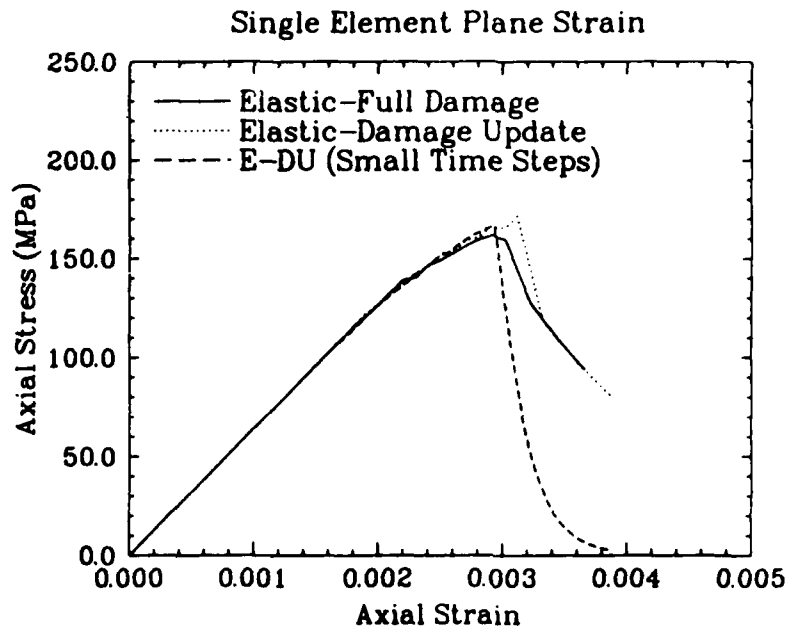
**Figure 10**

Results for a single element in plane strain compression using three different solution schemes.
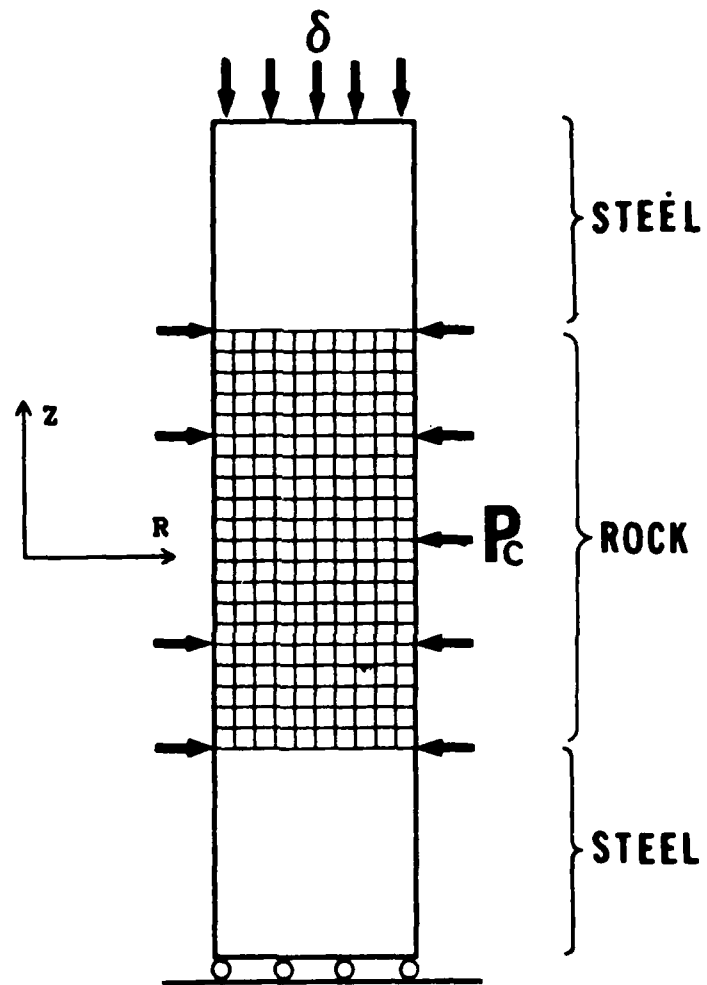
**Figure 11**

Finite element model of the triaxial test configuration. $\delta$ is the applied displacement and $P_c$ is the confining pressure.
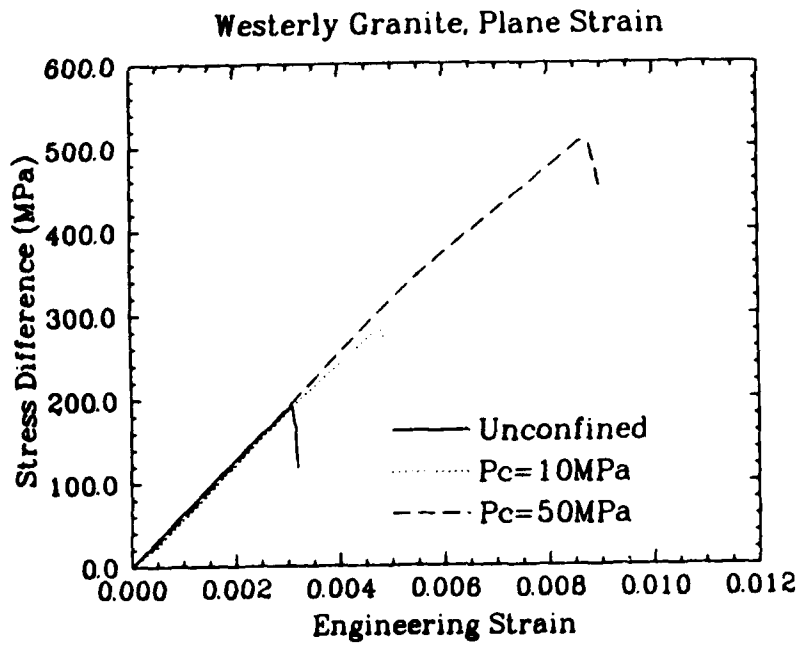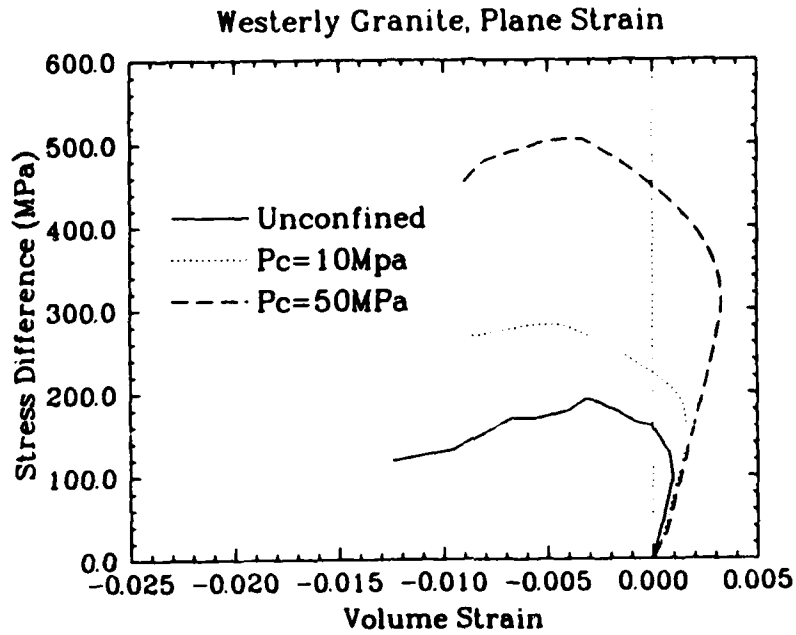
**Figure 12**

Stress-strain results calculated from the model triaxial compression tests at different confining pressures.

Westerly Granite – Plane Strain
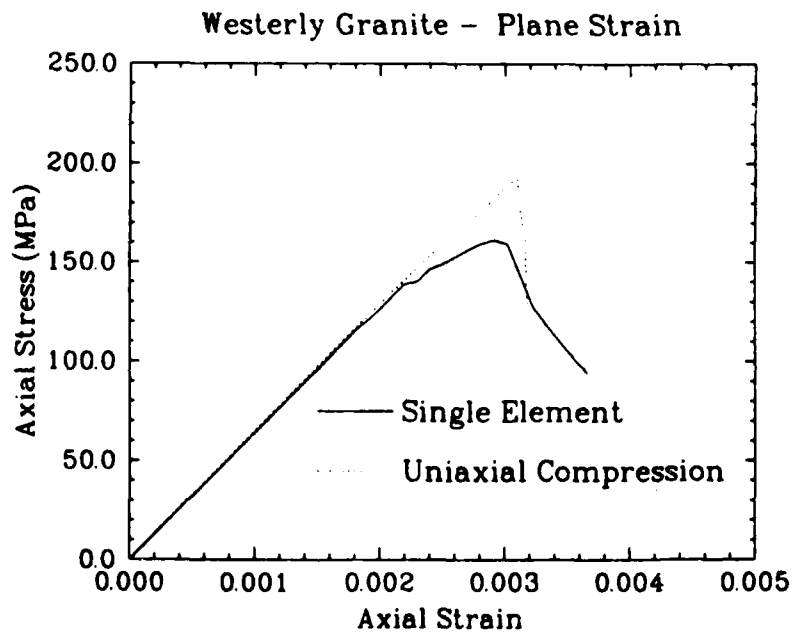
**Figure 13**

Comparison of the stress-strain response derived from
a simulated uniaxial compression test with the stress-
strain behavior of a single element in uniform uni-
axial compression.
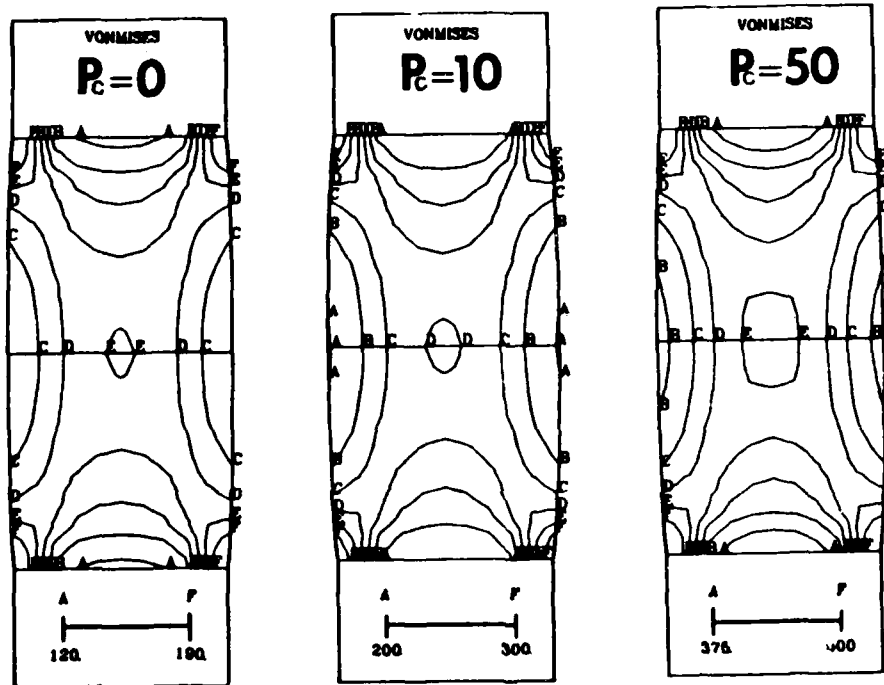
**Figure 14**

Contours of constant von Mises equivalent stress at a point near the ultimate stress for three different test conditions. The bar at the bottom of each figure gives the range of stress in MPa associated with the contours.
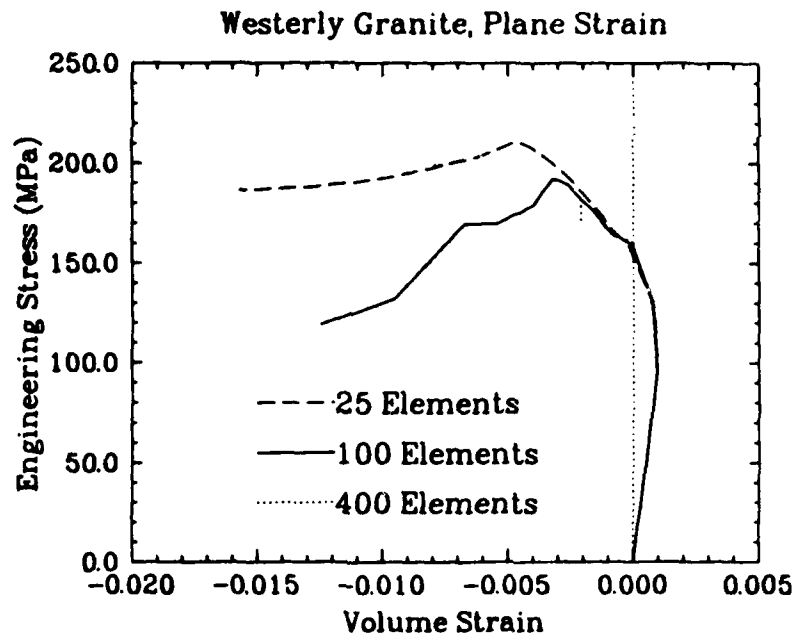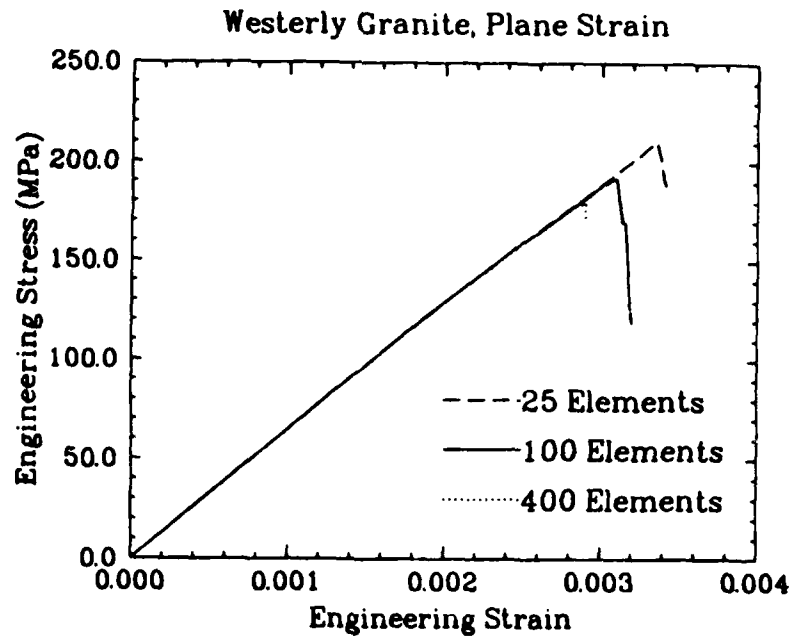
**Figure 15**

Stress-strain data calculated from model uniaxial compression tests using 25, 100, and 400 elements to model the rock.
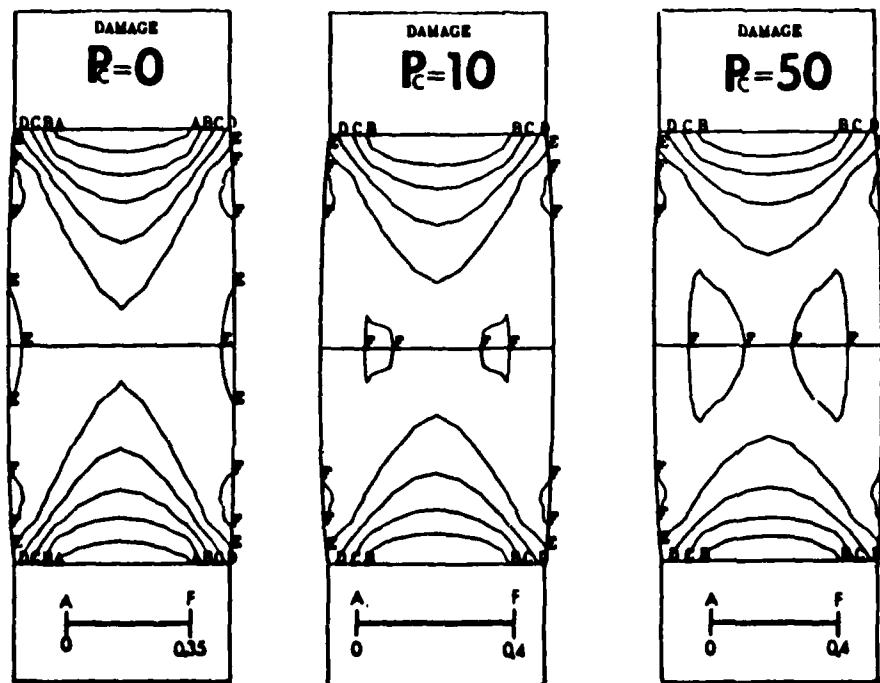
**Figure 16**

Contours of constant Damage at a point near the ultimate stress but before any failure has occurred. The scalar Damage is the magnitude of the Damage vector. The bar at the bottom of each figure gives the range of Damage associated with the contours.
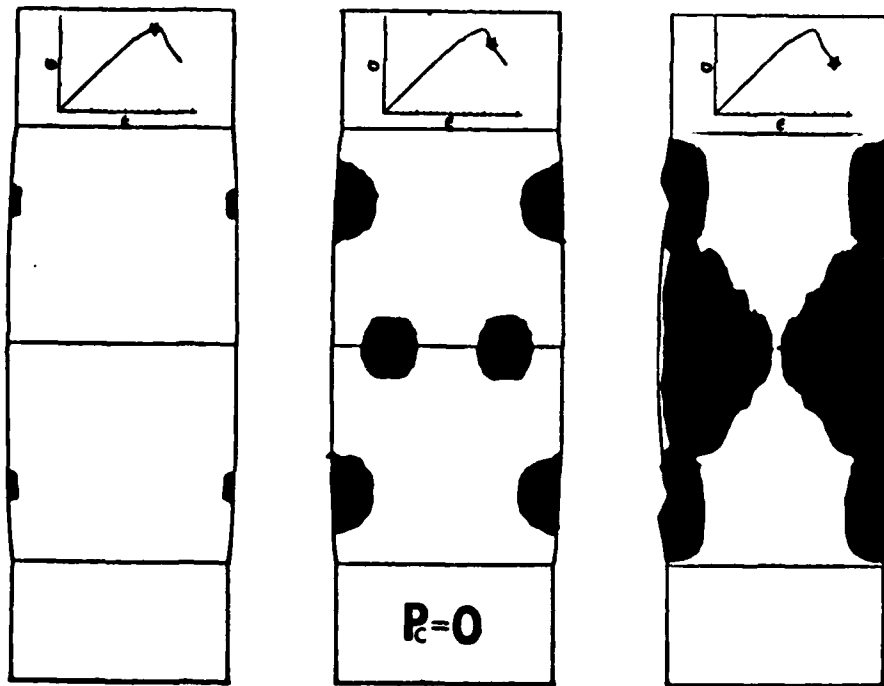
**Figure 17**

Progression of failure in a simulated plane strain uniaxial compression test. The dark areas represent elements that have gone into failure and are at some stage of softening. The schematic stress-strain curve at the top of each figure gives the approximate location on the specimen stress-strain response curve where the view is taken.
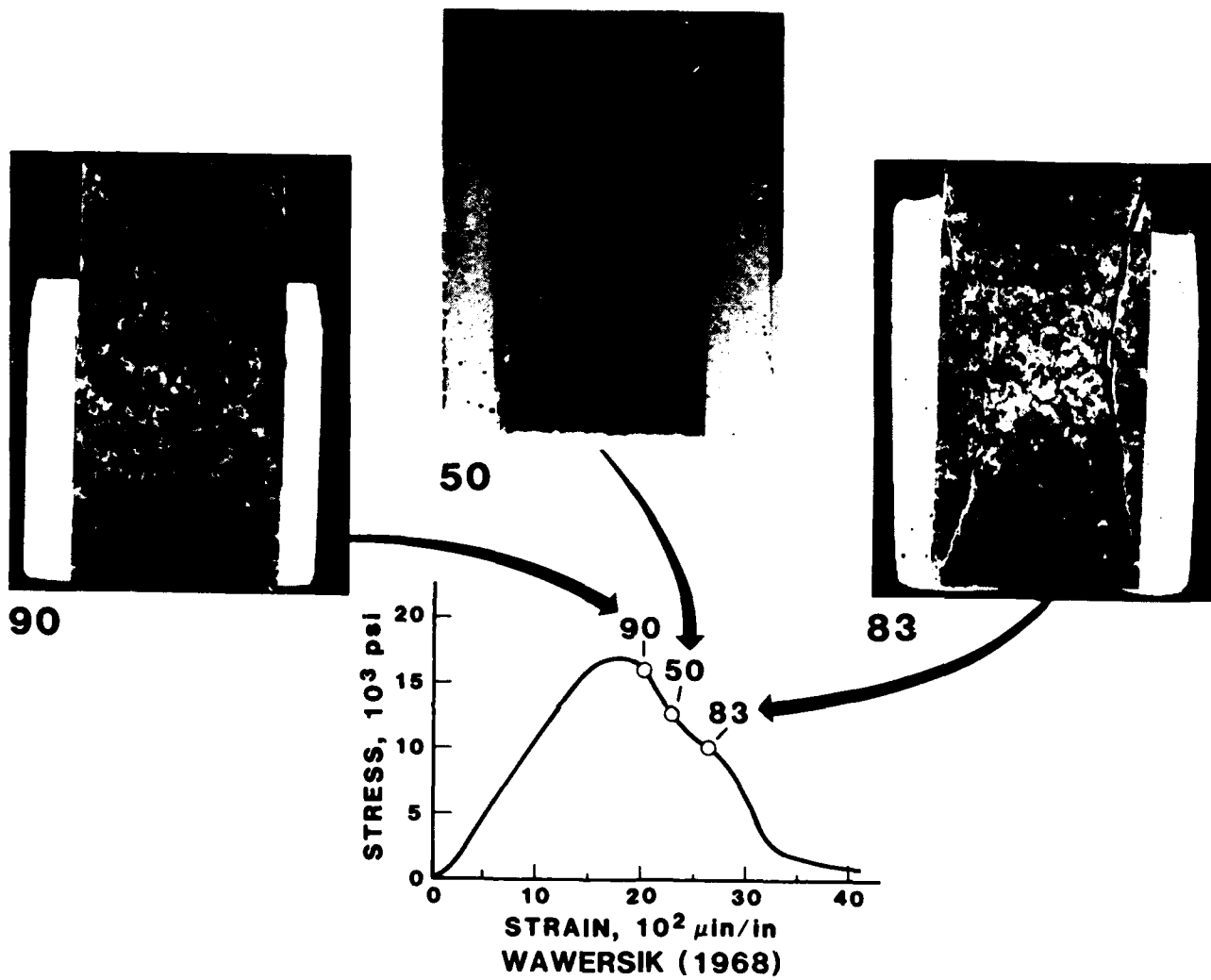
**Figure 18**

Sectioned, post-test samples of Tennessee marble from Wawersik [9]. Each sample is from a different uniaxial test that was stopped at the point indicated on the stress-strain curve. The lighter regions in the photographs of the sectioned samples are regions of higher damage.
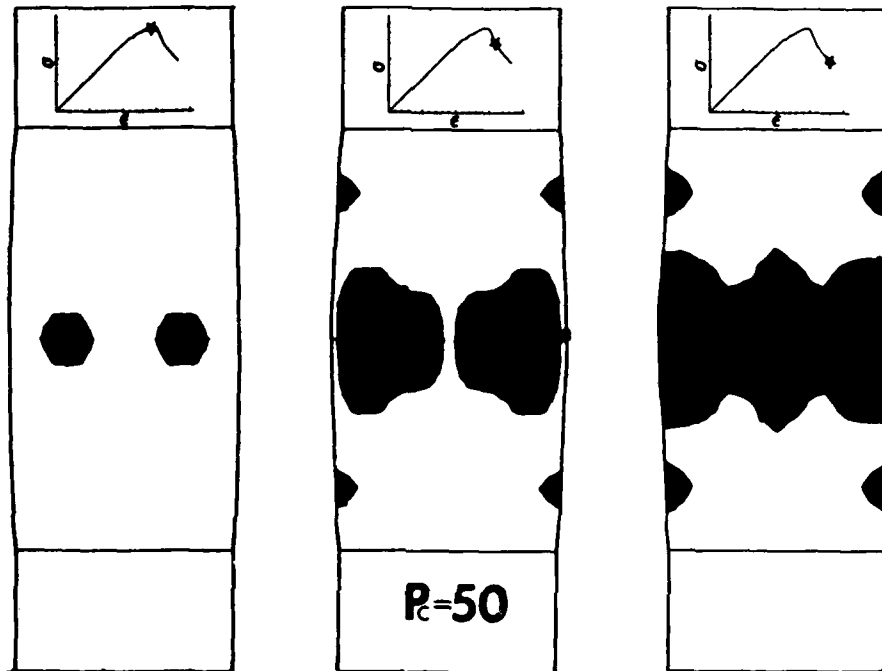
**Figure 19**

Progression of failure in a simulated plane strain triaxial compression test at 50 MPa. The dark areas represent elements that have gone into failure and are at some stage of softening. The schematic stress-strain curve at the top of each figure gives the approximate location on the specimen stress-strain response curve where the view is taken.
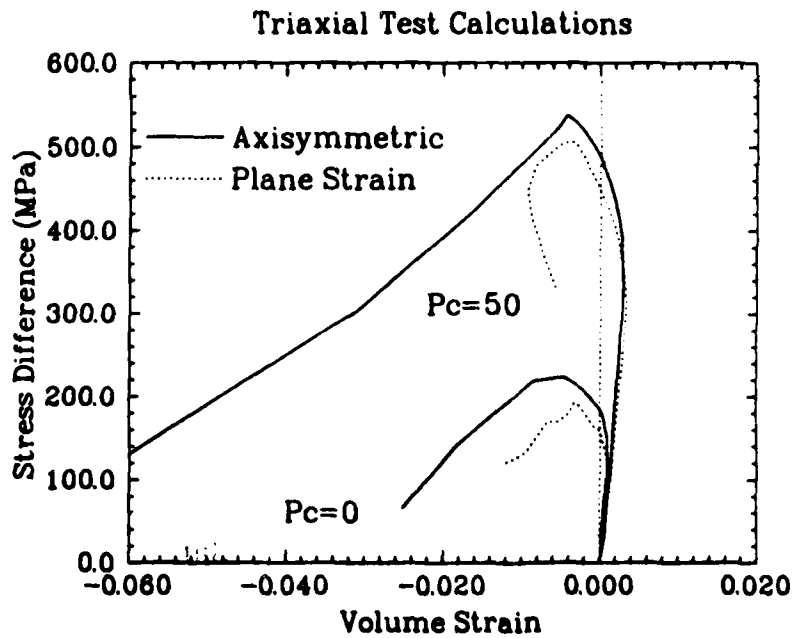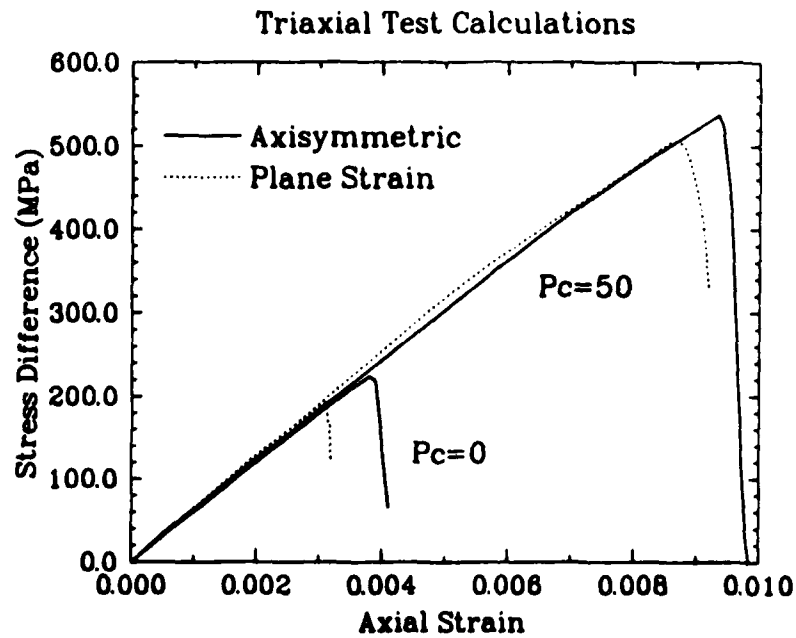
**Figure 20**

Comparison of stress-strain data calculated from tri-
axial compression test simulations using the axisym-
metric configuration with those calculated using the
plane-strain configuration.
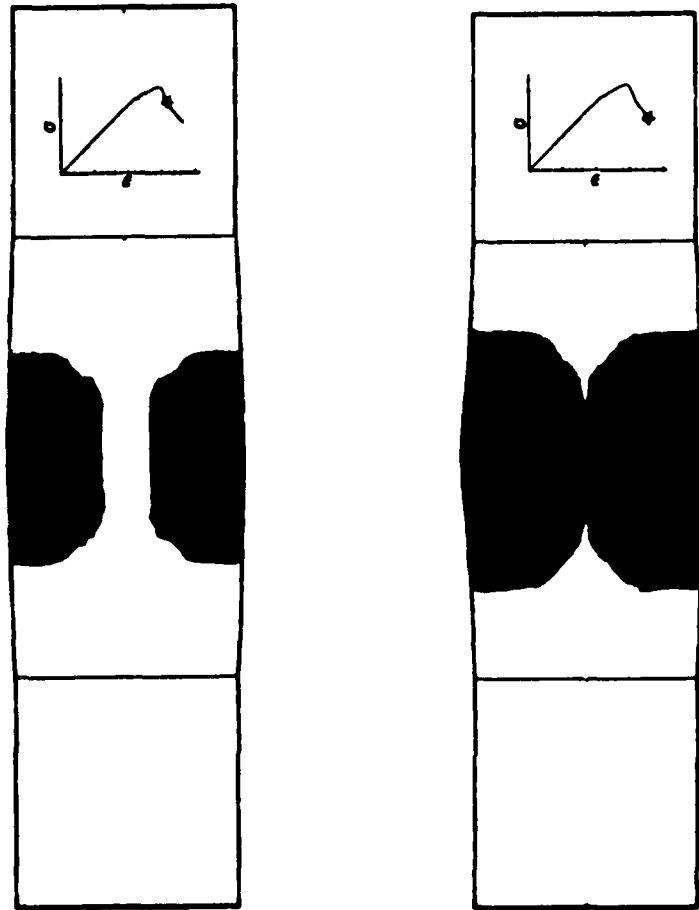
**Figure 21**

Progression of failure in a simulated uniaxial compression test in the axisymmetric configuration. The dark areas represent elements that have gone into failure and are at some stage of softening. The schematic stress-strain curve at the top of each figure gives the approximate location on the specimen stress-strain response curve where the view is taken.
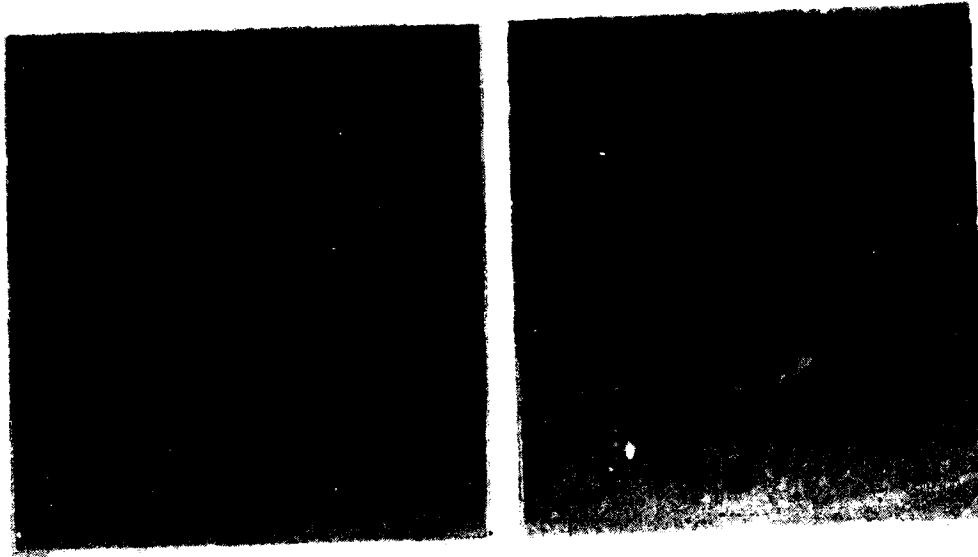
**Figure 22**

Photographs of an aluminum-filled epoxy sample after uniaxial compression. (a) Side view showing axial cracks similar to the axisymmetric hoop failure shown in Figure 21. (b) End view showing slabbing or hourglass fractures similar to the plane-strain failure shown in Figure 17.
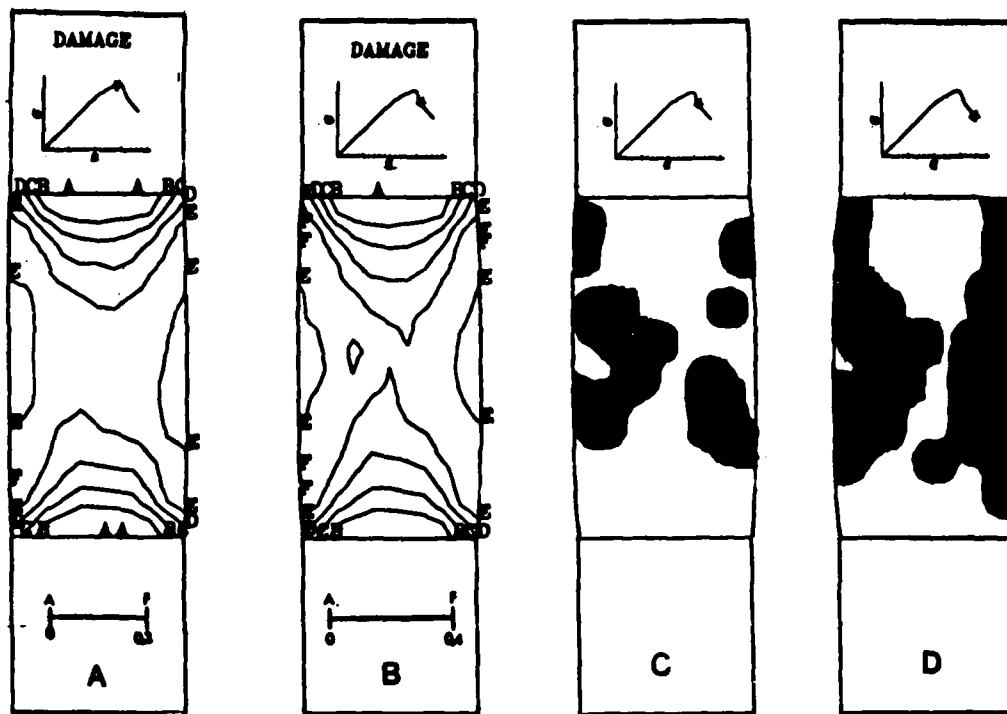
**Figure 23**

Results from uniaxial plane strain compression calculations using an initially random distribution of crack lengths. (a) and (b) are contours of constant Damage at points just before and just after peak stress. (c) and (d) show the progression of failure after the peak stress. Failed elements are shown by darkened regions.

# A MODEL TO PREDICT FRACTURE OF CONCRETE SUBJECTED TO VARYING STRAIN RATES

by
Surendra P. Shah
Professor of Civil Engineering
Director, Center for Concrete and Geomaterials
Northwestern University
Evanston, Illinois 60208

## 1. INTRODUCTION

Modern computer-aided analysis and use of concrete for special structures such as reactor containment vessels and missile storage silos, has led to a growing interest in the cracking behavior of concrete [1-4]. Such concrete structures are also likely to be subjected to short duration impulsive and impact loads in addition to static loads. Experimental results indicate that tensile, flexural and compressive strength of concrete increase with increase in rate of loading [5-7]. This implies that neglecting the 'rate effect' in structural design might result in underestimation of the strength of structures and hence uneconomical designs. On the other hand, there is experimental evidence to suggest that higher rate of loading might result in a brittle failure of concrete structures as compared to ductile failure at slow rate of loading [8-10].

In order to accurately evaluate the overall structural response under impact loading, a knowledge of the constitutive relationships and failure criteria of concrete, steel, and interface properties, over a wide range of strain rates (i.e., rates of loading) is essential. In this report, some relevant experimental results and an analytical model of concrete subjected to different rates of loading are discussed.

## 2. REVIEW OF DYNAMIC TEST METHODS

The effect of impact loading on mechanical properties of concrete has been reviewed in detail by Suaris and Shah [7], Mindess [11], Sierakowski

293

[12], and Reinhardt [13]. Many investigators (see for example, Reference 6) have studied the rate sensitivity of fracture strength of concrete in tension, flexure, and compression. Various test methods have been used for this purpose, as discussed next.

## 2.1 Test Methods

Conventional Drop Weight Tests: This is a simple qualitative test. In this test, a known weight is dropped on a specimen and the impact resistance is characterized by the number of blows required to either initiate visible cracking in the specimen or cause complete failure of the specimen. Evidently this method is dependent on the weight, size, and shape of hammer, drop height, and size of specimen. ACI Committee 544 recommends this test to evaluate the impact resistance of fiber reinforced concrete. Ramakrishnan et al. [14] used this technique to determine the performance of steel fiber reinforced concrete.

Explosive Test: This method involves use of explosive shocks for applying high rates of loading. This test is useful for studying scabbing and fragm ntation Bhargava and Rehnstrom [15] used explosives and high speed photography to study dynamic cracking behavior of plain and polymer modified concrete. Mayrhofer and Thor [16] used a blast-simulator to study the dynamic response of fibre and conventional reinforced concrete.

Charpy Impact Test: The Charpy Impact Test consists of a pendulum-type hammer striking a specimen, simulating either a cantilever beam or a three point bend specimen. This test was originally recommended for metals (ASTM). The impact toughness is characterized in terms of the energy required for total fracture of the specimen. The energy required for fracture is evaluated from the travel of the pendulum after the impact. The measured energy value includes the energy to fracture the specimen, energy absorbed by the testing system, and the kinetic energy imparted to the

294

specimen [17, 18]. Krenchel [19] and Johnston [20] used this test to evaluate the impact performance of steel fiber reinforced concrete in terms of energy absorption capacity relative to unreinforced matrix. The next step involved the use of an instrumented hammer in the conventional Charpy test. Thus the hammer load-time history could be obtained. Based on such Charpy impact tests of silicon carbide specimens, Abe, Chandan and Bradt [21] concluded that the energy calculated from the Charpy test is higher than the true fracture energy of the specimen and that the lower the true fracture energy, the higher is the discrepancy obtained from the Charpy test. Since the strength to weight ratio of concrete is much lower than that of metals, the conventional Charpy impact test could overestimate the energy absorption values of unreinforced matrix.

The above test methods do not facilitate rigorous quantitative analysis of the impact behavior of cement composites. One cannot obtain useul parameters for constitutive modeling purposes using the above experimental methods.

Instrumented Drop weight Test: The instrumented drop weight test consists of instrumented hammer and supports so that these serve as load cells. With the aid of adequate data acquisition systems, one can obtain load, displacement and strain versus time response of the specimen during the impact event. These results can be used to obtain design parameters such as modulus of rupture (MOR), Young's modulus, cracking strain, and energy absorbed (directly evaluated from load-deflection response) as functions of strain rate. Suaris and Shah [22] developed this test for studying the impact behavior of plain and fiber reinforced concrete (Figure 1). Recently, Bentur, Mindess and Banthia [24] developed a similar test set-up for testing large-sized concrete specimens.

Modified Instrumented Charpy Impact Test: Gopalaratnam, Shah and John

Figure 2. Modified instrumented Charpy impact testing system (17, 25, 26).

[17] developed the modified instrumented Charpy impact testing system (Figure 2). As the name suggests, the conventional Charpy machine was modified to include the following features among others [17, 25, 26]:

1) Concrete specimens larger than the conventional metal specimens could be tested.

2) Hammer and support loads could be recorded independently.

3) Deflections, strains, and crack growth could also be recorded.

This test set-up has been used for studying impact behavior of steel and glass fiber reinforced cement composites [18, 27], and fracture mechanics investigation of effect of impact loading on concrete [25, 26, 28]. Similar to the instrumented drop weight test, this method also yields paramters useful for constitutive modeling of concrete under impact loading.

Split Hopkinson Bar Test: The split Hopkinson bar test enables determination of stress-strain responses in compression and tension at high strain rates. The test was originally developed by Kolsky [29]. A schematic of this test set-up is shown in Figure 3. The specimen is located between two long bars, namely incident and transmtter bars. The specimen may be held in such a way that either a tensile or a compressive stress pulse, as desired, could pass through the specimen. The stess pulse is generated at the free end of the incident bar by an explosive charge or an impacting bullet. An excellent summary of the split Hopkinson bar technique is given in Reference 30. Reinhardt et. al. [1] and Malvern et. al. [32] used this method to study the high strain rate behavior of cement composites in uniaxial tension and compression, respectively.

Constant Strain Rate Test: Constant strain rate tests are deflection-controlled tests [see for example, References 22, 25 and 26]. Constant strain rate tests can be done in tension, flexure, and compression. This is an ideal test suitable for strain-softening materials such as concrte. But it may be difficult to achieve high strain rates in such tests.

## 2.2 Inertial Effects in High Strain Rate Tests

Inertial effects could become significant at higher rates of loading. Using a two degree of freedom model to represent the impact test set-up (see Figure 4), [Suaris and Shah, Reference 33] analyzed in detail the inertial effects in impact tests. The use of the hammer load signal alone can lead to erroneous results. The inertial loads could be neglected only if the hammer load cell response was identical to the support load cells. This required the use of a rubber pad to soften the contact zone between the hammer and the specimen. Suaris and Shah [33] validated this appraoch analytically using the model shown in Figure 4. Gopalaratnam, Shah and John [17] used this model to obtain guidelines for designing an impact test set-up, as discussed earlier.

Bentur et. al. [24] conducted instrumented drop weight impact tests on large-sized concrete specimens. The acceleration of the specimen was measured using accelerometers glued on the specimen. This enabled direct evaluation of the inertial effects experienced by the specimen. They reported that the inertial loads could be as high as 90% for concrete specimens. They also concluded that though the use of ruuber pad decreased the inertial effects, it also reduced the rate of loading, as expected. It should be noted that this was also observed by Suaris and Shah [33] and Gopalaratnam et. al. [17]. John [25] showed that the model shown in Figure 4 could be used to accurately predict the acceleration experienced by the specimen and hence the inertial effects obseved by Bentur et. A. [24].

## 2.3 Discussion

Several other studies using the various test methods described above have been conducted [34-47]. Based on the above review of dynamic test methods the following remarks can be made:

1. Instrumented impact tests (drop weight or Charpy) and splt Hopkinson bar tests can be used for developing constitutive models for concrete at impact rates.

2. Inertial effects have to be considered while analyzing the experimental results. In some cases direct measurements using accelerometers may be required.

3. To obtain the rate sensitivitiy of mechanical properties useful for constitutive modeling over a wide range of strain rates, instrumented impact (drop weight or Charpy) tests or split Hopkinson bar tests should be coupled with constant strain tests.


3. EXPERIMENTAL RESULTS OBTAINED FROM HIGH STRAIN RATE TESTS

Typical experimental load-deformation responses are shown in Figures 5-7. Figure 5 corresponds to uniaxial tension [13], Figure 6 to flexure [18], and Figure 7 to uniaxial compression [48]. The relevant conclusions regarding high strain rate behavior of concrete are listed below:

1. The peak strength increases with increase in rate of loading in tension, flexure, and compression (Figure 8 [49,50]).

2. The rate sensitivity (ratio of impact strength to static strength) is highest for tension and lowest for compression (Figure 8). Rate sensitivity in flexure is between that of tension and compression. This implies that rate sensitivity of mode I (tensile) cracking is probably responsible for the observed rate effects [49, 50, 51].

3. Young's modulus (E) is relaively rate independent from strain rate of $10^{-6}$ to 1.0 per second. This is shown in Figure 9, which was reported by Gopalaratnam and Shah [18] based on flexural impact results. This trend of relatively rate independent E was also observed by:

   a) Tinic and Bruhwiler [38] in uniaxial tension.

b) Suaris and Shah [49], and Ahmad and Shah [48] in compression.

c) John [25] in flexure based on load-crack mouth opening responses of notched beams at impact rates.

In contrast, Reinhardt [13] reported that E increaseswith increasing strain rate based on impact tensile tests. Their results indicated that the increase was about 25% at a strain rate of 1.0 per second.

4. Secant modulus evaluated at the peak load increases, see Figure 9. This was also observed by others in tension and compression [38, 48, 49]. This implies that the material behaves more linearly at high strain rates, i.e., prepeak nonlinearity decreases with increase in rate of loading.

5. John and Shah [26] used special brittle Krak Gages for studying the effect of impact loading on mode I crack growth in concrete, Figure 10. The experimental results indicate that prepeak nonlinearity in concrete is due to prepeak crack growth and this prepeak crack growth decreases with increasing strain rates, Figure 11.

6. The average crack velocity at strain rate of 0.4/sec. is less than 5% (about 100 m/sec.) of Rayleigh wave velocity in concrete, as observed by John and Shah (26). Bhargava and Rehnstrom (15) and Mindess et. al. (52) also reported similar crack velocities.

7. The deflection or strain at peak load also increases with the rate of loading (7, 13, 38, 48, 49).

8. The rate sensitivity of lower strength concrete is higher than that of higher strength concrete, Figures 12 (7, 8, 17, 28).

9. Most of the reported data correspond to strain rate less than or equal to 20 per sec. except those of Malvern et. al. (32) and Jawed et. al. (47).

299

## 4. MODELING OF CONCRETE BEHAVIOR UNDER HIGH STRAIN RATES

Some of the models proposed for predicting the rate sensitivity of fracture are described in this section [53-64].

**Thermally Activated Flaw Growth Models**: Many investigators have used thermally activated flaw growth models to predict the strain rate effects on fracture strength of materials such as concrete, ceramics and rocks. For example, Evans (62) assumed that the crack velocity is a power function of stress intensity factor (Equation 1) and derived a relationship between the fracture stress and rate of stress application as given by Equation 2. Note that Equation 2 was also derived by Charles (63).

$$V \propto K_I^N \tag{1}$$

$$V \propto (\dot{\sigma})^{1/N + 1} \tag{2}$$

in which $K_I$ = mode I stress intensity factor, $V$ = crack velocity, $\sigma_f$ fracture strength, $\dot{\sigma}$ = rate of stress application, and N is assumed to be rate independent. Mindess (11) reported a value of N = 30 for crack velocities up to $10^{-1}$ cm/sec. Based on impact crack growth measurements, John and Shah (26) concluded that log $K_I$ versus log $V$ relationship is nonlinear at higher rates of loading and hence Equation 1 is invalid at impact rates. Mihashi and Wittmann (64) derived an expression similar to Equation 2 (see Equation in Figure 13) by combining rate process theory and stochastic principles.

The rate process theory models were developed to predict crack under a constant load or a slowly increasing monotonically applied load. Under such loads crack growth is slow (crack velocity less than 1 mm/sec.). Hence this theory may not be valid at impact rates where crack growth is at much higher rate (15, 26, 51, 52), as shown in Figure 13. Kormeling (65) used the rate

theory to derive relations between fracture energy $(G_f)$, deformation rate and temperature.

**Dynamic Crack Models**: To determine the dynamic stress distribution around a fast moving crack tip, one can use equations of motion including the inertia terms. Freund (66) obtained dynamic elastic solutions for crack growth due to general loading. He concluded that the dynamic stress intensity factor decreases with increasing crack velocity as given by the following equations:

$$K_{ID} = k(V) \cdot K_{IS}$$

in which $k_{ID}$ = dynamic $K_I$, $K_{IS}$ = static $K_I$ for the same loading, and $k(V)$ = velocity correction factor, similar to the results of Broberg (67). The variation of $k(V)$ with crack velocity $(V)$ is shown in Figure 14. The maximum observed crack velocity at impact rates (strain rates about 1.0/sec.) is less than 5% of Rayleigh wave velocity $(C_R)$ (26, 51). For this small value of $V/C_R$, it can be seen in Figure 14 that the value $k(V)$ is close to 1.0 and hence $K_{ID} = K_{IS}$ in Equation 3.

Using the theory of linear elastic dynamic fracture mechanics for Heaviside loading of an isolated crack, Grady and Kipp (68) derived the following relationship between fracture strength, $\sigma_f$ and strain rate, $\dot{\epsilon}$, Equation 4.

$$\sigma_f \propto (\dot{\epsilon})^{1/3} \tag{4}$$

Not that Equation 4 is similar to Equation 2 with N = 2. This cubic rate dependence of fracture stress on strain rate was experimentally observed for a rock sample (Arkansas novaculite) at $\dot{\epsilon}$ = 0.8 x 10$^4$ to 2.5 x 10$^4$/sec. Equation 4 is applicable at very high rates only because it was derived

assuming that the crack travels at terminal velocity (acoustic velocity) after initiation. As discussed earlier, the observed crack velocity (V) is very low ($V/C_R$ < 5%) even at strain rates $\approx$ 1.0/sec (26, 51). Hence Equation 4 may not be applicable for concrte at strain rates observed so far.

From the above two sections, one can conclude that neither the rate process theory nor the elastic dynamic theory is capable of predicting the rate sensitivity of nonlinear material such as concrete in the strain rate regime of $10^{-7}$ to 10/sec.

Nonlinear Fracture Mechanics Model: For conditions where LEFM (linear elastic fracture mechanics) is applicable, one can calculate the critical stress intensity factor, $K_{Ic}$, from the notched beam tests using the measured peak load and initial notch depth, $a_o$. For cement based composites there is significant precritical (prepeak) nonlinear crack extension (also called "slow crack growth" or "process zone") (53-55). This can be seen in Figure 15. Crack growth was measured using Krak gages (see Figure 10) on one side of the specimen and strain was measured a the notch tip on the other side of the same specimen. The strain gage reading shows extensive "straining" (strain > 150 $\mu$ str) when the load response deviates from linearity. Close to this the Krack gage indicates crack initiation. One should include this prepeak crack growth for determining size independent $K_{Ic}$. It is very difficult to estimate the crack length based on surface measurements since the crack front is tortuous and discontinuous (26, 69-71)

To overcome this difficulty Jenq and Shah (53, 72) proposed an effective crack length approach to obtain a valid fracture toughness value. The effective crack length $a_e$ was defined such that the measured elastic crack mouth opening displacement was the same as that calculated using LEFM, Figure 16. They observed that $K_{Ic}$ and $CTOD_C$ (critical crack tip openinig displacement, (Figure 16) determined thus is essentially independent of size

302

of beam. Note that $CTOD_c$ is the elastic opening at the location of the initial notch tip when the initial notch, $a_o$, is assumed to grow to an effective crack, $a_e$, at the peak load. Note that $K_{Ic}$ defined by them is termed $K_{Ic}$. Jenq and Shah used this Two Parameter Fracture Model (TPFM) to explain the various size effect related phenomena in plain concrete (53, 72), fracture of steel fiber reinforced concrete (73), size effect in shear failure of reinforced concrete beas (74), and mixed mode fracture of concrete (75).

Based on the Two Parameter Fracture Model, John, Shah and Jenq (51) proposed a model to predict the rate sensitivity of mode I fracture of concrete. $K_{Ic}$ and E were assumed to be rate independent and $CTOD_c$ was assumed to decrease with increasing strain rates. John and Shah (28) used this model for studying high strength concrete, and the interaction of static strength and rate of loading. The proposed model predicts the generally observed trends in rate *effect in tension* (Figures 12 and 17), and flexure (Figures 18 and 19). The model also predicts the decrease of prepeak nonlinearity with increase in rate of loading, as shown in Figure 11. The difference in rate sensitivity in tension and flexure is predicted to be due to the size effect involved in the determination of flexural strength as shown in Figure 20. Note that a large beam haas the same rate sensitivity as uniaxial tension, Figure 20.

This model seems to be valid in the range $10^{-7}$ to 1.0/sec. This model was developed for Mode I fracture (as in the case of uniaxial tensile [76, 77] and flexural failure [26, 70, 72]. In actual failures, the fracture will be mixed mode (mode I, tensile, and mode II, shear) in nature. Experimental and theoretical study is in progress at Northwestern University to investigate the effect of rate of loading on mixed mode fracture of concrete (25). This study would be helpful in assessing the potential

variation of mode of failure of reinforced concrete structures with increasing strain rates.
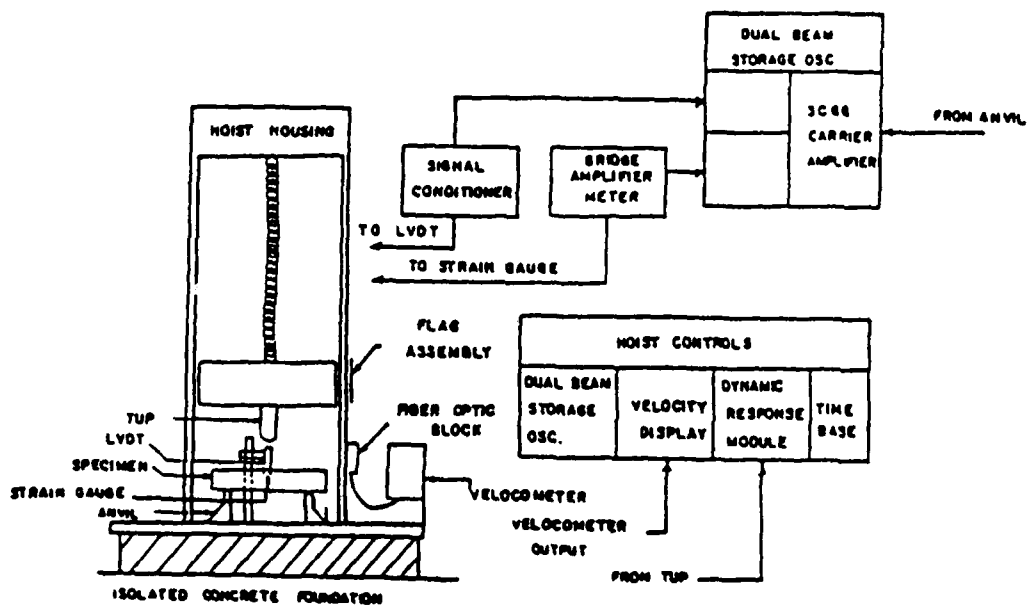
Figure 1.  Schematic of instrumented drop weight system (22).



① Energy scale (old, not used)
② Low blow fixture
③ Release mechanism
④ Pendulum
⑤ Instrumented tup
⑥ Isolated foundation
⑦ Instrumented anvil
⑧ Specimen
⑨ Fiber optic block
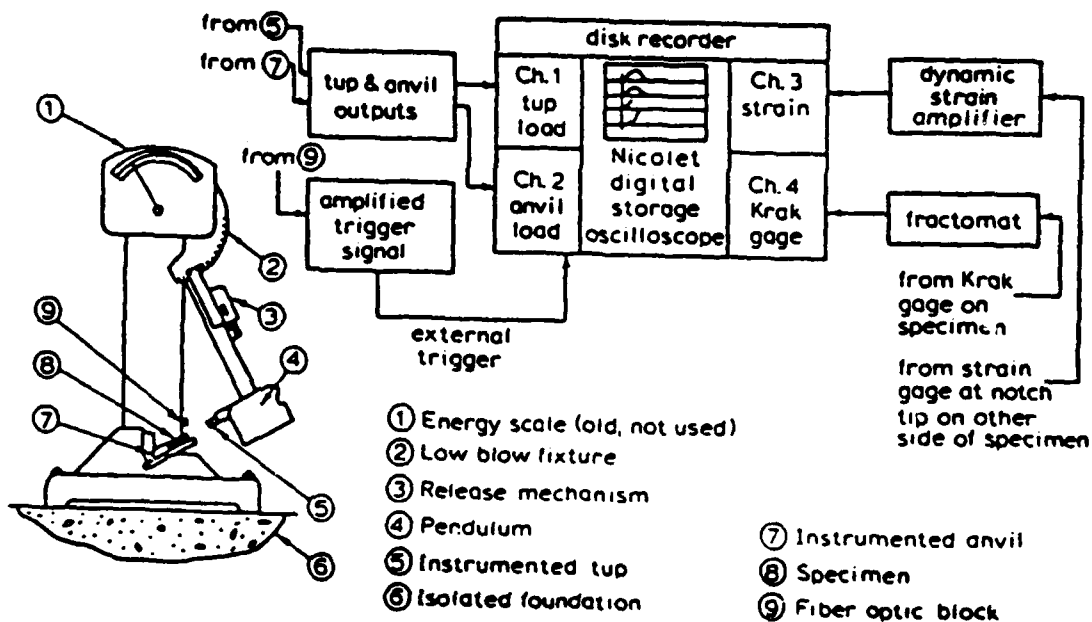
Figure 2.  Modified instrumented Charpy impact testing system (17, 25, 26).
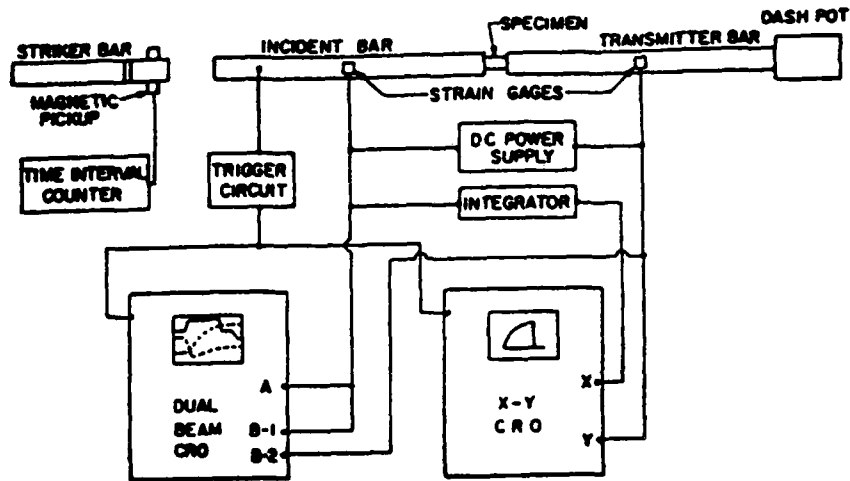
Figure 3. Schematic of compression split Hopkinson bar test set-up (30.



$m_h$ = mass of hammer

$m_b$ = mass of beam

$k_e$ = stiffness of contact zone

$k_b$ = stiffness of beam

$V_o$ = impact velocity of hammer
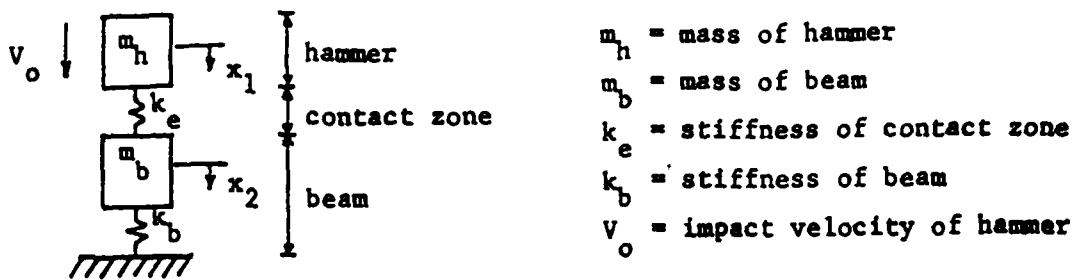
Figure 4. Two degree of freedom model (17, 33).
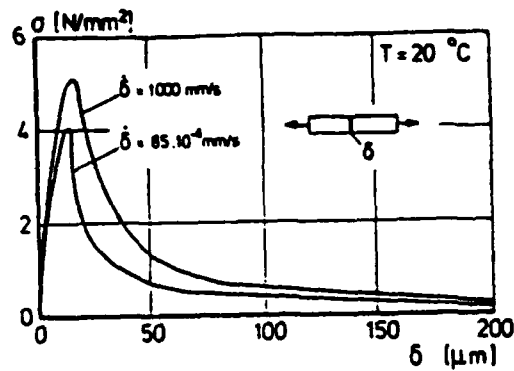


Figure 5. Uniaxial tension stress-strain curves of concrete
at two different rates of loading (13).
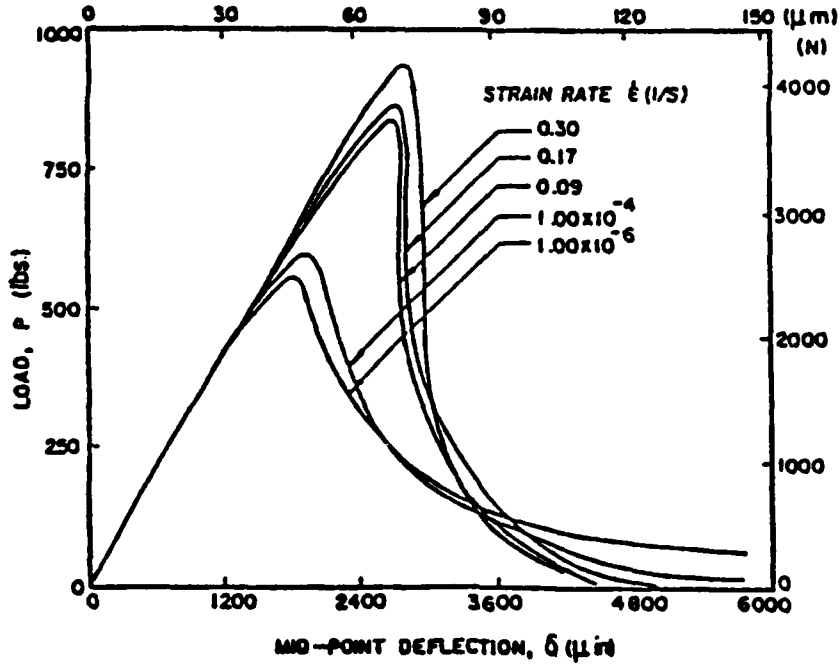
Figure 6. Typical load-deflection response of concrete in bending
at different rates of loading (18).
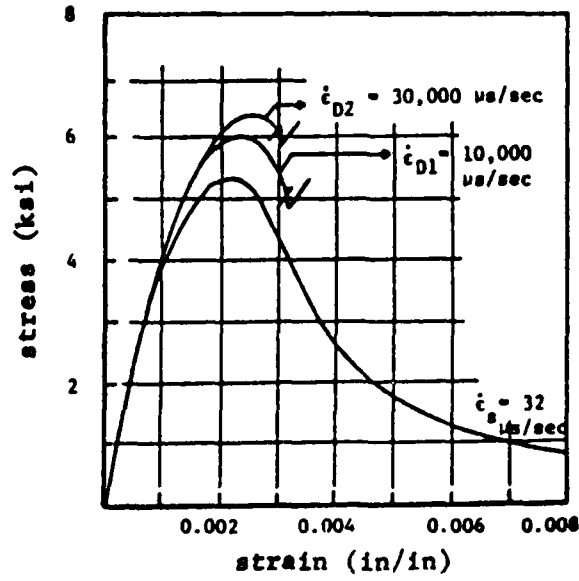


Figure 7. Typical effect of strain rate on the
compression stress-strain curve of
concrete (48).

307
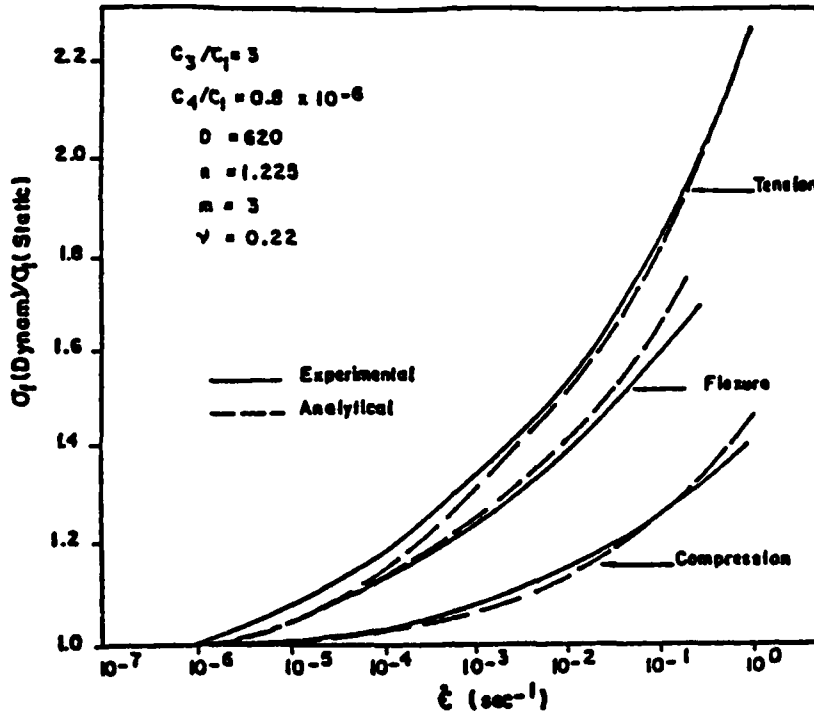
Figure 8.  Analytical and experimental curves for the effect of strain rate on the ultimate strength (49, 50).
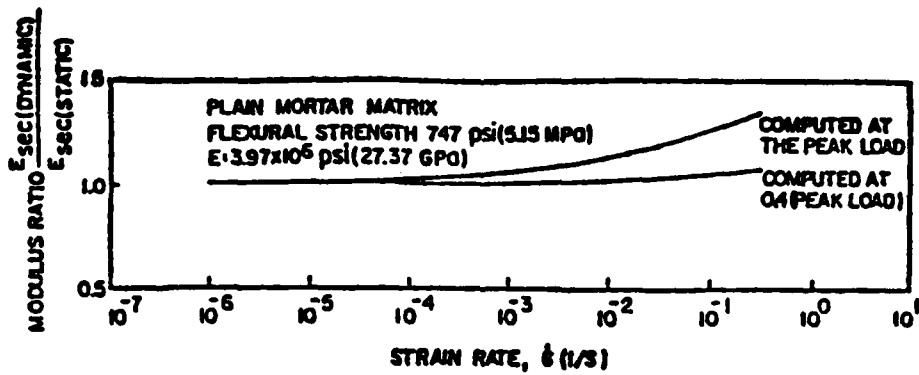


Figure 9.  Effect of strain rate on the elastic moduli of mortar (18).
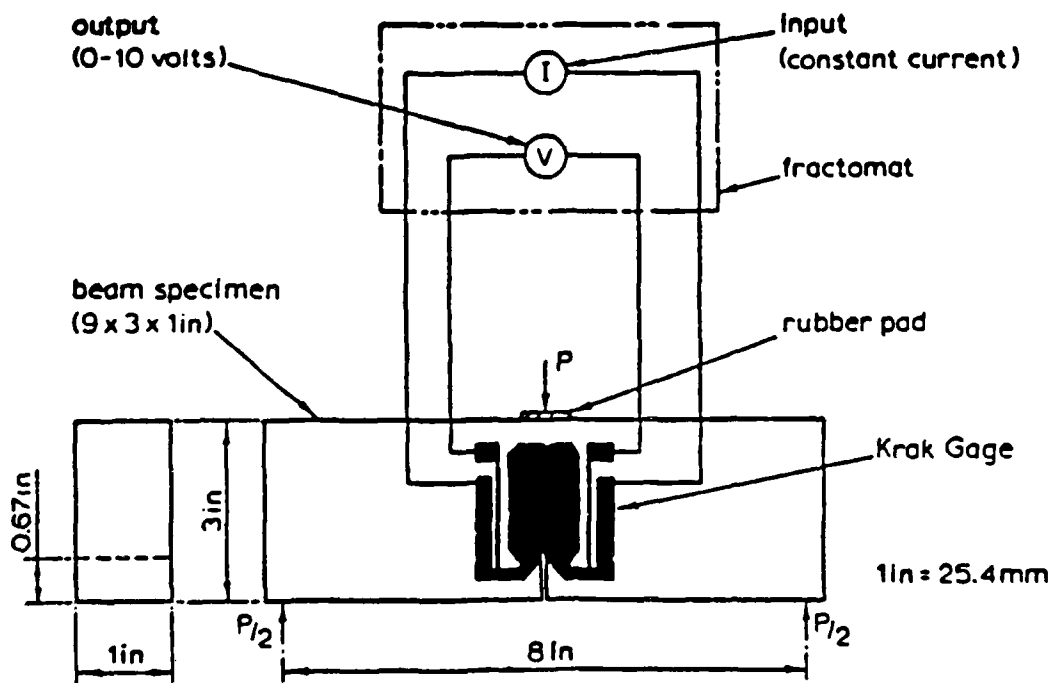
Figure 10.   Crack Growth measurement using Krak gages (26).
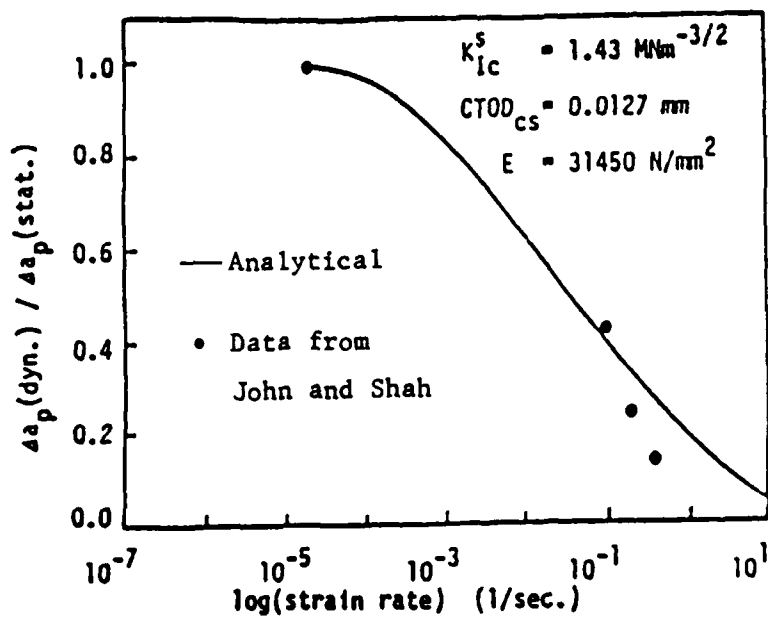


Figure 11.   Strain rate effect on precritical crack growth (26).
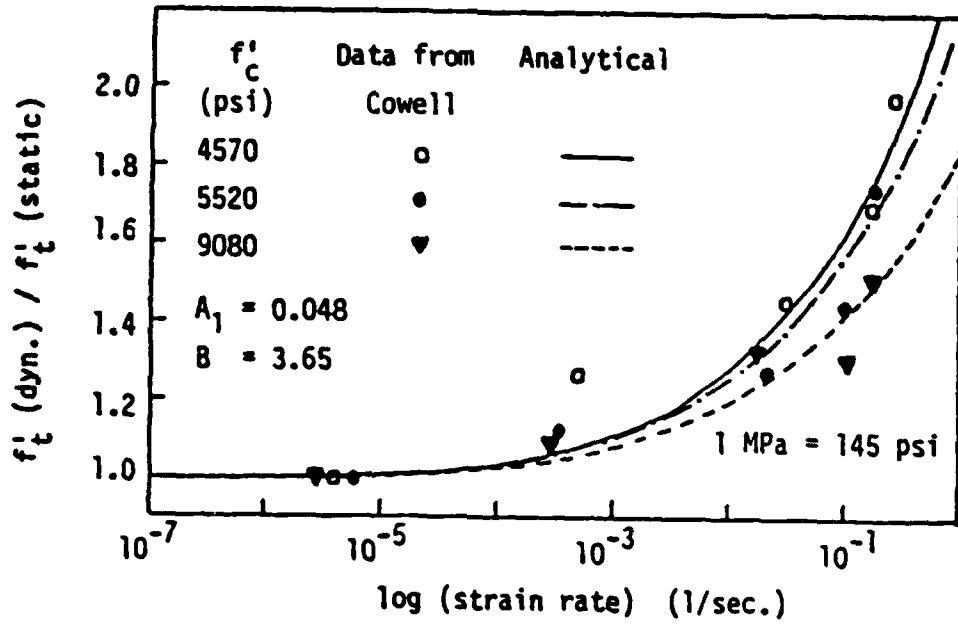
Figure 12.  Strain rate effect on tensile strength of concrete (28).
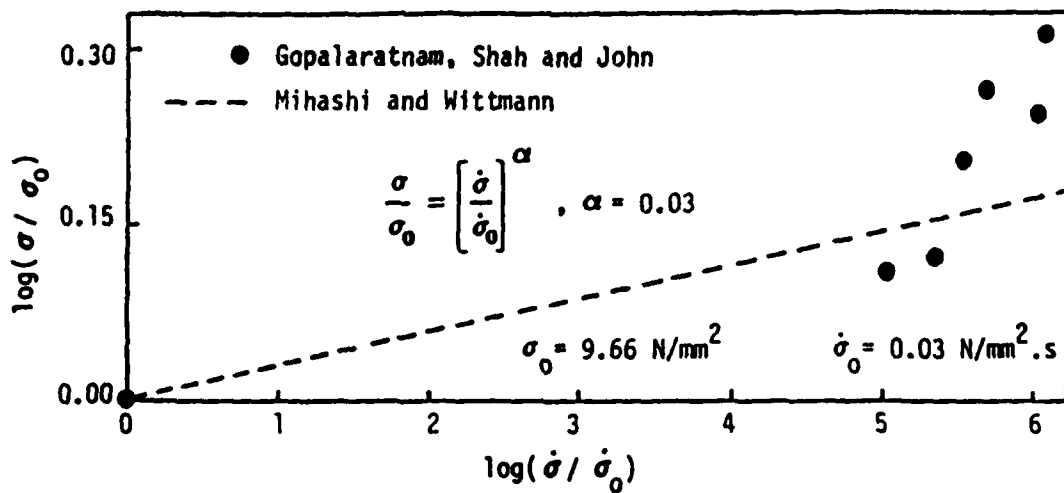


Figure 13.  Comparison of data from Reference 17 with rate theory equation.

310
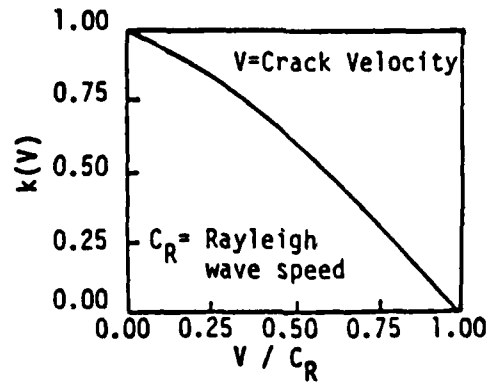
Figure 14. Variation of velocity correction
factor k(V) with crack velocity,
V (66).
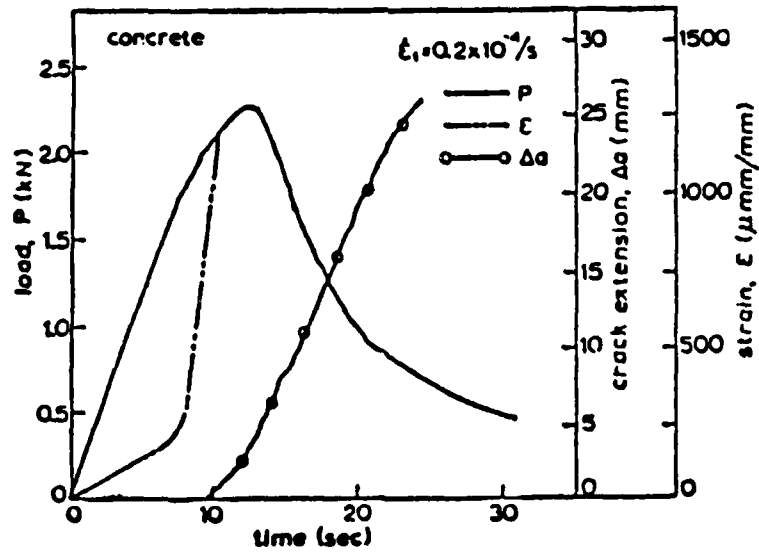


Figure 15. Typical crack growth test data (26).
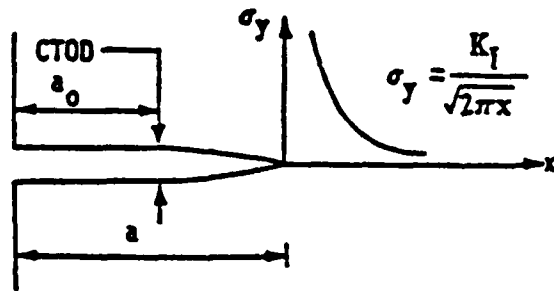
Effective Griffith Crack
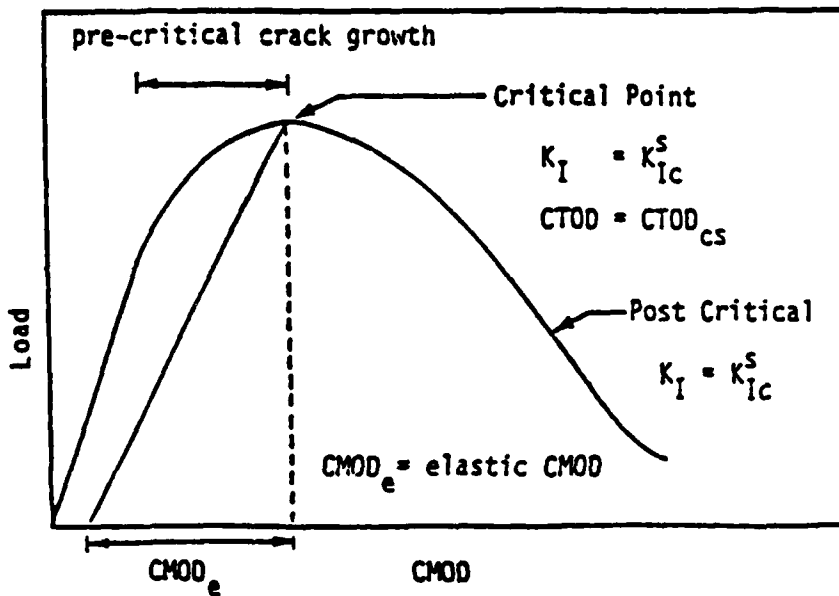


Typical Plot of Load vs. Crack Mouth Opening Displacement

Figure 16.  Two parameter fracture model (53, 72).

312
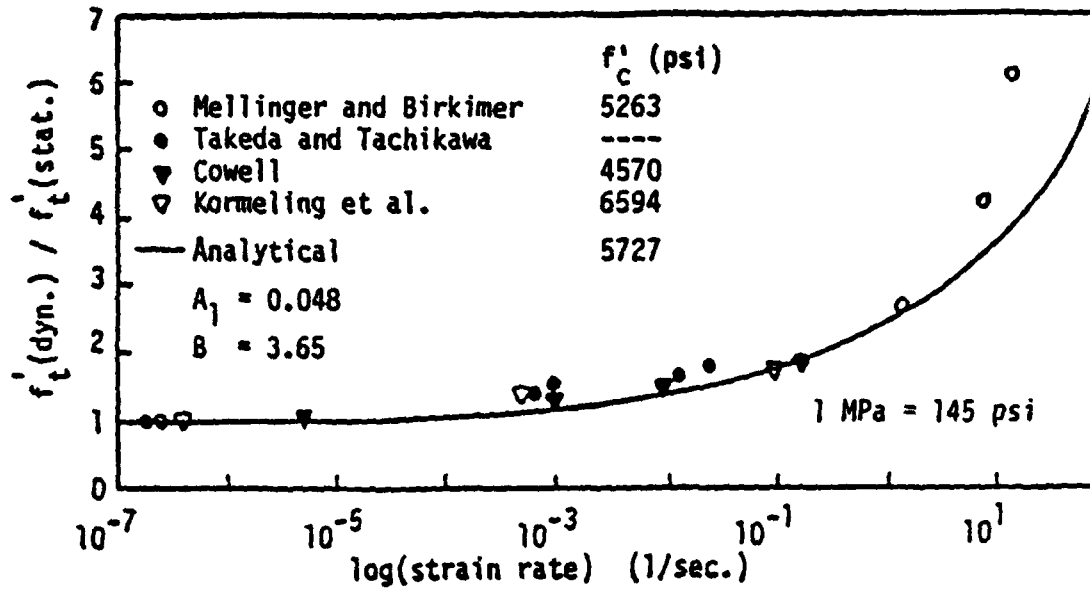
Figure 17. Strain rate effect on tensile strength of concrete (28).
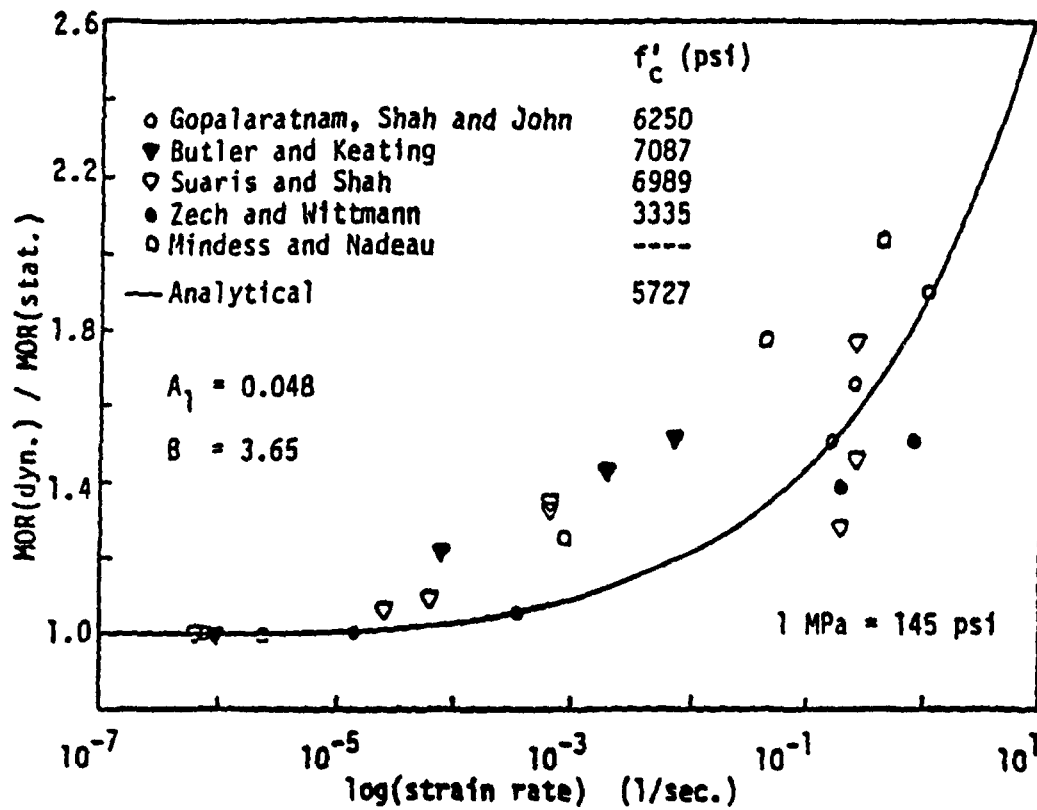


Figure 18. Strain rate effect on flexural strength of concrete (28).
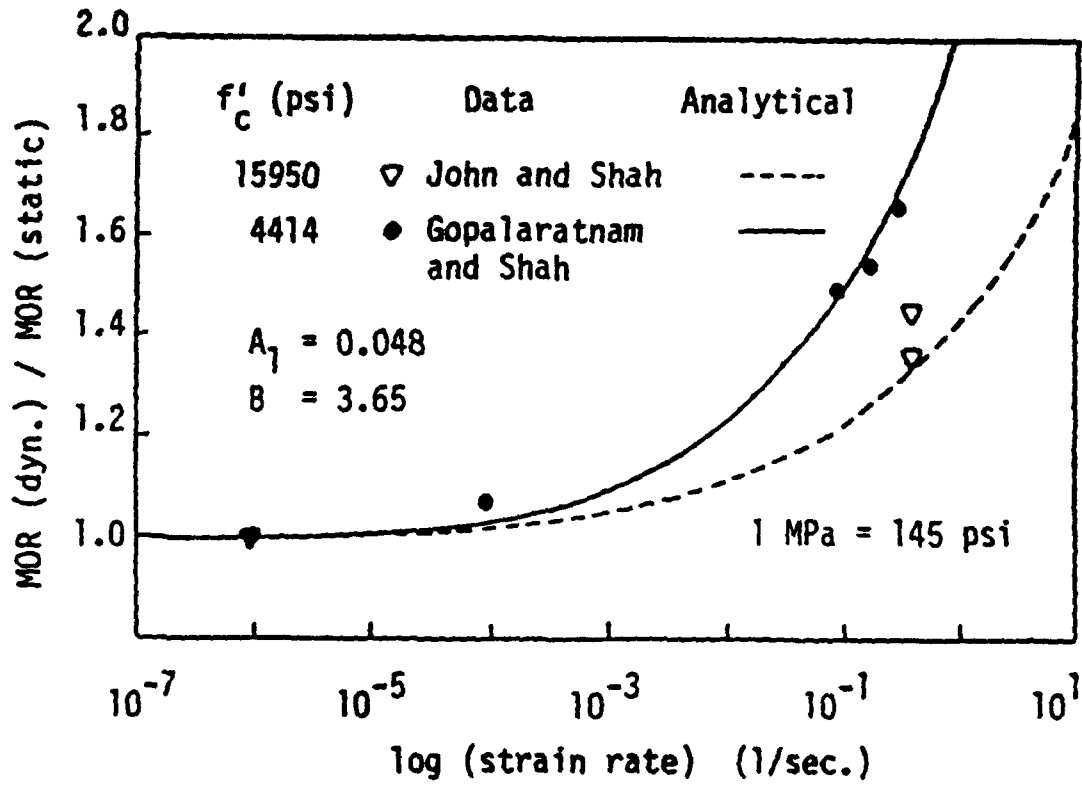
Figure 19. Interaction of strain rate and compressive strength on flexural strength (28).
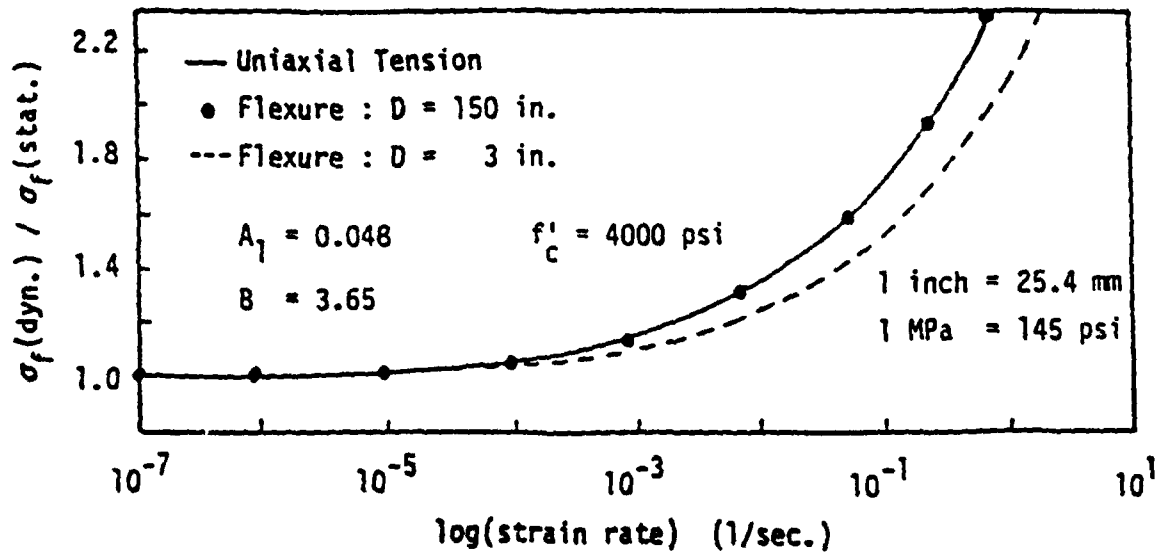


Figure 20. Model predicted size effect on rate sensitivity of flexural strength of concrete (28).

314

**REFERENCES**

(1) Shah, S. P. and Swartz, S. E. (Editors), June 1987. Proceedings, SEM-RILEM International Conference on Fracture of Concrete and Rock, Houston, TX, USA.

(2) Shah, S. P., (Editor), 1985. Application of fracture mechanics to cementitious composites, Proceedings, NATO Avanced Research Workshop, the Hague, Martinus Nijhoff.

(3) Bazant, Z. P. (Editor), 1985. Mechanics of geomaterials: Rocks, concretes, soils, New York, USA< John Wiley and Sons.

(4) Wittman, F. H. (Editor), 1986. Fracture toughness and fracture energy of concrete, The Netherlands, Elsevier Science.

(5) Concrete structures under impact and impulsive loading, June 1982. Proceedings, RILEM-CEB-IABSE-IASS Interassociation Symposium, Berlin (West), BAM.

(6) Mindess, S. and Shah, S. P. (Editors), 1986. Cement based composites: Strain rate effect on fracture, MRS Symposium Proceedings, 64.

(7) Suaris, W., and Shah, S. P., June 1982. Mechanical properties of materials under impact and impulsive loading, Introductory Report for the Interassociation (RILEM, CEB, IABSE, IASS) Symposium on Concrete Structures under Impact and Impulsive Loading, Berlin (West)), BAM, 33-62.

(8) Banthia, N. P., March 1987. Impact resistance of concrete, Ph.D. Thesis, Department of Civil Engineering, University of British Columbia, Canada.

(9) Mutsuyoshi, H., and Mahida, A., 1984. Properties and failure of reinforced concrete members subjected to dynamic loading, Transactions of the Japanese Concrete Institute, 6:521-528.

(10) Chung, L., and Shah, S. P., August 1987. Strain rate effects on bond stresses during earthquake loading, Pacific Conference on Earthquake Engineering, Organized by New Zealand National Society for Earthquake Engineering, Wairekei, New Zealand.

(11) Mindess, S., 1985. Rate of loading effects on the fracture of cementitious materials, Application of fracture mechanics to cementitious composites, (Editor: S. P. Shah), The Hague, Martinus Nijhoff, 617-636.

(12) Sierakowski, R. L., 1985. Dynamic effect in concrete materials, Application of fracture mechanics to cementitious composites, (Editor: S. P. Shah), The Hague, Martinus Nijhoff, 535-557).

(13) Reinhardt, H. W. 1986. In Cement based Composites: Strain rate effects on fracture, (Editors: S. Mindess and S. P. Shah), MRS Symposium Proceedings, 64:1-13.

(14) Ramakrishnan, V., Brandshaug, I., Coyle, W. V. and Schrader, E. K., May-June 1980. A comparative evaluation of concrete reinforced with

straight steel fibers with deformed ends glued together in bundles, ACI J., 77(3): 135-143.

(15) Bhargava, J. and Rehnstrom, A., May 1975. High speed photography for fracture studies of concrete, cement and concrete research, 5:239-248.

(16) Mayrhofer and Thor, June 1982. Dynamic response of fibre and steel reinforced concrete plates under simulated blast load, in concrete structurs under impact and impulsive loading, Proceedings, RILEM-CEB-IABSE-IASS Interassociation Symposium, Berlin (West), BAM, 279-288.

(17) Gopalaratnam, V. S., Shah, S. P. and John, R., June 1984. A modified instrumented Charpy test for cement based composites, Journal of Experimental Mechanics, SEM, 24(2): 102-111.

(18) Gopalaratnam, V. S., and Shah, S. P., 1985. Properties of steel fiber reinforced concrete subjected to impact loading, ACI Journal, 83(8):117-126.

(19) Krenchel, H., 1974. Fiber reinforced brittle matrix materials, SP-44, Detroit, ACI, 45-77.

(20) Johnston, C. D., 1974. Steel fiber reinforced mortar and concrete: A review of mechanical properties, fiber reinforced concrete, SP-44, ACI, 127-142.

(21) Abe, H., Chandan, H. C. and Bradt, R. C., 1978. Low blow Charpy impact of silicon carbides, American Ceramic Society Bulletin, 57(6):587-595.

(22) Suaris, W., and Shah, S. P., July 1983. Properties of concrete subjected to impact, Journal Structural Engineering, ASCE, 109(7):1727-1741.

(23) Naaman, A. E. and Gopalaratnam, V. S., November 1983. Impact properties of steel fiber reinforced concrete in bending. International Journal of Cement Composites and Lightweight Concrete, 5(4):225-233.

(24) Bentur, A., Mindess, S., and Banthia, N. P., 1986. The behavior of concrete under impact loading: Experimental procedures and method of analysis, Materials and Structures, RILEM, 19(113):371-378.

(25) John, R., Strain rate effects on fracture of cement based composites, Ph.D. thesis (supervised by S. P. Shah), Department of Civil Engineering, Northwestern University, Evanston, IL., 1987.

(26) John, R. and Shah, S. P., Summer 1986. Fracture of concrete subjected to impact loading, Journal of Cement, Concrete and Aggregates, STM, 8(1):24-32.

(27) Mobasher, B. and Shah, S. P. (in preparation). Impact behavior of glass fiber reinforced concrete, Department of Civil Engineering, Northwestern University, Evanston, IL., USA>

(28) John, R. and Shah, S. P., June 1987. Effect of high stength and rate of loading on fracture parameters of concrete. Proceedings of SEM-RILEM International Conference on Fracture of Concrete and Rock (Editors: S. P. Shah and S. E. Swartz), Houston, TX, USA>

(29) Kolsky, H., 1949. An investigation of the mechanical properties of materials at very high rates of loading, Proceedings, Phys. Soc., Sec. B62:676-700.

(30) Zukas, J. A., Nichclas, T., Swift, H. F. Greszczuk, L. B., and Curran, D. R., 1982. Impact Dynamics, New York, Johan A. Wiley and Sons.

(31) Reinhardt, H. W., Kormeling, H. A. and Zielinski, A. J., 1986. The Split Hopkinson bar, a versatile tool for the impact testing of concrete, Materials and Structures, RILEM, 19(109):55-63.

(32) Malvern, L. E., Tang, T., Jenkins, D. A., and Gong, J. C. 1986. In cement based composites: Strain rate effects on fracture (Editors: S. Mindess and S. P. Shah), MRS Symposium Proceedings, 64:119-118.

(33) Suaris, W., and Shah, S. P., Winter 1982. Inertial effects in the instrumented impact testing of cementitious composites, Journal of Cement, Concrete and Aggregates, ASTM, 3(2):77-83.

(34) Takeda, J. I., Tachikawa, H., and Fuimoto, K., June 1982. Mechanical properties of Concrete and steel in reinforced concrete structures subjected to impact or impulsive loadings, Concrete structures under impact and impulsive loading, RILEM-CEB-IABSE-IASS Interassociation Symposium, Berlin (West), BAM, 83-92.

(35) Cowell, W., June 1966. Dynamic properties of plain portland cement concrete, Tech. Rep. R447, U.S. Naval Engineering Laboratory, Port Hueneme, CA, USA.

(36) Mellinger, F. M. and Birkimer, D. L., April 1966. Measurements of stress and strain on cylindrical test specimens of rock and concrete under impact loading. Technical Report. 4-46, Department of the Army, Ohio River Division Laboratory, USA.

(37) Kormeling, H. A., Zielinski, A. J., and Reinhardt, H. W., May 1980. Experiments on concrete under single and repeated impact loading, Rep. 5-80-3, Stevin Laboratory, Delft University of Technology, Delft, The Netherlands.

(38) C. Tinic and E. Bruhwiler, 1985. Effects of compressive loads on the tensile strength of concrete at high strain rates, International Journal of Cement Composites and Lightweight Concrete 7(2); 103-108.

(39) Zielinski, A. J., 1986. Concrete under biaxial compressive-impact tensile loading, Fracture Toughness and Fracture Energy of Concrete, (Editor: F. H. Wittmann), The Netherlands, Elsevier Science, 479-489.

(40) Mindess, S. and Nadeau, J. S., 1977. Effect of loading rate on the flexural strength of cement and mortar, Bulletin of American Ceramic Society, 56(44):429-430.

(41) Butler, J. E. and Keating, J., 1980. Preliminary data derived using a flexural cyclic loading machine to test plain and fibrous concrete, Materials and Structures, 14(79):25-33.

(42) Zech, B. and Wittmann, F. H., 1980. Variability and mean value of strength as a function of load, ACI Journal, 77(5):358-362.

(43) Wecharatna,M. and Roland, E., May 1987. Strain rate effects as properties of cement-based composites under impact loading, Engineering Mechanics 5th Conference, ASCE, Buffalo, New York, USA, 113.

(44) Watstein, D., April 1953. Effect of strain rate on the compressive strength and elastic properties of concrete, ACI Journal, 49(8):729-744.

(45) Atchley, B. L. and Furr, H. L., November 1967. Strength and energy absorption capabilities of plain concrete under dynamic and static loading, ACI Journal, 745-756.

(46) Hughes, B. P. and Gregory, R., 1978. Compressive strength and ultimate strain of concrete under impact loading, Magazine of Concrete Research, 300(105):189-199.

(47) Jawed, I., Childs, G., Ritter, A., Winzer, S., Johnson, T., and Barker, D., 1987. High-strain-rate behavior of hydrated cement pasts, Cement and Concrete Research, 17(3):433-440.

(48) Ahmad, S. and Shah, S. P., Sept.-Oct., 1985. Behavior of hoop confined concrete under high strain rates, ACI J., 634-647.

(49) Suaris, W. and Shah, S. P., June 1984. Rate sensitive damage theory for brittle solids, Journal of Engineering Mechanics, ASCE, 110(6):985-997.

(50) Suaris, W. and Shah, S. P., March 1985. Constitutive model for dynamic loading of concrete," Journal of Structural Engineering, ASCE, 111(3):563-576.

(51) John, R., Shah, S. P., and Jenq, Y. -S., 1987. A fracture mechanics model to predict the rate sensitivity of mode I fracture of concrete, Cement and Concrete Research, 17(2):249-262.

(52) Mindess, S., Banthia, A., Ritter, A. and Skalny, J. P., 1986. Crack development in cementitious materials under impact loading, in Cement Based Composites: Strain Rate Effects on Fracture (Editors: S. Mindess and S. P. Shah), MRS Symposium Proceedings, 64:217-223.

(53) Jenq, Y. -S., and Shah, S. P., October 1985. A two parameter fracture model for concrete, Journal of Engineering Mechanics, ASCE, 111(10):1227-1241.

(54) Bazant, Z. P., Kim, J. K. and Pfeiffer, P., 1985. Continuum model for progressive cracking and identification of nonlinear fracture parameters, in Application of Fracture Mechanics to Cementitious Composites (Editor: S. P. Shah), The Netherlands, Martinus Nijhoff, 197-246.

(55) Hillerborg, A. Modeer, M., and Petersson, P. E., Nov. 1976. Analysis of crack formation and crack growth in concrete by means of fracture mechanics and finite elements, Cement and Concrete Research, 6(6):773-782.

(56) Takeda, J. and Tachikawa, H., August 1971. Deformations and fracture of concrete subjected to dynamic load, Proceedings, International Conference on Mechanical Behavior of Materials, Vol. IV, Concrete and Cement Paste, Glass and Ceramics, Kyoto, Japan, 4:267-277.

(57) Mlakar, P. F., Vitaya-Udom, K. P. and Cole, R. A., July-August 1985. Dynamic tensile-compressive behavior of concrete, ACI Journal, 82(4):484-481.

(58) Suaris, W. and Shah, S. P., May-June 1986. Discussion of Ref. 57, ACI Journal, 83(3):477-479.

(59) Takeda, J., Tachikawa, H. and Fujimoto, L., June 1982. Mechanical properties of concrete and steel in reinforced concrete structures subjected to impact or impulsive loads, Proceedings of RILEM-CEB-IABSE-IASS Interassociation Symposium, BAM, Berlin (West), 83-91.

(60) Kiger, S. A., and Getchell, J. V., September 1980. Vulnerability of shallow-buried flat roof structures, Technical Report S1-80-7, Report 1, 2, and 3, U. S. Army Engineer Waterways Experimental Station.

(61) Vos, E. and Reinhardt, H. W., September 1980. Bond resistance of deformed bars, plain bars and strands under impact loading, Report 5-80-6, Stevin Laboratory, Department of Civil Engineering, Delft University of Technology Delft, The Netherlands.

(62) Evans, A. G., June 1974. Slow crack growth in brittle materials under dynamic loading conditions, International Journal of Fracture, 10(2):251-259.

(63) Charles, R. J., December 1958. Dynamic fatigue of glass, Journal of Applied Physics, 29(12):1657-1662.

(64) Mihashi, H., and Wittmann, F. H. 1980. Stochastic approach to study the influence of rate of loading on strength of concrete, The Netherlands, Heron, 25(3).

(65) Kormeling H. A., 1986. The rate theory and the impact tensile behavior of plain concrete, in Fracture Toughness and Fracture Energy of Concrete, (Editor: F. H. Wittmann), The Netherlands, Elsevier Science, 467-477.

(66) Freund, L. B., 1972. Crack propagation in an elastic solid subjected to general loading: Parts I and II, Journal of Mechanics and Physics of Solids, 20:129-152.

(67) Broberg, K. B., 1960. the propagation of a brittle crack, Arkiv for Fysik, 18(6):159-192.

(68) Grady, D. E. and Kipp, M. E., 1979. The micromechanics of impact fracture of rock, International Journal of Rock Mechanics, Mining Science and Geomechanics Abstracts, 16:293-3-2.

(69) Diamond, S. and Bentur, A., 1985. On the cracking in concrete and fiber reinforced cements, in Application of Fracture Mechanics to Cementitious Composites (Editor· S. P. Shah), The Netherlands, Martinus Nijhoff, 87.

319

(70) Swartz, S. E. and Go, C. G., June 1984. Validity of compliance calibration to cracked concrete beams in bending, Experimental Mechanics, SEM, 24(2):129-134.

(71) Bascoul, A., Kharchi, F., and Maso, J. C., June 1987. Concerning the measurement of the fracture in a three points bending test on notched beams, Proceedings of SEM-RILEM International Conference on Fracture of Concrete and Rock, (Editors: S. P. Shah and S. E. Swartz), Houston, Texas, USA.

(72) Jenq, Y. S. and Shah, S. P. 1985. A fracture toughness criterion for concrete, Engineering Fracture Mechanics, 21(5):1055-1069.

(73) Jenq, Y. S. and Shah, S. P. 1986. Crack propagation resistance of fiber reinforced concrete, Journal of Structural Engineering, ASCE 112(10):19-34.

(74) Jenq, Y. S., June 1987. Fracture mechanics of cementitious composites, Ph. D. dissertation (Superivsed by S. P. Shah), Northwetern University, Evanston, IL, USA.

(75) Jenq, Y. S. and Shah, S. P., Accepted for publication, 1988. Mixed-mode fracture of concrete, in International Journal of Fracture.

(76) Gopalaratnam, V. S. and Shah, S. P., May-June 1985. Softening response of plain concrete in direct tension, ACI Journal, 82(3):310-323.

(77) Maji, A. and Shah, S. P., Process zone and acoustic measurements in concrete, Experimental Mechanics, SEM Paper No. 3609, March 1988.

# HIGH STRAIN RATE TESTING OF COMPOSITES

R. L. Sierakowski
Department of Civil Engineering
Ohio State University
Columbus, Ohio 43210

## Abstract

A review is presented of the high strain rate behavior of filamentary composite materials. The experimental techniques used in evaluating the dynamic performance of composites are chronicled as well as the types of composites materials studied by investigators. Research as to areas of needed research are addressed.

321

## Introduction

Dynamic loading effects occur in materials and structural elements by the application of rapidly applied loads produced over short time durations. For composite type materials, dynamic effects are particularly important due to concern with the impact resistance of these materials. Unlike metallic based materials, the multiphase structure of composites leads to complex interactions of the constituent elements. That is, at the fiber/matrix interface, the chances for micro-damage to develop at all dynamic loading levels are increased, leading to damage which, in turn, influences subsequent mechanical performance.

The complexity of the dynamic problem is further compounded by the fact that the intensity of the loading influences the loading rate, which affects the wave propagation and damage mechanisms occurrng in the composite material/structure. The distinction between material and structural response is pertinent in considering dynamic events since a clear definition between material response and structural response is an important issue for composites (Harding, [1]). Thus, in order to develop an understanding necessary for composite material behavior subjected to dynamic loading, it is necessary to study the interactive nature of dynamic events occurring during the loading process. As an example, in order to determine dynamic properties necessary for modelling dynamic events, it is necessary to study stress wave propagation as well as to know the material constitutive relations. However, to understand the wave propagation events the very same dynamic properties which are being sought must be known in order to input these parameters into the constitutive equations which are to be determined. Thus, understanding all three events must be synthesized in order to both understand and quantify dynamic effects.

This can be exemplified through Figure 1 shown below.
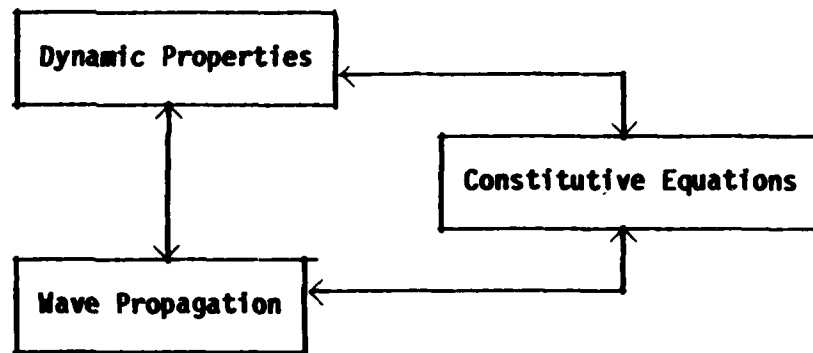


Figure 1.  Interactive Dynamic Effects

The aforementioned discussion is pertinent to the focus of two of the three issues highlighted in this workshop, these being:

- The ease with which model parameters can be determined directly from impact experiments

- Development in modeling related to the physical processes involved in deformation and failure

In order to pursue the aforementioned issues, it is useful to use experience gained from studies on the mechanical behavior of metals as a basis for predicting the general behavior of composites.

| $<10^{-3}$/sec | $10^{-3} - 10^{-1}$/sec | $10^{0} - 10^{1}$/sec | $10^{2} - 10^{4}$/sec | $>10^{4}$/sec |
|---|---|---|---|---|
| Constant Load Machines | Hydraulic or Screw Mechanics | Pneumatic or Mechanical Machines | Mechanical or Explosive Impact | Gas Gun or Expolosive Driven Plate Impact Devices |

Fig. 2  Loading Regimes and Experimental Test Techniques

As a reference point it is useful to refer to Figure 2 which illustrates a range of strain rate regimes with accompanying experimental test techniques. It is generally accepted that rate effects on metals (FCC, BCC, HCP, etc.)

323

generally become important in the range extending from 50 to 500/sec. The experimental procedures indicated have been used for obtaining data on such dynamic properties as:

strength
modulus
fracture toughness
damping
fracture surface energy
strain to failure

In the present case, primary focus will be given to studies of both continuous filament and discontinuous filament metal and non-metal matrix composites considering such parameters as fiber volume fraction, packing density, and fiber diameter. The issues important to the design of experiments for the dynamic testing of such composites are:

- Devising launch mechanisms to produce the desired stress state

- Fixturing specimens in the test assembly

- Selection of specimen geometry

- Test duration and equilibrium transit time

- Complexity of composite failure mechanisms

- Measuring transient parameters accurately

- Data collection, management, and interpretation

The dynamic test methods currently used for studying the dynamic properties of composites have been cited in the following table and each is discussed in the accompanying text. Included at the end of the text is both a reference list as cited and a bibliography for further use by the reader.

```
┌─────────────────────────────┐
│          TABLE I            │
│    Dynamic Test Methods     │
└─────────────────────────────┘
```

- Punch Tests

- Izod, Charpy Impact

- Drop Weight Tests

- Hydraulic/Pneumatic Machines

- Hopkinson Pressure Bar
  - Compression
  - Tension
  - Shear
  - Flexure

- Flyer Plate

For each of the cited test methods, a description of materials tested, loading rates, and data obtained from reference sources has been included.

```
┌─────────────────┐
│   Punch Tests   │
└─────────────────┘
```

```
┌──────────────────────────────────────┐
│ • Materials Tested                    │
│   - Weaves, Laminates                 │
│     (Pemaglass 22FE, NCRE, Graphite,  │
│     Kevlar, Glass)                    │
│                                       │
│ • Punch Loading Rates                 │
│   - 10⁻⁷ to 10 m/sec                  │
│   - Test Configuration                │
│     (Beams, Plates)                   │
│                                       │
│ • Data Obtained                       │
│   - Maximum Punch Load vs.            │
│     Punch Speed                       │
│   - Force Time Histories              │
│   - Fracture Damage                   │
└──────────────────────────────────────┘
```

- Punch Loading Rates
  - $10^{-7}$ to 10 m/sec
  - Test Configuration
    (Beams, Plates)

325

Punch tests have been performed in order to obtain data on maximum punch loads, force-time histories and fracture damage of composites. Harding [2], for example, has studied weaves and laminates consisting of epoxy and polyester based materials. As an example of the results obtained, the effect of punch speed on load-displacement for a glass/epoxy composite is shown in Figure 3 for punch speeds ranging from $10^{-7}$ to 16 m/sec. These data show that the maximum punch load increases by 250% for epoxy based materials and has been observed to increase by about 100% for polyester based materials. Further punch type tests have been performed on Kevlar-epoxy weaves as described by Duffey, Glass, Sutherland, [3], in which a series of low speed punch loads at less than 10 m/sec were performed. These results were used to compare with a theoretical finite element model by examining predicted and observed load-deflection curves. Some recent results on low speed impact in the 3 m/sec regime have been conducted, for example, by Shivakumar, Elber and Illg, [4]. In this study, two models were introduced, the first an energy balance and the second a spring mass model to predict impact force magnitude and duration as a function of impact velocity.

```
┌─────────────────────┐
│  CHARPY/IZOD TESTS  │
└─────────────────────┘
```

┌──────────────────────────────────────────────┐
│                                                │
│  • **Materials Tested**                        │
│                                                │
│     - Eglass/Epoxy, S-glass/Epoxy,             │
│       Kevlar 49, HMS-Graphite/Epoxy,           │
│       Thornel 75/Epoxy, Boron/Epoxy,           │
│       Modmore I/Epoxy,                         │
│       Modmore II/Epoxy,                        │
│       Boron/Aluminum                           │
│                                                │
│  • **Loading Rates**                           │
│                                                │
│     - .005 mm/sec to 1000 mm/sec               │
│       Test Configuration                       │
│       (Three Point Bending Tests)              │
│                                                │
│  • **Data Obtained**                           │
│                                                │
│     - Energy Absorption                        │
│     - Notch Sensitivity                        │
│     - Fracture Behavior                        │
│     - Rate Effects                             │
│       (Energy Absorption, Bending Strength)    │
│                                                │
└──────────────────────────────────────────────┘

Charpy/Izod tests have been widely used for obtaining such data as composite material energy absorption, specimen notch sensitivity, and composite fracture behavior. Such tests were originally designed to examine the energy absorbing qualities of metals and later used for studying resins and composites. Studies on composites using instrumented Charpy tests have been conducted, for example, by Beaumont, Riewald, and Zweben, [5]. These studies involved impact velocities of approximately 3.5 m/sec and for conditions where wave propagation effects were ignorable. A typical load history schematic for the impact event is shown in Figure 4. Based upon such data, a proposed Ductility Index was introduced by the authors defined as the ratio of initiation energy to propagation energy to evaluate the energy absorption within the material. This index can be considered as a useful screening tool for evalu-

327

ating the energy absorption of composites. In addition, both notched and unnotched (bend) Charpy tests provide an insight into the inherent differences between static and dynamic failure modes as observed, for example, by Krinke, Barber, Nicholas, [6] and shown in Figure 5. Most recently Ruiz and Mines, [7], and Mines and Ruiz [8] have performed instrumented Charpy tests on composites using V-notched and precracked fatigue specimens. For these tests, the recorded complex strain-time traces have been found to require electronic filtering to insure appropriate conversion to a force time diagram. A typical filtered Charpy load-time trace is shown in Figure 6.

Analytical work using FEM to evaluate the stress distribution of V notched Charpy type specimens in the near field, that is, in the vicinity of notches, and in the far field, has been studied by Chamis, [9]. An investigation of a variety of unidirectional composites including Boron, Graphite, Kevlar and Glass reinforced epoxy using NASTRAN as the FEM tool indicates a complex biaxial stress state in the vicinity of the notch involving transverse tension combined with interlaminar shear. Further away from the notch at the beam center, interlaminar shear appears to be the dominant fracture mode. Results of this analysis indicate that use of the Charpy test with a V notched specimen does not appear suitable for assessing non-metallic fiber composite impact resistance, because of the complex stress, strain, and strain rates encountered throughout the specimen.

```
┌─────────────────────────────┐
│                             │
│     DROP WEIGHT DEVICES     │
│                             │
└─────────────────────────────┘
```

```
┌─────────────────────────────────────────┐
│                                         │
│   • Materials                           │
│     - Eglass/Epoxy, S-glass/Epoxy       │
│       (ERL 2256), Graphite/Epoxy        │
│       (AS/3501), Hybrids                │
│       (ACIF-HT Carbon/Keylar 49/        │
│         Araldite F/AT 972)              │
│                                         │
│   • Loading Rate                        │
│     - 1 to 10 m/sec                     │
│     - Test Configuration (Beams)        │
│                                         │
│   • Data Obtained                       │
│     - Energy Absorption                 │
│     - Fracture Toughness                │
│     - Failure Mechanisms                │
│     - Strength Reduction                │
│     - Notch Sensitivity                 │
│                                         │
└─────────────────────────────────────────┘
```

## Drop Weight Tests

Drop Weight Tests have been used in a similar way to Charpy/Izod Tests to obtain dynamic properties data on material energy absorption, fracture toughness, failure mechanisms, strength reduction, and notch sensitivity. A schematic of such a drop test apparatus as used by Broutman and Rotem, [10], is shown in Figure 7. In this schematic, a drop weight with a preselected indentor tip is raised to a fixed height and released onto a specimen located on instrumented supports. Drop test results examining strength versus impact velocity for undirectional and cross-ply E glass/epoxy composites of differing geometries and drop weight heights have been studied for example by Broutman and Rotem, [10], and shown in Figure 8. Observations from these tests indicate that energy absorption is rate sensitive and that the principal mechanisms of energy absorption is delamination between layers. Studies on the impact strength of balanced angle ply composites have been examined for ex-

329

ample by Lifshitz, [11]. The importance of fiber orientation as it effects composite failure has been studied. For the E-glass/epoxy composites studied in Reference [11] a drop weight apparatus as shown schematically in Figure 9 was used. Some of the important results obtained from these studies include that for fiber orientations greater than $\pm45$, the maximum transverse strain theory agrees well with experiment and that the dynamic failure stress is of the order of 25% higher than the corresponding static value. More recent drop weight tests by G. Caprino, [12], for example, have examined predictive models for the residual tensile strength of carbon fiber composites. The Linear Elastic Fracture Mechanics model (LEFM) introduced has been shown to be useful for calculating residual tensile and compressive strength for low speed impacts. A typical residual strength curve is shown in Figure 10. Very recent drop weight tests on Kevlar/Carbon hybrid composites have been studied by Marom, Drukker, Weinberg, and Benloji, [13]. Results obtained from these experiments, which have been based on recorded force-time traces, indicate that the failure event in the carbon fibers always preceded that occurring in the Kevlar fibers, this attributed to the lower strain to failure for the graphite fibers. A typical impact energy curve as related to layer interchange and sequencing is shown in Figure 11.

---

**HYDRAULIC/PNEUMATIC MACHINES**

---

- **Materials**
  - Neat Resins (PMMA, CAB, Nylon, Polypropylene)
  - S-glass/Epoxy (828,871)

- **Loading Rates**
  - 1 to 50/sec/ 500/sec
  - Test Configuration (Tension)

- **Data Obtained**
  - Strain Rate Sensitivity
  - Failure Modes
  - Mechanical Properties
  - Constitutive Equation Modelling

---

## Hydraulic/Pneumatic Tests

Hydraulic/Pneumatic Tests have been conducted to obtain data on composite strain rate sensitivity, failure modes, dynamic material properties and constitutive equation modelling. Tests of this type are especially useful for controlled strain rate testing in the medium rate range. In this regard, Chou, Robertson, and Rainey, [14], studied the room temperature dynamic compressive behavior of a number of neat resins and their associated use for temperatures over a strain rate range extending from $10^{-4}$/sec to $10^{3}$/sec. A summary of work done on a variety of plastics has also been included by these authors and is noted in Figure 12. In particular, a unique open/closed loop testing machine has been designed for use in these experiments. The closed-loop mode incorporates a feedback system with a function generator for monitoring load and displacement. The open loop system uses fast acting valves with various orifice sizes, which when coupled with adjustable piston strokes insures a controlled displacement rate. Typical true stress-strain curves

331

obtained for a PMMA resin are shown in Figure 13, as well as true stress and strain rate behavior in Figure 14.

In the same time period Armenakas and Sciammarella [15], performed dynamic tests using a specially designed high speed apparatus in which an explosive type launch system was used. Specimens tested were plate like specimens fabricated from glass/epoxy and measurements were made by high speed photos taken of Moire patterns using a Beckman-Whitley camera. Stress-strain rate data for the glass/epoxy composite tested is shown in Figure 15. Some of the interesting observations made concerning composite failure include the fact that the number of fiber breaks at high rates is higher than at low rates and that the strain corresponding to the ultimate load is dependent on the strain at the ultimate load of the individual glass fibers.

Another interesting hydraulic/pneumatic device has been discussed by Matera and Albertson, [16]. This hydraulic/pneumatic device is shown in Figure 16 and uses gas and water, the latter placed in the upper chamber, while both chambers are initially at equal pressure. When the diaphragm shown in Figure 16 is ruptured, liquid is ejected, the piston moves up, with the pressure controlling the displacement rate. Strain measurements are made by means of a displacement transducer which is fixed to the upper bar which moves with the piston. This device allows strain rate measurements in the range 1 to 50/sec.

Among the most widely used tests for evaluating high strain rate effects in metals is the split Hopkinson pressure bar test. This type of test procedure has bee used to examine the dynamic response of materials in various modes of testing including compression, tension, and shear. Some of the important data obtained by using this test procedure include strain rate sensitivity, constituent properties, dynamic yield stress, damage propagation, and fracture mechanisms. The compression test represents one of the more fundamental testing modes for both metals and composites and a typical schematic of the test arrangement is shown in Figure 17, as described by

Chiddister and Malvern, [17]. Some of the important issues which need to be considered in both fixturing the test specimens and analyzing the data collected include minimizing radial inertia effects, accounting for wave propagation effects, and lubricating the specimen end faces. The latter is particularly important for composites insofar as the replication of the resultant failure modes is concerned. A somewhat more detailed view of the SHPB Compression apparatus showing the specimen configuration and wave transmission through the incident bar, the specimen, and the transmitter bar has been shown in Figure 18. This has been discussed in some early representative SHPB experiments performed by Lindholm [18], [19] on a variety of metals as well as some polymeric materials. Typical stress strain and rate dependent data for Cu is shown in Figure 19. This data obtained for a FCC type metal leads to a suggested form for the functional relationship between stress, strain, and strain rate as obtained from Figures 19 and 20 and is represented by an equation of the type $\sigma = \sigma_0 + \sigma_1 \log \dot{\varepsilon}$ where $\sigma_0$ refers to unit strain data and $\sigma_1(\varepsilon)$ increasing strain data. The form of this equation suggests a rate dependency which is due to a thermally activated process.

The application of the SHPB to epoxy based resins in a compression mode has also been studied by Lindholm [18]. Some typical static and dynamic curves are shown in Figure 21 for a specific epoxy. The rate sensitivity of this class of materials as well as the viscoelastic nature of the material is clearly evident.

Hauser [19] has examined experimental techniques for measuring the stress-strain relations of various classes of materials including metals, ceramics, and rock. Included in these studies was consideration of stress pulse shaping as related to the design of both the input/output bars for various loading modes including compression, tension, and shear. A schematic

334

of each mode of loading is shown in Figure 22. Variations of these loading modes have been applied to composites more recently. It should be noted that each of the aforementioned designs requires a dedicated SHPB configuration, launch mechanism, and specimen configuration and holding fixture. For the case of metals, and in an attempt to make the pressure bar versatile, Lindholm and Yeakley [21] proposed the design of a compressive SHPB bar which by specimen redesign could accomodate tensile specimens as shown in Figure 23. The introduction of a so-called hat type 'section for the tensile specimen was studied and this type of specimen showed no apparent geometrical effect when used for metallic based specimens. The application to composites, however, poses not only a manufacturing type problem but a geometrical/scaling problem as well. Some of the earliest work on the dynamic compressive testing of filamentry type composites was reported on by Sierakowski, et. al., [22]. These studies consisted of a systematic study of a carefully fabricated model system consisting of steel wire/epoxy specimens, with filament size, spacing, and volume fraction as parameters of study. Typical stress-strain curves for a particular filament size and volume fraction have been shown in Figure 24. The rate dependency of the composite system tested for various volume fractions and filament sizes is shown in Figure 25. Additional compressive bar high rate test data for E-glass/epoxy specimens has been shown in Figure 26. Further studies by Sierakowski, et. al., [23], on model steel wire/epoxy composites tested in compression on the SHPB examined fracture modes as well as the parameters mentioned above. Figure 27 shows the effect of volume percent reinforcement at both low and high strain rates as it effects peak stress. It is evident that in the dynamic case a peak stress associated with a filament size and volume fraction of reinforcement is evident, while such an observation is not true at low rates. This can be partly attributed to dif-

335

ferences in observed failure modes between low and high strain rates shown in Figure 28. Some high rate compression tests in controlled filament reinforced metal based composites have been conducted by Ross and Sierakowski, [24] for a Tungsten/Copper Composite in the SHPB. Once again, filament size and volume fraction were examined as related to how rate effects influence the flow stress of the material. Typical results are shown in Figure 29 with corresponding stress-strain curves shown in Figure 30. Additional tests on metal based composite systems in compression using a SHPB were conducted by Sierakowski and Lemkey, [25], on a model material (Al-Al$_3$Ni). Such composites have filaments aligned in situ in the matrix material using the process of rapid solidification. Typical stress-strain rate data as well as dynamic stress-strain data for this material are shown in Figures 31,32. An interesting observation is that even though the matrix is ductile a strain softening phenomena is observed for high loading rates. Some additional tests on metal based systems have been conducted by Weimer, et. al., [26], and Krause, [27]. A summary table of rate effect data obtained from these studies for various metal based composite systems is shown in Figure 33 with some of the particular compressive pressure bar design and specimen fixturing for the high strength composites tested is shown in Figure 34. Some of the interesting failure modes observed during these tests has been included in Figure 35. These may be compared to the steel-epoxy modes shown previously. Most recently, Bai and Harding [28] have studied fracture initiation under high rates of loading for glass/epoxy composites. The first observed sign of damage for single layer composites appears to be when failure occurs along the direction of the axially aligned reinforcement, while for the case of the multi-layer composites, it was found that longitudinal splitting may play an important role in the initial failure process.

336

```
┌─────────────────────────────┐
│   HOPKINSON PRESSURE BAR     │
└─────────────────────────────┘

        ┌──────────────┐
        │   TENSION     │
        └──────────────┘
```

```
┌──────────────────────────────────────────┐
│  • Materials                               │
│    -  Al-Al₃Ni, Ni-Nb-Al, FP/Al           │
│       SiC/6061, SMC, CFR (Polyester        │
│       KFR (Polyester), Glass/Epoxy         │
│       Carbon/Glass/Epoxy                   │
│       Carbon/Kevlar/Epoxy                  │
│       Woven Carbon/Epoxy                   │
│       Graphite/Epoxy                       │
│                                            │
│  • Loading Rates                           │
│    -  10² - 10⁴/sec                        │
│    -  Test Configurations                  │
│       (Tensile Coupons)                    │
└──────────────────────────────────────────┘
```

Considerable interest in the dynamic tensile testing of filamentary composites has occurred in recent years. A number of important issues related to the overall design of the tensile pressure bar system as well as the specimen configuration and fixturing occur for the tensile case. An early pressure bar apparatus capable of rates to 2000/sec, was suggested by Harding, [29], and used for testing a number of metal based materials. Such a configuration is shown schematically in Figure 36.

One of the earliest tests on composite type specimens tested in a tensile mode was performed by Matera and Albertini, [16]. These tests were performed on eutectic type composites $Al-Al_3Ni$ and Ni-Nb-Al using a modified pressure bar apparatus shown schematically in Figure 37. Some typical strength versus

strain rate data for Al-Al$_3$Ni composites is shown in Figure 38 for a range of temperatures. It has been noted that the response of this system to high strain rates is controlled mainly by the aluminum rich matrix. Continued improvement in tensile pressure bar device for high strain rate testing of metal based materials has been suggested by Tatro, et. al., [30], and Nicholas, [31] and [32]. Each of the systems shown schematically in Figures 39,40 represent a different configuration for both introducing the dynamic stress into the specimen as well as specimen configuration and fixturing; all important elements for filamentry composite specimens.

Results obtained from the first test procedure, Tatro, et. al., [30], has shown that difficulties exist in the design of the specimen gripping as well as specimen size effects, which has resulted in a wide scatter in test results. A more reproducible tensile pressure bar scheme for metals is that of Nicholas, [31], which uses a threaded type specimen. Data obtained for a wide variety of metals has been shown to be in agreement with other investigators. A modification of the aforementioned tensile device for testing particulate, short fiber, and continuous fiber type composites was introduced by Ross, et. al., [33]. Particular attention was paid to the design of the specimen holding configuration as shown schematically in Figure 41. For the SiC/606/Al, SMC, and FP/Al composites, which can be machined to produce threaded specimens, high strain rate data can be obtained. Also, for some types of composites which cannot be machined, a smooth contoured waisted type specimen may be useful. Most recently, Welsh and Harding, [34], have conducted high rate tensile tests using the pressure bar for a variety of continuous filament composites. Materials tested include carbon, glass, and Kevlar reinforced polyester resins. Some typical results obtained for several strain rates for carbon and glass are shown in Figure 42. It has been ob-

served that there is an effect of strain rate on failure strength and the fracture appearance for impact loading. An extension of tensile dynamic response for hybrid type composites was studied by Saka and Harding, [35]. A typical waisted type specimen used in the studies is shown in Figure 43 with a schematic of the SHPB arrangement and wave diagram shown in Figure 44. Some dynamic stress-strain curves obtained for various types of composites are shown in Figure 45. It has been observed by Saka and Harding, [35], that fracture for carbon fiber reinforced plastics show limited fiber pull out with local cracking in the resin in planes perpendicular to the applied load. For the case of glass fiber reinforced plastics an extended damage zone with no clearly defined fracture surface and considerable fiber pull-out has been noted. Additional studies on the behavior of glass/epoxy, graphite/epoxy and carbon/glass hybrids has been reported on by Saka and Harding, [36]. A schematic of the test configuration used in the study as well as typical results obtained for a glass weave composite relating stress to strain rate is shown in Figures 46, 47. Of note in these results, is that the yield stress shows a more significant increase with strain rate than does the maximum stress. Most recently Liu and Chiem, [37], have proposed a tensile test device for composites patterned after the overall test device of Tatro, 1980 [30], and the specimen configuration/fixture of Ross, et. al., [33]. A schematic of the bar apparatus and Lagrangian wave diagram are shown in Figure 48 with typical stress-strain data obtained for woven carbon/epoxy composites shown in Figure 49.

While the tensile HPB has been modified for use with composites, another high rate technique based upon an expanding ring as proposed by Hoggat and Recht, [38], has been modified for use with composite type specimens. While this technique offers an opportunity to obtain extremely high strain rates however, it is difficult to determine the stresses accurately. The technique does however provide for a uniform deformation in the specimen and avoids wave propagation effects. A schematic of this device as proposed by Hoggat and Recht, [38], for thin metal rings is shown in Figure 50. An extension of this device to graphite/epoxy composites with different ply constructions has been studied by Daniel, et. al., [39]. A schematic of the device is shown in Figure 57 with a typical dynamic stress-strain curve shown for the composite studied shown in Figure 52. While a dynamic stress-strain curve is obtained, difficulties noted are that the specimens need to be of tubular construction with accompanying difficulty in machining and the loading procedure requires an explosive discharge.

```
┌─────────────────────────────┐
│   HOPKINSON PRESSURE BAR     │
└─────────────────────────────┘

        ┌──────────┐
        │  SHEAR   │
        └──────────┘

┌────────────────────────────────────────┐
│  •  Materials                           │
│                                         │
│     -  Polymethylene Oxide,             │
│        Polycarbonate Graphite/Epoxy     │
│        Polyamide                        │
│                                         │
│  •  Loading Rates                       │
│                                         │
│     -  $10^2$ - $10^4$/sec              │
│     -  Test Configurations              │
│        (Short Cylinder, Thin Walled     │
│        Tubes, Beams)                    │
└────────────────────────────────────────┘
```

One of the important test modes for composites is the shear configuration. Torsional pressure bars have been developed for metals in order to eliminate such effects as friction and transverse stresses due to radial inertia as present in axial loading. Duffy, [40] has used a torsional pressure bar as shown in Figure 53 to test thin walled tubes of metal materials. To test matrix materials made of a variety of plastics, Vinh and Khalil, [41], have used a special torsional impact machine of the type shown schematically in Figure 54 for polymethylene which in turn has been used in the development of dynamic constitutive equations. Further, torsional PB bar development for large strain measurement of metals has been contributed by Stevenson, [42]. The specimen fixity for these experiments has made use of an epoxy resin cement.

The dynamic fragmentation of ceramic type materials using the torsional PB has been studied by Costin and Grady, [43]. Most recently, Gilat and Pao, [44], have developed a torsional PB for studying the dynamic response of various materials including polymer doped hydraulic cements, Sierakowski, Gilat and Wolfe, [45]. A schematic of both the pressure bar and wave diagram as well as typical shear stress-strain curves for the polymer hydraulic cements are shown in Figures 55,56.

While all the aforementioned torsional pressure bar designs could be extended to the testing of various classes of composites, few have been. Recently Warner and Dharan, [46], have suggested a pressure bar experimental arrangement for the testing of composite short beam shear specimens as shown in Figure 57. Both the interlaminar and transverse shear configurations for the composite beams have been tested using this experimental arrangement with data for the interlaminar shear mode shown in Figure 58. It has been observed that the interlaminar shear remains relatively constant for all loading rates while the transverse shear decreases with increasing strain rate.

```
┌─────────────────────────────┐
│   HOPKINSON PRESSURE BAR     │
└─────────────────────────────┘

        ┌─────────────┐
        │   FLEXURE   │
        └─────────────┘

┌───────────────────────────────┐
│  • Materials                   │
│    -  Steel                    │
│                                │
│  • Loading Rates               │
│    -  $10^2$ - $10^4$/sec      │
│    -  Test Configurations      │
│       (Beams)                  │
│                                │
│  • Data Obtained               │
│    -  Fracture Toughness       │
│    -  Crack Initiation         │
│    -  Load Time History        │
└───────────────────────────────┘
```

A modification of the Hopkinson Pressure Bar for studying the fracture toughness of materials has been examined by Mines and Ruiz, [8] and Ruiz and Hines, [7]. The technique devised is shown schematically in Figure 59 with recorded strain-time histories also shown in Figure 59. Some difficulties that are associated with data reduction for Charpy tests are accountability for inertia forces within the specimen, output trace oscillations, and the question as to whether specimen fracture occurs at the maximum load. Some of these difficulties can be avoided by tests using a pressure bar type test technique. Specifically, the HPB provides a technique for obtaining a well defined impulse load in which fracture occurs before reflection of the stress waves at the distal end of the bars. Also, the load application is sufficient in time to encompass the fracture time and such occurrences as specimen movement in the loading anvils is eliminated.

343

While the technique has not been adopted to composites, it appears that such an application may be useful.

```
┌──────────────────────────┐
│                          │
│      FLYER PLATE TESTS    │
│                          │
└──────────────────────────┘
```

- **Materials**
  - Quartz Cloth Reinforced Phenolic

- **Loading Rates**
  - $10^4$ -$10^6$/sec
  - Test Configurations
    (Beams, Plates)

- **Data Obtained**
  - Constitutive Modelling
    Parameters
  - Pulse Attenuation
  - Dynamic Fracture
  - Stress Wave Induced Damage
  - Material Properties Degradation

In order to study the response of materials at very high pressures and under a state of uniaxial strain, loading rates, flyer plate tests have been used with applications to composites related to composites of the cloth reinforced type. As an example of the technique, the single and double flyer plate impact apparatus described by Berkowitz and Cohen, [47] and [48], is shown in Figure 60. Some classes of stress wave induced damage for composites dynamically loaded in such experimental arrangements is shown in Figure 61. Some of the important design issues for flyer plate experiments include the launch mechanism, which usually involves an explosive type discharge or magnetic driven propulsion, alignment of the flyer plate in free flight, and instrumentation of the target material.

344

Recently, Rajendran and Bless, [49], have surveyed high strain rate material behavior and reviewed and described some new experimental techniques including a double flyer plate technique. While such techniques have not been applied to composites, this application does indeed seem feasible.

CONCLUDING REMARKS

It should be noted that in the design of experiments for studying the dynamic behavior of composites, a clear distinction needs to be made between material versus structural response. This has been noted in a recent review by Harding, [1], concerning the effect of high strain rates on material properties. In particular, the material response is exemplified by insensitivity to load application and specimen geometry while structural response is related to both specimen geometry and material properties. Thus, the design of experiments is compounded by the difficulty to distinguish carefully between these two response modes.

As noted in the present review, a description of dynamic test methods developed for obtaining high strain rate data on the mechanical response of metals and extended to composites has been reviewed. Since composites are multiphase materials, the dynamic test data as reported on for metals has importance as related to the performance of metal matrix composites. In addition, rate dependent data for non-metallic matrices has also been studied, however, less information is generally available on the rate dependency of the fiber phase of composites due to the inherent difficulties in the testing of filaments and fiber bundles. The characterization of the constituents is indeed important to assessing the performance of composites of the fiber reinforced type, however, the complex interaction occurring between the reinforcing fibers and matrix phase result in difficulties in assessing the rate dependency of the constituent phases. This type of complex behavior has been

345

noted as for example that as the rate of testing is increased, the corresponding failure mode changes. Thus, while some progress in extending dynamic test techniques to composites and developing new rate dependent tests for composites has been made, assessing the mechanical behavior of composites will rest with the ability to clearly distinguish the response mode of the specimens tested, that is, to specifically note the geometrical and material properties features associated with the specimens tested. At issue, therefore, are such important factors as the processing variables involved in specimen fabrication, quality control of same, role of the fiber/matrix interface, environmental conditioning of the specimens, and selection of individual constituent phases, that is, the respective matrices and fibers selected for study.

The effect of high strain rates on composite material properties can at best be stated as a rapidly developing field. Much of the development for this class of materials is based upon understanding and experience gained from metal materials. For filamentary type materials, which represent a significant interest class of composites, a number of important research issues arise. Among these are the complex interactions occurring between the fiber and matrix, the effect of fiber coatings on composite performance, and the quantification of microdamage on composite response and failure. All of these issues reflect upon the difficulties associated not only with static strength measurements but also with the design of high rate test devices. This does not address other important factors and parameters significantly affecting material strength including time and temperature effects, moisture effects for polymer matrix composites, and the processing/fabrication aspects of various classes of composites.
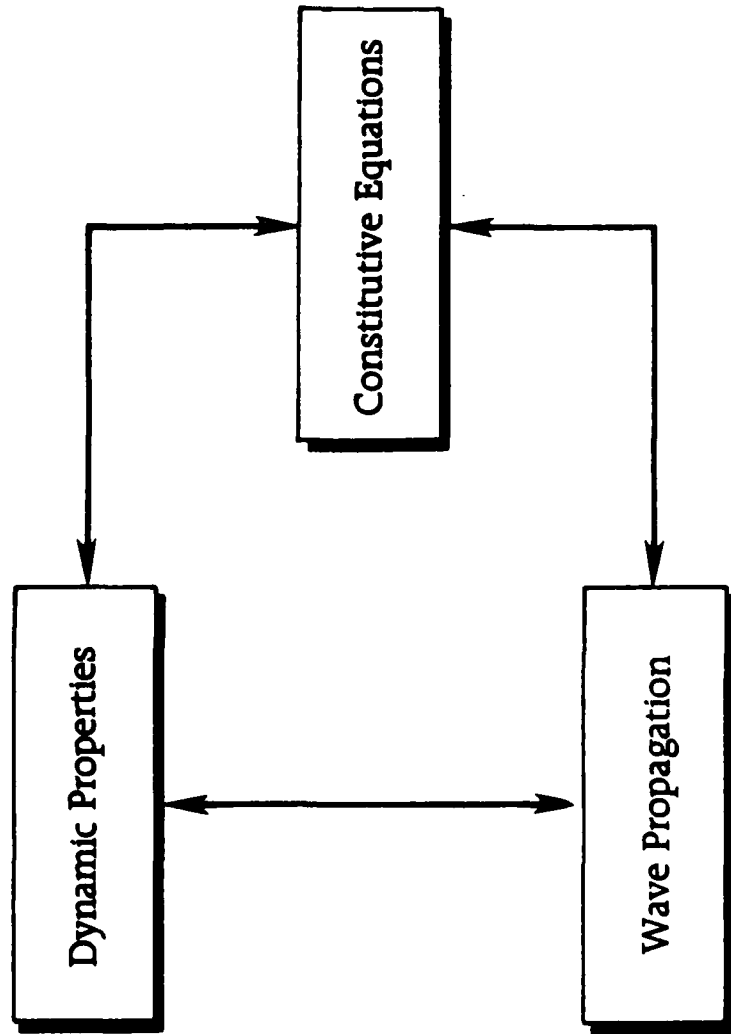
Figure 1 -    Interactive Dynamic Effects
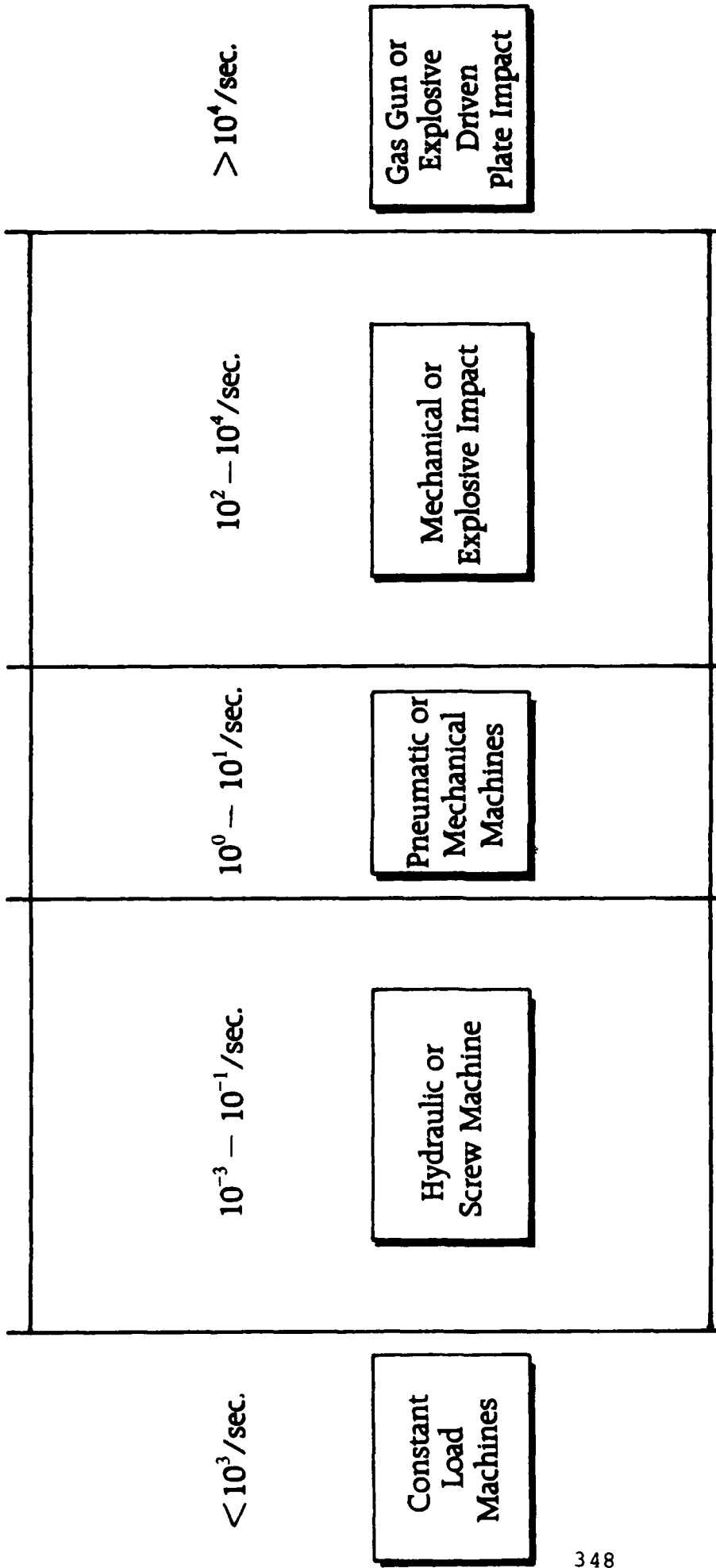
Figure 2 -    Loading Regimes and Experimental Test Techniques
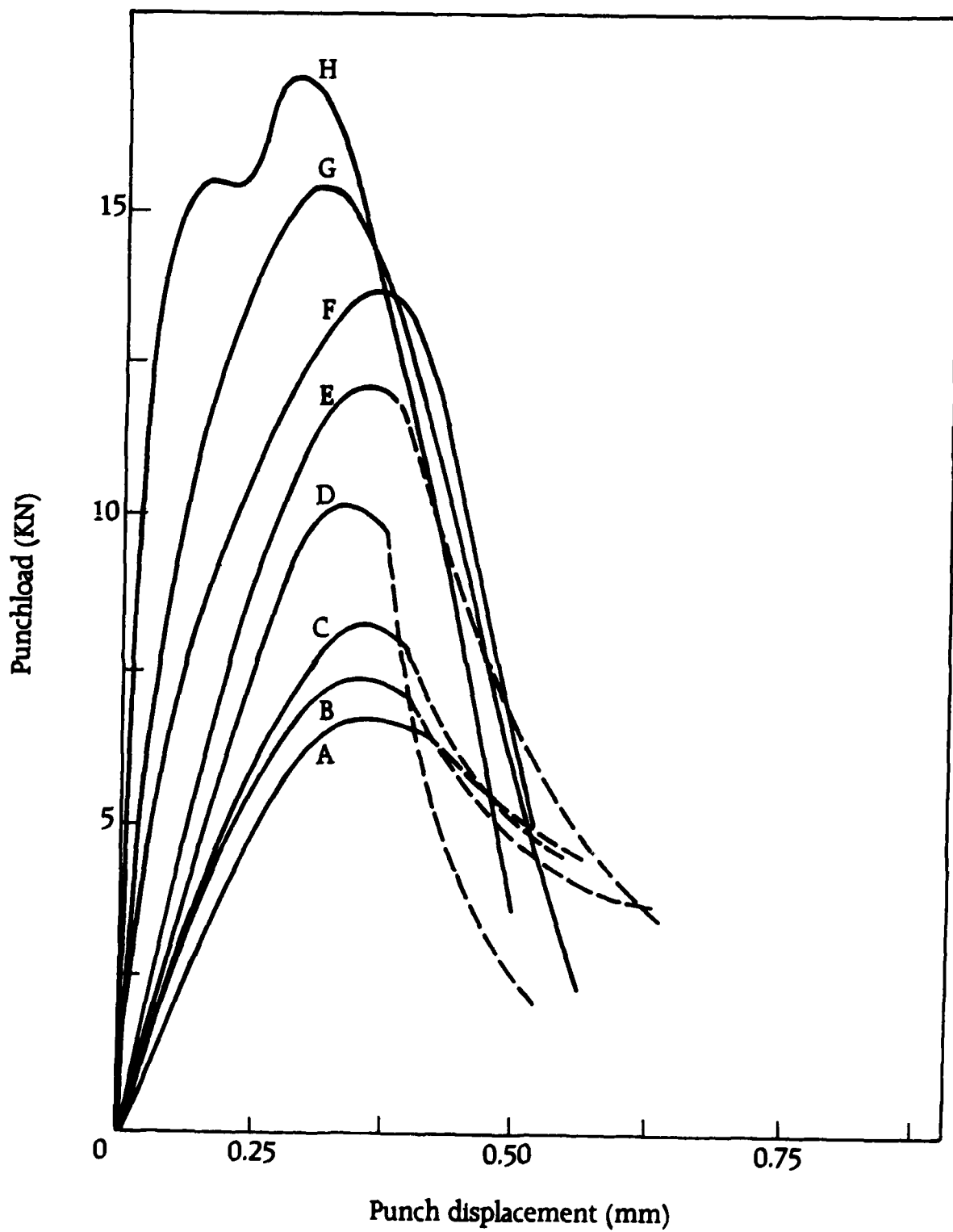
Figure 3 -    Punch Tests, Glass/Epoxy, Punch Speeds $2.5 \times 10^{-7}$ to 16 m/sec., Reference [2]

$$E = \int Fvdt$$

$$E = E_i + E_p$$

Propagation phase

Ductility index

$$DI = \frac{E_p}{E_i}$$

Initiation phase
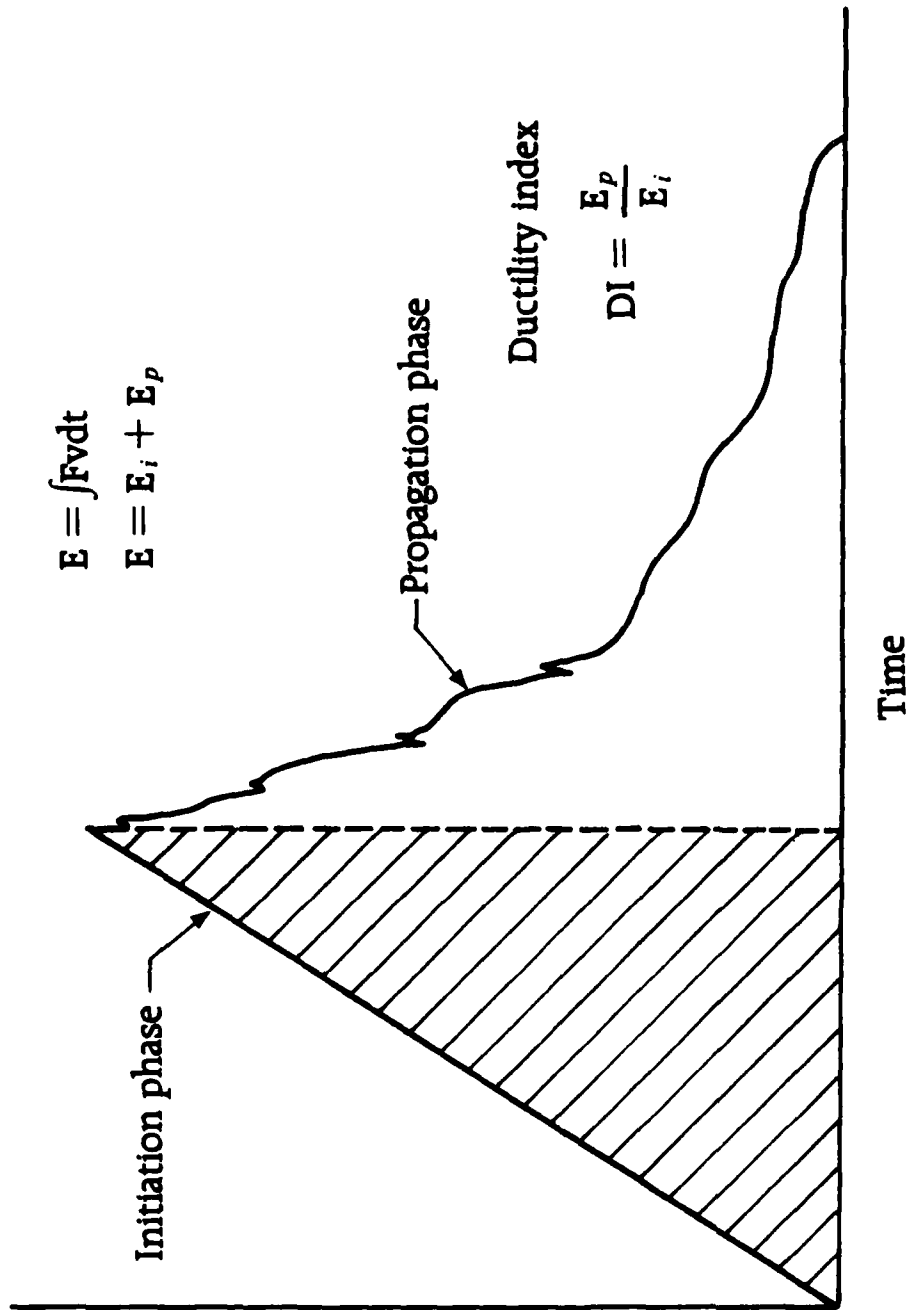
Time

Figure 4 -    Load History Impact Test, Reference [5]
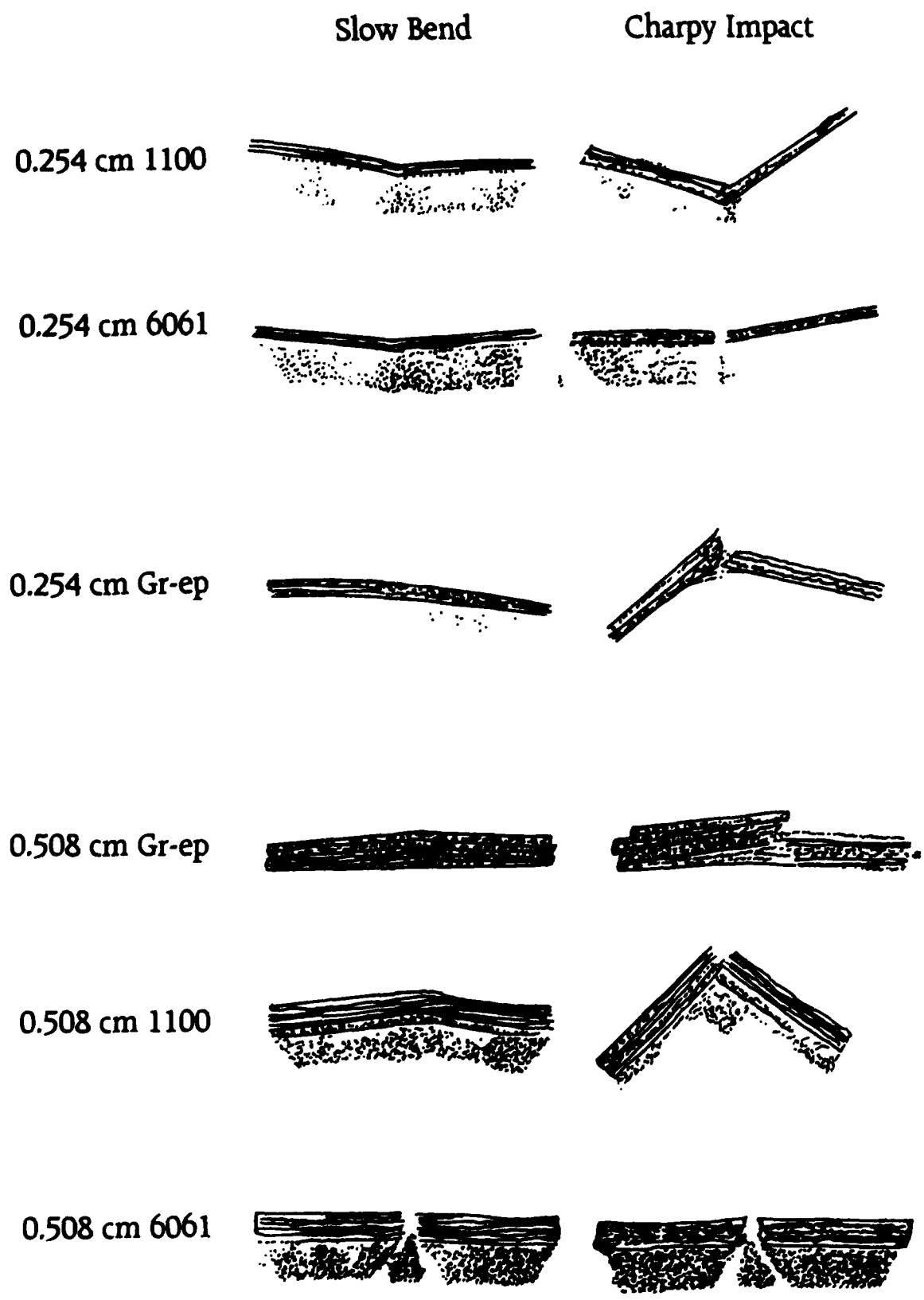
Figure 5 –   Slow Bend and Charpy Impact Test Failure Modes, Beam-Aluminum
(1100,6061), Graphite-Epoxy, Reference [6]
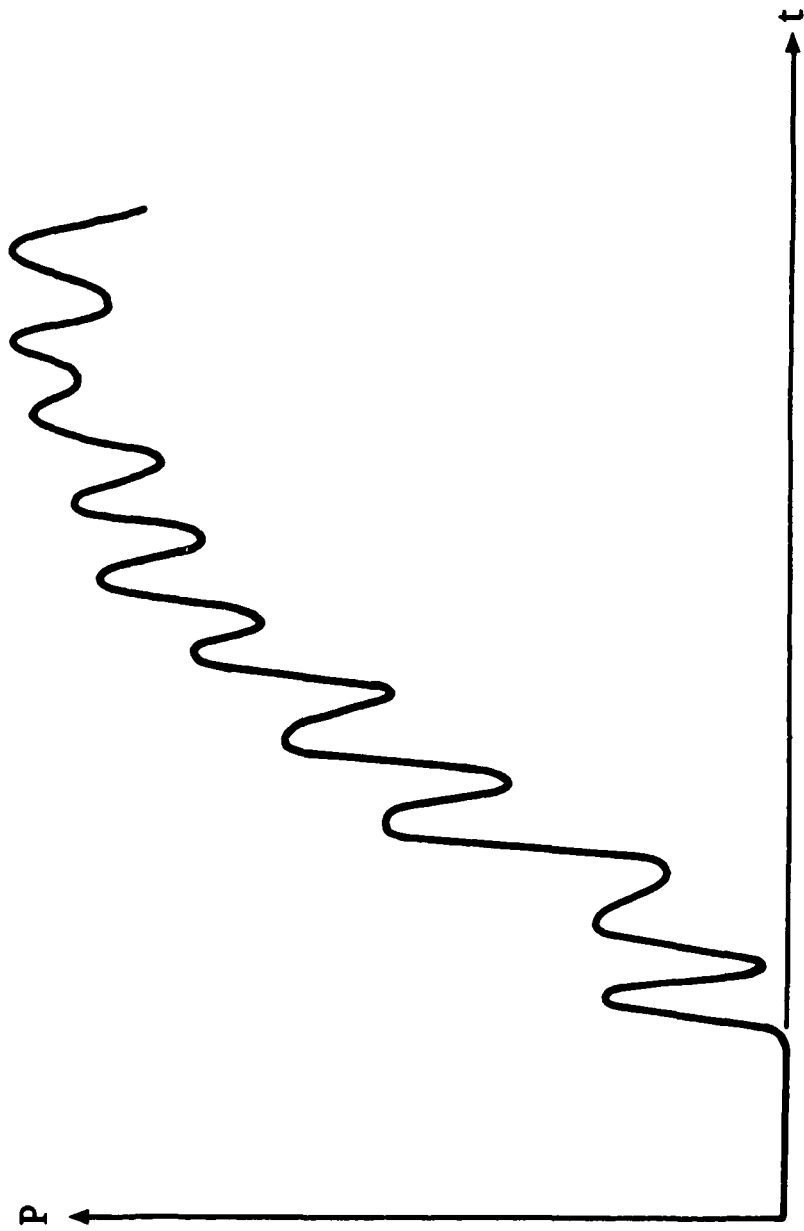
Figure 6 - Time Response Charpy Test, Reference [7]
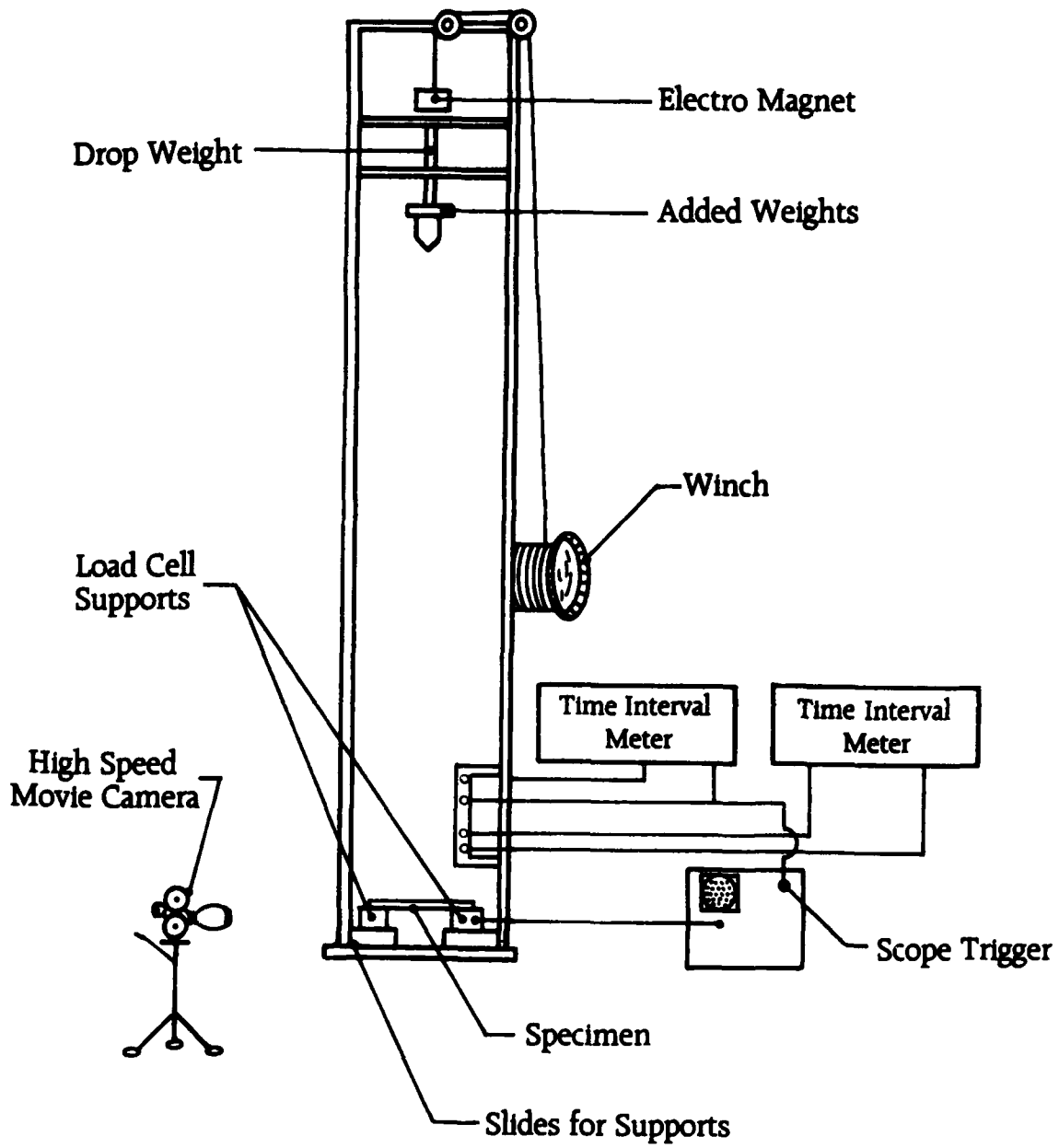
Figure 7 -    Drop Weight Apparatus, Reference [10]
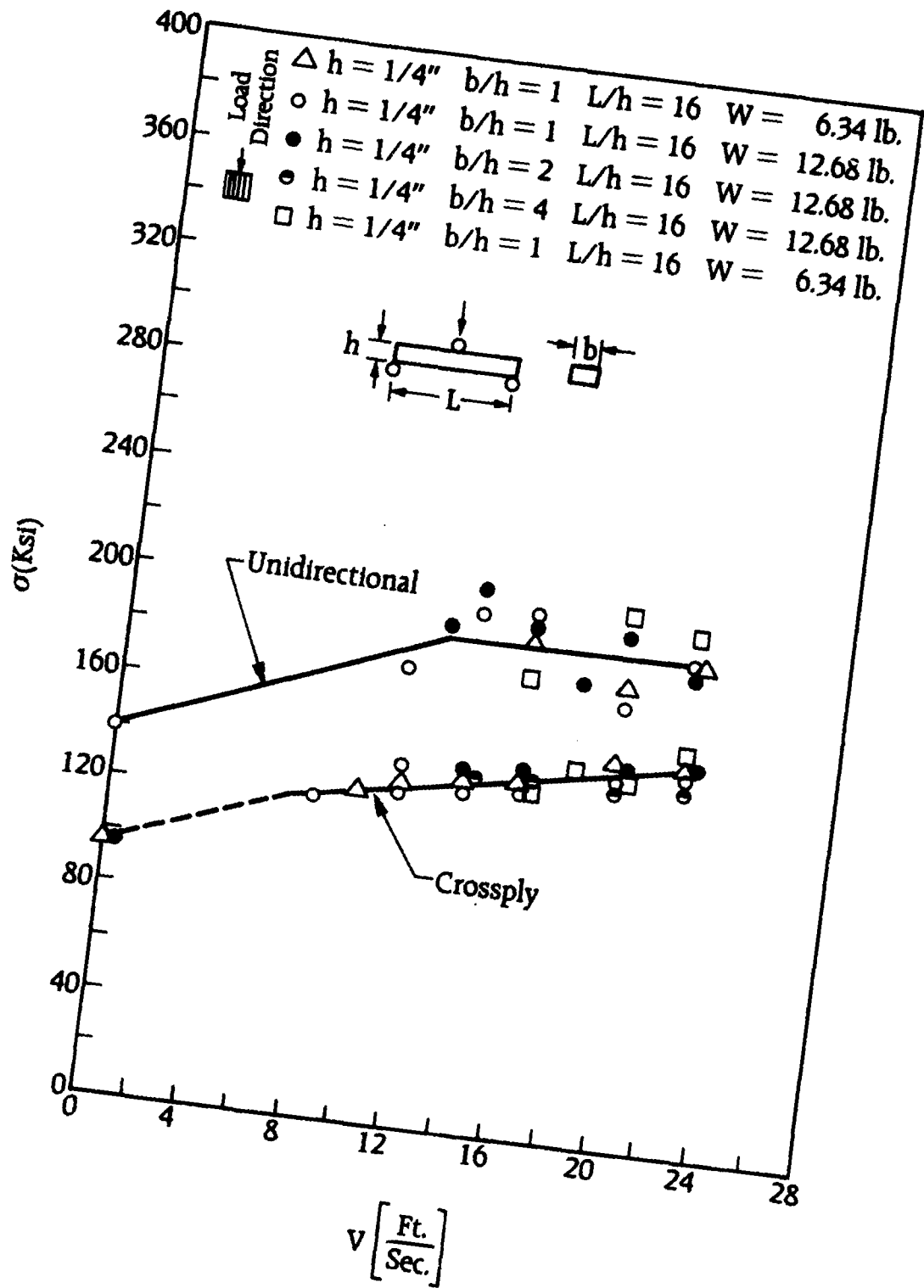
Figure 8 –    E-Glass/Epoxy Strength vs. Impact Velocity, Reference [10]
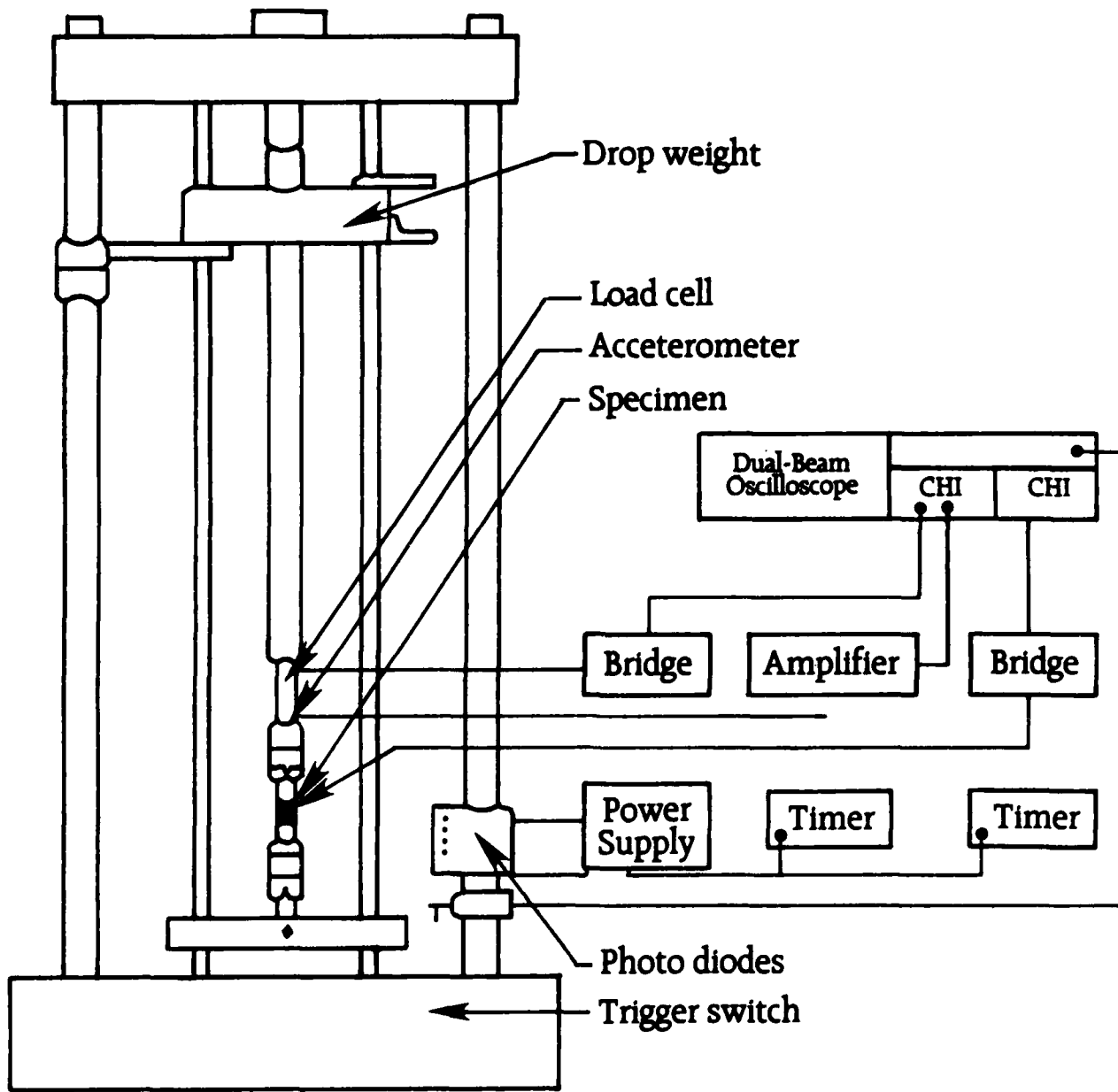
Figure 9 – Schematic for Dynamic Loading Apparatus, Reference [11]

355
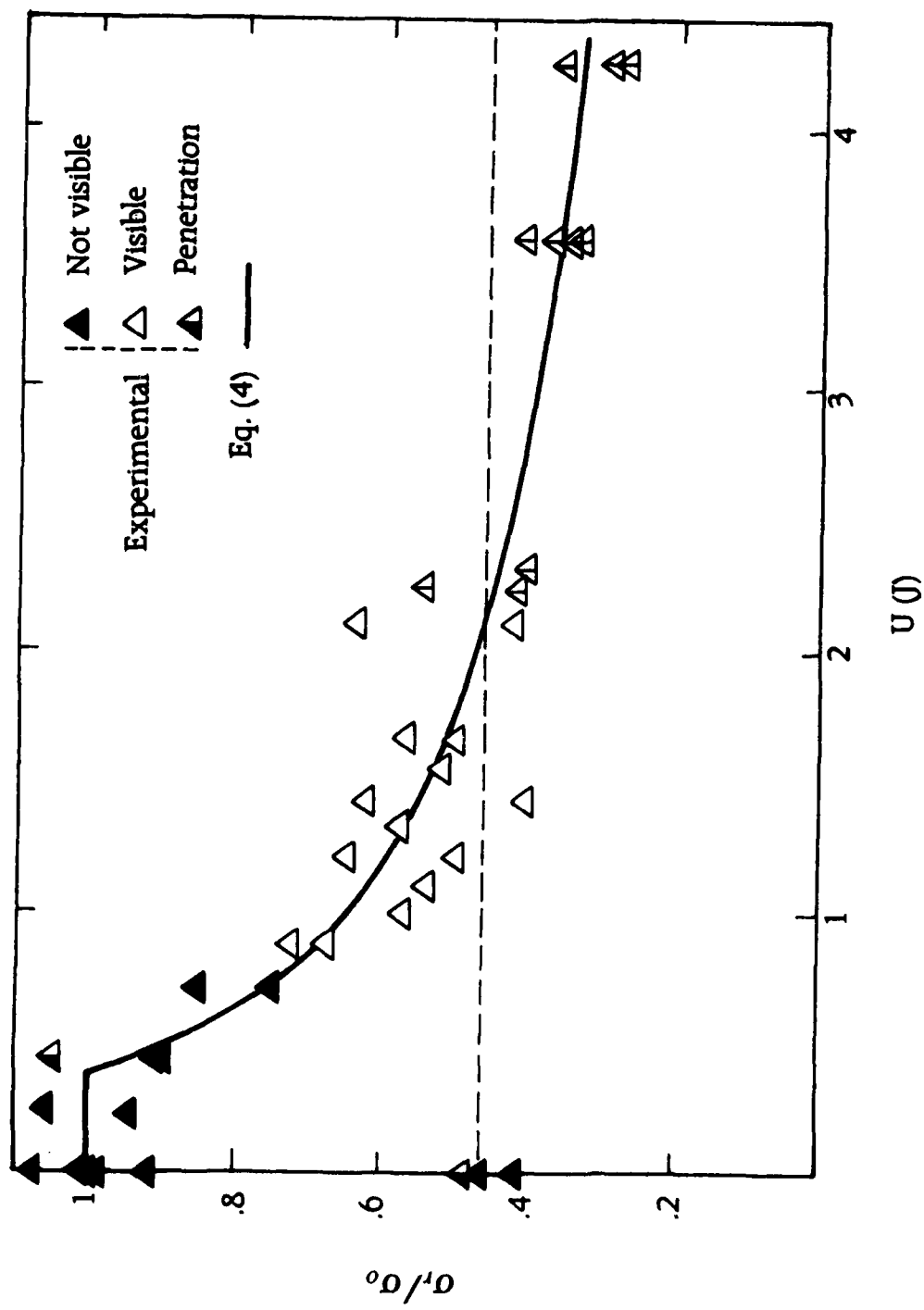
Figure 10 – Residual Tensile Strength vs. Applied Energy Graphite/Epoxy $(0/\pm45)_2$, Reference [12]
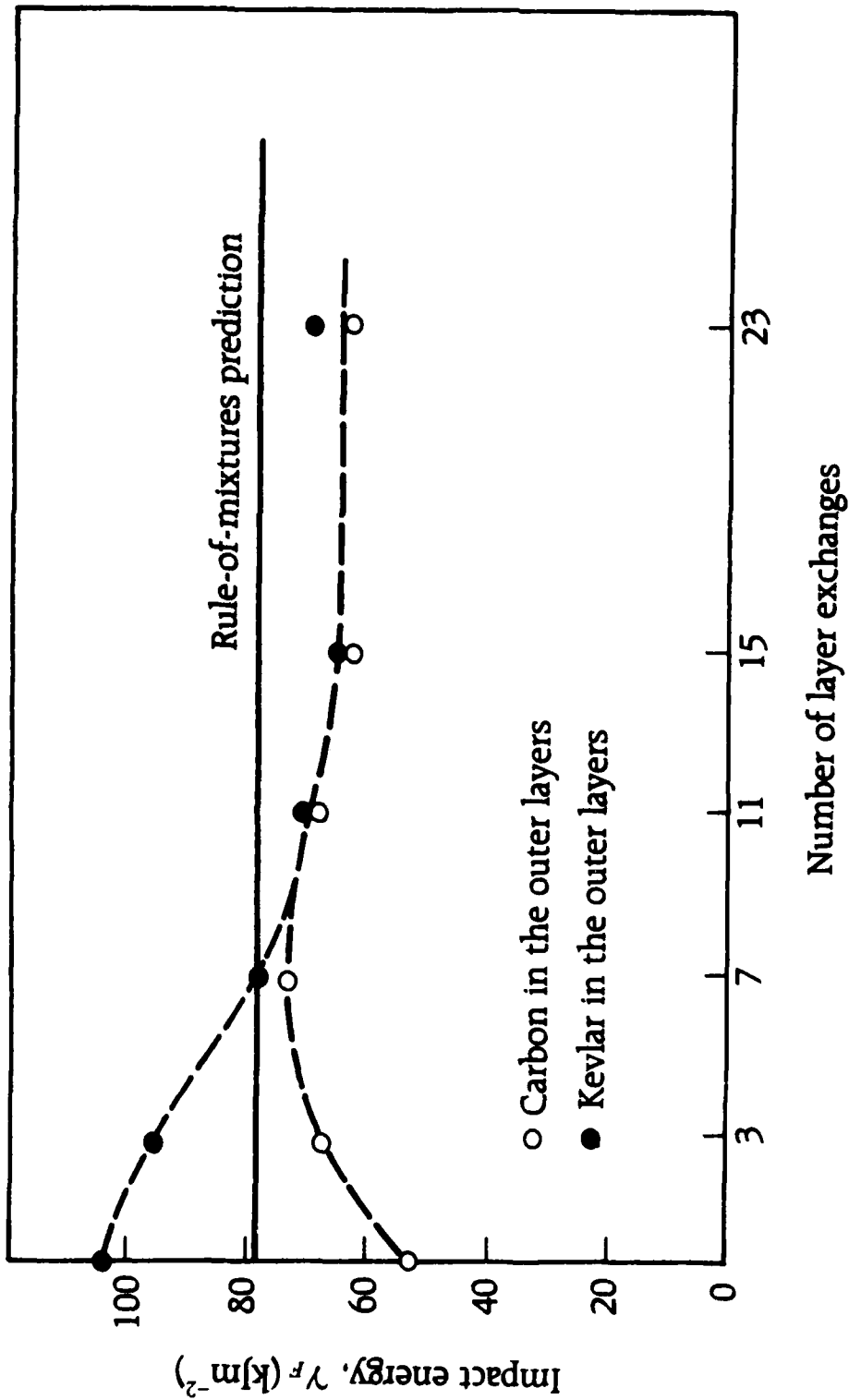
Figure 11 –   Impact Energy Related to Layer Exchanges, Reference [13]

| Investigator | Date | Materials | Strain Rate $s^{-1}$ | Temp °K |
|---|---|---|---|---|
| Kolsky[2] | 1949 | polyethylene | 1,900-7,500 | 293 |
| | | PMMA | 575 | 292 |
| | | natural rubber | 5,000 | 290 |
| Back, Campbell[3] | 1957 | phenol formaldehyde | 500 | Room |
| | | phenol formaldehye composite | 500 | |
| Ripperger[4] | 1958 | polyethylene | 2,200-5,700 | 210;300;340 |
| | | PTFE | 2,200 | 300 |
| | | nylon | 2,200 | 300 |
| | | CAB (Tenite M) | 2,200 | 300 |
| | | CAB (Tenite H) | 2,200 | 300 |
| | | polystyrene | 2,200 | 300 |
| | | polyvinylidene chloride | 2,200 | 300 |
| Volterra, Barton[5] | 1958 | natural rubber | 41 | 274;294 |
| | | hard rubber | 25 | |
| | | polychloroprene (Neoprene GNA) | 33 | |
| | 1963 | polyethylene | 0.4-16 | 233-323 |
| | | ethyl cellulose | 0.4-7.4 | |
| | | CAB | 0.4-4.3 | |
| Tardif, Marquis[7] | 1963 | PMMA | 150-590 | Room |
| | | polycarbonate | 327-1028 | |
| | | nylon | 500;860 | |
| | | polyacetal | 450;670 | |
| | | PTFE | 570-1,420 | |
| | | epoxy | 150-690 | |
| Davies, Hunter[8] | 1963 | PMMA | 1,550-5,600 | Room |
| | | nylon 6 | 2,000-8,000 | |
| | | polyethylene | 1,270-3,700 | |
| | | PTFE | 1,430 | |
| | | PVC | 1,250 | |
| Lindholm[9] | 1964 | epoxy | 930 | Room |
| Hoge[10] | 1965 | polypropylene | 0.6-1,610 | Room |
| Maiden, Green[11,12] | 1966 | PMMA | 0.005-1,210 | Room |
| Hold[13] | 1968 | PMMA | $10^{-5}$-1,000 | 273-388 |
| Dao[14] | 1969 | polyethylene nylon 6-6 | 0.00033-33 | 77-450 |
| Meikle[15] | 1969 | PMMA | 0.07-33 | 200-360 |

Figure 12 -    Strain Rate Effects for Neat Resins, Reference [14]
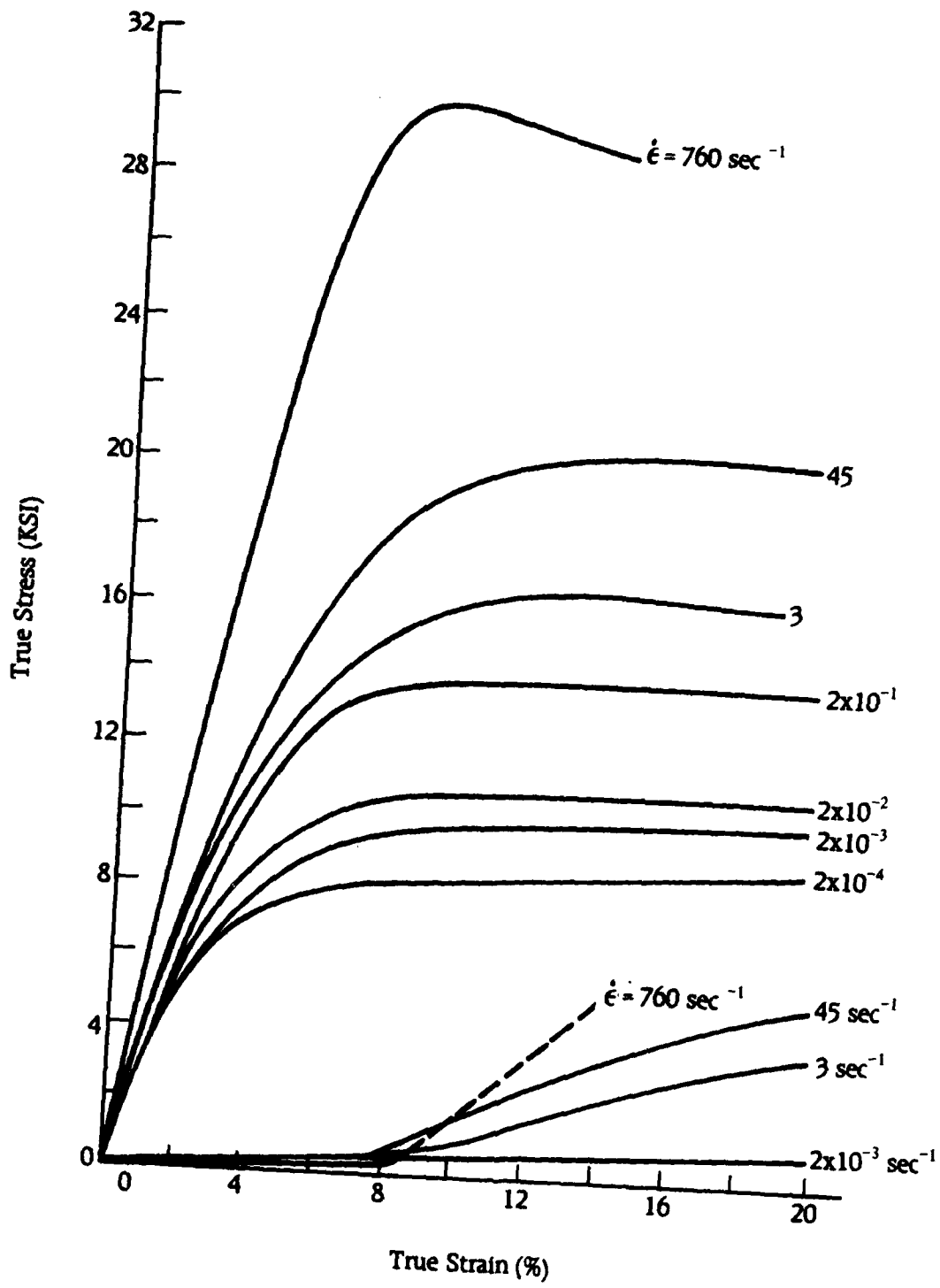
Figure 13 -   Stress - Strain Curves PMMA, Reference [14]
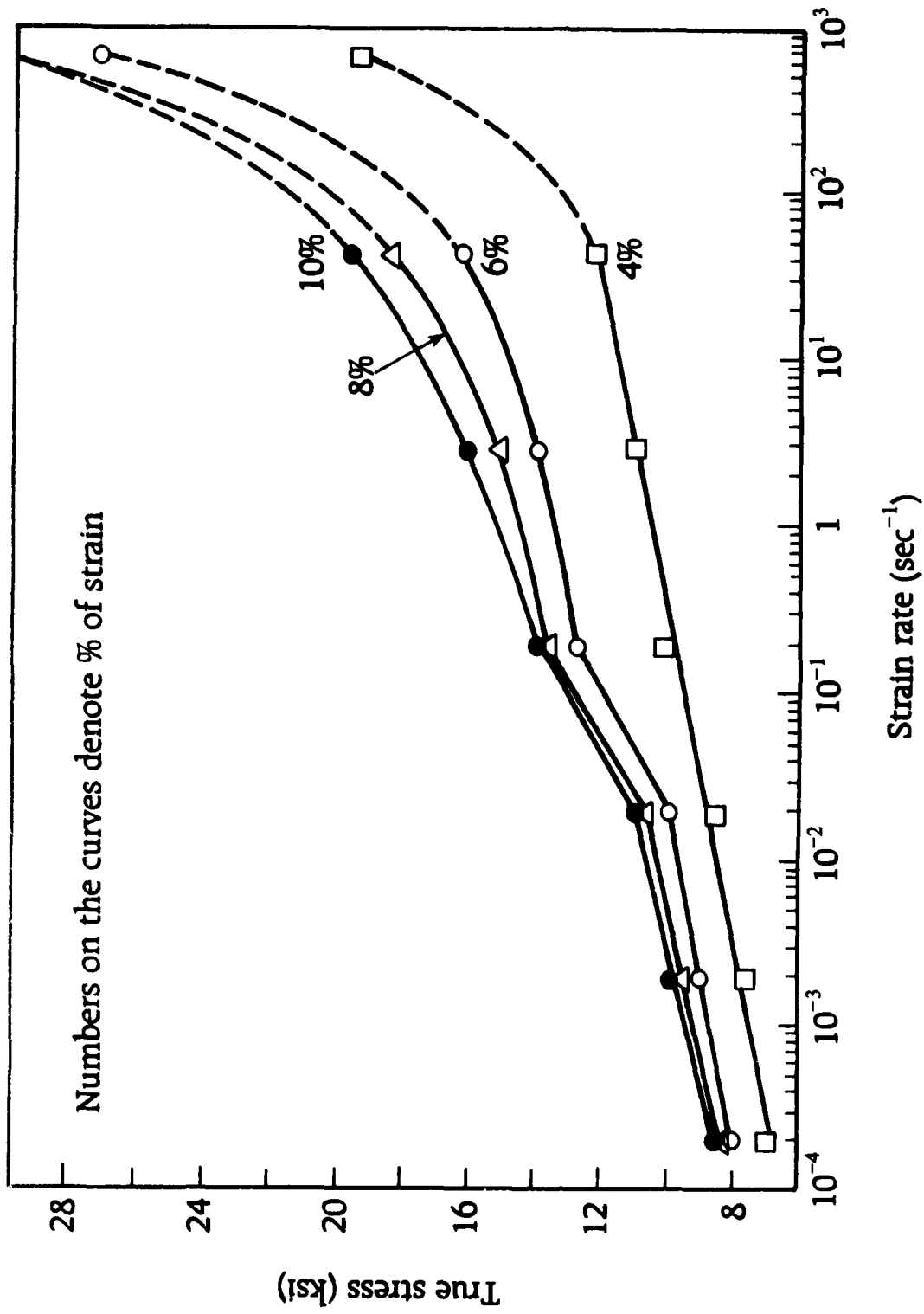
Figure 14 - Stress vs. Strain Rate PMMA, Reference [14]
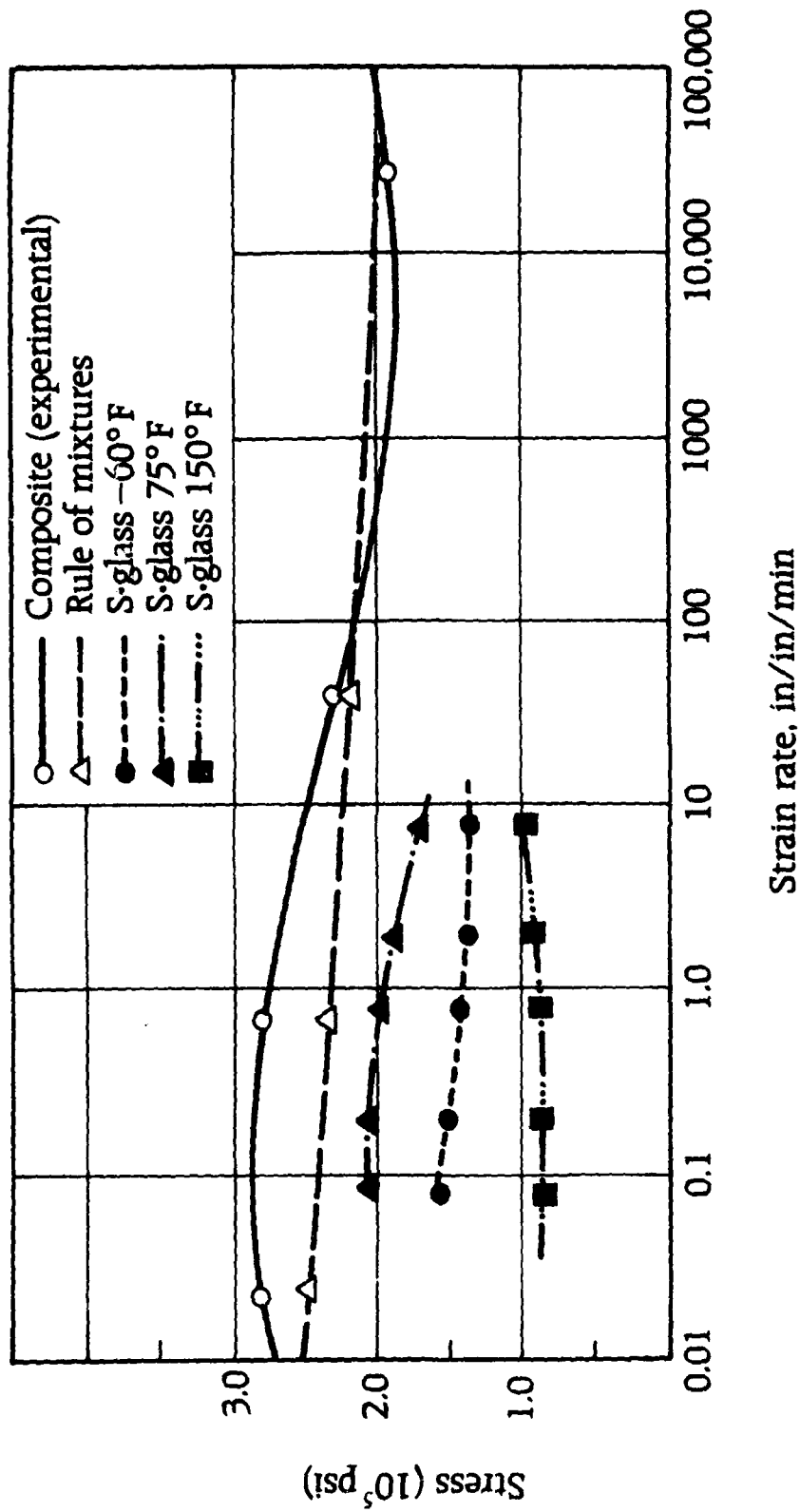
Figure 15 —  Stress vs. Strain Rate S-Glass/Epoxy, Reference [15]
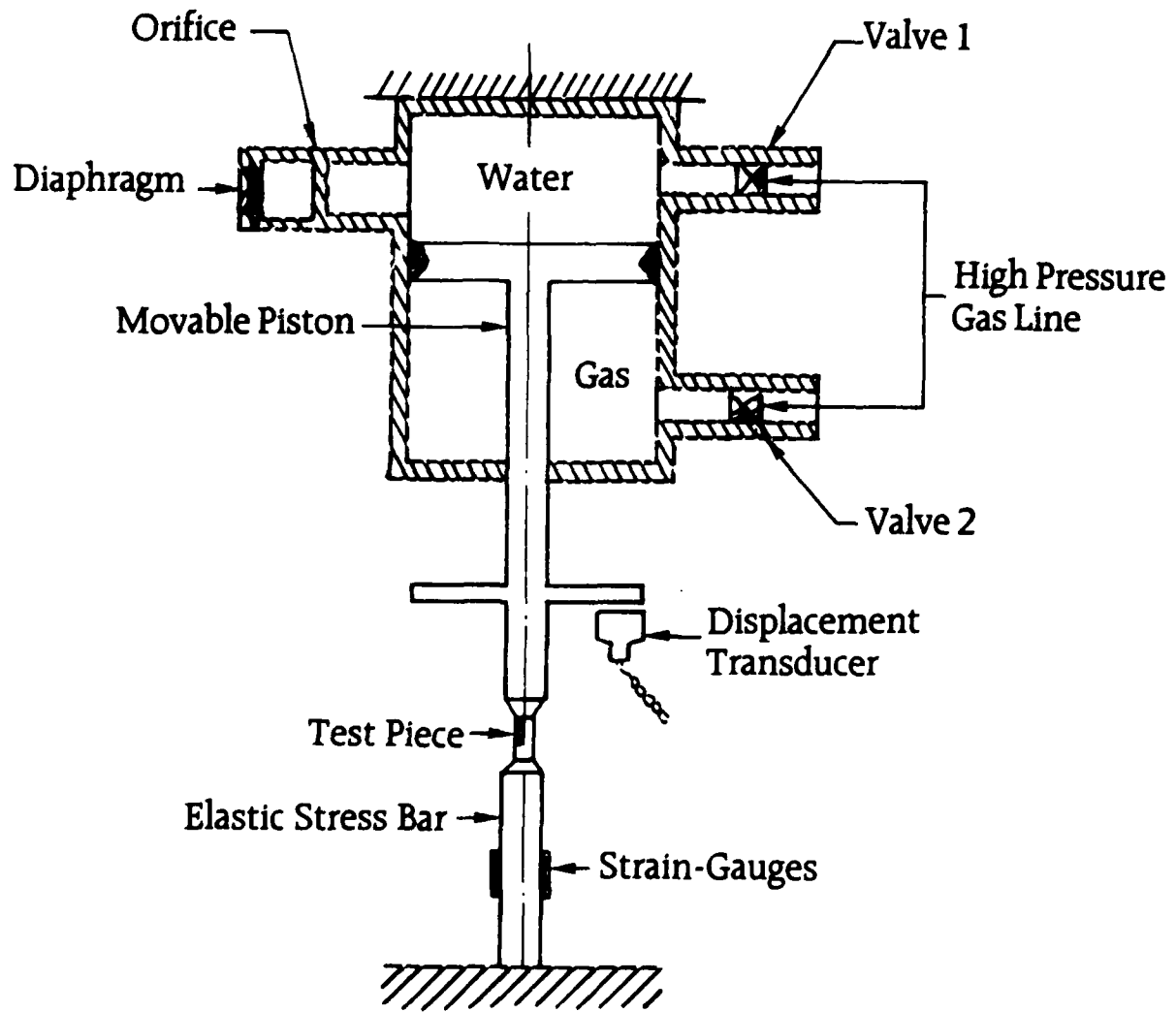
Figure 16 -    Pneumatic-Hydraulic Testing Apparatus, Reference [16]
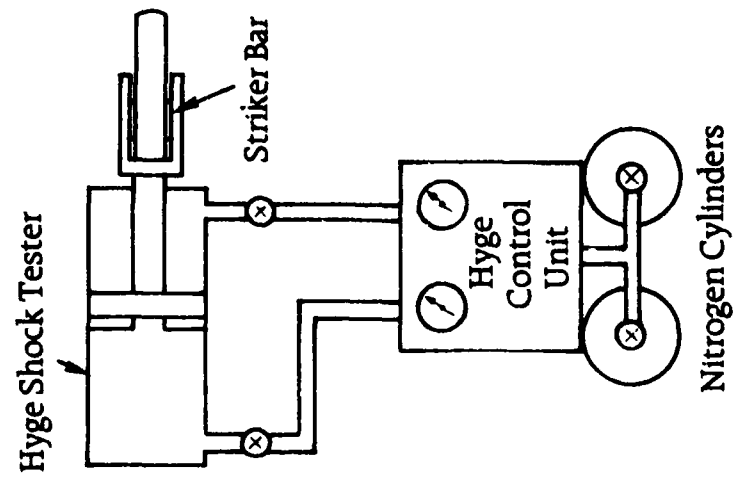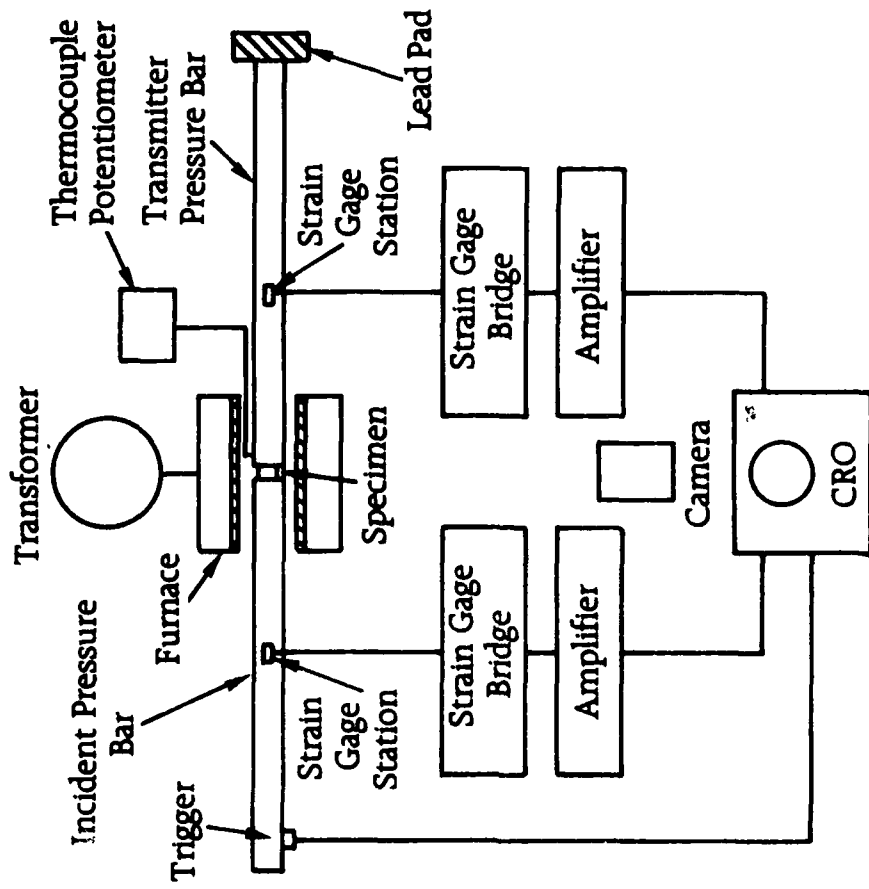
Figure 17 - Schematic SHPB Apparatus, Reference [17]
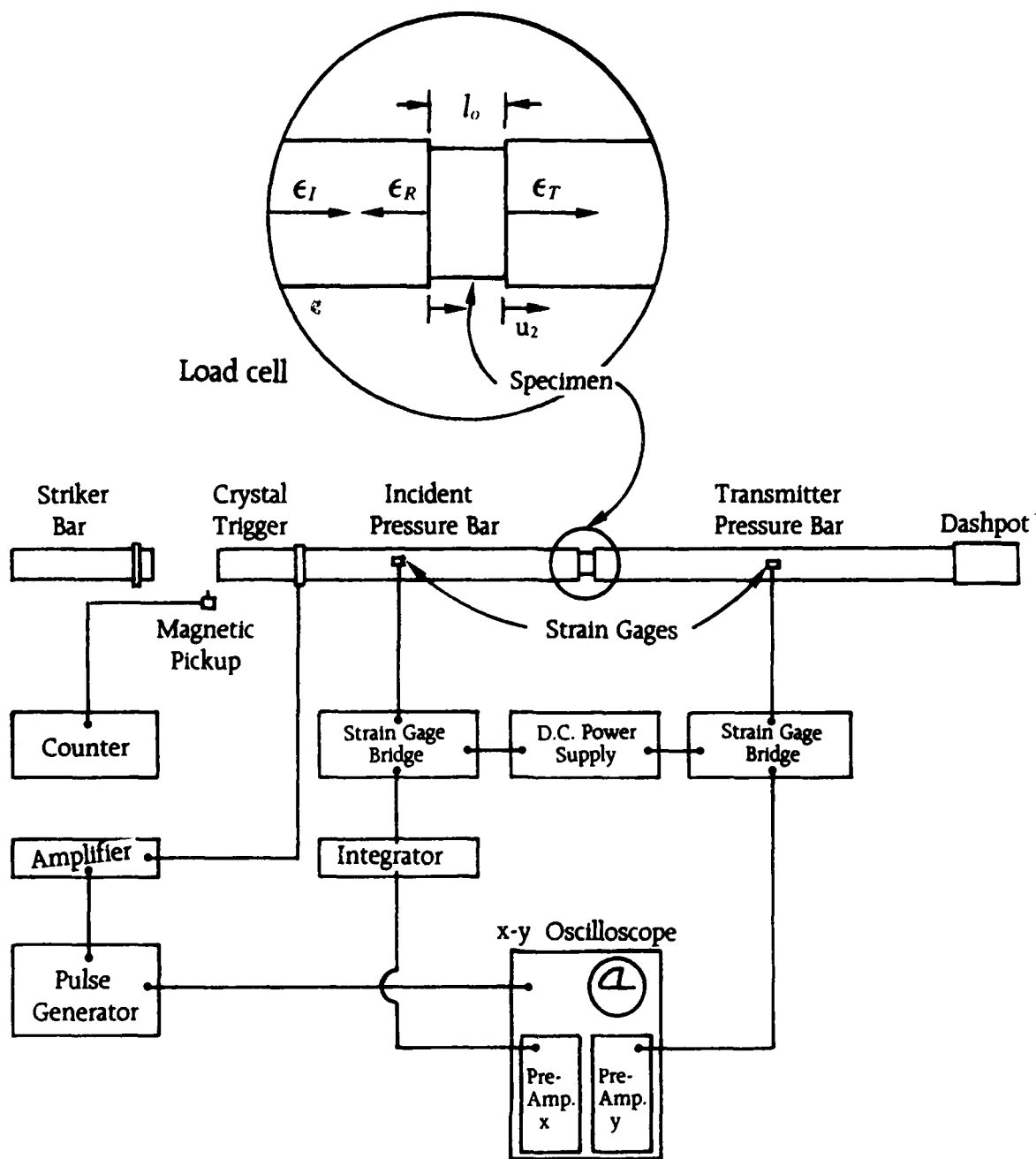
Figure 18 -    Schematic SHPB Compression Apparatus, Reference [18]
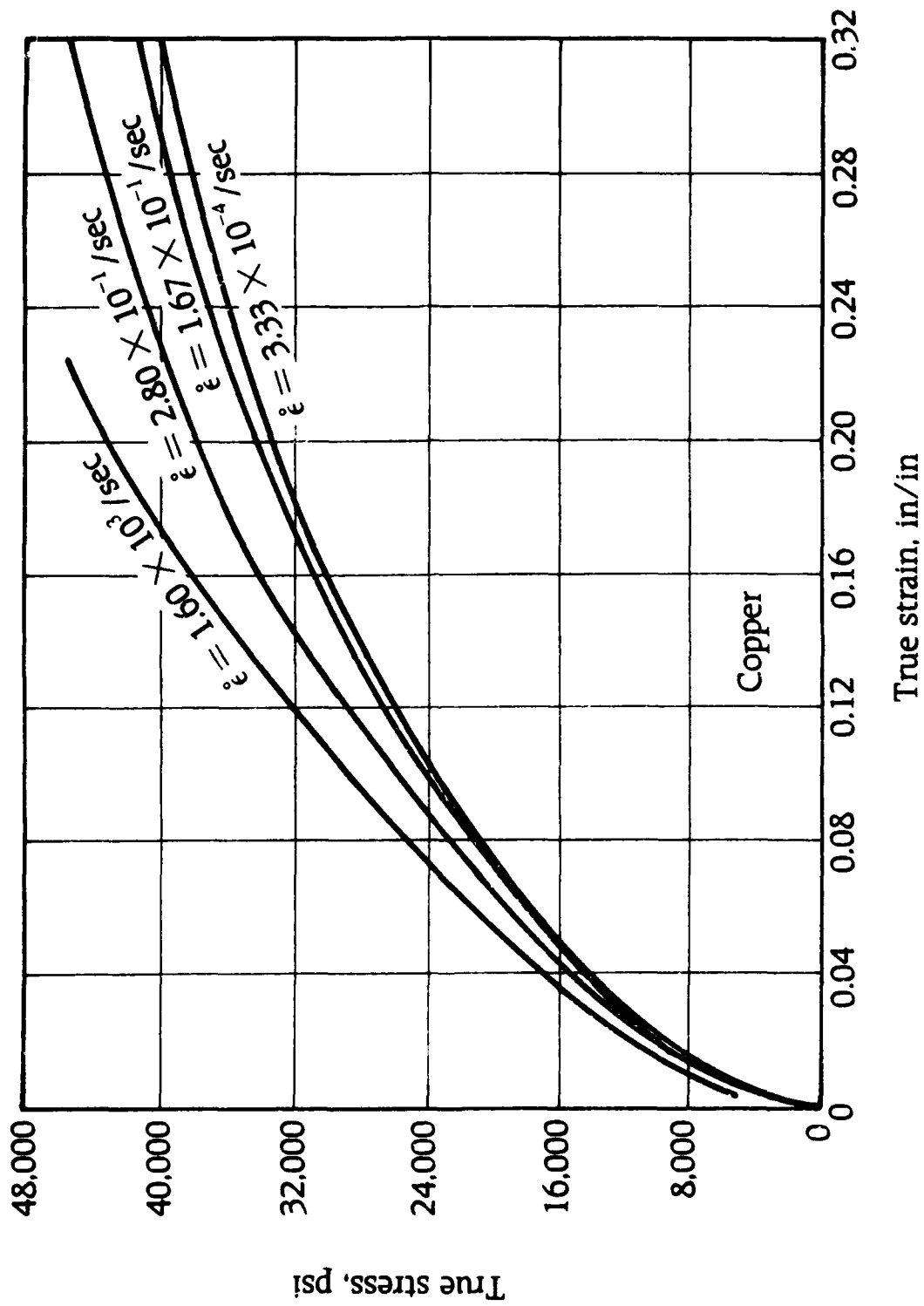
Figure 19 -   Stress – Strain Curves for Cu, Reference [18]
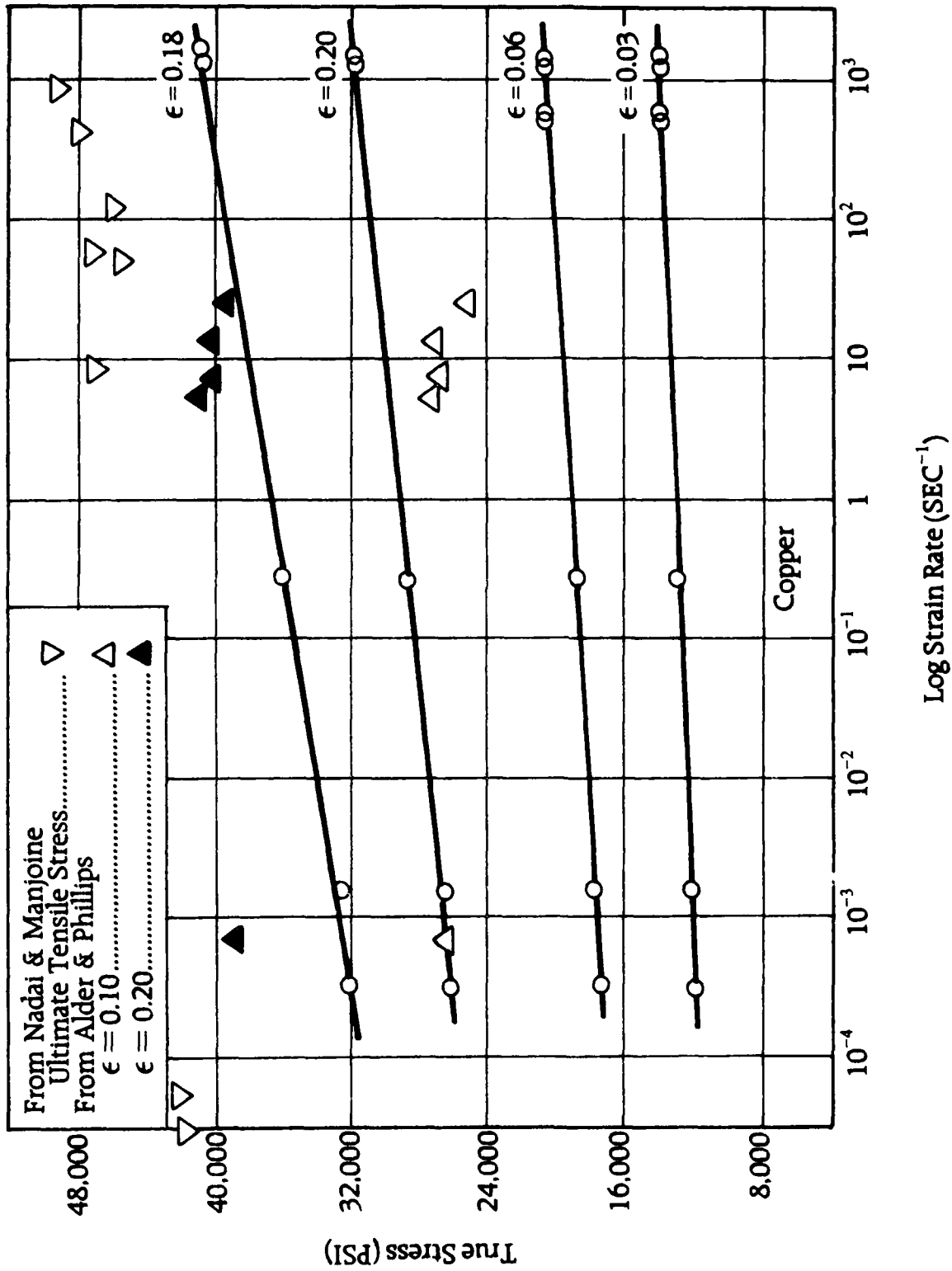
Figure 20 – Stress vs. Strain Rate for Cu, Reference [18]
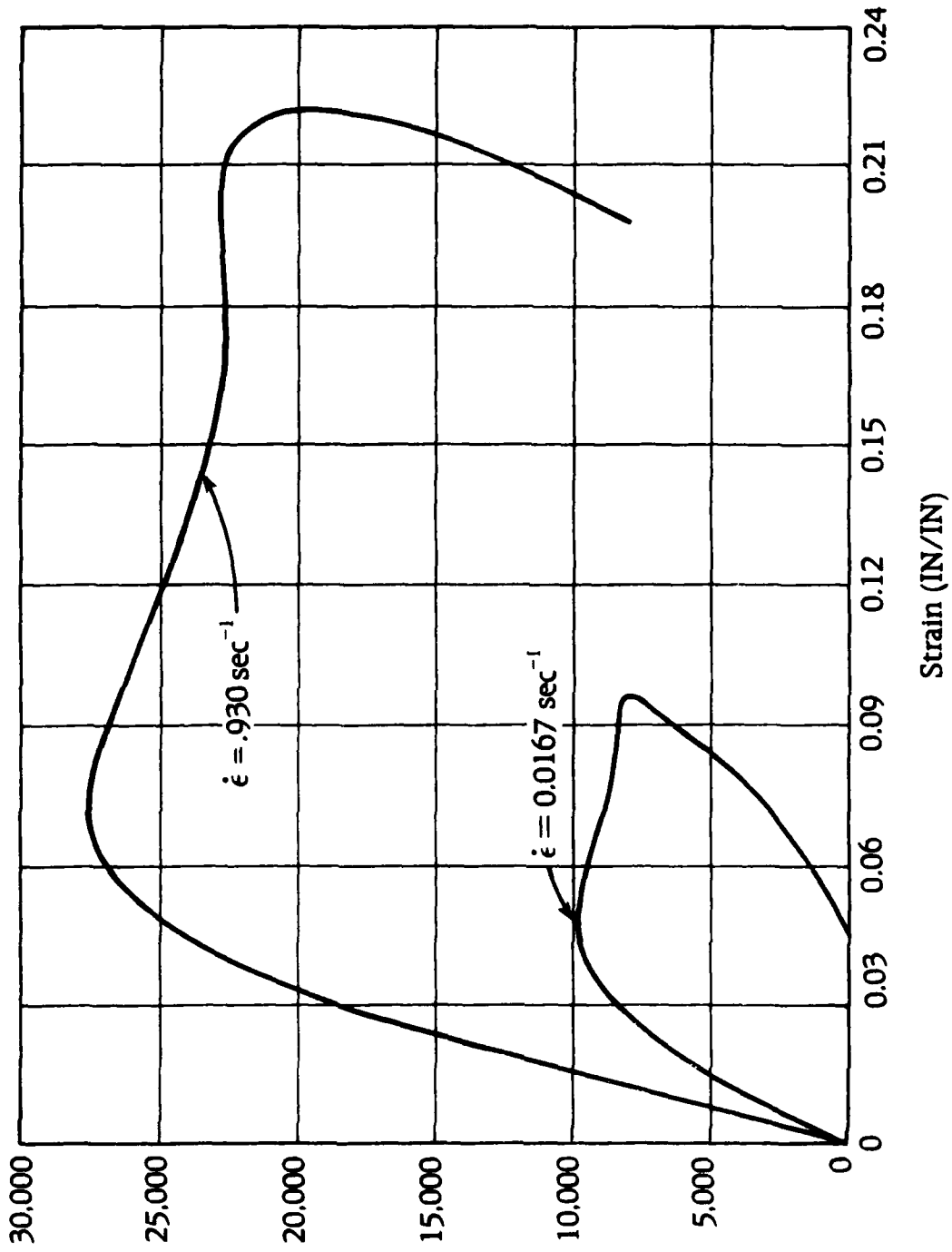
Figure 21 - Stress - Strain Curves for Epoxy, Reference [18]

367

**a. Static**          **B. Quasi-static**          **c. Dynamic**
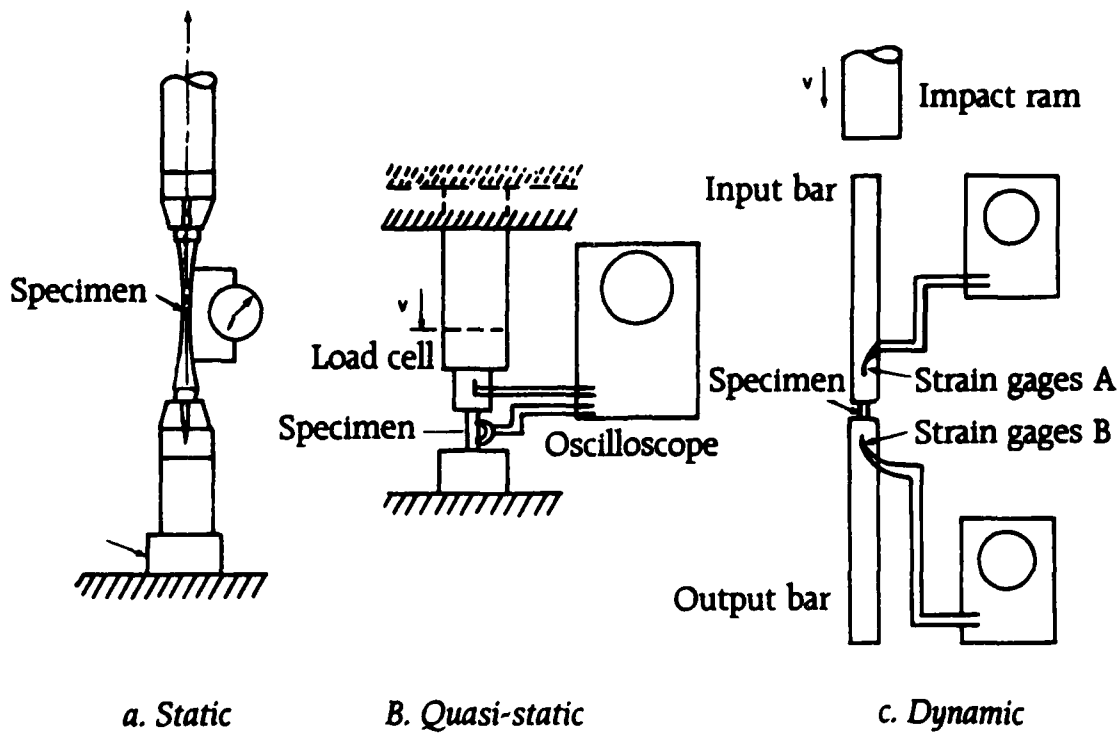
Schematic Materials Test Configurations
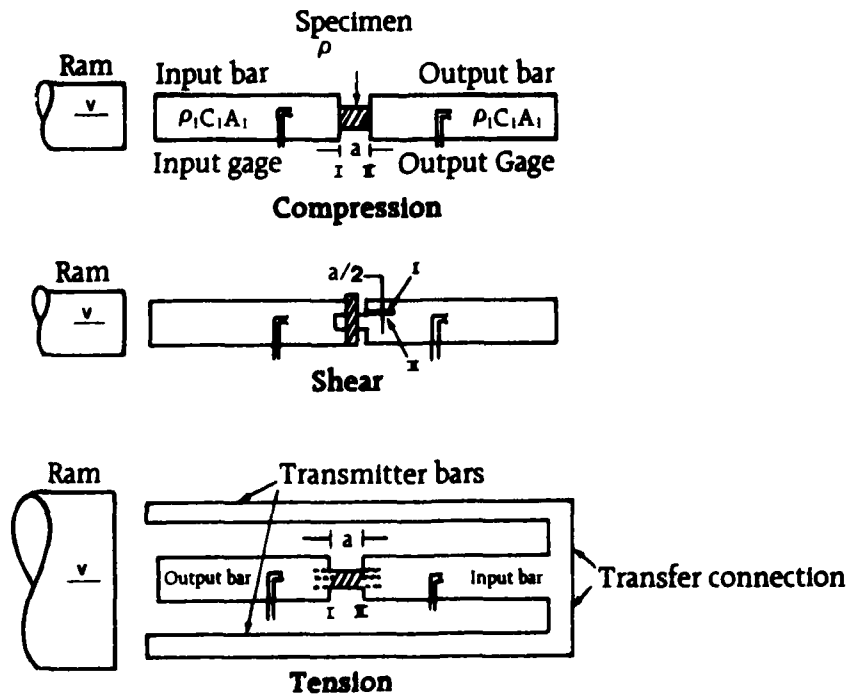


**Figure 22 -**     Schematic Compression, Shear, Tension SHPB Arrangements, Reference [20]

Guard Rings (Brass)

Epoxy

Teflon Support Ring

Teflon Support Ring

Specimen

Transmitter Pressure Bar

$l_0$

Case (Brass)

Active Capacitance Ring

**Compression**

Specimen

Incident Pressure Bar

Transmitter Pressure Bar

$l_0$
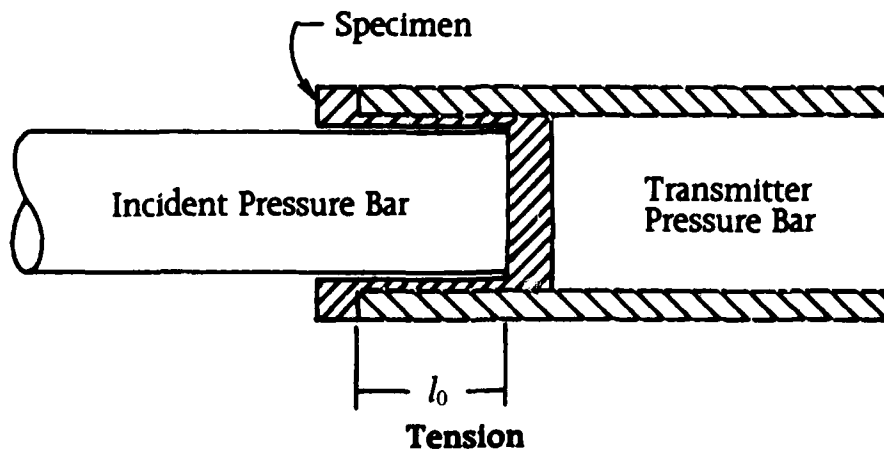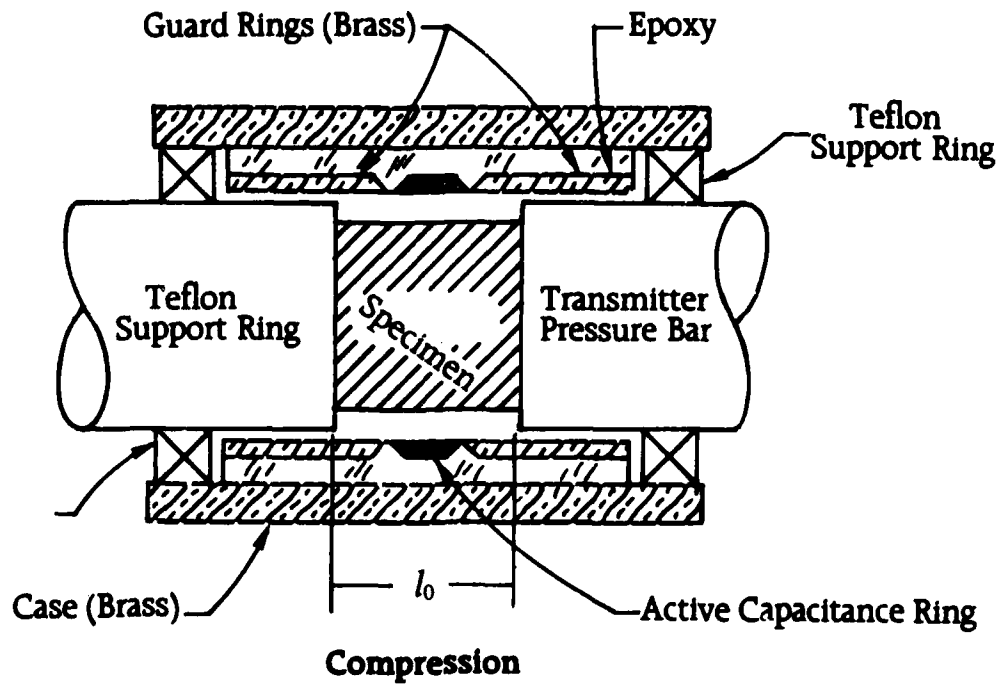
**Tension**

Figure 23 –    Schematic Compression and Tension Specimens, Reference [21]

369
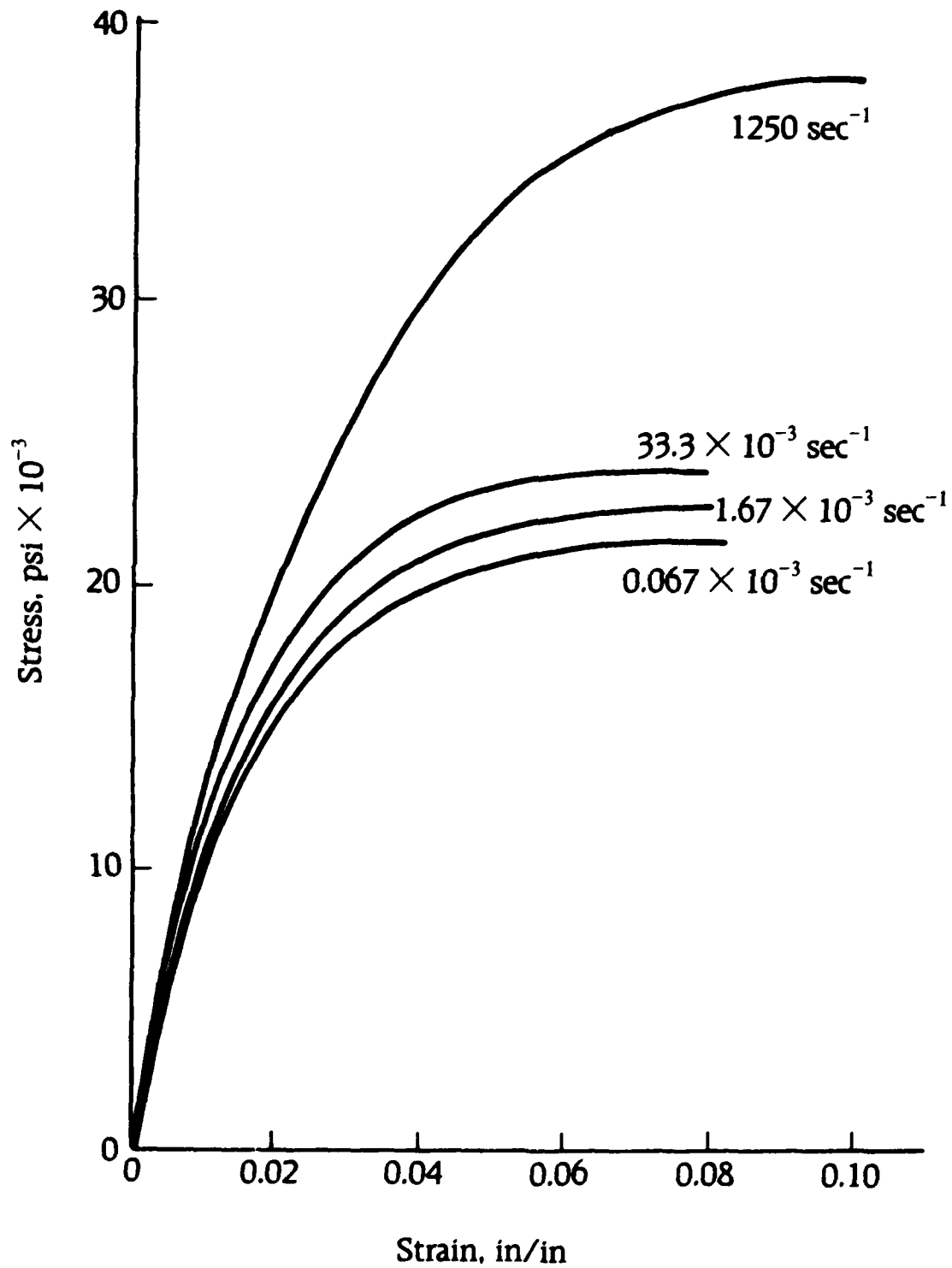
Figure 24 –    Stress – Strain Curves for Steel/Epoxy Filament Diameter .016", $V^f$ 10%, Reference [22]
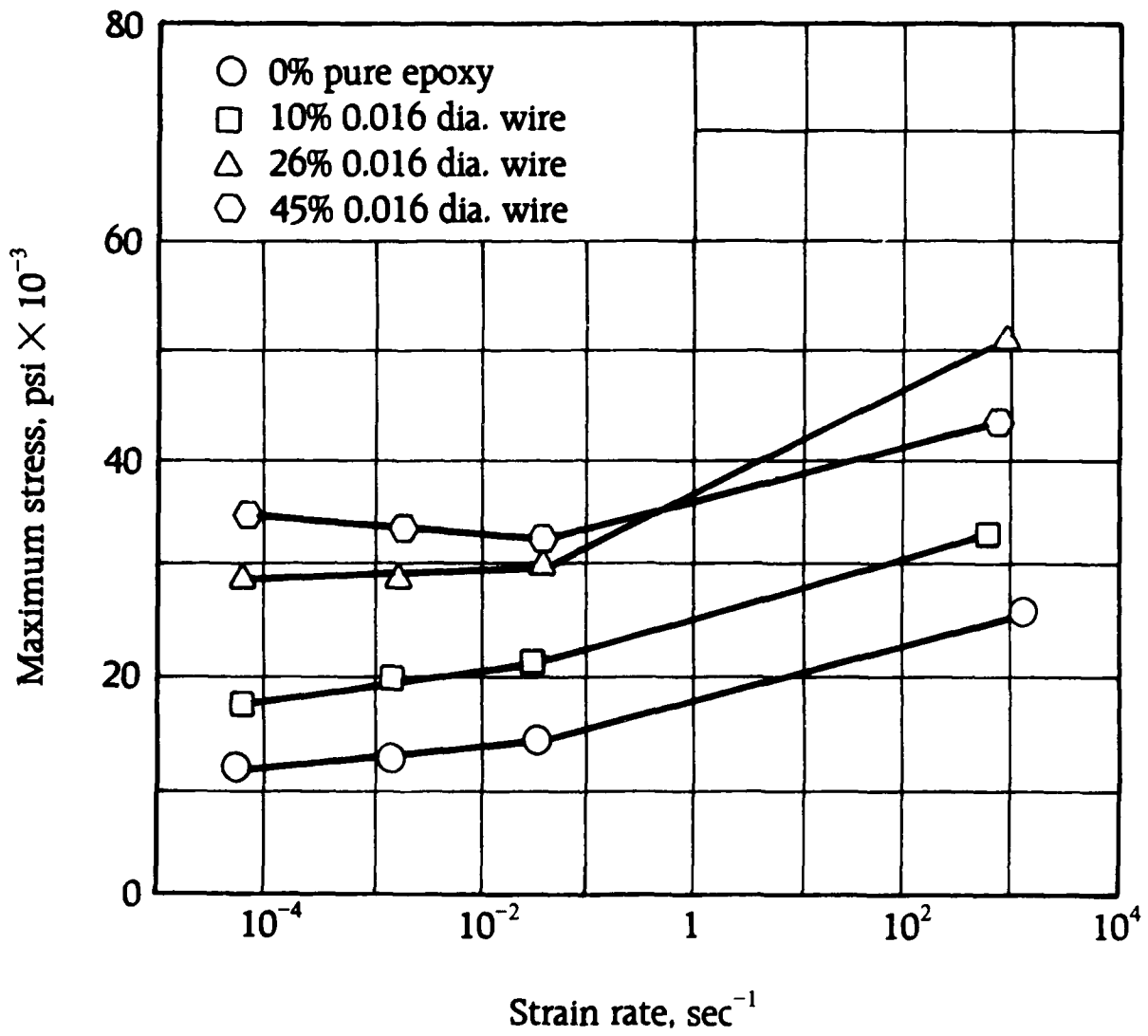
Figure 25 –    Stress vs. Strain Rate Steel/Epoxy - Various Filament Sizes, Reference [22]

371
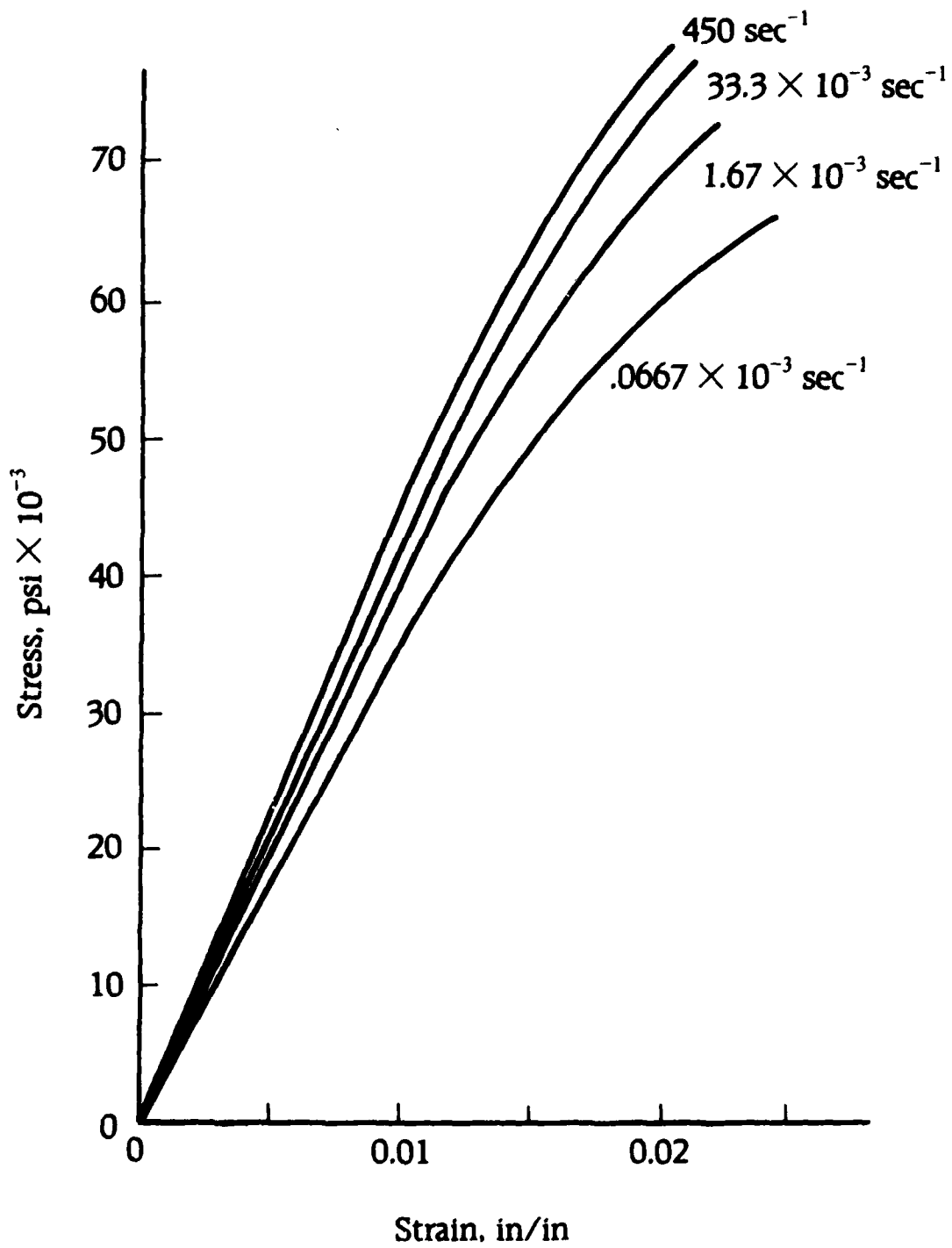
Figure 26 –     Stress – Strain Curves for Glass/Epoxy, Reference [22]

372
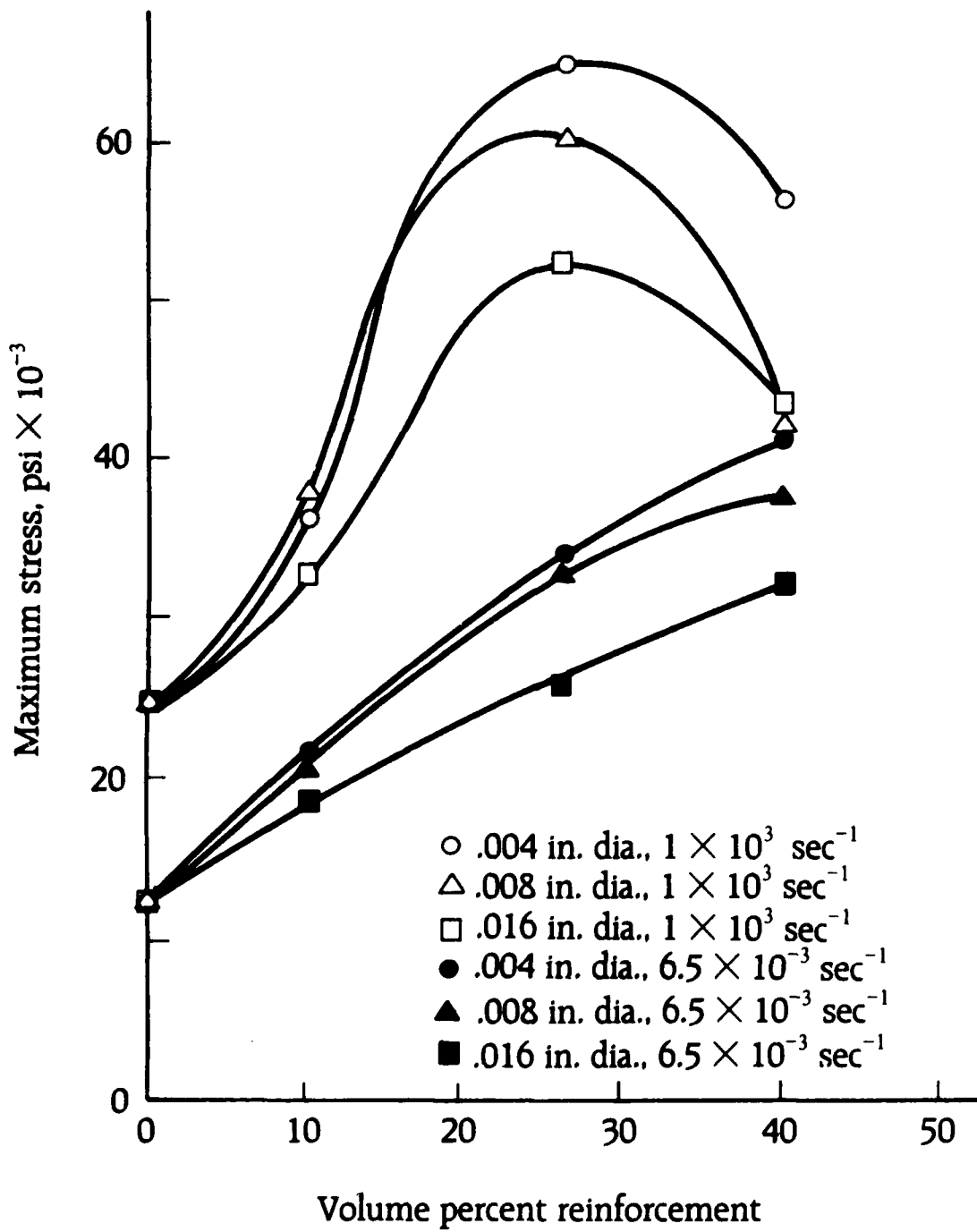
Figure 27 -    Ultimate Compression Stress Steel/Epoxy, Reference [23]
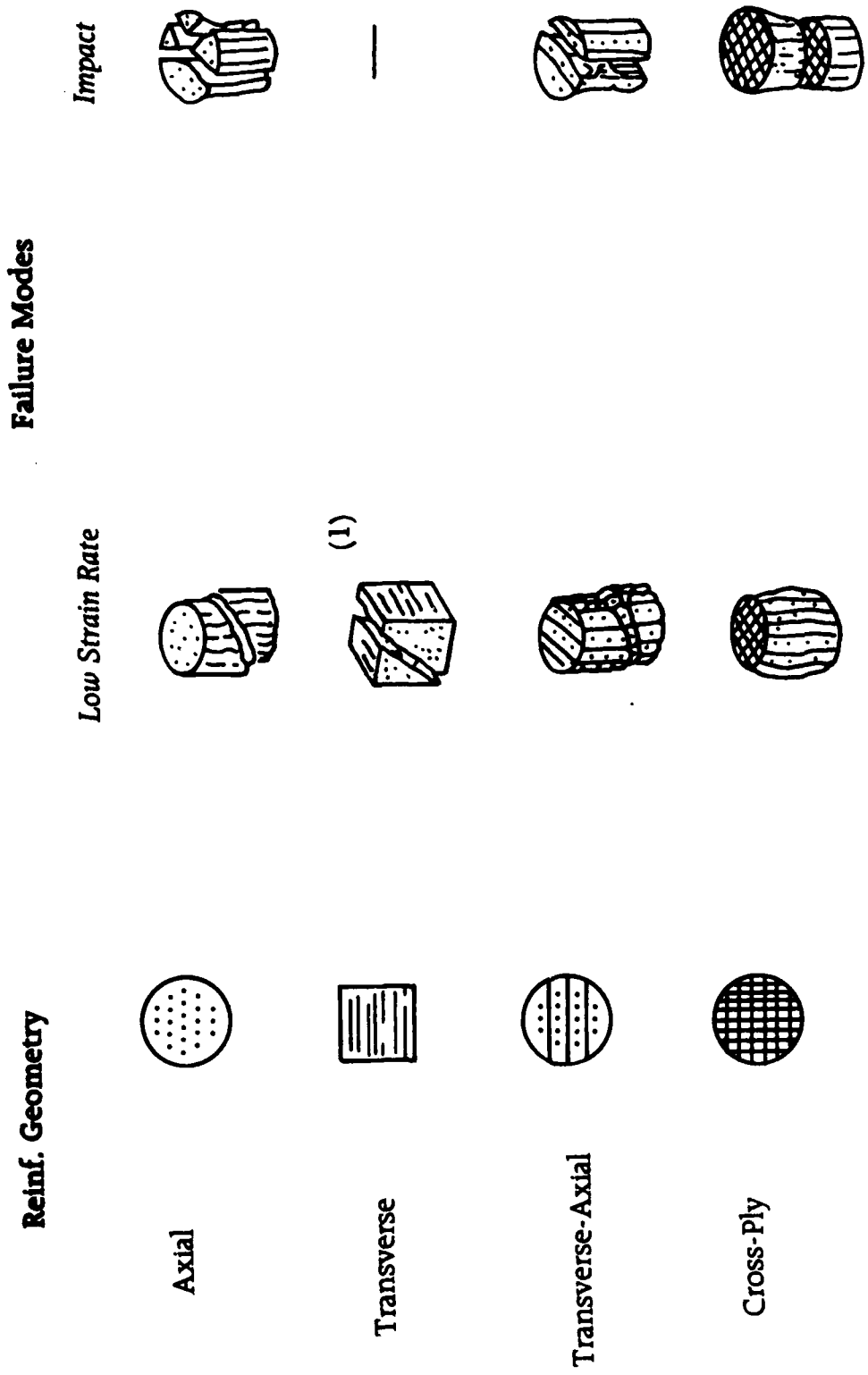
Figure 28 - Static/Dynamic Failure Modes Steel/Epoxy, Reference [23]

374
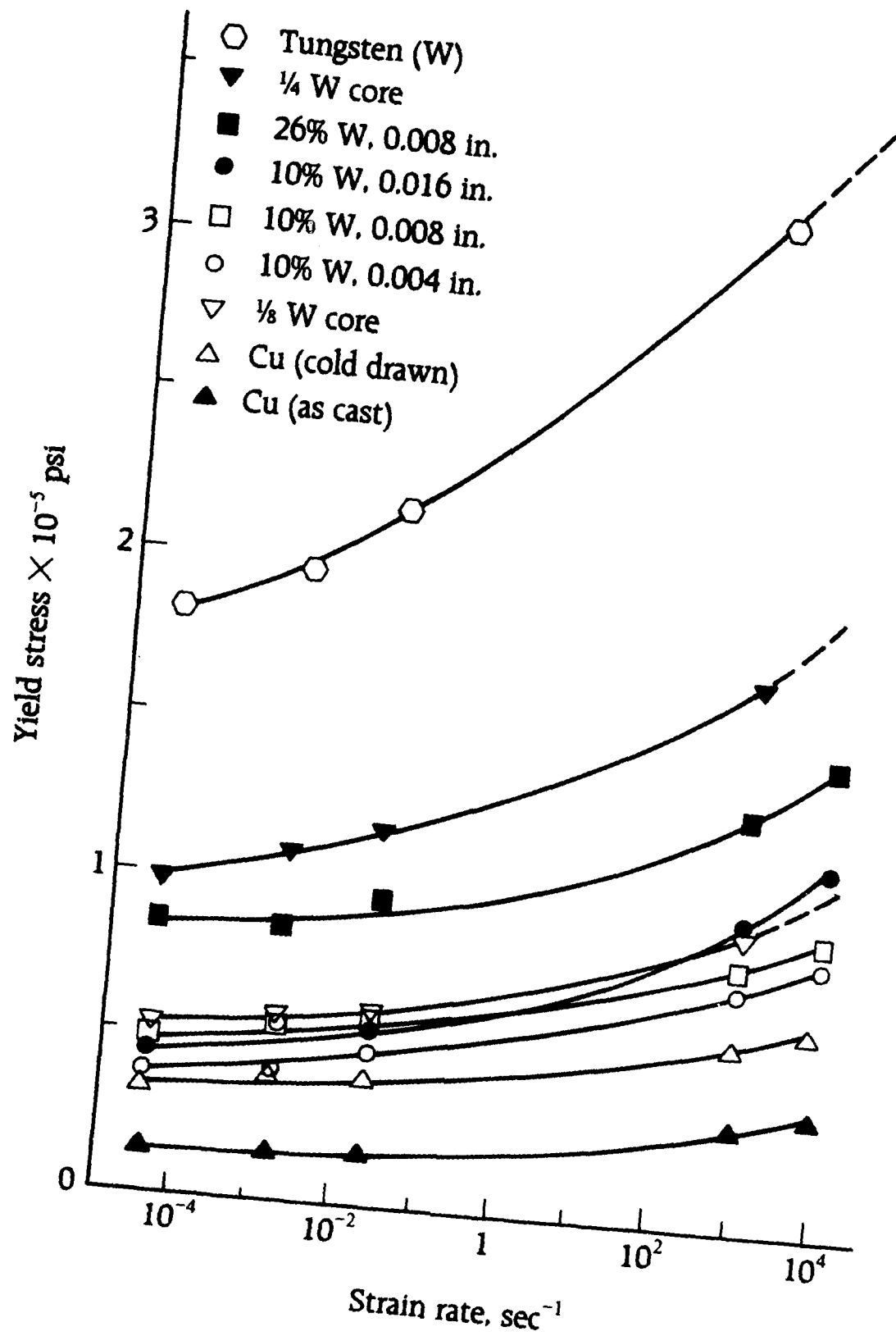
Figure 29 — Stress - Strain Curves for Cu W, Reference [24]

375
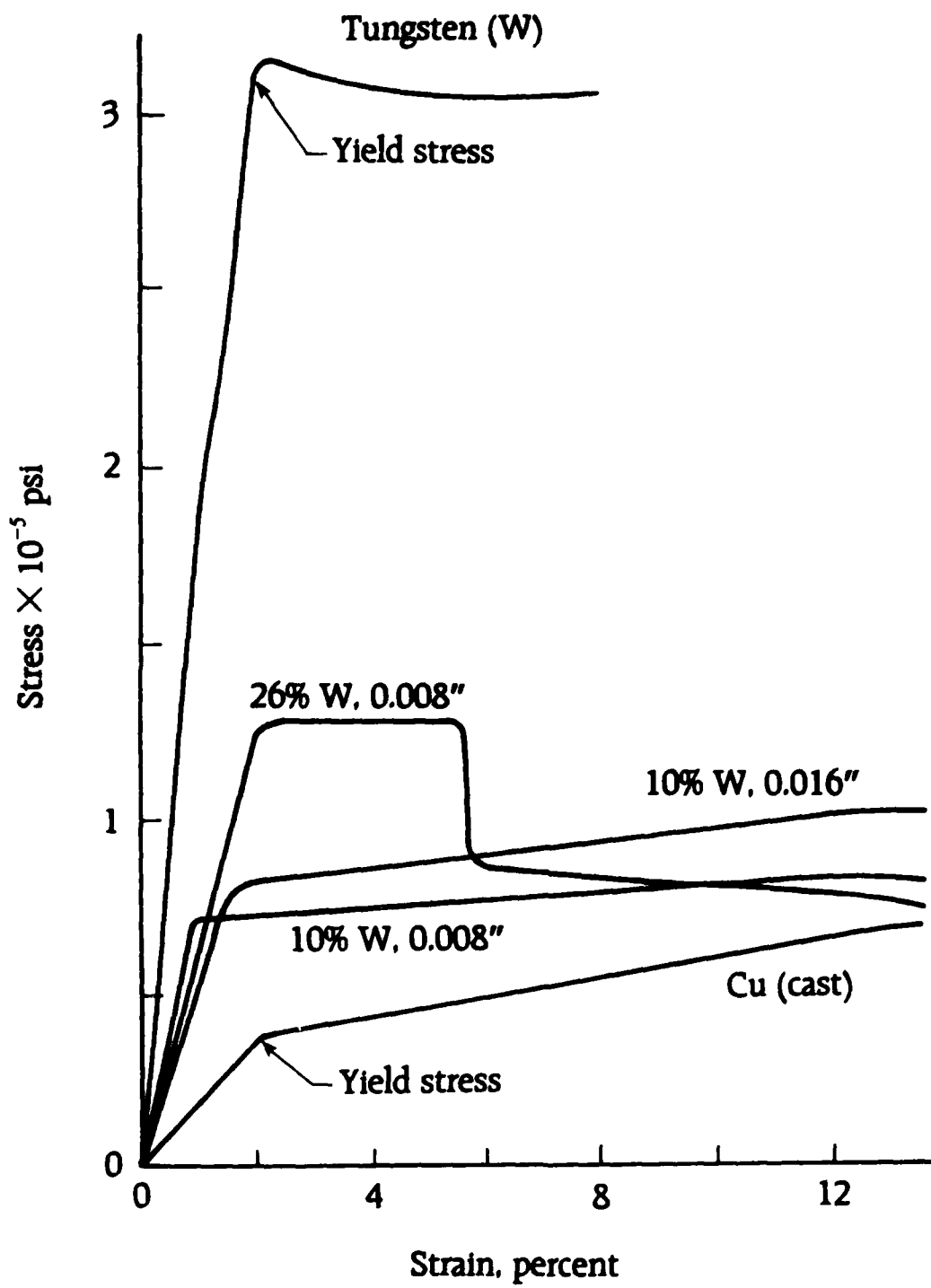
Figure 30 -    Yield Stress vs. Strain Rate for Cu W, Reference [24]
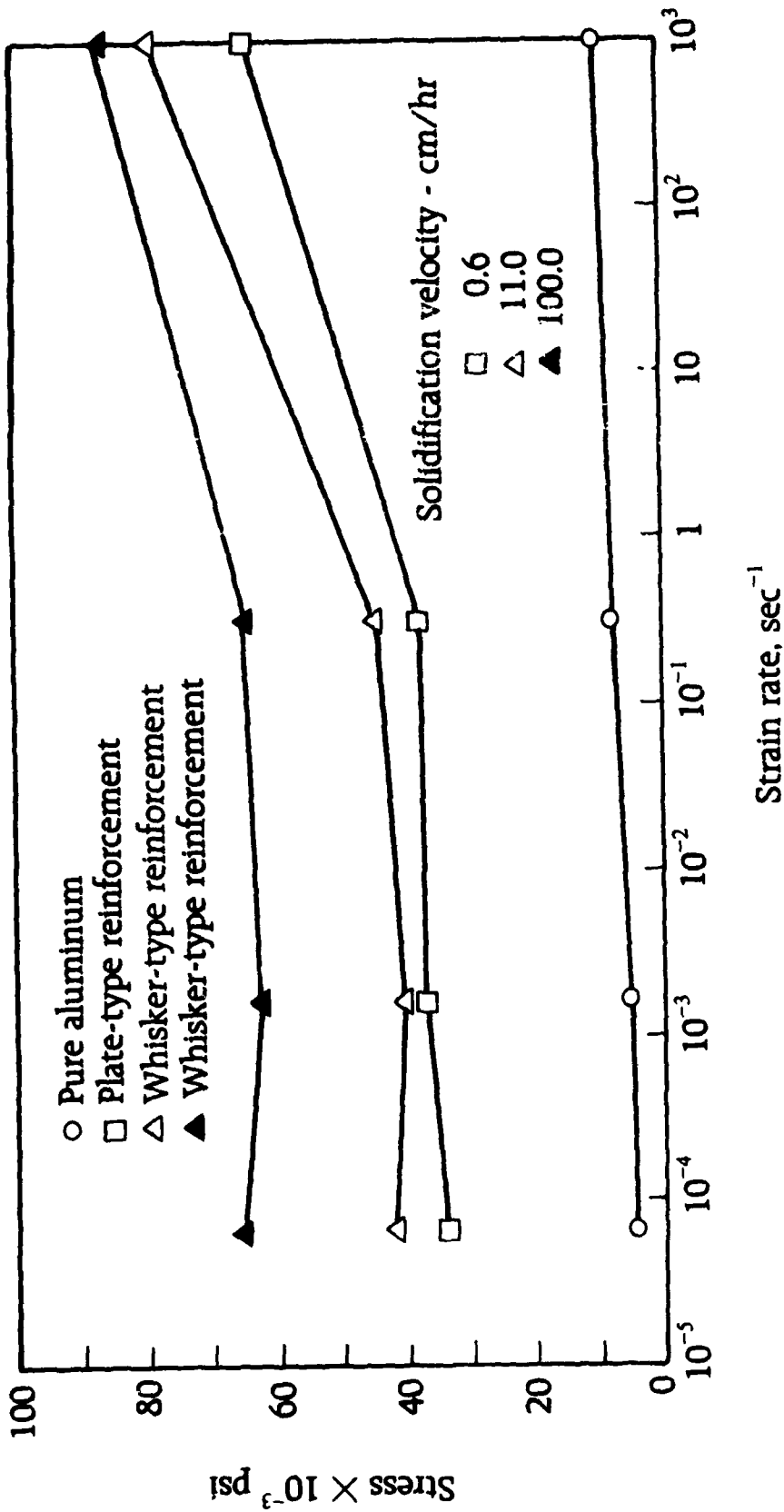
Figure 31 - Composite Stress vs. Strain Rate Al-Al₃Ni, Reference [25]
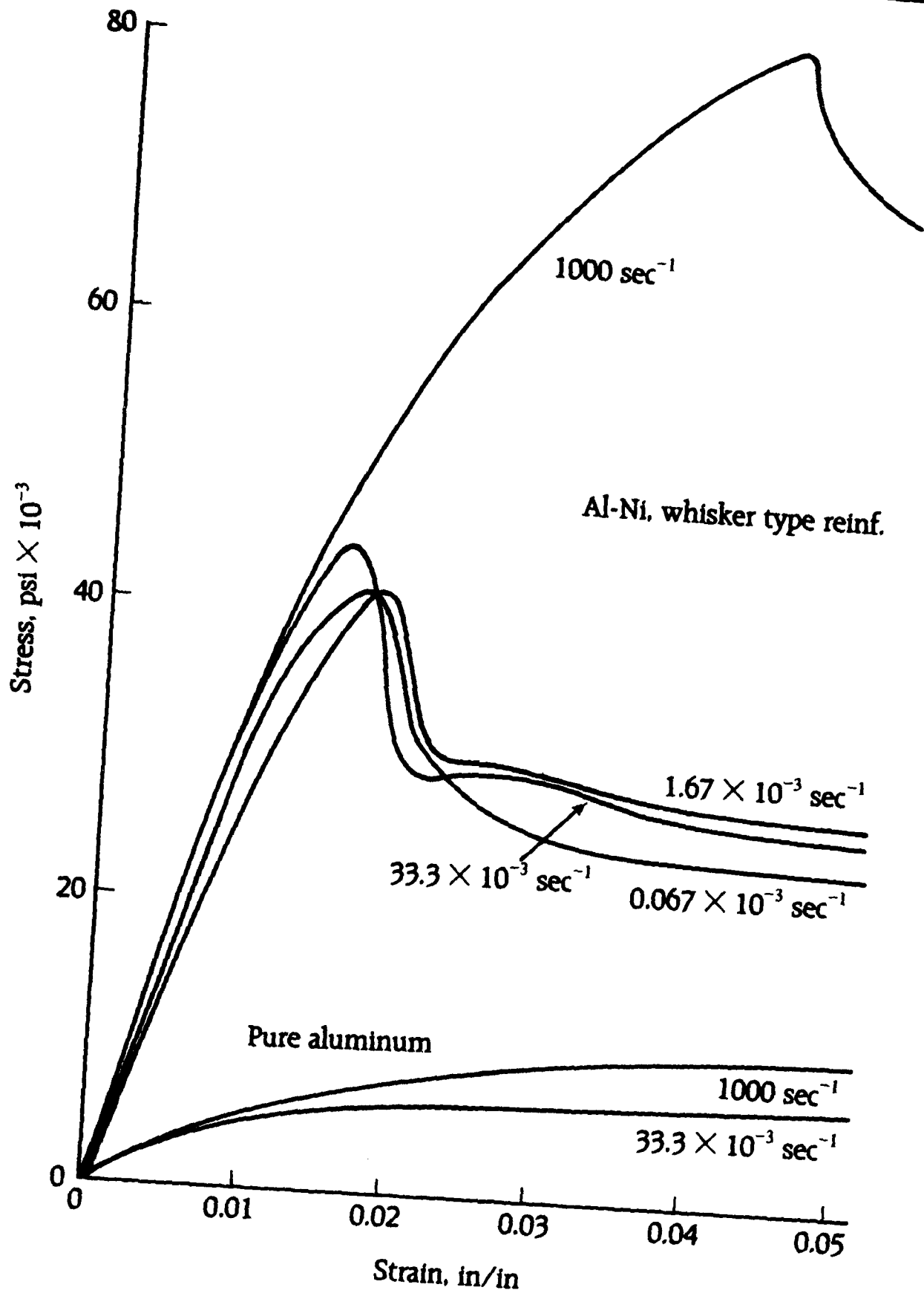
Figure 32 - Stress - Strain Curves Al-Al$_3$Ni Composite, Reference [25]

378

| Material Designation | Strain Rate $\dot{\epsilon}(s^{-1})$ | Yield Stress (MPa) | Flow Stress at Strain $\epsilon^C$(MPa) | Final Compressive Strain[a] $\epsilon^C$(%) |
|---|---|---|---|---|
| DU/45W(AF) | $1 \times 10^{-4}$ | 1365 | 1968 | 9.0 |
|  | $1.6 \times 10^3$ | 2010 | 2234 | 8.1 |
|  | $3.3 \times 10^3$ | 2000 | 2423 | 16.6 |
| DU/45W-3Re(HT) | $1 \times 10^{-4}$ | 1480 | 2180 | 12.7 |
|  | $1.5 \times 10^3$ | 2320 | 2530 | 7.6 |
|  | $2.6 \times 10^3$ | 2440 | 2640 | 13.3 |
| St/45W-1ThO$_2$(HT) | $1 \times 10^{-4}$ | 1120 | 1460 | 9.0 |
|  | $7 \times 10^2$ | 2310 | 2350 | 3.3 |
|  | $7 \times 10^2$ | 2160 | 2350 | 3.5 |
|  | $2 \times 10^3$ | 2430 | 2410 | 10.2 |

Figure 33 –    Quasistatic and Dynamic Longitudinal Compressive Strength of W Fiber-Reinforced Metal Matrix Composites, Reference [27]

379
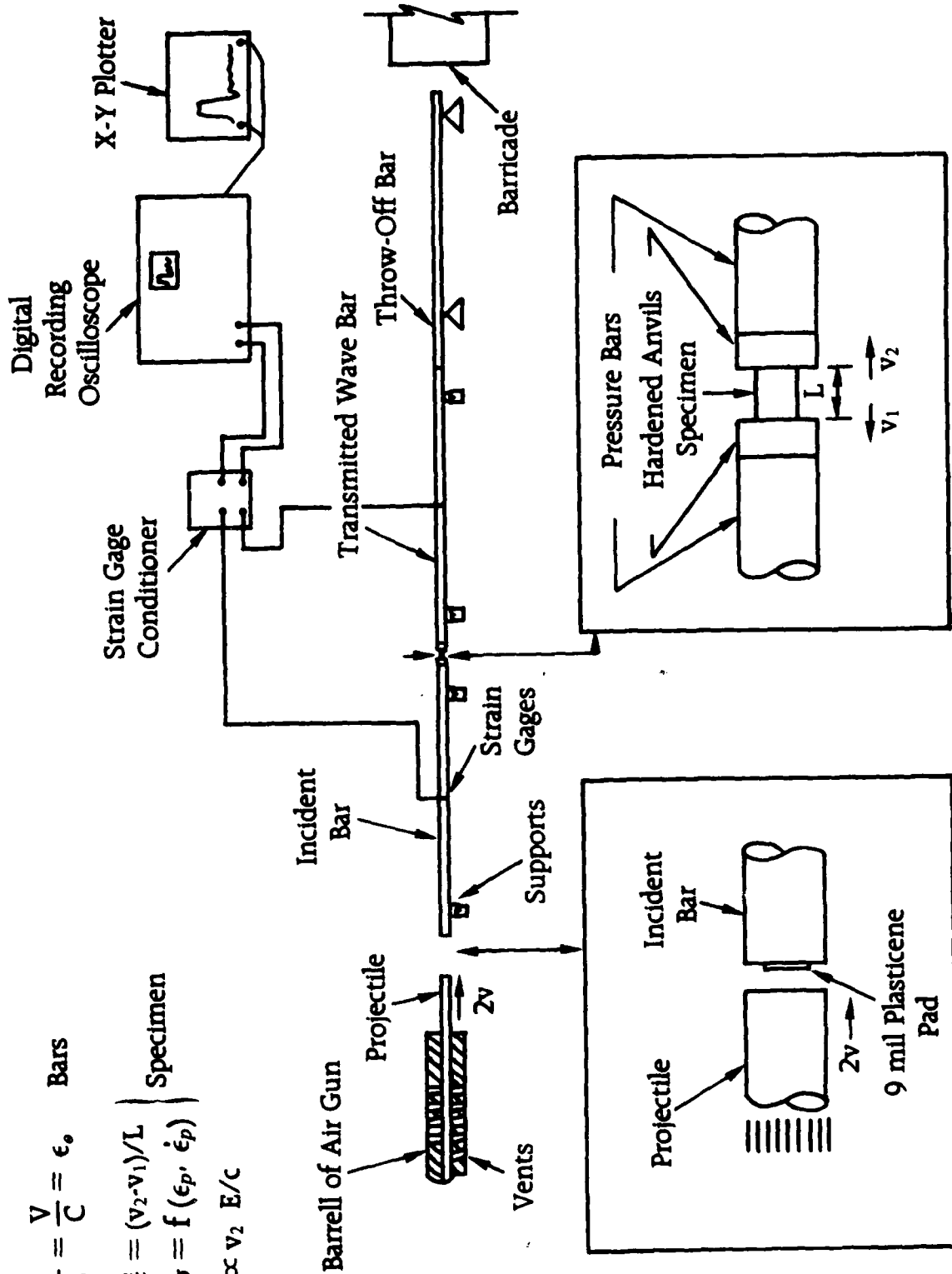
Figure 34 – Schematic Compression SHPB used for MMC (Tungsten/Al, Tungsten/Steel, Du/Tungsten), Reference [27]
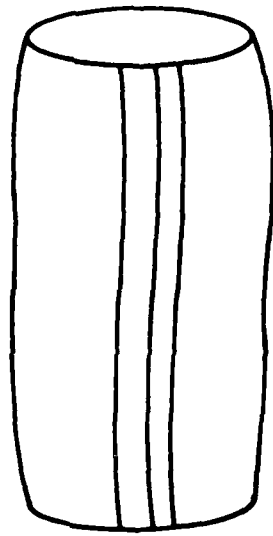
**Plastic Buckling**
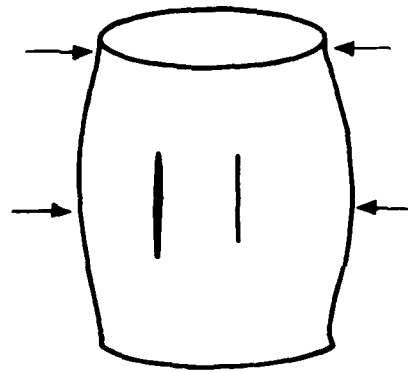
**Barreling with Longitudinal Splitting**
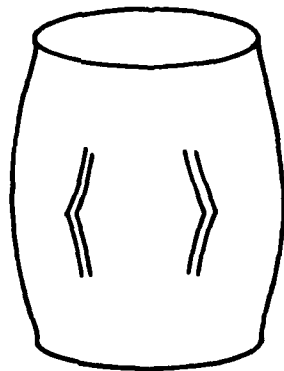
**Fiber Buckling**
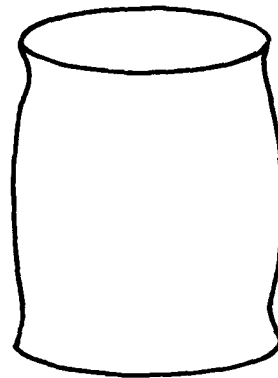
**Brooming**

Figure 35 -    Schematic Compressed Failure Specimen Modes, Reference [27]
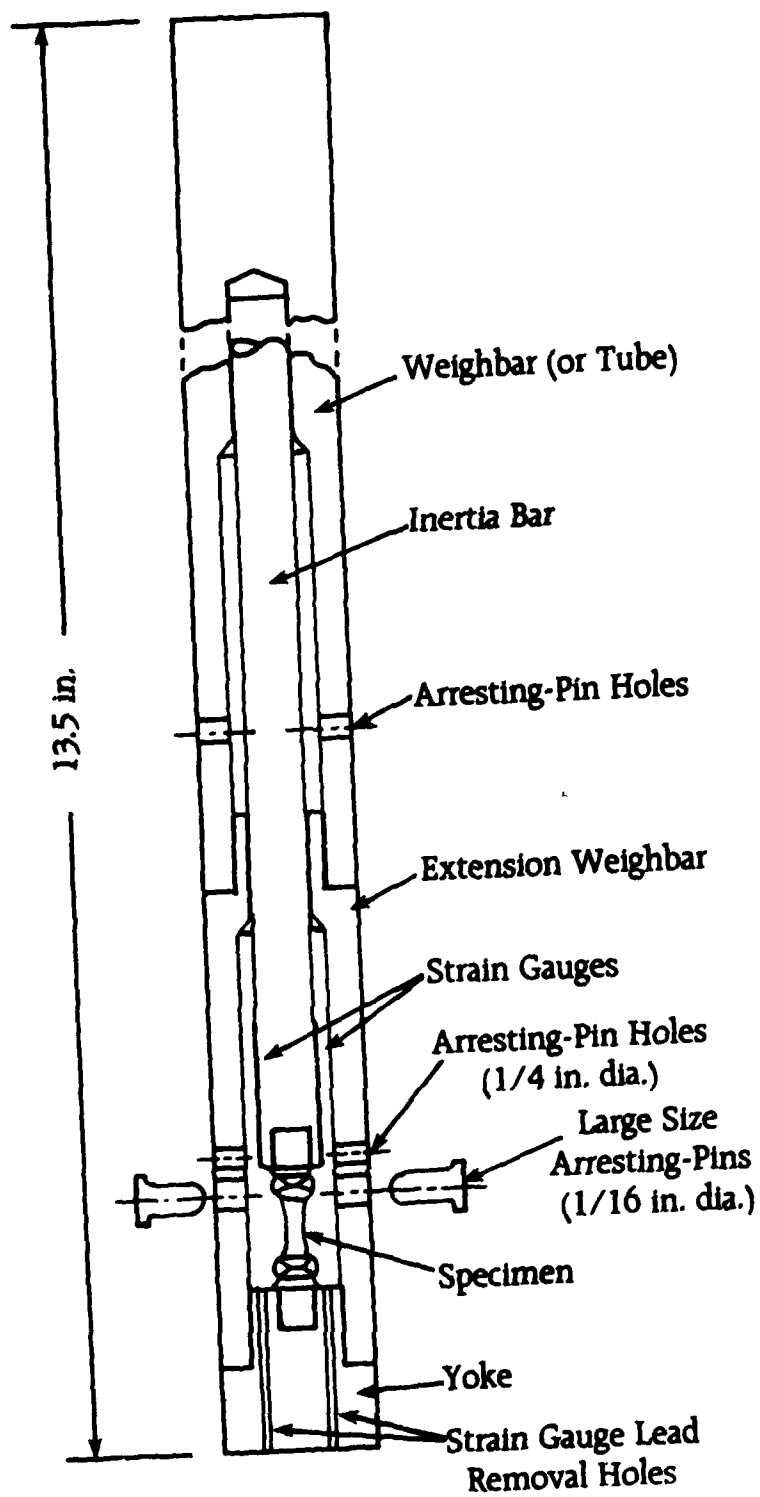
Figure 36 -    Tensile PB Apparatus, Reference [29]
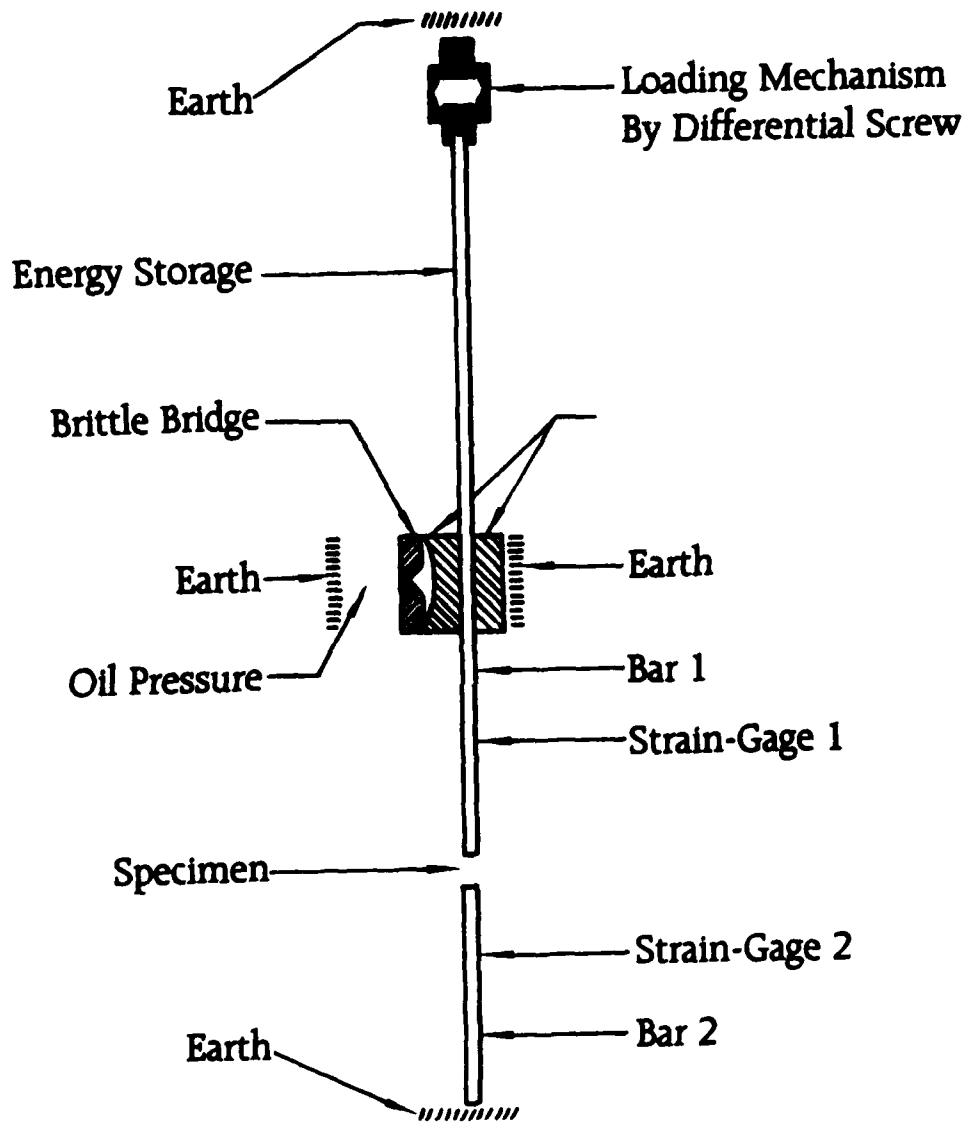
Figure 37 -    Schematic Hopkinson Pressure Bar System, Reference [16]

383
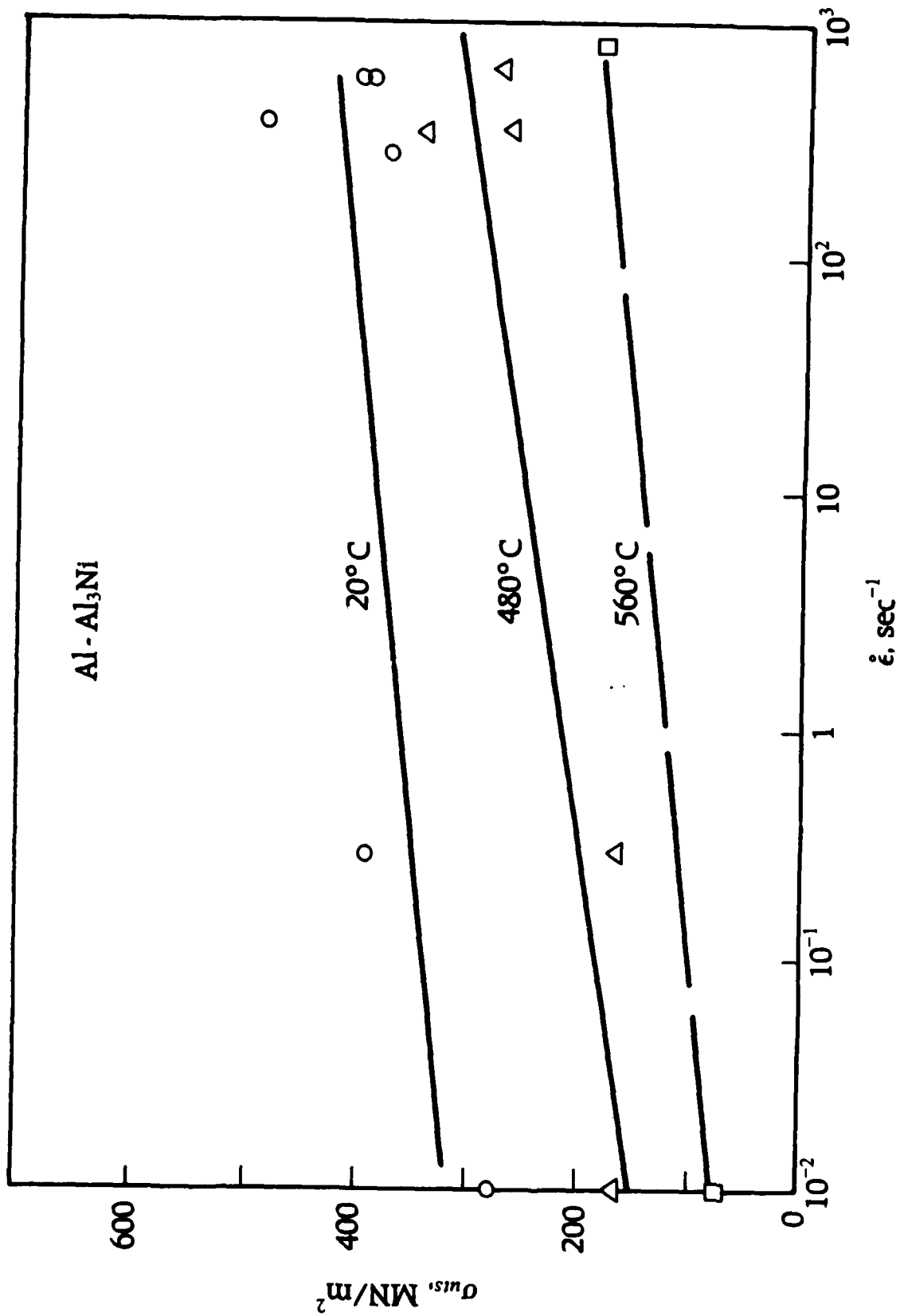
Figure 38 – Strength vs. Strain Rate and Temperature for Al-Al₃Ni, Reference [16]
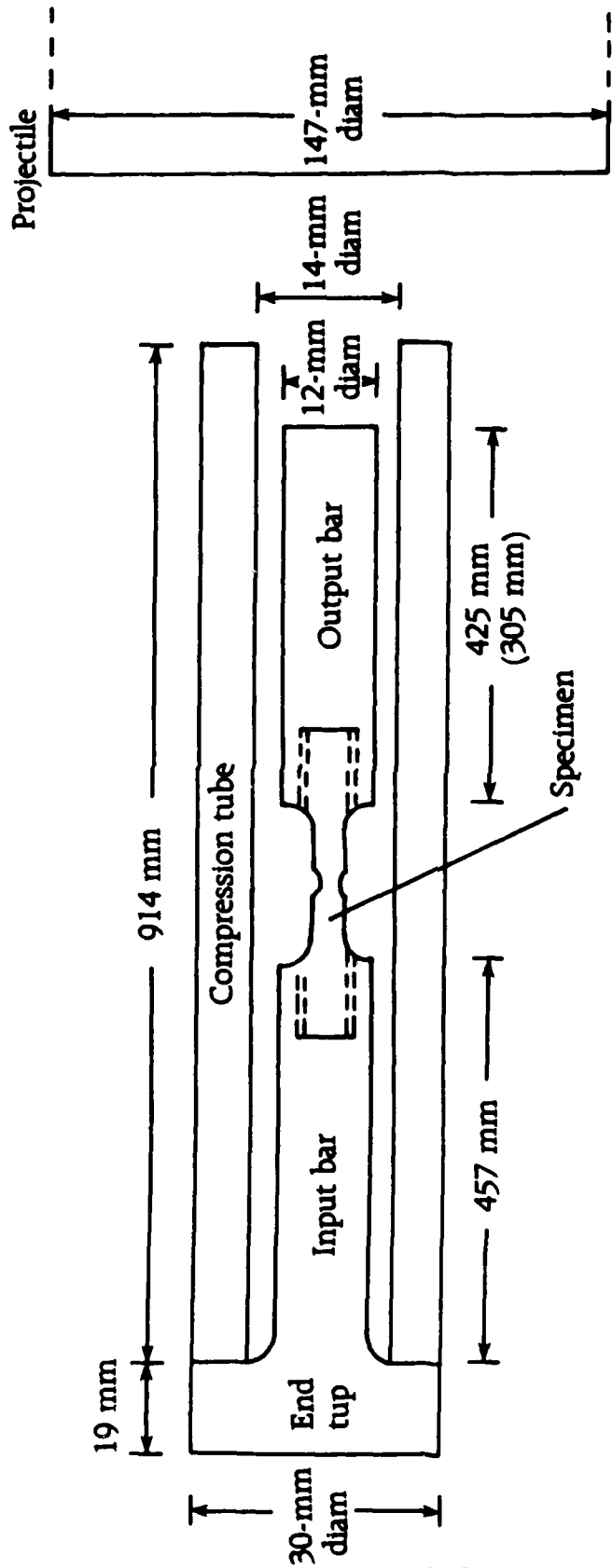
Figure 39 – Schematic SHPB Tensile System, Reference [30]

385
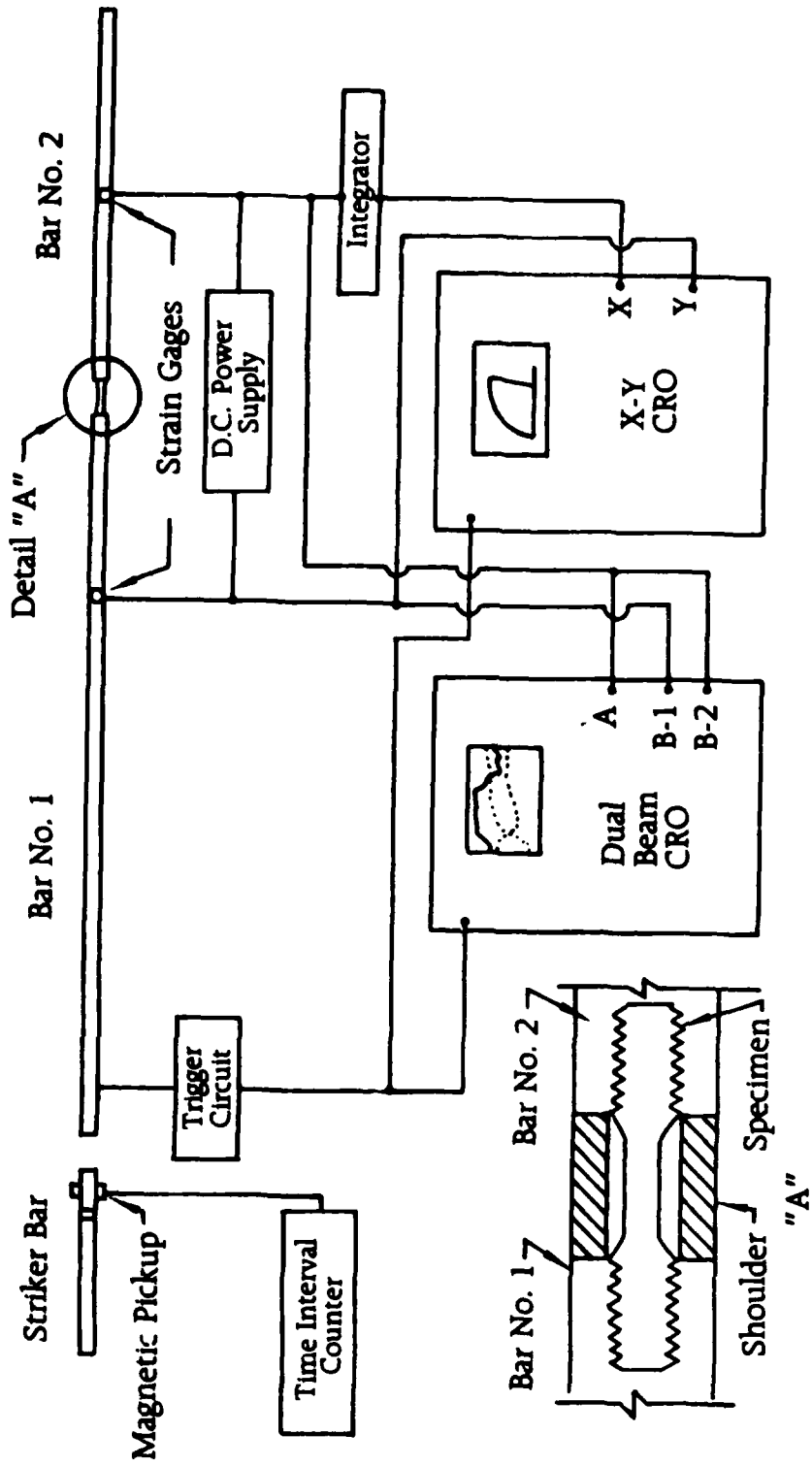
Figure 40 –   Schematic Tensile SHPB Apparatus, Reference [31]
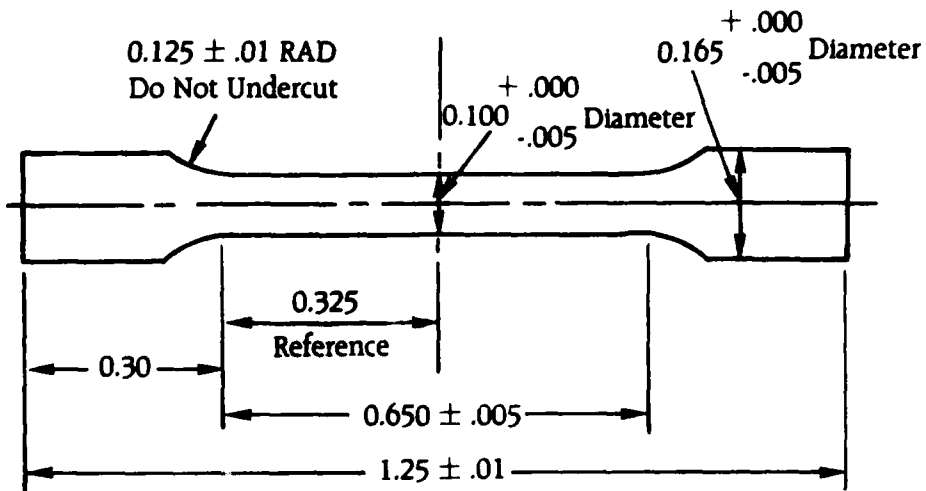
**Tensile Specimen**
Scale 4 x Size

(a) Machine Drawing (Dimensions in Inches)
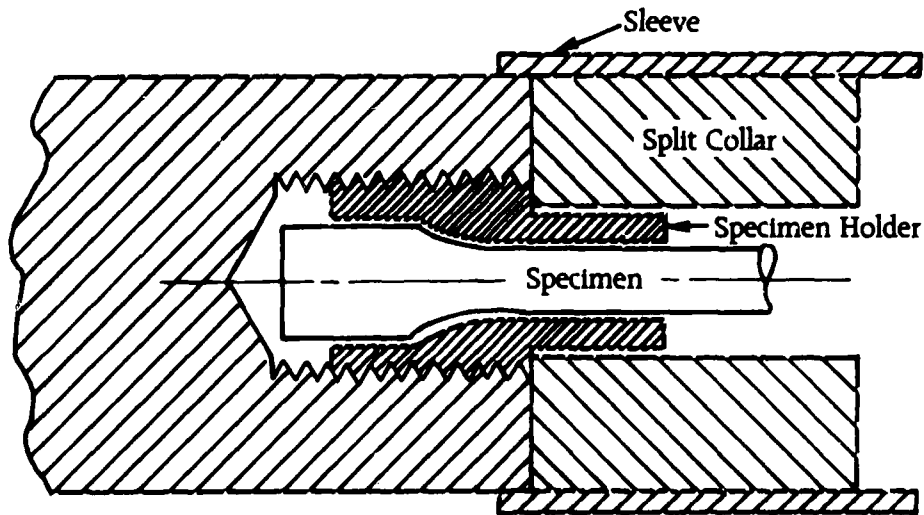


(b) Specimen Inserted in Bar

Figure 41 -     Specimen Configurations Tensile SHPB FP/Al, SiC/6061, SMC
Composites, Reference [33]
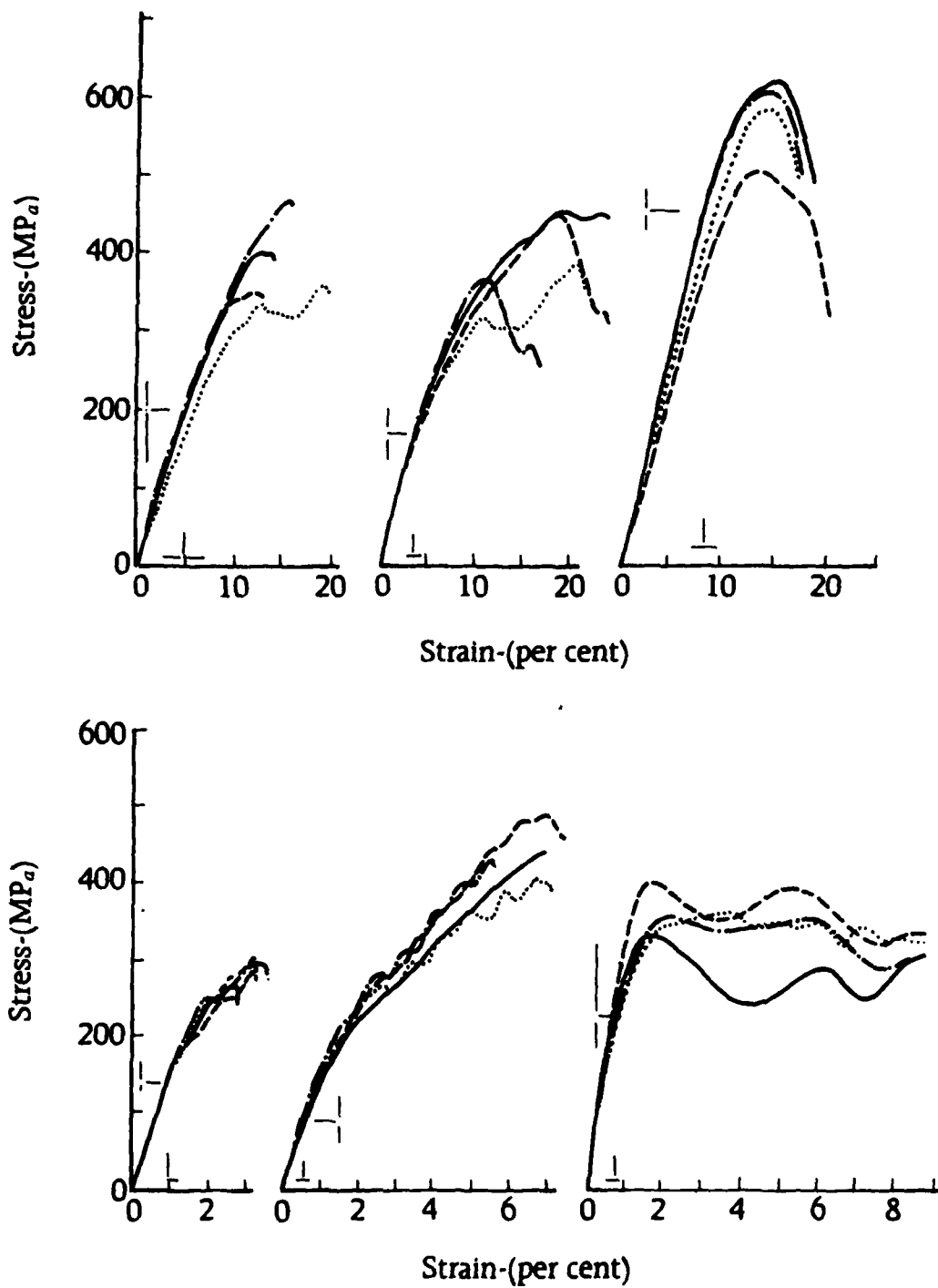
Figure 42 -    Tensile Stress - Strain Curves CFRP and GFRP at Three Strain
              Rates:  $10^{-4}$/sec., 10/sec., 700/sec., Reference [34]

All Carbon
50% fibre by wt.

Carbon-glass 2(b)
Wt. fraction,
C:G=2.95

Carbon-glass 2(a)
Wt. fraction,
C:G=1.48

Carbon-glass 1
Wt. fraction,
C:G=0.66

All Glass
50% fibre by wt.

389
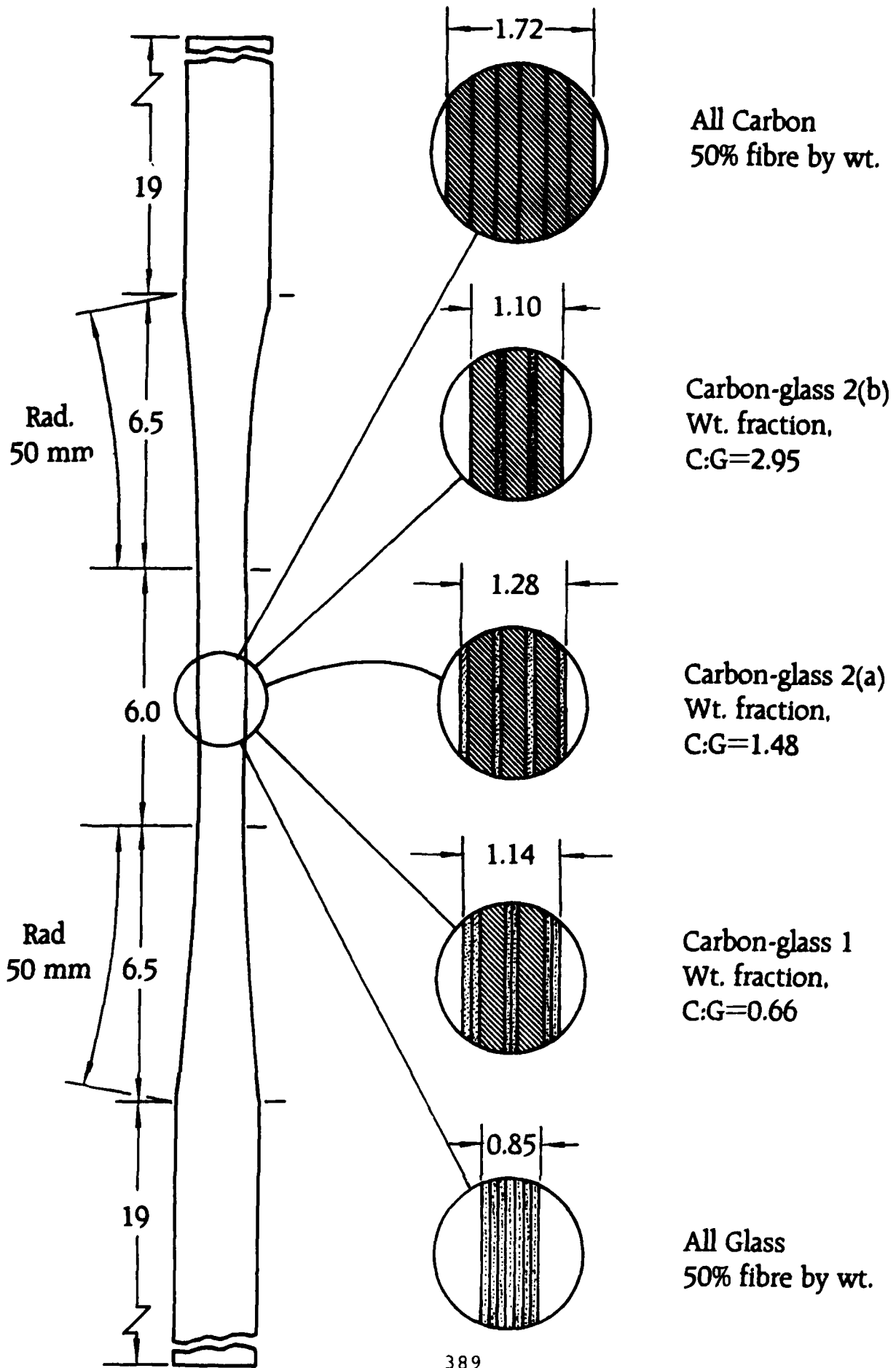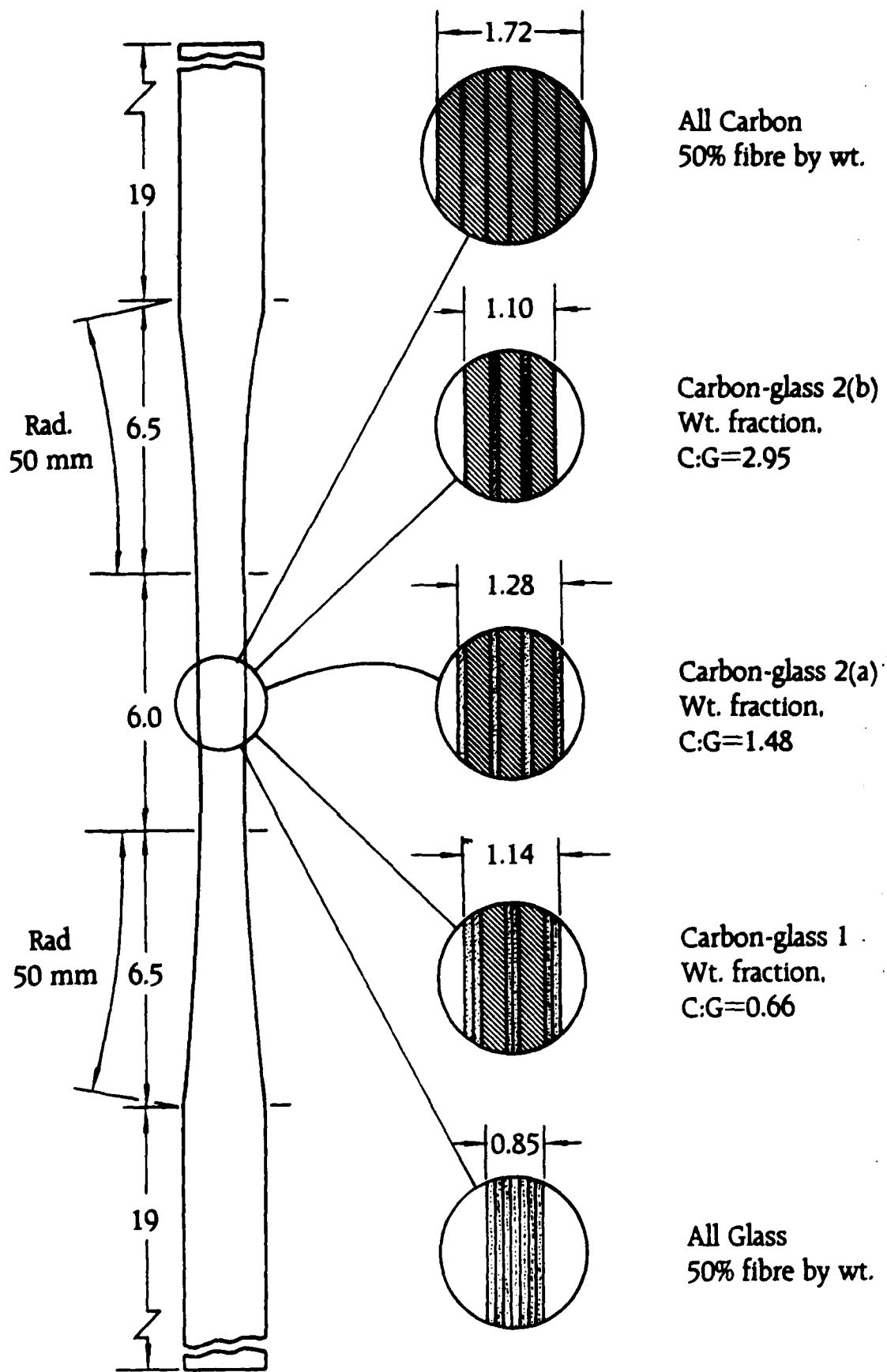
Figure 43 -    Test Specimen Configurations, Reference [35]
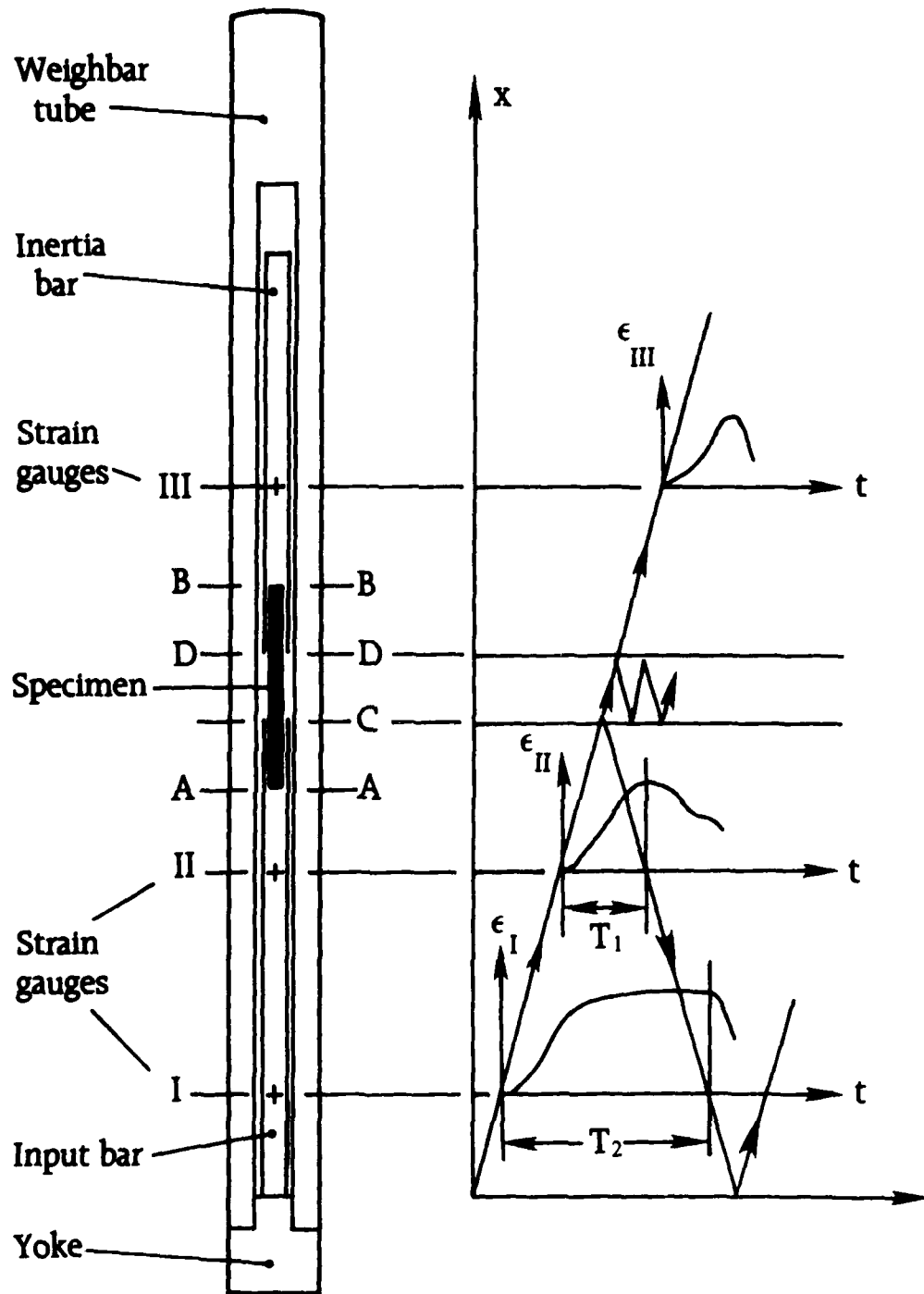
Figure 44 - Schematic Tensile SHPB Arrangement and Wave Diagram, Reference [35]

391
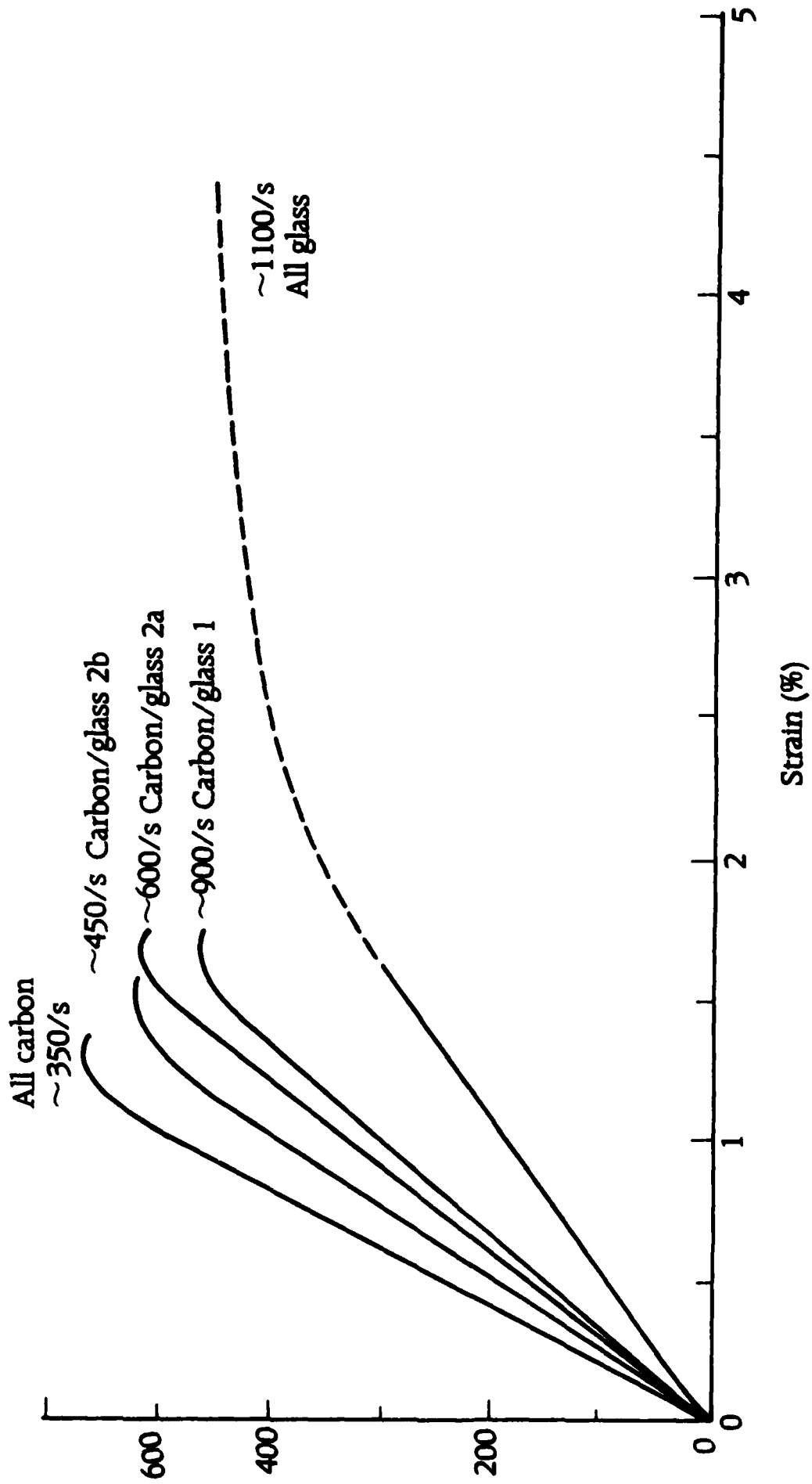
Figure 45 – Dynamic Stress-Strain Curves for Various Composites, Reference [35]
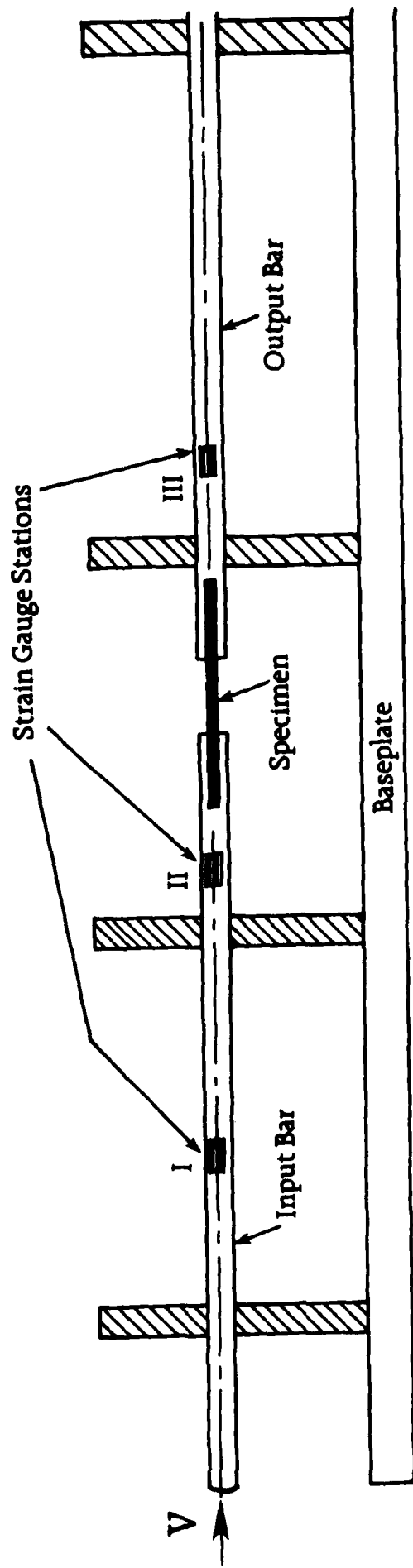
Fig. 12a   Test Rig for Impact Compression Tests
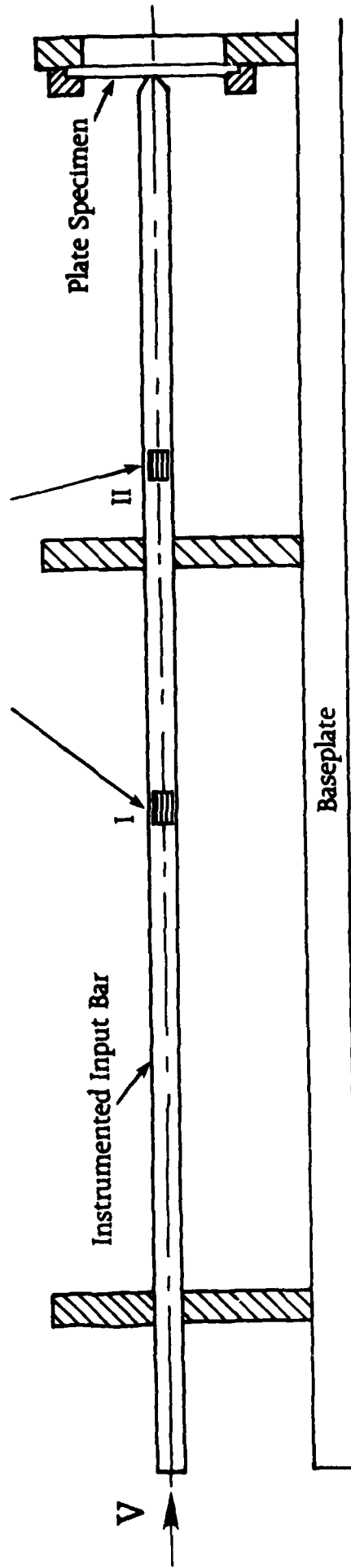
Figure 46 –   Test Configuration Pressure Bar Tests, Reference [36]

393

b. 'Yield' and Maximum Stress
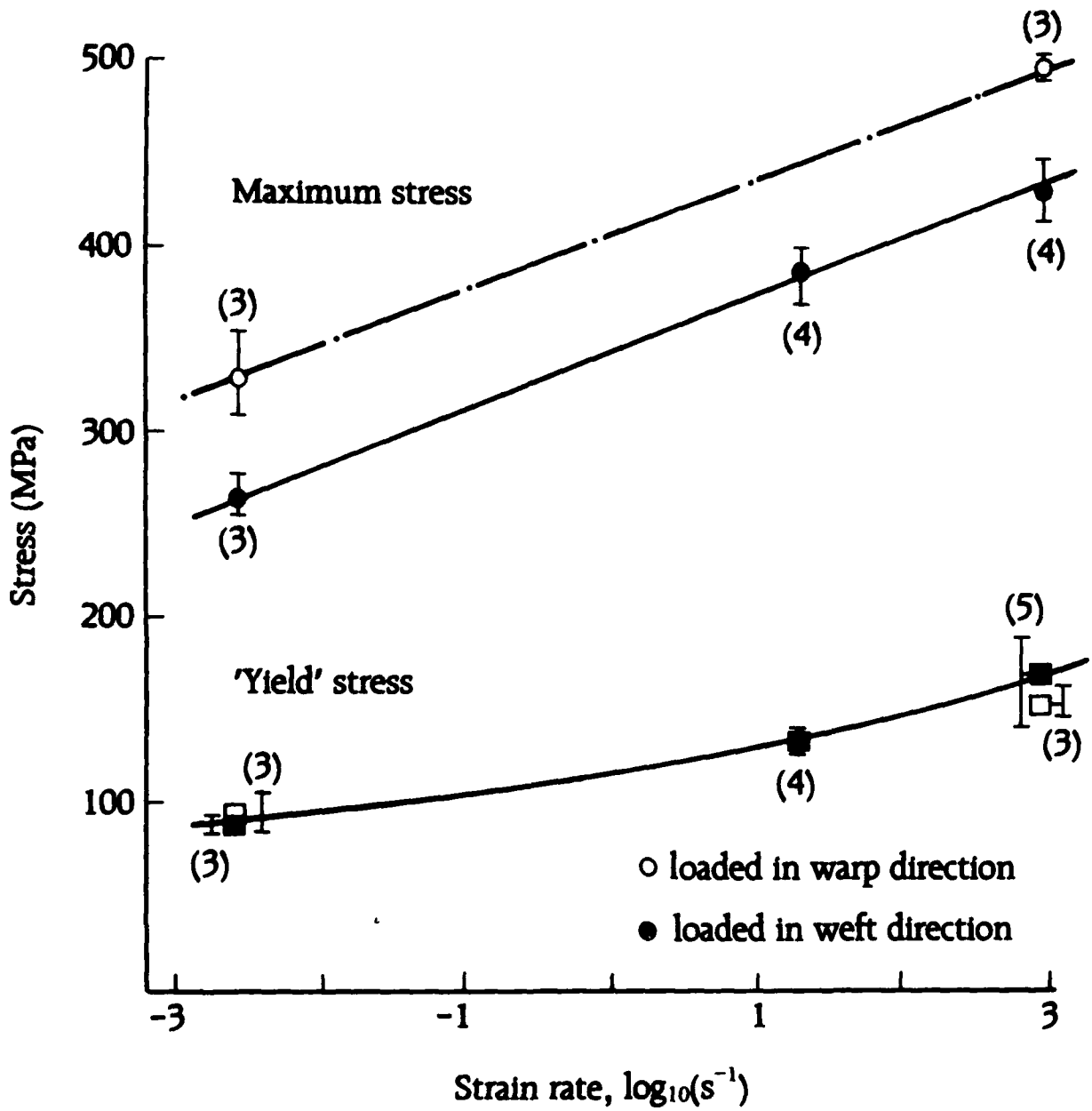
Figure 47 -    Strain Rate Effects All Glass Composites, Reference [36]
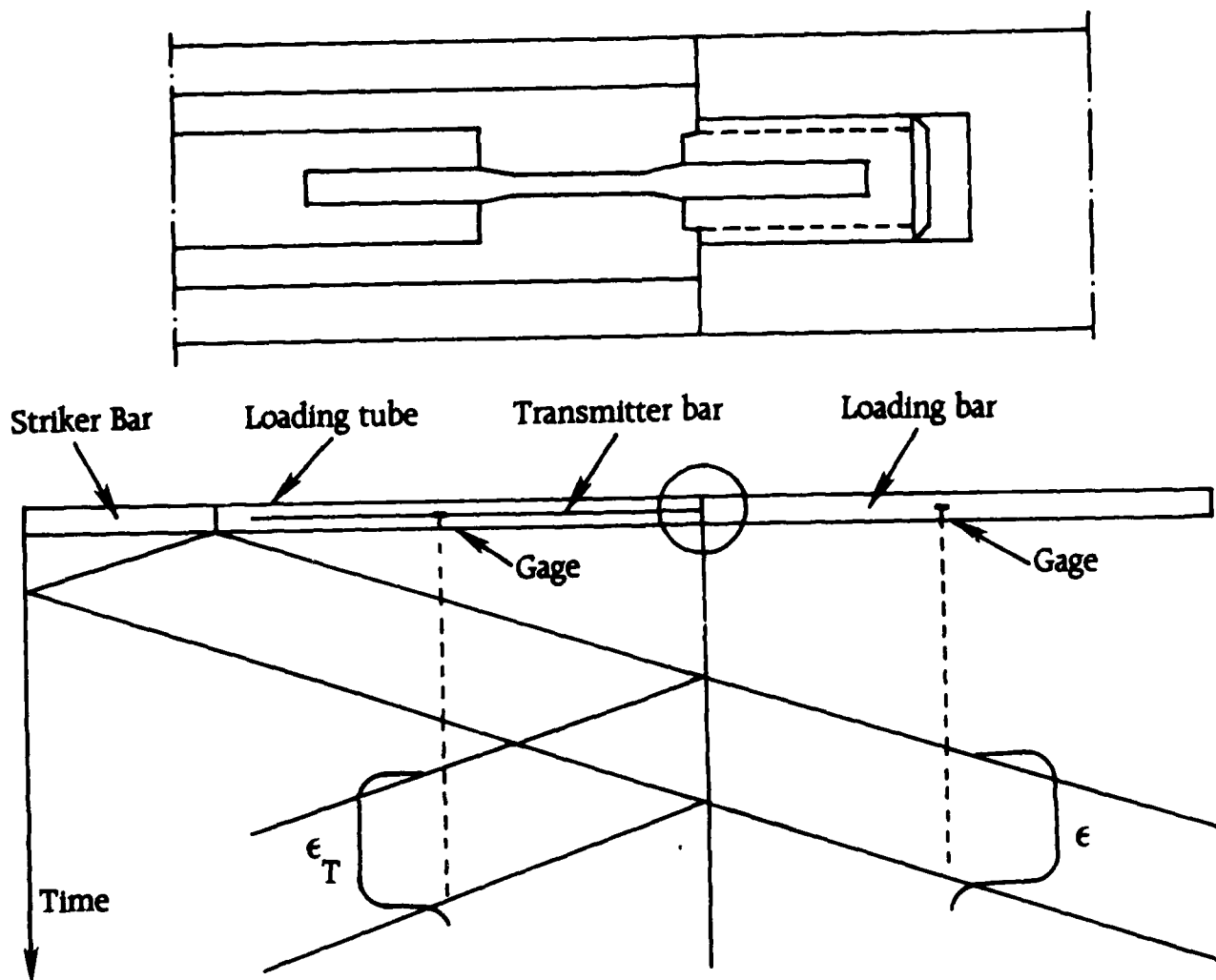
Figure 48 -     Schematic Tensile SHPB, Reference [37]
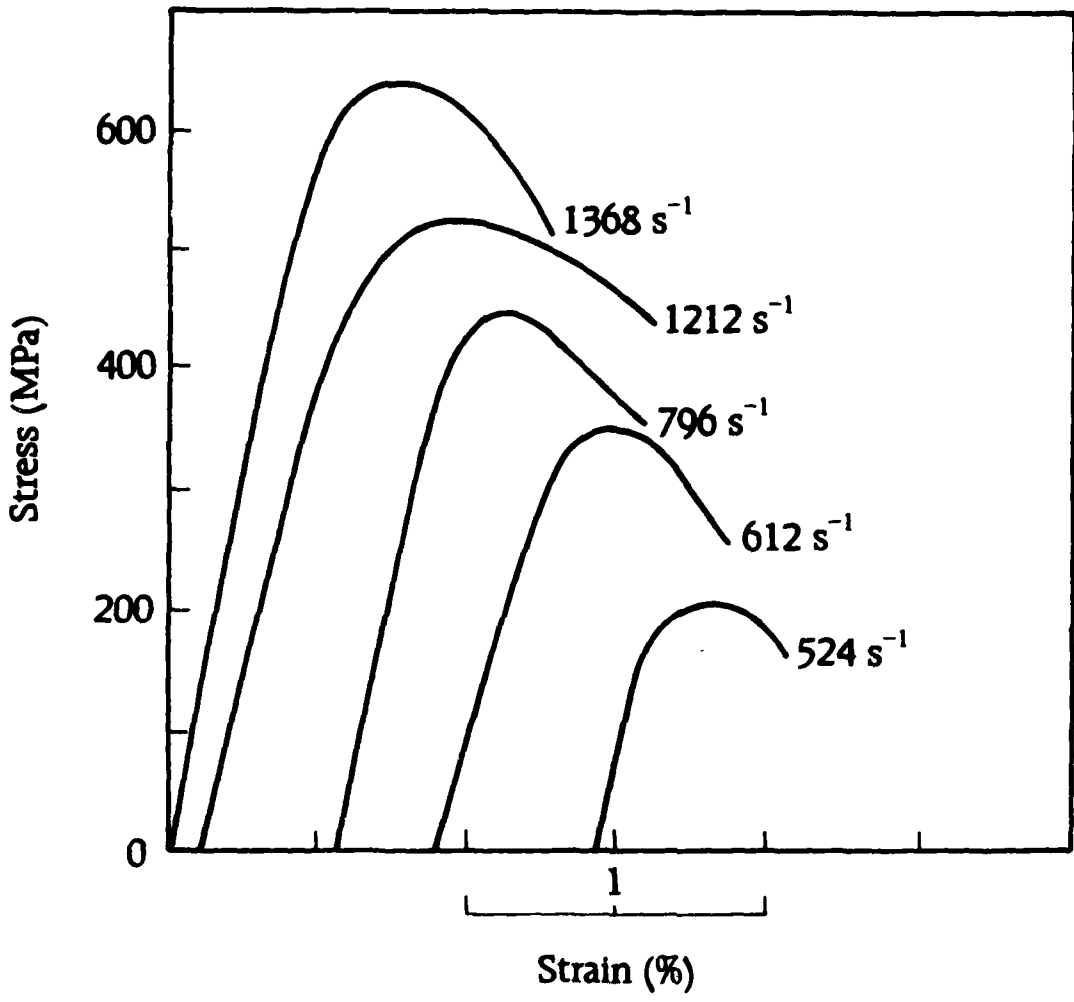
Figure 49 –     Tensile SHPB Stress – Strain Curves Woven Carbon/Epoxy
                Composites, Reference [37]
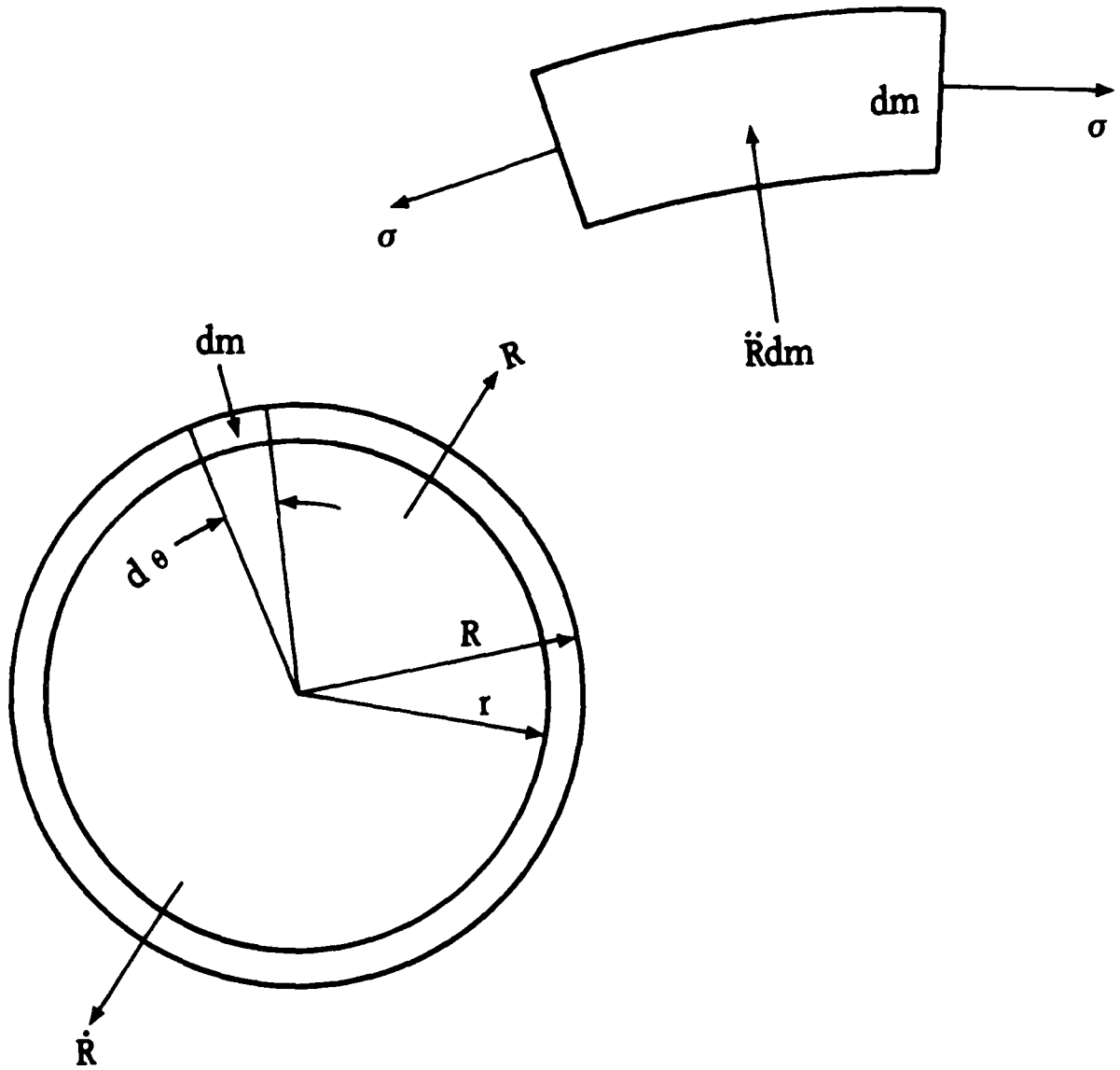
Figure 50 -    Schematic Expansion Thin Ring, Reference [38]
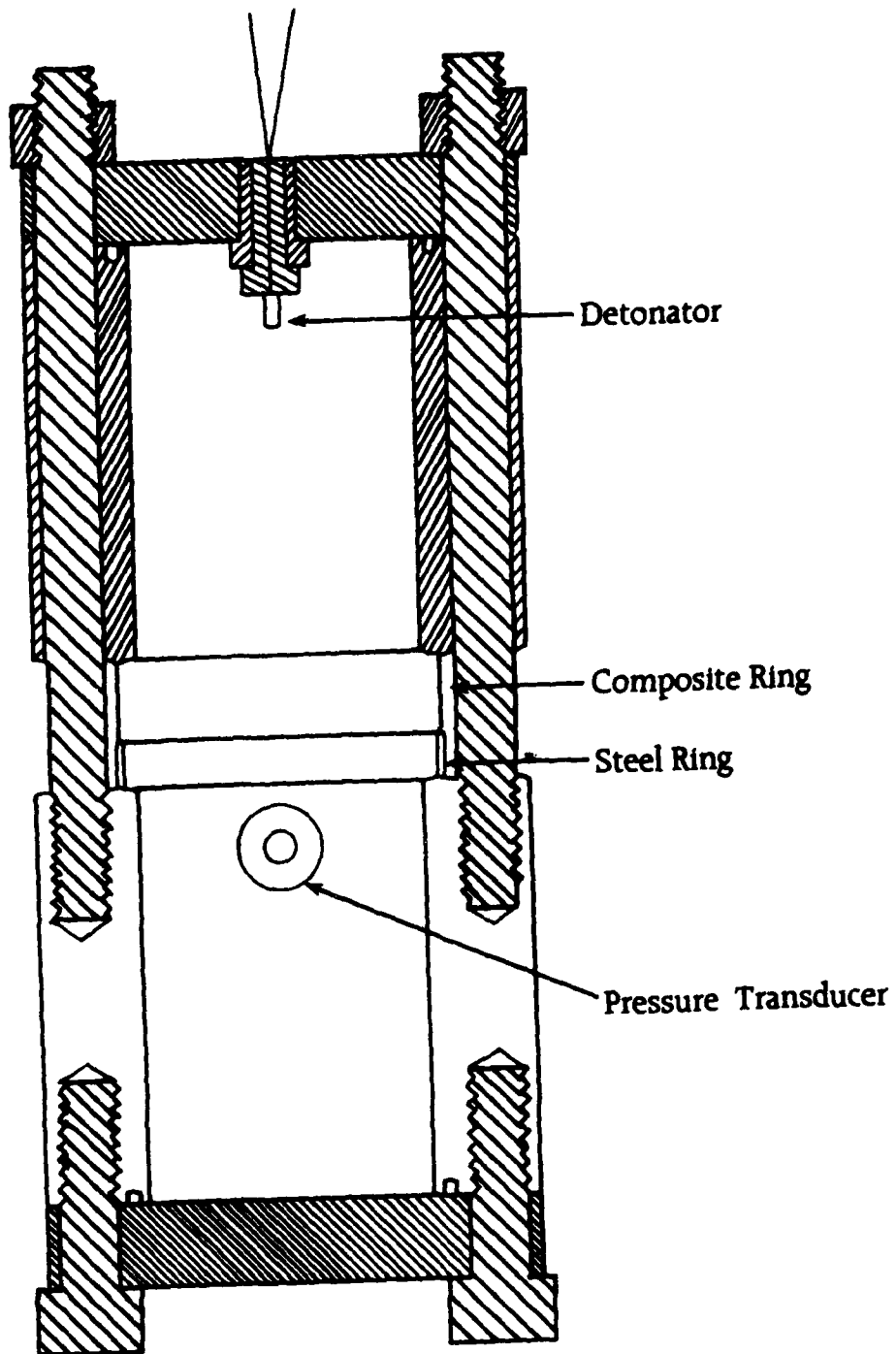
Figure 51 -      Schematic Tensile Split Ring Testing Fixture, Reference [39]
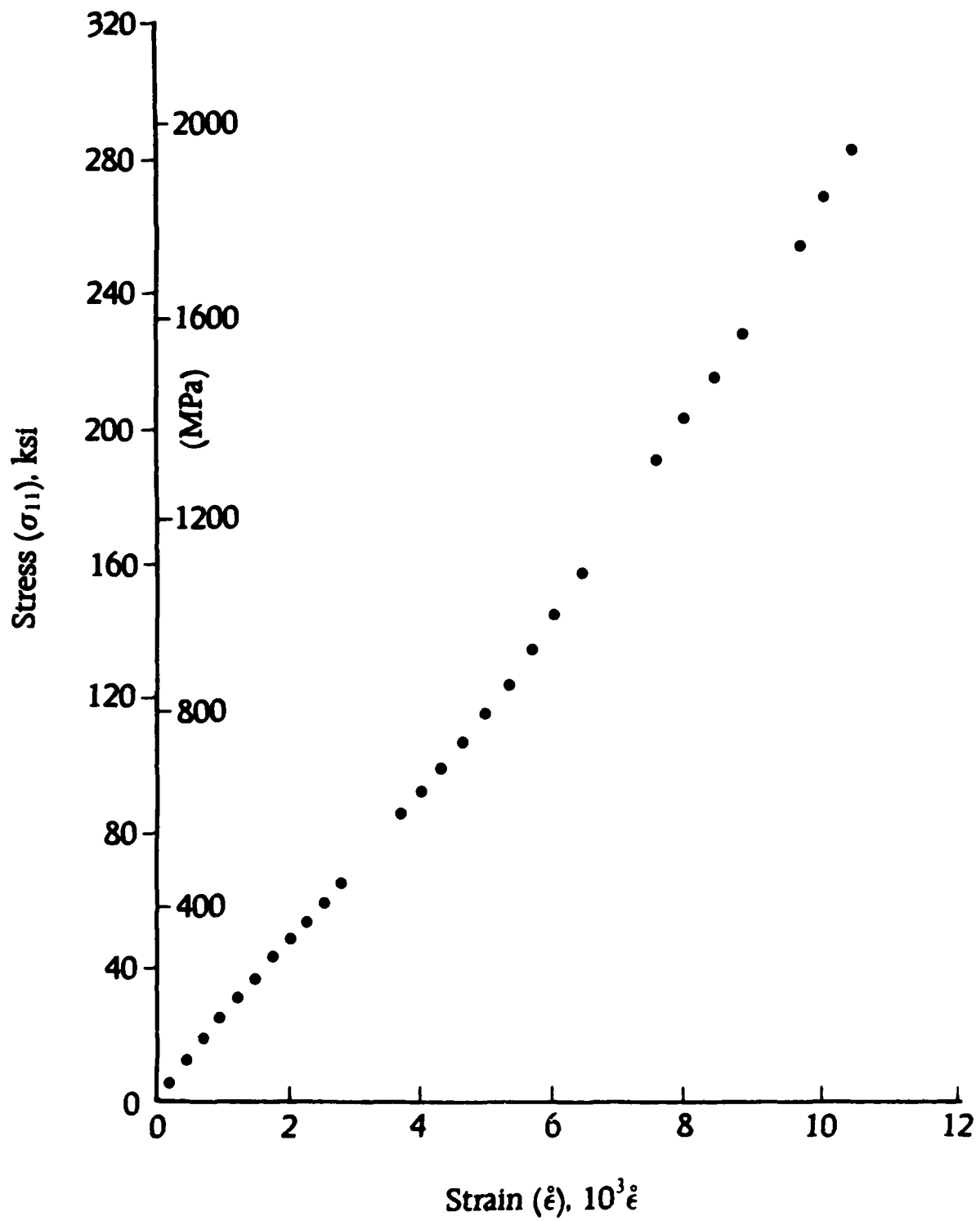
Figure 52 -     Dynamic Tensile Stress-Strain Curve, Graphite Epoxy (SP
                288/AS), Reference [39]
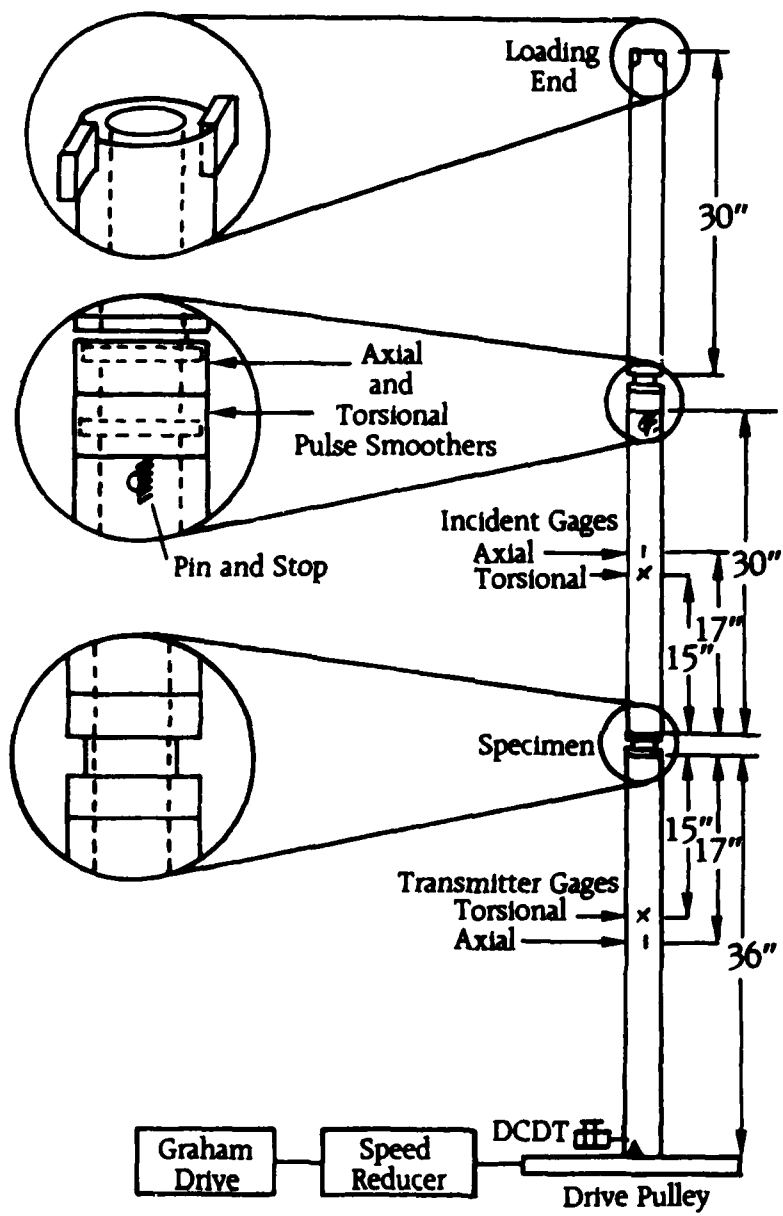
Figure 53 -    Schematic Torsional Pressure Bar, Reference [40]

400
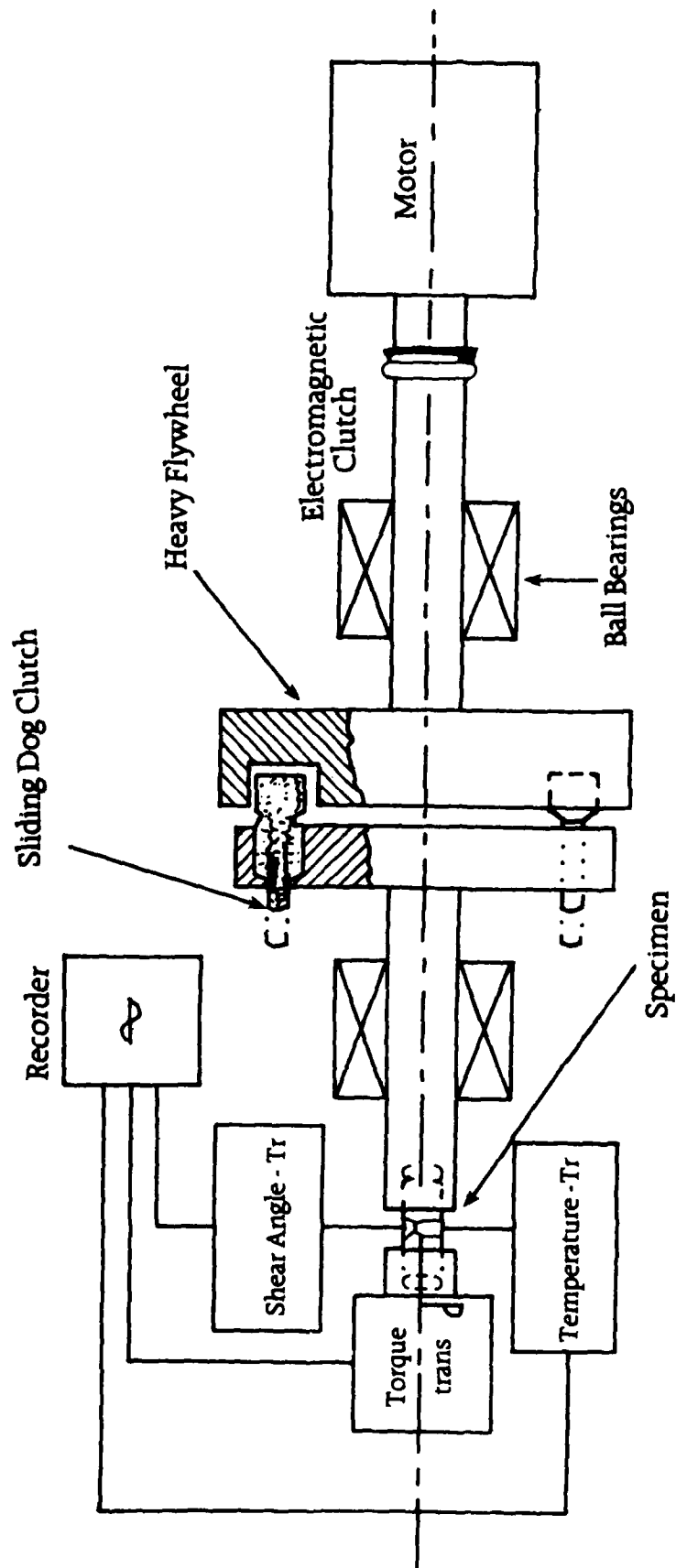
Figure 54 - Torsional Dynamic Apparatus, Reference [41]
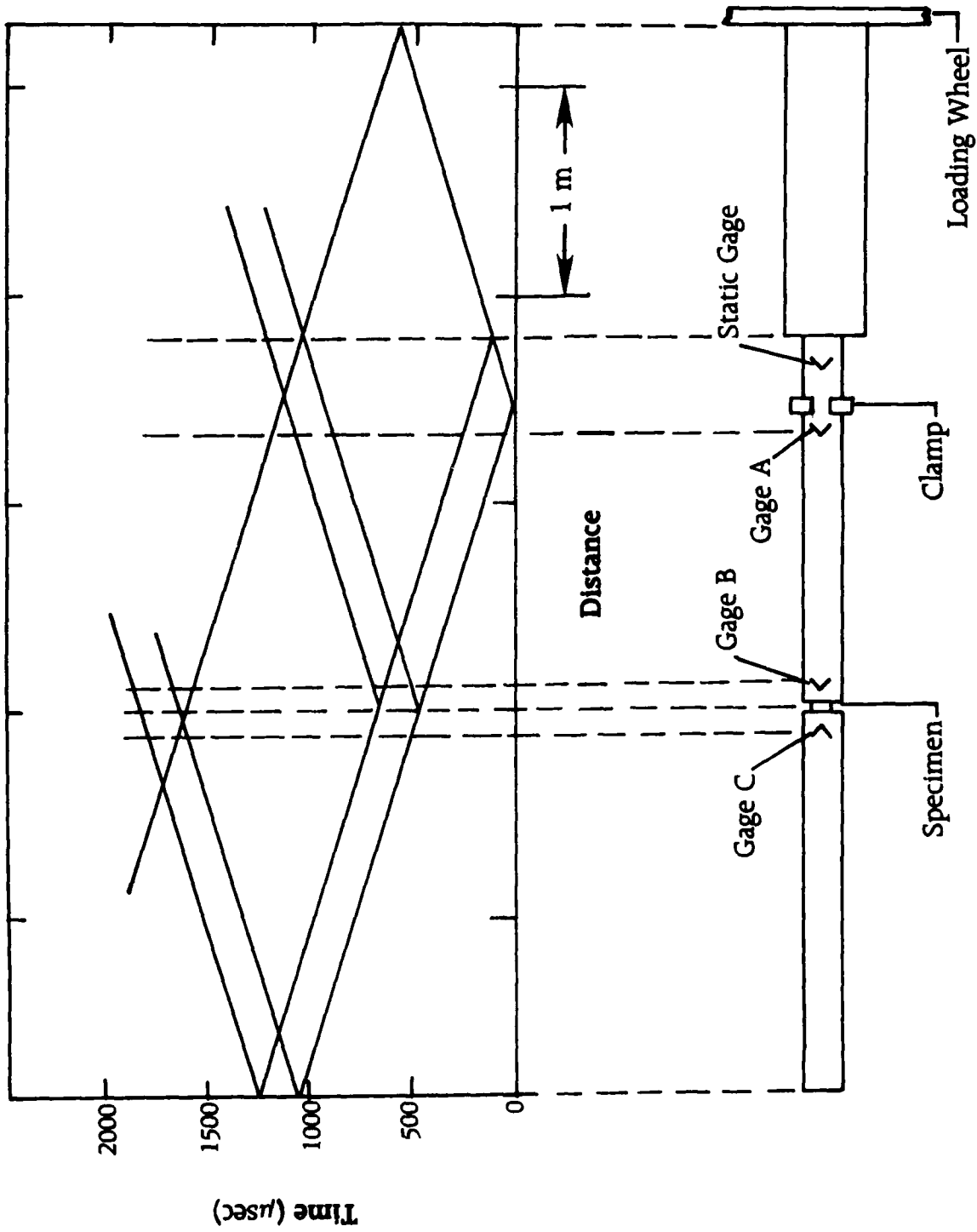
Figure 55 – Schematic Torsional Pressure Bar and Lagrangian Wave Diagram, Reference [44]

402
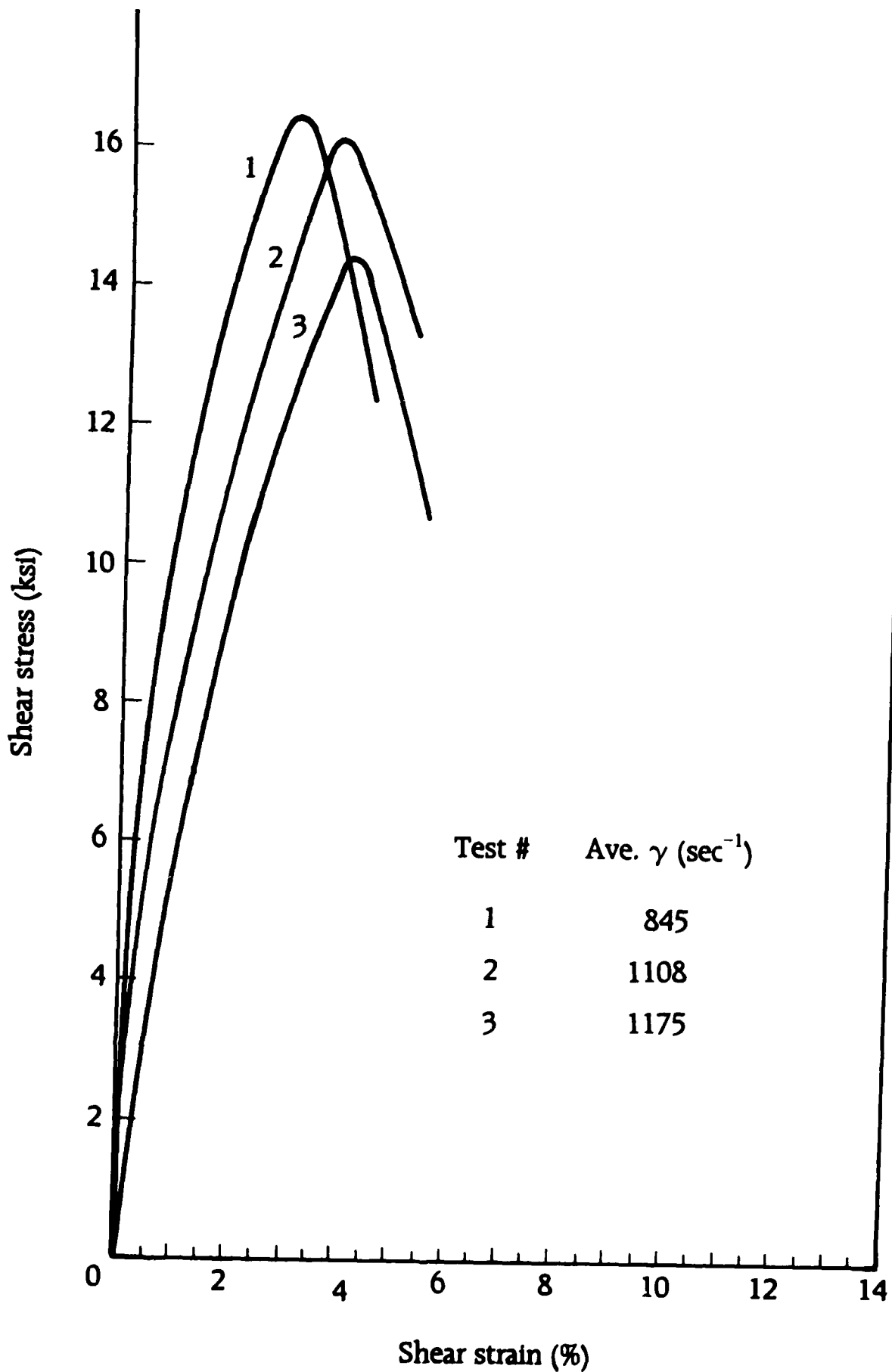
Figure 56 –     Dynamic Shear Stress - Strain Curves Hydraulic Cement, Reference [45]
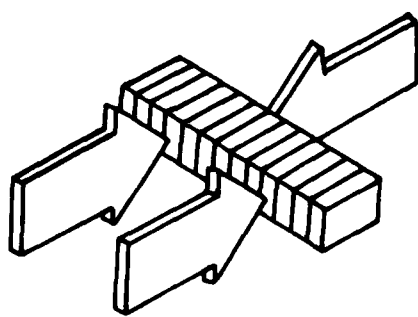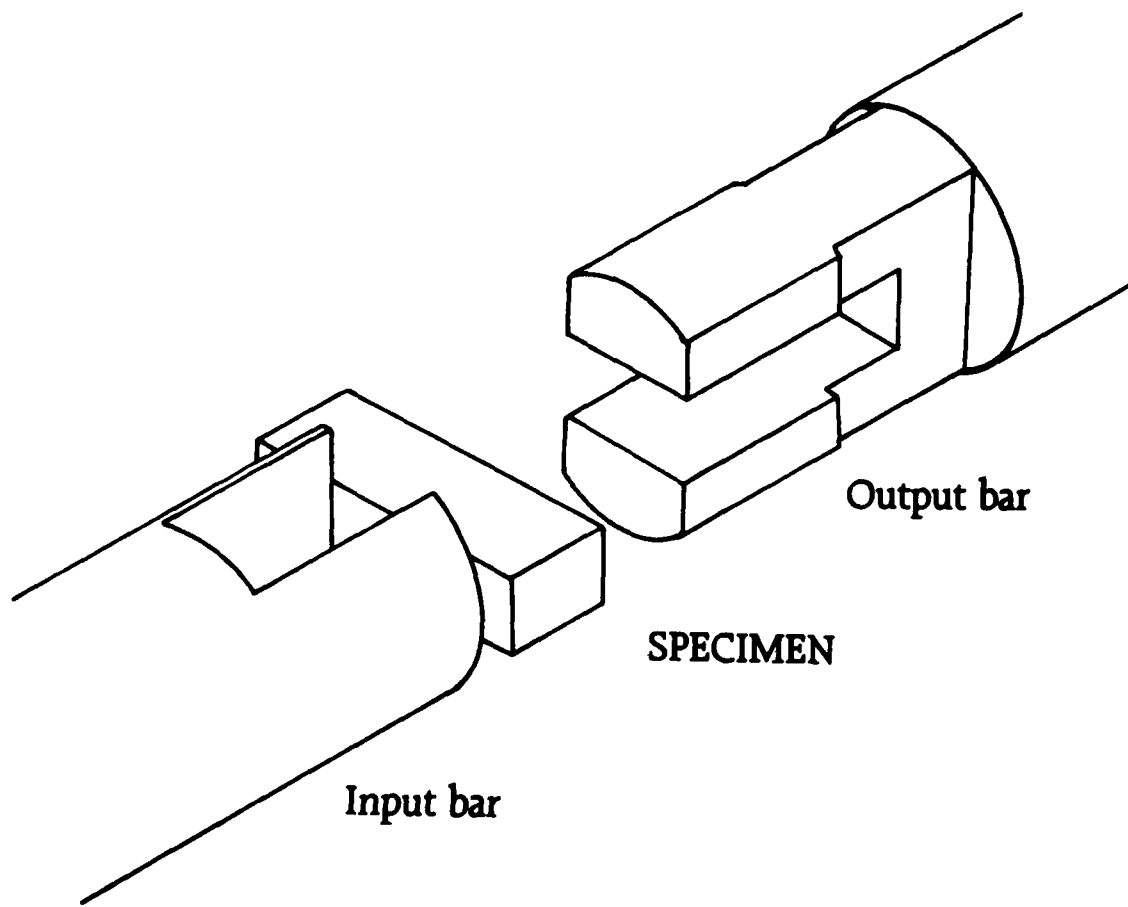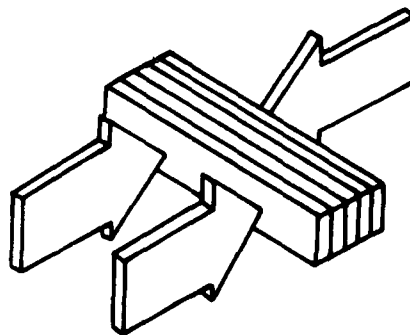
(a) Interlaminar shear      (b) Transverse shear

Figure 57 -    Schematic Shear PB Test for Composites, Reference [46]
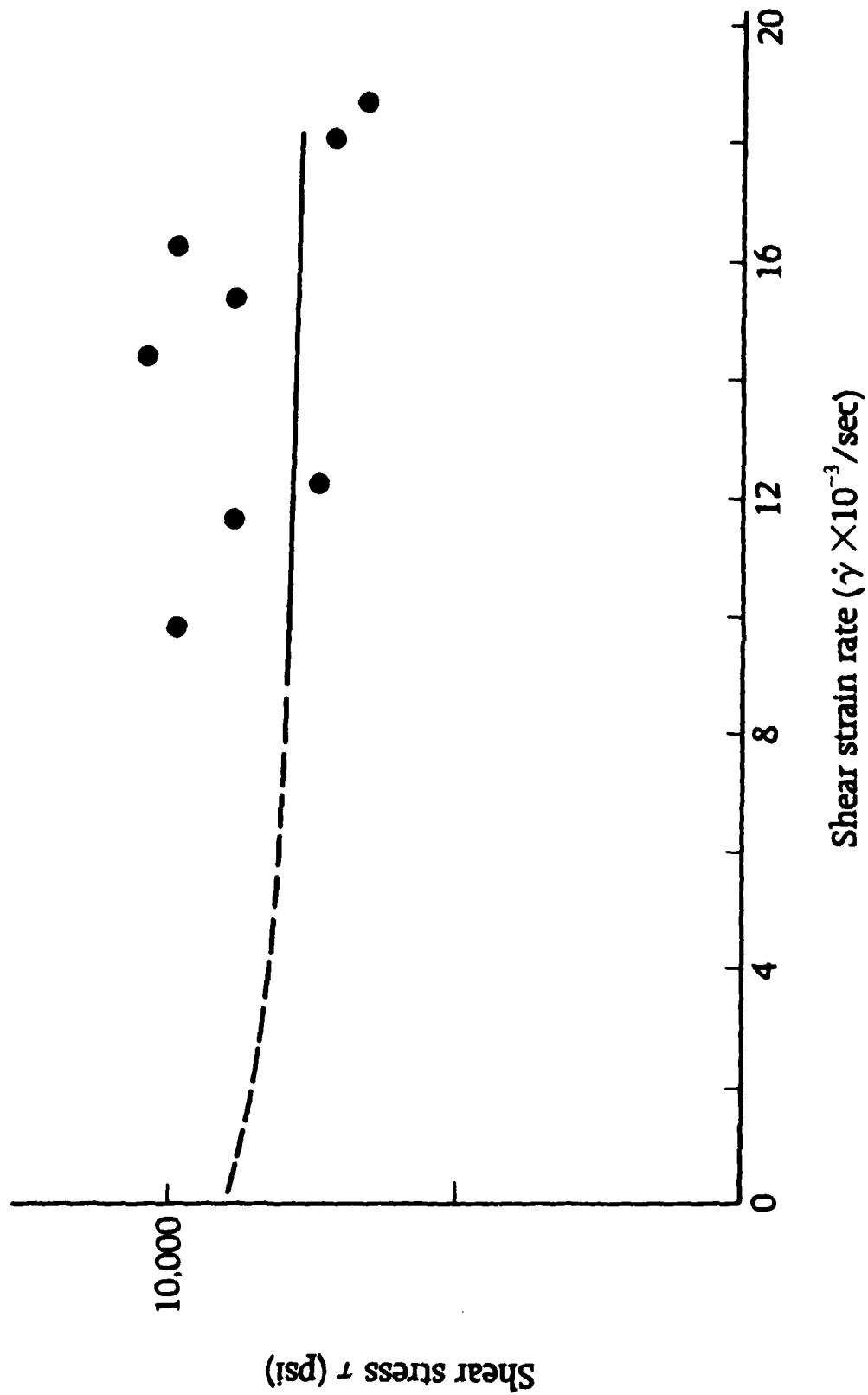
Figure 58 -   Results of Dynamic Interlaminar Shear Stress vs. Strain Rate, Reference [46]
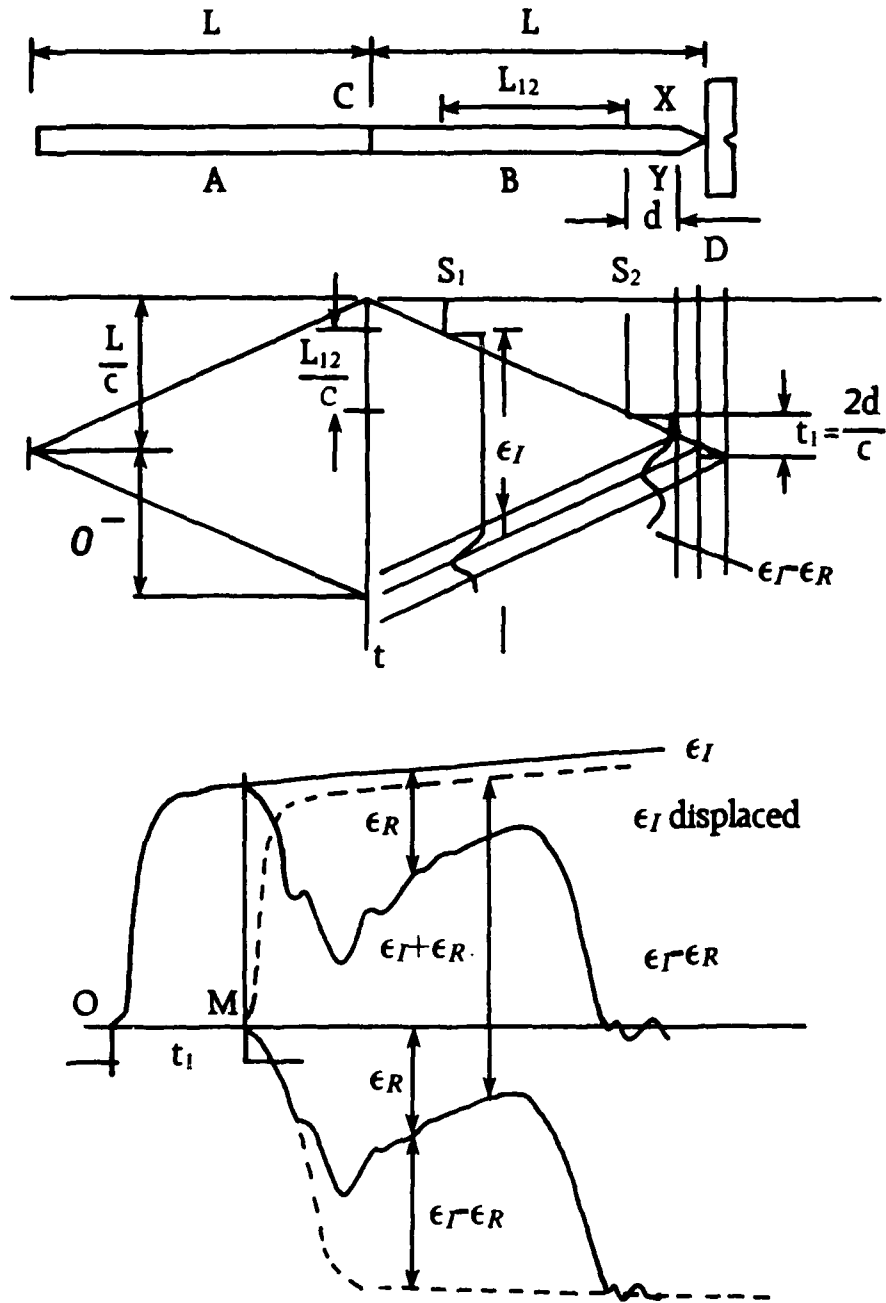
5,000

Figure 59 -     HPB Fracture Apparatus Stress Wave Diagram, Reference [7]

406
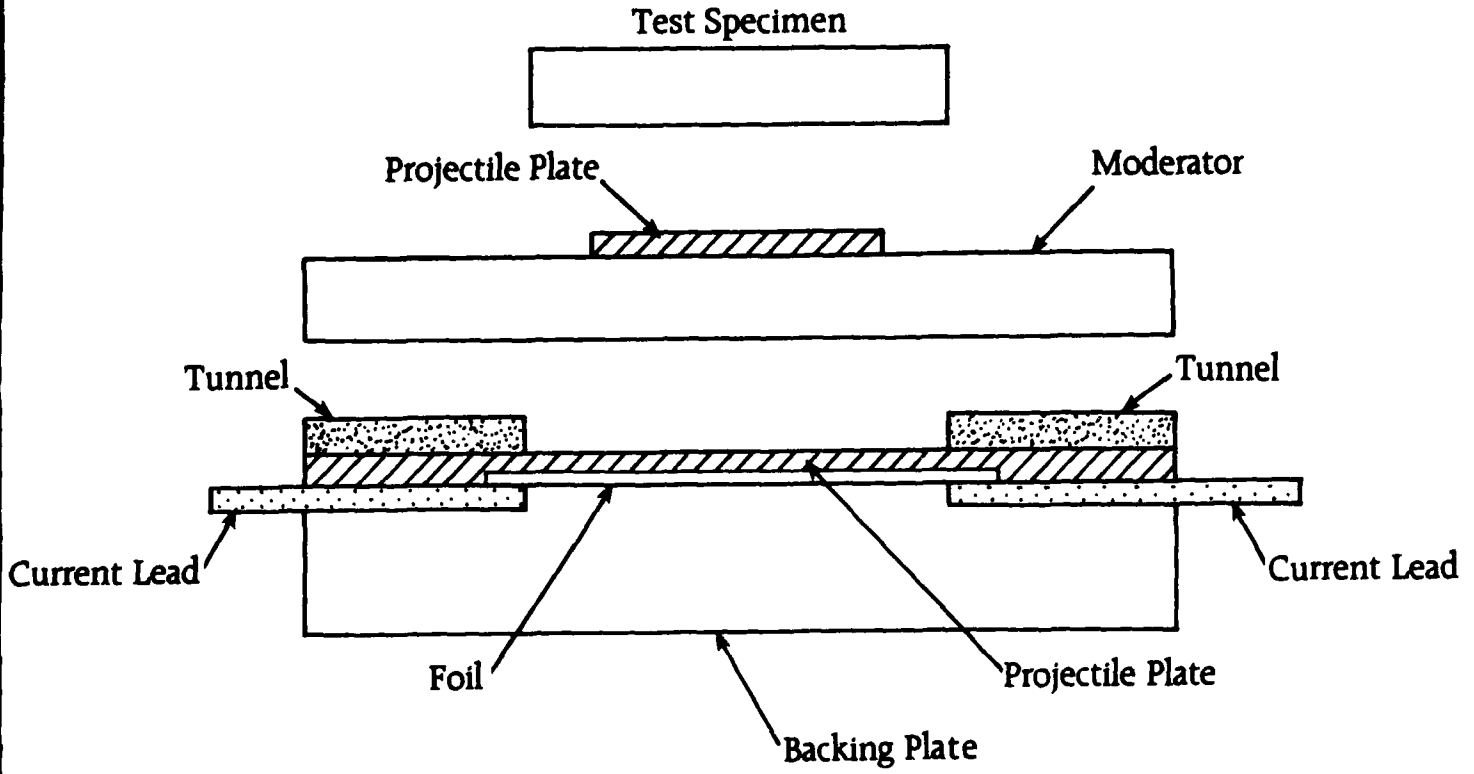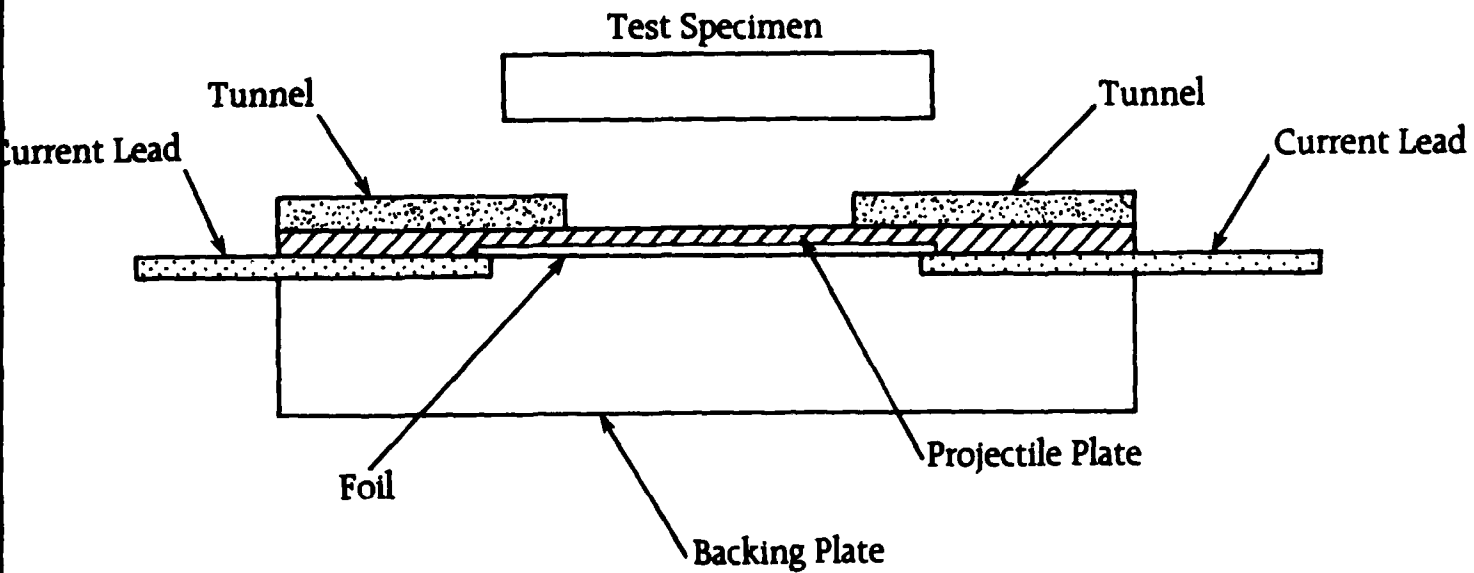
Figure 60 -        Single and Double Flyer Plate Impact Apparatus, Reference [47]
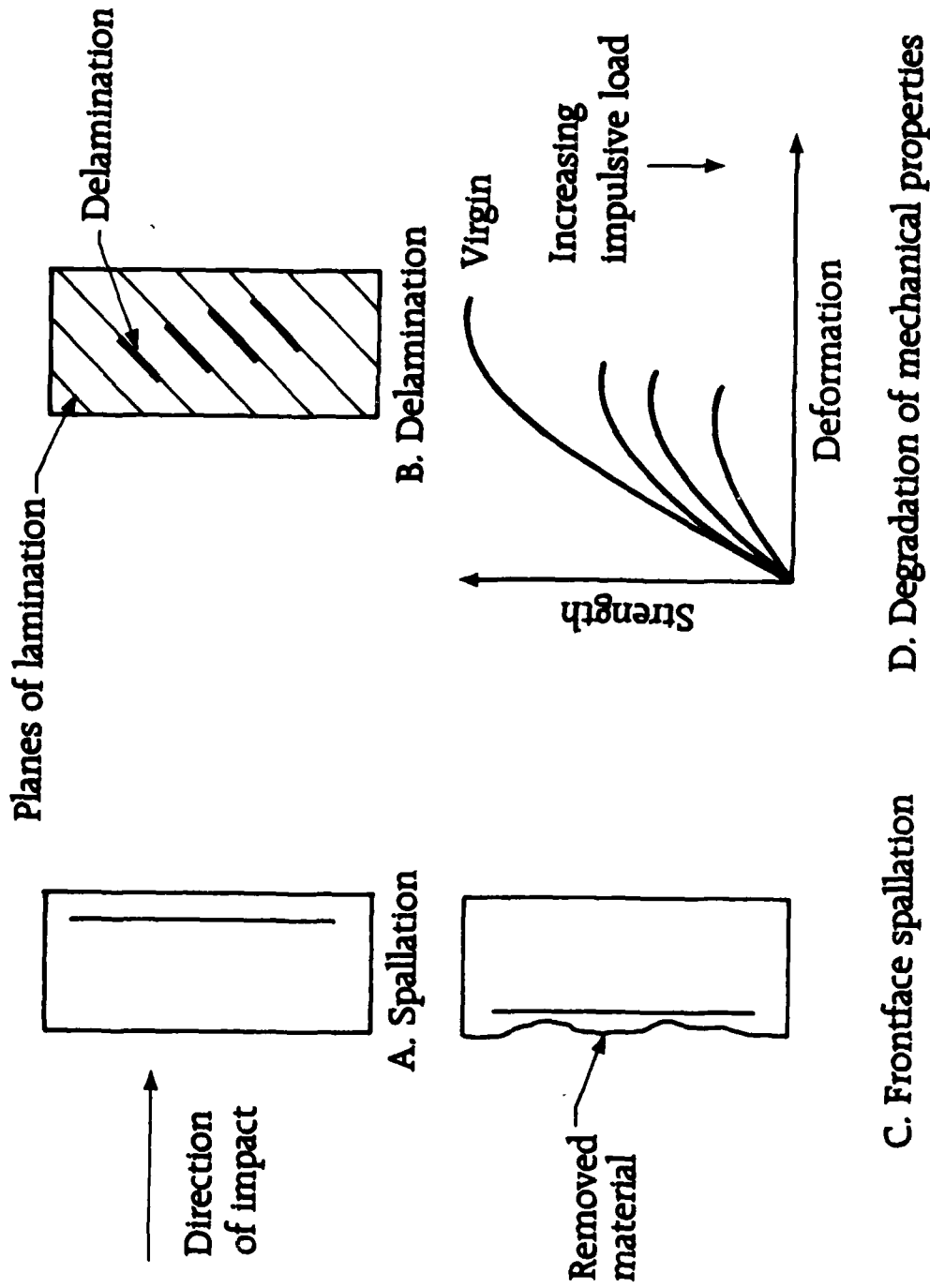
Figure 61 - Classes of Stress Wave Induced Damage, Reference [47]

# SECTION IV

# NUMERICAL SIMULATIONS

# IMPLEMENTATION OF SIMPLIFIED CONSTITUTIVE MODELS IN LARGE COMPUTER CODES

Gordon R. Johnson
Honeywell Incorporated
Armament Systems Division
Brooklyn Park, Minnesota 55428

## INTRODUCTION

For a wide range of problems involving high velocity impact and explosive detonation, material models can have an important effect on computed responses. Examples of some of these types of computations are shown in Figure 1. Although computational analyses are currently very helpful, there remains much to be accomplished in developing material models for both strength and fracture. This paper will: 1) briefly describe the computational algorithms for the material response, 2) present and compare some simplified models, and 3) discuss how the appropriate constants may be obtained.

## COMPUTATIONAL ALGORITHMS FOR DYNAMIC MATERIAL RESPONSE

A schematic representation of the computational algorithm is shown in Figure 2. Note that the stresses must be obtained from the strains and strain rates, rather than determining the strains and strain rates from the stresses.

Most computer codes use a computational procedure similar to that initially presented by Wilkins [1] for use in the HEMP code. For axisymmetric geometry, the three normal stresses are expressed as:

$$\sigma_r = s_r - (P + Q) \tag{1}$$

$$\sigma_z = s_z - (P + Q) \tag{2}$$

$$\sigma_\theta = s_\theta - (P + Q) \tag{3}$$

where $s_r$, $s_z$, and $s_\theta$ are deviator stresses; $P$ is the hydrostatic pressure; and $Q$ is the artificial viscosity. The shear stress is represented by $\tau_{rz}$.

The deviator and shear stresses are updated in an incremental manner for each time increment. Trial values of these stresses at time $= t + \Delta t$ are:

$$s_r^{t+\Delta t} = s_r^t + 2G\dot{e}_r\Delta t - 2\tau_{rz}^t\omega_{rz}\Delta t \tag{4}$$

$$s_z^{t+\Delta t} = s_z^t + 2G\dot{e}_z\Delta t + 2\tau_{rz}^t\omega_{rz}\Delta t \tag{5}$$

$$s_\theta^{t+\Delta t} = s_\theta^t + 2G\dot{e}_\theta\Delta t \tag{6}$$

$$\tau_{rz}^{t+\Delta t} = \tau_{rz}^t + G\gamma_{rz}\Delta t + (\sigma_r^t - \sigma_z^t)\,\omega_{rz}\Delta t \tag{7}$$

In Eq. (4), $s_r^{t+\Delta t}$ is the trial radial deviator stress at time $= t + \Delta t$, $s_r^t$ is the radial deviator stress at time $= t$, G is the elastic shear modulus, $\dot{e}_r$ is the deviator strain rate in the radial direction, $\Delta t$ is the integration time increment, $\tau_{rz}^t$ is the shear stress at time $= t$ and $\omega_{rz}$ is the rate of rotation in the r-z plane. The second term $(2G\dot{e}_r\Delta t)$ is the incremental stress due to the incremental strain $(\dot{e}_r\Delta t)$ during the time increment. The third term $(2\tau_{rz}^t\omega_{rz}\Delta t)$ is due to shear stresses from the previous time increment, which now act as normal stresses due to the new orientation of the element, caused by an incremental rotation $(\omega_{rz}\Delta t)$ during the time increment. The axial, hoop, and shear stresses $(s_z, s_\theta, \tau_{rz})$ have a similar form except that the hoop stress does not have a contribution from rotated shear stresses.

The updated stresses in Eqs. (4) to (7) are trial stresses only, and they may need to be reduced if they are greater than the strength of the material. This determination can be made by computing the von Mises equivalent stress:

$$\sigma = \left[\frac{1}{2}[(s_r - s_z)^2 + (s_z - s_\theta)^2 + (\sigma_\theta - s_r)^2] + 3\tau_{rz}^2\right]^{1/2} \tag{8}$$

410

If $\bar{\sigma}$ is not greater than the equivalent tensile strength of the material, $\sigma_{max}$, the final deviator and shear stresses are in the elastic range, and are as given in Eqs. (4) to (7). If $\bar{\sigma}$ is greater than $\sigma_{max}$, then the material is in the plastic range and the stresses in Eqs. (4) to (7) must be multiplied by the factor $(\sigma_{max}/\bar{\sigma})$. When the reduced deviator and shear stresses are put into Eq. (8), the result is always $\bar{\sigma} = \sigma_{max}$. The primary purpose of the strength model is to determine $\sigma_{max}$. This will be described in more detail later.

The hydrostatic pressure is dependent on the volumetric strain and the internal energy in the element. The Mie-Gruniesen Equation of State [2] is commonly used for metals and can be expressed in the following form:

$$P = (K_1\mu + K_2\mu^2 + K_3\mu^3)(1 - \lceil \mu/2) + E_s(1 + \mu) \tag{9}$$

where $\mu = \rho/\rho_0 - 1 = V_0/V - 1$, and $E_s$ is internal energy per initial volume. The initial and current densities are $\rho_0$ and $\rho$, and the initial and current volumes are $V_0$ and $V$. The four material constants are $K_1$, $K_2$, $K_3$, and the Gruneisen coefficient, $\lceil$. For small spherical volumetric strains, Eq. (9) reduces to $P = K_1\mu$, where $K_1$ is analogous to the elastic bulk modulus.

For high pressures, the effect of the internal energy, $E_s$, can be significant. Therefore, it is necessary to solve the pressure and internal energy equations simultaneously, which ensures that the pressure and energy are consistent with one another.

The artificial viscosity, Q, tends to damp out localized oscillations near the leading edge of wave fronts. It is called artificial because it is a numerically induced viscosity rather than a real material viscosity.

There appears to be a general concensus that the equation of state models (pressure as a function of volume and energy) and data are adequate for most computations involving metals. As a result, more attention needs to be focused on strength and fracture models.

## COMPUTATIONAL STRENGTH MODELS

In the preceding section, the strength of the material was designated as $\sigma_{max}$, for clarity, but will now be simplified to $\sigma = \sigma_{max}$. A good computation strength model, then, is one which will accurately predict $\sigma$ as a function of the strain, strain rate, temperature, and/or pressure.

One of the more commonly used simplified models for metals is that developed by Johnson and Cook [3]. In this model, the equivalent tensile flow stress is given by

$$\sigma = [A + B \, \varepsilon^n][1 + C \, \ln \dot{\varepsilon}^*][1 - T^{*m}] \tag{10}$$

where $\varepsilon$ is the equivalent plastic strain, $\dot{\varepsilon}^* = \dot{\varepsilon}/\dot{\varepsilon}_0$ is the dimensionless plastic strain rate for $\dot{\varepsilon}_0 = 1.0 s^{-1}$, and $T^* = (T - T_{room})/(T_{melt} - T_{room})$ is the homologous temperature for $0 \le T^* \le 1.0$. The five material constants are A, B, n, C, and m.

The expression in the first set of brackets gives the stress as a function of strain for $\dot{\varepsilon}^* = 1.0$ and $T^* = 0$. The expressions in the second and third sets of brackets represent the effects of strain rate and temperature, respectively. At the melting temperature ($T^* = 1.0$), the stress goes to zero for all strains and strain rates. The basic form of the model is readily adaptable to most computer codes, since it uses variables ($\varepsilon$, $\dot{\varepsilon}^*$, $T^*$) that are available in the codes.

The Johnson-Cook model: 1) is simple to implement, 2) does not require excessive computing time or memory, 3) can be used for a variety of metals, 4) allows constants to be readily obtained from a limited number of laboratory tests, and 5) enables the effects of the important variables to be identifiable and separable.

The primary disadvantage of this model is that it is empirical, and therefore, has no sound physical basis. Thus, exceptional care must be exercised when using it for extrapolated values of $\varepsilon$, $\dot{\varepsilon}^*$, and $T^*$.

Although various test techniques can be used to obtain constants for this model, the following approach has commonly been used [3]. First, the yield and strain hardening constants (A, B, n) are obtained from isothermal tension and torsion tests at relatively low strain rates ($\dot{\varepsilon}^* \le 1.0$). Next, the strain rate constant, C, is determined from torsion tests at various strain rates, and from tension tests (quasi-static and Hopkinson bar) at two strain rates. Finally, the thermal softening constant, m, is determined from Hopkinson bar tests at various temperatures.

The Zerilli-Armstrong model is based on dislocation mechanics, and is therefore more physically based than the Johnson-Cook Model. The Zerilli-Armstrong model has two forms:

one for face-centered cubic (fcc) metals and another for body-centered cubic (bcc) metals [4]. The expression for fcc metals is:

$$\sigma = C_0 + C_2 \varepsilon^{1/2} \exp(-C_3 T + C_4 T \ln\dot{\varepsilon}) \tag{11}$$

where $\varepsilon$ is the equivalent plastic strain, $\dot{\varepsilon}$ is the equivalent strain rate, and T is the absolute temperature. The four constants are $C_0$, $C_2$, $C_3$, and $C_4$. Here the initial yield stress, $C_0$, is independent of strain rate and temperature. Also, the stress does not necessarily go to zero at the melting temperature. Reference 4 provides a discussion of how $C_0$ is affected by solute and grain size.

The expression for bcc metals is:

$$\sigma = C_0 + C_1 \exp(-C_3 T + C_4 T \ln\dot{\varepsilon}) + C_5 \varepsilon^n \tag{12}$$

where the variables ($\varepsilon$, $\dot{\varepsilon}$, T) are as defined for Eq. (11) and the six constants are $C_0$, $C_1$, $C_3$, $C_4$, $C_5$, and n. Here the initial yield stress is a function of $C_0$, $C_1$, $C_3$, and $C_4$. Again, the stress does not necessarily go to zero at the melting temperature.

In Eq. (11), the strain, strain rate, and temperature are all coupled together for the fcc model. In Eq. (12), however, the effect of strain hardening is separated from the coupled strain rate and temperature for the bcc model.

The fact that the Zerilli-Armstrong model is based on dislocation mechanics appears to make it preferable to the Johnson-Cook model. On the other hand, the more complex form of the Zerilli-Armstrong model appears to make it more difficult to obtain the appropriate constants. Both are easily implemented into the codes.

Figure 3 shows a comparison of isothermal and adiabatic stress-strain relationships for the two models of interest. This is done for OFHC Copper (fcc) and Armco Iron (bcc). The temperature for the adiabatic relationships is due to the plastic work of deformation. Constants for both models were obtained from essentially the same data base [3, 4].

For the OFHC Copper, the Johnson-Cook model predicts higher adiabatic stresses at lower strains, and lower stresses at higher strains. For both the OFHC Copper and the Armco Iron,

the Johnson-Cook model predicts less of a strain rate effect than does the Zerilli-Armstrong model. Generally, however, the adiabatic responses are similar for the two models. The isothermal responses vary more, but it is difficult to actually attain an isothermal response at the high strain rates shown.

There remains much uncertainty about the behavior of metals under the combination of very high strain rates ($10^5 < \dot{\varepsilon} < 10^7 s^{-1}$) and large strains ($\varepsilon > 0.5$). This is due to the wide range of proposed models and to the general lack of test data under these conditions. It is the author's opinion that the most important problem to be addressed is to develop physically based models that accurately predict adiabatic stress-strain behavior at large strains and high strain rates. If the results are presented in a form similar to that shown in Figure 3, then a meaningful evaluation and comparison of the models can be made. At this time, there is not general agreement by researchers working in this area.

Additionally, while the von Mises flow rule is commonly used, it is well known that simple tension-torsion comparisons cannot always be adequately accounted for when using this flow rule. Also, material history effects can be important when dealing with changing strain rates and changing strain directions.

Returning again to the Johnson-Cook and Zerilli-Armstrong models, one way of evaluating these models is to compare computed results with cylinder-impact test results, such as shown in Figure 4.

To quantify the degree of agreement between computed shapes and test data, an average error has been defined as

$$\tilde{\Delta} = \frac{1}{3} \left[ \frac{|\Delta L|}{L} + \frac{|\Delta D|}{D} + \frac{|\Delta W|}{W} \right] \tag{13}$$

where L, D, and W are the deformed length, diameter and bulge (diameter at 0.2 $L_0$ from the deformed end) from the test results; and $\Delta L$, $\Delta D$, and $\Delta W$ are the differences between the computed and test results. Note that both models give good general agreement, but the Zerilli-Armstrong model gives better agreement.

The maximum computed equivalent strains ($\varepsilon_{max}$) in Figure 4 range from 1.57 to 2.04. The strain distributions, however, show that the overwhelming majority of the elements experience

equivalent strains less than 0.6. Therefore, the comparisons in Figure 4 tend to reflect the accuracy of the model for relatively low strains ($\varepsilon < 0.6$), but do not necessarily provide a good indication for larger strains ($\varepsilon > 0.6$). This is a very important limitation associated with cylinder impact test data. A more detailed discussion of this limitation is provided in Reference 5.

The simplified models of Eqs. (1), (2) and (3) represent the stress as an explicit function of the strain, strain rate, and temperature. This is very desirable from a computational viewpoint. However, there are several more complicated models [6-9], which include loading history, but require iterative procedures to obtain the equivalent stress, $\sigma$. Although all of these models are physically based, there are differences. It would be very helpful and interesting to have an assessment of each model's predictions for a limited number of identical materials.

Although the preceding discussion has focused on metals, there is a need to develop improved models for other materials such as sand, soil, rock, concrete, and ceramics. These materials have little ductility, when compared to metals, but the strength can be dependent on the hydrostatic pressure. As an example, Figure 5 shows a schematic representation of a computational model for ceramics. Note that the strength before and after fracture is highly dependent on the pressure.

## DETERMINATION OF CONSTANTS FROM CYLINDER IMPACT TEST DATA

The preceding discussion presented the simplified Johnson-Cook and Zerilli-Armstrong models. Constants for these models were obtained primarily from torsion tests at various strain rates, Hopkinson bar tests at various temperatures, and quasi-static tension tests [3,4].

Another option is to obtain some of the constants from a cylinder impact test. This is described in more detail in Reference 5, along with some potential problems associated with the approach.

Figure 6 shows how cylinder impact test data can be used to obtain constants for various forms of the Johnson-Cook model. The adiabatic stress-strain relationships are shown in Figure 7, and the constitutive model constants are given in Table 1. The adiabatic stresses are shown only to the maximum strains attained in the computed results.

For Case A-1, only the length, L, of the deformed cylinder (OFHC Copper) is matched with the computational result. Because only one deformed dimension is matched, only one

415

independent strength constant (representing a constant flow stress) can be obtained. Note that there are significant discrepancies between the test and computational results at the deformed end of the cylinder.

Case B-1 allows for linear strain hardening. By matching both the deformed length, L, and the maximum diameter, D, it is possible to obtain the two constants for the linear hardening. Here the computed result is in good general agreement with the test result, with a relatively small error of $\bar{\Delta}$ = 0.005. One reason for the good correlation is that the cylinder tends to conserve volume; and the intermediate diameter, W, must be consistent with the conserved volume. Applying this model to larger strains than those experienced in the computed results of Case B, however, would probably lead to excessively high stresses. It is well known that thermal softening tends to decrease the rate of strain hardening at large strains, as shown in Figure 3.

It is possible to obtain a more realistic model, again solving for only two constants, by assuming linear thermal softening (m = 1.0). This also provides a good correlation with the test data ($\bar{\Delta}$ = 0.012), as shown in Case C-1 of Figure 6, and it allows the thermal softening to reduce the stresses somewhat at the larger strains.

Cases D-1 and E-1 are based on the complete Johnson-Cook model of Eq. 1. Although there are five constants in this model (A, B, n, C, m), only the three yield and strain hardening constants (A, B, n) are determined from the test data. The strain rate constant, C, and the thermal softening constant, m, must be approximated or obtained from other sources. Because there are now three constants, it is possible to match three deformed dimensions: the length, L; the maximum diameter, D; and an intermediate diameter, W. Note again, however, that the intermediate diameter, W, is not totally independent.

Case D-1 is the result obtained if nothing is known about the strain rate or thermal softening characteristics of the material. Here, the strain rate constant is set to C = 0, and the thermal softening is assumed to be linear, or m = 1.0. Case E-1 uses the previously determined strain rate and thermal softening constants from Reference 3 and Figure 3. Even though there is little apparent difference between Cases D-1 and E-1 for this problem, for some other problems (with wider ranges of strain rates and temperatures), the Case E-1 constants will probably provide better results. Also included in Table 1 and Figure 7 are data from Reference 3 and Figure 3.

Looking at Figure 7, it can be seen that there is a significant discrepancy in the various adiabatic stress-strain relationships, especially at the larger strains. Yet, with the exception of Case A-1, they all provide a generally good correlation with the date data. The reason for this situation is provided in the distribution of strain. Although some of the elements experience equivalent plastic strains as high as 2.04, most of the elements experience strains less than 0.6. Looking back to this specific range of strains in Figure 7, there is good general agreement (except for Case A-1) between the various adiabatic stress-strain relationships. Therefore, because the various models essentially agree with one another in this relatively narrow band of strain, it would be expected that they would give similar results for computed solutions whose strains fall within this narrow band, and whose strain rates are similar to those experienced in the cylinder impact tests.

In the lower portion of Figure 6, the same approach was attempted for the Armco Iron. For Case A-2, only the length, L, was matched, giving a constant flow stress. For Case B-2, the length, L, and diameter, D, were matched using linear strain hardening. For Case C-2, linear thermal softening (m = 1.0) was included with the linear strain hardening, and the two dimensions (L, D) were matched.

The result of this discussion is that it is possible to determine constants from the cylinder impact test, but that great care should be taken to not extrapolate beyond the range of strains and strain rates that govern the results of the test.

## SUMMARY AND CONCLUSIONS

This paper has attempted to describe how simplified constitutive models can be implemented into large computer codes. It has also described some ways of obtaining constants for these models.

There are currently several simplified models and several more complicated models in existence and/or in development. It is not generally obvious what the distinguishing features are for each of these models, and what differences in material response are predicted by the various models. A comprehensive assessment and comparison of these models would be helpful.

417

# REFERENCES

1. Wilkins, M.L., "Calculation of Elastic-Plastic Flow," *Methods in Computational Physics*, Vol. 3, Academic Press, New York, 1964.

2. Walsh, J.M., et al., "Shock Wave Compressions of Twenty-Seven Metals," Equations of State of Metals, *Physical Review*, Vol. 108, No. 2, 1957.

3. Johnson, G.R. and W.H. Cook, "A Constitutive Model and Data for Metals Subjected to Large Strains, High Strain Rates and High Temperatures," *Proceedings of Seventh International Symposium on Ballistics*, The Hague, The Netherlands, 1983.

4. Zerilli, F.J. and R.W. Armstrong, "Dislocation-Mechanics-Based Constitutive Relations for Material Dynamics Calculation" *Journal of Applied Physics*, Vol. 61, No. 5, 1987.

5. Johnson, G.R. and T.J. Holmquist, "Evaluation of Cylinder Impact Test Data for Constitutive Model Constants," *Journal of Applied Physics*, In Press, 1988.

6. Follansbee, P.S. and U.F. Kocks, "A Constitutive Description of the Deformation of Copper Based on the Use of the Mechanical Threshold Stress as an Internal State Variable," *Acta Metall*. Vol. 36, No. 1, 1988.

7. Steinberg, D.J. and C.M. Lund, "A Constitutive Model for Strain Rates from $10^{-4}$ to $10^6$ $s^{-1}$," *Journal de Physique*, Collogue C3, 1988.

8. Klepaczko, J.R., "Constitutive Modeling in Dynamic Plasticity Based on Physical State Variables - A Review," *Journal de Physique*, Collogue C3, 1988.

9. Bodner, S.R. and Y. Partom, "Constitutive Equations for Elastic-Viscoplastic Strain Hardening Materials," *Journal of Applied Mechanics*, ASME, Vol. 42, 1975.

Table 1.   OFHC Copper and Armco Iron Constants for the Johnson-Cook Model as Determined by Various Methods

| CONSTANTS FOR JOHNSON-COOK MODEL $\sigma = [A+B\varepsilon^n][1+C\ln\dot{\varepsilon}^*][1-T^{*m}]$ | | | | | | |
|---|---|---|---|---|---|---|
| OFHC COPPER | | | | | | |
| CASE | A (MPa) | B (MPa) | n | C | m | $\overline{\Delta}$ |
| REF. 3 | 90 | 292 | 0.31 | 0.025 | 1.09 | 0.063 |
| A-1 | 250 | 0.0 | - | 0.0 | - | 0.231 |
| B-1 | 157 | 425 | 1.00 | 0.0 | - | 0.005 |
| C-1 | 150 | 490 | 1.00 | 0.0 | 1.00 | 0.012 |
| D-1 | 118 | 484 | 0.74 | 0.0 | 1.00 | 0.0 |
| E-1 | 98 | 368 | 0.70 | 0.025 | 1.09 | 0.0 |
| ARMCO IRON | | | | | | |
| REF. 3 | 175 | 380 | 0.32 | 0.060 | 0.55 | 0.025 |
| A-2 | 593 | 0 | - | 0.0 | - | 0.041 |
| B-2 | 555 | 134 | 1.00 | 0.0 | - | 0.001 |
| C-2 | 553 | 230 | 1.00 | 0.0 | 1.00 | 0.004 |
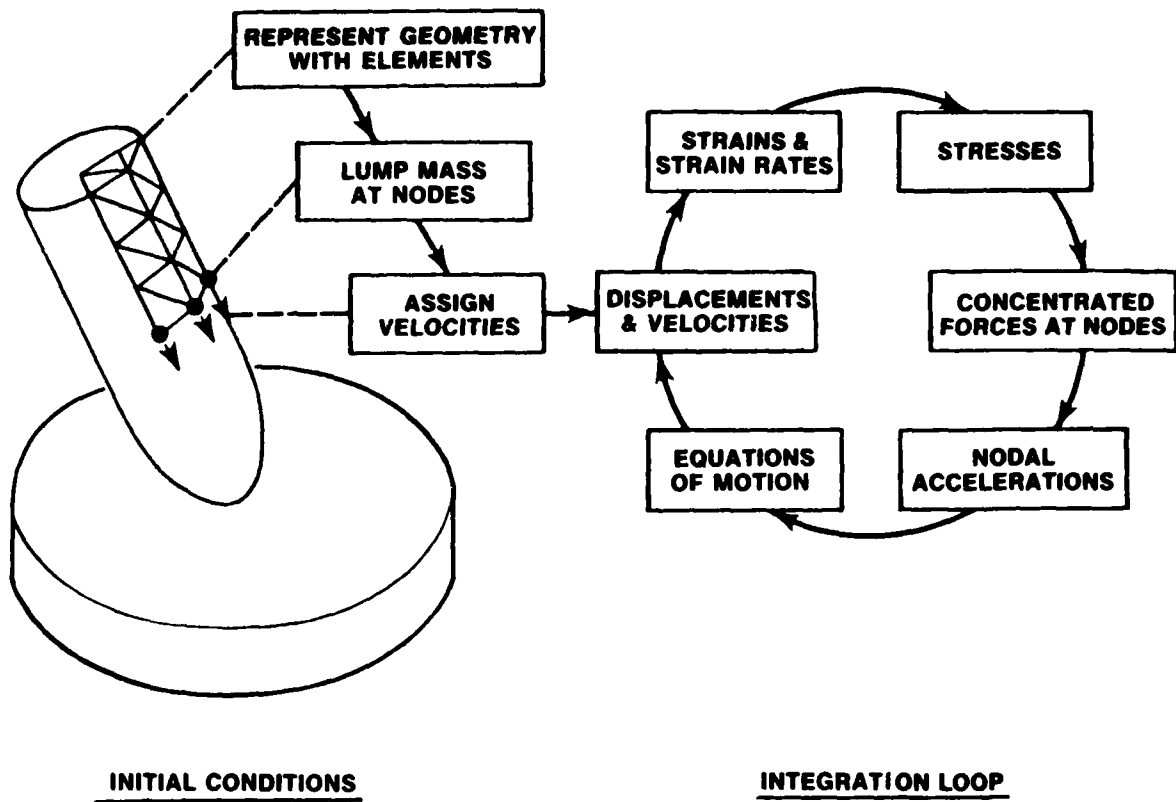
Figure 1. Schematic Representation of the Computational Technique Used in the EPIC-2 and EPIC-3 Codes
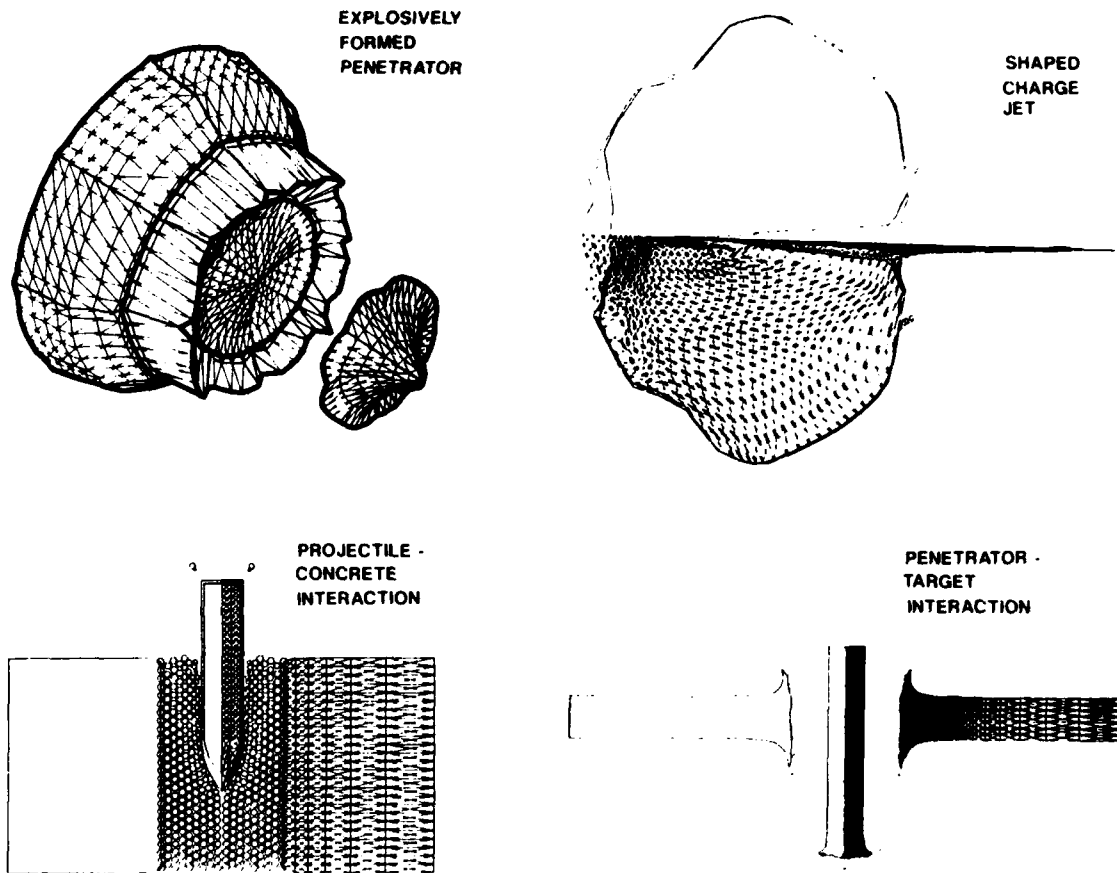
Figure 2. Examples of Impact and Explosive Detonation Computations Performed with the EPIC-2 and EPIC-3 Codes
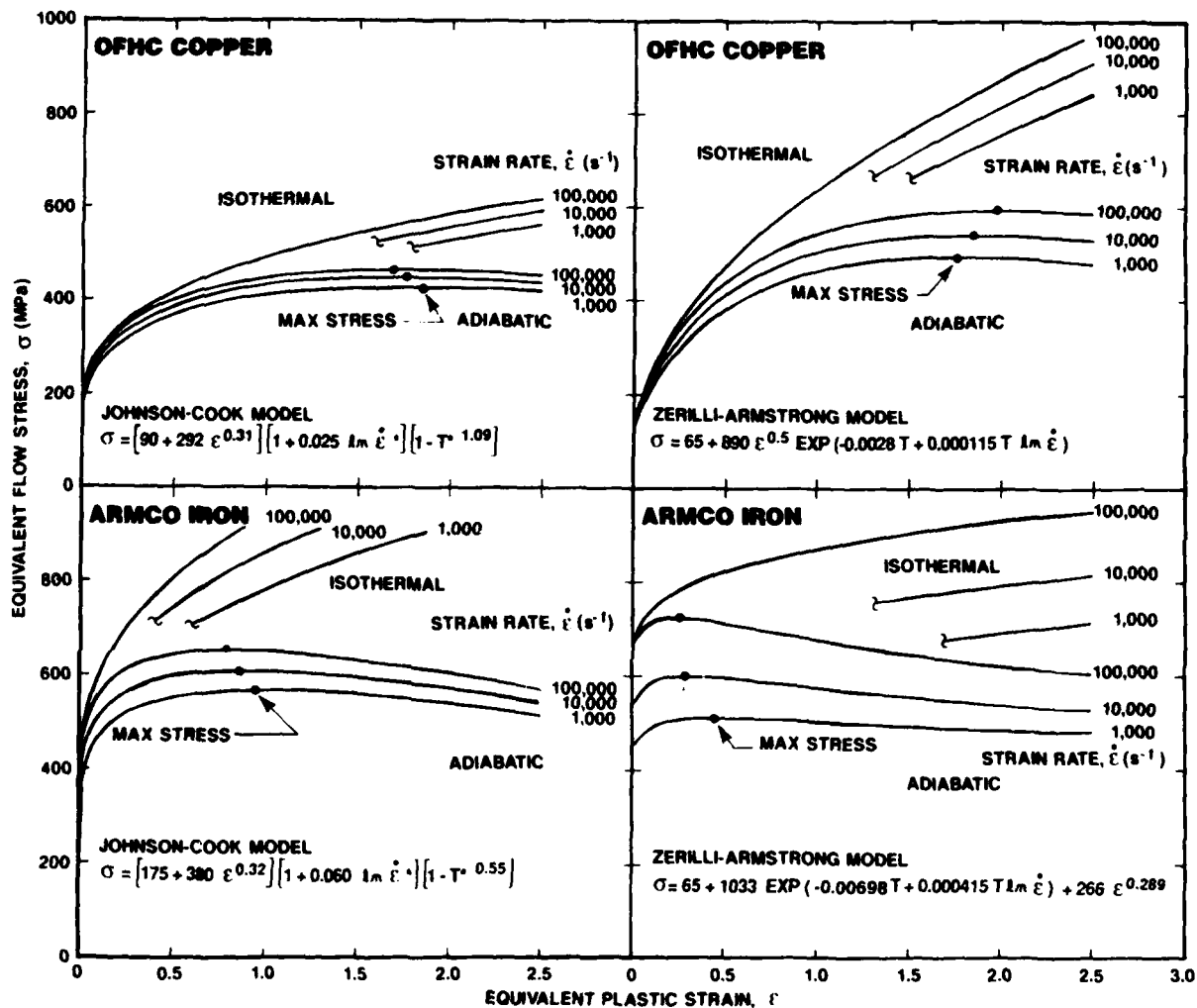
Figure 3.    Isothermal and Adiabatic Stress-Strain Relationships for OFHC Copper and Armco Iron Using the Johnson-Cook and Zerilli-Armstrong Models

422

OFHC COPPER
(JOHNSON-COOK MODEL)

$\overline{\Delta} = 0.063$

$\varepsilon_{MAX} = 2.04$

V = 190 M/S

OFHC COPPER
(ZERILLI-ARMSTRONG MODEL)

$\overline{\Delta} = 0.018$

$\varepsilon_{MAX} = 1.57$

V = 190 M/S

ARMCO IRON
(JOHNSON-COOK MODEL)

$\overline{\Delta} = 0.025$

$\varepsilon_{MAX} = 1.80$

V = 221 M/S

ARMCO IRON
(ZERILLI-ARMSTRONG MODEL)

$\overline{\Delta} = 0.004$

$\varepsilon_{MAX} = 1.91$

V = 221 M/S

NOTES:

- $\overline{\Delta} = \frac{1}{3}\left[\frac{|\Delta L|}{L_{TEST}} + \frac{|\Delta D|}{D_{TEST}} \quad \frac{|\Delta W|}{W_{TEST}}\right]$

- $\varepsilon_{MAX}$ IS MAXIMUM COMPUTED EQUIVALENT PLASTIC STRAIN

- INITIAL LENGTHS, $L_o$ = 25.4mm

- INITIAL DIAMETERS, $D_o$ = 7.6mm

- PLASTIC STRAIN CONTOURS SHOWN AT $\overline{\varepsilon}$ = 0.1, 0.3, 0.4, 0.5, 0.6, 1.0, 1.2, 1.5

- TEST DATA DENOTED BY DOTS (...)
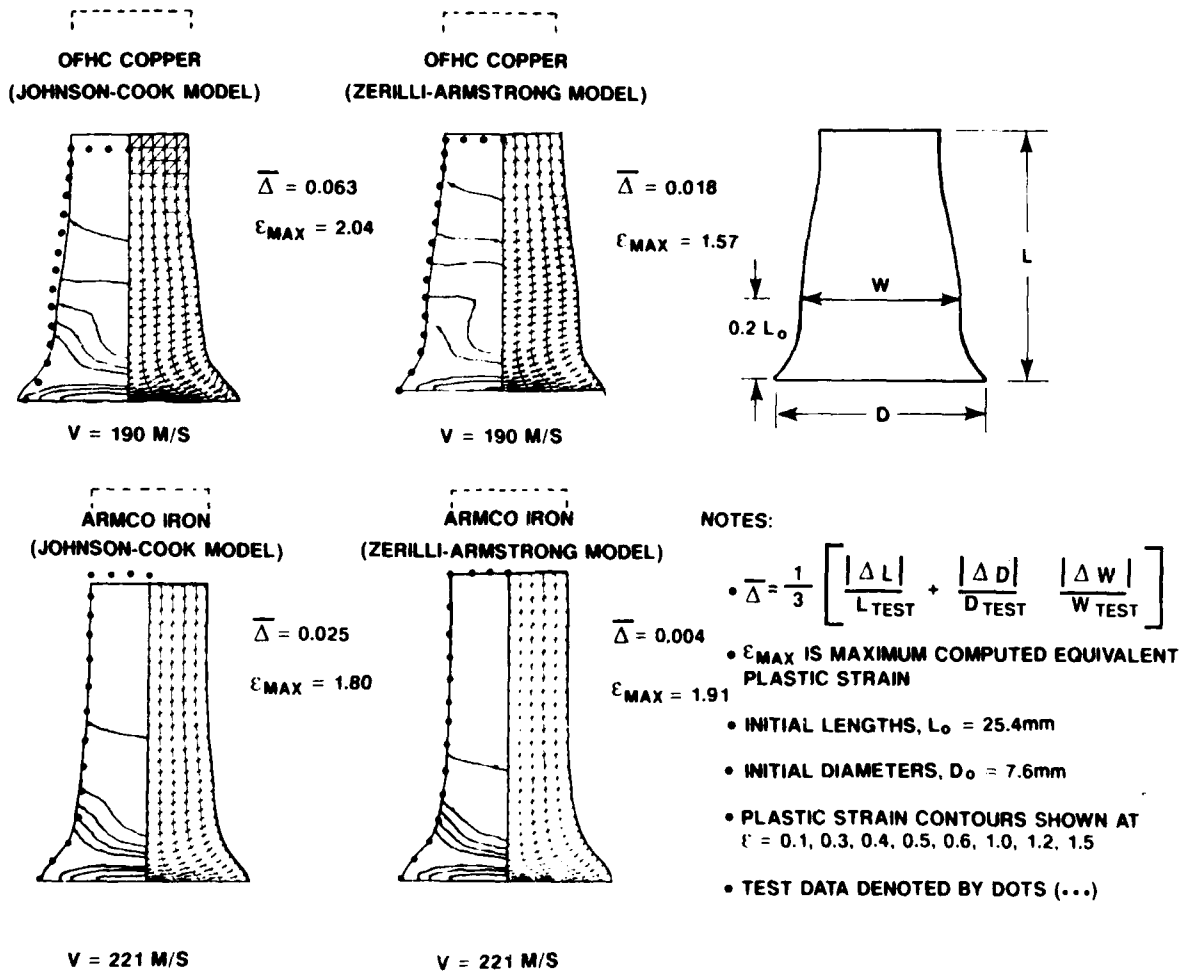
Figure 4. Comparison of Cylinder Impact Test Results and Computed Shapes for OFHC Copper and Armco Iron Using the Johnson-Cook and Zerilli-Armstrong Models

423
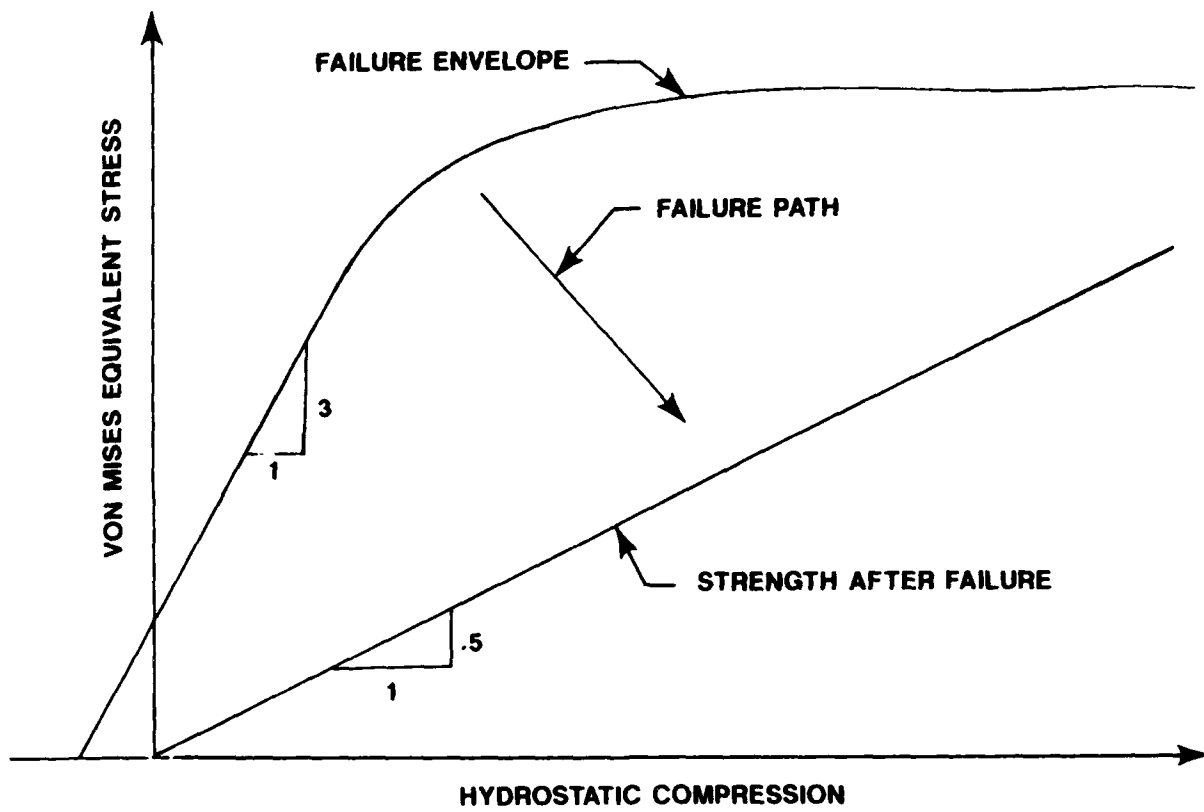
Figure 5. Schematic Representation of a Simplified Constitutive Model for Ceramics

OFHC COPPER

CASE A-1  CASE B-1  CASE C-1  CASE D-1  CASE E-1

$\overline{\Delta} = 0.231$   $\overline{\Delta} = 0.005$   $\overline{\Delta} = 0.012$   $\overline{\Delta} = 0.0$   $\overline{\Delta} = 0.0$
$\varepsilon_{MAX} = 5.09$   $\varepsilon_{MAX} = 1.67$   $\varepsilon_{MAX} = 1.68$   $\varepsilon_{MAX} = 1.66$   $\varepsilon_{MAX} = 1.64$

ARMCO IRON

CASE A-2  CASE B-2  CASE C-2

$\overline{\Delta} = 0.041$   $\overline{\Delta} = 0.001$   $\overline{\Delta} = 0.004$
$\varepsilon_{MAX} = 2.65$   $\varepsilon_{MAX} = 2.08$   $\varepsilon_{MAX} = 2.07$
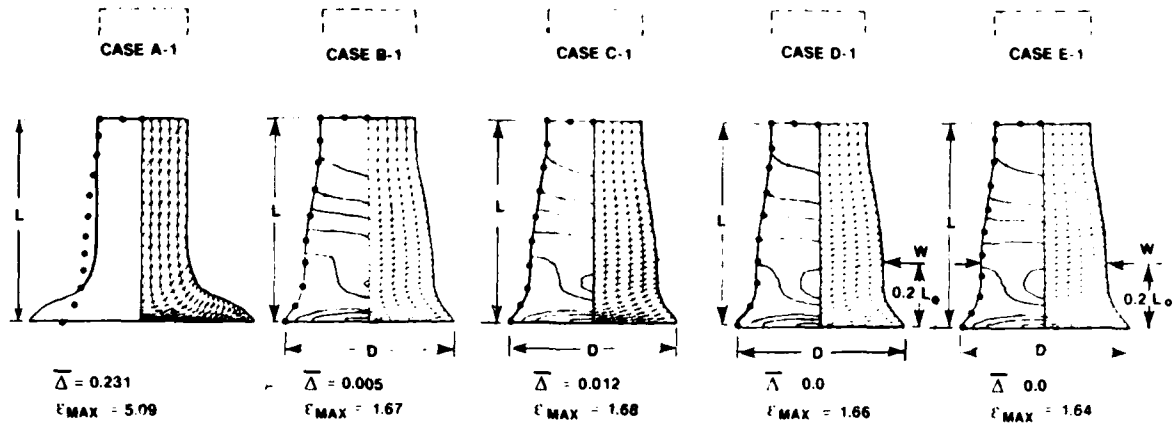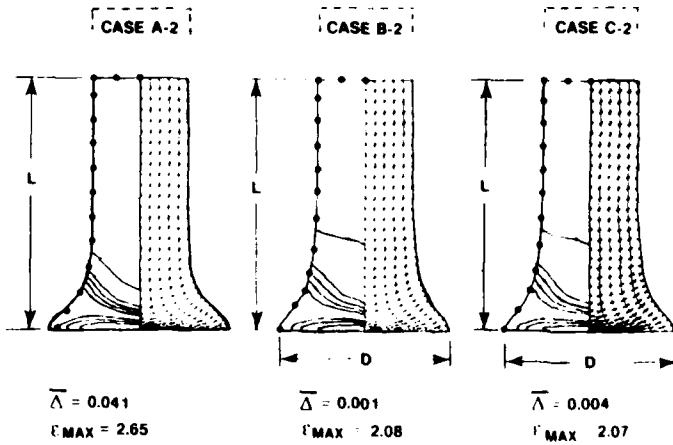
NOTES:

• OFHC COPPER CYLINDER ($L_o = 25.4mm$, $D_o = 7.6mm$, $L_{TEST} = 16.2mm$, $D_{TEST} = 13.5mm$, $W_{TEST} = 10.1mm$)

• ARMCO IRON CYLINDER ($L_o = 25.4mm$, $D_o = 7.6mm$, $L_{TEST} = 19.8$, $D_{TEST} = 13.7mm$, $W_{TEST} = 8.6mm$)

• IMPACT VELOCITIES = 190 M/S (OFHC COPPER) AND 221 M/S (ARMCO IRON)

• TEST RESULTS INDICATED BY DOTS ••••

• EQUIVALENT PLASTICS STRAIN CONTOURS SHOWN AT 0.1, 0.3, 0.4, 0.5, 0.6, 1.0, 1.2, 1.5

Figure 6.  Examples of Cylinder Impact Test Results Used to Determine OFHC Copper and Armco Iron Constants for the Johnson-Cook Model

425
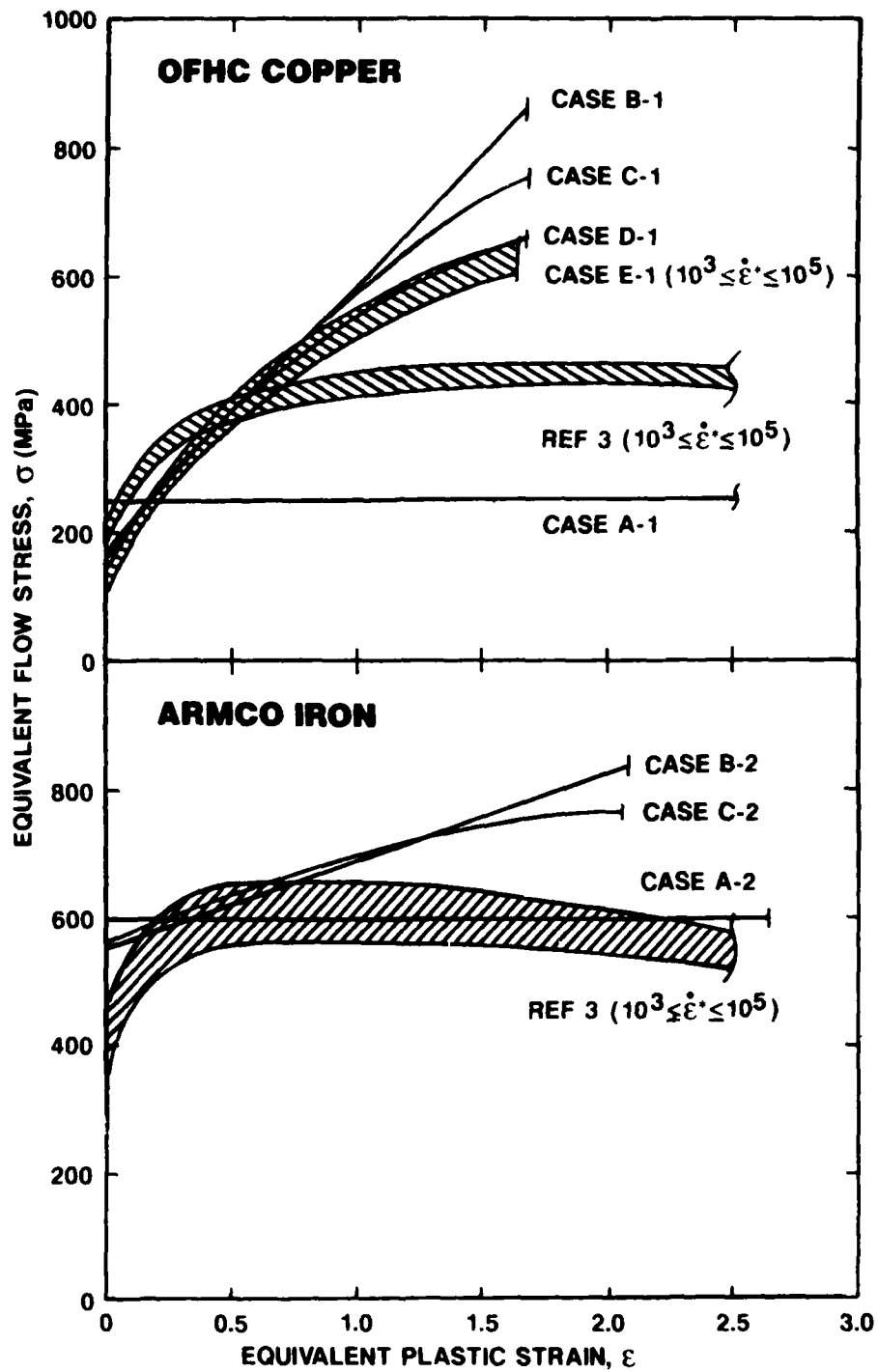
Figure 7. Comparison of Adiabatic Stress-Strain Relationships for OFHC Copper and Armco Iron Constants Using Various Forms of the Johnson-Cook Model

# YIELDING AND ROTATION OF A MULTIPLE-PLANE PLASTICITY MODEL COMPARED WITH TRADITIONAL MODELS

By Lynn Seaman

SRI International

Menlo Park, CA 94025

Traditional isotropic plasticity models can represent equivalent stress, total plastic strain, and work hardening fairly well, if the material remains approximately isotropic. If large material rotations occur or the material develops significant anisotropy, more complex models are required. In this paper, we explore a multiple-slip-plane plasticity model for its response to rotations, work hardening, and strain-rate effects. Hence, this single model can represent all these effects. Our purpose is to examine the accuracy with which this model can treat these effects.

We first introduce the general characteristics of a multiple-plane plasticity model, termed SHEAR4 [1,2,3]. Then computations are made with the model for comparison with stress results from simple isotropic yield models. These simple models are extended to include work hardening and strain-rate effects, and further comparisons are made. Finally, an analysis of material rotation under large shear strain is made, and the SHEAR4 results are compared with exact results.

The SHEAR4 model is based on the slip-plane concept formulated by Batdorf and Budiansky [4]. Its operation is very similar in concept to the two-plane model of Peirce, Asaro, and Needleman [5]. They were providing for the specific slip planes of a single crystal in their study. Bazant has developed a series of multiple-

plane models to represent initially isotropic materials [6, 7, 8]. Generally, he has found it necessary to use a large number of planes (20 or more) to represent adequately an isotropic behavior. Another multiple-plane model with characteristics to SHEAR4 is that of Zienkiewicz and Pande [9], which they used to represent shearing behavior in rocks.

## NATURE OF THE MULTIPLE-PLANE PLASTICITY MODEL

The SHEAR4 model is a multiple-plane plasticity model onto which the shear band microprocesses have been added. The multiple-plane feature can be viewed in two equally valid ways:

1. A discretization of all possible orientations for slipping in a globally isotropic polycrystalline material, or

2. A representation of the actual slip planes in a single crystal.

The planes in the SHEAR4 model can be initially oriented to represent either isotropic behavior or specific planes.

The selected orientations (shown in Figure 1) are central to the model formulation because all plastic strain as well as localization (shear banding) occurs on these orientations. Some of the possible sets of orientations that could be used in the model are listed in Table 1. Each of these sets of orientations is complete and isotropic: it does not favor any quadrant around a point. Our selection of orientation sets was guided by our experimental data in which shear bands tended to occur on $45°$ lines. Therefore, we selected the 9-plane set from the table, the set shown in Figure 1.

428

Table 1

ORIENTATION OPTIONS FOR SHEAR SLIP MODELING[a]

| No. of Planes 2-D | 3-D | Coordinate Axes | 45° Planes[b] | Equiangular Planes[d] |
|---|---|---|---|---|
| 3 | 3 | X, Y, Z | None | None |
| 5 | 7 | X, Y, Z | None | (X,Y,Z), (-X,Y,Z) [(X,-Y,Z), (-X,-Y,Z)][c] |
| 7 | 9 | X, Y, Z | XY, YZ, XZ, (-X,Y) [(-Y,Z), (-X,Z)][c] | None |
| 9 | 13 | X, Y, Z | XY, YZ, XZ, (-X,Y) [(-Y,Z), (-X,Z)][c] | (X,Y,Z), (-X,Y,Z) [(X,-Y,Z), (-X,-Y,Z)][c] |

[a] The 2-D state is taken as either plane strain or axisymmetry. There are no shears in the YZ and XZ directions. This symmetry requires that some planes be identical; e.g., YZ and (-Y,Z). For 2-D problems, these pairs of planes can be treated as single planes. Orientations are designated by the directions of the normals to the damage planes.

[b] Normals to these slip planes are at 45 degrees between the coordinate directions; e.g., -X,Y means the normal is at 45 degrees between the -X and Y axes.

[c] Orientations listed in brackets are needed only for 3-D symmetry.

[d] Normals to the equiangular planes are directed along lines that have equal angles to each of the listed coordinate axes.

For a calculation, the planes are given initial orientations in the external coordinate directions. Hence, the orientations could be aligned initially to favor some directionality of the material. During the computation, each orientation is allowed to rotate with the deformation of the material such that relative orientations do not stay fixed.

For stress-strain relations, the material is represented by a standard thermoelastic-plastic model with work hardening and strain-rate dependence. The material elastically deformed is isotropic; hence, its stress tensor can be separated into pressure and deviatoric components. Whereas the material is initially isotropic, the presence of differentially hardened slip planes and shear bands can lead to highly anisotropic behavior for the material element containing both elastically deformed material and slip on the planes. The stress calculations are made using Cauchy stresses in the current configuration.

The pressure is given by the Mie-Grüneisen relation:

$$P = C\mu + D\mu^2 + S\mu^3 + \Gamma\rho_o(E - E_H) \tag{1}$$

where

$\mu = \rho_s/\rho_o - 1$, the compression strain,

$\rho_s$, $\rho_o$ are current and initial solid density,

$C$, $D$, and $S$ are coefficients with the units of moduli (this series defines the Hugoniot for the material),

$\Gamma$ is the Grüneisen ratio (dimensionless),

$E$ is the internal energy (energy per unit mass), and

$E_H$ is the energy at the same density ($\rho_s$) on the Hugoniot.

With this formulation, the pressure responds to thermal and mechanical effects, while the deviator stress is normally a function of the mechanical changes.

The deviator stress is computed from the standard elastic relation:

$$\sigma'_{ij} = \sigma'_{ij_o} + 2G\Delta\epsilon'^{E}_{ij} \tag{2}$$

where

$G$ is the shear modulus,

$\sigma'_{ij}$ and $\sigma'_{ij_o}$ are the deviator stresses after and before the current strain increment, and

$\Delta\epsilon'^{E}_{ij}$ is the incremental change in the elastic deviator strain.

As usual, the total deviator strain is separated into elastic and plastic components:

$$\Delta\epsilon'_{ij} = \Delta\epsilon'^{E}_{ij} + \Delta\epsilon'^{P}_{ij} \tag{3}$$

The next step for computing the deviator stresses is to determine the plastic strain increments. These plastic strains are computed on the individual planes in the SHEAR4 model.

The following steps are followed in computing the plastic strains:

- Impose the strain increment tensor $[\Delta\epsilon^{T}]$.

- Treating all the strain increment as elastic, compute the stress tensor $[\sigma^{N}]$ from Eq. (2).

- Transform $[\sigma^{N}]$ to normal and shear stresses ($\sigma^{N}_{kn}$ and $\sigma^{N}_{kr}$) on each plane ($k^{th}$ plane).

- Relax the shear stress components $\sigma_{kr}^N$ according to the standard stress relaxation equation:

$$\frac{d\sigma_{kr}}{dt} = 2G\frac{\Delta\epsilon_k'^T}{\Delta t} - \frac{\sigma_{kr} - Y_k}{T_c} = \frac{\sigma_{kr}^N - \sigma_{kro}}{\Delta t} - \frac{\sigma_{kr} - Y_k}{T_c} \qquad (4)$$

- Compute the plastic strains $\Delta\epsilon_k^P$ on each plane, and assemble these strains into the tensor $\Delta\epsilon^P$.

- Recompute the stress tensor $[\sigma]$ from the elastic strain, based on the difference between the total and plastic strain tensors: $[\Delta\epsilon^T] - [\Delta\epsilon^P]$

The yield strength on each plane is allowed to work harden according to the plastic strain $\epsilon_k^P$ that accumulates on that plane.

With this plastic flow procedure, natural anisotropy develops in the material because the plastic strain stored on each plane (and hence the yield strength on that plane) reflects the directions of the loading history.

## COMPARISON OF STRESSES WITH SIMPLE YIELD MODELS

Because yielding occurs only on specific planes, the SHEAR4 model yields at a somewhat higher stress than isotropic models that are able to yield on the plane with the highest shear stress. Therefore, we loaded the model under simple stress conditions and compared its response to that of the Mises and Tresca models.

In the Mises model, yielding occurs when the scalar quantity $\bar{\sigma}$ reaches the yield strength $Y$. In the Tresca model, yielding occurs on specific planes when the shear stress on that plane exceeds $Y/2$. If we require that the Tresca and Mises models give the same yield condition in simple tension, then the Tresca model gives a shear

432

yielding strength that is just $\sqrt{3}/2$ of the strength from the Mises model. Because SHEAR4 also provides yielding on specific planes, we might expect its behavior to be somewhat like that of the Tresca model. However, the SHEAR4 planes are not necessarily at the plane of maximum shear stress; therefore, SHEAR4 generally provides a higher yield strength than the Tresca model.

For the initial comparisons, we made simulations with nominal steel properties using an initial yield strength of 1 GPa, a work-hardening modulus of 3.2 GPa, and a stress relaxation time constant of 10 ns.

The first simulations with the SHEAR4 model are for a tensile loading applied in the z-direction. A strain of 8% was applied in the z-direction, and strains of -4% were applied in the X- and Y-directions. Thus, the volume was preserved and a simple tension test was approximated. The loading rate was $8 \times 10^4$ per second in the z-direction. After loading for 1 $\mu$s, straining was stopped and the stress was allowed to relax. The computed stress history is shown in Figure 2. This figure also shows the history of the threshold stress or static yield stress, $Y_{st}$. Work hardening gradually increases this yield value until point A, when loading ceases. At point A, the stress begins to relax back to the static value. Because of the short time constant, the relaxation is very rapid and the overshoot of the stress is only about 0.1 GPa. The orientation of the planes is ideal for this loading so the initial yielding matches that for both Mises and Tresca. However, neither the work hardening nor the stress relaxation follows the patterns of those models.

To test the effect of the stress-relaxation time constant, we next simulated the same loading with a time constant of $T_c = 10^{-7}$ seconds. The loading is along the

X-direction, but with the slip planes oriented such that the results are identical to those for loading in the z-direction. The resulting stress history is shown in Figure 3. The overshoot in stress is about 1.25 GPa. In a standard Mises model with stress relaxation in the form of Eq. (4), the overshoot would be $3GT_c\dot{\epsilon} = 1.92$ GPa, or 1.5 times the observed value here. (The 0.1 GPa noted above for a time constant of $10^{-8}$ seconds is nearly half the expected value of 0.192 GPa.) The stress relaxation rate seen in Figure 3 corresponds to a relaxation time of about 5 $\times$ $10^{-8}$, or just half the one used. Hence, the effective time constant for SHEAR4 appears to be about half that obtained with a Mises model. To obtain similar time effects, we should use $T_c \approx 2T_{Mises}$.

The next yielding studies were made to determine the effect of the initial slip plane configuration on the apparent yield strength of the SHEAR4 model. Therefore, we applied a simple tension loading for a range of initial orientations of the slip planes. A uniaxial tensile loading was applied in the X-direction at a strain rate of $8 \times 10^4$ until a strain of 8% was reached (1 $\mu$s). At that point, loading was stopped, and the strain was held constant for the same period of time. Then unloading was imposed at the same rate for the same period of time, and the cell was again held at a constant strain. The loading and unloading pattern used in the computations is shown in the inset in Figure 4. The SHEAR4 computations were made with six different initial orientations of the slip planes in the X-Y plane. The first orientation was that shown in Figure 1. Second, planes 1 through 8 were rotated $9^o$ from X in the X-Y plane. For orientations 3 through 6, the planes were shifted by $9^o$ degree increments until the first plane was at $45^o$. The resulting $\bar{\sigma}$ at loading points A, B, C, and D are shown for each initial configuration in Figures

4 and 5. The pattern of loading is such that the stress overshoots to point A, then gradually reduces to point B through the stress relaxation process, unloads elastically through zero to yielding in the opposite direction at point C, and then relaxes to point D.

The expected pattern of loading is shown by the "Mises Static" line in Figure 4. The expected pattern, including work hardening and strain-rate effects, is shown in the diagram at right in Figure 5. Clearly, the values from the six computations only roughly approximate these Mises values. Without work hardening and strain-rate effects, yield strengths are higher than the Mises strength because of nonoptimal orientation of the planes. Work hardening occurs at about half the rate in the Mises model because only the plastic strain taken on the local plane is considered in SHEAR4, not the total plastic strain taken on all planes. On the active planes, this local plastic strain tends to be about half the equivalent plastic strain in the usual global definition. As noted earlier, the time constant in SHEAR4 has a smaller effect than in an isotropic model, so the stress overshoot is only about half that of the standard model. In summary, the work-hardening and strain-rate effects contribute to decreasing the yield strength computed in SHEAR4, whereas the nonoptimal placement of the slip planes introduces a random increase in the strength compared with a Mises model.

## ANALYSIS OF ROTATION

We first consider the rotations occurring in a block of material undergoing large shear strains as background for examining the accuracy of the multiple-plane calculations. The multiple-plane model is used to simulate various loading

paths and the results of the calculations are compared with analytical results. The large-shear problem is illustrated in Figure 6, in which a block is being distorted in simple shear. The block is sheared by moving points 2 and 3 by $u\Delta t$. The apparent rotation from the Jaumann procedure is

$$\Delta\alpha = \frac{u\Delta t}{2\Delta y} \tag{5}$$

For an example of the difficulty with large rotation problems, consider the case in which the incremental motion in Figure 6(a) gives an angular change of $\Delta\alpha = 1^{\circ}$. Then continue the motion for 180 increments. Line 03 rotates by about $2^{\circ}$ per increment initially. However, as it moves from the vertical, the angular change per increment reduces. Line 02 initially rotates by $\Delta\alpha$ per increment; hence, its rotation matches the "average" rotation. But this line also moves away from $45^{\circ}$, and so thereafter its rotations are less than $\Delta\alpha$ per increment. The state after $180^{\circ}$ of motion is shown in Figure 6(b). Equation (5) would give a total angular change of $180^{\circ}$. Yet from Figure 6(b), it is clear that none of the bounding lines rotated more than $90^{\circ}$, so the average rotation must be less than $45^{\circ}$. (The actual average rotation is about $38^{\circ}$.)

## Types of Rotation to Consider

The rotation information for a block of material can be used in at least three ways and can account for three different effects:

1. Transformation of the stress tensor to account for the material rotation.

2. Rotation of micro features, such as cracks or planes of anisotropy.

3. Average rotation of the cell material.

436

In a recent article [10] it was found necessary to distinguish between these three types of rotation because they are in fact different and because their individual importance depends on the material being used and the information required from the computation. This is a problem that has been studied thoroughly by Dienes [11]. The following observations were made based on the constitutive relation under study:

1. Isotropic elastic material: Rotation corrections are needed for shear strains on the order of 1. As shown in Figure 7, the usual Jaumann correction is not adequate.

2. Isotropic plastic material: Jaumann's or Dienes' method or no correction is sufficient for stress computations, but Dienes' method is needed to compute the average rotations. Figure 8 compares stresses computed by Dienes' method and by Jaumann's method for material with a large yield strength; there is no difference even for this very large yield strength.

3. Anisotropic material with material orientations that are fixed with respect to each other: Dienes' method should be used to account for the location of the material orientations.

4. General anisotropic material or material with developing anisotropy: The relative orientations of planes in the material are not fixed, so individual planes must be treated. The average cell rotation (by any method) is not useful for orienting the planes or for stress computations.

Analysis of Rotation of Lines

The rotation analysis is developed first for the motion of a line in a linear velocity field. This result is applied to the rotation of material features such as microcracks. Then the line analysis is applied to determine the average rotation of a block undergoing large shear deformation.

A line segment L in a linear velocity field will be stretched (or shortened) and rotated. We consider only the rotation aspect. The rotation rate $d\theta/dt$ is given by the dot product

$$\frac{d\theta}{dt} = -\frac{1}{|L|}\frac{d\vec{\delta}\cdot\vec{n}}{dt} \tag{6}$$

where $\vec{n}$ is the unit normal to the line L. $\vec{\delta}$ is the displacement of one end of the line with respect to the other, and $L$ is the line length. The linear velocity field is written in terms of velocities $u$ and $v$ in the $x$- and $y$-directions. The $d\vec{\delta}/dt$ can be written in terms of the $x$- and $y$-coordinates and the $\Delta x$ and $\Delta y$ lengths of the line.

$$\frac{1}{|L|}\frac{d\vec{\delta}}{dt} = \vec{i}\frac{(\partial u/\partial x)\Delta x + (\partial u/\partial y)\Delta y}{|L|} + \vec{j}\frac{(\partial v/\partial x)\Delta x + (\partial v/\partial y)\Delta y}{|L|}$$

$$= \vec{i}\left(\frac{\partial u}{\partial x}\cos\theta + \frac{\partial u}{\partial y}\sin\theta\right) + \vec{j}\left(\frac{\partial v}{\partial x}\cos\theta + \frac{\partial v}{\partial y}\sin\theta\right). \tag{7}$$

The angle $\theta$ is the angle of the line with respect to the $x$- coordinate, measured positively counterclockwise. Similarly, the normal vector $\vec{n}$ is

$$\vec{n} = \vec{i}\sin\theta - \vec{j}\cos\theta. \tag{8}$$

When the expressions for $d\vec{\delta}/dt$ and $\vec{n}$ are placed in Eq. (6), the rotation rate is obtained:

$$\frac{d\theta}{dt} = -\frac{\partial u}{\partial x}\sin\theta\cos\theta - \frac{\partial u}{\partial y}\sin^2\theta + \frac{\partial v}{\partial x}\cos^2\theta + \frac{\partial v}{\partial y}\sin\theta\cos\theta. \tag{9}$$

Equation (9) is used to obtain the rotation for lines or other line-like features in two-dimensional calculations.

Next we consider the rotation of several lines in a block of material as a means of obtaining the average rotation of the material. We assume that the block has a large number of lines drawn on it. Then the block is sheared, and the motion of the lines is followed. If a simple shear $\omega = d\alpha/dt = \partial u/\partial y$ is applied, then the rotation rate $d\theta/dt$ of a line originally at an angle $\theta_o$ from the $x$-axis is

$$\frac{d\theta}{dt} = -\omega \sin^2 \theta = -\frac{d\alpha}{dt} \sin^2 \theta. \tag{10}$$

For a constant $\omega$, this equation can be integrated over time to obtain

$$\cot \theta = \cot \theta_o + \Delta\alpha \tag{11}$$

or

$$\Delta\theta = \theta - \theta_o = \text{arccot}(\cot \theta_o + \Delta\alpha) - \theta_o. \tag{12}$$

Now we can find the average rotation for a cell by finding the average $\Delta\theta$ for a large number of planes. A set of 36 planes uniformly distributed from $\theta_o = 0^o$ to $175^o$ was studied. Simple shear strain such as that in Figure 6 was imposed in $1^o$ increments for 180 steps. As shown in Figure 9, the rotations of the planes varied from $0^o$ to $115^o$.

We tracked the rotations of sets of lines during the shearing calculation and examined the accuracy that could be achieved with this method, compared with the preceding exact analysis. First we used 18 orthogonal pairs of lines. The average rotations of pairs that were initially orthogonal ranged from $36^o$ to $80^o$, compared with the exact value of $57.52^o = \arctan \pi/2$. The range in these average

rotations is shown in Figure 10. The abscissa of this plot gives the range from the minimum to the maximum rotation for any pair of lines, normalized by the exact value for the rotation. The figure shows also results for nine sets of four planes each, six sets of six planes each, four sets of nine planes each and two sets of 18 planes each. Clearly, the error in the average angle decreases markedly with the increase in the number of planes used. As expected, the error increases with the total rotation imposed. Hence, the correct rotation of the material can be found by following the rotation of sets of lines, but this procedure does not provide high accuracy unless a large number of lines are used.

Rotations with the Multiple-Plane Model

With this rotation information we can examine the operation of a multiple-plane model to determine how well it represents large rotations. For the model we use four planes to describe shearing in the x-y plane; hence, we expect to obtain uncertainties of about 7.4° (from Figure 10) for a nominal rotation of 180°.

The inaccuracies noted previously for small amounts of total strain are simply enlarged for large shear strain. Figure 11 shows the resulting Mises stress for loading in simple shear to an equivalent plastic strain of 1.4. Curves are given for six initial configurations of the planes. Because of the grouping of the planes, periods of apparent hardening and softening are caused by the locations of the planes, not by material behavior.

Similar computations were made to examine the grouping of the slip planes, using the same six starting locations for the four base planes. A shear strain of 2 was imposed along the y-axis. The motion of these four planes is given in Figure

12 as a function of the initial position of each plane. The positions of the planes for no strain and with the first plane at $0°$ are shown as dots along the abscissa. After a strain of 2.0 the three planes originally at $0°$, $45°$, and $90°$ are now spaced only from $65°$ to $90°$, whereas the plane originally at $135°$ is finally at $225°$. Yet $225°$ corresponds to $45°$, so all four planes are actually within the range of $45°$ to $90°$; these planes will poorly represent shearing that would require slip from $0°$ to $45°$ or from $90°$ to $180°$. Without appropriately placed slip planes, the stresses may be too high. A similar bunching of the planes occurs when the first plane starts at $45°$, but for other configurations the final distribution of planes is more uniform with angle.

## SUMMARY

Problems still exist in the computation of stress and rotation in material that develops anisotropy and undergoes large strains, especially large shear strains.

Standard tensor solutions appear inappropriate to account for rotations in anisotropic materials. Therefore, we have considered multiple-plane models which can, in principle, account correctly for rotations.

We examined stress computations under large strains for several loading paths in a nine-plane model (SHEAR4). The results follow:

- The nominal yield stress reached depends ($\pm$ 10%) on the orientation of the planes with respect to the loading direction. For large strains, the variation of the yield stress with orientation increases significantly.

- Work hardening occurs at about half the rate it would in a Mises model for

the same work-hardening modulus.

- The time constant $T_c$ in the multiple-plane model causes relaxation and overstress comparable to $T_c/2$ for a Mises-type model.

- After large shear strains, the original planes can become grouped together in orientation and poorly represent an isotropic material. The material then responds with increased apparent yield strength.

Multiple-plane models can readily represent a large range of rotation, damage, and yield phenomena, but attention should be given to accuracy problems associated with the limited number of planes used when these planes are a discretization of isotropic slipping material. However, when modelling deformation of a single crystal, as by Peirce, Asaro, and Needleman [5], the multiple-plane models should give accurate results.

# REFERENCES

1. Seaman, L. and James L. Dein, "Representing Shear Band Damage at High Strain Rates," Proceedings of the IUTAM Symposium on Nonlinear Deformation Waves, Tallinn, Estonia, held August 1982, published by Springer-Verlag, Berlin, 1983.

2. Curran, D. R. and L. Seaman, "Computational Models for Nucleation, Growth, and Coalescence of Adiabatic Shear Bands," American Physical Society Conference of Shock Waves in Condensed Matter, July 1985, Spokane, Washington.

3. Curran, D. R., L. Seaman, and D. A. Shockey, "Dynamic Failure of Solids," Physics Reports, 147, Numbers 5 & 6, 253, March 1987.

4. Batdorf, S. B. and B. Budiansky, "A Mathematical Theory of Plasticity Based on the Concept of Slip," Tech Note No. 1871 of National Advisory Committee for Aeronautics, April 1949, Washington.

5. Peirce, D., R. J. Asaro, and A. Needleman, "An Analysis of Nonuniform and Localized Deformation in Ductile Single Crystals," Report MRL E-138, Brown University for National Science Foundation, Oct 1981.

6. Bazant, Zdenek P., and Pere C. Prat, "Creep of Anisotropic Clay: New Microplane Model," Jour. of Eng. Mech., ASCE, 113, No. 7, 1050, July 1987.

7. Bazant, Zdenek P., and B. H. Oh, "Microplane Model for Progressive Fracture of Concrete and Rock," Jour. of Eng. Mech., ASCE, 111, No. 4., 559, April 1985.

8. Bazant, Zdenek P. and Pere C. Prat, "Microplane Model for Brittle-Plastic Material: I. Theory," Jour. of Eng. Mech., ASCE, 114, No. 10, 1672, Oct. 1988.

9. Zienkiewicz, O. C., and G. N. Pande, "Time-Dependent Multilaminate Model of Rocks - A Numerical Study of Deformation and Failure of Rock Masses," Int. Jour. for Num. and Analytical Methods in Geomechanics, 1, 219, 1977.

10. Seaman, L., "Rotation Transformations for Two-Dimensional Calculations," Int. J. Solids Structures, 24, No. 7, 735, 1988.

11. Dienes, J. K., "On the Analysis of Rotation and Stress Rate in Deforming Bodies," Acta Mech., 32, 217, 1979.
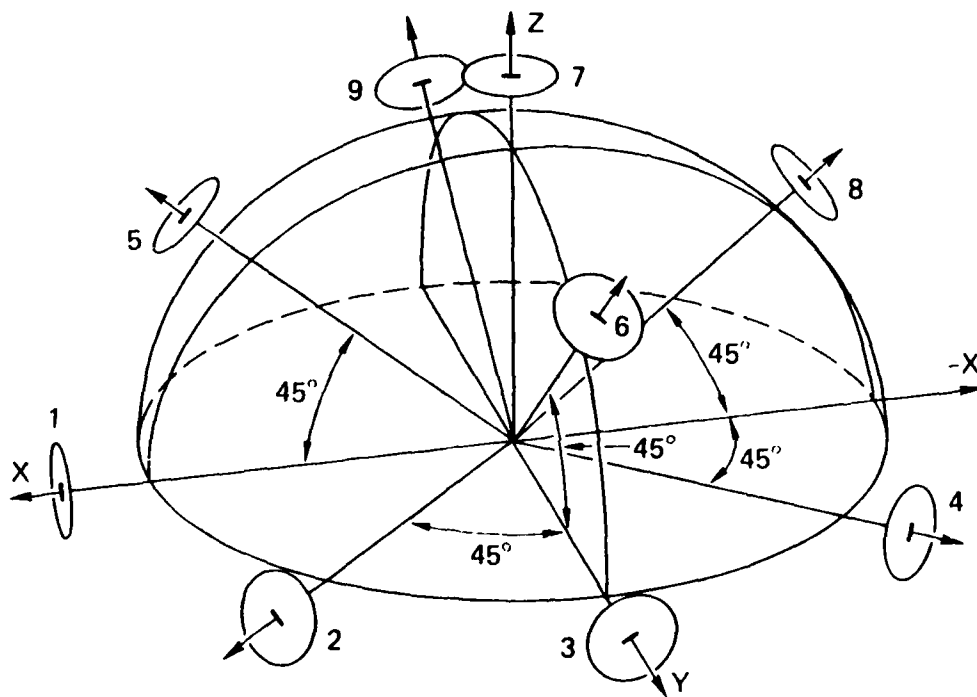
MA-7893-3A

Figure 1. Initial Configuration of the Slip Plane Orientations in the SHEAR4 Model

445
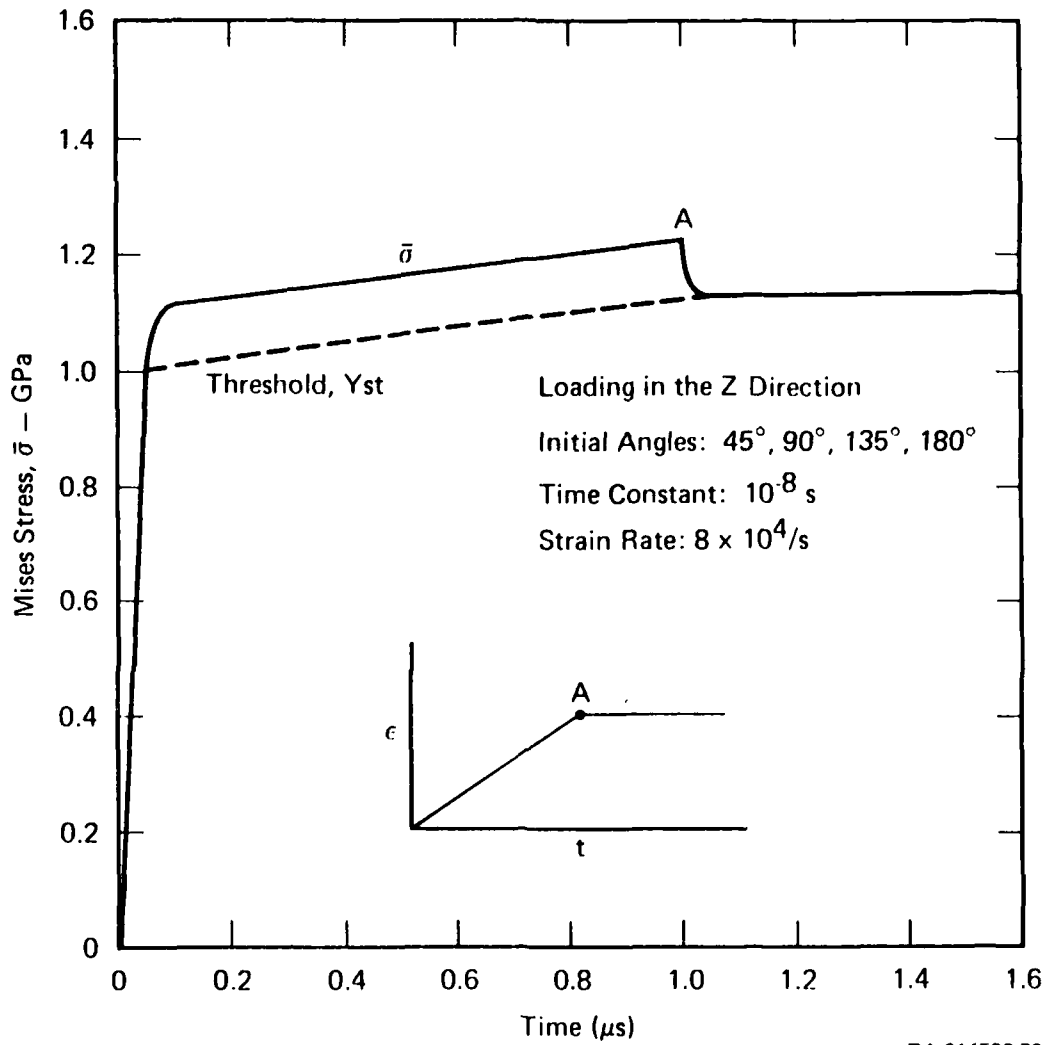
Figure 2. Rate-Dependent, Work-Hardening Path Followed by SHEAR4
Loading for a Time Constant of $10^{-8}$ seconds

446

Loading in the X Direction

Initial Angles: 0°, 45°, 90°, 135°

Time Constant: $10^{-7}$ s

Strain Rate: $8 \times 10^4$/s
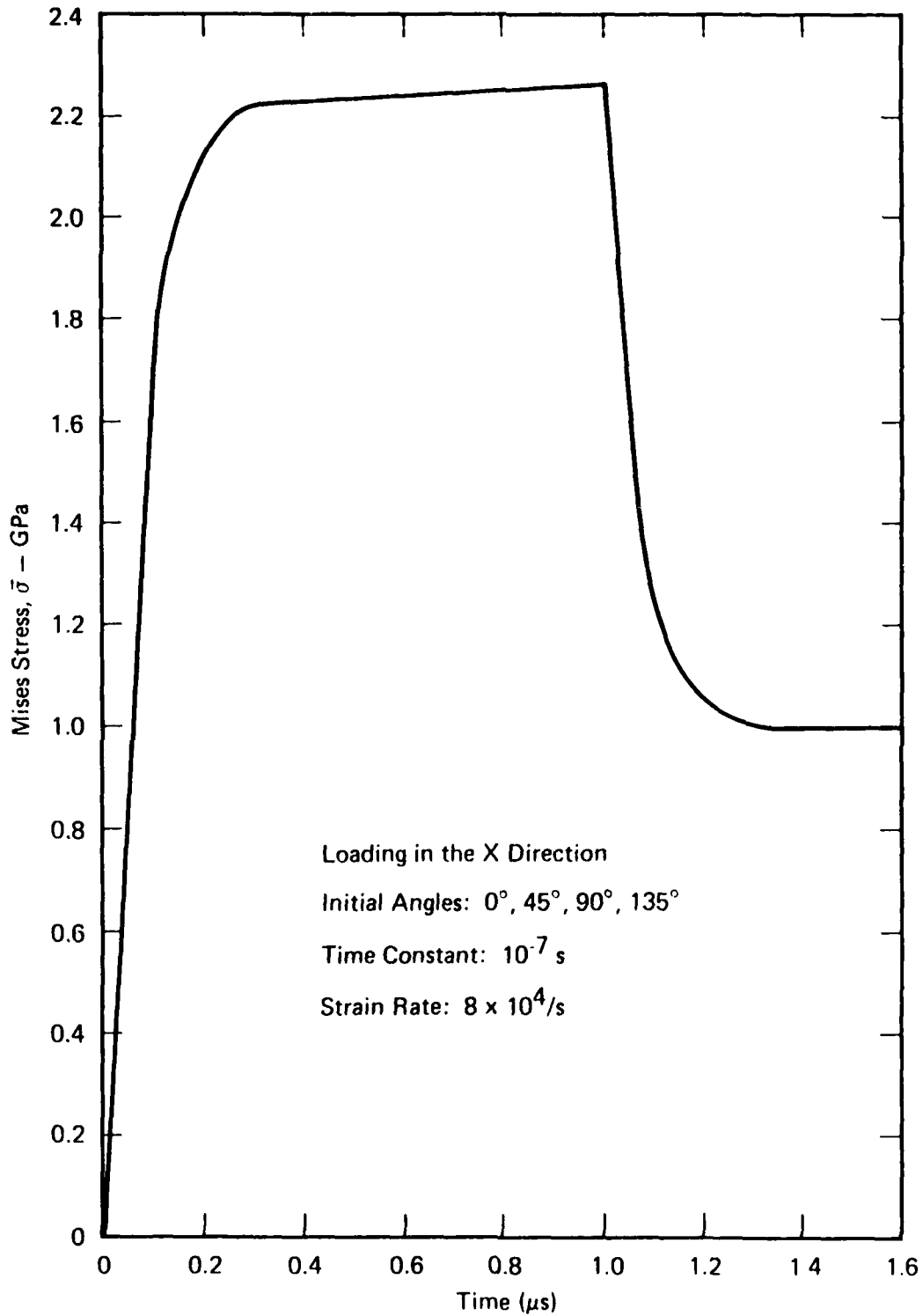
RA-314522-51

Figure 3. Rate-Dependent, Nonwork-Hardening Path Followed by SHEAR4 during Loading for a Time Constant of $10^{-7}$ seconds

447
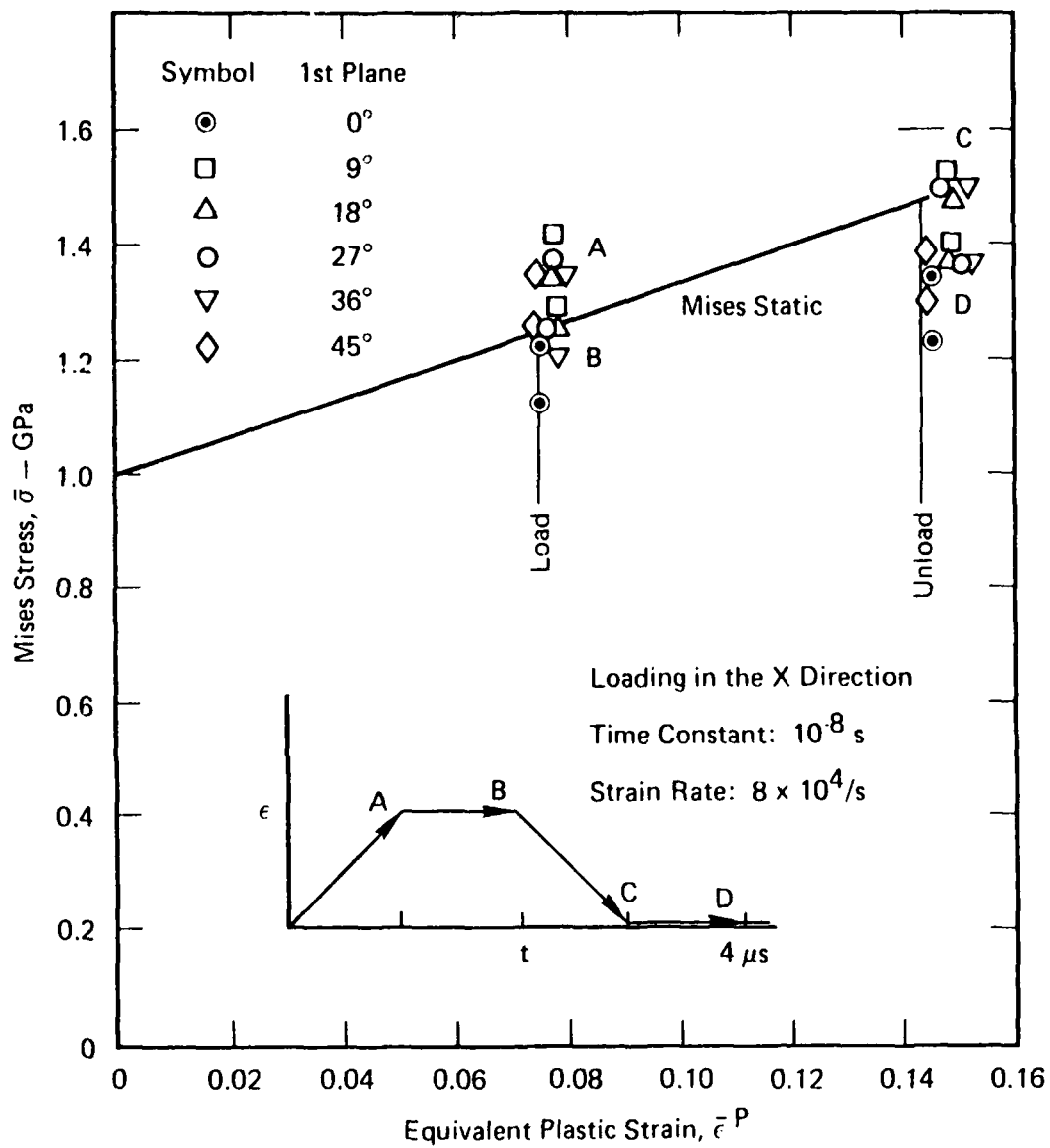
Figure 4. Comparison of the Equivalent or Mises Stress from SHEAR4
with That from a Mises Model for a Loading and Unloading
Path (time constant = $10^{-8}$ seconds)
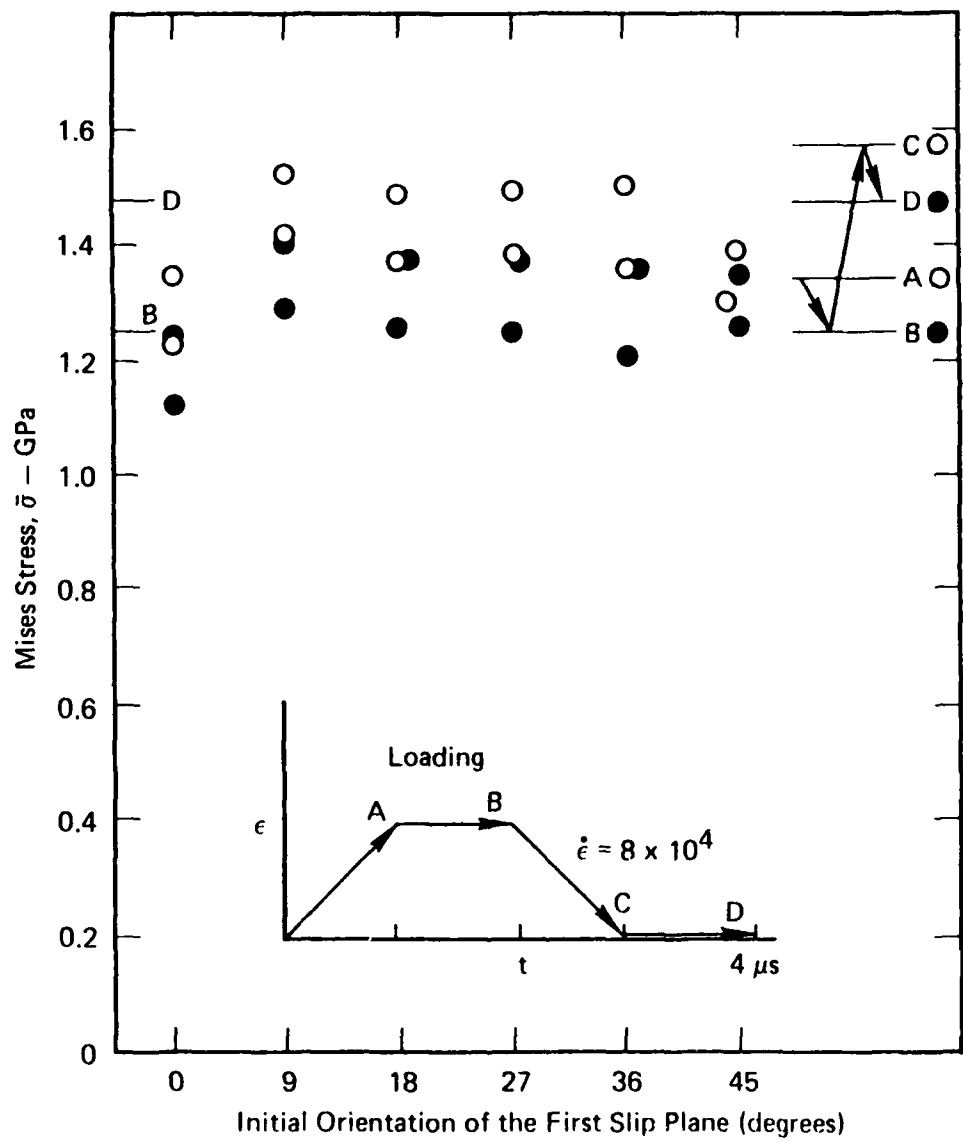
Figure 5. Variation of the Yield Response of the SHEAR4
Model as a Function of the Initial Orientation of
the Slip Planes

Mises Stress, $\bar{\sigma}$ – GPa

Initial Orientation of the First Slip Plane (degrees)

Loading

$\dot{\epsilon} = 8 \times 10^4$

4 µs

RA-314522-49

449
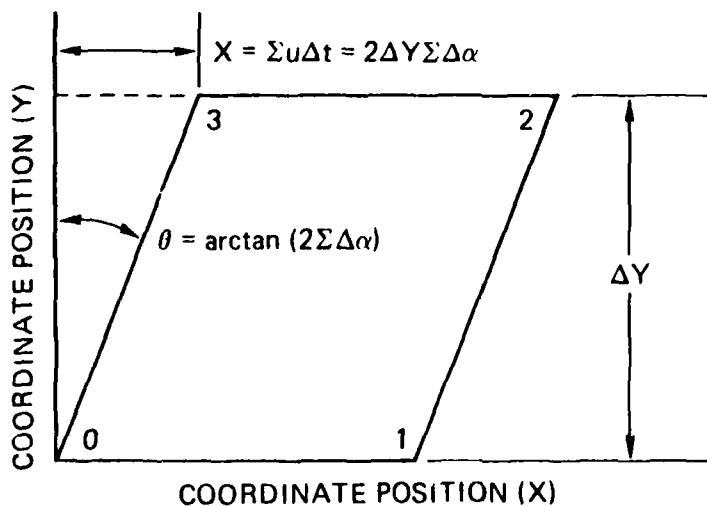
(a) Distorted Block After Several Strain Increments
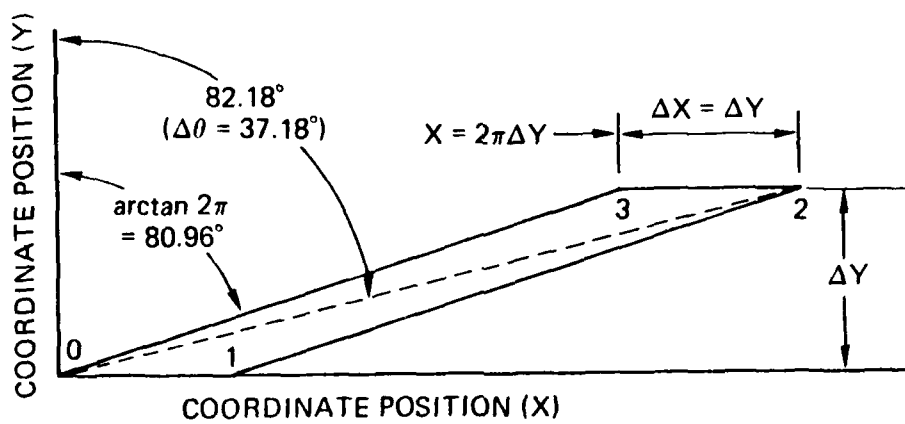
(b) Configuration for $\Sigma\Delta\alpha = \pi$

RA-314522-13

Figure 6. Configuration of a Block Undergoing Simple Shear

450
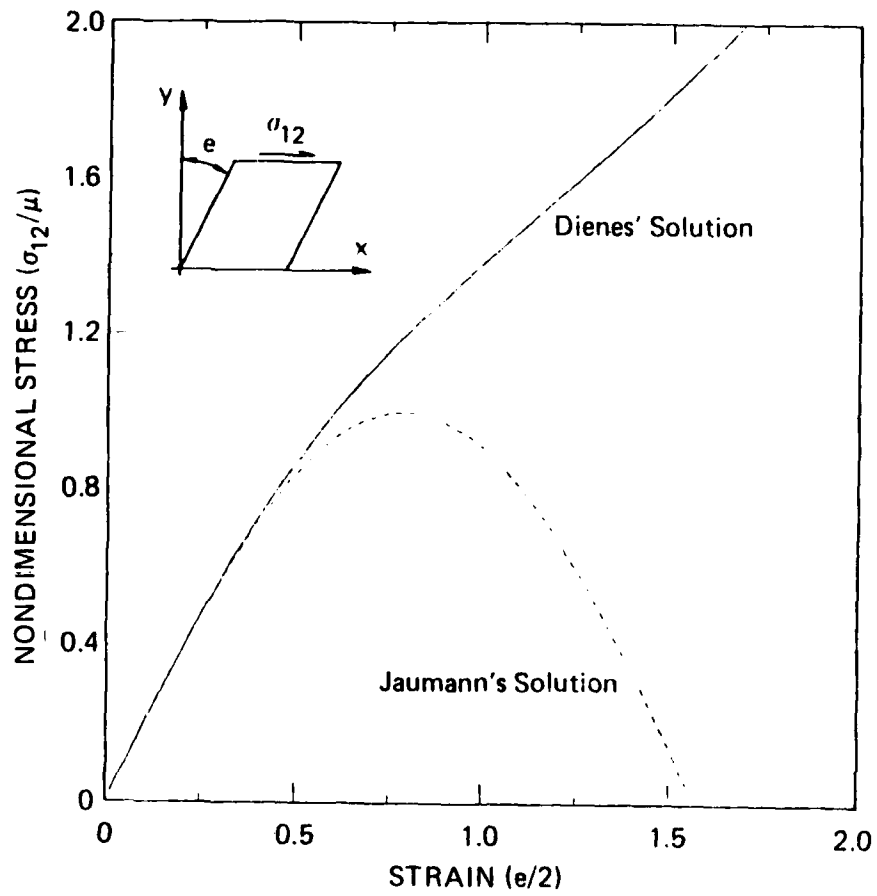
(a) Comparison of Shear Stresses for Simple Shear
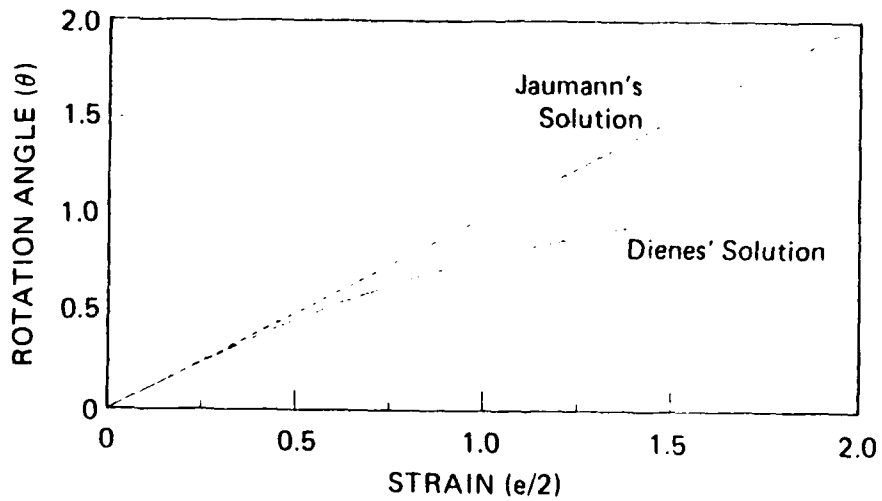
(b) Comparison of Rotation Angles

JA-6423-21

Figure 7. Comparison of Shear Stress and Angle of Rotation
Computed by the Methods of Dienes and Jaumann
in Simple Shear

451
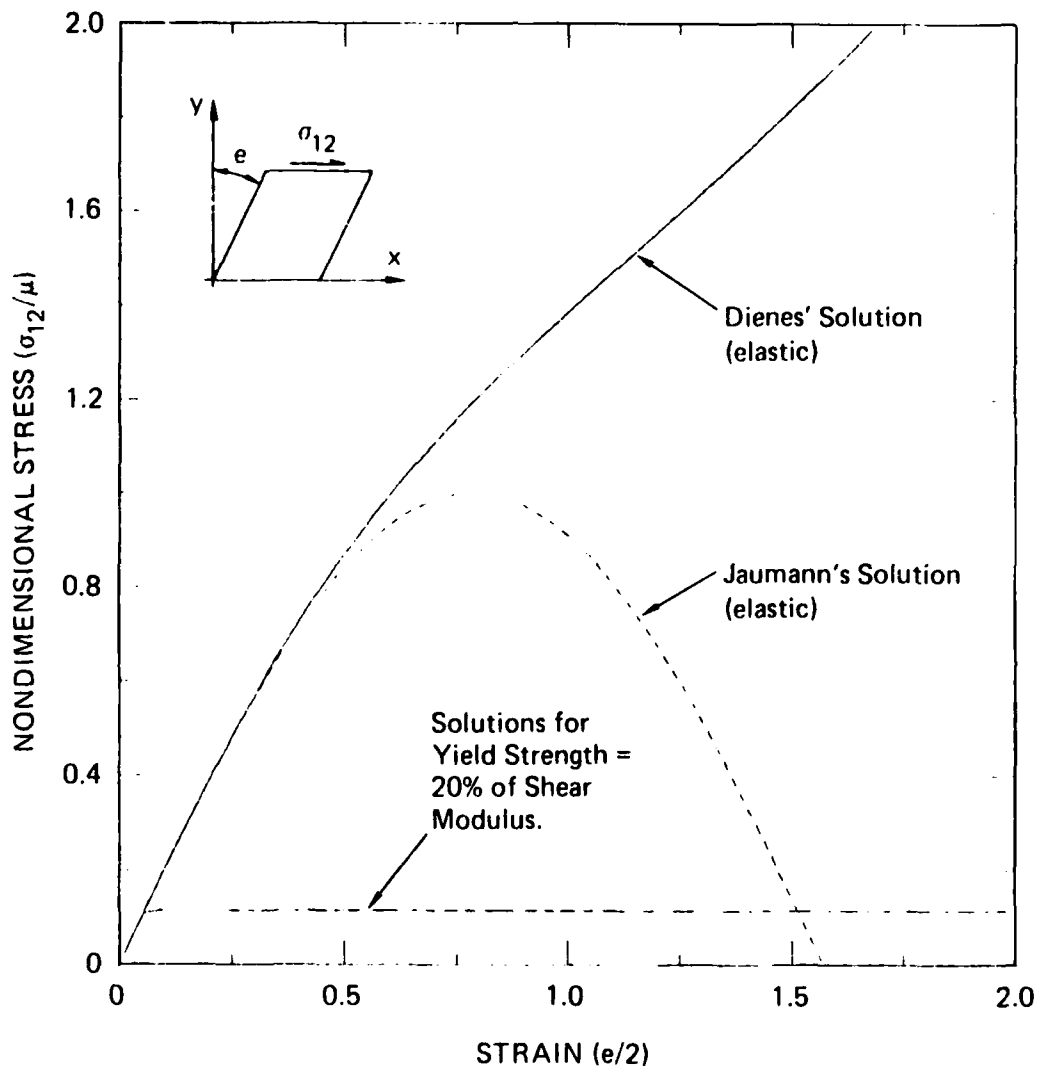
Figure 8. Comparison of Shear Stresses from Dienes' and Jaumann's Solutions for Elastic and Plastic Cases

JA-6423-24

452
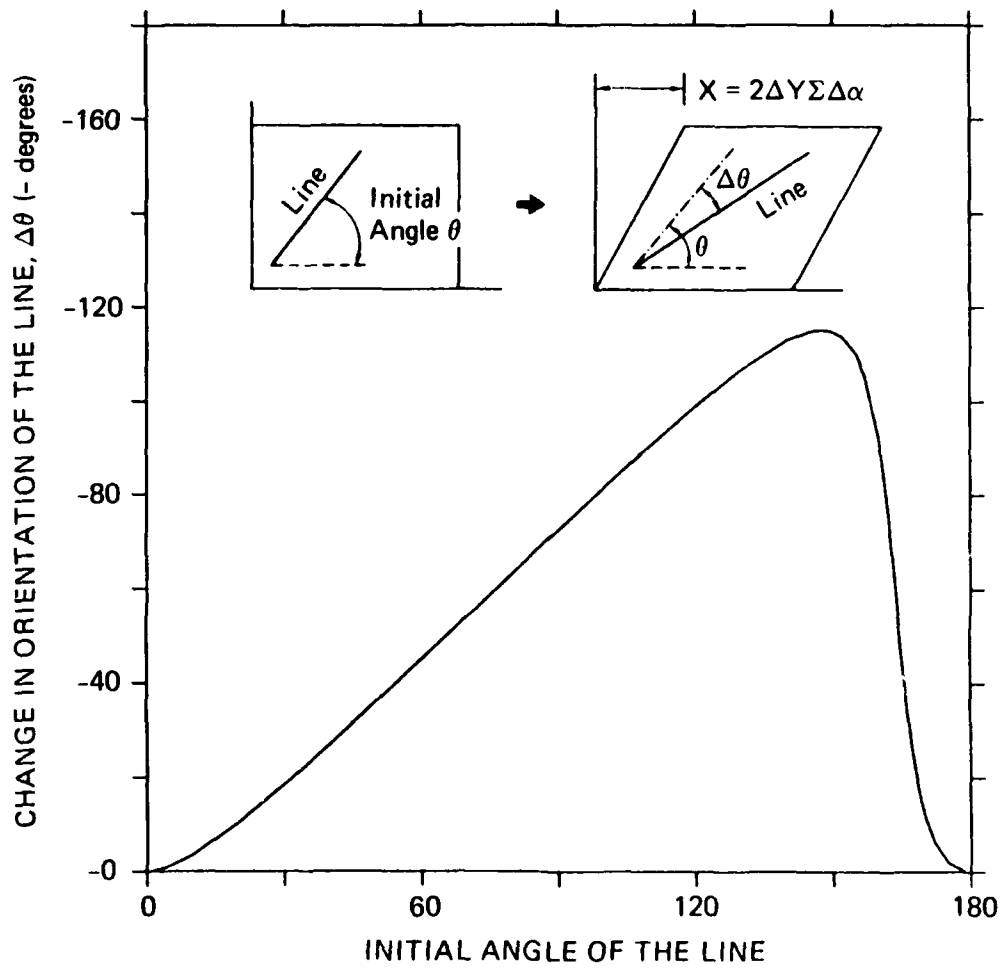
Figure 9. Change in Orientation of Lines in a Block Undergoing Simple Shear as a Function of the Initial Line Orientation (Nominal Rotation of 180°)
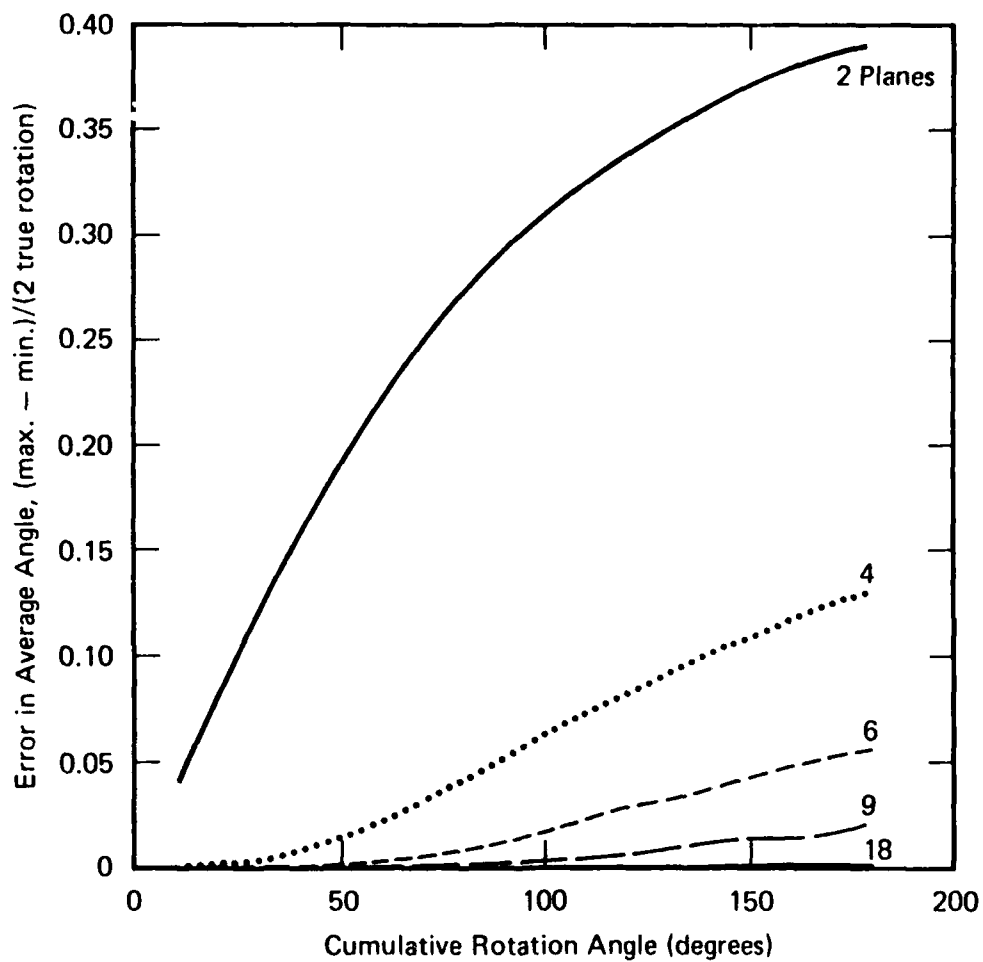
RA-314522-15

Figure 10. Posible Errors Obtained by Using the Average Rotation of Sets of
2, 4, 6, 9, or 18 Lines to Compute the Average Rotation of the Cell

454
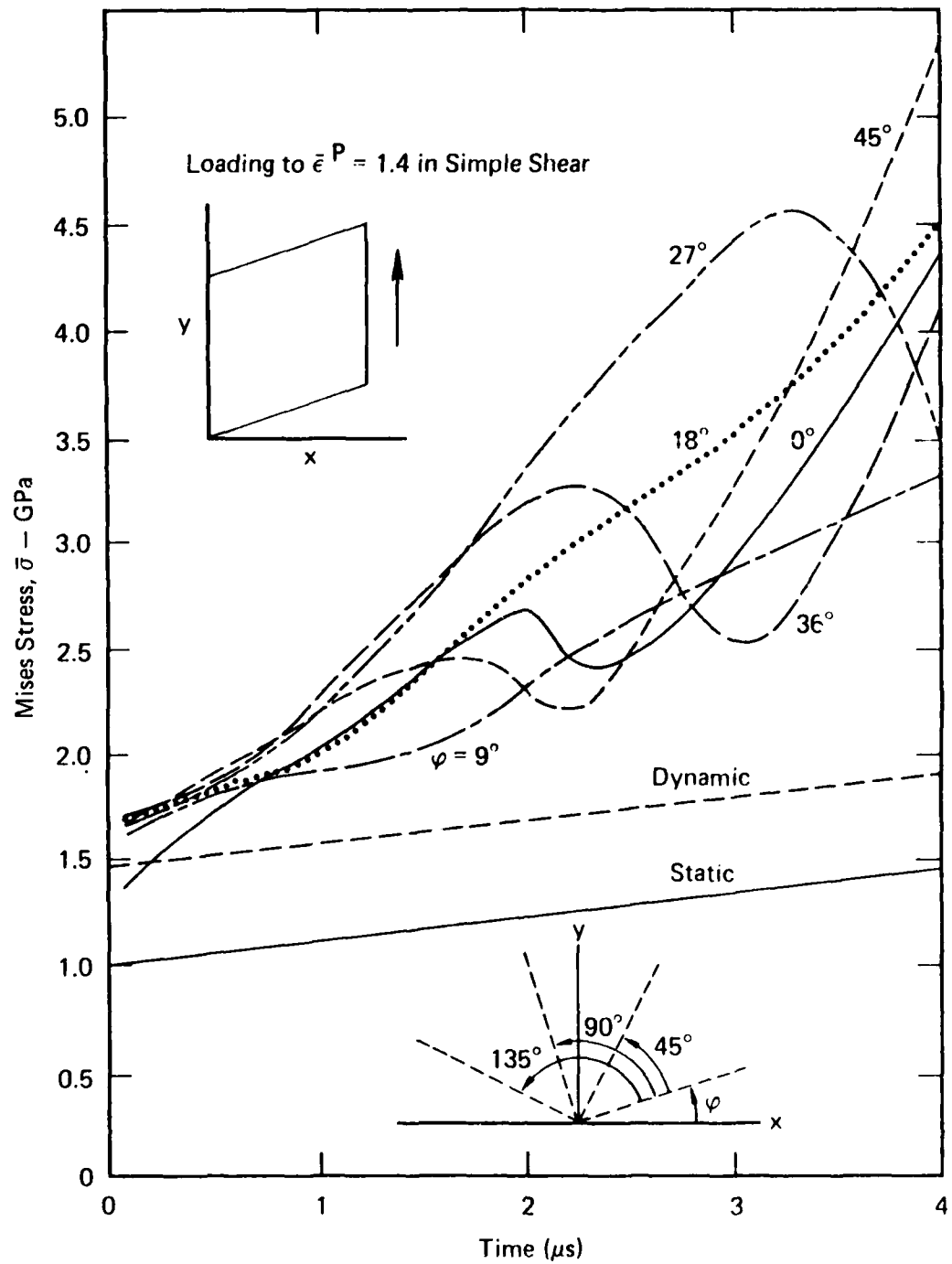
Figure 11. Variation of the Mises Stress under Large Shear Strain
for Several Initial Slip Plane Configurations

455
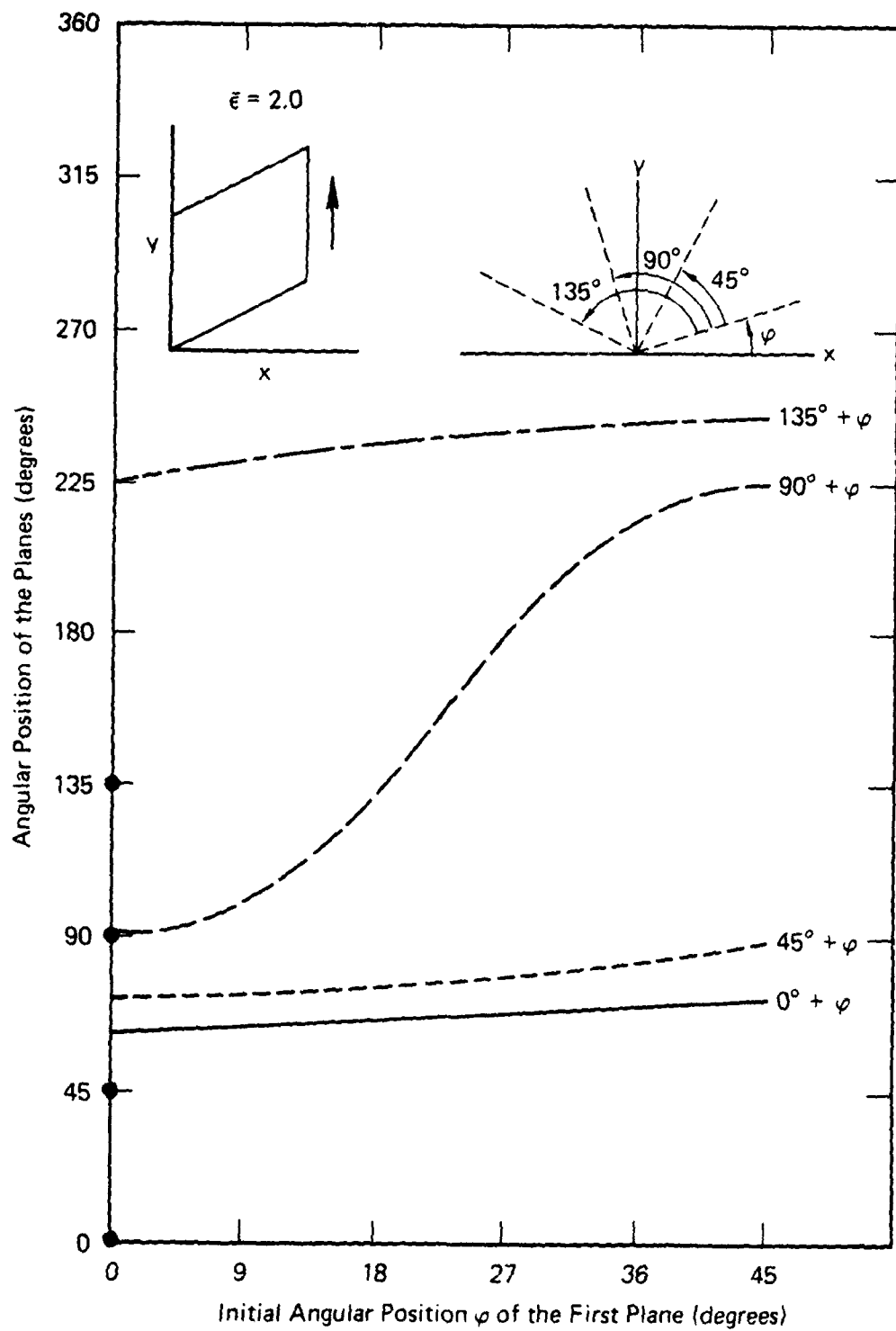
Figure 12. Variation of Slip Plane Motions as a Function of the
Initial Position of the Planes

456

# APPLICATIONS OF THE BODNER-PARTOM MODEL

William H. Cook
Air Force Armament Laboratory
AFATL/MNW
Eglin AFB, FL 32542-5434

## INTRODUCTION

The Bodner-Partom constitutive model represents a well documented, state variable, viscoplastic constitutive model with several apparent advantages for applications in continuum mechanics wave propagation codes (hydrocodes) [1,2]. The model has recently been implemented in versions of the STEALTH and EPIC-2 HYDROCODES [3,4] at the University of Dayton Research Institute, and sufficient software and documentation have been provided to the EPIC-2 user community for use of this model with the EPIC2 86 version of the code currently available to Government sponsored users through Eglin AFB [5]. This paper documents some preliminary experiences with the application of the Bodner-Partom model to elementary validation test problems and problems of interest to the conventional weapon development community.

## BACKGROUND

The Bodner-Partom constitutive model separates total deformation rate into elastic (geometrically reversible) and plastic (geometrically irreversible) components that are

loading and unloading. The formulation includes strain hardening as a function of plastic work, rate of deformation effects, and strain rate history effects. The model implemented here assumes isotropy, although more recent developments of the model have been proposed allowing the treatment of modest anisotropy. This implementation modifies the originally isothermal Bodner-Partom model to account for thermal softening effects through a modification of the strain rate hardening term. The model avoids the necessity for yield criterion and loading or unloading conditions. The state variable approach is developed with metallurgical implication associated with dislocation theory concepts. A limiting strain rate is assumed in the model-- generally 100,000,000 per second.

The model takes the form:

$$\dot{\epsilon}^{P}_{ij} = D_o \exp\left\{-\left[\frac{Z^2}{3J_2}\right]^n \frac{n+1}{2n}\right\} \frac{S_{ij}}{\sqrt{J_2}} \tag{1}$$

$$Z = Z_1 - (Z_1 - Z_o) \exp\left\{-m W_p\right\} \tag{2}$$

where Z is the inelastic state variable representing resistance to plastic flow caused by microstructural barriers impeding dislocation motion.

$$W_p = \sigma_{ij} \epsilon^p_{ij} \tag{3}$$

$$n = n_o \left\{1 - T^{*A}\right\} \qquad (4)$$

where n controls rate dependency

$$m = m_o + m_1 e^{-W} p \qquad (5)$$

where m controls the rate of work hardening.

In these equations, and throughout this paper, the following notations apply:

$\sigma$      total stresses

$S$      deviatoric stresses

$J_2$      second invariant of deviatoric stresses

$\epsilon^p$, $\epsilon^e$, $\epsilon$      plastic, elastic, and total strain rates

Einsteinian summation convention is denoted by subscripts except on constants.

It should be noted that strain rates are expressed as a function of stresses in this model, and solving for stresses in terms of strain rates is not possible. Hydrocodes universally require the solution of incremental stresses from incremental strain rates, demanding an iterative solution for stresses when the Bodner-Partom model is implemented in a hydrocode.

The model requires eight material constants summarized below:

$D_o$   limiting value of plastic strain rate in shear

$Z_o$   initial value of

$Z_1$   saturation state for $(0 \leq z \leq Z_1)$

$m_o$   work hardening coefficient

$m_1$   secondary work hardening coefficient

$\alpha$   another secondary work hardening coefficient

$n_o$   strain rate coefficient (large is rate sensitive)

$A$   thermal softening exponent

Special software has been developed by the University of Dayton Research Institute for determination of the first four constants described above, based on at least three tensile tests at different strain rates [6]. The software is essentially a computer aided graphical approach providing four options for the evaluation of material test data to determine Bodner-Partom material constants. The four options are:

1.    Determine the four basic material constants allowing user interaction for adjustments. Constants determined are:

$$Z_o \quad Z_1 \quad m_o \quad n_o$$

2. Graphically compare stress-strain curves of tensile or compressive tests against curves generated from the Bodner-Partom model with specific values for the constants determined in Option 1.

3. Graphically compare stress-strain curves of best-fit plots from tensile or compressive tests against curves generated from the Bodner-Partom model with specific values for the constants determined in Option 1.

4. Solve the Bodner-Partom model for selected strain rates, displaying the stress-strain curve for a range of preselected stresses based on specific values for the constants determined in Option 1.

In all cases, this software assumes a limiting shear strain rate of 100,000,000 per second. Constants are determined sequentially so that errors in determining the first constant can effect the selection of subsequent constants. The user must determine the following material constants iteratively with assistance from graphic displays of model fits to test data:

$$\alpha \quad m_1 \quad A$$

SOLUTION TECHNIQUE FOR BODNER-PARTOM MODEL

The Bodner-Partom model represents material plastic strain rate as a function of material constants, a state variable related to plastic work, and the stress state. Within

461

## BASIS FOR COMPARISON

The Johnson-Cook constitutive model was used as a basis of comparison for this study [7]. This five-parameter empirical model has been demonstrated to provide realistic solutions to hydrocode predictions of a very broad class of applications to extremely dynamic events such as impact, penetration, and explosive acceleration of metals. The Johnson-Cook model has the form:

$$\bar{\sigma} = [A + B\,\bar{\epsilon}^n]\,[1 + C\,\ell n\,\bar{\epsilon}*]\,[1 - T^{*M}] \qquad (6)$$

where:

$\bar{\sigma}$    Equivalent Stress

$\bar{\epsilon}$    Effective Strain

$\epsilon^*$    Strain Rate
(dimensionless, normalized by 1/seconds)

$T^*$    Homologous Temperature
(dimensionless (T-Troom)/(Tmelt-Troom))

and the five material constants are:

A    Yield Strength

B    Work Hardening Coefficient

n    Work Hardening Exponent

C    Strain Rate Coefficient

M    Thermal Softening Coefficient

hydrocodes, stresses must be determined from incremental strains, so the Bodner-Partom model must be inverted to represent stress as a function of strain. This is not directly possible, so an iterative solution technique is required.

The iterative solution seeks deviatoric stresses, total stresses, and plastic strain rates at the current cycle. These values are known for the previous cycle, along with values for the current cycle for total strain rate, volumetric strains, and pressure. The elastic constants are also known. The iterative solution used here is essentially an Euler scheme using a first order forward difference to determine the new stress state. A trial stress state is chosen and placed in the Bodner-Partom model, which provides trial plastic strain rates. Elastic strain rates are calculated and added to the trial plastic strain rates for a trial total strain. Deviatoric stress rates are calculated using the elastic constants and the elastic strain rates. Total stress rates are determined by adding the pressure terms. Finally, a trial total stress state is established by adding the incremental stress rate times the time step to the stresses known for the previous cycle stresses for the element being considered. The stresses calculated are compared to the originally estimated stresses, and the process iterates to an acceptable level of difference between estimated and calculated stresses.

## BASIS FOR COMPARISON

The Johnson-Cook constitutive model was used as a basis of comparison for this study [7]. This five-parameter empirical model has been demonstrated to provide realistic solutions to hydrocode predictions of a very broad class of applications to extremely dynamic events such as impact, penetration, and explosive acceleration of metals. The Johnson-Cook model has the form:

$$\bar{\sigma} = [A + B \, \bar{\epsilon}^n] \, [1 + c \, \ell n \, \dot{\bar{\epsilon}}*] \, [1 - T^{*M}] \qquad (6)$$

where:

$\sigma$    Equivalent Stress

$\epsilon$    Effective Strain

$\dot{\bar{\epsilon}}^*$    Strain Rate
(dimensionless, normalized by 1/seconds)

$T^*$    Homologous Temperature
(dimensionless (T-Troom)/(Tmelt-Troom))

and the five material constants are:

A    Yield Strength

B    Work Hardening Coefficient

n    Work Hardening Exponent

C    Strain Rate Coefficient

M    Thermal Softening Coefficient

## COMPARISON OF MATERIAL CONSTANTS

Table 1 provides a comparison of the material constants used in this study for the Bodner-Partom Model as compared to the Johnson-Cook Model. In all cases, the material constants for the Johnson-Cook Model are derived from laboratory experiments and are taken as provided in the EPIC-2 material library. The Bodner-Partom material constants were derived from laboratory experiments for all cases but the second set of copper data. The Bodner-Partom constants for the Oxygen Free High Conductivity (OFHC) copper were determined from the OFHC Johnson-Cook model. In almost all applications in this study, the OFHC data for the Bodner-Partom model as derived from the Johnson-Cook model were used as a basis of comparison. The only exception was a test case for a plate impacting a rod, where independently determined constants for different sets of material were used.

The eight material constants required by the Bodner-Partom model suggests a more complex data set requirement than actually usually exists, since two of the constants are only required for materials such as copper where the work hardening effects demand extra constants for a reasonable fit, and since the constant $D_o$ is usually safely presumed to be 100,000,000. On the other hand, the Bodner-Partom model as implemented here is complicated by the requirement to provide 7 additional parameters associated with

465

the convergence criterion for the iterative solution of the model.

APPLICATIONS

Five test cases were used to evaluate the performance of the Bodner-Partom model relative to the Johnson-Cook model in applications of the EPIC-2 hydrocode to problems representative of simple high strain rate impact problems or complex problems of interest to the conventional weapons development community. These problems consisted of a cylinder impacting a rigid surface (Taylor impact), a simulated high strain rate tensile test with loading reversal, a plate impacting a rod, a rod penetrating a plate, and an explosively formed penetrator (EFP).

The Taylor cylinder impact calculation relates to a test often used to determine material parameters for constitutive models used in calculations of high strain rate deformation processes. Figure 1 shows the initial configuration for this calculation, and establishes the standard format used throughout this paper for initial configurations. For the axisymmetric calculations performed, the top half of the figure shows a material map and the bottom half shows the initial gridding. Figure 2 shows the comparison of the results of a 1-inch long, 0.3-inch diameter OFHC copper rod impacting a rigid surface at 6000 inches per second, with the stress profiles for the deformed cylinder at 60 microseconds depicted for the Bodner-Partom model

on top and the Johnson-Cook model below.  This is the standard
format used for results plots throughout this paper.  In all
figures, the Bodner-Partom model is denoted BP and the Johnson-
Cook model is denoted EPIC since it is the default constitutive
model in the EPIC hydrocode.  The close comparison of the two
models in terms of both deformation and stress profiles is
notable.  For this low temperature, high strain rate (average
strain rates of around 20,000 per second), and moderate strain
conditions, the models are nearly alike.

The second test case simulated a high strain rate tensile
test.  Figure 3 illustrates the initial configuration and the
velocity boundary condition used to simulate the tensile test
with loading reversal at two different levels of high strain
rates.  This calculation used a 0.125-inch diameter by 0.375-inch
long OFHC copper cylinder fixed at one end with an applied
velocity boundary on the other end with velocity as a function of
time as shown in the Figure 3 and outlined below:

| TIME $\mu$/sec | VELOCITY (inches/second) | AVERAGE STRAIN RATE SOUGHT (1/sec) |
|---|---|---|
| 0-100 | 150 | 400 |
| 100-200 | -150 | -400 |
| 200-300 | 750 | 2000 |
| 300-400 | -750 | -2000 |
| 400-500 | 15C | 400 |
| 500-600 | -150 | -400 |

These values and the configuration of the specimen were selected
to be representative of a potential Hopkinson bar test.

Variables associated with element 116 were recorded as a function of time, and the equivalent uniaxial stress is plotted as a function of effective strain in Figure 4 for both the Bodner-Partom and Johnson-Cook models. It is important to note here that although full reversal of loading occurred, because of the use of equivalent stresses and effective strains, all values are positive. Equivalent stress is given as:

$$\bar{\sigma} = \sqrt{\frac{3}{2}} \left( s_{11}^2 + s_{22}^2 + s_{33}^2 \right) + 3 \left( s_{12}^2 + s_{13}^2 + s_{23}^2 \right) \tag{7}$$

Effective strain is computed as:

$$\bar{\epsilon} = \sqrt{\frac{2}{9}} \left[ \left( \epsilon_{11} - \epsilon_{22} \right)^2 + \left( \epsilon_{11} - \epsilon_{33} \right)^2 + \left( \epsilon_{22} - \epsilon_{33} \right)^2 + 6 \left( \epsilon_{12}^2 + \epsilon_{13}^2 + \epsilon_{23}^2 \right) \right] \tag{8}$$

The instantaneous strain rate effects of the models are obvious, but the strain rate history effects that should be observable with the Bodner-Partom model are not clear, perhaps because of the modest difference in strain rates and levels of strain rate effects in OFHC copper. Figure 5 shows the achieved strain rates at element 116 as predicted by EPIC, and Figure 6 shows the results at completion as well as three times during loading. Geometrically, the results are almost identical, and the stress profiles compare favorably.

The third test application was a plate impacting a rod, selected to observe the modeling of wave propagation in a long

rod with the two constitutive models. A 1-inch diameter by 6-inch long stationary rod of steel was impacted by a 2-inch square by 0.6-inch thick steel plate at 7716 inches per second. In the Bodner-Partom calculation, the rod was 1008 steel and the plate was 1020 steel, while for the Johnson-Cook calculation 1006 steel and Armco iron were used. Figure 7 shows the initial configuration and the location of element 835 where all element data were recorded as functions of time. Figure 8 illustrates the equivalent stress vs. time curves observed at element 835 for the two different models with the slightly different sets of materials. Because of these differences in materials, direct comparisons cannot be expected, but the predicted profiles demonstrate the ability of the Bodner-Partom model to follow stress wave propagation without introducing spurious results. Figure 9 shows the final profiles and stress contours, which are slightly different due to differences in materials modeled.

The last two test applications represent standard conventional weapon applications with correspondingly more severe deformations. Figure 10 shows the initial configuration for a 2-inch long, 1-inch diameter OFHC copper rod penetrating a stationary 6-inch square by 1-inch thick 4340 steel plate at 100,000 inches per second. Failure of both the penetrator and the target were permitted using the erosion capabilities of the EPIC code, where for strains greater than 150% the elements were deleted and only the mass of the nodes remained in the

calculation. Since failure keys on the strain values, it was anticipated that small changes in the material models might result in large solution differences. Only slight differences were observed, as shown in the results in Figure 11.

The final test application was an explosively formed penetrator as shown in Figure 12. This has traditionally represented one of the most severe tests of a constitutive model seen in the conventional weapon design process. It encompasses a wide range of high temperatures, large strains, and high strain rates with relatively high pressures. Various designs can lead to segments of the liner being in an extremely wide design space involving strains, strain rates, temperatures, and pressures. As shown in Figure 13, although the final geometries are similar, and considering the sensitivity of the problems to the constitutive model they are very closely alike, the differences in final stress contours are significant. Selecting one result as more correct than the other would be extremely difficult since experimental results of recovered slugs have potential for deformations during the recovery process and flash radiography generally cannot thoroughly resolve voids in the tail section. Both predictions represent what have historically been considered good results, but since the Bodner-Partom model material data set was derived from the Johnson-Cook data, and in view of the examples presented previously, a more similar solution might have been expected. The sequential derivation of the material

constants for the Bodner-Partom model and the approach towards the treatment of the thermal softening are suggested as the likely differences in the results.

Generally, it may be concluded from this set of five applications, that for a comparable set of material inputs, the results from the Bodner-Partom model duplicate the results of the Johnson-Cook model. These conclusions are valid only for the range of applications represented by the five tests, and further evaluation with complex loading conditions and loading in other ranges of strain, strain rate, temperature, and pressure are desirable. Applications had been sought to demonstrate the inherent advantages of the strain rate history effect embodied in the state variable approach of the Bodner-Partom model, but no such applications relevant to conventional weapon modeling were obvious.

TIMING COMPARISONS

The Bodner-Partom model suffered severely in timing comparisons with the simpler Johnson-Cook model. The implementation in the EPIC code was done primarily with modularity of coding as a goal, so computational efficiency no doubt suffered. The Bodner-Partom model implementation involved that addition of 14 new subroutines to the code for a total addition of 1889 lines to a baseline code of 12,407 lines. The additions were commented extensively and are self-documenting.

Also, these changes were performed in a way to be easily extended to support failure models that consider a matrix material with material properties that could be modified by void formation to provide aggregate material response for damage based failure model development. This contributed partially to the time intensive results of the Bodner-Partom calculations. Overall, these timings were at least three to four times longer than the Johnson-Cook model for very simple problems with modest deformations, and as much as 23 times longer for conventional weapon design applications involving very large strains and high strain rates. Timings for the five applications considered are given in Table 2. Note that in all cases the Johnson-Cook model was used with a sound speed fraction of 0.9, where the Bodner-Partom model required reduction of the sound speed fraction to as low as 0.5 to achieve convergence. (Sound speed fraction is a multiplier on the maximum allowable time step determined by the Courant condition.) Also, in the conventional weapons applications, the convergence criteria for the Bodner-Partom model were extended beyond 10 time step cuts and 100 iterations per cell per cycle in order to achieve convergence. The calculations with the Bodner-Partom model had to be repeated in each case as acceptable convergence criteria were determined. As experience with the model develops, this situation would probably be vastly improved, but the additional complexity and potential for failed solution cannot be eliminated.

Table 3 illustrates profiles of performance for the EPIC code on the third test case for the plate impacting a rod with and without the Bodner-Partom model on an ULTRIX VAX 8650 using the f77 compiler without optimization. Note that in Table 2 timings for the third test case were for the same machine but for the VAX FORT compiler with optimization selected by default. Profiling could not be accomplished with optimization on this system. In this case the calculation required 6121 seconds with the Bodner-Partom model and 1875 seconds with the Johnson-Cook model for a factor of 3.26 in timing. The Bodner-Partom related subroutines took 35.5% of the run time, compared to 19.2% of the total run time required for the same calculation with the Johnson-Cook model. It should be noted that a large percent of total time as reported by this profiler is used by intrinsic mathematical functions, so direct comparison of these percentages and the slowdown of the total calculation are not straightforward. The Bodner-Partom model makes much greater use of the exponentiation and power expansion intrinsic functions. Also, the overall time increased due to the reduced sound speed fraction required by the Bodner-Partom model. This reduced sound speed fraction was found to be more efficient than further subcuts of time in the iterative solution technique, and in some cases was the only approach that led to convergence.

## ADVANTAGES AND DISADVANTAGES OF BODNER-PARTOM MODEL

The Bodner-Partom model is probably superior to most of the models in current use in hydrocode applications. The model has been implemented and demonstrated in versions of the EPIC-2 and STEALTH hydrocodes. The model is well documented and well known throughout the research community. It embodies the concept of a limiting strain rate that is the subject of much recent experimental research. The model is applicable over a relatively wide range of strain rates, and includes history dependence through a state variable approach. Relatively straightforward techniques for the determination of the material constants exists and have been implemented in interactive graphic based software. The model has no discontinuity at a yield point and does not require a yield criterion or loading/unloading conditions.

Drawbacks for the Bodner-Partom model do exist, and the selection of this model for particular applications must consider the balance between these disadvantages relative to the aforementioned advantages. The model is not easily conceptualized, and although some meaning can be given to the material constants, that meaning is often not direct. Furthermore, the sequential determination of the material constants from test data can lead to diverse sets of material constants, particularly for the last several constants established, when different researchers establish those constants, even from the same test data. The convergence schemes

necessary for the implementation of this class of model in the structure of a typical hydrocode necessitate several constants related to the convergence criteria that impose an extra burden on the user of the code. The selection of these values would probably improve with more use of the model, eventually becoming fairly simple. Finally, and most importantly, for the implementation of the model reviewed here, the coding was extremely extensive, and the increase in computer time required to achieve a solution was high. More efficient coding is possible, and improved convergence schemes could increase the efficiency of the model in hydrocodes. For applications where large strain rates lead to large strains per time step in hydrocodes, the Bodner-Partom model incurs high costs relative to the empirical class of model such as the Johnson-Cook model.

SUMMARY AND CONCLUSIONS

An implementation of the Bodner-Partom constitutive model in the EPIC-2 hydrocode has been successfully applied to several demonstration problems. The results of calculations with the Bodner-Partom model compare directly to results obtained with the Johnson-Cook constitutive model, where material parameters for the Bodner-Partom model were determined from matches to the Johnson-Cook model. Applications which demand the complexity of the Bodner-Partom model need to be identified to justify its use in the present form. Better coding efficiency and better convergence schemes for the iterative solution of this model are

desirable for cost effective applications. Recently, an improved solution scheme based on a Diagonally Implicit Runge-Kutta (DIRK) algorithm has been successfully developed at the University of Dayton Research Institute. The preliminary results indicate substantial improvements in the timings. Also, for user simplicity, several of the convergence criterion related constants are internally handled by the code and the solution convergence seems to be assured in each computer run. However, the timing efficiency for conventional weapon design applications using this new DIRK scheme is yet to be established.

# REFERENCES

1. Bodner, S. R. and Partom, Y., "A Large Deformation Elastic-Viscoplastic Analysis of a Thick-Walled Spherical Shell," J Appl Mech, Vol 39, 1972, pp 751-757

2. Bodner, S. R. and Partom, Y., "Constitutive Equations for Elastic-Viscoplastic Strain Hardening Materials,"J Appl Mech, Vol 42, 1975, pp395-389

3. "STEALTH- A Lagrangian Explicit Finite Difference Code for Solids Structures, and Thermohydraulic Analysis," Electrical Power Research Institute, Palo Alto, CA, EPRI NP-2080, Nov 1981

4. Johnson, G. R., "A Computer Program for Elastic-Plastic Impact Computations in 2 Dimensions Plus Spin," U.S. Army Ballistic Research Laboratory, Aberdeen Proving Ground, MD, ARBRL-CR-00373, June 1978

5. Johnson, G. R. and Stryk, R. A., "User Instructions for the EPIC-2 Code," U.S. Air Force Armament Laboratory, Eglin AFB, FL, AFATL-TR-86-51, Sept 1986

6. Rajendran, A. H. and Geers, E. J., "BPSOLVE- A Program to Determine Bodner-Partom Model Parameters," University of Dayton Research Institute, Dayton, OH, UDR-TR-86-95, Aug 1986

7. Johnson, G. R. and Cook, W. H.," A Constitutive Model and Data for Metals Subjected to Large Strains, High Strain Rates and High Temperatures," Seventh International Symposium on Ballistics, The Hague, The Netherlands, April 1983

## COMPARISON OF MATERIAL CONSTANTS

### EPIC

|       |          | Armco Iron | 1006   | 4340    | OFHC Cu |
|-------|----------|------------|--------|---------|---------|
| A     | (PSI)    | 25,400     | 50,800 | 114,900 | 13,000  |
| B     | (PSI)    | 55,100     | 39,900 | 73,900  | 42,300  |
| n     | (-)      | 0.32       | 0.36   | 0.26    | 0.31    |
| C     | (-)      | 0.060      | 0.022  | 0.014   | 0.025   |
| m     | (-)      | 0.55       | 1.00   | 1.03    | 1.09    |

### BODNER-PARTOM

|           |          | 1008       | 1020       | OFHC Cu (1) | OFHC Cu (2) |
|-----------|----------|------------|------------|-------------|-------------|
| $D_0$     | (1/sec)  | 1.0e8      | 1.0e8      | 1.0e8       | 1.0e8       |
| $Z_0$     | (PSI)    | 797,710    | 92,824     | 116,030     | 47,860      |
| $Z_1$     | (PSI)    | 1,015,300  | 134,890    | 949,997     | 123,276     |
| $m_0$     | (1/PSI)  | .00010342  | .00020684  | .0000759    | .0000276    |
| $m_1$     | (1/PSI)  | 0.0        | 0.0        | .0010340    | .0001720    |
| $\propto$ | (1/PSI)  | 0.0        | 0.0        | .0100003    | .0008270    |
| $n_0$     | (-)      | 0.4        | 4.0        | 0.4         | 2.8         |
| A         | (-)      | 0.0        | 0.0        | 0.0         | 0.85        |

(1) UDRI published constants from independant laboratory experiments
(2) Derived form fits to EPIC default constitutive model as part of this study

### TYPICAL CONVERGENCE CONSTANTS

| | |
|---|---|
| Max strain per time step (-)      | .0001 |
| Min eff plastic flow stress (PSI) | .15   |
| Convergence tolerance (-)         | .0001 |
| Relaxation factor (-)             | 1.0   |
| Max iterations (-)                | 10    |
| Max number of time cuts (-)       | 10    |
| Time step cut factor (-)          | 2     |

Table 1.  Material Constants

TIMING COMPARISONS OF THE
BODNER-PARTOM MODEL IN EPIC2
WITH THE DEFAULT EPIC2 MODEL

| | EPIC2 MODEL | | BODNER PARTOM MODEL | | | RATIO |
|---|---|---|---|---|---|---|
| | Time | SSF | Time | SSF | % Elem | |
| Taylor Impact | 690 | 0.9 | 2919 | 0.7 | 100 | 4.2 |
| Tensile Test | 2883 | 0.9 | 10084 | 0.9 | 100 | 3.5 |
| Plate on Rod | 532 | 0.9 | 1638 | 0.7 | 100 | 3.1 |
| Rod Penetration | 243 | 0.9 | 5768 | 0.5 | 31 | 23.7 |
| EFP | 1591 | 0.9 | 11598 | 0.6 | 10 | 7.3 |

Table 2.   Timing Results

# TIMING DATA

The Bodner-Partom changes to EPIC-2 include 1889
lines of FORTRAN coding added to the 12,407 lines
in the baseline EPIC-2 code

This includes the addition of 14 subroutines:
>BODNER
>BODPAR
>INIBPS
>CMPBPS
>ESTBPS
>AVHYMX
>NEWWPM
>EPIJ
>NEWPRS
>NEWSIJ
>CHKBPS
>NEWEST
>UPDBPS
>NEWBPS

## TIME SPENT IN SUBROUTINES

| EPIC | | BODNER-PARTOM | | |
|------|------|------|------|------|
| ELOOP1 | 21.3 % | ELOOP1 | | 8.8 % |
| STRESS | 13.9 | MIEGRU | | 7.9 |
| MIEGRU | 5.3 | CHKBPS | * | 4.0 |
| NLOOP | 2.9 | NEWPRS | * | 3.9 |
| | | INIBPS | * | 3.8 |
| | | NEWSIJ | * | 3.4 |
| | | NEWWPM | * | 3.2 |
| | | ESTBPS | * | 2.9 |
| | | BODNER | * | 2.2 |
| | | EPIJ | * | 2.2 |
| | | UPDBPS | * | 1.6 |
| | | NEWBPS | * | 1.5 |
| | | CMPBPS | * | 1.5 |
| | | AVHYMX | * | 1.5 |
| | | BODPAR | * | 1.4 |
| | | NEWEST | * | 1.3 |
| | | NLOOP | | 1.1 |

EPIJ ⟩ 35.5 %

(1875 seconds)                    (6121 seconds)

Table 3.   Profile Results

480

TAYLOR IMPACT TEST

RIGID
SURFACE

ROD VELOCITY
6000 IN/SEC
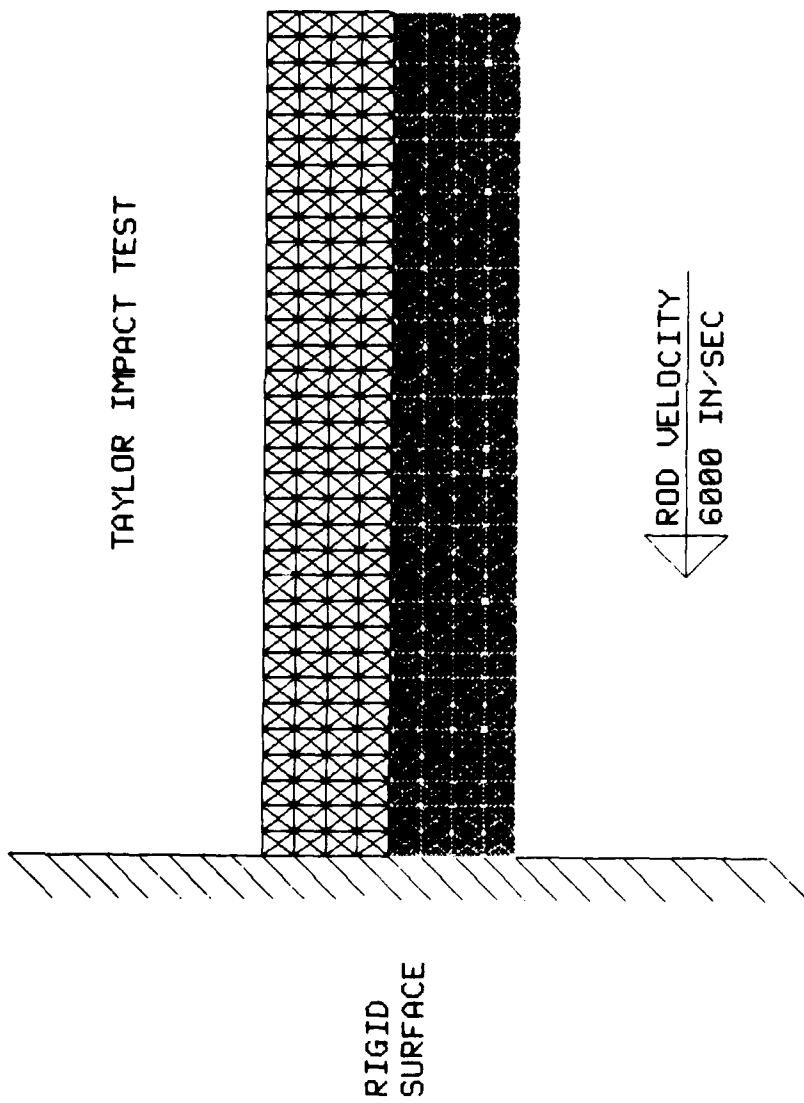
Figure 1. Initial Configuration of Taylor Cylinder Impact

481

TAYLOR IMPACT TEST
STRESS CONTOURS (PSI)

55000.
51333.
47667.
44000.
40333.
36667.
33900.
29333.
25667.
22000.
18333.
14667.
11000.
7333.
3667.
0.

60 MICROSECONDS

BP
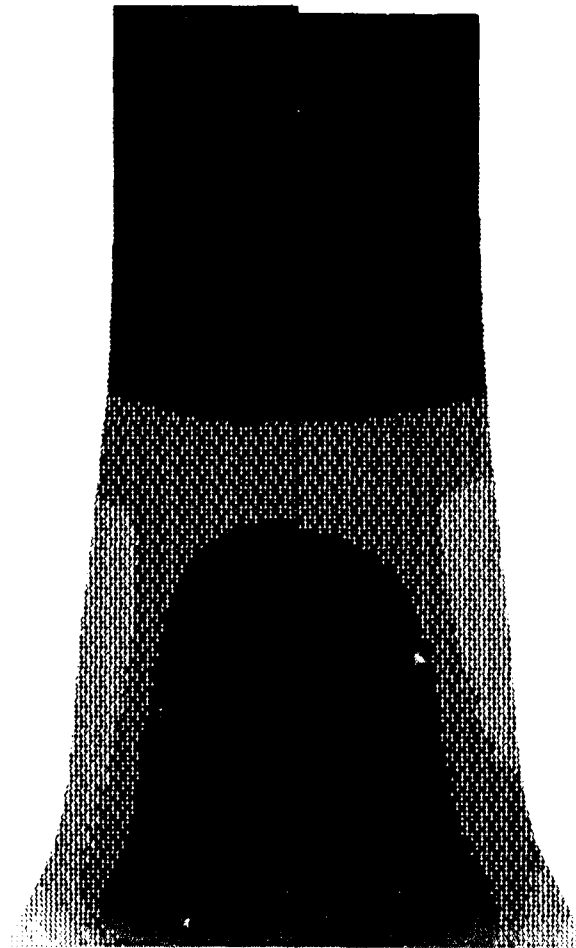
EPIC
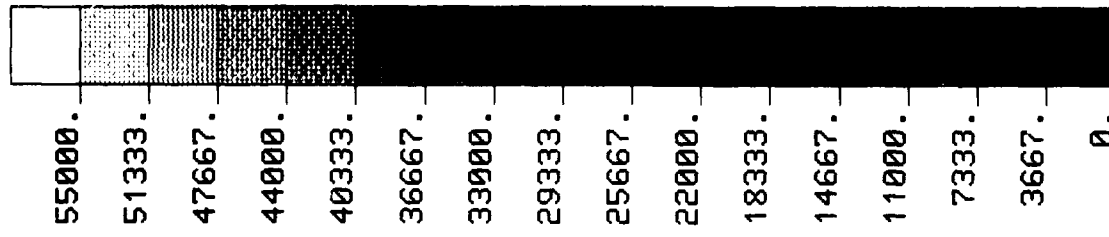
Figure 2.  Taylor Cylinder Impact at 60 usec
Stress Contours
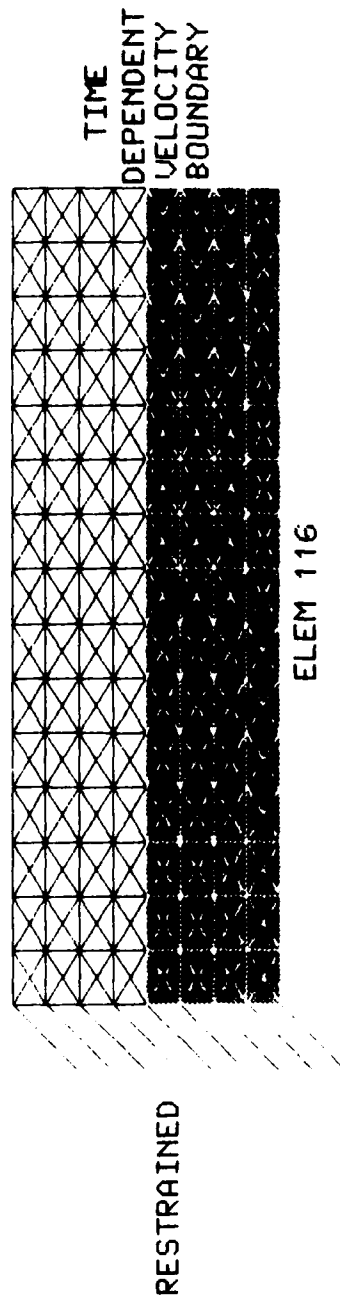
Figure 3.  Initial Configuration of Simulated Tensile Test
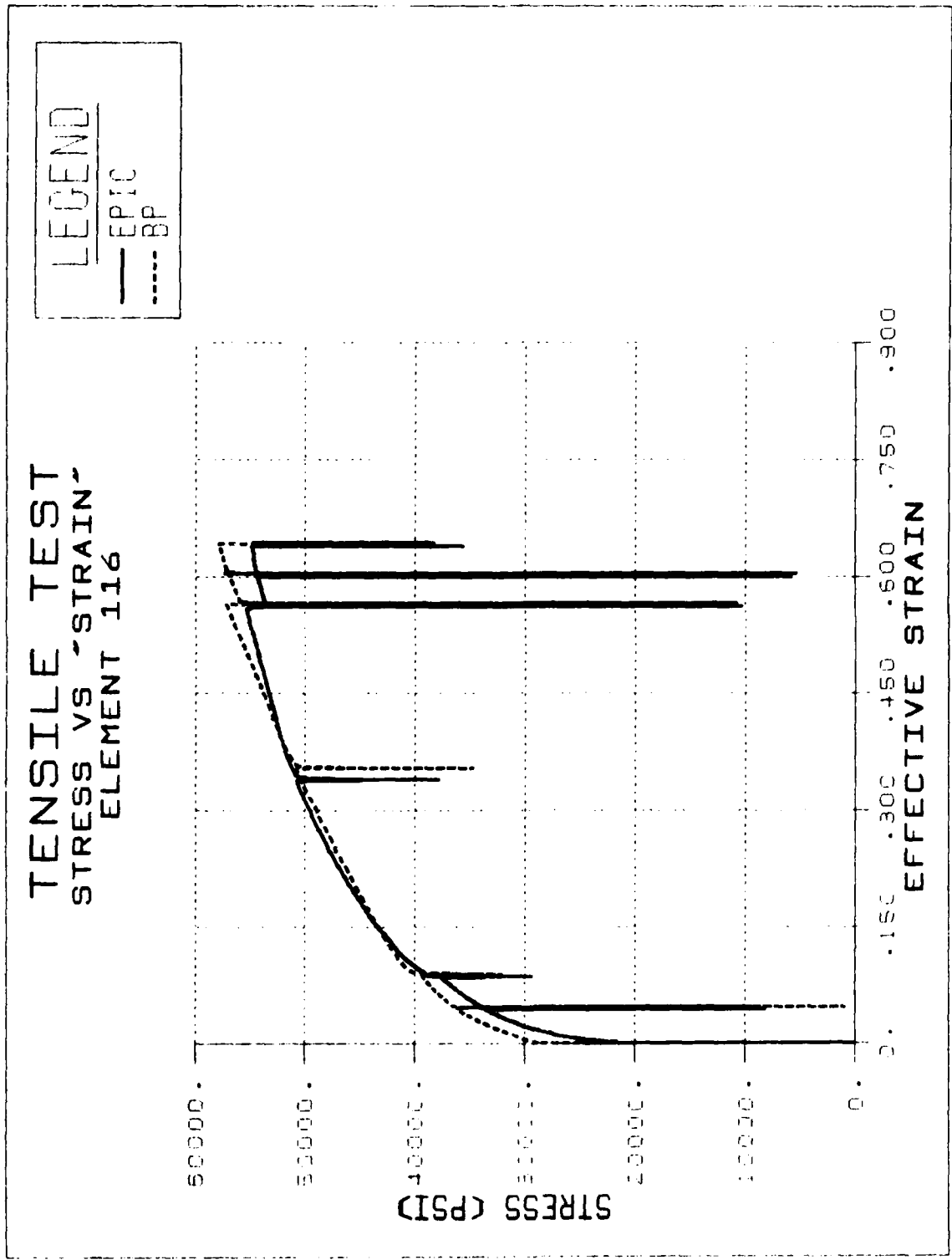
Figure 4.  Simulated Tensile Test Results at Element 116
Equivalent Stress vs Effective Strain
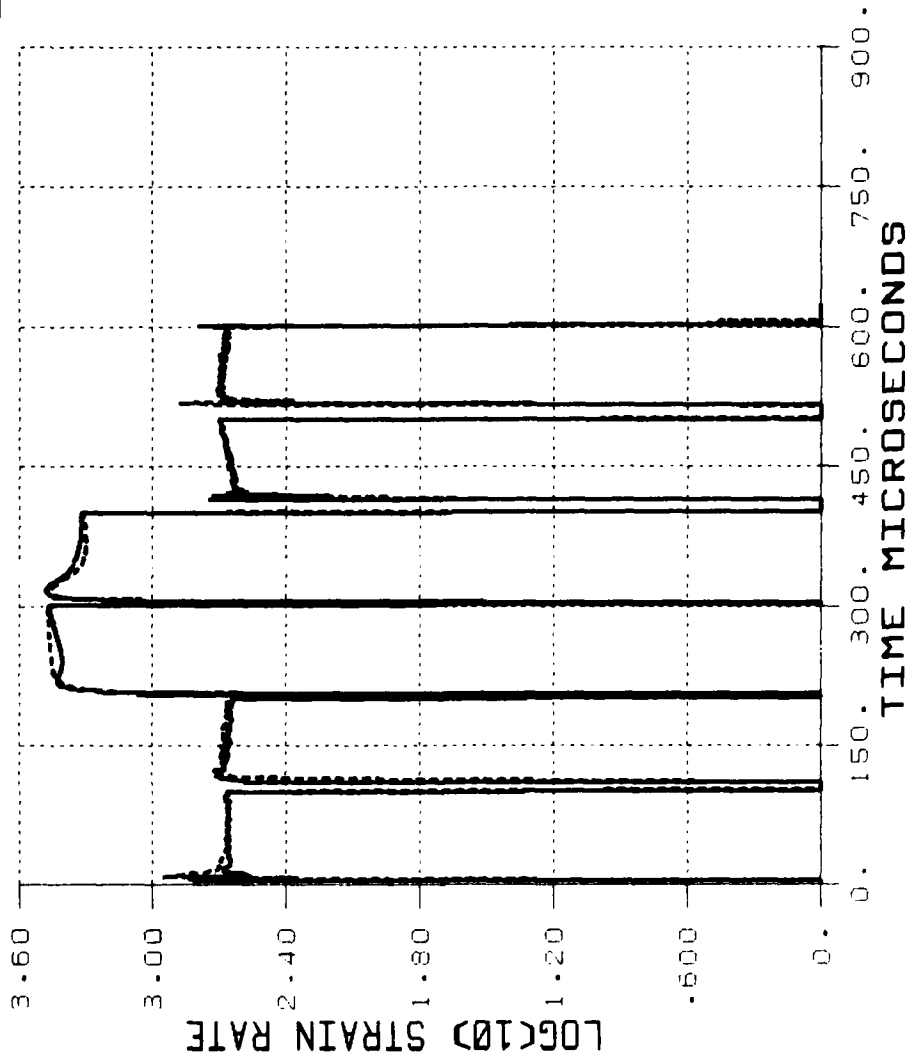
Figure 5.   Simulated Tensile Test Results at Element 116
            Effective Strain Rate vs Time
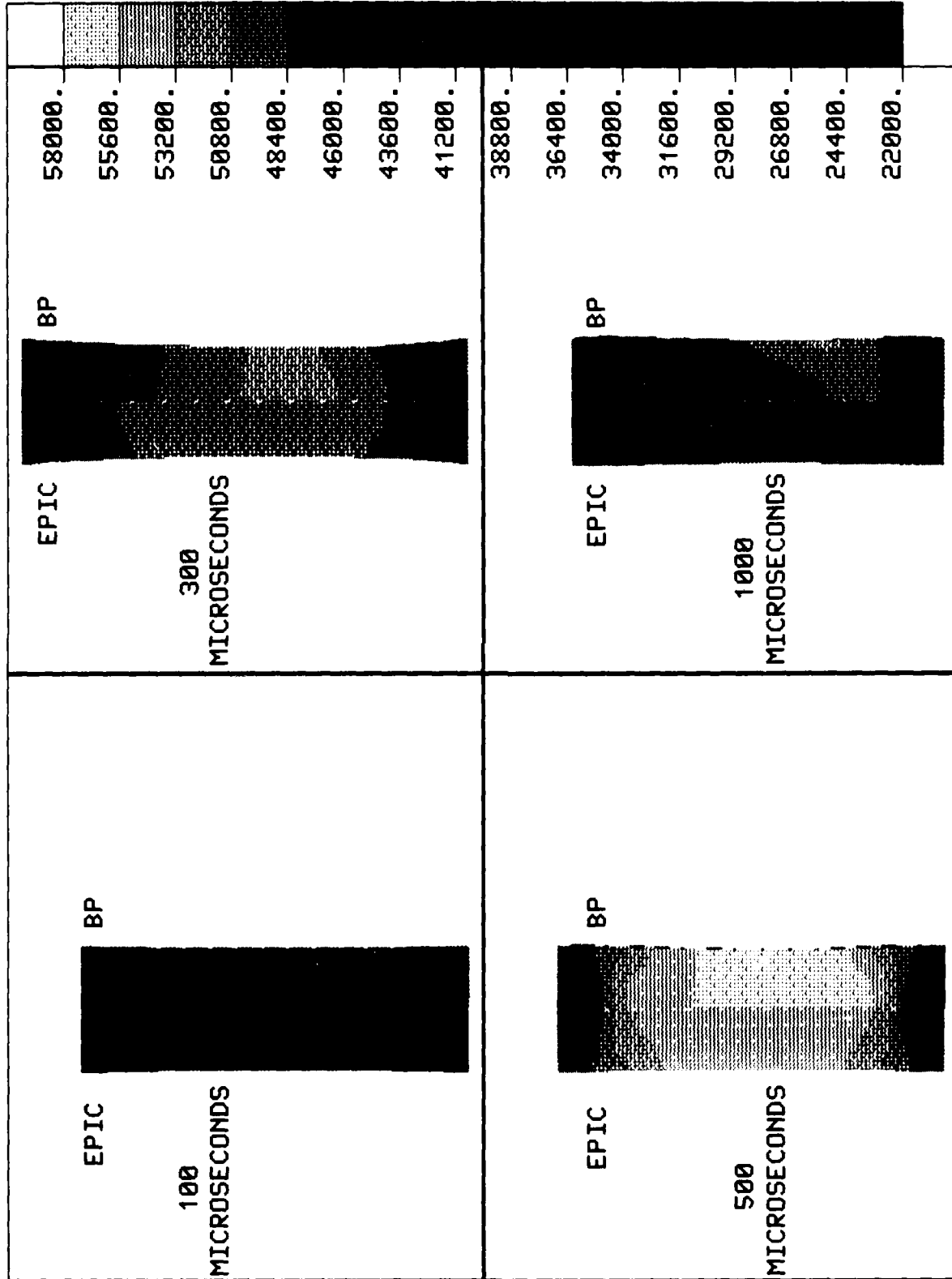
Figure 6. Simulated Tensile Test Results at 100, 300, 500, & 1000 usec
Stress Contours

PLATE ON ROD
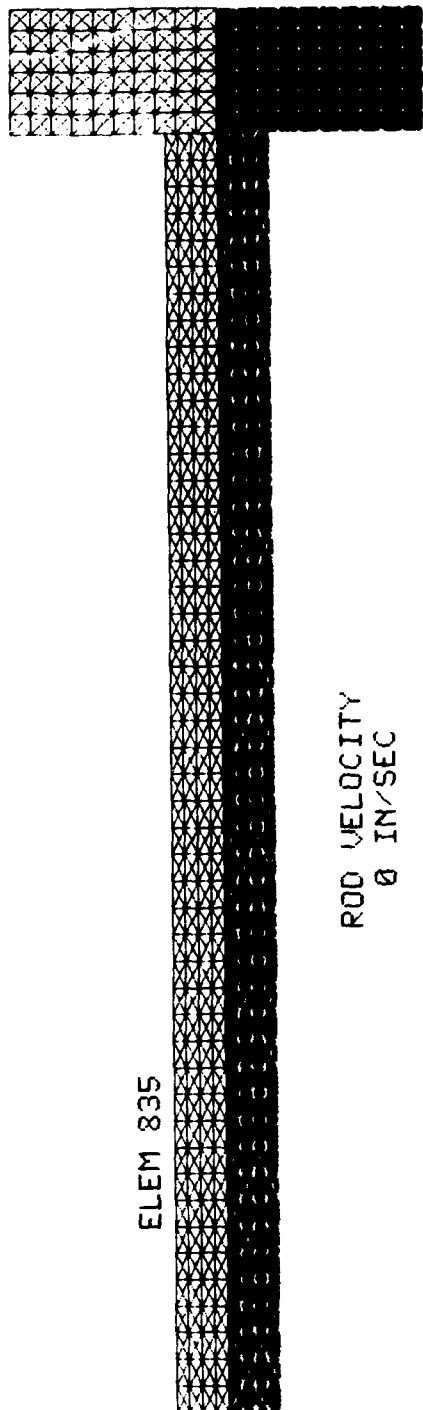
ELEM 835

ROD VELOCITY
0 IN/SEC

PLATE VELOCITY
7716 IN/SEC

Figure 7.   Initial Configuration of Plate Impacting Rod

487
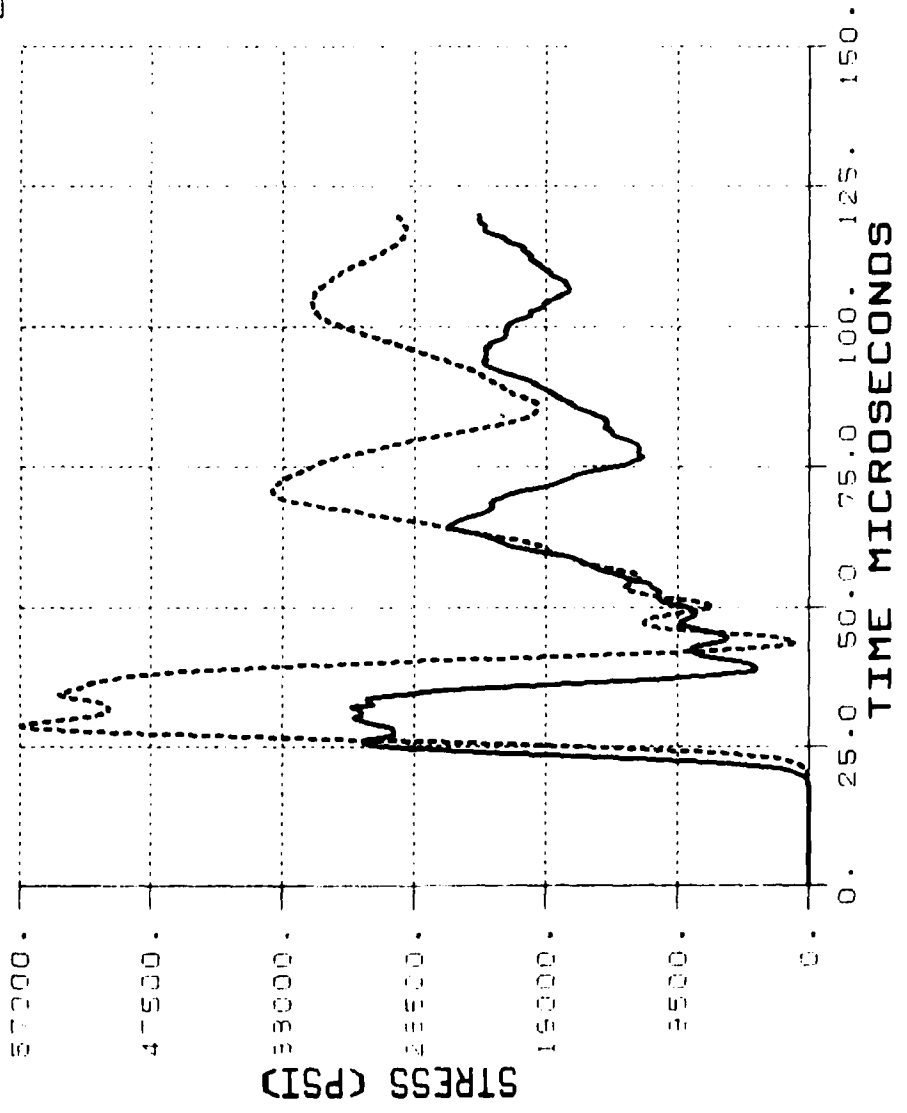
Figure 8. Plate Impacting Rod
Stress vs Time at Element 835

PLATE ON ROD
STRESS CONTOURS (PSI)

120 MICROSECONDS
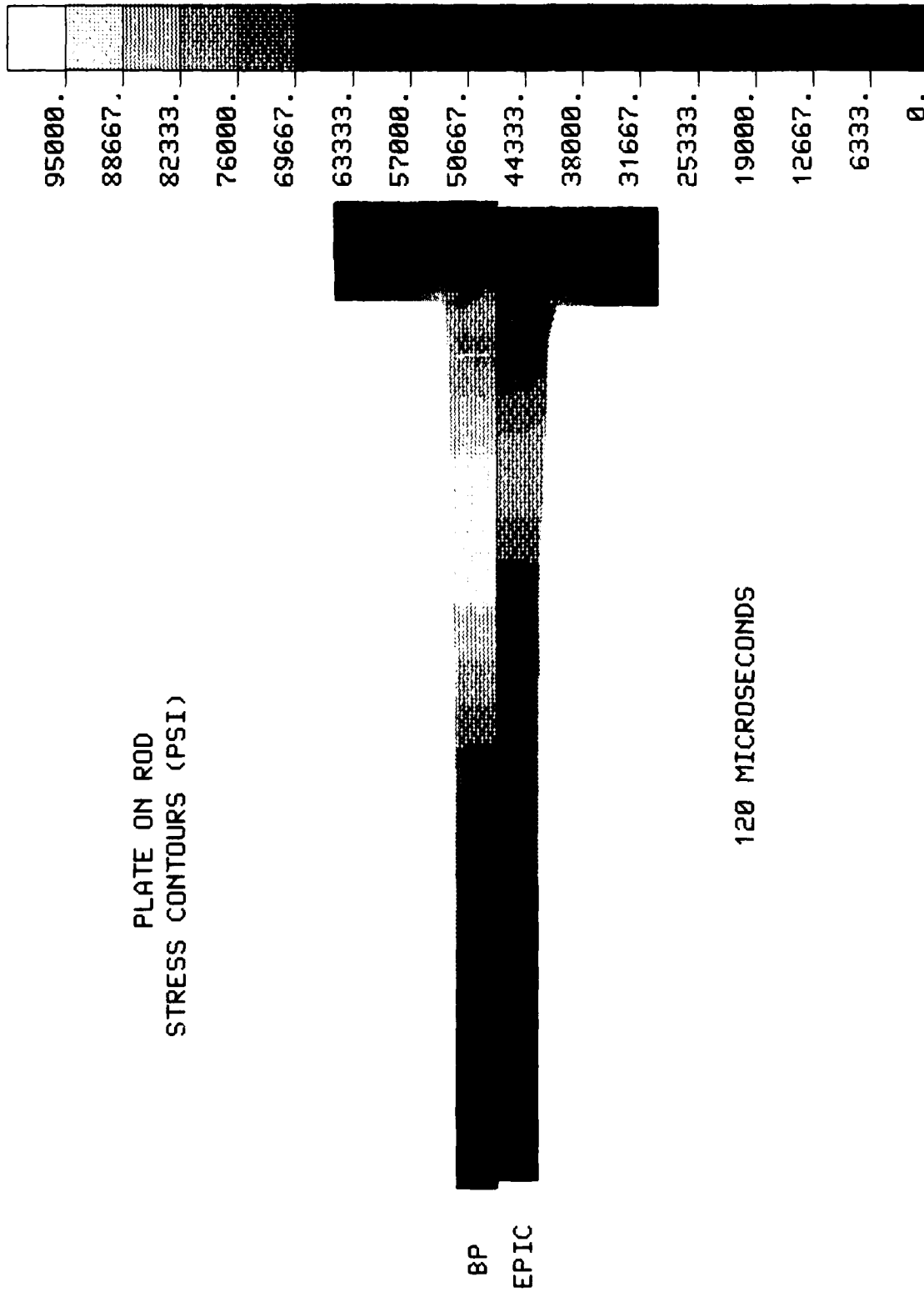
Figure 9.  Plate Impacting Rod
Stress Contours
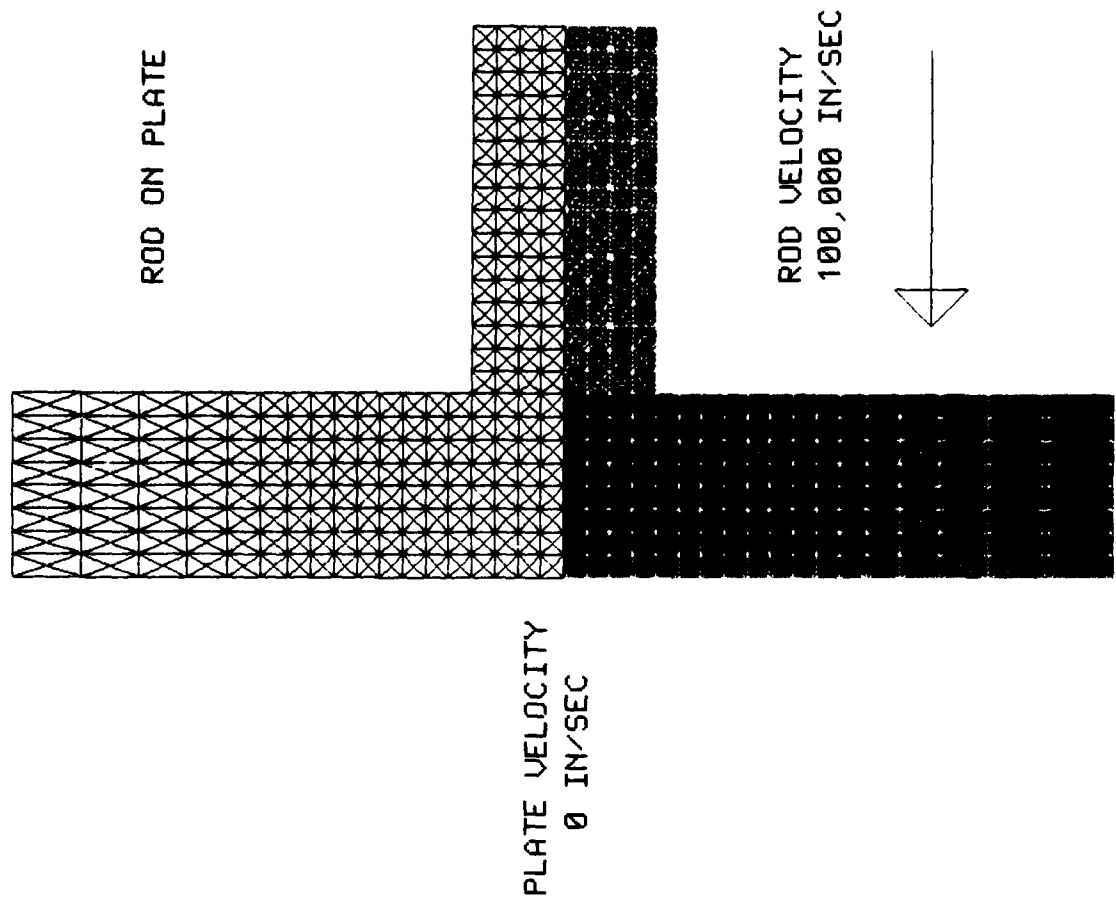
Figure 10. Initial Configuration of Rod Penetrating Plate

ROD ON PLATE
STRESS CONTOURS (PSI)

40 MICROSECONDS
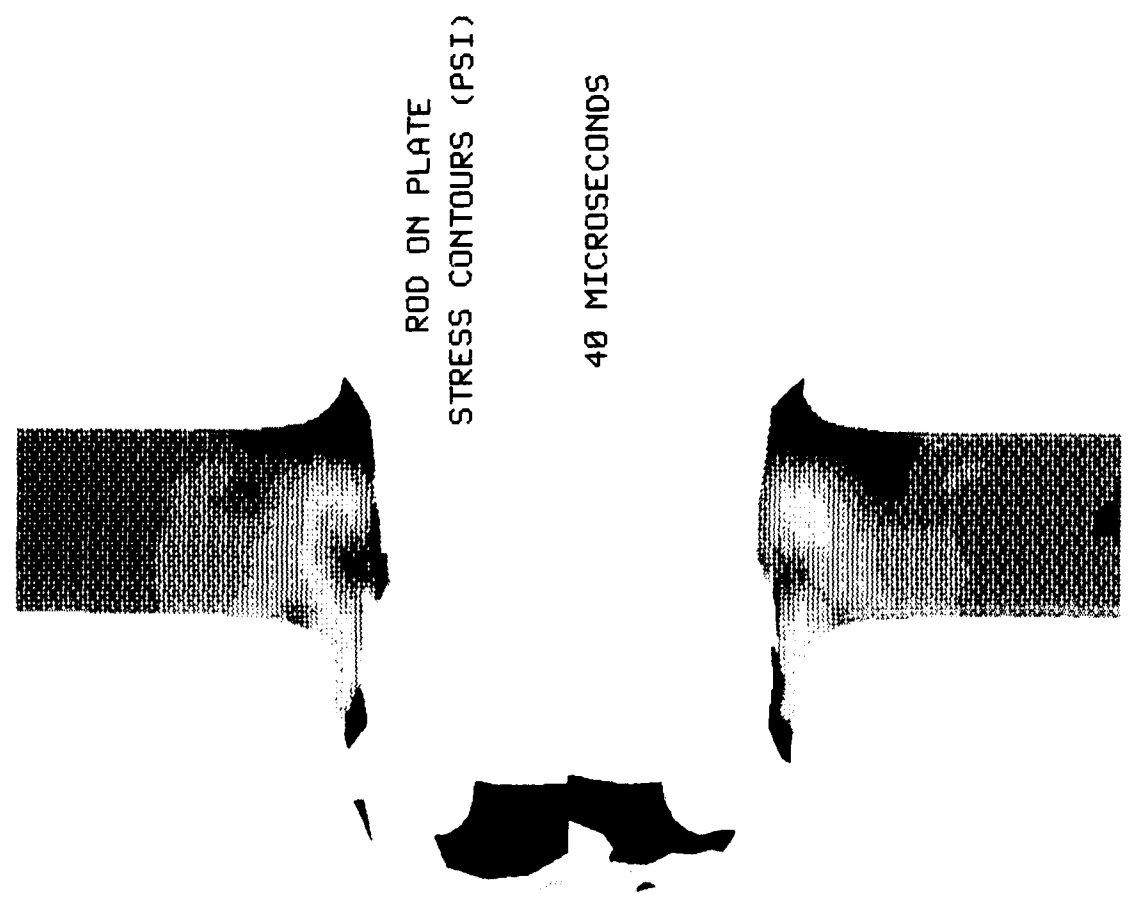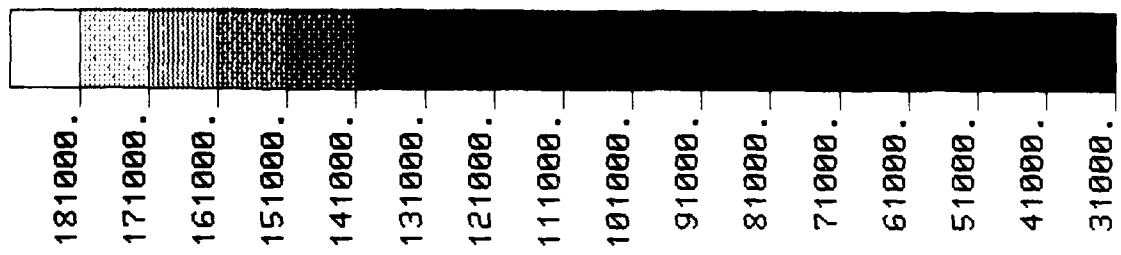
Figure 11. Rod Penetrating Plate
Stress Contours
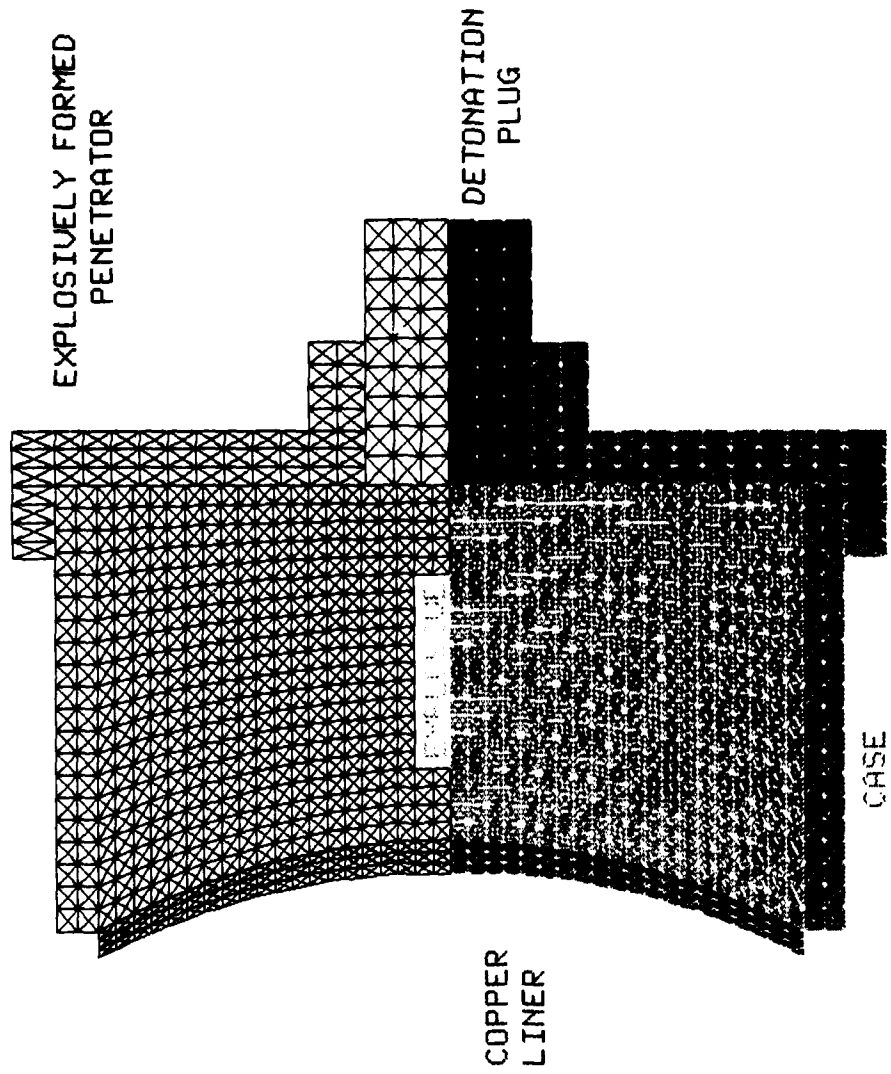
Figure 12. Initial Configuration of Explosively Formed Penetrator

EXPLOSIVELY FORMED PENETRATOR
STRESS CONTOURS (PSI)

80000.
76500.
73000.
69500.
66000.
62500.
59000.
55500.
52000.
48500.
45000.
41500.
38000.
34500.
31000.
27500.

BP
EPIC

100 MICROSECONDS
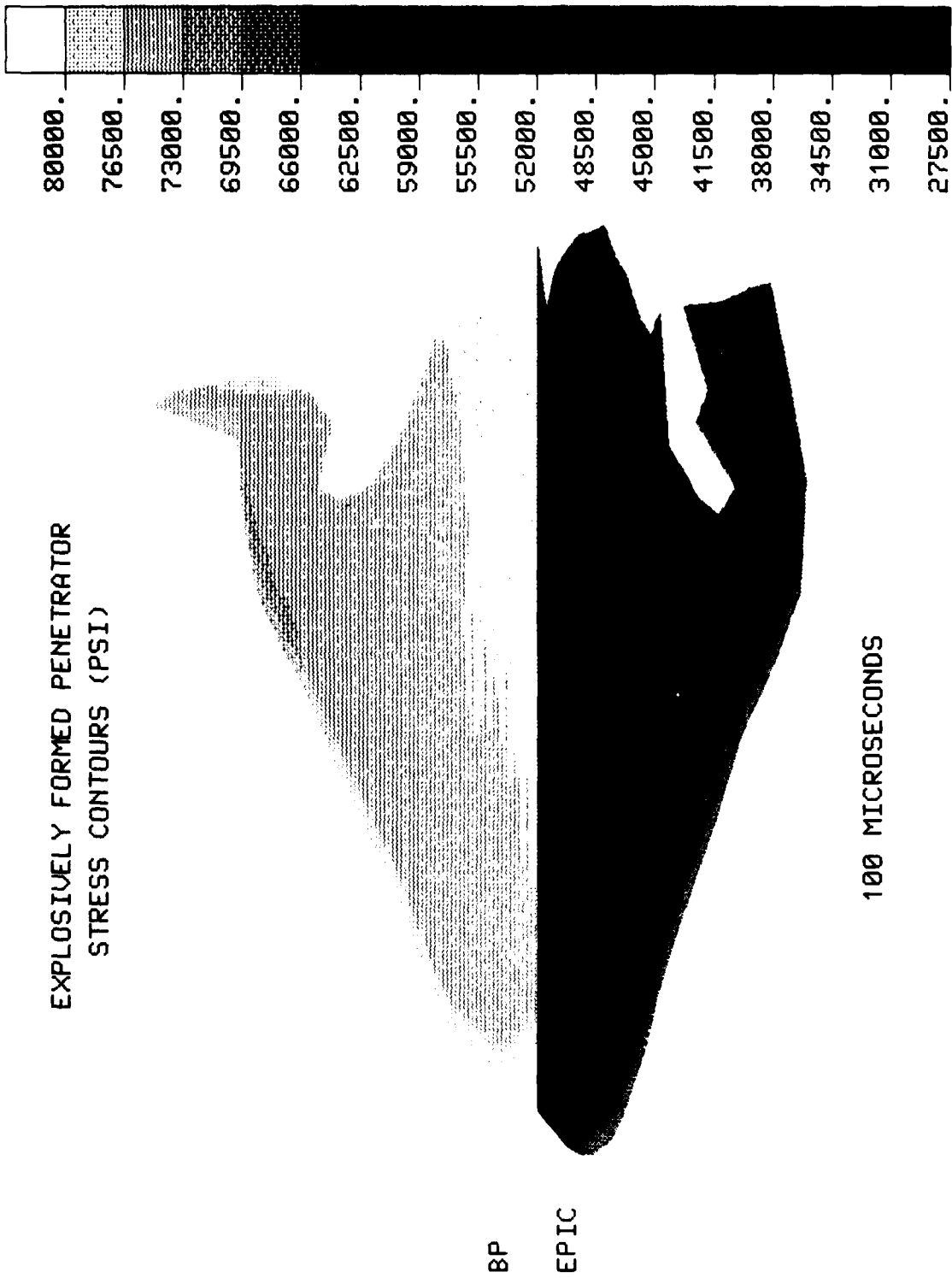
Figure 13. Explosively Formed Penetrator
Stress Contours

# APPENDIX

# LIST OF ATTENDEES

Dr. Stephen Bless
University of Dayton
Research Institute
Dayton, OH 45469

Mr. William Cook
AFATL/MNW
AF Armament Laboratory
Eglin AFB, Florida
Florida 32542-5434

Dr. Gordon Johnson
7225 Northland Drive
Brooklyn Park, NM 55428
MN 48-3700

Prof. S. P. Shah
Dept. of Civil Engineering
Technological Institute
Northwestern University
2145 Sheridan Road
Evanston, IL 60208

Dr. S. N. Brar
University of Dayton
Research Institute
Dayton, OH 45469

Prof. I. M. Fyfe
Dept. of Aeronautics and
Astronautics - MS FS-10
University of Washington
Seattle, WA 98195

Mr. R. Garrett
Code R32
Naval Surface Weapon Ctr.
10901 New Hampshire Ave.
Silver Spring, MD 20903-5000

Prof. R. L. Sierakowski
470 Hitchcock Hall
2070 Neil Avenue
Columbus, OH 43210

Dr. E. P. Chen
Division 1523
Sandia National Laboratory
Albuquerque, NM 87185

Dr. L. S. Costin
Division 6314
Sandia National Lab
Box 5800
Albuquerque, NM 87185

Dr. Amos Gilat
Dept. of Engineering Mechs.
165 W. Woodruss Ave.
Columbus, OH 43210

Mr. J. Kroupa
University of Dayton
Research Institute
Dayton, OH 45469

Mr. Charlie Smith
Code U-12
Naval Surface Warfare Ctr.
10901 New Hampshire Ave.
Silver Spring, MD 20903-5000

Dr. Tony Chou
SLCMT-MRD
Army Material Tech. Lab.
Watertown, MA 02172

Dr. Datta Dandekar
SLCMT-MRD
Army Materials Tech. Lab.
Watertown, MA 02172

Dr. Y. Horie
Army Research Office
Engineering Science Div.
P.O. Box 12211
Research Triangle Park
North Carolina 27709

Dr. T. Nicholas
AFWAL/MLLN
WPAFB
Dayton, OH 45433

Dr. Spencer Wu
AFOSR/NA
Building #410
Bolling Air Force Base
Washington, D.C. 20332

Prof. R. J. Clifton
Division of Engineering
Brown University
Providence, RI 02912

Dr. Gene Farnum
Mail Stop G-756
Los Alamos National Lab.
Los Alamos, NM 87545

Dr. Reji John
University of Dayton
Research Institute
Dayton, OH 45469

Dr. A. M. Rajendran
University of Dayton
Research Institute
Dayton, OH 45469

Dr. Barbara Yoon
3054 Franklin Canyon Drive
Beverley Hills, CA 90210

Dr. P. S. Follansbee
MS G 730
Los Alamos National Lab.
Los Alamos, NM 87545

Dr. L. Seaman
SRI International
333 Ravenwood Avenue
Menlow Park, CA 94025

A-1